Thermomechanical Factors Influencing Weld Metal Hydrogen Assisted Cold Cracking

By

Rahim N. Kurji

A thesis submitted in partial fulfilment of the degree of Doctor of Philosophy at the

School of Mechanical Engineering

The University of Adelaide

Australia

Submitted: 31st October 2016

Accepted: 20th February 2017

In The Name Of Allah the Most Beneficent the Most Merciful

Abstract

Hydrogen Assisted Cold Cracking is a phenomena that manifests itself in weldments when a critical hydrogen concentration is trapped within a susceptible microstructure and subjected to a threshold level of stress and poses a significant threat to pipeline girth weld integrity, in particular the root pass of girth welds.

This thesis explores the thermomechanical factors influencing the formation of Weld Metal Hydrogen Assisted Cold Cracks (WMHACC) in High Strength Low Alloy line pipe steel when welded with cellulosic electrodes using the Manual Metal Arc Welding process. The overarching objective of this body of work is to delineate a safe boundary across which the characteristics of weld metal samples can be defined to enhance the understanding of the factors which influence the formation of weld metal hydrogen cracks. The significance of achieving this objective is the improved ability to predict the onset of the phenomenon, consequently facilitating the development of strategies, which can be assimilated by industry to minimise the presence of cold cracks increasing the safety and reliably of pipeline girth welds. To address the overarching objective and address the limitations identified though the literature review, in particular the limited number of studies focusing on welding in the Australian context, a three-part experimental and analytical program was developed and undertaken.

Development of an Enhanced Weldability Test. To facilitate deposition of tests welds under high restraint in a range of heat inputs which reflected the desired test window, an enhanced weldability test, the MWIC, was designed and commissioned. The test's geometry and characteristics were based on the well-established Welding Institute of Canada Weldability test, but was enhanced to allow for deposition of welds at very low heat inputs, of which no published cracking data exits. Additionally, the test was modified to allow for the extraction of critical welding data, facilitating its use as a research tool.

Delineation of Safe Welding Envelope. Using the MWIC test, deposition envelopes were created for thick (20mm) and thin (10mm) sections of API 5L X70 line pipe steel welded with E6010 electrodes under high and low restraint. Welds were deposited at low heat inputs (<1kJ/mm) over a range of preheats and examined under magnification to establish the critical/ threshold preheats above which no cracking was observed.

Characterisation of weld metal samples across the derived cracking boundary. The weldability test samples generated from weldability testing were characterised using a range

of macroscopic, microstructural, and micromechanical techniques to establish the interrelationship between cracking and thermomechanical parameters. The influence of heat input on bead eccentricity was established and its consequent effect on the welds susceptibly to hydrogen cracking was proposed. The potential interrelationship between solidification and hydrogen cracks was discussed in relation to restraint levels. The inefficiency of the currently accepted hardness threshold of 350HV used to predict the onset of HAZ-HACC as a proxy for Weld Metal Hydrogen Assisted Cold Cracking susceptibly was established for all test cases. Additionally, the use of micromechanical properties as a proxy, in particular the use of the ratio of E/H was introduced as a means of quantifying susceptibly to WMHACC.

Declaration

I certify that this work contains no material which has been accepted for the award of any other degree or diploma in my name, in any university or other tertiary institution and, to the best of my knowledge and belief, contains no material previously published or written by another person, except where due reference has been made in the text. In addition, I certify that no part of this work will, in the future, be used in a submission in my name, for any other degree or diploma in any university or other tertiary institution without the prior approval of the University of Adelaide and where applicable, any partner institution responsible for the joint-award of this degree.

I give consent to this copy of my thesis, when deposited in the University Library, being made available for loan and photocopying, subject to the provisions of the Copyright Act 1968.

I acknowledge that copyright of published works contained within this thesis resides with the copyright holder(s) of those works.

I also give permission for the digital version of my thesis to be made available on the web, via the University's digital research repository, the Library Search and also through web search engines, unless permission has been granted by the University to restrict access for a period of time.

_____ _____

Rahim N. Kurji Date

List of Publications

The following journal and conference publications are of close relevance to the present work and are included in the appendices:

Conference Publications:

1. Kurji, R., Lavigne, O. and Ghomashchi, R., 'Micromechanical Characterisation of Hydrogen Assisted Cold Cracking Using Instrumented Indentation' In: 5th IIW Welding Research and Collaboration Colloquium, Limburg, Germany, 2015

2. Kurji, R., Costin, W., Brown, I., Ghomashchi, R., An Improved Welding Institute Of Canada Test And The Interrelationship Between Weld Metal Microstructure And Hydrogen Assisted Cold Cracking. In: 4th IIW Welding Research and Collaboration Colloquium, Wollongong Australia, 2014

3. Kurji, R., Griggs, J., Linton, V., Barbaro, F., Kotousov, A., Gamboa, E., Ghomashchi, R., and Coniglio, N., 'An Improved Welding Institute of Canada test for Evaluation of High Strength Pipeline Steel Weldability', Paper No:S11-03, 6th International Pipeline Technology Conference, 7-9 October 2013, Ostend, Belgium

4. Coniglio, N., Barbaro, F., Linton, V., Gamboa, E., and Kurji, R., 'Hydrogen Assisted Cold Cracking Susceptibility of Weld Metal Deposited by Cellulosic Shielded Metal Arc Welding Consumables', In: Proceedings of the 8th International Pipeline Conference, IPC2010, Calgary, Canada, 2010. IPC2010-31680.

Journal publications:

1. Kurji, R., Coniglio, N., Griggs, J. and R. Ghomashchi, Modified WIC test: an efficient and effective tool for evaluating pipeline girth weldability. Science and Technology of Welding and Joining- Accepted 25th Aug 2016

2. Kurji, R., O. Lavigne, and R. Ghomashchi, Micromechanical characterisation of weld metal susceptibility to hydrogen-assisted cold cracking using instrumented indentation. Welding in the World, 2016. 60(5): p. 883-897

3. Ghomashchi, R., W. Costin, and R. Kurji, Evolution of weld metal microstructure in shielded metal arc welding of X70 HSLA steel with cellulosic electrodes: A case study. Materials Characterization, 2015. 107: p. 317-326.

4. Kurji, R. and N. Coniglio, Towards the establishment of weldability test standards for hydrogen-assisted cold cracking. The International Journal of Advanced Manufacturing Technology, 2015. 77(9-12): p. 1581-1597.

Acknowledgements

This work was funded by the Energy Pipelines CRC, supported through the Australian Government's Cooperative Research Centres Program. The cash and in-kind support from APIA through its Research and Standards Committee is also gratefully acknowledged.

First and foremost, I am grateful to my principle supervisor A/Prof Reza Ghomashchi, for his tireless help, patience and guidance. His meticulous nature, and love for science has always been and will always be, a source of inspiration.

I would also like to thank A/Prof Andrei Kotousov and Dr Erwin Gamboa. Without their immense support, completing this body of work would not have been possible. I am also immensely grateful to A/Prof Zonghan Xie and Dr Olivier Lavigne for their support and expertise in the field of micromechanical characterisation. Many thanks to Ian Brown for his advice.

I grateful to the Energy Pipeline CRC Program 1 industry advisory board, for their support, advice and counsel. I would like to thank Leigh Fletcher, John Piper, Vijay Vijayaraghavan and Cameron Dinnis for their advice and support.

I would like to particularly thank Neville Cornish for not only being an unwavering source of support and providing unlimited access to the resources at Australian Welding Solutions by being my 'on call-no charge' Welding Engineer.

None of this work would have been possible without the help of the Mechanical Engineer staff of the University of Adelaide. My dear friend and master welder Pascal Symons, or Dr P. as he is affectionately known; your ability to feel out welding defects still astounds me. You sir are a legend!

The mechanical workshop, Garry Clarke, Scott Letton, Richard Pateman, Mr Robert Dempster, Bill Finch, Anthony Herzich, Stephen Kloeden, Steven Smith, who were always there, any time of the day to help with beating the AutoRon into submission, preparing MWIC specimens, fixing my messes and always ready to have a laugh. You are the pillars of the engineering department. The electronics workshop; Philip Schmidt, Norio Itsumi, Lydia Zhang, Derek Franklin who were able to isolate phantom signals, calibrate equipment, fix plugs and basically keep me sane when instrumentation failed - I thank you

The extraordinary administrative team at the School of Mechanical Engineering: Yvette, Wendy, Loretta, Baily and Tracy, Steven, Margret and Fei - who made getting to conferences, organizing purchases and logistics an absolute breeze - thank you.

Adelaide Microscopy, Dr Ben Wade, Dr Ken Neubauer, Dr Animesh Basak - for all help getting the SEM/ EDX work done. Without your help, I still would be trying to focus in on those inclusions to get the perfect image.

I cannot forget the support of Chris Jones from BlueScope Steel, Australia and Celia Olivero and Patrick Chapon from HORIBA in France. Many thanks to Phillip J. Resendez from Technical Toolboxes, Ltd. and Cliff Johnson, President of Pipeline Research Council International (PRCI), and Dr Yu-Ping Yang, from EWI for the resources they made available to facilitate my research. I would also like to thank Marie Quintana & Matt Jones from Lincoln Electric for supplying the welding consumables and Bao Steel China, for the test martial.

To my colleagues, Walter Costin and Krzysztof Borkowski- thank you for the late-night laughs as we struggled with the complexities of trying to understand the mechanisms of hydrogen embrittlement and the equally baffling complexities of EndNote. Special thanks to Houman Alipooramirabad and James Griggs for all your help with FEA.

Of all the people I have met in this journey, who have worked tirelessly to support me, there are three people to whom I will never be able to fully express my appreciation.

Professor Frank Barbaro- who spent countless hours providing advice and support, who always had a kind word to say regardless of how badly I had messed up, and who knew the best places to eat in Wollongong- thank you.

Professor Valerie Linton, my mentor, who never gave up on me, who invent time so that she could check up on me, who read countless drafts, which must have infuriated her, who gave me every opportunity to excel and even made sure that I had my vegetables- thank you.

My dearest friend and first supervisor, Dr Nicolas Coniglio (AKA Boss) who got me into the world of welding. I will forever remember the first time you took me to the welding bays at the Thebarton laboratories and got me to deposit my first weld bead. You are a scientist of the highest calibre and I am eternally indebted to you.

In saying all that, I believe this body of work is what it is, because of my family. My mom Parin, who instilled in me my love for science and research as I watch her lecture at the University of Nairobi from a young age, my father Nazmudin, who taught me through his actions as a father never to give up and to live life with commitment and attention to detail and of course my sister, Jaameeta, my best friend and biggest fan.

Finally, my darling Sarah. It's your love and support that made this a reality.

…. We are the pilgrims, master; we shall go always a little further…
-James Elroy Flecker

Contents

List of Figures

List of Tables

List of Equations

List of Abbreviations

AF:	acicular ferrite
CE:	carbon equivalent
FCAL:	force control experiments
FCM:	force control mode
GBF:	grain boundary ferrite
G-BOP:	gapped bead-on-plate
GD-OES:	glow discharge optical emission spectrometry
HACC:	hydrogen assisted cold cracking
HAZ:	heat-affected zone
HAZHACC:	heat-affected zone hydrogen assisted cold cracking
HE:	hydrogen embrittlement
HELP:	hydrogen-enhanced localised plasticity
HSLA:	high-strength low-alloy steel
HV:	Vickers hardness units
IG:	intergranular
IIW:	International Institute of Welding
LCS:	lower critical stress
MAOP:	maximum allowable operating pressure
MCAL:	manual control experiments

MCM:	manual control mode
MVC:	microvoid coalescence
MWIC:	modified Welding Institute of Canada
NMI:	non-metallic inclusion
QC:	quasi-cleavage
ROI:	region of interest
RRC:	rigid restraint cracking
RSD:	relative standard deviation
SMAW:	shielded metal arc welding
TRC:	tensile restraint cracking
VCAL:	voltage control experiments
VCM:	voltage control mode
WIC:	Welding Institute of Canada
WF:	Widmanstätten Ferrite
WMHACC:	weld metal hydrogen assisted cold cracking

CHAPTER 1

Introduction

1 Introduction

The pipeline construction process, in particular the deposition of the root pass of a girth weld, creates conditions which leaves weldments vulnerable to a range of defects. One such defect that poses a significant threat to pipeline integrity is hydrogen assisted cold cracking (HACC). Hydrogen assisted cold cracks, or simply cold cracks, manifest themselves in a weld when a critical concentration of hydrogen trapped within a susceptible microstructure interacts with it when subjected to a threshold level of stress [1-7]. The resulting loss of weld integrity has been responsible for multiple pipeline failures over the past five decades [8-10]. HACC has traditionally been associated with the heat affected zone (HAZ) of ferritic steel welds. Significant improvements in the steelmaking process, particularly the thermomechanically controlled processing of steels, has facilitated the development of high-strength steels with low alloy contents and a homogenous microstructure with improved resistance to HACC. However, the as-cast microstructure of the weld metal maintains its susceptibility to HACC as a result of its composition and inherently complex and inhomogeneous structure. Consequently, the reliability of traditional proxies used to predict the onset of the phenomenon has been challenged with the introduction of this newer generation of higher-strength steels. This thesis examines the thermomechanical factors influencing the formation of weld metal hydrogen assisted cold cracks (WMHACC), in high-strength low-alloy (HSLA) line pipe steel. The overarching objective of this thesis is to delineate a boundary within which crack-free welds can be deposited and to assess the suitability of traditional proxies to assess the susceptibility of welds to WMHACC when welded in the Australian context. The local weld metal micromechanical properties are introduced as a novel, potential alternative to assessing the susceptibility of welds to HACC. To construct the context within which this thesis is being undertaken, this introductory chapter outlines the pipeline construction process, particularly the susceptibility of newer-generation steels to the formation of weld metal hydrogen cracks.

1.1 Pipeline Construction

In Australia and around the world, pipeline construction procedures are subject to government regulation and contractual compliance which are harmonised with the underlying principles of defect mitigation. Australia is unique, however, in that its pipeline construction is dominated by thin-walled small-diameter pipelines and an aversion to the use of preheat, due to the cost it imposes on pipeline construction [11]. Historically, the preference for the construction of

these types of pipelines has been to use shielded metal arc welding (SMAW) processes with cellulosic-based electrodes.

SMAW, also known as Manual Metal Arc Welding (MMAW), is a constant current process that dominated fusion welding until the beginning of the 1980s. Since then, advances in technology have facilitated the development of alternative techniques, each with their distinctive strengths and weaknesses. SMAW has nevertheless maintained its dominance in the oil and gas pipeline industry, as the technology has proven itself to be reliable in extreme weather conditions and in challenging terrain, a common feature of onshore pipeline construction. Moreover, the simplicity of the process has ensured that the capital cost of employing SMAW in the field has always remained significantly lower than alternative welding processes [12, 13].

Smart and Bilston [14] carried out a detailed study on the process of onshore pipeline construction. The process, illustrated in Figure 1, begins with the preparation of a right of way and the excavation of a trench to accommodate laying pipe. Pipe sections, generally 12-18m in length, are welded above ground to form stringers. These stringers are then lowered into the trench and tied in before a battery of usually ultrasonically or radiographic testing is carried out to ensure the integrity of the joined sections. The rate at which pipeline construction progresses is critically linked to the rate at which the welding of the root pass of the front joint is completed [14].

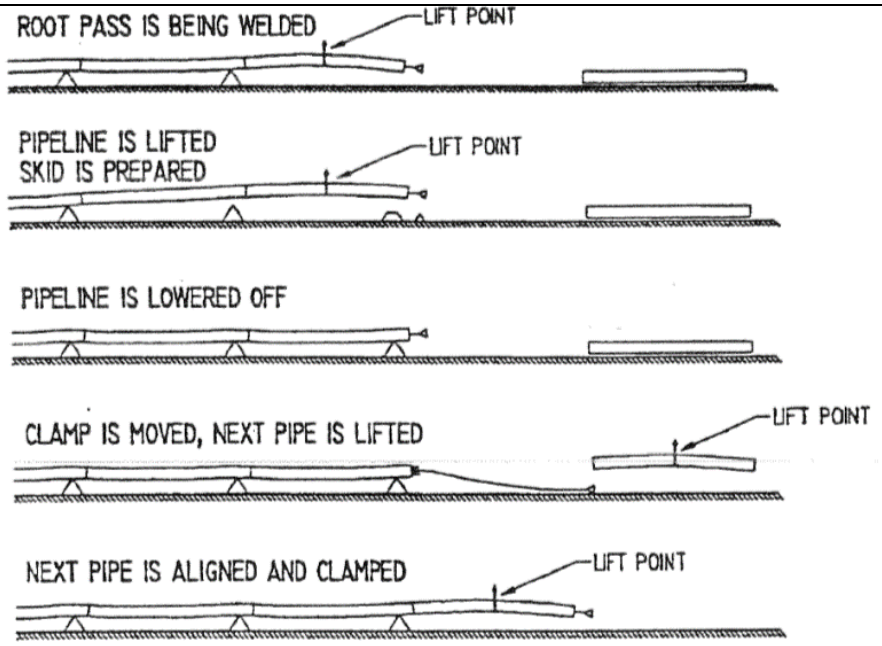

Figure 1: Welding sequence employed in pipeline construction [14]

To maximise productivity, the root pass is welded while the free pipe is supported by a side boom at mid-length. Once the root pass is partially completed, the line-up clamp is released, pulled towards the new joint and clamped to the leading edge, and the pipeline is lifted by the side boom and a skid is prepared to support the free pipe at the correct height to maintain alignment of the string. The pipeline is then lowered onto the skid and the side boom moves to the next pipe and lifts it. The new pipe is added to the string and brought into position over the line-up clamp. Once the root pass has been completed, a hot pass is added. The parameters and delay times between the passes are dictated by the project specific Welding Procedure Specification (WPS). In Australia, common practice dictates that 50–70% of the root pass is to be completed before lifting and lowering onto a supporting skid to improve productivity. The pipeline construction process in particular the lifting action introduces stresses and strains at the bottom dead centre position of the pipe. This consequently influencees the susceptibility of the root pass to HACC.

1.2 **Cellulosic Electrodes**

Cellulosic electrodes are favoured for pipeline construction as they give high burn-off rates, forceful arcs and produce a light, fast-freezing slag that is ideal for the vertical down technique. Cellulosic electrodes typically contain about 25 wt% cellulose ($C_6H_{10}O_5$) that combusts to produce carbon dioxide, carbon monoxide and water vapour. According to Linnert [15], a typical covering for a cellulosic EXX10 electrode consists of 21 wt% cellulose as a gas former and 29 wt% volatile matter and moisture. Decomposition of the water in the welding arc produces copious amount of monatomic hydrogen which is readily adsorbed by the molten weld metal.

Hydrogen trapped in steel is known to have a deleterious effect on the reliability and integrity of the deposited weld, although the exact mechanism governing the process of hydrogen-influenced embrittlement remains a matter of debate. The superheated temperatures generated by the welding arc increases the solubility of hydrogen in molten steel, facilitating the formation of weld metal saturated with hydrogen. As the weld metal cools and solidifies, hydrogen solubility decreases and hydrogen is redistributed through the process of diffusion and lost into the atmosphere through the process of effusion. However, once a critical concentration of hydrogen is trapped within a susceptible microstructure and is subjected to a threshold level of stress, hydrogen cracks can form and potentially result in the catastrophic failure of the joint. However, cellulosic electrodes

remain favoured as deep penetration and spray deposition of the weld metal [15], is critical in pipeline construction where one-sided root pass welding is required.

1.3 **Stove Pipe Welding Technique**

Although the principles of SMAW are applied to pipeline welding, the exact technique employed is markedly different from conventional positional welding methods, especially the use of the stove pipe technique, which involves circumferential welding in which the arc is ‘buried’. The technique requires specially trained welders to force the electrode into the groove, shortening the arc length and increasing the current; this increases the melt temperature and allows exceptional root penetration through the formation of a ‘keyhole’ through the constricted arc and high amounts of hydrogen. The pressure of the arc, vapour pressure and recoil pressure arising from the vaporisation of the melt are balanced against the opposing pressure due to gravity and surface tension to determine the actual depth of the keyhole [16].

The hydrogen introduced into the welding arc as a result of the disassociation of moisture trapped in the cellulosic flux increases the thermal conductivity of the arc and acts to concentrate and constrict the arc, producing deep penetration. Additionally, the recombination of monatomic hydrogen at the metal surface releases significant enthalpy and thus increases melting efficiency [17]. As the keyhole moves, molten metal at its front and sides flows to backfill the space formed in the direction opposite to the keyhole motion [16]. It is important to note that steady-state conditions are difficult to maintain because of variations in welding conditions and parameters caused by the process itself. This affects not only the stability of the keyhole in terms of its size and shape but also the thermophysical properties of the melt.

A significant ramification of the keyholes’ instability—due to their transient and dynamic nature—is its effect on the resultant weld bead geometry and the porosity that it can introduce to the weld metal. ‘Windows’ and porosity occur when the rate of solidification of the weld bead exceeds the rate at which the liquid metal can backfill the void associated with the moving keyhole [18]. Moreover, variations in the stability of the keyhole lead to irregularities and eccentricity in the bead profile, which serves as a stress concentrator and hence a preferential site to which hydrogen can diffuse to. Consequently, the formation of the keyhole, which has been identified as a requirement for effective weld penetration of the root pass [19], increases the risk of HACC because of its potential to increase the prevalence of stress concentrators.

Regardless of the diameter or wall thickness of the pipe being laid, the pipe-laying sequence and process remain relatively constant. Although tried and tested over decades, this sequence, and the use of the SMAW process with cellulosic electrodes introduces copious amounts of hydrogen and a stress state which can promote the formation of HACC.

1.4 Thermomechanically Controlled Processed Steels

Development in the field of steel production has considerably improved the quality of line pipe steel. Improvements in the thermomechanically controlled processing of steels have facilitated the development of higher-grade steels with a lower carbon content and a lower proportion of microalloying elements. These leaner, cleaner steels have an increased strength with good toughness and ductility and have shown greater resistance to cold cracking in the HAZ but not in the weld metal [2, 20-22].

Although numerous strategies have been adopted in codes internationally for the prevention of heat-affected zone hydrogen assisted cold cracking (HAZHACC), no mitigating strategies have as yet been incorporated into any major world standard for the prevention of weld metal hydrogen assisted cold cracking (WMHACC) [23-25]. Understanding the thermomechanical factors affecting WMHACC is critical in order to propose a scientifically sound strategy to mitigate this phenomenon.

1.5 Motivation and Research Objectives

Hydrogen plays a dichotomous role in root pass girth welding; it both facilitates the economic deposition of welds and has the capacity to cause a range of dangerous defects. The challenge faced by industry is finding the margin in which hydrogen's benefits can be harnessed without succumbing to the defects it promotes.

Numerous studies have been commissioned to investigate the formation of HAZHACC. Much of this information has been integrated into the industrial context through codes and standards. In contrast, there is little published information addressing the specific conditions governing the formation of WMHACC and consequently little guidance from which safe welding conditions can be derived [26]. Therefore, it is not surprising that current welding standards are limited in addressing the issue of avoiding hydrogen cracking in weld metal [27, 28].

Some standards provide overarching measures to minimise the risk of WMHACC. The American standard for the welding of structural steel (AWS D1.1:2010 [29]) and the American standards for the welding of pipelines and related facilities (API 1104:2014 [30]) simply advise testing when there is believed to be a risk of WMHACC, whereas the British standard (BS 5135:1984 [31]) proposes the use of low hydrogen electrodes (< 2.5 ml/100 g) or the application of high post heat to minimise the volume of residual hydrogen (200 °C post heat for 2–3 hours). These measures can add a significant economic burden to production. Other standards do not address the issue of WMHACC in any detail at all. Standards such as the Australian Standard (AS2885.2 [23]) and the European standards (EN 1011-2:2001 [24]) do not offer any guidance on how to reliably assess the risk of WMHACC.

Whilst the existence of some standards do acknowledge the possibility of weld metal cracking under certain conditions, there is no universally accepted and experimentally validated methodology to quantify the risk of WMHACC or calculate the threshold preheats needed to mitigate the risk of WMHACC. To address this gap, this thesis examines the thermomechanical factors that influence the formation of weld metal hydrogen cracks.

The thesis is structured into four main sections.

Literature Review

The literature review critically examines hydrogen cracking as a phenomenon and discusses the weldability tests that are used to assess susceptibility of weld metals to HACC. The current methods used to predict the onset of HACC and their limitations are discussed. The relevant empirical cracking data is consolidated and discussed to form the basis on which the weldability testing in this thesis is based. An article entitled ‘Towards the establishment of weldability test standards for hydrogen-assisted cold cracking’ based on this section has been published in *The International Journal of Advanced Manufacturing.*

Development of a Weldability Test

To carry out weldability testing within the parameter range identified in the literature review, an enhanced weldability test is designed. The second key section of this thesis examines the development of this weldability test, which was presented at *6th International Pipeline Technology Conference in Ostend Belgium (2013)* and at the *4th IIW Welding Research and*

Collaboration Colloquium, Wollongong, Australia (2014), and subsequently published in the *Science and Technology of Welding and Joining (2016).*

Delineation of a Safe Welding Envelope

The enhanced weldability test is used as a tool to delineate a safe welding boundary for conditions not examined in the published literature. The development of the safe welding boundary and the features of the cracking boundary are presented in the third section of this thesis. A journal article detailing the empirically derived cracking envelopes and the interaction between observed crack types will be submitted to the *Science and Technology of Welding and Joining* entitled 'Investigating the Dependence of Hydrogen Assisted Cold Cracking on Solidification Cracking in the Root Pass of Pipeline Girth Welds'.

Analysis of Weldability Test Samples

The fourth section of the thesis focuses on presenting and discussing the microstructural and micromechanical properties of samples prepared from weldability tests across the safe welding boundary introduced in section three. Two journal articles were published based on these results. The first journal article, 'Evolution of weld metal microstructure in shielded metal arc welding of X70 HSLA steel with cellulosic electrodes – A case study', was published in *Materials Characterization (2015).* The second article, 'Micromechanical characterisation of weld metal susceptibility to hydrogen assisted cold cracking using instrumented indentation' was published in *Welding In the World (2016).* A presentation based on these results was also presented at the *5th IIW Welding Research and Collaboration Colloquium (2015)* in Limburg, Germany.

From the analysis of thermomechanical factors that influence the formation of WMHACC, the thesis provides a platform from which the weld metals' micromechanical properties can be used as a proxy to assess WMHACC susceptibility.

CHAPTER 2

Literature Review

2 Literature Review

The objective of this literature review is to establish the foundation necessary to investigate the factors influencing the formation of WMHACC in the Australian context. Pipeline construction in the Australian oil and gas industry, especially transmission pipelines, is dominated by thin-walled small diameter pipes welded using SMAW with cellulosic electrodes. The use of higher grades of HSLA steels is driven by savings in the gross tonnage of steel used in construction but has raised concerns over the increased vulnerability of weldments to WMHACC.

In this literature review, the development and weldability of HSLA steels are discussed with a focus on the how weld metal solidification morphology, solid-state transformations and elemental chemistry influence the development of crack-susceptible microstructures. The introduction, diffusion and trapping of hydrogen within these microstructures are discussed and the key factors influencing the formation of weld metal hydrogen cracking are established. The phenomenological consequence of the interaction of these key factors is explored through a review of the hypothesised mechanisms governing HACC.

To substantiate a suitable methodology for evaluating the susceptibility of weldments to WMHACC, a critical review of weldability tests is presented. Previously derived empirical boundaries are outlined and a critical welding parameter range, for which no published data exists, is identified. The current methods used to predict the onset of the phenomenon are reviewed and their limitations highlighted. To address these limitations, the use of instrumented indentation as a novel alternative is explored from a theoretical perspective. The critical review of the literature presented in this chapter forms the basis on which the research gaps and aims are founded, identified and presented in Chapter 3 of this thesis.

2.1 Hydrogen Assisted Cold Cracking

HACC is generally accepted [28, 32-46] to be the phenomenological consequence of a critical concentration of hydrogen trapped in a susceptible microstructure subject to a threshold level of stress. Traditionally, hydrogen cracks have been known to manifest in the coarse grained HAZ and are frequently described as toe cracking, root cracking or under-bead cracking, depending on the location of the crack [47]. HACC is also commonly referred to as cold cracking, as it is well established that cracks develop when a critical concentration of residual hydrogen is allowed to incubate in a susceptible microstructure for a period of time. The

length of this incubation period depends on the interrelationship between the three critical factors of residual hydrogen concentration, microstructure and level of stress that influence the formation of cold cracks.

Given the complexity of this interrelationship and the fact that no universal consensus exists as to the exact mechanism by which hydrogen cracking is governed, it is not surprising that there is not yet a codified method in industry which can be used to estimate the time within which a hydrogen crack will manifest after deposition of a weld. As the risk of hydrogen cracking is directly related to the proportion of hydrogen trapped within a weld, the introduction and trapping of hydrogen in a weld is an important factor to consider when assessing the susceptibility of a given weld to cold cracking. Similarly, understanding both the characteristics and features that make a microstructure susceptible and the threshold levels of stress above which hydrogen cracks are likely to initiate and propagate is essential in determining the thermomechanical factors that influence HACC.

2.1.1 Weld Metal Hydrogen Assisted Cold Cracking

Hydrogen cracking is traditionally associated with cracking that initiates and propagates through the HAZ. However, with improvements in the steelmaking process and a consequent reduction in steel hardenability, there is evidence to suggest that there is an increased tendency for HACC to occur in the weld metal rather than the HAZ [43, 48, 49]. The prevalence of WMHACC over HAZHACC has been suggested to be the consequence of changes in the alloy content and as-cast microstructure of the parent plate. Modern alloy designs have raised the austenite (γ) to ferrite (α) transformation temperatures of the HAZ to a point where the ferrite transformation occurs in the HAZ before the weld metal [2]. As the solubility of hydrogen in ferrite is lower than in austenite, hydrogen is rejected from the HAZ and accumulates in the weld metal; the higher diffusivity of hydrogen in ferrite favours this process. The consequence is the preferential accumulation of hydrogen in the weld metal.

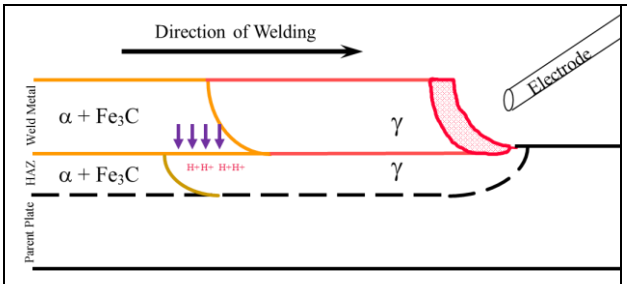

Figure 2: HAZHACC. The austenite (γ) to ferrite (α) transformation is suggested to occur in the weld metal before the HAZ, leaving the HAZ to act effectively as a hydrogen

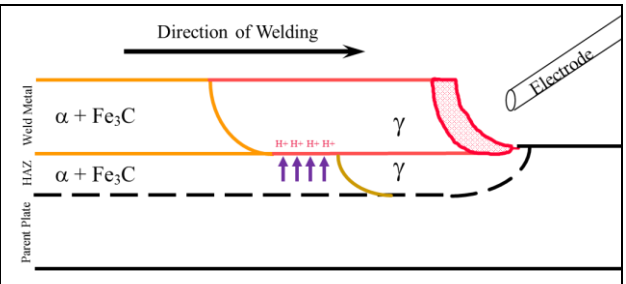

Figure 3: WMHACC. Modern alloy designs favour the austenite (γ) to ferrite (α) transformation in the HAZ before the WM. This transforms the WM into an effective hydrogen

sink. Hydrogen accumulates in areas of high triaxial stress within the HAZ, creating conditions which favour the formation of hydrogen cracks.	sink, within which hydrogen can accumulate in areas of high triaxial stress, creating conditions which favour the formation of hydrogen cracks.

Ferritic steels are comparatively more susceptible to HACC as a result of their body-centred cubic crystal structure [50]. This closely packed structure allows greater mobility of hydrogen. The following section discusses the interaction between hydrogen, stress and weld metal microstructure and the role they all play in increasing the susceptibility of a weld to failure as a result of hydrogen cracking.

2.2 High Strength Steels and their Weldability

As highlighted in Chapter 1, HSLA steels are widely used in the oil and gas industry for the construction of transmission pipelines. This section explores the characteristics of HSLA steels with the aim of identifying key factors which affect the mechanical properties and weldability of these steels. The evolution of the steels' microstructure is discussed and the effect of two critical factors, solidification and non-metallic inclusions (NMI's), are described. The section concludes by discussing these effects on susceptibility specifically to HACC.

2.2.1 High-Strength Low-Alloy Steels

HSLA steels are favoured in pipeline construction because of their high strength, toughness, ductility and formability. Given that they are exhibit a relatively better resistance to corrosion than general low C-Mn steels, it is readily apparent why HSLA steels present themselves as prime candidates for the production of oil and gas transmission pipelines. Their strength-to-weight ratio facilitates the formation of low-weight structures at a relatively low cost. Over the past 50 years, yield strength levels have doubled from the API 5L X42 to X52 (289–358 MPa) grades of the 1950s to the API 5L X100 and above (689 MPa) grades available today. To achieve the desired tensile strengths of over 500 MPa for operating pressures of 12–20 MPa, the focus in industry has been not only on controlling alloying content but on refining the steelmaking processing itself.

Microalloyed steels (also known as hot-rolled HSLA steels) are low-carbon steels (< 0.2 wt% C) alloyed with elements to produce minimum yield strengths between 275 and 550 MPa and a ductile to brittle transition temperature of approximately -60 °C. Elements such as manganese (< 1.5 wt.%), silicon (< 0.7 wt.%), niobium (< 0.05 wt.%), vanadium (< 0.1 wt%) and titanium (< 0.07 wt.%) are used to promote grain refinement and precipitation hardening.

Niobium (Nb), vanadium (V) and titanium (Ti) have a strong affinity for carbon and nitrogen and consequently are strong formers of nitrides and carbides. This makes them effective in limiting grain boundary movement and grain growth, both of which are key factors in producing high-strength, high toughness steels.

The use of thermomechanically controlled processing and the addition of small amounts of Ni, Mo and Cr can produce steel with yield strengths of 550 MPa and above. Major changes such as the introduction of basic oxygen steelmaking, improvements in the accuracy of process control and reductions in sulphur and phosphorus content have improved the control of steel composition and the homogeneity of the product. Homogeneity has been further improved by the move from ingot cast to continuous slab casting technology and its subsequent extensive refinement, minimising the consequences and extent of centreline segregation. The introduction of thermomechanically controlled processing has enabled further reductions of both carbon content and microalloying content, while increasing parent metal strength and toughness without sacrificing weldability.

Although steels of greater yield strength (> 690 MPa) can be produced by manipulation of the austenisation process and by quenching and tempering, those yield strengths are far higher than what is demanded in the Australian context for onshore pipeline construction. Furthermore, the risk of hydrogen cracking requires extremely rigid control of welding processes, including but not limited to the use of high preheat and low hydrogen electrodes, which makes them an economically unattractive option.

2.2.2 Development of High-Strength Low-Alloy Steels

Traditionally, carbon and manganese were used to increase the tensile strength of mild steel at the cost of weldability. However, the introduction of microalloying allowed for an increase in strength without significant increase in carbon. Nb, V and Ti, along with Mn, Si, Cr, Mo, Ni and Al, used in conjunction with thermomechanical treatments have allowed for the development and production of high-strength, high toughness weldable steels.

The initial development of microalloyed steels can be attributed to several factors, the most pertinent of which is an increase in transportation costs [51]. There was and is an ever-present need to increase the strength of steels to lower the thicknesses employed without compromising weldability, in order to deliver a lower net cost of production. This need has driven the development of microalloyed steels and production techniques resulting in metallurgically clean, fine-grained homogenous steels. These new steels are characterised by

low sulphur content and a reduced amount of micro-constituents that are detrimental to toughness such as oxides, inclusions and pearlite. The reliance on carbon and alloy content for strength has been replaced by complex thermomechanical processing routes and accelerated cooling that has facilitated the development of low carbon equivalent steels which have excellent toughness and enhanced weldability as a result of their refined grain structure. The fine-grained structure, higher strength and improved resistance to crack propagation allow for the steels to be employed in pipelines operating at higher pressures. In addition, lower alloying additions and a finer-grained structure have helped improve the toughness profile of the HAZ reducing susceptibility to cold cracking.

2.3 The Welding Metallurgy of HSLA Steels

The integrity of a welded joint is known to be dependent not only on the symmetry of the deposited weld bead and thus its ability to transfer load across the ligament but also the micromechanical properties and the degree of homogeneity within the constituents of the ligament. The weld metal microstructure established during the cooling of the weld cycle will dramatically influence the load-bearing capacity of the joint. It is for this reason that there is a large amount of research dedicated to determining the ideal thermochemical factors to produce a desirable microstructure. As a result of this research, numerous methods have been developed to identifying various phases and micro-constituents. For ferritic steels, the IIW classification [52] is widely accepted. However an alternative detailed description of weld metal microstructure appears in Thewlis [53] .

The microstructure developed during coalescence depends on the complex interactions of the elemental constituents of the parent plate, the filler metal, the electrode flux and the thermal cycle to which the weld is subjected. The interaction will not only affect the resulting chemical composition and alloy concentration, but also the solidification structure and the size and distribution of non-metal inclusions, a key variable affecting the homogeneity and integrity of the ligament. Figure 4 schematically represents the transformations that occur in the weld during cooling.

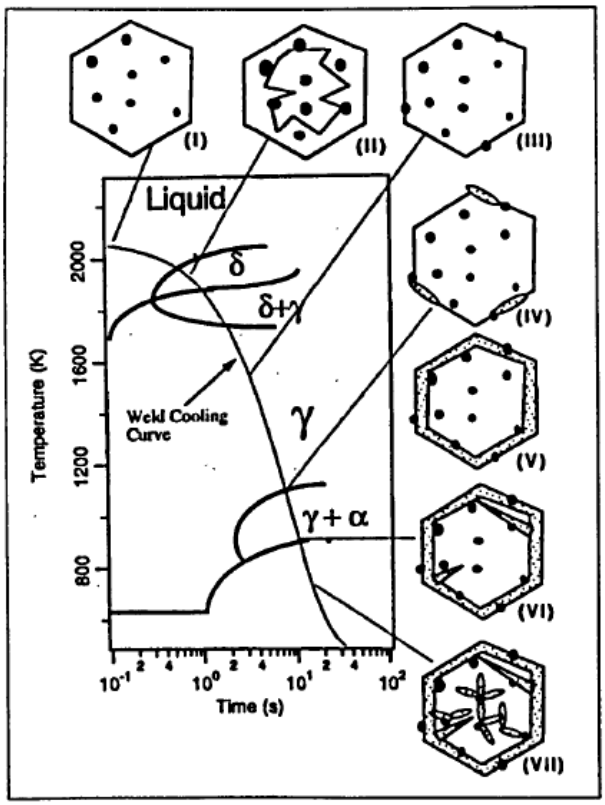

Figure 4: Schematic representation of a continuous cooling transformation diagram presenting the basic steps involved in weld metal microstructure development: (I) inclusion formation; (II) solidification; (III) austenite phase; (IV) beginning of primary ferrite nucleation and growth of ferrite side plates; (V) finishing of primary ferrite growth; (VI) nucleation and growth of ferrite side plates; and (VIII) acicular ferrite formation [54].

Although the metallurgical transformation temperatures are largely the same in welding as in steel production, the microstructures that evolve during welding are meaningfully different. This results partly from the welding process itself, especially the interaction of molten deposits with the ionising column of the welding arc. A significant amount of oxygen is introduced into the weld, increasing the volume fraction of inclusions in the weld metal. These inclusions influence the austenite to ferrite transformation, restrict grain growth and offer alternative nucleation sites leading to the formation of AF or ferrite side plates.

During weld metal solidification, elemental segregation is known to take place as a result of the rapid cooling conditions [55, 56]. This inevitably leads to impurities being concentrated within inter-cellular boundaries or inter-dendritic regions. This influences the kinetics of the posterior solid-state transformation and thus the resulting microstructure. This section of the literature briefly reviews and discusses the development of weld metal microstructures. The role of microstructural constituents are discussed, followed by a brief overview of the significance of NMIs and weld metal chemistry.

2.3.1 Weld Metal Solidification

It has been established that the properties of the weld metal are affected not only by its grain structure, but also by the degree of elemental segregation and the presence of NMIs [55-57]. Solidification behaviour, especially solidification kinetics, affects these factors and consequently the properties of the deposited weld. As a result, the propensity of a weld deposit to succumb to a welding defect depends in part on the solidification behaviour of the weld [58].

The molten material deposited from the electrode wets the partially molten parent metal, creating an interface from which the solidification process continues. The macroscopic solidification rate depends on the net thermal gradient. This in turn depends on all the factors that affect the net heat input, such as current, voltage and travel speeds, and the net heat loss, which depends on factors that could affect cooling rates, including plate thicknesses and boundary conditions like ambient temperature and preheat [59].

The macroscopic shape of the solid-liquid interface remains relatively constant throughout the weld deposit as long as the weld is not subject to conditions, such as start and end effects, that would significantly alter the cooling rates; however, the physical motion within the weld metal is not constant. Electromagnetic stirring creates a large amount of internal turbulence which results in mixing of the molten metal and may affect the elemental distribution throughout the weld.

Weld solidification initiates at the fusion boundary; partially melted grains at the fusion boundary serve as nuclei for the growth of columnar grains. The relationship between the width of the columnar grains and the weld austenite grain size depends on the HAZ grain morphology. Although the exact mode of solidification depends on the chemical composition of the weld, microalloyed ferritic steel welds solidify as delta ferrite which decomposes to austenite on further cooling. In time, the austenite grains will cross the primary delta ferrite grain boundaries, eliminating the prior structure [60].

The thermal gradient plays a pivotal role in the mode of growth of the grain structure. The columnar grain structure is governed by the extent of constitutional supercooling, which is influenced by the composition and thermal gradient. The higher the thermal gradient, the lower the constitutional supercooling and the consequent difference in growth mode. As the thermal gradient decreases, the growth modes change in the following order: planar, cellular, cellular dendritic, columnar dendritic, and equiaxed dendritic [60-63].

The growth rate patterns of cellular and dendritic solidification in combination with rapid cooling rates may result in extensive elemental segregation. Elemental segregation into inter-columnar regions may result in intergranular embrittlement. As demonstrated by [64], when hydrogen and intergranular impurities are present, brittle fracture may occur at lower stress levels than when they are not present.

It is important to note that the solidification mode, although significant, is only part of the process that determines the resulting weld metal microstructure. Numerous studies have suggested that AF is the optimal microstructure for high-strength ferritic steel weld metal. The next section discusses the evolution of ferritic weld metal, typical weld metal microstructures and the process by which AF is formed.

2.3.2 Solid-State Transformations

A weld deposit will undergo a range of phase transformations as it solidifies. Typically, weld pool solidification commences with (1) the epitaxial growth of elongated columnar delta-ferrite (δ) at the fusion boundary, followed by (2) the inward growth of austenite *(γ)* on the δ-ferrite grain boundaries and then by (3) the inward growth of allotriomorphic (grain boundary) ferrite *(α)* on the γ-γ- grain boundaries (see Figure 5 and Figure 6).

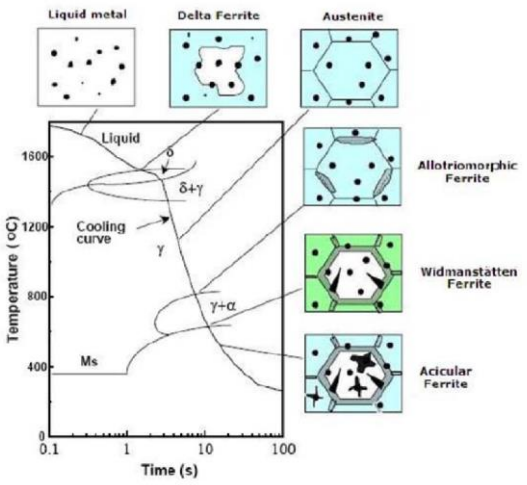

Figure 5: Schematic diagram of microstructure evolution in steel welds. Modified from Bhadeshia and Svenson [57].

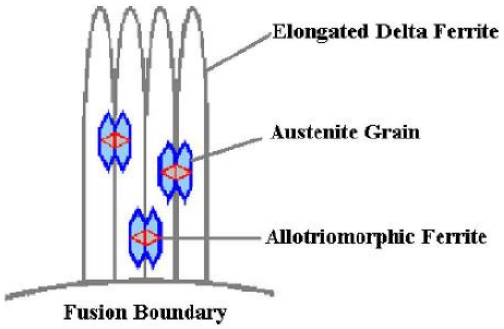

Figure 6: A typical steel weld deposit will undergo two solid-state transformations which start as elongated δ-ferrite. The austenite would then normally grow along the δ-ferrite grain boundaries before moving into the grain.

Allotriomorphic ferrite, Widmanstätten ferrite (WF) and Acicular ferrite (AF) are the three major ferritic constituents that form in the solidified weld metal; AF is favoured in high

strength steel weld metal, as it provides optimum weld metal mechanical properties due to its small plate size, interlocking microstructure and high angle grain boundaries [53, 60, 65, 66].

2.3.2.1 Austenite

The size and shape of austenite grains plays a significant role in the evolution of the final weld metal microstructure, which derives itself from the established austenite morphology (Figure 7). As was noted above, the presence of AF is known to correlate with improved weld metal toughness [66]. According to Basu and Raman [67], the prior austenite grain size and the presence of NMIs are critical factors in determining the prevalence of AF in a weld. The role of NMIs as nucleation sites for AF are discussed later in this chapter. Regardless of the relation to austenite grain size, Suito et al. [68] have reported that the distribution of fine inclusion particles refined both the austenite grain size and the final weld metal microstructure.

Finer austenite grain sizes result in an increase in the number of grain boundary surfaces which serve as nucleation sites for bainite over AF [57, 69].

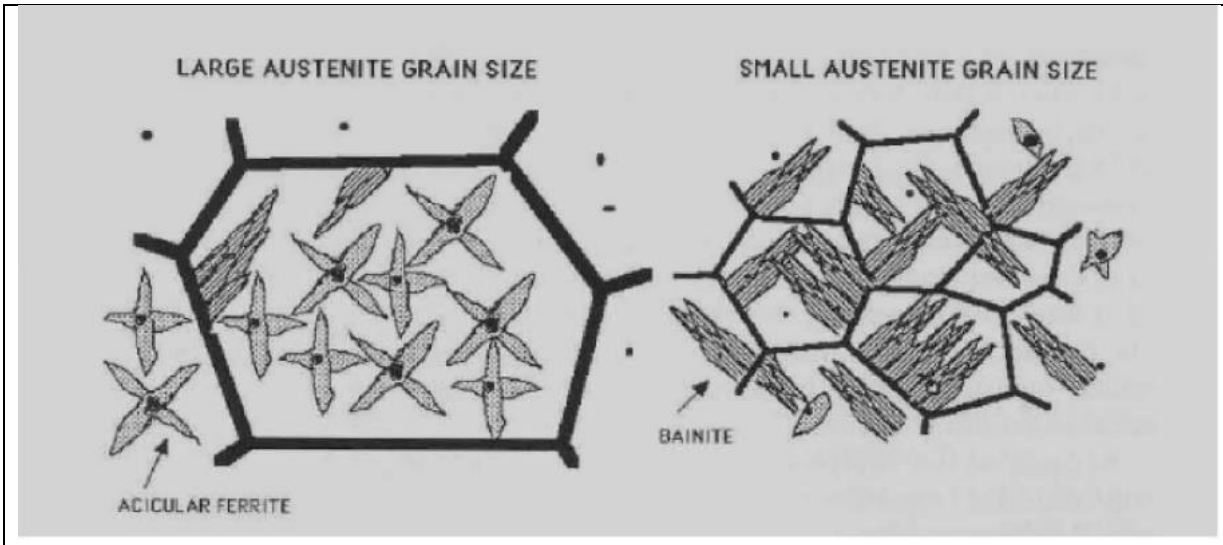

Figure 7: Austenite grain size vs. dominant microstructure. As the illustration shows, a smaller grain size will mean a larger density of intergranular nucleation sites that favour the formation of bainite. Conversely, a relatively large austenite grain size favours the formation of AF [57].

The magnitude of the heat input influences the resulting austenite grain size. An increase in the heat input increases the weld metal austenite grain size, which favours the formation of AF in the place of bainite resulting in a decrease in hardness [70]. Depending on the magnitude of the heat input, it may also serve to coarsen the austenite grain size in the HAZ. At very high heat inputs, the cooling rate may retard to the point that a higher proportion of polygonal ferrite is formed, corresponding to a reduction in the amount of AF. In addition to

the larger austenite grain size, high heat heightens the probability of inclusions being absorbed by the slag, resulting in a potential drop in the volume fraction of inclusions. As noted above, the austenite grain size and inclusion content are critical factors that influence the prevalence of AF in weld metal.

2.3.2.2 Allotriomorphic Ferrite

Allotriomorphic ferrite *(α)* (polygonal or grain boundary ferrite (GBF)) is the first phase to form on cooling below the AC_3 temperature at which austenite becomes unstable [57]. Although the formation of allotriomorphic ferrite may promote the formation of AF [66], excessive amounts are detrimental to weld metal toughness [70]. However, it is the competitive growth between allotriomorphic ferrite and bainite that is of greatest benefit to the weld, as bainite sheaves are known to be inefficient crack arrestors [66, 71], so their formation is highly undesirable. Allotriomorphic ferrite will compete against the formation of bainite during austenite ferrite transformation. The formation of allotriomorphic ferrite renders the grain boundaries inert, removing nucleation sites for bainite and forcing the formation of AF instead.

2.3.2.3 Widmanstätten Ferrite

Widmanstätten Ferrite (WF) is the second phase to form on cooling below the AC_3 temperature. It may nucleate directly from the austenite grain (primary WF), but it usually grows from allotriomorphic ferrite (secondary WF). The formation of WF does not involve the diffusion of substitutional solutes; rather, it forms by displacive transformations that are usually preceded by reconstructive transformations [72]. Displacive transformation are rapid transformations that constitute minor changes to the crystal structure through a re-alignment of crystal lattice, whereas reconstructive transformations are small and include the decomposition of chemical bonds and recombination into a new crystal structure. When the net carbon content is low, the formation of WF may prevent the formation of AF, as Widmanstätten plates can grow across the austenite grains [72].

2.3.2.4 Acicular Ferrite

Acicular ferrite (AF) forms within prior austenite grains in an interlocking basket weave pattern that strongly resists crack propagation as a result of its small grain size (typically 1–3 μm) with high angle grain boundaries [60]. According to Bhadeshia [73], AF is intergranularly nucleated bainite and thus forms at a lower temperature than WF. It forms through displacive

transformaiton at temperatures below primary ferrite at faster cooling rates. However, unlike ferrite side plates, AF nucleates on inclusions rather than grain boundaries [66, 74, 75]. This intra-granular nucleation and growth of AF on or around inclusions will occur until they are impinged by neighbouring grains. It thus follows that the growth of AF is limited by the density and distribution of NMIs. However, as suggested by [76], it is the inclusion type, size and distribution rather than the total volume fraction of inclusions that determines the prevalence of AF. The role of NMIs are discussed in more detail in Section 2.3.3.

Austenite grain size also plays a role. The transformation from austenite to AF is controlled by the size of the austenite grain; smaller size results in bainite forming preferentially over AF, as smaller austenite grains will provide an increase in austenite grain boundaries upon which the bainite can nucleate [57]. Austenite grain size is influenced by the weld metal chemistry; during solidification, elemental segregation leads to a change in composition that stabilises austenite, which may inhibit the nucleation of AF [77]. The role of weld metal chemistry is discussed in Section 2.3.4.

There is a strong resemblance between AF and bainite; however, it is the nucleation sites—AF from NMIs and bainite from austenite grain boundaries—that distinguish the two micro-constituents. The nucleation of AF on inclusions within the austenite grain form isolated plates radiating from a point rather than the sheaf morphology of classic bainite. This results in isolated laths with high aspect ratios. AF is desirable for its correlation with improved strength and toughness; its fine interwoven pattern improves cleavage toughness, as the multi-directional plates serve as an interface to deter propagating cracks [70].

Factors influencing the nucleation of AF have been the subject of much research and debate, a detailed review of which is far beyond the scope of this study. Nevertheless, it is established that the nucleation of AF depends on its ability to contest and dominate the conditions for its nucleation.

2.3.3 Non-Metallic Inclusions

2.3.3.1 Formation of Non-Metallic Inclusions

The formation of NMIs is the first reaction known to impact the final weld metal microstructure. Oxidation, not only in the ionising column of the arc but also in the molten metal itself produce these inclusions, which end up trapped in the bulk of the weld metal. Generally, NMIs in carbon-manganese and low-alloy steels are the oxidation products of aluminium, titanium, silicon and manganese [78]. Although it has been hypothesised that

NMIs form in order of decreasing stability (or the value of the standard free energy of formation) and thus in a fixed sequence (Al_2O_3, Ti_2O_3, SiO_2 and MnO) regardless of alloy composition, experimental data suggests that stability actually results from the reactant concentration, which in turn depends on alloy composition and solidification kinetics that influences the degree of segregation [79].

During solidification, elements segregate to the solid-liquid interface and concentrate within inter-dendritic spaces. The Scheil equation can be used to describe this segregation, as it estimates the concentration of different solutes if solid diffusion is neglected. As the formation of NMIs depends not only on the concentration of different alloying elements but also on their interactions, the Scheil equation serves as only part of the solution to determining the formation of simple and complex NMIs. Numerous attempts have been made to develop a theoretical model to predict the formation of NMIs in steel welds. Kluken and Grong [80] developed a model for the formation of inclusions, theorising the nucleation of oxides as a consequence of supercooling. Eijk and Grong [81] later proposed a mechanism based on work using Ti, Al and Ca deoxidizers in steel; their model was based on thermodynamic analysis and validated using experimental data. They concluded that solid-state products such as MnS, TiN and $MnOTiO_2$ are by-products of a series of reactions occurring in liquid metal. Babu and David [82] employed computational thermodynamics to predict the formation of NMIs and facilitated the development of de-oxidation diagrams, which are instrumental in describing the formation of inclusions over a range of welding processes and compositions and rely on equilibrium thermodynamics. However, these methods do not describe the size, distribution or morphology of NMIs; these are the NMI properties that collectively and significantly influence weld metal transformations, the resulting mechanical properties of the weld and the ligament.

Kinetic models such as Babu et al [83] and Hong's [84] have been developed to allow for the estimation of NMI size and density. They both rely on the kinetics of the reactions, in particular nucleation rates and diffusion rates. Models such as Babu et al [83] predict the de-oxidation sequence from calculated time temperature transformation diagrams. Hong [84] expands on Babu and David's [82] work by taking into account temperature and velocity fields within the weld metal itself. Although these theoretical models demonstrate significant progress in predicting the formation of NMIs, there is no evidence to suggest that there is as yet a universal model that can be used to predict NMI formation. What is universally accepted is that NMIs play a role in the mechanical properties of HSLA steel weld metal. The

following section briefly explores NMIs' influence on the mechanical properties of steel weld metals.

2.3.3.2 Effect of NMIs on Weld Metal Properties

Both the size and distribution of NMIs play a critical role in the development of weld metal microstructure and thus strongly influence the weld's mechanical properties. It is generally accepted that the presence of NMIs plays a dichotomous role in the overall mechanical properties of a weld: NMIs may serve as initiation sites for planar defects but also may promote the formation of AF, which improves weld toughness and thus retards crack propagation [84].

Numerous studies have investigated the formation of AF and the effects of inclusion composition on that formation [56]. The importance of the size and distribution of NMIs are outlined in studies by Lee et al. [66], Barbaro et al. [85], Ricks et al. [86] and Cochrane [87]. Lee et al. [66] concluded that with low-carbon steels, the larger the inclusions of $Si0_2$, MnO and Al_2O_3, the higher the probability of AF nucleation, especially with inclusions greater than 0.2 µm; they reported that the probability of AF nucleation reached 1 for inclusions greater than 1.1 µm, whereas Barbaro et al. [85] suggested that particle size of 0.4–0.6 µm was required. Ricks et al. [86] suggested that the energy barrier to AF nucleation actually decreased as inclusion sizes increased to 1 µm. In all the cases reviewed, they found no evidence to suggest that inclusions inhibit the nucleation of AF. However, as suggested by Choi and Hill [88], a sufficiently high volume fraction of inclusions may limit austenite grain size, thus favouring the formation of ferrite side plates.

In addition to the provision of nucleation sites, inclusions can refine the weld metal microstructure by pinning and prevent the growth of the austenite grains. Cochrane [87], in investigating the influence of inclusion morphology on microstructure and weld toughness, suggested that the distribution of inclusions affects the degree of austenite grain refinement by reducing the mobility of the austenite grain boundary. This effect has been referred to as Zener pinning [68, 89], which does not necessarily control austenite grain size but will influence morphology by counteracting the driving forces attempting to enlarge grain size. As noted above, smaller austenite grains favour the formation of microstructural constituents other than AF.

2.3.4 **Alloying Additions**

Sections 2.3.1 and 2.3.2 briefly discussed the role of solidification and solid-state transformations in the development of weld metal microstructure. This section outlines the effect of chemical composition on the formation of microstructural constituents and mechanical properties, as summarised in Table 1. Numerous reviews [56, 78, 90, 91] have discussed the effect of alloying additions on the microstructural and mechanical properties of steel welds. It is universally accepted that a change in the alloy composition of either a consumable or a parent material will change the microstructural and mechanical properties of the resulting weld.

2.3.4.1 Carbon

Carbon is among the most influential elements with regards to weldability of steels. Although the solid solution hardening effect of carbon is very high, it is of relatively little importance given the low solubility (≈ 0.01 wt%) of carbon in ferrite. However, a change in net carbon content will significantly affect the resultant microstructure [78, 90, 92]; an increase in carbon content decreases the width of columnar grains, reducing the austenite grain size, which in turn may promote intergranular transformations. In addition, an increase in carbon content results in thinner ferrite veins at prior austenite grain boundaries and increases the amount of second phases such as martensite constituents and austenite martensite carbides.

2.3.4.2 Manganese

Manganese is a cost-effective alloying addition that is used to control strength and toughness [90]. Although it has only a moderate solid solution strengthening effect, it significantly affects the formation of AF. In particular, it has been reported that for welds with less than 1.0 wt% of manganese, the formation of AF is highly unlikely, whereas for welds with an manganese content of 1.4–1.8 wt% the resulting weld metal microstructure will consist mainly of AF [93]. Above this range, upper bainite is expected to form, resulting in a decrease in weld metal toughness. It has also been reported that strength is linearly proportional to increases in manganese content.

2.3.4.3 Silicon

Silicon is a common alloying addition for use as a de-oxidant with moderate solid solution strengthening effect [78]. Silicon differs, though, in being used in quantities below 0.5 wt%,

as it reduces ductility in large quantities. In addition, although higher silicon content will increase yield strength, the marginal gains per unit increase in silicon content is decreasing and non-linear. Silicon and manganese work in tandem to influence the properties of AF [90]. With a high manganese content, an increase in silicon content increases the aspect ratio of AF. Silicon also increases the amount of retained austenite by inhibiting the formation of cementite.

2.3.4.4 Nickel

Nickel is used to improve toughness and increase hardenability; although comparatively less effective than manganese, chromium or molybdenum [90], nickel improves weld metal toughness regardless of weld metal microstructure. Nickel does promote the formation of AF at the expense of GBF [90] and an increase in nickel content increases the AF's aspect ratio. However, when combined with high manganese content, a nickel content of more than 2.2 wt% will result in the formation of martensite with an increase in the proportion of ferrite with second phase.

Weld metal hardness is also affected by nickel content. Kang et al.[77] demonstrated that weld metal hardness increases linearly as manganese and nickel content increases in low-carbon steel welds as a result of solid solution strengthening and the formation of hard phases. In addition, weld metal toughness deteriorates with high levels of nickel in combination with manganese, leading to an increased probability of intergranular fracture.

2.3.4.5 Chromium

Chromium is an alloy addition used to enhance weld metal strength. It has been demonstrated to increase both tensile and yield strengths, along with hardenability. In terms of its effect on weld metal microstructure, chromium, like nickel, works in tandem with manganese. At 1 wt%. manganese, the optimum chromium content for the formation of AF is 1 wt%. As the manganese content increases, the chromium content required to optimise the formation of AF decreases. Increasing the chromium content beyond this threshold promotes the formation of bainite [71].

2.3.4.6 Molybdenum

Molybdenum is an alloying strengthener with greater efficacy than manganese. However, molybdenum can have significant detrimental effects on weld metal toughness when

disproportionality high levels are used. 0.2–0.3 wt% of molybdenum suppresses the growth of GBF and promotes the formation of AF [90], while 0.5 wt% refined AF to a considerable extent. However, subsequent additions have been suggested to increase the formation of ferrite with aligned second phase, thus reducing the proportion of AF present.

2.3.4.7 Titanium

Titanium has been reported to be among the most favourable alloying additions to weld metal for the formation of AF. This has been suggested to be a result of the formation of titanium oxides on the surface of NMIs that serve as nucleation sides for AF. Evans and Baily [90] reported that 15 ppm of titanium in the flux of a rutile electrode will produce a weld microstructure dominated by AF. However, it must be noted that in order for titanium to be effective, a sufficient quantity of manganese content in the weld metal is also required. Evans [90] reported that, for a weld with 1.4–1.8 wt% manganese, 30 ppm of titanium is required. In addition to the promotion of AF in the weld metal, titanium has been shown to increase the strength of the weld metal while slightly reducing ductility.

2.3.4.8 Aluminium

Being a strong oxidising agent, aluminium has a stronger affinity for oxygen than titanium or manganese and will therefore affect the formation of oxides that serve as nucleation sites [55]. However, aluminium's effect depends on the oxygen potential of the weld metal. At high oxygen concentrations aluminium's effect will be low; the converse is also true. Aluminium in low quantities favours the formation of GBF and AF, but as aluminium content increases, microstructures tend to be upper bainite, which increases hardenability, reduces the formation of AF and affects weld metal toughness [90, 92]

2.3.4.9 Oxygen

Oxygen plays a critical role in the formation of weld metal microstructure. Low oxygen content favours the formation of bainite, whereas high oxygen content favours the formation of WF. For the optimal formation of AF, David and Garland [59] reported that 0.03–0.06 wt% oxygen is required, while Potapov [94] suggested a narrower range of 0.02–0.035 wt% of oxygen for optimal weld metal mechanical properties. To manipulate the net oxygen content, de-oxidants are added to ensure that the desired microstructural transformation and consequent microstructural properties are obtained.

2.3.4.10 Sulphur and Phosphorus

Sulphur and phosphorus are regarded as impurities, as they negatively affect weld metal toughness. An increase in sulphur content decreases the proportion of AF in favour of ferrite with aligned second phase, which results in a deterioration of toughness. In addition, an increase in sulphur has been reported to reduce ductility [95].

Table 1: Effects of alloying additions on weld metal properties.

Element	Wt%	Alloying Consequence
C	0.03–0.10	• Matrix strengthening by precipitation
Mn	1.6–2.0	• Delaying austenite decomposition during accelerated cooling • Substitutionally strengthening effect • Decreases ductile to brittle transformation temperature • Critical in the formation of fine-grained lower bainite
Si	< 0.6	• Solid solution strengthening resulting in increase in strength
Nb	0.03–0.06	• Reduces temperature range in which recrystallisation is possible between rolling passes • Retards recrystallisation and inhibits austenite grain growth, which improves strength and toughness by grain refinement
Ti	0.005–0.03	• Grain refinement by suppressing the coarsening of austenite grains (TiN formation) • Strong ferrite strengthener • Combined with free Ni to avoid detrimental effect of free Ni on hardenability
Ni	0.2–1.0	• Improves low temperature toughness without impairing weldability • Forms less hardened microstructural constituents than Mg and Mo that are detrimental to low temperature toughness
V	0.03–0.08	• Leads to precipitation strengthening during tempering treatment • Strong ferrite strengthener
Mo	0.2–0.6	• Improves hardenability and thus promotes the formation of the desired lower bainite microstructure

2.3.5 **Austenite Grain Size and Martensite Start Temperature**

The austenite grain size and martensitic start temperature depend on the alloying constituents and significantly affect the resulting weld metal microstructure. Bhadeshia and Svenson [57] suggested the following relationship between austenite grain size and alloying elements:

Equation 2-1: Prediction of columnar austenite grain size [57].

$$L(\mu m) = 64.5 - 445.8C + 139Si + 7.6Mn + 16HI,$$

where:

L = predicted columnar austenite grain size,
C = weight percent carbon,
Si = weight percent silicon,
Mn = weight percent Manganese and
HI = heat input in kJ/mm.

As the equation suggests, a change in carbon, silicon or manganese will alter the prior austenite grain size, as will a change in the net heat input. However, excessive alloying prevents the formation of allotriomorphic ferrite, which may lead to impurities' segregating to the grain boundaries, resulting in intergranular fracture at the columnar austenite grain boundaries.

The formation of martensite may begin over a wide temperature range (from 500 °C to below room temperature), depending on the elemental constituents [57]. Rapid cooling is associated with the formation of martensite, as this suppresses the higher temperature diffusion controlled formation of ferrite, pearlite and bainite. Increasing the alloying content generally corresponds to lowering the martensitic start temperature, which implies that higher-alloyed steels will require a less steep cooling rate to increase the formation of martensite. In addition, Yang and Bhadeshia [96] have shown that a decrease in martensite start temperature leads to a reduction in austenite grain size. It has been suggested, based on these observations, that alloy content will affect the austenite grain size and the martensitic start temperature [97].

2.3.6 Martensite Start Temperature and Hydrogen

In addition to the effect on mechanical properties of the weld metal, weld metal microstructure influences the migration of hydrogen through the weld and its subsequent susceptibility to HACC. The solubility and permeability of different microstructures depends on their crystal structure.

Hydrogen is highly soluble in austenite as it has a face-centred cubic structure. Ferrite, on the other hand, has a body-centred cubic structure with a significantly higher hydrogen diffusion coefficient but lower solubility than austenite [98]. The differences in solubility and diffusion coefficients facilitate the non-uniform distribution of hydrogen across the weld [35]. It therefore stands to reason that a change in the alloy composition of the parent material

influences the transformation temperatures of the HAZ and the weld metal, changing the decomposition behaviour of austenite. This influences the distribution of hydrogen, which in turn influences the location of defects like hydrogen cracks.

Granjon [33] and Olson [43] have extensively discussed the distribution of hydrogen in low-alloy steels during phase transformations. Olson [43] reports that when the austenite-martensite transformation occurs in the HAZ at a higher temperature than the weld metal, the weld metal acts as a hydrogen sink; excess hydrogen may accumulate in the weld metal, promoting cracking. However, if the transformation occurs at a higher temperature in the weld metal than in the HAZ, hydrogen will accumulate under the fusion line. Olson [99] illustrates this relationship with the following equation.

Equation 2-2: Martensitic start temperature [99].

$$\Delta M_s = M_{WM} - M_{HAZ},$$

where

ΔM_s = change in martensitic start temperature

M_{WM} = martensitic start temperature weld metal

M_{HAZ} = martensitic start temperature HAZ

Case (a) if $\Delta M_s > 0$ hydrogen will accumulate in the parent metal HAZ

Case (b) if $\Delta M_s < 0$ hydrogen will accumulate in the weld metal

The consequence of alloying conditions on the susceptibility of a weldment to hydrogen cracking thus becomes apparent. Olson [100] aptly illustrates the relationship by use of a typically overmatched weldment. An overmatched weld has a higher alloying content, resulting in a lower transformation temperature than the parent plate, so the austenite phase retains a high level of hydrogen, which is available during the austenite transformation into ferrite. Hence, the probability of weld metal hydrogen cracking is greater.

2.3.7 **Concluding Remarks**

Alloying addition influences the weld metal microstructure and mechanical properties. The complex interrelationship between alloying elements and the effect of welding parameters has been researched extensively, both empirically and through metallurgical modelling. To understand the role that weld metal chemistry plays in the resistance to defects more fully, the role of alloying elements on the resulting weld metal properties and microstructure has been

briefly discussed. The relationship between austenite grain size and martensitic start temperature has been outlined and the role of alloying content in the distribution of hydrogen has been explored. From this review, it is concluded that weld metal alloying content plays a role in the susceptibility of a weld to HACC.

2.4 The Role of Hydrogen in HACC

2.4.1 Introduction of Hydrogen into a Weld

Hydrogen can be introduced into the weld from numerous sources [4, 5, 32, 101]: moisture in the flux and atmosphere, hydrocarbon-based contaminants such as oil or grease on the surface of the joint being welded or even hydrogen in the welding electrode itself. The energy generated in the plasma arc column facilitates the dissociation of diatomic hydrogen into monatomic hydrogen, which can be readily adsorbed by the molten metal [102-105]. Monatomic hydrogen may be positively charged, but when retained as a solute during solidification, its charge is neutralised by free electrons in the metal [106]. This process of neutralisation changes the electronic structure of the host metal, consequently changing the cohesive forces between metal atoms. This change is believed to be the root cause of brittle fracture [102]. Unlike diatomic hydrogen, the dissociated hydrogen atoms are small enough to diffuse into the metal lattice [107]. Their distribution is driven thermodynamically, where hydrogen migrates to energetically favourable areas within a weldment's microstructure (voids, NMIs and grain boundaries). It is this process of migration and subsequent interaction that is believed to be the basis for HACC [102, 108].

Troiano [109] was the first to postulate that dissolved hydrogen migrates to areas of high triaxial stress and results in an abnormal concentration of hydrogen in stressed regions. Li et al. [110] demonstrated that, from a thermodynamic perspective under equilibrium conditions, hydrogen will concentrate in a region subject to tensile stresses. Their hypotheses suggested that an increase in stress lowers chemical potential, creating a possible imbalance that the migration of hydrogen serves to bring back into equilibrium. This process of diffusion driven by chemical potential can be described by Fick's law: to achieve equilibrium, atomic hydrogen diffuses to areas of high stress as they have lower chemical energy states. Under certain circumstances, hydrogen will become trapped in the plastic strain field around discontinuities.

2.4.2 Solubility of Hydrogen in a Weld

The general solubility of diatomic gases in liquid metals is described by Sieverts' law [24], which defines the solubility of hydrogen in liquid steel as proportional to the square root of the partial pressure of the diatomic gas above the melt for an isothermal closed system in equilibrium concentration. In the absence of an electric arc, Sieverts' law is sufficient to describe the solubility of diatomic hydrogen and can be used to calculate the solubility limit of hydrogen gas in a molten weld pool.

However, there are suggestions in the literature [111-113] that Sieverts' law does not consider the dissolution of monatomic hydrogen and ionisation of hydrogen in welding arcs and therefore underestimates the proportion of hydrogen in the molten metal. In addition, it has been shown [112] that when liquid metal is in contact with arc plasma the solubility of diatomic gas is significantly higher that than predicted by Sieverts' law. Gedeon's [112] model takes into account the effect of arc plasma on hydrogen solubility, the disassociation of diatomic hydrogen into monatomic hydrogen and the dissolution of monatomic hydrogen in the weld pool. The model is based on the assumption that the temperature of the plasma is sufficient to cause disassociation of diatomic hydrogen and the adsorption of hydrogen that takes place at the liquid metal interface. Gedeon's model implies that the majority of monatomic absorption takes place at the cooler edge of the weld pool, closer to the fusion line [24, 111]. This is in direct contrast to Sieverts' law, which suggests that absorption is highest in the high-temperature region of the weld pool directly under the arc.

Figure 8 illustrates the solubility patterns of hydrogen as a function of partial pressure and temperature for both Gedeon's and Sieverts' models. The former suggests that hydrogen solubility is a linear function of partial pressure for a given temperature, and decreases monotonically with an increase in reaction temperature.

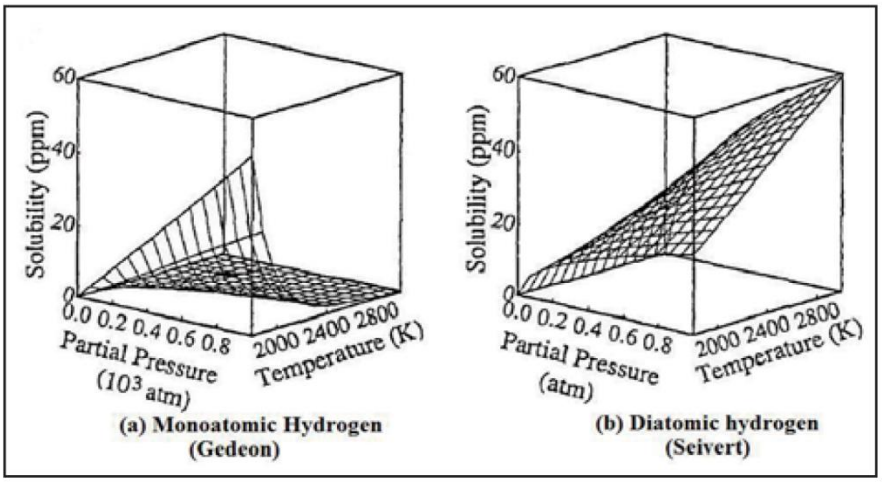

Figure 8: A comparison of the solubility distribution of hydrogen in the weld pool per Gedeon's (a) and Sieverts' (b) models.

Mundra et al. [114] provide sufficient experimental and analytical evidence to support Gedeon's model.

2.4.3 Solubility of Hydrogen in Phases of Steel

Hydrogen solubility in steel depends on temperature, pressure and the crystal structure of constituent phases in steels [55, 57, 115]. Hydrogen solubility increases when ferrite (α) transforms to austenite (γ) and drops when ferrite (α) transforms to delta ferrite (δ). Solubility increases with temperature, with a maximum solubility of 34 wppm reported at 1600 °C at 1 atm (i.e., in liquid phase) [116, 117]. When cooled under non-equilibrium conditions, hydrogen retained in the steel can be above the solubility limit.

2.4.4 Migration of Hydrogen through a Weld

The diffusion of the hydrogen absorbed into the weld pool is described by Fick's 2nd law (Equation 2-3), assuming that the concentration of hydrogen does not change with respect to time:

Equation 2-3: Fick's 2nd law.

$$\frac{\partial C}{\partial t} = D\nabla^2 C,$$

where:

D = Lattice diffusivity of hydrogen
C = Concentration of hydrogen diffusing in steel
∇^2 = Laplace Operator

Equation 2-4: Laplace operator employed in Fick's law.

$$\nabla^2 = \frac{\partial^2}{\partial x^2} + \frac{\partial^2}{\partial y^2} + \frac{\partial^2}{\partial z^2}$$

The assumption of a steady state implies that Fick's law does not consider hydrogen trapping effects or that the gradient and local concentration of hydrogen will decrease with time, but it has been demonstrated to produce a reasonable approximation when small elements of the diffusing material are considered. In reality, however, hydrogen diffusion through a weld is influenced by numerous factors that have been categorised by Böllinghaus et al. [98] into three effects: trapping effects, surface effects and liquid state effects. Diffusion of supersaturated hydrogen is primarily impeded by the presence of traps in the crystal structure.

2.4.5 Hydrogen Traps

Hydrogen is irregularly distributed through a steel weld deposit as a result of the inhomogeneity within the weld and the attractive forces these inhomogeneities exert on mobile hydrogen atoms. Long-range interactions relative to atomic spacing depend on the elastic strain field, while short-range interactions are chemical in nature and are described in terms of the hydrogen atoms' ability to bind to a defect [118]. Hydrogen has a tendency to reside in atomic and microstructural imperfections such as vacancies, voids, dislocations, grain boundaries and second-phase particles. This phenomenon is referred to as hydrogen trapping [104, 119, 120]. As hydrogen traps prevent the diffusion of mobile hydrogen, the residual hydrogen content after the process of effusion has ceased is believed to be a function of the number and types of hydrogen traps present. Hydrogen traps are classified by their ability to trap hydrogen atoms, which is a function of binding energy [55, 106, 121-123]. Table 2 summarises the classification of the three categories of traps and the release temperatures associated with each category.

Table 2: Classification of hydrogen traps [104, 119, 120].

Hydrogen Trap Classification	Examples	Binding Energy (kJ/mol)	Release Temperature (^{O}C)
Very Reversible	Interstitial lattice sites, elastic stress fields, dislocations	7.7	
Reversible	Substitutional atoms, grain boundaries, dislocations, ferrite/carbide and ferrite/cementite interfaces, tempered martensite	17-36	112-270

Irreversible	Microvoids , Fe_2O_3, Fe_3O_4, MnS, Al_2O_3 , TiC, Ce_2O_3	35-112	305-750

On one end of the classification spectrum, very reversible hydrogen traps house and provide little resistance to mobile hydrogen, while traps with high binding energy house and are commonly referred to as strong traps. Reversible traps lie in the middle of the classification spectrum and have a dichotomous role, acting as both hydrogen sinks and hydrogen sources.

Depending on trap energy, the hydrogen residing in the trap may increase or decrease the solubility and thus the apparent diffusivity of hydrogen [100, 124]. Hydrogen traps can affect resistance to HACC. Pressouyre and Bernstine [119] suggested that high-density traps with high binding energies such as TiC particles that have activation energies in excess of 60 kJ/mol can delay HACC. Conversely, a low density of heterogeneously disturbed traps could accelerate the HACC process. As the reversible nature of hydrogen traps is associated with temperature, an increase in temperature can change an irreversible trap to a reversible trap [119].

The net hydrogen content in a weld will be the sum of the diffusible hydrogen, hydrogen accumulated around stress concentrators and trapped hydrogen. The density of trapping sites will influence the maximum trapped hydrogen concentration. As a saturated hydrogen trap is not expected to accommodate any more diffusible hydrogen [125], any additional hydrogen is free to diffuse throughout the microstructure, so hydrogen traps can be used to limit the accumulation of hydrogen at potential initiation sites [122, 126] and inhibit the initiation of HACC.

Olson et al. [43] and Cwiek [113] suggest that hydrogen traps could be used to immobilise diffusible hydrogen and prevent it from reaching and accumulating at susceptible sites. The influence of traps has also been examined by Choo et al. [127] and Lee and Lee [128], whose findings agree with Oriani's [129] results that an increase in the volume and density of traps decreases the amount of hydrogen available for diffusion.

Pressouyre's [130] work, however, contradicts these results, suggesting that an excessive number of traps can actually accelerate the process of hydrogen cracking. Katano et al.'s [131] work on high-strength Cr-Mo steel provides evidence to suggest that hydrogen traps serve as sources for hydrogen at temperatures above 100 °C.

From these varied results what can be hypothesised with confidence is that the nature of the trap plays an important role in influencing the rate of hydrogen cracking. Irreversible traps with their high binding energy are more likely to inhibit the diffusion of hydrogen into susceptible regions. However, given the complexity required to engineer hydrogen traps to reduce susceptibility to hydrogen cracking, it is not surprising that the focus in terms of hydrogen has been on reducing the amount of hydrogen introduced into the weld and preventing the saturation of existing hydrogen traps [132]. Olson et al. [43] findings agree with Oriani [133] in that an increased volume of traps decreases the amount of hydrogen available for diffusion.

2.5 **Role of Stress**

The non-equilibrium contraction resulting from the thermal cycle experienced during cooling subjects a weld to conditions that promote the build-up of residual stresses [134, 135] and may subject the weld to reaction stresses. Residual stresses, which are in short-range equilibrium, arise as a result of inhomogeneous thermal gradients in the joint. Conversely, reaction stresses, which are long-range stresses, manifest themselves when free thermal shrinkage is prevented [135, 136]. Although hydrogen cracking in welds is generally associated with the presence of residual stresses [136, 137], the exact role of these stresses is still under contention, as there is no consensus as to the exact mechanism that governs hydrogen cracking. This is discussed in further detail in Section 2.6.

2.5.1.1 Initiation of Hydrogen Cracks

Although stress is considered to be the mechanical aspect that drives the propagation of hydrogen cracks, microscopic stresses within the weld are known to influence the local distribution of hydrogen and thus influence the susceptibility of initiation sites. Plastically deformed areas, form within a weldments as result of the welding thermal cycle. Within these areas, macroscopic stresses are known be non-uniformly distributed. Hydrogen cracks have been shown to propagate where microscopic stresses are higher due to concentrated plastic flow [138-142]. The loss of macroscopic ductility is the manifestation of extensive local plastic deformation.

As noted in Section 2.4.4, it has been suggested in the literature that, on a microscopic scale, hydrogen diffuses through a weld and concentrates at inhomogeneities within the weldment. The formation of dislocations during plastic deformation transports hydrogen to areas of high triaxial stress through dislocation movement. Beachem [143] and Sofronis [142] both propose

the hypothesis that hydrogen induces material degradation by intensifying local material deformation. Beachem [143] suggests that hydrogen diffuses into the metal lattice ahead of the crack tip and intensifies plastic deformation. However, more recent work suggests that crack propagation and hydrogen diffusion are a yoked phenomenon and result in intense shear bands [142, 144]. Sofronis [142] suggests that shear localisation combined with high hydrogen contraction leads to failure, as the material yields on a microscopic scale. This therefore links the decrease in macroscopic ductility with an increase in local microscopic plastic deformation.

Yurioka and Suzuki [32] suggest that hydrogen cracking in both the HAZ and the weld metal depend on the stress intensity factor at the crack tip. Extending the work of Karppi et al. [145], Gao and Cao [146] conclude that plastic deformation at the tip of a crack influences the concentration of hydrogen and thus is a pivotal component in inflecting the transportation and distribution of hydrogen. Gao and Cao [146] attribute the accumulation of hydrogen to the trapping effect of dislocations. These observations are supported by Liang et al. [147], Kuipers [148] and Sofronis [149].

2.5.1.2 Propagation of Hydrogen Cracks

Satoh [136] has shown that, in single-pass welds, reaction stresses play a primary role in increasing the risk of cracking in butt joints, whereas residual stresses play a secondary role. Restraint intensity (R_F) [32, 136, 150, 151] can be used to encapsulate the effect of stresses developed as a result of external restraint. R_F is defined as the force per unit length of a weld required to contract or expand by a unit length in the direction normal to the weld length [32]. Consequently, R_F increases as plate thickness increases. For a hydrogen crack to propagate, the dominant stress component needs to be perpendicular to the orientation of the crack itself. In the case of HAZ under bead root cracking, the transverse net stress across the weld throat is critical [152, 153].

2.6 **Hydrogen Assisted Cold Cracking Mechanisms**

Several reviews [154-156] on the phenomenon of hydrogen embrittlement (HE) conclude that residual stresses are the driving force in the development of HACC at room temperature. While several models have been proposed, none has yet been accepted by the broad scientific community; the most important theories advanced to describe HACC formation are described below.

2.6.1 Stress-Induced Pressure-Based Theories

The pressure theory postulated by Zapffe in 1941 [5, 34, 157] represents the oldest proposed mechanism for HE. According to Zapffe, atomic hydrogen diffuses and recombines to molecules in internal defects and then generates high internal pressure within those defects. If the precipitation of molecular hydrogen is sufficient, nucleation and growth of micro-cracks may occur at lower externally applied stress because of the assistance of hydrogen pressure in developing a crack from these defects, so the required stress to generate a crack in the solid with hydrogen is less than what is required without hydrogen. The presence of micro-cracks and voids in which the hydrogen pressure can reach critical values is necessary for the operation of this mechanism. However, many authors [158, 159] have shown that micro-cracks or cavities need not be present to initiate the embrittlement process, since macroscopic hydrogen cracks can nucleate from dislocation pileups under the influence of external stress.

2.6.2 Hydride Formation-Based Theories

Other theories have correlated HE with stress-induced hydride formation. Metal-hydrogen hydrides [160] may induce local strain by volume expansion of the metal lattice. The hydride formation model proposes that cracking occurs through the formation and cracking of hydrides at the crack tip, where the hydride stabilizes under the hydrostatic stress field. Hydrides usually possess a lower elastic modulus and larger molar volume than the metallic matrix. While no stable hydride of iron forms below 2 GPa hydrogen pressure, calculation suggests that saturation can occur at room temperature near the crack tip, permitting hydride formation. This suggests that the hydride formation model could apply to iron on an atomic scale [161]. The hydride theories require the presence of hydrides that form ahead of the crack tip when local hydrogen amounts exceed critical values.

2.6.3 Dislocation Mobility Enhancement Theories

Dislocation-based theories assume that hydrogen affects the motion of dislocations during plastic deformation. Hydrogen atoms are believed to accumulate locally around dislocations, thus forming Cottrell atmospheres that are dragged by the dislocations. The formation of Cottrell atmospheres is the result of the interaction of hydrogen with the tensile stress field adjacent to a dislocation.

At first, the Cottrell atmospheres were believed to reduce dislocation mobility [162], suggesting that brittle failure in hydrogenated specimens occurs because hydrogen increases

the energy barrier for the emission of dislocations ahead of the crack tip, reducing the amount of plastic deformation. Later, however, Beachem [155] experimentally observed in a wedge-loaded test specimen the change in fracture mode from intergranular (IG) to quasi-cleavage (QC) to microvoid coalescence (MVC) with increasing stress intensity factors and hydrogen concentration at the crack tip [155]; these results have since been confirmed by Oriani [133] and Gedeon [111]. As Figure 9 illustrates, the plastic deformation is greater with MVC than with QC or IG fracture modes. Observations of tear ridges and dimples on fracture surfaces of hydrogen-embrittled steels were associated with hydrogen enhancing dislocation movement.

The theory of slip softening due to enhanced dislocation mobility [163] assumes that the decrease of the barrier to dislocation movement with hydrogen results in greater flow stress and easier plastic deformation locally, which agrees with enhanced hydrogen evolution caused by plastically deforming steel [161]. The characteristic loss of ductility with HE is a macroscopic observation and does not preclude significant localised plasticity on a microscopic scale. Combining the stress intensity and hydrogen content defines the conditions needed for fracture, as illustrated by the critical stress intensity-hydrogen mapping concept shown in Figure 10. The energetically favourable IG process is thought to be pre-empted at high stress intensity factors by the kinetically faster MVC and QC processes. Moreover, the slower crack growth rates with IG permit hydrogen diffusion ahead of the crack tip, resulting in greater hydrogen amounts at the grain boundaries and creating more favourable conditions for grain boundary plasticity.

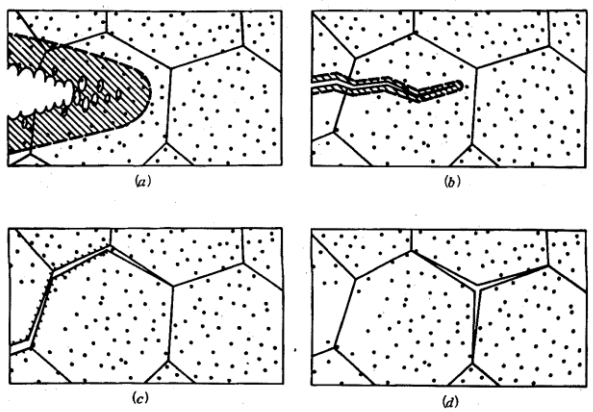

Figure 9**:** Schematic for (a) high, (b) intermediate and (c) low stress intensity factor of microscopic fracture modes: (a) MVC, (b) QC, (c) IG and (d) IG with the assistance of hydrogen pressure [163].

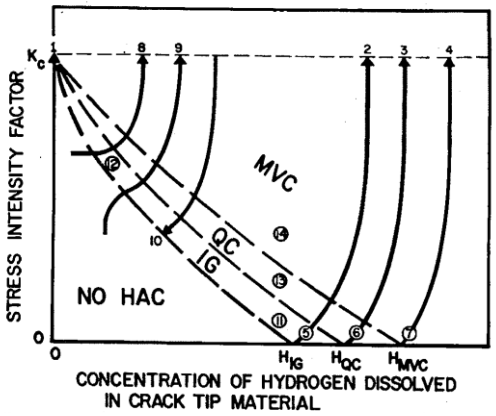

Figure 10: Critical stress intensity factor hydrogen concentration map, demarking regions for MVC, QC and IG fracture modes [163].

The concept of hydrogen's enhancing dislocation mobility was later revived by Lynch [164] and Birnbaum [165]. The slip, dimples and tear ridges on the fracture surface of nickel specimens tested in gaseous hydrogen environments demonstrate dislocation activity that suggests a crack growth due to localised plastic deformation [164]. Lynch first suggested that hydrogen shielding was restricted to the surface, while Birnbaum later showed that it can occur in the bulk. Following these theories, the hydrogen-enhanced localised plasticity (HELP) theory [165] was proposed to evaluate hydrogen cracking susceptibility and explain the effect of hydrogen on dislocation mobility. Hydrogen forms an atmosphere around the dislocation due to its elastic stress field; this atmosphere shields the dislocation by reducing the interaction energy between the dislocation and the obstacle. This facilitates dislocation movement (i.e. localised plastic deformation).

In order to effect dislocation mobility, the Cottrell atmospheres must follow the dislocations during metal straining. Dislocation velocity varies with the strain rate applied to the specimen, while the Cottrell atmospheres' velocity is limited by the diffusivity of hydrogen. The Cottrell atmospheres must be thermodynamically stable to accumulate locally, which means that the temperature must be below critical value.

2.6.4 **Adsorption Theories**

Surface adsorption theories assume that hydrogen adsorbed on the metal surface reduces the surface energy and consequently the strength and ductility of the material [160, 166, 167]. This is possibly because of the formation of a layer of hydrogen ions at the juvenile surface of a crack initiated in the metal bulk [168]. Adsorbed hydrogen may also force the metal atoms into orientations corresponding to the plane of least density and highest energy within the crystal lattice structure [162]. Building upon the analogy between liquid metal and HE,

Lynch [164] suggests that HACC occurs through an adsorption-induced localised-slip process.

Figure 11 confirms the linear relationship between grain size and rupture stress, so the easy crack nucleation and growth in hydrogen-charged specimens may be due to decreases in binding forces caused by hydrogen dissolution. While grain size may be a major factor in the extent of embrittlement (assuming a role is played by the grain boundaries), HE has also been found in single crystals [166].

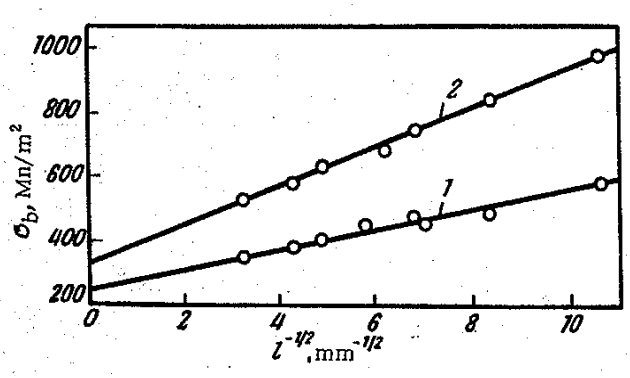

Figure 11: Rupture stress as a function of the inverse of the square root of the grain size at 291 °K for a low-carbon steel (1) hydrogenated and (2) hydrogen-free specimens [166].

Another approach is based on the Griffith criterion. Petch [167] proposed that the HE mechanism could be supplied by hydrogen adsorption on a Griffith crack surface; if the surface tension drops with hydrogen contamination, the fracture stress will drop as well. Moreover, the kinetics relating to the hydrogen adsorption rate at the freshly created crack surfaces explains the delay and discontinuous growth characteristics of HE. Brittle failure may be due to some factors that reduce the work of plastic deformation during crack nucleation and propagation rather than a deterioration of the surface energy. The plastic deformation is due to the nucleation and movement of dislocations emitted at the crack tip; for example, ductile crack growth involves initiation, growth and coalescence of voids ahead of a pre-existing crack tip. Although some experimental evidence does support the adsorption theory, there is also evidence against it: the theory underestimates the work needed for fracture; it cannot account for the discontinuous crack propagation characteristic of HACC; and it cannot explain why oxygen, with a greater heat of adsorption, not only fails to promote cracking but also stops the hydrogen embrittling effect [161].

2.6.5 Hydrogen-Induced Decohesion Theories

Hydrogen embrittlement may arise from the development of localised tensile stress regions into the material. Hydrogen atoms in interstitial lattice sites [32] may induce local strain by volume expansion of the metal lattice [162]; the interatomic dilation of the lattice should result in a decrease in the atomic cohesive strength.

Trapping refers to the fact that interstitial atoms often find interstices associated with lattice imperfections to be energetically preferable to normal sites. This leads to a requirement for additional energy, referred to as the binding energy, to leave the site. Trapping causes a delay of diffusion of interstitial atoms near these sites. Hydrogen traps may be interstitials, vacancies or dislocations [169]. The role of dislocations in HE and trapping is poorly understood, with dislocations appearing to be both effective hydrogen traps and means of hydrogen transportation.

Oriani [104] developed a theoretical approach to account for trapping sites' effect on hydrogen diffusion behaviour in steel. By applying this theory to experimental data from the literature, Oriani found characteristics in trapping sites that are in the range of 4–8 kcal/mol H in the different experiments. With these data, Oriani concluded that the increase amount of hydrogen absorption with cold work is due to the increasing dislocation and micro-crack surface densities.

The decohesion theory [105, 109, 170] proposes that dissolved hydrogen lowers the maximum cohesive force between the atoms of the alloy in the iron lattice, at grain boundaries and at interfaces. This occurs ahead of the crack tip, where hydrogen accumulates in the triaxial tensile region under the driving force arising from stress potential gradients. The reason for the cohesion's lowering along the grain boundaries enriched by impurity segregation remains poorly understood. It has been shown experimentally that the impurities not only segregate to the grain boundaries but also chemically react with the metallic components, which suggests that electrons and their bonding characteristics are responsible for the embrittling effect. In other words, in this view the electronic structure of the involved elements and its arrangement after the chemical reaction must be considered to understand the cohesion reduction.

Surface adsorption theories [171] assume that hydrogen present on metal surfaces reduces the metal surface energy [160, 166], and will thus decrease the critical stress when considering a Griffith crack. Griffith's criterion was developed to explain the failure of brittle materials. The

application of the adsorption theory to HACC remains in question because crack initiation and propagation have been assumed to take place through rupture of material within a limited distance ahead of the crack tip in the area of maximum stresses and strains that are normal in the crack plane. Hence, the energy that is required for fracture in the material is associated almost entirely with plastic deformation; changes in surface energy should not be significant. Other disagreements with this model have been reported, such as an underestimation of the required energy for creating new fracture surfaces and non-consideration of continuous crack propagation processes. Thus, the adsorption theory has not proven quite adequate enough to account for the dynamic stages of crack propagation.

2.6.6 Hydrogen Trapping-Based Theories

The hydrogen trapping theory was originally developed by Oriani [104] to explain the slower apparent diffusion of hydrogen in ferritic steels compared to the lattice diffusion of hydrogen at temperatures below 200 °C. The important view that dislocation transport and trapping are competitive processes was pioneered by Tien [172], who used a kinetic model to show that hydrogen transportation as Cottrell atmosphere bound to dislocation is faster than lattice diffusion.

When a dislocation with a hydrogen cloud intersects an inclusion (Figure 12), the amount of hydrogen stripped off is that which is distributed along the dislocation line that intersects the inclusion. The diffusion along the dislocation restores cloud uniformity as the dislocation moves away, after which the hydrogen lattice diffusion from inclusion to the matrix distributes hydrogen. Tien [172] calculated that an increase in stacking fault energy reduces hydrogen transportation and small inclusions (< 1 μm) rather than large inclusions play an essential role in hydrogen-assisted cracking.

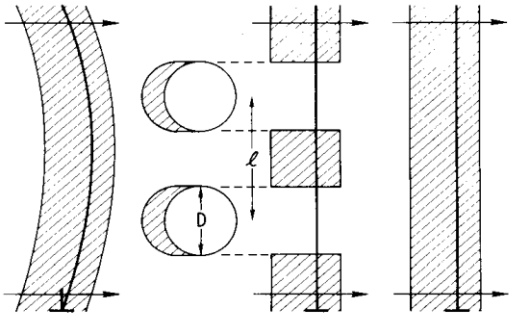

Figure 12: Schematic of moving dislocation with hydrogen cloud stripped off at particles of effective size D and spacing l. [172].

Hydrogen traps can be of various natures; among the defects where hydrogen may accumulate, there are trap sites on the surface and subsurface, edge dislocations, grain boundaries and vacancies [120]. Konstantarakis [173] has proposed that the dispersion of inclusions will affect the cracking susceptibility of high-strength steel weld metal. A fine dispersion of inclusion increases hydrogen trapping by increasing the surface of the traps. The crack is assumed to stop when it reaches the outside of the plastic zone previously developed ahead of the crack tip and with low local hydrogen content. Diffusion of hydrogen will be impeded by trapping such as titanium and titanium-carbon interfaces [108]. Moving dislocations transport hydrogen faster than can be achieved by diffusive transport [108]. In steels, voids form readily by interfacial decohesion around inclusions, by cracking of second phase particles and by high stresses produced by plastic incompatibility in regions between particles [108].

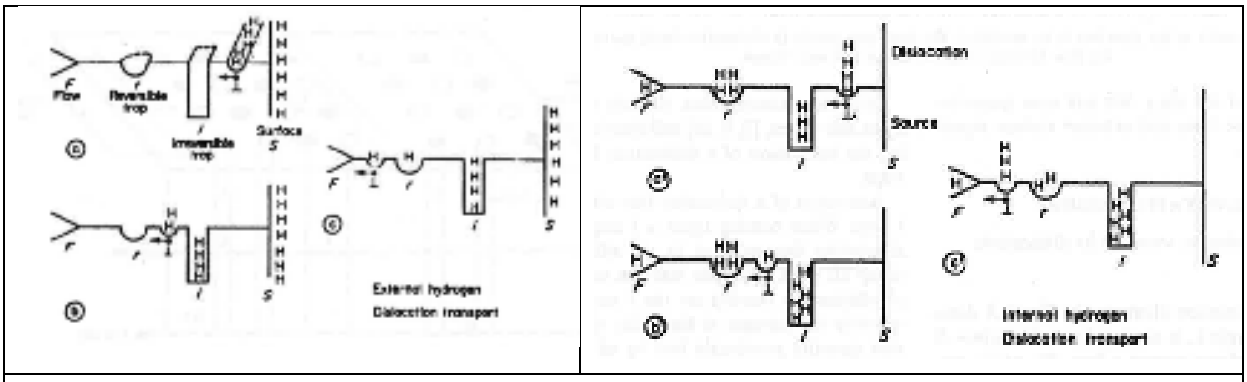

Figure 13: Hydrogen transportation by dislocation to flaw when (a, b, c) external and (a', b', c') internal hydrogen is involved [174].

The embrittling index was taken as the minimum hydrogen concentration in a weld metal to generate susceptibility to HACC [108]. Using this index, it was found that HACC susceptibility is lower in microstructures containing continuous GBF and martensite austenite carbide with retained austenite as opposed to AF, and a high density of fine and homogeneously dispersed inclusions as opposed to large inclusions. When investigating the effect of hydrogen on fracture mode, Oriani [108] found that microstructures composed of continuous GBF and AF, discontinuous GBF and AF and coarse AF change the fracture mode from MVC to IG with increasing hydrogen. These results, however, contradict Beachem's work [155].

2.6.7 **Concluding Remarks**

From the literature reviewed, it is evident that there is no universally accepted mechanism that can be used to describe and substantiate experimentally the cold cracking phenomenon.

However, what is universally accepted is that, regardless of the theories postulated to describe the phenomenon, a critical concentration of hydrogen in a susceptible microstructure subject to a mechanical driving force is the foundation for all theories. It may be argued that as experiments are devised to explore the micromechanical aspects of HACC, the industrial practicality of the generated results may be lost, as the condition limitations imposed by laboratory testing are not physically achievable when welding in the field. Hence, when investigating the phenomenon with the underlying aim of proposing a strategy to predict and eventually to mitigate cold cracking, the conditions tested must to a large degree emulate what would be encountered in the field. A mechanism validated by tests under these conditions would ensure a true representation of the field-encountered phenomenon.

2.7 **Weldability Tests**

A variety of weldability tests have been specifically designed to generate HACC by promoting special restraint conditions in the weldment, as indicated in the numerous reviews on the subject [5, 28, 34, 175, 176]. Weldability testing techniques can be classified into two categories: full-scale and small-scale. This section discusses the characteristics and strengths of the tests within these two categories.

2.7.1 Full-Scale Weldability Tests

Full-scale testing has been adopted in an effort to bypass the difficulties inherent in predicting field behaviour from small-scale laboratory tests. This testing consists of welding pipes using the intended construction procedure and submitting the root pass weld after completion to a constraint similar to the one encountered during pipe lifting in the field. The stresses generated by the lifting operation depend in part on pipe diameter, lifting point and lifting height [177]. The lifting-originated stress may be applied either by simply lifting one end of the pipe with the pipe's own weight providing the bending stresses [177] or by using a four-point bending frame with the bending force supplied at the outboard load points by two groups of three hydraulic jacks acting on the pipe through contoured saddles (Figure 14) [178]. However, due to the complexity of full-scale tests, the vast dimensions and a lack of standardisation, smaller-scale restraint cracking tests have been developed to evaluate weldability in laboratories, limiting the full-scale weldability tests to a validation role using in-field welding procedures. The in-field procedures that can be investigated are the effect of clamp release and lifting operations during pipeline construction on stresses generated in girth welds [14].

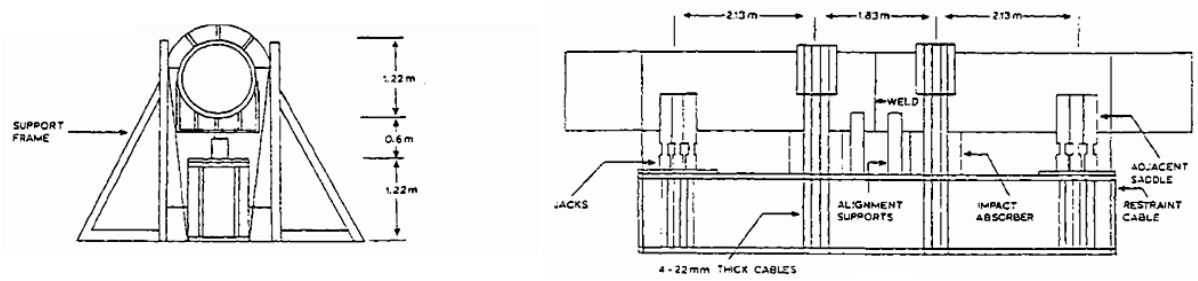

Figure 14: Experimental set-up of full-scale pipeline weldability test [178].

2.7.2 Small-Scale Weldability Tests

Small-scale weldability tests for laboratory investigations are either extrinsic (involving external loading) or intrinsic (self-restrained). Extrinsic weldability tests promote cracking by external loading of the specimen and seek to isolate metallurgical factors from mechanical ones by applying a controlled restraint, with the weldability being directly related to the applied stress (crack versus no-crack) for a given alloy and welding condition. The delay between the load application and the welding completion could affect, among other parameters, the location of the crack (Figure 15) and thus should be explicitly defined within the test procedure. On the other hand, intrinsic weldability tests are designed so that cracking is promoted by the stresses induced from thermal contraction and solidification shrinkage of the welded region against the resistance of the surrounding parts of the test piece itself or of an external restraint jig. However, the complex interactions involved make it difficult to isolate the metallurgical from the mechanical factors. In addition to the differences in stress distribution, the stress history follows two different paths, as indicated by Figure 16, in which the stress evolution [5, 32, 179] is superimposed on the Beachem diagram. As time passes, hydrogen accumulates at the crack tip until the attainment of a critical hydrogen level, at which point the crack propagates. In an intrinsic test, residual stress is relaxed and stress intensity factor decreases with crack growth, eventually arresting the crack. However, in an extrinsic test, the constant loading value generates an increase in stress intensity over time as the crack grows. The drop of hydrogen content at the crack tip follows the lower hydrogen amount required for crack growth at higher stress intensity factors or the effusion of hydrogen from the weld.

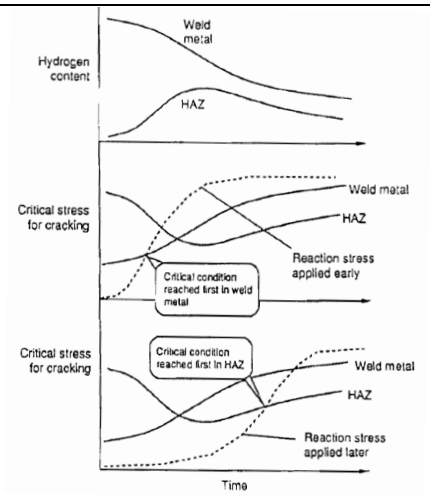

Figure 15: Model for determining crack location [34].

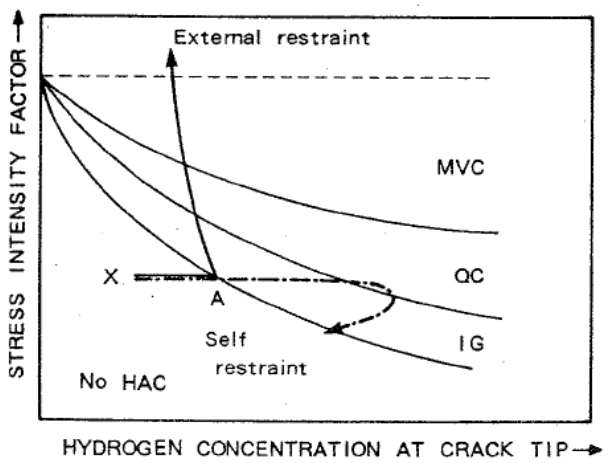

Figure 16: Superposition on Beachem diagram of stress history at crack tip (indicated by lines with arrows) for external loading and self-restraint cracking tests [32].

2.7.3 Extrinsic Weldability Tests

2.7.3.1 Implant Test

The implant test [34, 45, 180-182] investigates the formation of HACC in the HAZ. It consists of depositing a butt weld on a plate in which a cylindrical sample, referred to as an implant, is inserted and pre-placed on the weld path with the notch of the implant located in the HAZ (Figure 17). This test imposes a stress independent of the welding procedure, but has the major drawback of difficulty in locating the notch properly so that it fails at the same location within the HAZ for each test in a series. The ability to position the notch precisely within the HAZ is improved by replacing the single circumferential notch of the implant with a helical notch so that the entire HAZ is traversed by the helical notch [182]. The failure is then initiated in the most crack-susceptible microstructure. This test was successfully applied to investigate the HAZHACC susceptibility of SMAW metals deposited by cellulosic and low hydrogen consumables on HSLA, including X65 and X70 pipeline steels [45, 179, 181]. Using this test, the relationship between the applied stress and time to fracture can be established for a set of welding conditions, quantifying the critical stress below which no crack occurs (Figure 18). When equipped with acoustic emission sensors, the crack is shown to grow in an intermittent manner in the HAZ (Figure 19) [179], suggesting that hydrogen transport to the crack tip is a critical requirement for HACC propagation. This test was also successful in establishing the relationship between fracture mode, stress intensity factor and hydrogen content (Figure 20) [163], revealing a new zone at high hydrogen contents not specified in the similar map first proposed by Beachem. This test is not suitable for

investigating the formation of HACC in the weld metal but does work in the HAZ of pipeline girth welds.

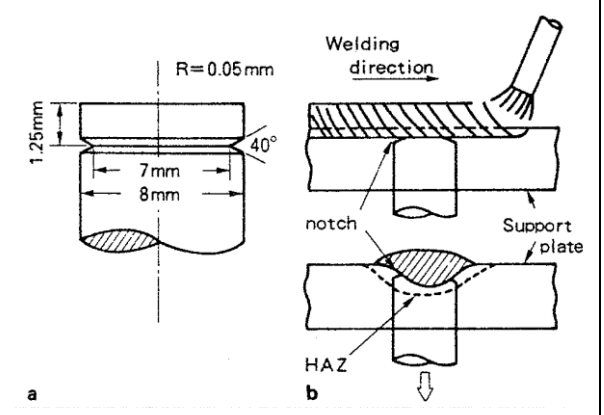

Figure 17: Experimental set-up of (a) implant and (b) implant test [179].

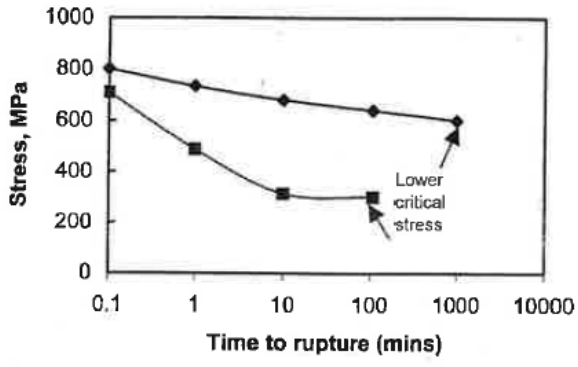

Figure 18: Stress to fracture-time to failure map for two different materials tested using the implant test [177].

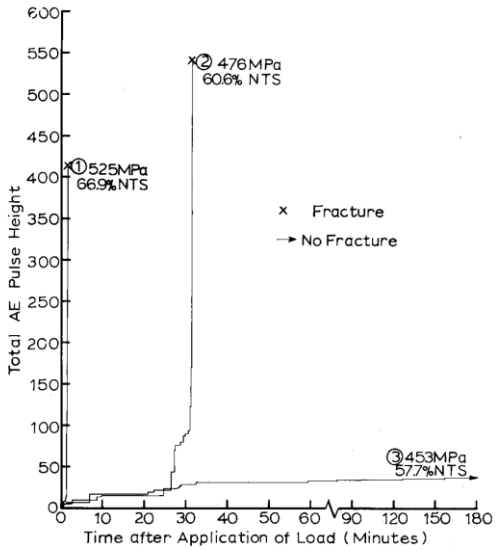

Figure 19: Intermittent crack growth in implant test as measured by acoustic emission for a given percentage of the notch tensile strength [179].

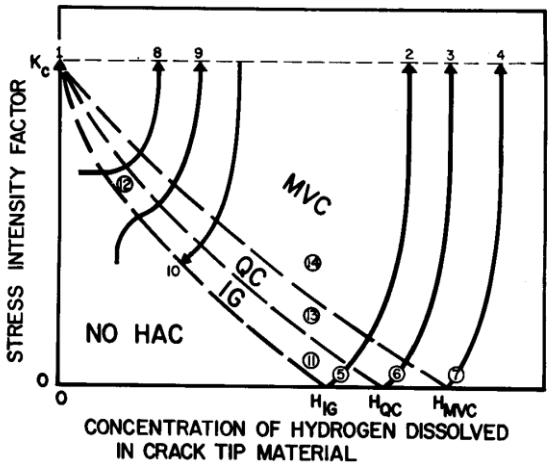

Figure 20: Suggested interrelationship between stress intensity factor, dissolved hydrogen content and fracture mode: IG, QC and MVC [163].

2.7.3.2 The Bending Test

The bending test was introduced to investigate the crack susceptibility of completed welds [34, 183-185], especially of pipeline girth welds [34, 184, 185]. The procedure consists of subjecting the weld metal, after welding has been completed, to controlled amounts of strain either by bending the specimen around a curved mandrel or forcing it to conform to the surface radius of a die block (Figure 21). The specimen is bent around the curved mandrel whose axis is parallel to the welding direction. The weld specimen can be kept at low temperatures to immobilize hydrogen prior to testing [34] or machined from the initial weld 24 hours after weld completion [184, 185]. The latter method consists of using the bending

test as an opener of pre-existing cracks to facilitate their observation and enumeration. The bending is carried out at room temperature and slow loading rates (strain rates) so as to maximize the embrittling effects of hydrogen. The initiation of a significant number of cracks is indicated by a load drop on the load-deflection curve. The total deflection at the first significant load drop [34] or a crack-length criterion [185] is taken as the crack sensitivity index. Using crack-length criteria as a weldability index, this test has been successful in ranking the cracking susceptibility of X70 pipeline girth welds performed with cellulosic E6010, E8010 and E9010 welding consumables under various welding conditions [184, 185]. However, it has several drawbacks. The inhomogeneity of the applied strain at various weld thicknesses makes it difficult to quantify of the critical conditions to promote cracking.

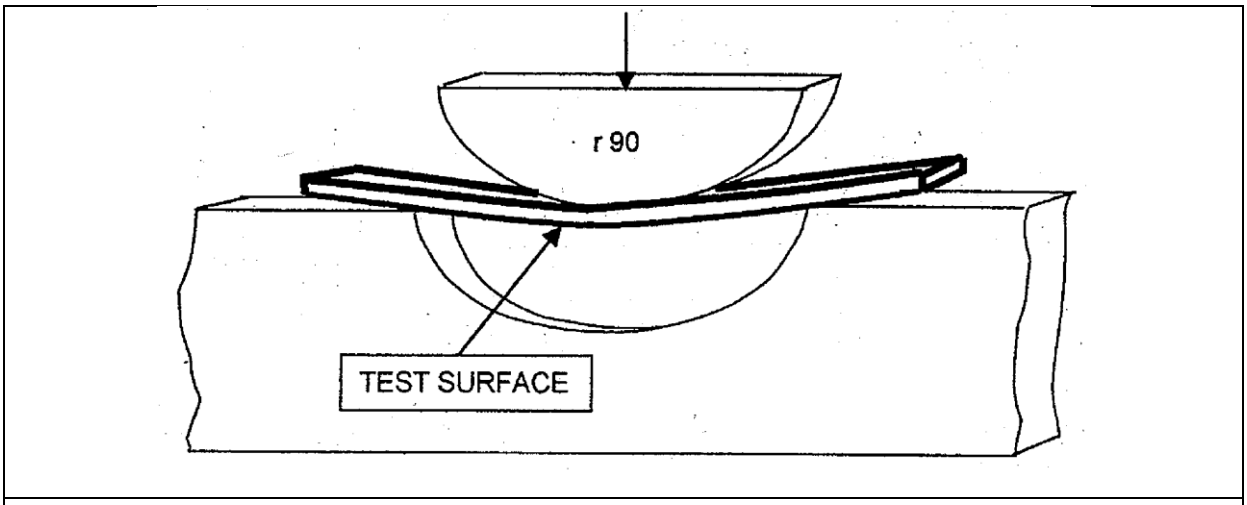

Figure 21: Experimental set-up of bending weldability test [184].

2.7.3.3 The Transverse Controlled Loading Test

Weldability tests have been developed to investigate the conditions for crack formation through the application of a controlled load transverse to the welding direction. The tensile restraint cracking (TRC) test, illustrated in the top right corner of Figure 22, consists of depositing a butt weld between two plates and then applying a constant load transverse to the welding direction in order to provide the critical stress at the onset of HACC [32]. This test examines root cracking in butt welds and the relationship between stress and time to failure (Figure 23). Other extrinsic weldability tests have been designed to promote a controlled strain across the weld metal. In the rigid restraint cracking (RRC) test (Figure 23), the transverse load is adjusted as the weld cools down in order to maintain a predefined local strain across the weld as measured through an extensometer, resulting in a quantifiable stiffness or restraint [1, 5]. The RRC test (Figure 23) was used to investigate the cracking susceptibility of weld metals deposited by cellulosic E6010, E8010 and E9010 consumables

in grooves of X70 and X80 pipeline steels with both symmetric Y and single-bevel joints, with an estimated R_F of 64 GPa for a 10 mm-thick X70 base metal [1]. The RRC provides the critical restraint length as the test result while the TRC provides the critical restraint stress. A good correlation exists between results generated by TRC and RRC, where the critical restraint length has been converted into critical stress [32]. Despite different stress histories, the RRC and TRC both give similar stress time to fracture curves, so stress might be the main driving force behind HACC.

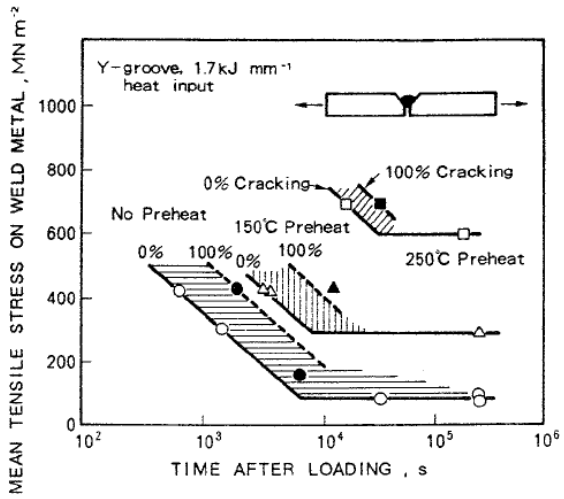

Figure 22: Stress to fracture time to failure relationship measured using the TRC test for a 700 MN.m-2 yield strength steel [32].

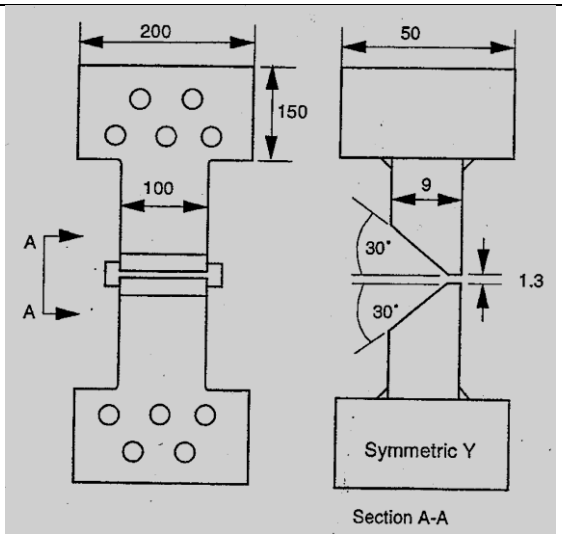

Figure 23: Experimental set-up of the RRC test with symmetric Y-groove [1].

2.7.4 **Intrinsic Weldability Tests**

2.7.4.1 Multi-Pass Gap-Filling Weldability Tests

Multi-pass gap-filling weldability tests are designed to investigate the cracking susceptibility in multi-pass welds. The cracking may be enhanced by accelerating the cooling rate of the weld metal by filling a gap between two water-cooled ducts (Figure 24). The window-type cruciform restraint test [32] consists of an inserted plate rigidly welded, in which the tensile residual stresses act in the short transverse direction initiating lamellar tears at the mid-thickness of the inserted plate (Figure 25). In particular, a type of lamellar tear that begins at the weld metal toe is believed to be a type of HACC. The Cranfield test [32] consists of filling the gap between two plates at a 45° relative angle, with the tensile stresses arising at the root from the angular distortion brought about during multi-pass welding (Figure 26). The stress distribution favours root cracking that could grow into a lamellar tear. These tests are however not suitable for the investigation of cracking in pipeline girth welds because of the

overly large differences in terms of stress, thermal distributions and histories compared to in-field pipeline girth welding.

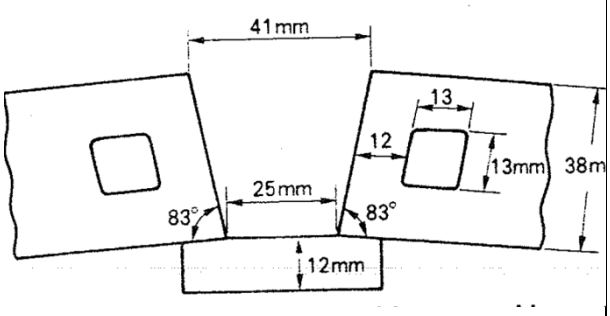

Figure 24: Experimental set-up of water-cooled ducts multi-pass test [32].

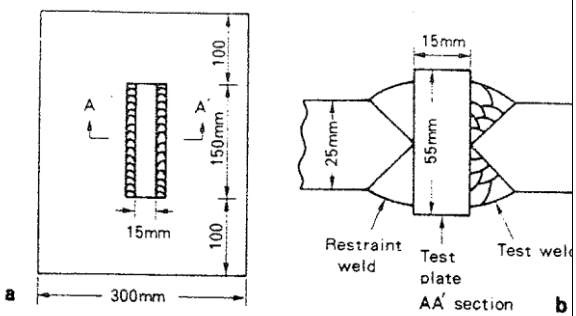

Figure 25: Experimental set-up of window-type cruciform restraint test [32].

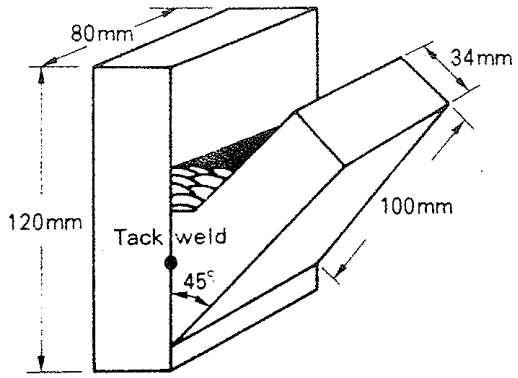

Figure 26: Experimental set-up of Cranfield test [32].

2.7.4.2 Single-Pass Block-Joining Tests

Single-pass block-joining tests rely on the design of two metallic pieces to be joined for the formation of HACC. The restraint circular weldability test [32] consists of making a circular bead-on-plate weld. Among the numerous configurations of this test are the restraint circular groove (Figure 27), the restraint circular U-groove and the circular patch. The non-restraint fillet weld test [32], also referred to as the T-test, consists of welding two plates in an inverted-T configuration (Figure 28). This test was used to investigate the fillet root cracking possibly caused by severe HAZ hardening [32] and the non-uniform local deformation of the vertical plate promoted by the weld thermal cycle. The controlled thermal severity test [186-188] consists of welding a cubic block to a plate (Figure 29) to enhance the formation of HAZHACC. This test focuses on determining a critical cooling rate for cracking [34]. In order to increase cracking susceptibility, weld metal cooling may be accelerated by plunging the end of the block opposite to the one just welded vertically in flowing cold water [34]. This test can be used to find critical HAZ hardness or critical preheat temperature, at which no

HACC forms, by changing the welding heat input [32]. These tests are, however, not suitable for the investigation of cracking in pipeline girth welds because of the overly large differences in terms of stress, thermal distributions and histories compared to in-field pipeline girth welding.

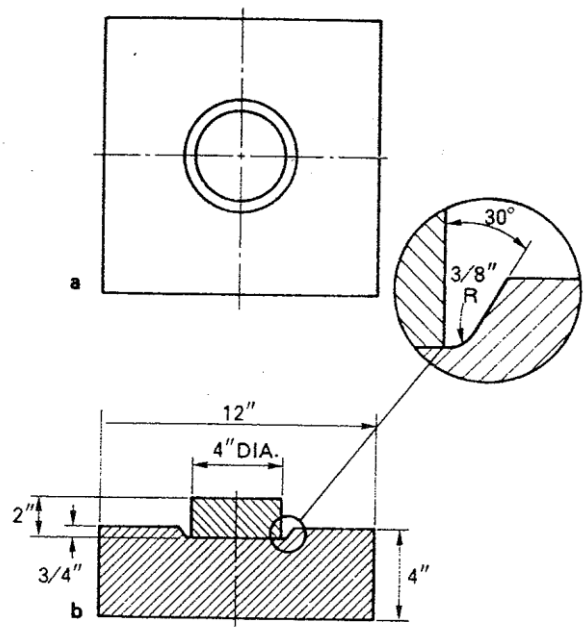

Figure 27: Experimental set-up of British Welding Research Association (BWRA) circular patch test [32].

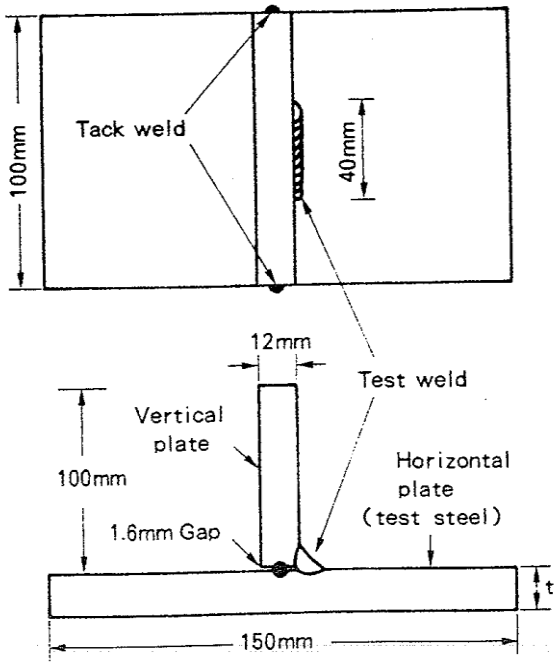

Figure 28: Experimental set-up of non-restraint fillet weld test [32].

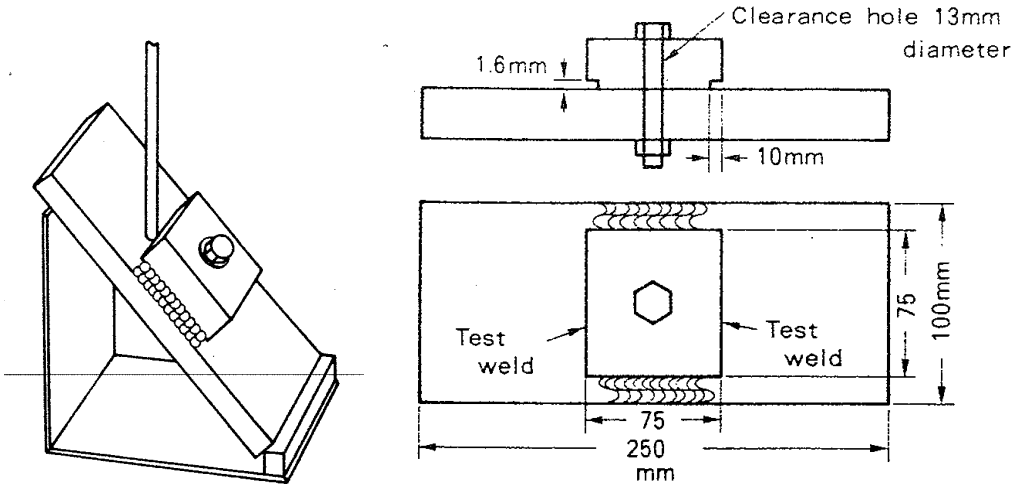

Figure 29: Experimental set-up of the controlled thermal severity test [32].

Gapped Bead-on-Plate Weldability Test

The gapped bead-on-plate (G-BOP) test [32, 34, 39, 42, 189, 190], illustrated in Figure 30, was initially developed as a simple and inexpensive test to investigate weld metal's

susceptibility to HACC [39]. Welding over a transverse gap was recognised to enhance the initiation of transverse weld metal HACC at the gap by longitudinal residual stresses. Consequently, the G-BOP test consists of depositing a bead-on-plate weld over a gap formed when two blocks, one with a shallow recess machined into it, are clamped together. The longitudinal stress across the gap is measured during welding by instrumenting the blocks [39, 42]; one possibility is illustrated in Figure 30 with strain gauges measuring the longitudinal weld contraction. The evolution of the longitudinal stress shown in Figure 31 reveals an increase due to thermal contraction followed by a drop when the crack grows. Experiments have shown that the composition of the G-BOP blocks affect the test result because of the high base metal dilution in the weld. To overcome this issue, a weld metal with low base-metal dilution (below 10%) was obtained by machining grooves in the G-BOP test blocks and filling them with the relevant consumable, creating what are known as buttered regions, and then depositing the test weld over these buttered regions (Figure 32) [190]. The crack-length criteria and critical preheat temperature to avoid cracking were taken as weldability indexes. The G-BOP test has also been coupled with a back propagation artificial neural network in order to evaluate the likelihood of HACC formation [191]. The G-BOP test promoting transverse weld metal HACC is not suitable for investigating the conditions promoting longitudinal weld metal HACC formation in pipeline girth welds.

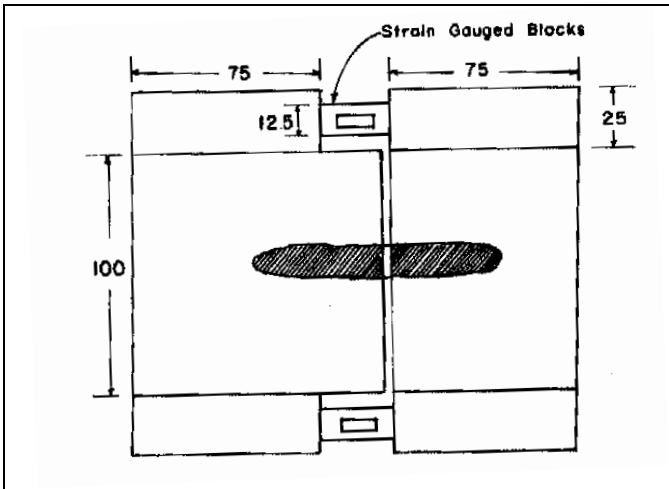

Figure 30: Experimental set-up of G-BOP test with instrumentation for stress measurement [42].

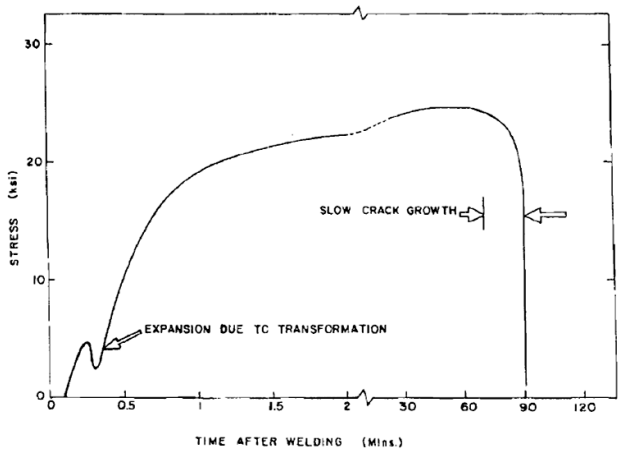

Figure 31: Stress across gap measured in instrumented G-BOP test showing time of crack initiation and growth [39].

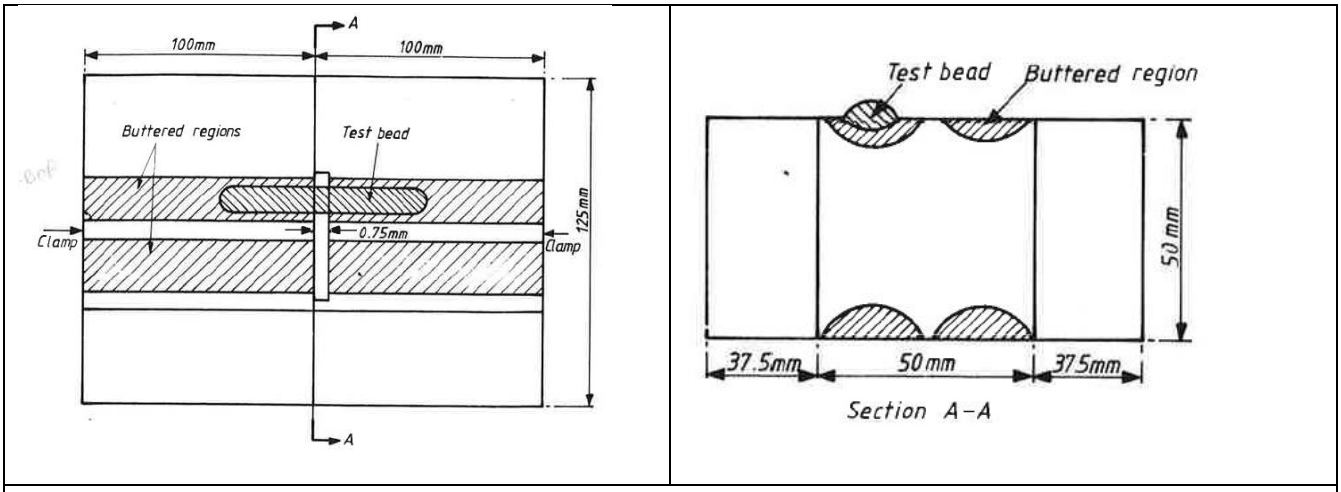

Figure 32:Experimental set-up of G-BOP test used to minimize block chemistry effect [190].

One-Plate Self-Restraint Weldability Tests

Another group of weldability tests consists of depositing a bead-on-plate single-pass layer within a groove machined into the middle of a plate with no external restraining fixture. One-plate self-restraint weldability tests are designed so that the only restraint is provided by the test plate configuration. The major differences between these tests lie in the plate geometry and weld preparation, which affects local stress distribution and consequent crack initiation site. These tests have been successful in assessing the welding behaviour of pipeline steels [177]. The cracking percentage at a fixed temperature or the critical preheat temperature to eliminate cracking are taken as weldability indexes.

The Lehigh U-groove, also referred to as the Stout test [32], consists of depositing a butt weld in a U-groove (Figure 33); it was specifically developed to assess the weldability of pipeline steels. The U-groove favours HACC initiation at the root of the weld metal rather than in the HAZ [32, 177] and is thus preferred for assessing the susceptibility of weld metal to HACC [32]. The geometry of the Stout test best reproduces the field situation when considering the bending stresses arising from shrinkage in pipe welds, with cracks initiating at the root of the weld bead [177]. The restraint can be varied by changing the depth of the edge slits [34] which are saw-cuts machined along the sides of a specimen.

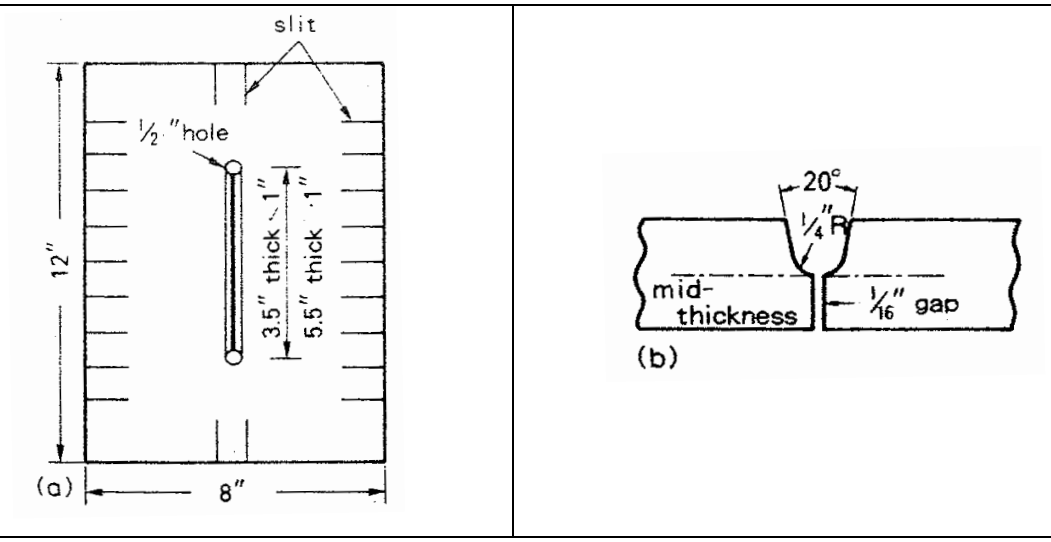

Figure 33: Experimental set-up of a Lehigh U-groove restraint test [32].

The Lehigh slot test [179] was developed for assessing the weldability of HSLA pipeline steels and consists of depositing a weld metal in a 2.4 mm-wide slot machined in the middle of the plate (Figure 34). The slot gap can have an enormous effect on crack location, with the HACC crack moving from weld metal to the HAZ when the slot width goes from 1 to 2 mm [179]. This test was used to assess the weldability of line pipe steel with E8010 cellulosic SMAW electrode [178]. This test is simpler in execution than the original Lehigh test with slide slits. As the crack propagates, the subsequent relaxation of the load changes the fracture mode from MVC to QC to IG [179], in agreement with Beachem's theory [163]. The temperature-controlled tinting of the cracked areas provides information on the crack extent over time [178]. The reproducibility of results with the slot test is not satisfactory when using crack percentage as the cracking susceptibility index, except at very high or very low levels of cracking [178], so the critical preheat to avoid cracking is preferred as the cracking susceptibility index [178]. Acoustic emission sensors have been successfully integrated into the test to record crack growth development [179], revealing that HACC growth in weld metal is intermittent (Figure 35). Such intermittent growth accords with the findings made using the implant test (recall Figure 19).

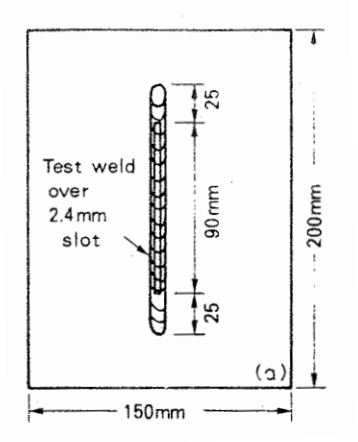

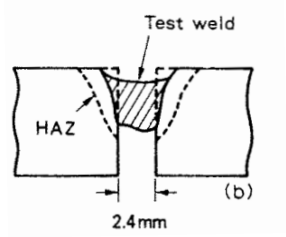

Figure 34: Experimental set-up of Lehigh slot weldability test [179].

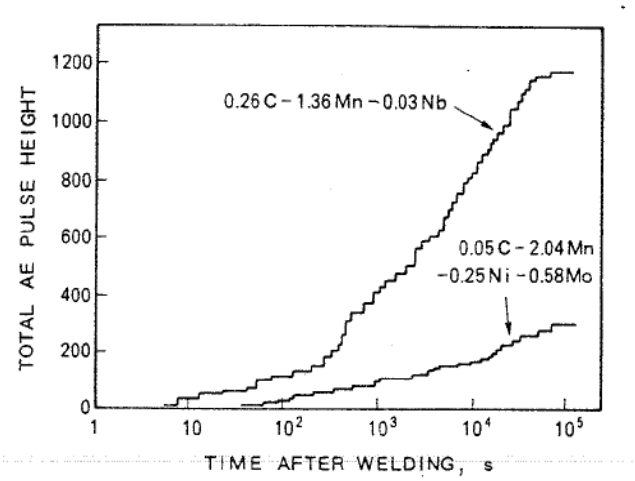

Figure 35: Intermittent crack growth recorded by acoustic emission in Lehigh slot test [179].

The Tekken test [32, 177], also called the Y-groove restraint test, was originally developed with a Y-groove at the centre thickness of the test piece (Figure 36), resulting in cracks beginning in the HAZ and extending into the weld metal [177]. A Y-groove restraint test primarily examines the HAZ root cracking that occurs in a single-pass butt weld [32]. This test has been successfully used to evaluate the critical hydrogen content required for cracking [192]. Because of the higher severity of the Tekken test compared to the controlled thermal severity test, weld metals in the Tekken test require minimum preheat temperatures of at least 50 ˚C higher than the controlled thermal severity test to avoid cracking [32]. The G-BOP is also slightly more severe than the Tekken test, in that higher preheats are required to avoid cracking, but both tests ranked the weld metals in the same order in terms of their HACC susceptibility [39]. However, comparability between the results of these two tests is limited, since the Tekken and G-BOP tests promote longitudinal and transverse cracking respectively. The test weld is deposited at the centre of the plate, parallel to the long axis. The weld length is restricted from 30% to 50% of the plate width in order to predict R_F [177]. The Tekken test has been used to investigate X80 pipeline steel weldability with E8018 electrodes, including the effect of plate thickness on cracking susceptibility [20].

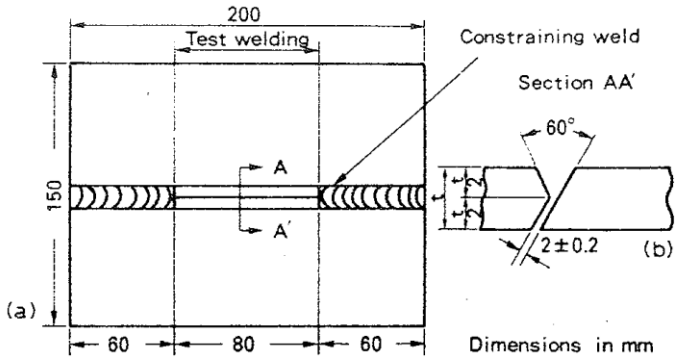

Figure 36: Experimental set-up of Y-groove restraint (Tekken) test [5].

Yurioka and Kasuya [101] have proposed a chart method to determine the necessary preheat temperature to avoid cracking in steel weld metals. Their method is based upon master curves experimentally obtained for each set of welding conditions. The established data to predict the preheat temperature required for pipeline welding is illustrated in Figure 37. The carbon equivalent values *CEN* and CE_{IIW} used in this method are given by:

Equation 2-5: Carbon equivalent CEN [101].

$$CEN = C + \left(0.75 + 0.25\tanh\left[20\left(C - 0.12\right)\right]\right)\cdot\left(\frac{Si}{24} + \frac{Mn}{6} + \frac{Cu}{15} + \frac{Ni}{20} + \frac{Cr + Mo + Nb + V}{5} + 5B\right)$$

Equation 2-6: Carbon equivalent CE_{IIW} [32].

$$CE_{IIW} = C + \frac{Mn}{6} + \frac{Ni + Cu}{15} + \frac{Cr + Mo + V}{5}$$

Figure 37a illustrates the *CEN* value correction versus weld metal hydrogen content, revealing a nearly logarithmic effect. Figure 37b illustrates *CEN* correction versus CE_{IIW} and welding heat input. The *CEN* increment is negative at high heat inputs because of the reduction in HAZ hardness arising from slower cooling. Figure 37c shows the critical preheat temperature measured in a Y-groove self-restraint cracking test as a function of the plate thickness and weld metal *CEN* value. These curves are valid for weld metal hydrogen contents of 5 ml/100g (as measured by gas chromatograph or mercury method), welding heat input of 1.7 kJ/mm, and ambient temperature of 10 °C. Figure 37b illustrates the required correction to apply to the preheat temperature for welding practice in the field compared to the laboratory Y-groove

restraint testing results, depending on steel yield strength. Assuming that the known variables are weld metal composition, yield strength and hydrogen content in addition to the plate thickness and welding heat input, the corrections to the *CEN* value from the hydrogen content (Figure 37a) and those due to the heat input (Figure 37b) can be applied to give total correction for the *CEN* value. This corrected *CEN* value and the plate thickness can then be used to determine the minimum preheat temperature necessary to avoid cracking in the Y-groove self-restraint cracking test (Figure 37c). Finally, the yield strength of the steel defines the correction for the critical preheat temperature to be applied in the field (Figure 37d) [32].

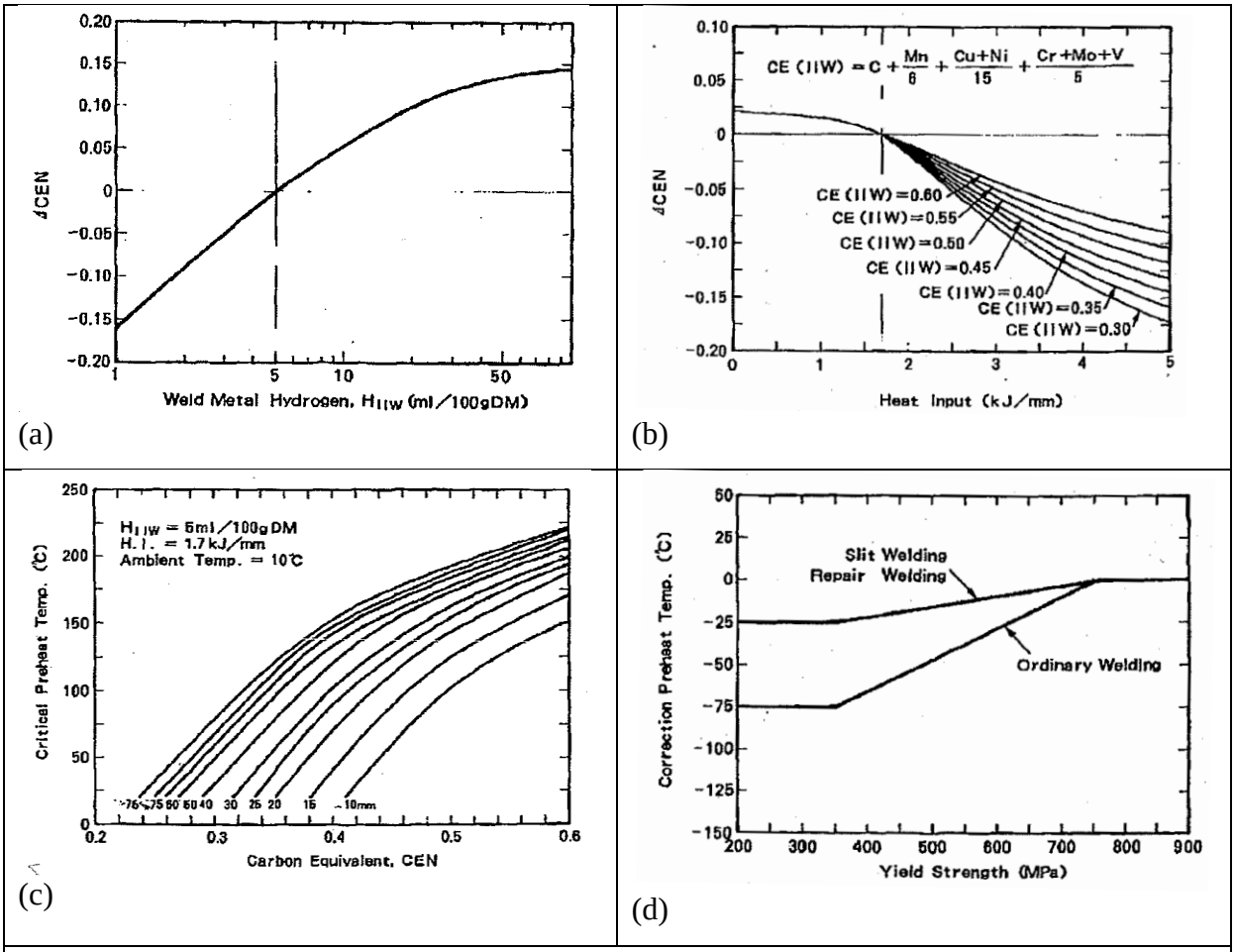

Figure 37: Maps used in Yurioka's chart method for evaluating critical preheat temperature to avoid cracking for welding practice: (a) carbon equivalent (*CEN*) value correction as a function of weld metal hydrogen content; (b) *CEN* value correction as a function of welding heat input and carbon equivalent (CE_{IIW}) value; (c) critical preheat temperature for laboratory Y-groove restraint testing as a function of plate thickness and *CEN* value at indicated test conditions; and (d) critical preheat temperature correction from laboratory test to welding practice as a function of steel yield strength [32].

Highly Restrained Two-Plate Weldability Test

The last group of intrinsic weldability tests consists of depositing a bead-on-plate single-pass layer within a groove separating two highly restrained plates. The instrumented restraint cracking test [32] and the restraint root cracking test [178], also referred to as the Schnadt-Fisco test (Figure 38) consist of depositing a weld in a single V-groove between two test

plates kept in a restraint frame; the R_F is controlled by varying the restraint beam cross section. However, the restraint levels in the Schnadt-Fisco test are generally too low to provide an HACC ranking [177, 178], and the minimum preheat temperature to avoid cracking in E8010 cellulosic SMAW of HSLA pipeline steels is lower than what has been measured in full-scale tests [178].

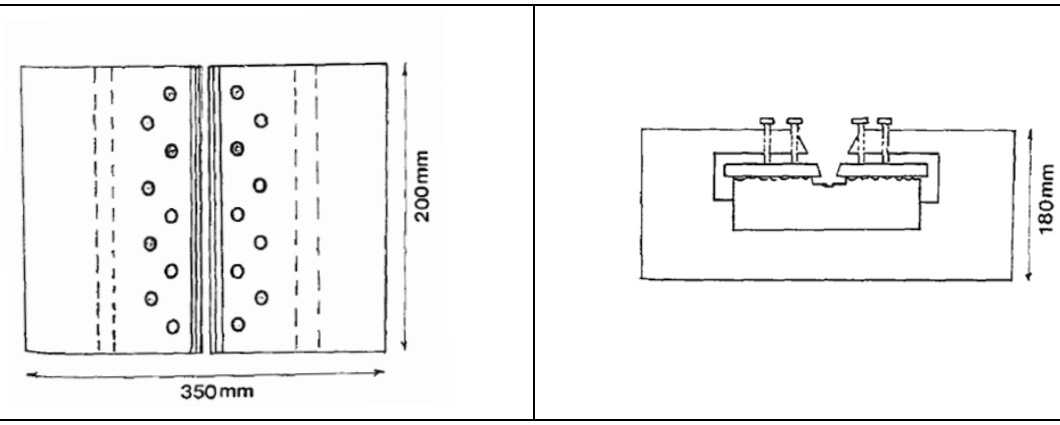

Figure 38: Experimental set-up of Schnadt-Fisco test [178].

The H-slit restraint test [32] consists of machining two test plates into one larger plate and controlling the R_F by varying the slit length (B_S), indicated in Figure 39. The H-slit test was designed to generate higher and more uniform reaction stresses, which creates a barrier to heat flow beyond the end of the weld and maximizes weld contraction across the weld portion [34]. This test has been used to determine the crack-no crack (CNC) boundary conditions in terms of bending and tensile restraint intensities (Figure 40).

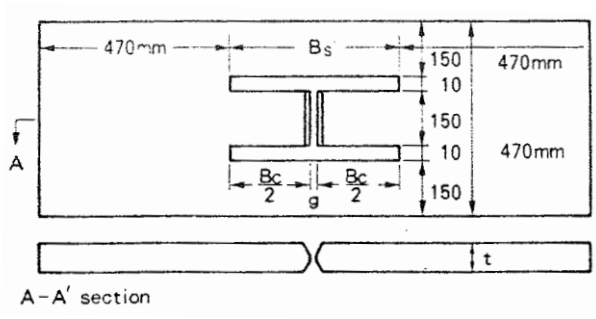

Figure 39: Experimental set-up of H-Slit restraint test [5].

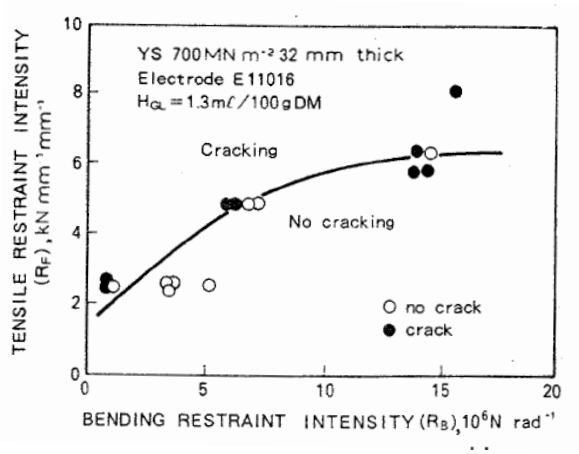

Figure 40: Bending-tensile restrain intensities mapping showing cracking boundary conditions in H-slit restraint test [5].

The Welding Institute of Canada (WIC) test [20, 45, 178, 193] and the window-type restraint multiple-layer cracking [194] tests (Figure 41) consist of depositing a single-pass weld metal

into a V-groove separating two restraint test plates clamped with anchor welds to a stiffener tee or plate respectively, with the R_F controlled by the anchor welds. The window-type restraint multiple-layer cracking test [194] can be used with thick test plates (e.g., 50 mm in Figure 42); it was developed to provide higher restraints than in the pipe girth welds, so that if no crack forms in the test, then the pipeline girth weld should be crack-free [194]. These two tests have the virtue of promoting HACC in both the HAZ and weld metal [32], which is invaluable for research purposes. The WIC test (Figure 41) has been benchmarked as a procedure for developing in-field pipeline welding requirements [20, 176-178, 195]. The weld-free distance between the anchor welds needs to be carefully controlled, as the maximum stress encountered by the weld metal depends on this distance. Based on work by Sato et al. [151], Graville [34] estimates that the stress in weld metal doubles its maximum value when reducing restraint length from 100 to 25 mm (Figure 43). Traditionally, the weld metal in the WIC test groove was deposited manually in the flat position, but this procedure has limited repeatability (± 0.1 kJ/mm heat input) due to the variations in welding conditions inherent in manual welding [196]. Moreover, a vertical-down welding direction should be used, as that is more representative of in-field pipeline conditions. These arguments highlight the issues raised by the traditional procedure when using the WIC test. Therefore, a recent modification of the WIC test procedure includes the mechanised deposition of the weld in the vertical-down direction and the introduction of run-on and run-off tabs (Figure 41) to reduce the start and stop effects on the weld metal's cracking susceptibility [193].

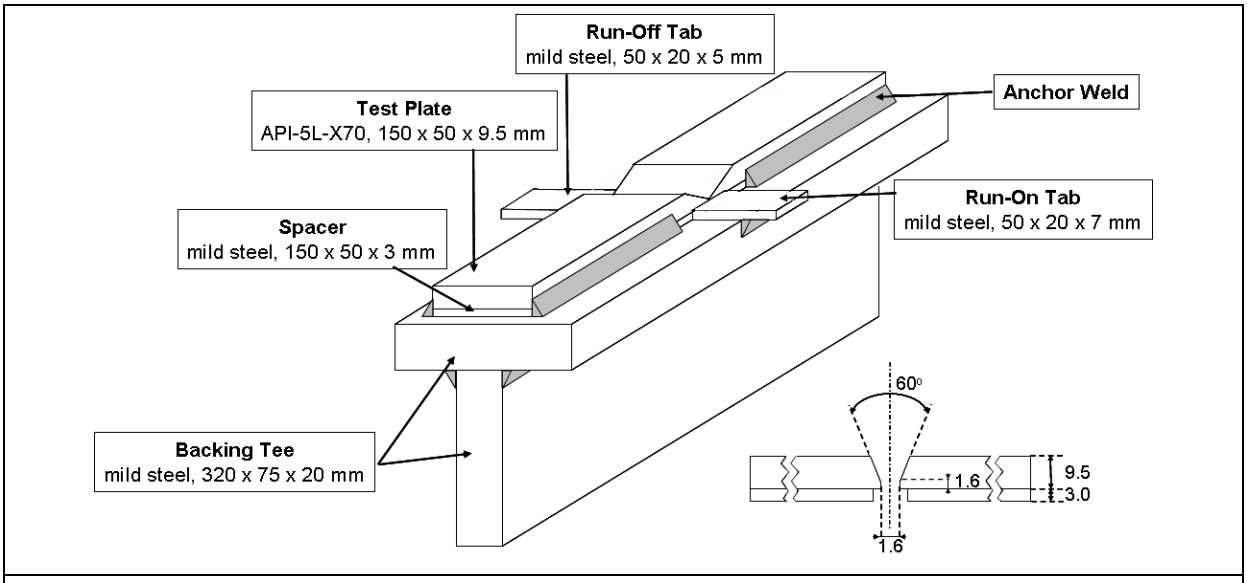

Figure 41: Experimental set-up of WIC test [193].

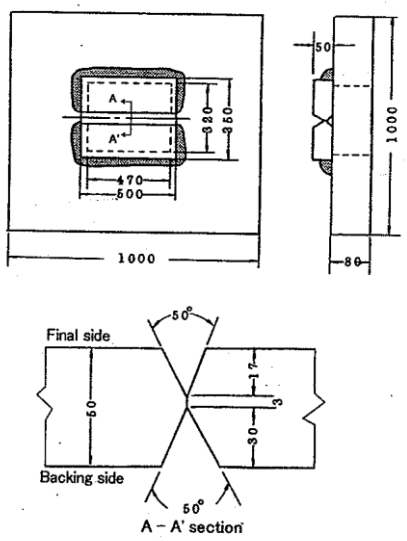

Figure 42: Experimental set-up of window-type restraint cracking test [194].

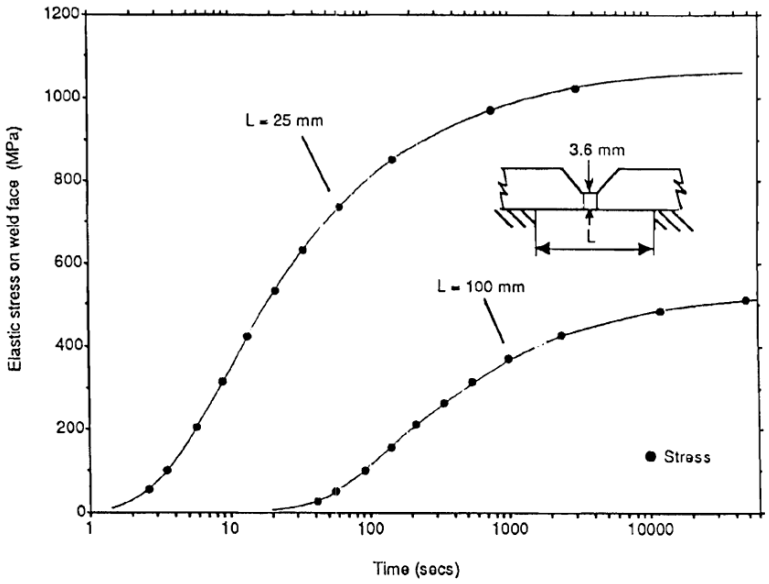

Figure 43: Reaction stress estimated for two restraint lengths using a one-dimensional analysis [34].

2.7.5 **Concluding Remarks**

There are a wide range of tests devised to investigate the cracking susceptibility of weld metals in welded structures, a few of which find application in studying pipeline girth weld integrity. Tests today are usually limited by their lack of instrumentation and the difficulty of varying the restraint conditions, leading to estimating the crack susceptibility through a simple CNC criterion. The WIC test is selected in this study to investigate the weld metal HACC susceptibility in pipeline girth weld, because this test has successfully been used to simulate the root pass cracking that is due to lifting stresses in pipeline girth welds [34]. Because of the configuration of the test, stresses are generated transverse to the welding direction and are thus ideal to promote the formation of longitudinal HACC in the weld metal for testing purposes. This test is selected for weldability testing because of its legitimacy in investigating conditions to form longitudinal weld metal HACC and the important associated scholarly data that enables a comparison of the behaviour of our consumables with other tests.

While the WIC test has been popular for investigating pipeline girth weld integrity, the difficulty of access to the weld metal for local strain measurements and the important constraints during the specimen machining in terms of both cost and workshop time are limiting factors for broad investigations. Therefore, modifications of the traditional WIC test are required to overcome these limitations, though the modified test must still provide sufficient levels of restraint to generate HACC and access to the back side of the weld metal for measuring the local strain conditions for cracking. Instrumentation access should include a

local strain measurement system in the vicinity and across the weld metal continuously from weld start to HACC formation.

2.8 The Welding Institute of Canada Weldability Test

The WIC restraint cracking test subjects a weld butt to high reaction stresses. It is particularly intended to examine root cracking in pipeline girth welds by controlling the R_F in a V-butt joint, and has been used to simulate the root pass cracking due to lifting stresses in pipeline girth welds [34]. The WIC test consists of depositing a single-pass weld metal into a V-prep groove separating two restraint test plates clamped with anchor welds to a stiffener tee (Figure 41). The single-V pipeline preparation concentrates stresses at the upper surface of the weld, as occurs with the lifting stresses experienced pipeline construction in practice [34, 177]. The R_F is controlled by the length of the anchor weld-free region—the restraint length—about which the weld joint under test is centred. Frictional effects within the restraint weld are avoided by shimming the test sample off the backing plate, allowing any bending related to an asymmetric weld bead to occur freely. The backing tees are attached to the bottom of the base to provide high stiffness and prevent joint rotation. Run-on and run-off tabs can be used to eliminate cracking tendencies due to weld starting or stopping and promote a steady-state weld within the groove [193]. This test can promote HACC in either the HAZ area or the weld metal area, which is helpful for research testing purposes [5]. The welded joint is usually removed from the WIC specimen 24 hours after welding completion by sawing the test assembly just inside the restraint length, avoiding the ends of the anchor welds; the weld zone is assessed for cracking. This 24 hour-delay for crack analysis is reasonable, according to the measurements of Alam et al. [20] that are shown in Figure 44 for a WIC test specimen with a restraint length of 25 mm. A clip gauge was positioned after weld completion across the weld metal in order to measure the local strain. The results show a sudden increase in the strain value 350 seconds after welding completion (part B of the curve in Figure 44), which is related to crack formation.

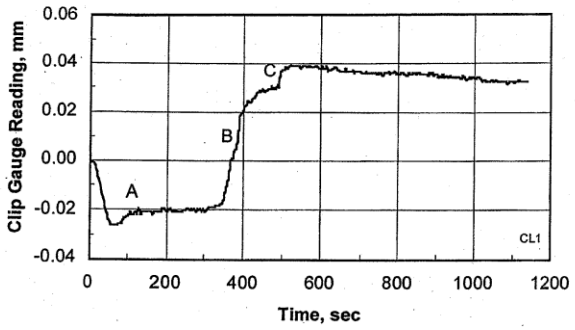

Figure 44: Measured local deformation by clip gauge across weld metal after welding completion in WIC test: (A) initial contraction, (B) onset of cracking and (C) second stage of cracking [20].

2.8.1 Preheat Temperature Effect

For the WIC test, the minimum preheat temperature to avoid cracking can be chosen as the cracking susceptibility index. The critical preheat temperature depends not only on the welding conditions and weld metal chemistry, but also on the high-low misalignment of the two test plates separated by the V-groove, which results in an increase in the critical preheat temperature to avoid cracking [5]. This test has been successful in comparing the HACC susceptibility of weld metals deposited by cellulosic SMAW consumables for a range of steels and conditions [20, 31, 178, 197-199]. The details of these effects are discussed in Section 2.9.

The weldability improvement at higher preheat temperatures may be related to the slower cooling rate [20], which offers more time for hydrogen effusion and lowers the weld metal hydrogen content upon reaching room temperature (Figure 45) [5]. Testing showed that the primary factor controlling weld metal cracking was hydrogen diffusion through control of the cooling time to 100 $^{\circ}$C [2]. Preheating to a minimum temperature is required to extend the weld metal cooling duration and deposit a weld metal containing a hydrogen content below the critical level for welding and service conditions [4, 20].

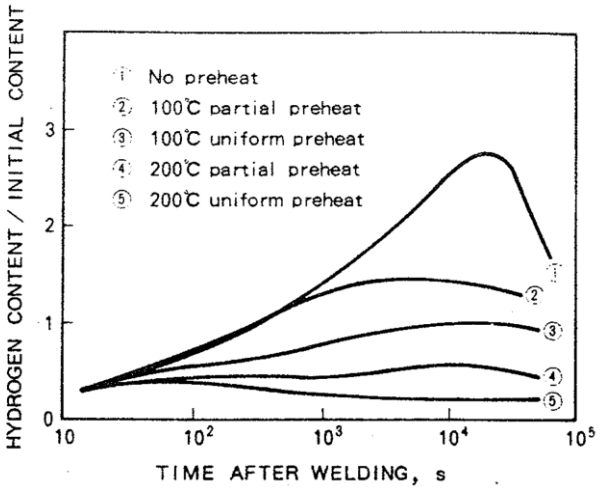

Figure 45: Weld metal hydrogen content evolution after welding completion at weld root of single-bevel weld under various preheat conditions, as calculated by the finite difference method [5].

Further development of the WIC test has involved the mechanised vertical-down deposition of the weld metal [193, 196]. This procedure improves the control of the welding conditions and thus the consistency and repeatability of the tests. Tests were carried out on the specimen detailed in Figure 46 with an anchor weld-free region, referred to as the restraint length, of 30mm in length. SMAW metals were deposited using commercial E8010 cellulosic welding consumables into the groove machined between the API 5L X70 steel test plates. In these conditions, the results showed that the heat input, while varying up to 0.2 kJ/mm with manual weld deposition, was kept constant with mechanised deposition. Moreover, thanks to the consistency in heat input used, differences in weldability were revealed not only between the consumables of different brands, but also for consumables different vintages of the same brand, as Figure 46 shows. The bars for each alloy indicated approximately the minimum preheat to avoid cracking; cracks form at higher preheat in the consumables from more recent vintages, reflecting their lower weldability.

While the minimum preheat temperature to avoid cracking has been a popular choice as a HACC susceptibility index, its usefulness in characterizing the HACC susceptibility of Australian pipeline girth welds raises two major issues. First, small-diameter pipes are welded in Australia without preheat, so the laboratory quantification cannot be used as such in the field. Second, minimum preheat temperature does not directly represent the driving force to form HACC in the weld metal; therefore, the minimum R_F needed to form a crack is more attractive as a tool to define the CNC boundary condition.

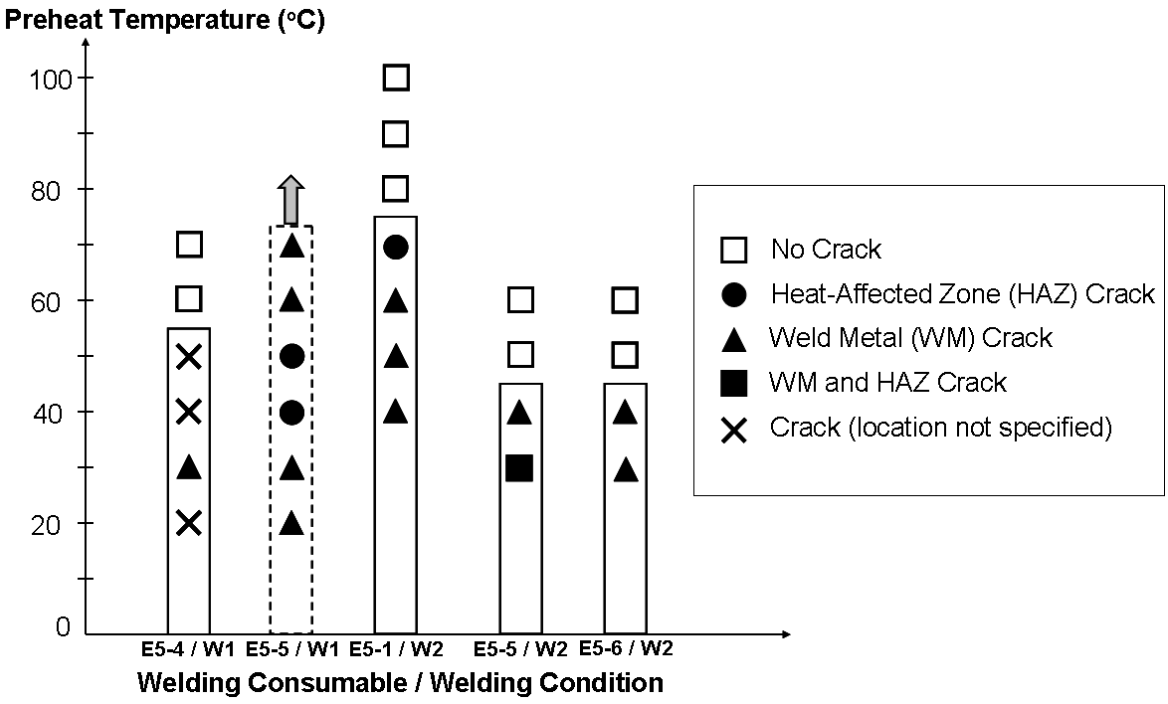

Figure 46: Comparison of WIC test results for cellulosic SMAW consumables (E5-1, E5-4, E5-5, E5-6) and welding conditions W1 (manual deposition) and W2 (mechanised deposition), showing observed HACC behaviour varying with preheat temperature [196].

2.8.2 Restraint Intensity Effect

The R_F in the WIC test is controlled by the restraint length, i.e. the weld-free region between the anchor welds (see Figure 41). Only a limited number of experiments have been conducted to investigate the effect of restraint length on the severity of the test. Rothwell, as cited by Barbaro [2], investigated the cracking susceptibility of HSLA steel line pipe using the WIC test, finding that a decrease in the R_F tends to shift the cracking from the weld metal to the HAZ. The calculation of the R_F and its relationship to the weld metal stresses in the direction transverse to the welding direction have been summarised by Yurioka [5] . The tensile R_F is given by:

Equation 2-7: Tensile R_F factor.

$$R_F = \frac{Eh}{l} = \eta r_f h ,$$

where E is Young's modulus, h is plate thickness, l is restraint length, R_F is a restraint coefficient, and η is a correction factor for the plate thickness. The R_F values are given in Figure 47 as a function of restraint length. A correction factor η is required because the full thickness of the plate does not necessarily work as a restraint against contraction of the weld; effective R_F reduces with an increase in plate thickness. This factor is given by:

Equation 2-8: R_F correction factor.

$$\eta = \exp\left(\frac{5.6 - h}{80.3}\right)$$

and is valid for h between 5 and 100 mm. The resultant reaction stress (σ_R), also referred to as the restraint stress, is expressed by:

Equation 2-9: Resultant reaction stress σ_R.

$$\sigma_R = \frac{SR_F}{h_w},$$

where S is the total contraction in mm and h_w is the height of the weld metal throat. These calculations show that a longer restraint length results in smaller restraint intensities and smaller transverse stresses in the weld metal, which agrees with the notion of a decrease in crack percentage with increased restraint length (Figure 48). Recent WIC testing [20] indicates that the maximum stress encountered in practice through restraint and bending is unlikely to exceed that imposed by the standard restraint length in the WIC test (16.4 kN/mm^2 for 8.6 mm-thick plate) and that restraint conditions are less critical than weld metal hydrogen content in inducing HACC. The lower cracking susceptibility at smaller restraint intensities may also be related in part to the increase in cooling time from 800 ˚C to 100 ˚C ($t_{8/1}$) with a decrease in R_F (Figure 49) leading to a greater amount of hydrogen diffusing out of the weld metal during cooling [20]. This decrease in cooling rate may be related to the seating error x of the test plate (Figure 50) in the WIC test due to curvature of the plate [34]; the bad thermal conduction from the test plate to the support leads to the fact that the heat from the welding process is evacuated largely through the anchor welds to the backing tees.

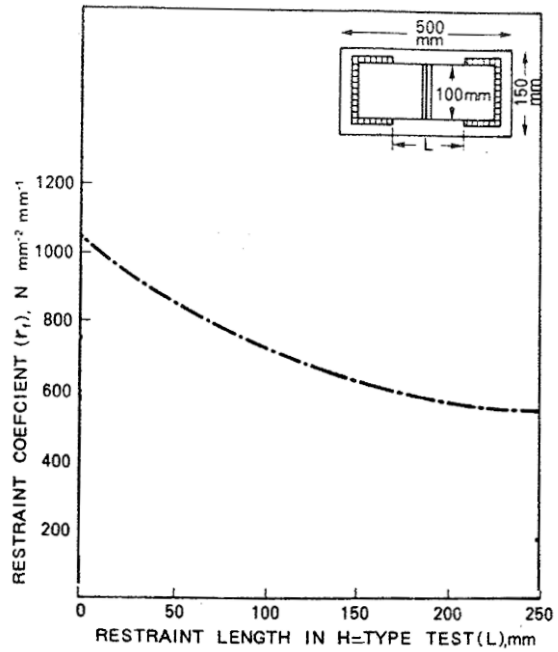

Figure 47: Restraint coefficient (r_f) as a function of restraint length in the WIC test to be used for the calculations in Equation 2-7 [5].

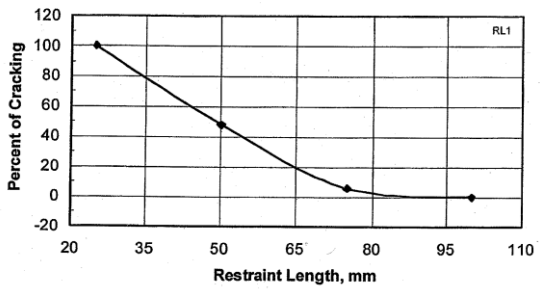

Figure 48**:** Percentage of cracking as a function of restraint length in the WIC test [20].

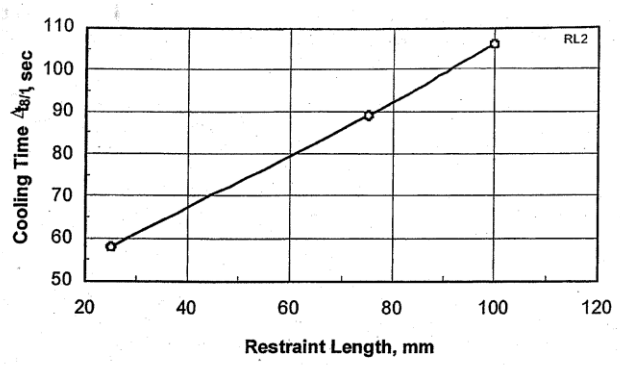

Figure 49**:** Weld cooling time from 800 °C to 100 °C in the WIC test as a function of restraint length without preheating [20].

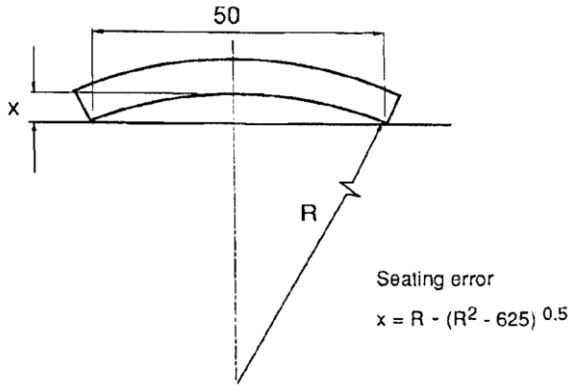

Figure 50**:** Seating of curved pipe specimen in the WIC test, indicating the seating error *x* [34].

Experimental measurements show that the critical preheat temperature and the R_F in a WIC test represent the conditions needed for crack growth. Combining these two factors defines the conditions needed for cracking, as plotted in Figure 51 [20]. The critical R_F-preheat temperature mapping concept was proposed by Alam et al. [20]. Lower restraint intensities require lower preheat temperatures to avoid cracking.

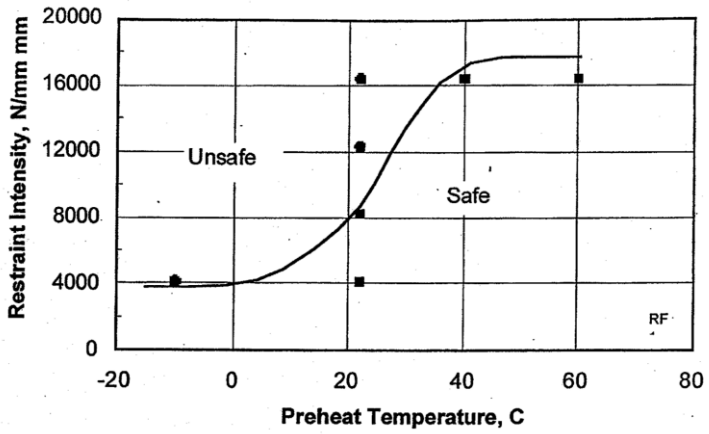

Figure 51: Critical R_F-preheat temperature map demarking cracking regions using the WIC test [20].

2.8.3 Weldability Quantification

Quantifying weldability is necessary to rank the alloys at a minimum, and ideally to quantify explicitly the conditions required for cracking. Even if a simple CNC criterion can be used, other weldability indexes will hopefully lead to a more nuanced ranking. While crack length and preheat criteria do permit ranking, strain criteria relate to an actual cracking mechanism, allowing for future predictions.

2.8.4 Crack Length Criteria

Crack length measurements are commonly used to characterize HACC susceptibility and are often reported in terms of mean, maximum or total cumulative crack length, as it is generally assumed that for fixed testing conditions, an alloy with higher cracking susceptibility will result in more extensive cracking. These parameters are commonly used for intrinsic tests to quantify cracking susceptibility. The number of cracks may also be used to evaluate an alloy's cracking susceptibility, as when the bending test is used to assess the cracking susceptibility of pipeline girth welds [185].

2.8.5 Strain Criteria

Assuming that all thermo-metallurgical factors like constant alloy composition and cooling rate are held constant, it is useful to concentrate on the thermomechanical conditions required for crack formation. Measuring local strain in the vicinity of the weld during the entire welding cycle poses some unique challenges, such as the high temperatures encountered in welding. In response, Japanese researchers have introduced a new concept referred to as R_F [5]. The R_F defines, for a given test configuration, the relationship between deformation and

stress generated in the weld metal and is explicitly given for the WIC test, recalling Equation 2-7. This concept enables ranking the alloys' susceptibility in terms of stresses encountered, assuming that this relationship is similar for different welds because the weld metals possess a comparable Young modulus. In order to estimate closely the stress encountered by the weld metal, the groove shape is of particular importance to determining the stress distribution within the weld metal, especially in- or out-of-plane strain conditions (Figure 52). This knowledge is important to evaluate the planarity of the strain conditions and the bending stresses that arise. The groove geometry will affect the stress concentration factor at the root of the weld, as laid out in Figure 53.

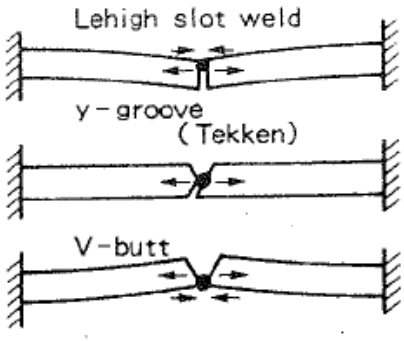

Figure 52: Effect of weld eccentricity on local stress at weld root in different groove configurations [5].

Groove Type	Kt	Groove Type	Kt
Oblique y	4.0	Single bevel-3	6.9
Double Vee	3.7	Single bevel-4	3.5
Single bevel-1	5.8	Symmetric Y	4.2
Single bevel-2	5.4		

Figure 53: Stress concentration factor (K_t) at the root of the weld of basic joint geometry [5].

2.8.6 Thermal Criteria

Critical preheat temperature to avoid cracking is an important parameter for the industry, as it may be the only way to avoid cracking during pipeline construction. Work has been carried out to relate the critical preheat temperatures of in-field pipeline welding to those found in laboratory tests [178]. Statistical tools used to evaluate the HACC susceptibility in weld metals account for the hydrogen content in combination with the thermal history [3, 177, 200]. The results suggest that a linear [201] or logarithmic [4, 194] effect of hydrogen concentration on the critical preheat temperature is necessary to avoid cracking. A higher preheat temperature is believed to reduce the cooling rate and thus reduce the hydrogen content in the weld metal and cracking susceptibility.

2.9 Empirical Testing Using the WIC Test

In the literature review (Section 2.8), the WIC test was identified as the best weldability test to replicate high-restraint butt welds. In particular, its adoption by the pipeline industry as a benchmark weldability test was attributed, among other things, to the fact that its geometry and restraint levels that the intrinsic test generates during weldability testing are comparable to those generated in single-pass girth welds in the field.

The literature review extended the discussion on the WIC test by examining the test's features and the effects of welding conditions on the test's behaviour. The WIC test has been used to identify the critical preheat needed to minimise the risk of HACC for a number of different HSLA steels welded over a wide range of heat inputs and thicknesses using electrodes of varying strength. In addition to single-pass welds, the WIC test has also been used to ascertain the critical preheat required to minimise cracking risk for a range of steel-consumable combinations for multi-pass welding [20, 28, 31, 193, 197, 198, 202-204].

Since its development in the late 1970s, the WIC test has been used in multiple studies to ascertain the weldability of a range of steel compositions and electrode-steel combinations. This section of the literature review focuses on the results from two major studies commissioned to investigate, using the WIC test, the field weldability of high-strength pipeline steels. From the literature found to date, these studies were closely aligned with the overarching objective of this thesis and are pivotal in streamlining the research gaps which are presented in Chapter 3. In particular, this section of the literature review explores the effect of pipeline welding procedural variables on the weldability of HSLA steels using the traditional WIC test.

2.9.1 Weldability Studies Using the WIC Weldability Test

2.9.1.1 Field Weldability Using the WIC test

In 1986, after the API-5L line pipe specification amended its standards to allow the use of HSLA line pipe steels with yield strengths of around 520 MPa, the American Gas Association, in conjunction with the Welding Institute in the UK and the Edison Welding Institute in the US, funded a three-year study designed to investigate the weldability of a number of high-strength pipeline steels, especially API 5L X80 (522N/mm^2). Noble and Pargeter [198] authored a report investigating the field weldability of high-strength pipeline steels as part of a larger study aimed at investigating the weldability of HSLA steels with carbon content ranging from 0.02 wt% to 0.08 wt%. The authors conducted small-scale weldability testing using SMAW with the traditional WIC test in addition to full-scale testing on pipe sections using both GMAW and SMAW. As this thesis focuses on SMAW, only the SMAW results and discussion will be detailed below.

Noble and Pargeter conducted testing on two pipe sections of API-5L- X80 (522N/mm^2) line pipe steel. The thicker of the two sections originated from the NKK Corporation in Japan; it had an outer diameter of 1070 mm and a wall thickness of 15.5 mm. The steel was on-line accelerated cooled and had a microstructure comprising of fine-grained ferrite and elongated colonies of pearlite. The steel had carbon content of 0.068 wt% and a carbon equivalent (CE) of 0.39. The thinner of the two sections was reported as originating from an undisclosed US manufacturer. This section of pipe had an outer diameter of 406 mm and a wall thickness of 9.5 mm. The steel was reported as having an essentially bainitic structure with a carbon level of 0.12 wt% and a CE_{IIW} of 0.38. The detailed chemical composition of the pipe sections used for testing appear in Table 3.

Table 3: Line pipe steel composition for weldability tests conducted on the traditional WIC specimens by Noble and Pargeter [198].

Steel	C	Mn	P	S	Si	Cu	Sn	Ni	Cr	Mo	Al	V	Nb	Ti	B
NKK	0.068	1.72	0.013	0.001	0.24	0.007	0.001	0.013	0.059	0.10	0.034	0.079	0.026	0.010	0.0002
US	0.120	1.27	0.016	0.006	0.18	0.010	0.001	0.008	0.026	0.18	0.016	0.041	0.002	0.001	0.0001

Weldability testing on both full-scale and the traditional WIC specimens was conducted with a range of cellulosic electrodes, as detailed in Table 4.

Table 4: Electrode combination used by Noble and Pargeter [198] for SMAW weldability tests conducted with the traditional WIC test.

Small-Scale SMAW Weldability Testing	Full-Scale SMAW Testing
4 mm AWS A5.5-81 E9010	4 mm AWS A5.5-81 E8010
4 mm AWS A5.5-81 E8010	4 mm AWS A5.5-81 E9010
	5 mm AWS A5.5-81 E8010

Using the traditional WIC geometric configuration, Noble and Pargeter employed a single V-groove butt joint prep with a bevel angle of 60°. For the 15.5 mm thickness, the authors specified a root face and gap of 2.0 mm, while a root gap of 1.7 mm and a root face of 1.5 mm was specified for the 9.5 mm-thick pipe. Although in Noble and Pargeter's publication a dimensional tolerance of ± 0.1 mm was specified only for the root gap on the 9.5 mm-thick plate, it is reasonable to assume that this degree of accuracy was used for the joint preparation in the 15.5 mm plate as well; at least, there was no information provided to the contrary.

For the two thicknesses and electrodes specified, Noble and Pargeter aimed to define the minimum or threshold preheat at which no cracking was observed in the metallurgically prepared samples. It is important to note, however, that Noble and Pargeter tolerated small crack like defects at the toe of the welds, as they were unable to establish whether they were hydrogen cracks or whether they resulted from incomplete fusion with the sidewall. Noble and Pargeter allowed the entire test assembly to cool in still air for a 48-hour incubation period instead of the standard 24-hour period.

Table 5: Weldability test sequence employed by Noble and Pargeter [198]

Task	Electrode	Thickness	Heat input	Restraint	Objective
1	E9010	15.5 mm	1 kJ/mm	25 mm	Single-pass testing on NKK Steel using E9010 electrodes to determine threshold preheat where no hydrogen cracking is present
2	E8010	15.5 mm	1 kJ/mm	25 mm	Single-pass testing on NKK Steel using E8010 electrodes to determine threshold preheat where no hydrogen cracking is present
3	E9010	9.5 mm	1 kJ/mm	25 mm	Single-pass testing on American steel using E9010 electrodes to determine threshold preheat where no hydrogen cracking is present

Table 5 summarises the small-scale weldability testing sequence on traditional WIC samples employed by Noble and Pargeter; it details a heat input of 1 kJ/mm was targeted for all tests. For the thicker steel sections sourced from Japan, single-pass root runs were deposited using 4 mm E8010 and 4 mm E9010 electrodes. However, for the thinner test plates sourced from the

US, single-pass root runs were deposited using only 4 mm E9010 electrodes. The authors gave no justification as to why this testing sequence was employed. In addition to examining the test samples for cracking, Noble and Pargeter extracted the critical cooling parameters ($t_{8/5}$ and t_{100}) by plunging a thermocouple into the molten weld pool just behind the arc; the temperature was monitored at a frequency of 5Hz.

2.9.1.2 Investigation of WIC Test Variables

The second major study presented and discussed is an investigation into WIC test variables authored by Cola in 1991 [197]. Since its adoption in North America as a standardised weldability test to establish threshold preheats necessary to avoid hydrogen cracking in the root region of circumferential welds, the WIC test has been acknowledged to be a conservative test. North et al. [178] indicated that the threshold preheat temperatures developed from WIC weldability test data are in the regions of 25–35 °C above those required in the field.

Cola suggested that in order to formulate economical welding procedures with accurate levels of preheat, further analysis of the WIC test was needed, which served as the overarching justification for his work. Testing was conducted by Cola [197] for the Pipeline Research Council International at the Edison Welding Institute on 20 mm- and 6.4 mm-thick X80 steel from 914 mm-diameter pipes manufactured by Nippon Steel in Japan. The steel was manufactured using accelerated cooling and had a microstructure comprising of fine-grained ferrite and elongated colonies of pearlite. The chemical composition appears in Table 6.

Table 6: Line pipe steel composition for weldability tests conducted on the traditional WIC specimen by Cola [197].

C	Mn	P	Si	Cu	Ni	Cr	Mo	Al	V	Nb	Ti	CE	P_{CM}
0.06	1.82	0.004	0.26	0.27	0.88	0.12	0.13	0.026	0.058	0.018	0.012	0.502	0.209

A total of 214 tests were conducted on this steel in 11 weldability tasks using five different electrode types, including cellulosic and basic electrodes. The electrodes ranged from low strength (E60XX) to high strength (E100XX). The electrodes' designations and chemical compositions are listed in Table 7 and Table 8. It is important to note that the chemical composition of the electrodes was derived experimentally using optical emission spectroscopy. A multi-pass (> 10 passes) pad weld was deposited to avoid base metal dilution. (See Table 10 for detailed test procedures employed by Cola [197]).

Table 7: Electrode combination used by Cola [197] for SMAW weldability tests conducted with the traditional WIC test.

Electrode Designation	Electrode Type	Classification
Cel 90	4 mm Cellulosic	AWS 5.5-81 (E9010)
XP 90	4 mm Cellulosic	AWS 5.5-81 (E9010)
XP 70	4 mm Cellulosic	AWS 5.5-81 (E7010)
Cel 70	4 mm Cellulosic	AWS 5.5-81 (E6010)
B 90	4 mm Basic	AWS 5.5-81 (E10018)

Table 8: Elemental composition of electrodes used by Cola in weldability testing [197].

	C	Mn	P	S	Si	Cu	Ni	Cr	Mo	V	Ti	[H]
Cel80	0.22	1.04	0.017	0.008	0.33	0.016	0.2	0.21	0.003	0.006	0.021	49.23
XP90	0.13	0.86	0.007	0.015	0.21	0.103	0.66	0.13	0.22	0.03	0.011	41.72
Cel70	0.17	0.62	0.014	0.011	0.19	0.013	0.02	0.02	0.002	0.005	0.013	48.77
XP70	0.13	0.82	0.006	0.012	0.32	0.094	0.79	0.03	0.009	0.007	0.015	74.82
B 90	0.10	1.70	0.017	0.009	0.39	0.026	1.49	0.03	0.006	0.007	0.013	4.28

The WIC test commissioned for weldability testing has a 3 mm root gap and a symmetric Y-joint preparation. The entire test sample was preheated to the appropriate weld preheat before welding commenced. In line with traditionally established test procedures, the test assembly was cooled in still air and allowed to incubate for 72 hours before metallurgical sections were removed for analysis. This was marginally different from Noble and Pargeter's 48-hour incubation time.

Table 9: Weldability test designation and parameters employed by Cola [197].

Task	Electrode	Thickness	Heat input	Restraint	Objective
A	XP-90	20 mm	1 kJ/mm	25 mm	Single-pass baseline testing using E9010 electrodes.
A1	Cel 90	20 mm	1 kJ/mm	25 mm	Single-pass baseline testing using E9010 electrodes.
B	E9010	20 mm	1 kJ/mm	Multiple	Examining the effects of restraint length on cracking susceptibility for single-pass welds.
C	Cel 70	20 mm	1 kJ/mm	25 mm	Examining the cracking susceptibility of single-pass welds deposited using E6010 electrodes.

C1	XP 70	20 mm	1 kJ/mm	25 mm	Examining the cracking susceptibility of single-pass welds deposited using E7010 electrodes.
D	B90	20 mm	1 kJ/mm	25 mm	Examining the cracking susceptibility of single-pass welds deposited using high-strength low-hydrogen (E10018) electrodes.
E	XP-90	20 mm	Root Pass: 1 kJ/mm Hot Pass: 1.2-1.4 kJ/mm	25 mm	Examining the cracking susceptibility of double-pass welds using E9010 electrodes. The inter-pass delay is 10 min.
F	Root Pass: XP70 Hot Pass:XP90	20 mm	Root Pass: 1 kJ/mm Hot Pass: 1.2-1.4 kJ/mm	25 mm	Examining the cracking susceptibility of double-pass welds using XP-70 electrodes for the root pass and XP90 electrodes for the hot pass. The inter-pass delay is 10 min.
G	Root:XP70 Hot Pass: B90	20 mm	Root Pass: 1 kJ/mm Hot Pass: 1.2-1.4 kJ/mm	25 mm	Examining the cracking susceptibility of double-pass welds using XP-70 electrodes for the root pass and E10018 electrodes for the hot pass. The inter-pass delay is 10 min.
G1	Root:XP90 Hot Pass: B90	20 mm	Root Pass: 1 kJ/mm Hot Pass: 1.2-1.4 kJ/mm	25 mm	Examining the cracking susceptibility of double-pass welds using XP-90 electrodes for the root pass and E10018 electrodes for the hot pass. The inter-pass delay is 10 min.
H	Root:XP90 Hot Pass: XP90	20 mm	Root Pass: 1 kJ/mm Hot Pass: 1.2-1.4 kJ/mm	25 mm	Examining the cracking susceptibility of double-pass welds using E9010 electrodes. The inter-pass delay is 30 min.
I	XP90	6.4 mm	1 kJ/mm	25 mm	Single-pass baseline testing using E9010 electrodes.

2.9.2 **Empirical Cracking Boundaries**

2.9.2.1 E9010/E8010 Electrodes

Noble and Pargeter [199] conducted testing on 15.5 mm-thick parent plates (N.K.K steel) using both E8010 and E9010 electrodes, reporting that all cracking observed in welds were in the weld metal, not the HAZ. The cracking data generated by Noble and Pargeter can be represented as cracking boundaries (Figure 54 and Figure 55).

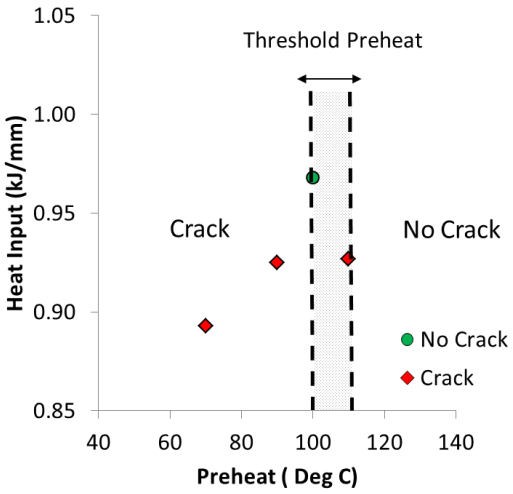

Figure 54: Critical preheat for 15.5 mm-thick pipe welded on the traditional WIC specimen using E8010 electrodes.

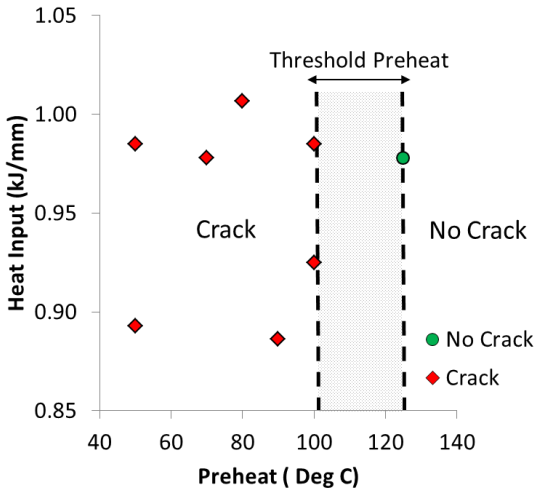

Figure 55: Critical preheat for 15.5 mm-thick pipe welded on the traditional WIC specimen using E9010 electrodes.

From the empirical results generated, Noble and Pargeter [199] proposed threshold preheats in excess of 100 °C. For welds deposited with E8010 electrodes they reported a small crack like defect at the weld toe at a preheat of 110 °C. Similarly, for the weld deposited with the E9010 electrodes, Noble and Pargeter [199] reported small cracks at the weld toe at a preheat of 100 °C. At a preheat of 125 °C, welds deposited with E9010 electrodes were reported as being crack-free. From these results they suggested that welds deposited with E9010 electrodes had threshold preheats of 100 °C to 125 °C and welds deposited with E8010 electrodes had threshold preheats of 100 °C to 110 °C. They also reported that, regardless of the electrode used for weldability testing, the weld microstructure consisted primarily of AF with some GBF. Hardness values for the coarse grain HAZ averaged 264 HV (Vickers hardness units) to 287 HV, with maximum hardness values ranging from 275 HV to 348 HV; they were insensitive to preheat.

On the 9.5 mm-thick plate, weldability testing was conducted using only E9010 electrodes. Noble and Pargeter [199] reported that, as was the case with the thick plate sections sourced from Japan, cracking was only observed in the weld metal, not the HAZ, in the American steel. The cracking data generated by Noble and Pargeter [199] can be represented as cracking boundaries, as illustrated in Figure 56.

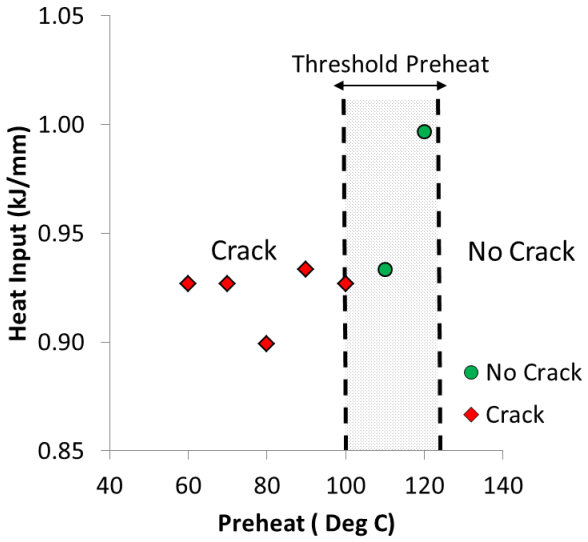

Figure 56: Critical preheat for 9.5 mm-thick pipe welded on the traditional WIC specimen using E9010 electrodes.

For welds deposited on thin test sections, Noble and Pargeter [199] reported a threshold preheat of 110 °C. The authors reported a microstructure consisting of primarily ferrite with aligned second phase for welds deposited with a lower preheat and a finer microstructure with a greater proportion of AF observed at higher preheats. Hardness values measured in the coarse grain HAZ ranged from 246–265 HV, with peak hardness values varying between 265 and 268 HV. The authors noted that the average weld metal hardness values were lower than those measured with the thicker test sections, which may have been as a result of the lower CE of the thinner parent plate and the longer $t_{8/5}$ cooling times associated with the thicker test sections. Nevertheless, as was the case with the thick sections, the authors reported no discernible connection between weld metal hardness and preheat levels.

Noble and Pargeter suggested that, although the WIC test was developed to compare weld metal cracking susceptibility and inherently favours the formation of cracking in this location, the data generated in their study from both small- and full-scale testing suggested that for the steel tested (i.e. for CE tested) and comparable welding parameters, cracking occurred exclusively in the weld metal. The authors compared their results with data generated from a study conducted by Pargeter [205] and concluded that this observation was similar for steels with lower CEs. The authors presented a table, reproduced as Table 10, to compare previously published threshold preheats with the Japanese and American steels that they tested.

Table 10: Critical preheats for various grades of line pipe steel tested by Noble and Pargeter [199].

Steel	Carbon Content wt%	CE_{IIW}	Cracking Threshold Preheat °C
1B465	0.02	0.28	70
1B469	0.08	0.39	90
1B486	0.05	0.35	90
1B487	0.02	0.26	70
NKK	0.07	0.39	100
US	0.12	0.38	110

Pargeter [205] conducted all WIC testing using an E9010 electrode which Noble and Pargeter [199] reported as having similar levels of reported diffusible hydrogen (38.1–49.1 ml/100g deposited weld metal) to the electrodes used in their study. Noble and Pargeter hypothesised that an increase in the threshold preheats appeared to be related to the carbon content of the pipe material, as would be anticipated from dilution effects; however, they went on to suggest that the relationship between CE and threshold preheats for the tests they conducted was unclear. When reviewing the 1986 results published by Pargeter [205], there is evidence to suggest that as the CE_{IIW} increases, the threshold preheat increases linearly. It is important to note, however, that when considering the Pargeter's 1986 results with Noble and Pargeter's, the both data sets support a positive linear trend (Figure 57).

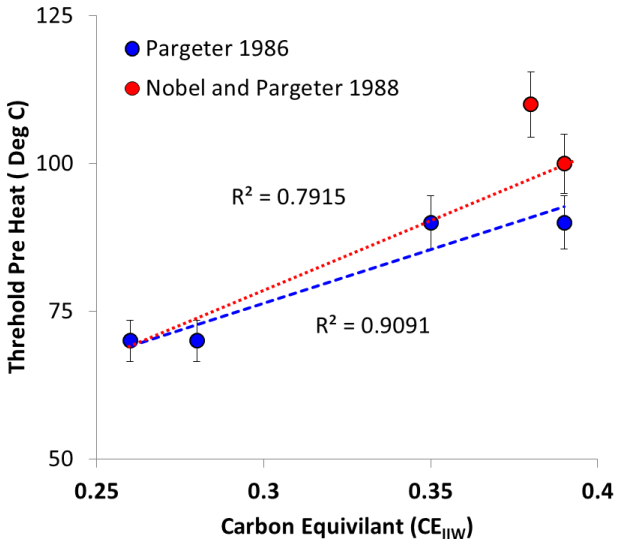

Figure 57: Threshold preheats for line pipe steels of different elemental compositions tested by Noble and Pargeter [199] and Pargeter [205] .

Overall, from both small- and full-scale weldability testing, Noble and Pargeter concluded that there is a greater risk of WMHACC than HAZHACC when depositing SMAW welds

using cellulosic electrodes of matching strength on HSLA line pipe steel such as API 5L X80. Additionally, they concluded that the minimum preheat needed to avoid WMHACC in WIC tests conducted with E9010 electrodes on X80 plate was 110 °C. Noble and Pargeter concluded that there is no clear effect on threshold preheat and strength of consumables. Although the CE of the two steels tested were comparable, the chemical composition of the steel sourced from Japan had slightly higher concentrations of Cr, C, Ni and Mo. This would not have only influenced the strength of the plates but also may have affected elemental segregation and thus cracking susceptibility [206].

For weldability testing conducted by Cola [197], weld metal hydrogen cracking was also the predominant type of cracking observed in the specimens tested. Cola also reported that cracking usually began at one of the corners of the root, primarily at the fusion boundary before propagating immediately into the weld metal. For weldability tests conducted using E9010 electrodes on 20 mm-thick plates (Figure 58), Cola suggested a threshold preheat of 70 °C to 80° C [197]. The variation in threshold preheat was suggested by Cola to be a consequence of different brands of electrodes used in testing. It is important to note that the results generated by Cola contradict those published by Noble and Pargeter [199], who reported a threshold preheat of 100 °C to 125 °C, even though testing was conducted on steels with a slightly lower carbon content and consequently lower CE.

Additionally, North et al. [178], who also tested E9010 electrodes on base materials with a P_{cm} of 0.200 and 0.183, established a threshold preheat of 120 °C, similar to Noble and Pargeter [199] but different than Cola [197]. North et al. [178] employed a shim to introduce misalignment but maintained restraint levels at R_F = 25 mm to approximate full-scale pipe welding conditions, just as Cola [197] and Noble and Pargeter [199] did.

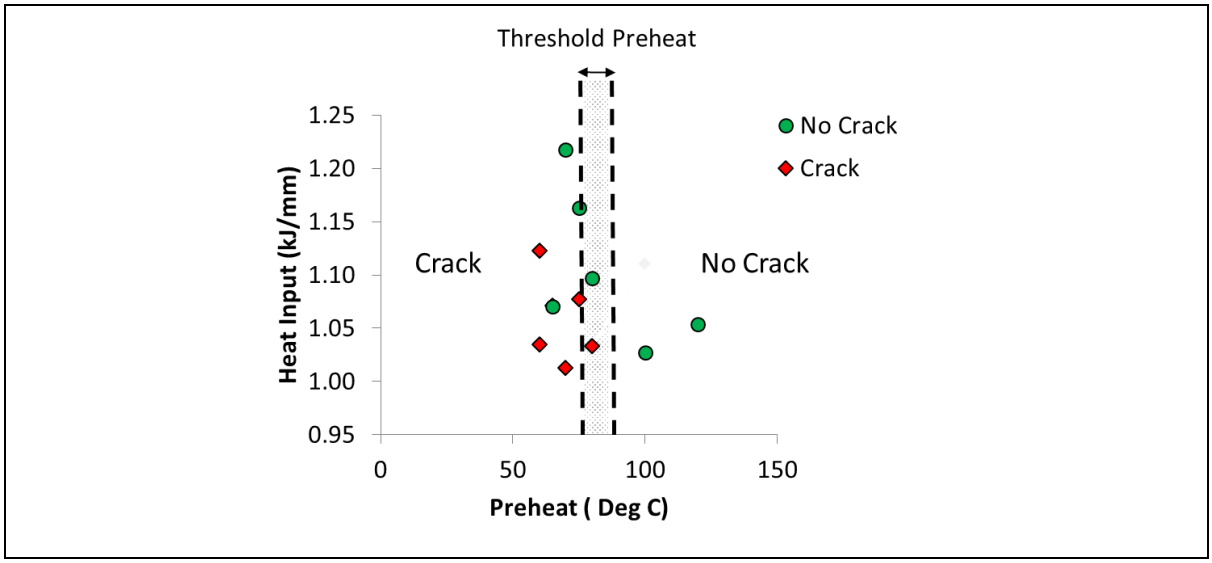

Figure 58: Single-pass weldability tests conducted on 20 mm-thick plate at heat inputs targeted at 1 kJ/mm using two different brands of E9010 electrodes. Cola [197] proposed a threshold preheat of 70–80 °C to minimise the risk of hydrogen cracking.

Cola extended testing to thin plates of 6.4 mm and concluded that the threshold preheat decreased by approximately 40 °C for the thinner plates (Figure 59). Cola attributed this to a lower level of restraint as the wall thickness had declined.

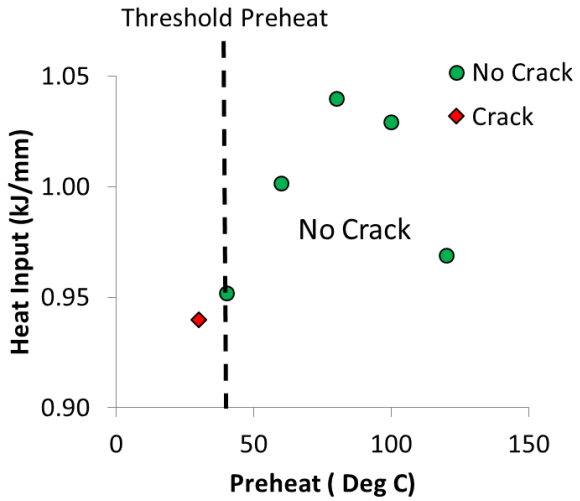

Figure 59: Single-pass weldability tests conducted on 6.4 mm-thick plate at heat inputs targeted at 1 kJ/mm using E9010 electrodes. Cola proposed a critical preheat of 40 °C to minimise the risk of hydrogen cracking.

Cola extended testing to assess the influence of the deposition of the hot pass on hydrogen cracking susceptibility. Welding was conducted using E9010 electrodes for the root and hot pass with two inter-pass delays (of 10 min and 30 min) tested; the results are illustrated in Figure 60.

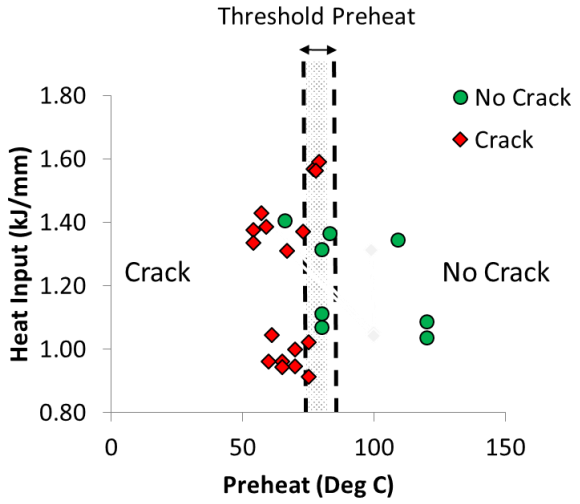

Figure 60: Multi-pass weldability tests conducted on 20 mm-thick plate at heat inputs targeted at 1 kJ/mm for the root pass and 1.2-1.4 kJ/mm for the hot pass, using E9010 electrodes and two inter-pass delays times (10 min and 30 min). Cola [197] proposed a critical preheat of 70–75 °C to minimise the risk of hydrogen cracking.

Cola [197] concluded from this testing that there was no significant difference between the critical preheat levels, particularly when the delay time between the root and hot pass was greater than 10 min. Cola hypothesised that this was as a direct result of cracking occurring before the deposition of the hot pass. In addition to a root pass-hot pass combination using E9010 electors, Cola also tested an E9010 (root pass) and E10018 (hot pass) combination to investigate the effects of overmatching the hot pass on hydrogen cracking susceptibility (Figure 61). Based on the empirical data generated, Cola suggested that a preheat of 105–110 °C is required, which as expected is greater than the preheat required for single-pass welds deposited with only E9010 electrodes.

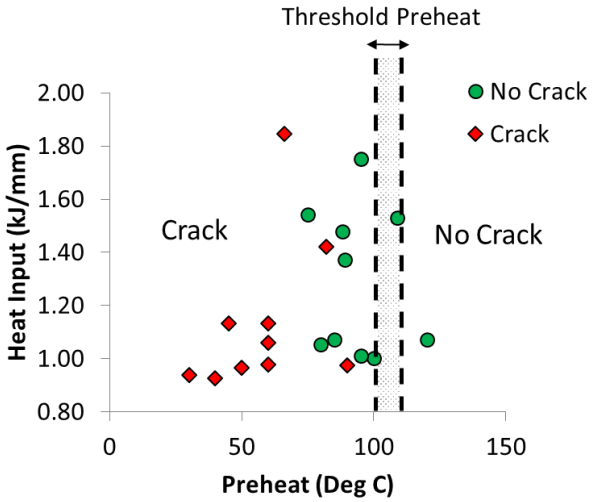

Figure 61: Multi-pass weldability tests conducted on 20 mm-thick plate at heat inputs targeted at 1 kJ/mm for the root pass and 1.2–1.4 kJ/mm for the hot pass, using E9010 and E10018 electors. Cola proposed a critical threshold preheat of 105–110 °C to minimise the risk of hydrogen cracking.

Single-pass weldability tested conducted using E9010 electrodes showed a nearly negligible difference in the critical preheat required to eliminate evidence of cracking. Cola reported that the variation in preheat was less than expected given the difference in elemental chemistry of the brands being tested.

As reported earlier, for a richer, higher-alloy chemistry, a higher preheat to mitigate the onset of hydrogen cracking is expected. When using the preheat predictors proposed by Yurioka [4], it is expected that the alloyed CEL 90 electrodes should require a preheat of 95 °C, whereas the leaner XP 90 electrodes should require a preheat of about 70 °C. Although the empirical results reported by Cola did not match the expected results, the ordering of the results was similar. This supports the preposition that electrodes with richer chemistries require higher preheats to reduce HACC susceptibility. In terms of the critical cooling rates ($t_{8/5}$ and t_{100}), an increase in the preheat applied resulted in an increase in the t_{100} and an

increase in the heat input lead to a marginal increase in the $t_{8/5}$, as expected. A review of the cooling rates for samples produced by two different brands of electrodes suggested that there was no significant difference in the cooling rates between different brands of E9010 electors.

For weldability tests conducted using E9010 electrodes, Cola [197] reported higher hardness's for samples on the cracked side of the empirically derived cracking boundary. Additionally and as expected, the hardness values were greater with Cel 90-type (rich chemistry) electrodes than with the XP90 (lean chemistry) electrodes. The theoretical basis for this expectation is the associated increase in hardenability of weld metal when depositing welds with higher alloying contents. Based on the empirical testing results, Cola proposed that the difference in hardenability accounted for the difference in cracking susceptibility and therefore the threshold preheat. Additionally, Cola compared the empirical testing results to the theoretical threshold preheats calculated using Yurioka's CEN hardness criteria. Cola acknowledged that the differences in the values could be attributed not to the sensitivity of the test but to the precision with which the tests were conducted.

When compared with results published by Noble and Pargeter [199] for X80 line pipe steel welded with similar E9010 type electrodes, there were significant differences in the threshold preheats (100–125°C), even though the hardness values were similar. In contrast, the results published by Pargeter were in much closer agreement with Cola's. Pargeter [205] reported threshold preheats of 80–90° C and hardnesses similar to that of Cola [197] and of Noble and Pargeter [199].

For double-pass welds using an E9010/E9010 electrode combination, Cola [197] reported a delay time of 10 min or more between the root and hot passes did not significantly influence cracking susceptibility; the threshold preheats reported for single-pass and double-pass welds were also similar. The similarity in cracking susceptibility can be explained by the fact that a delay time of 10 min or more between passes is sufficiently long to allow the temperatures of the WIC specimen to drop to a temperature similar to that of a WIC specimen with only one pass deposited.

The WIC test was designed to be a cracking susceptibility test for single- rather than multi-pass welds. The design of the weldability test permits rapid development of stresses after welding and therefore promotes cracking in the first pass of welds, so a second pass would have little effect on reducing crack susceptibility. Nevertheless, the deposition of the hot pass tempers the root pass, reduces hardness, improves toughness and decreases the amount of

residual hydrogen in the weld ligament. Thus, a root pass and a hot pass deposited in close succession should require a lower threshold preheat than a single-pass weld.

2.9.2.2 E7010/E6010 Electrodes

To test the susceptibility of undermatched welds, Cola [197] deposited single-pass welds using E6010 and E7010 electrodes. When comparing the results generated for single-pass welds deposited with E9010 electrodes, Cola suggested that for single-pass welds the critical preheat decreases with decreasing electrode strength. A similar trend is observed when comparing Cola's [197] results to that of Noble and Pargeter [199]. In the case of the empirical testing, Cola concluded that the critical preheat for single-pass welds deposited on 20 mm-thick plate using E6010 electrodes was 60 °C. Similarly, the threshold preheat was 60–65 °C for E7010 electrodes. Cola identified a maximum difference of 20 °C in threshold preheat levels between E9010 and E7010 electrodes and 20 °C between E7010 and E6010 electrodes.

It is important to note that, although Cola's results were inconsistent with those published by Noble and Pargeter [199], who reported no difference in preheat levels between E8010 and E9010 electrodes, there is much evidence in the literature [3, 20, 28, 33, 36, 81, 100, 193, 207-214] to suggest that as electrode strength decreases, the threshold or critical preheat required to avoid cracking also decreases. The discrepancies in the results support the notion that in order to test the difference in electrode chemistry and strength on hydrogen cracking susceptibility, there has to be a significant difference in the strength and thus the elemental composition of the electrodes tested.

A review of Cola's weldability test results also shows that for double-pass welds a lower preheat was required when depositing the root pass with an E7010 electrode and a combination of either an E9010 or E10018 electrode than with a single-pass E7010 electrode. These results further support the proposition that the root pass is the most vulnerable pass in the welding sequence.

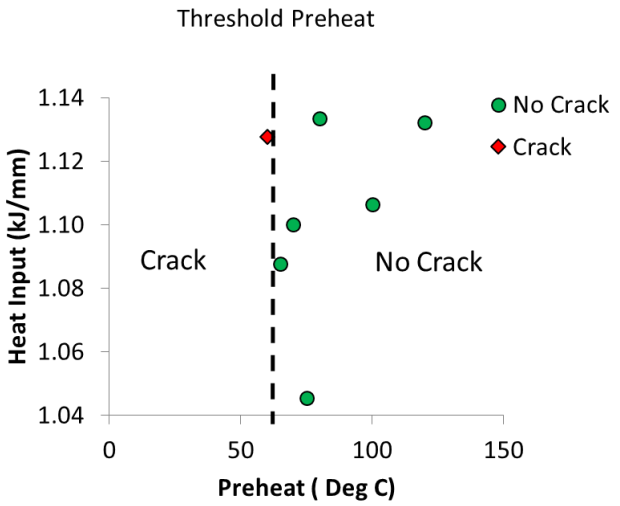

Figure 62: Single-pass weldability tests conducted on 20 mm-thick plate at heat inputs targeted at 1 kJ/mm for the root pass using E6010 electrodes. Cola proposed a critical preheat of 60–65 °C to minimise the risk of hydrogen cracking.

For welds deposited with E6010 electrodes (Figure 62), Cola proposed a threshold preheat of 60–70°C, which are within the range proposed by Signes and Howe [45] who reported a threshold preheat of 45 °C and 85 °C for E6010 and E7010 electrodes respectively. The base metal composition in Signes and Howe's study ranged from P_{CM} = 0.17 to P_{CM} = 0.20, whereas the base metal composition in Cola's study was P_{CM} = 0.21. Cola reported the same threshold preheat (60 °C) for single-pass E7010 (Figure 63) welds and double-pass WIC tests (E7010/E9010). Cola suggested that this was to be expected, as it was the E7010 electrode in the root pass that controlled weld metal cracking, and the threshold preheats should thus be similar. Nevertheless, it is reasonable to suggest that the addition of an E9010 pass has the potential to increase the transverse residual tensile stresses in the root pass and should lead to an increase in the threshold preheat needed to avoid cracking. However, Cola [197] noted that as it has been demonstrated that the critical stress required for fracture of a single-pass E7010 weld is lower than that required for an E9010 weld, it can be concluded that the cracking susceptibility of an E7010 root pass is not altered by the addition of an E9010 hot pass. Cola justified this conclusion by pointing out that, in the data reviewed, cracking only occurred in the weld metal initiated at the root notch and propagated through the root pass.

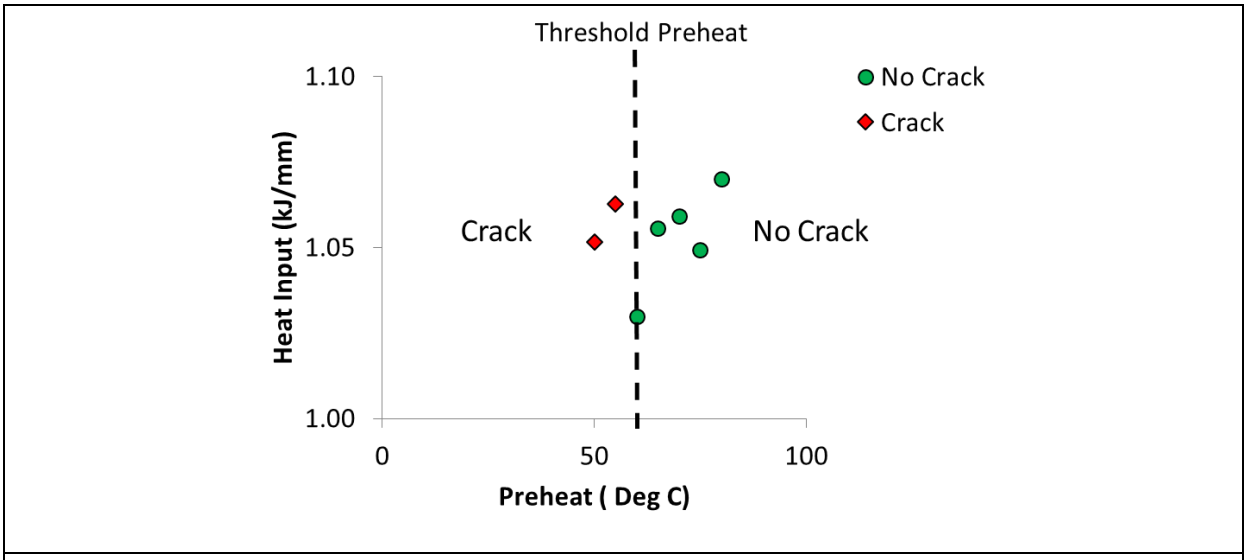

Figure 63: Single-pass weldability tests conducted on 20 mm-thick plate at heat inputs targeted at 1 kJ/mm for the root pass using E7010 electrodes. Cola [197] proposed a threshold preheat of 60 °C to minimise the risk of hydrogen cracking.

2.9.2.3 E10018 Electrodes

In addition to E6010, E7010 and E9010 electrodes, Cola [197] conducted limited testing on E10018 electrodes. These high-strength low-hydrogen electrodes are typically not recommended for use with X70/X80 line pipe steel when depositing the weld for the root pass or the hot pass of a girth weld, though if they are used, they do represent the effect of a significantly overmatched root pass. From the results generated, Cola [197] suggested a threshold preheat of 110–115 °C for single-pass welds. Cola reported that cracking occurred primarily in the HAZ, which he suggested was a result of overmatching. Cola also concluded that for double-pass welds (Figure 65), an increase in the strength of the root pass resulted in a higher critical preheat needed to eliminate evidence of hydrogen cracking.

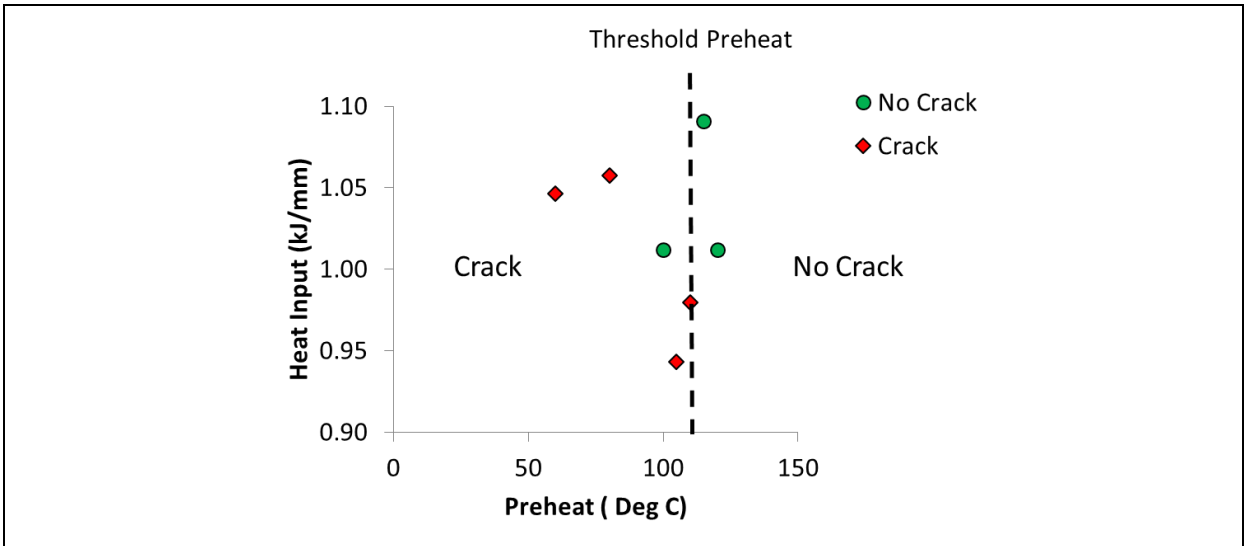

Figure 64: Single-pass weldability tests conducted on 20 mm-thick plate at heat inputs targeted at 1 kJ/mm for the root pass using E10018 electrodes. Cola proposed a critical preheat of 110 °C to minimise the risk of hydrogen cracking.

When examining the difference in where the cracking manifest, it is important to account for two key differences between the electrodes considered. The E10018 is an all-position low-hydrogen potassium- and iron-powered based electrode with estimated tensile and yield strengths of 690 MPa (100 ksi) and 600 MPa (87 ksi) respectively. The hydrogen content introduced into the weld metal is on the order of 4.2 ml/100 grams of deposited weld metal. Conversely, the E9010 electrode is an all-position cellulosic and sodium-based electrode with estimated tensile and yield strengths 620 MPa (90 ksi) and 552 MPa (80 ksi) respectively. Additionally, the cellulosic electrode introduces hydrogen into the weld metal on the order of 42 ml/100g of deposited weld metal, so a cellulosic electrode introduces 10 times more hydrogen than a low-hydrogen electrode. Considering that the yield strength of the base plate is 552 MPa (80 ksi), the E9010 produced a slightly undermatched weld, whereas the E10018 electrode produced an overmatched weld. These factors suggest that the yield strength and local stress ratio are greater for an E9010 than for an E10018 weld. Cola [197] postulated that, given the higher hydrogen content, yield strength and local stress ratio of the E9010 weld, it is reasonable to suggest the propensity for weld metal cracking will be greater in the E9010 electrode than in the E10018. Nevertheless, overmatching and undermatching welds may influence the threshold cracking stress, which was not addressed in Cola's study.

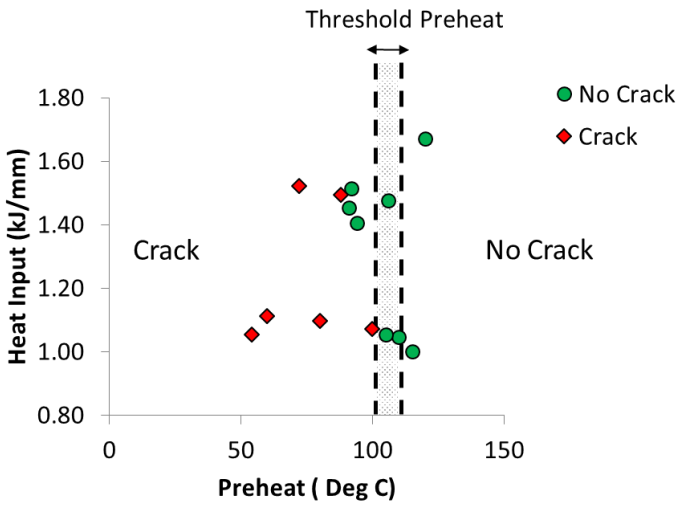

Figure 65: Multi-pass weldability tests conducted on 20 mm-thick plate at heat inputs targeted at 1 kJ/mm for the root pass and 1.2–1.4 kJ/mm for the hot pass, using E9010 and E10018 electrodes. Cola [197] proposed a critical preheat of 105–110 °C to minimise the risk of hydrogen cracking.

For double-pass welds Cola observed that the E9010/E10018 electrode combination had a higher threshold pre heat than the E9010/E9010 combination (Figure 65), even though it was the root pass of the E9010/E10018 that appeared to be sensitive to crack formation. Cola

sought to explain this anomaly by examining the weld cooling times, $t_{8/5}$, hardness and visual appearance for the E9010/E10018 and the E9010/E9010 combinations.

Cola [197] concluded that the $t_{8/5}$ cooling times were similar, as were the hardness values and trends such as higher hardnesses for cracked samples vs non-cracked samples. Cola reported no anomalies in the weld profile of the welds; the weld beads appeared to be centred in the joints for both electrode combinations. Cola therefore concluded that the empirical data collected offered no evidence to explain the difference in the threshold preheat required for the E9010/E9010 and E9010/E10018 electrode combinations. Cola [197] proposed further tests to analyse with greater precision the factors governing the differences in threshold preheat.

2.9.3 Correlation of Thermal Data

Noble and Pargeter [199] reported no correlation between $t_{8/5}$ times and preheat. However, the authors stipulated that they noted a high degree of scatter in their $t_{8/5}$ cooling data, which might have been the reason why they were not able to discern a credible correlation between the parameters. However, preheat has a dominant influence on t_{100}, not on $t_{8/5}$, so it is reasonable to suggest that this may have also contributed to the fact that Noble and Pargeter [199] were not able to derive a correlation between the two parameters. Nevertheless, the authors did report a positive correlation between t_{100} and preheat. It is important to note that Noble and Pargeter [199] were only able to record data for 300 seconds. Cooling times (t_{100}) greater than 300 seconds were simply coded as > 300. Cola [197] did not discuss the correlation between welding parameters and critical cooling rates, but a review of the published data sets reveals results similar to Noble and Pargeter's [199].

2.9.4 Hardness Surveys

Vickers hardness tests were conducted by Cola on selected weld samples across the weld metal and HAZ using a 1-kg load. 15 indentations were made on single-pass welds and 22 on double-pass welds. From the results generated, Cola concluded that for all weldability tests conducted an increase in the level of preheat applied resulted in a decrease in weld metal hardness. This result is similar to what was observed by Noble and Pargeter [199] for single-pass welds deposited with E9010 electrodes. Cola [197] went on to conclude that the higher alloy content in the electrodes produced welds with higher hardnesses. For single-pass welds deposited with E6010 and E7010 electrodes with comparable heat inputs, Cola reported a hardness range of 225–283 HV. For E9010 and E10018 electrodes, hardnesses ranged from

260 HV to 313 HV. For double-pass welds deposited with E7010/E9010 and E9010/E9010 combinations, the weld metal hardness ranged from 201 HV to 303 HV. The HAZ hardness was reported to be lower for double-pass than single-pass welds with comparable electrode selection, which can be explained by the tempering effect of the second pass on the HAZ created by the first pass.

2.9.5 Concluding Remarks

The WIC test has been used for many years as a conservative tool to predict the critical preheat levels needed to avoid hydrogen cracking. It has been especially favoured for small-scale testing, primarily due to its ability to relate a critical test parameter like preheat to full-scale behaviour. Weldability testing has been used to generate multiple safe welding envelopes for a range of steel/electrode combinations.

The Root Pass

The WIC test was originally designed to evaluate the cracking susceptibility of single-pass welds, as the design allows for the rapid build-up of stresses after the first pass, reducing the influence of the second pass on cracking susceptibility. In the field, however, the second pass will have an effect on cracking susceptibility by reducing local stresses on ligaments. Additionally, the hot pass tempers the root pass, increasing toughness, reducing hardness and reducing the residual hydrogen content in the weld. From a review of empirical studies [31, 178, 182, 197, 199], it was established that the root pass is indeed the most vulnerable pass in the pipeline laying process.

Heat Input Test Range

It was established in the literature review that the lower the heat input with which the root pass is deposited, the greater susceptibility to HACC. In the North American context a heat input of 1 kJ/mm is considered low for the thickness and grade of steels currently in use. It is therefore not surprising that extensive weldability testing has been carried out on multiple heat inputs greater than 1 kJ/mm with a range of electrode-steel combination for line pipe steels. No test data was found for weldability tests below 1 kJ/mm on line pipe steels. However, as noted above, in the Australian context the root passes of girth welds are deposited with heat inputs as low as 0.5 kJ/mm. No published data was found that examined the critical preheats needed to avoid hydrogen cracking for heat inputs lower than 1 kJ/mm (Figure 66). This significant gap in published data represents a key area that needs to be

investigated to establish a comprehensive safe welding envelope, especially outside the North American context.

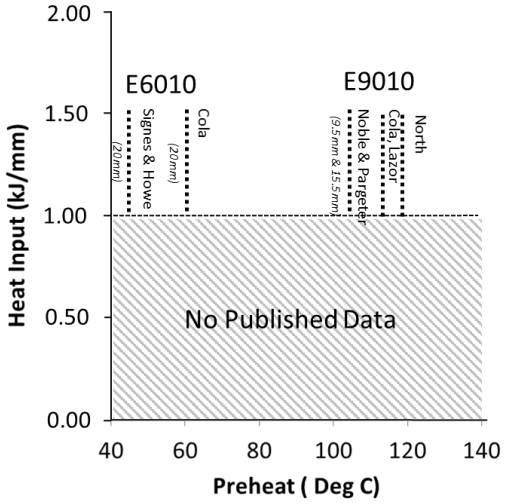

Figure 66: Empirical safe welding envelope established though weldability testing [31, 45, 178, 197, 199] on the WIC specimen for various electrodes on HSLA steels with a P_{CM} range of 0.17 to 0.22.

Empirical Boundaries

Cellulosic electrodes are generally used to deposit the root pass of a girth weld for HSLA line pipe steels as a result of their ability to deposit at high travel speeds and their excellent penetration. However, they introduce copious amounts of hydrogen into the weld, which makes the welds particularly susceptible to HACC. To prevent excess hydrogen introduced into the weld, critical preheats are identified above which no hydrogen cracking is expected. Extensive weldability testing has been carried out with E8010 and E9010 electrodes and a limited number of tests have been carried out using E6010 and E7010 electrodes (Figure 66). From these tests, variations in the critical preheat were identified, but there was no definitive explanation for these variations. It was also established the weldments heat affected zone's hardness, which historically has been used as a proxy for HAZ hydrogen cracking, cannot be used as a definitive tool to quantify crack susceptibility of the weld metal.

2.10 Prediction and Prevention of HACC in Welds

For hydrogen cracks to begin and propagate, a critical concentration of hydrogen must be in a susceptible microstructure and the local stress concentration must be at a critical threshold. If one of these factors is absent, it is improbable that the phenomenon will manifest. However, the interrelation of variables that influence the three factors of hydrogen concentration, hardness and local stress concentration make the prediction and control of hydrogen cracking

a daunting task. Causal factor diagrams such as Yurioka's [4] are used to illustrate the interrelation of variables (Figure 67).

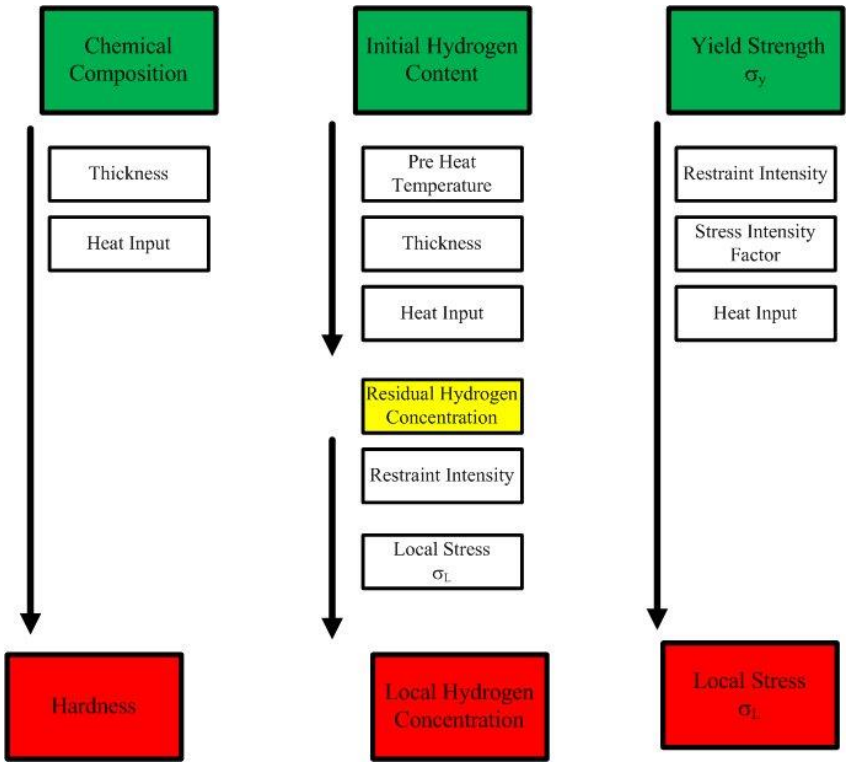

Figure 67: Diagrammatic representation of interrelationship of variables that influence causal factors governing hydrogen cracks [4].

Numerous methods for prediction and prevention of hydrogen cracking have been proposed, though most have been for the prevention of cracking in the HAZ. This section of the literature review discusses the various methods used for the prediction and control of hydrogen cracking.

2.10.1 **Carbon Equivalent (CE)**

The influence of individual alloying elements on the resulting weld metal microstructural features, constituents and properties were introduced in Section 2.3.4. The effect of the collective or bulk chemical composition on the weldability of steels can be encapsulated by the concept of CE. The CE normalises the composition to a single number and estimates the hardenability of the parent materials, which is indicative of the likelihood to form hard martensitic microstructures. Table 11 below lists a selection of the CEs developed to date.

Table 11: CE formulas and their applicability.

CE Formula	Application according to Yurioka [32]	Application According to Talas et al. [215]	Reference
Group A			
$CE_{IIW} = C + \frac{Mn}{6} + \frac{Ni + Cu}{15} + \frac{Cr + Mo + V}{5}$	C ≥ 0.08 %	C-Mn steels with high C Content	[216]
$CE_{WES} = C + \frac{Si}{24} + \frac{Mn}{6} + \frac{Ni}{40} + \frac{Cr}{5} + \frac{Mo}{4} + \frac{V}{14}$			[217]
Group B			
$CE_{DNV} = C + \frac{Si}{24} + \frac{Mn}{10} + \frac{Ni + Cu}{40} + \frac{Cr}{5} + \frac{Mo}{4} + \frac{V}{10}$	0.08 % ≤ C ≤ 0.12%	Steels with lower C contents	[218]
$CE_{T} = C + \frac{Mn}{10} + \frac{Cu}{20} + \frac{Ni}{40} + \frac{Cr}{20} + \frac{Mo}{10}$			[219]
Group C			
$Pcm = C + \frac{Si}{30} + \frac{Mn}{20} + \frac{Cu}{20} + \frac{Ni}{60} + \frac{Cr}{20} + \frac{Mo}{15} + \frac{V}{10} + 5B$	C ≤ 0.12%	Pipeline steels	[220]
$CE_{PLS} = C + \frac{Si}{25} + \frac{Mn}{16} + \frac{Cu}{16} + \frac{Ni}{60} + \frac{Cr}{20} + \frac{Mo}{40} + \frac{V}{15}$			[221]
$CE_{HSLA} = C + \frac{Mn}{16} - \frac{Ni}{50} + \frac{Cr}{23} + \frac{Mo}{7} + \frac{Nb}{5} + \frac{V}{9}$			[35]
Group D			
$CE_{N} = C + (0.75 + 0.25\tanh[20(C - 0.12)]) \times (\frac{Si}{24} + \frac{Mn}{6} + \frac{Cu}{15} + \frac{Ni}{20} + \frac{Cr + Mo + Nb + V}{5} + 5B$	C ≤ 0.3%	All steels	[222]

The derivation of the CE is empirical in nature, so each formula is limited to a particular chemical composition of steel, cooling rate ($t_{8/5}$) and plate thickness. Consequently, there is no universal CE that can be used as a proxy for weldability [223-228]. Moreover, having been derived empirically, both systematic and random experimental errors add a degree of uncertainty to any correlation derived from the use of the formulae.

The predictive utility of CEs has been further eroded with the introduction of high-strength low-alloy steels. Traditionally, metallurgical properties and weldability were dictated by the carbon content in the steel. As carbon levels have dropped and carbon equivalent levels have progressively decreased, other metallurgical factors such as the prior austenite grain size have become increasingly more important than the effect of chemistry [4, 229, 230].

2.10.2 **Hardness Control Criterion**

Although the literature review has demonstrated the limitations of using hardness on its own as a measure of weld metal cracking susceptibility, historically it has been used to establish a threshold above which a weld would not be qualified for service. One of the key hardness control thresholds that was established was codified in BS5135 [31]. Developed by the Welding Institute, the monograms proposed identified the critical preheats required to retard cooling rates to such an extent that a steel with a CE_{IIW} > 0.2% for combined thickness from 10–150 mm and heat input from 1–8 kJ/mm could be welded without the risk of cracking at a given level of restraint. The nomogram was based on the observation that the incidence of

HAZ cracking is significantly reduced when HAZ hardness value reaches a critical level. By limiting the cooling rates through the application of preheat, critical HAZ hardness will never be reached. This approach worked well for steel with a CE_{IIW} range of 0.46–0.58. However, given the composition of modern steels, especially its carbon content, this approach would have to be used with a great degree of caution.

2.10.3 Hydrogen Control Criterion

The development of hydrogen control criteria stemmed from the fact that cracking did not always occur when critical hardness was exceeded. The control of the residual hydrogen content is based on the principle that the application of preheat to a weld ligament will retard the cooling rate. As the weld cools, hydrogen has the opportunity to effuse out of the weldment. The rate of effusion and consequently the volume of hydrogen that will effuse out depends on the time it takes the weld to cool to 100 °C (t_{100}). As discussed in Section 2.4.5, hydrogen is less mobile below 100 °C and can thus cause embrittlement in the local microstructure within which it is trapped. In practical terms, controlling the hydrogen content is the simplest approach. A preheat can be estimated based on a combination of welding variables such as alloy composition and thickness, thus allowing for a greater fabrication flexibility in terms of the selection of heat input, pass sequence and level of restraint, as compromises do not have to be made to avoid hydrogen cracking. Preheated welds can tolerate higher hardness levels than non-preheated welds.

Ito and Bessho

Ito and Bessho [231] derived an empirical correlation between the parent plates' chemistry, restraint levels, hydrogen content and cracking susceptibility based on a large number of groove weld Tekken tests for a range of alloy steels (0.07 < C < 0.22 wt%). A cracking parameter P_W was proposed, which links the composition characterisation parameter P_{CM}, diffusible hydrogen content (using the glycerine method), H_{JIS} (ml/100g) and intensity of restraint K (kg/mm^2):

Equation 2-10: Cracking parameter P_W proposed by Ito and Bessho [231].

$$P_w = P_{cm} + \frac{H_{JIS}}{60} + \frac{K}{40 \times 10^3}$$

The authors pointed out that the cooling time to 100 °C is related to the residual hydrogen content in the weld, so increasing the time it takes the weld to cool to 100 °C would decrease

the risk of susceptibility to HACC. The critical preheat was then defined as the preheat level at which no more cracks were observed experimentally for a given composition and restraint level. The cooling time was measured experimentally; based on an extrapolation of the data, critical preheat criteria such as Equation 2-11 were proposed:

Equation 2-11: Extrapolation of critical cooling times proposed by Ito and Bessho.

$$t_{100} > (t_{100})_{cr} = 1.4 \times 10^4 (P_w - 0.28)^2$$

Several other cracking parameters, such as those in Suzuki et al. [192] and Yurioka et al. [101], have been developed using a similar approach to Ito and Bessho [231]. The studies by Ito and Bessho [231], Suzuki et al. [232] and Yurioka et al. [228] use the Tekken weldability test to establish empirical safe welding boundaries. The differences in the models arise from the degree of refinement of the hydrogen diffusion equation and the method used to determine the stress of the weld. In the Tekken test, root cracks are initiated in the root notch of a single-pass short bead with severe restraint. Therefore the criteria developed, especially the critical preheats, are considered conservative, especially when compared with multi-pass welding, which is the norm in field welding.

Yurioka

Yurioka's [101] proposed methodology, with its cracking criterion CI-t_{100} described by Equation 2-12, takes into account the theoretical elastic stress concentration factor at the weld root or toe (K_t) and the mean yield strength of the weld metal (σ_w). Cracking can be avoided if the actual cooling time t_{100} is greater than the critical cooling time $(t_{100})_{cr}$:

Equation 2-12: Correction factor for Yurioka's critical cooling rate estimator.

$$CI = CE_N + 0.15 \log H_{GL} 0.70 \log\left(0.0017 K_t \sigma_w\right)$$

Equation 2-13: Yurioka's critical cooling rate (t_{100})cr estimator for the prevention of HACC.

$$\left(t_{100}\right)_{cr} = \exp\left(68.05CI^3 - 181.77CI^2 + 163.80CI - 41.65\right)$$

The use of the CE CE_N (Equation 2-14) takes in to account the factor A(C) (Equation 2-15). For a carbon content of less than 0.08%, A(C) approaches 0.5, while at carbon content greater than 0.18%, A(C) approaches 1, as illustrated in Figure 68.

Equation 2-14: CE used in Yurioka's critical cooling rate estimator.

$$CE_N = C + A(C)\left(\frac{Si}{24} + \frac{Mn}{6} + \frac{Cu}{15} + \frac{Ni}{20} + \frac{Cr + Mo + V + Nb}{5} + 5B\right)$$

Equation 2-15: Accommodation factor A(C) relating CEN, CE_{IIW} and P_{CM}.

$$A(C) = 0.75 + \tanh\{20\times(C - 0.12)\}$$

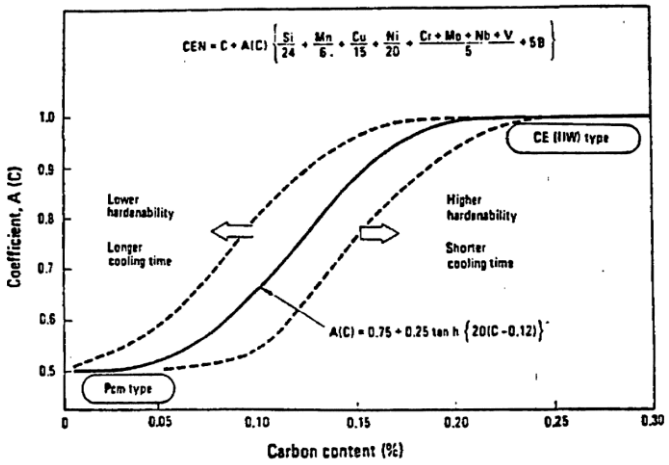

Figure 68: Accommodation factor relating CEN, CE_{IIW} and P_{CM}.

To demonstrate the validity of the proposed predictor, Yurioka performed a series of Stout's line pipe cold cracking tests on 20 different grades of steel with carbon content ranging from 0.018% to 0.25%, including low-alloy steels. In rating CEs in order of decreasing correlation coefficients, Yurioka demonstrated that CE_N had the highest correlation, implying the superiority of his proposed criterion.

Suzuki

Although accurate, Yurioka's formula requires prior knowledge of K_t and σ_w. In 1986 Suzuki [232] published a predictor which he claimed to be more accurate than any he had published before and had proven to be as accurate as the method published by Ito and Bessho [231]. The critical preheat temperate to avoid cracking in low-carbon steels (C > 0.037 wt%) is given by Equation 2-16**,** where *O* is the critical preheat temperature, *h* is the thickness of the plate and H_D is the amount of diffusible hydrogen (ml/100g) of the deposited weld metal.

Equation 2-16: Critical preheat temperature to avoid hydrogen cracking, proposed by Suzuki [232].

$$(O)_{Cr} = 68\log(h) + 97\log(H_D) + 459\tan^{-1}(3C) + 41Si + 67Mn + 23Cu + 12Ni + 151\tan^{-1}(0.7Cr) + 29\tan^{-1}(3Mo) + 139V + 24\tan^{-1}(300B) - 354$$

Graville

Graville [37] proposed a variation on the traditional hydrogen criterion method, effectively introducing a more generalised approach. He hypothesised that cracking could only occur if a critical concentration of hydrogen remained in the weld after it had cooled to 50 °C. He suggested that the amount of hydrogen diffusing out of the weld could be represented by the diffusion parameter βτ, where β is a geometric factor and $\beta = \int_{1500}^{TR} D(t)dt = \sum D\Delta t$, where D is the diffusion coefficient for hydrogen over time. For a given material, τ is related directly to the time needed to cool to 50 °C. Therefore the residual hydrogen concentration H_R is represented by:

Equation 2-17: Relationship between residual hydrogen concentration diffusion parameter proposed by Graville [37].

$$H_R = H_0 \exp(-\beta_0 \tau)$$

τ increases as the cooling rate decreases, especially between 300°C and 100 °C. The critical residual hydrogen concentration is described by Equation 2-18**.**

Equation 2-18: Relationship between critical hydrogen concentration diffusion parameter proposed by Graville [37].

$$H_{Cr} = H_0 exp(-\beta_0 \tau_{cr})$$

The critical values for βτ for the onset of cracking are empirically related to hydrogen content and composition:

Equation 2-19: Relationship between composition, residual hydrogen concertation and diffusion parameter.

$$\beta_0 \tau_{cr} = 12P_{cm} + logH_{IIW} + Constant,$$

where P_{cm} is the Ito-Bessho [220] CE, H_{IIW} is the hydrogen content (ml/100g) of deposited metal and the constant term depends on restraint levels. When the residual hydrogen concentration exceeds the critical hydrogen concentration, there is the risk of a weld's

succumbing to HACC. Figure 69 illustrates the relationship between $(\beta\tau)_{Crit}$ and βτ and reported that $\frac{\beta}{\beta_0} = 2.3$ and $\beta = 49cm^2$ with the G-BOP test [37].

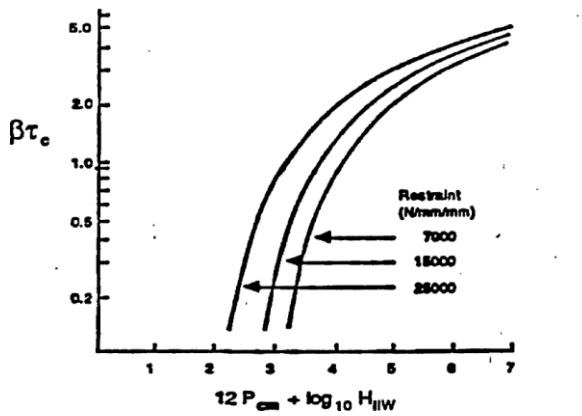

Figure 69: Determination of preheat temperate from βτ parameter [37].

2.10.4 **Stress Control Criterion**

Numerous studies have been commissioned with the aim of identifying the lower critical stress (LCS) needed for cracking to initiate and propagate as a function of influential variables like elemental constituents as represented by CE, diffusible hydrogen content, hardness and critical cooling rates (t_{100}, $t_{8/5}$), etc. The relationships derived are generally only applicable for the class of steel with which they were developed; it is accepted that no relationship with universal applicability has been developed to date.

Ito's Formula

In 1976 Ito et al. [233] proposed the following formula for estimating the LCS in high-strength steels with a P_{CM} range of 0.136–0.271 and a diffusible hydrogen content of 0.7–3.7 ml/100g (JIS method). The relationship was developed using the implant cracking test.

Equation 2-20: Relationship proposed by Ito et al. [233] used to estimate the LCS for the onset of HACC.

$$LCS\left(\frac{kg}{mm^2}\right) = -242P_{CM} - 22.5\log[H] + 50\log t_{100} - 3$$

Weldability tests were carried out at 0.97 kJ/mm and 1.7 kJ/mm at two preheats: 60 °C and 150 °C. The implant samples used were of circular notch geometry and the implants were positioned in a V-groove in the support plate. Although demonstrated to be accurate for the steels tested by Ito et al., Lundin et al. [47] showed that Ito's formula underestimated the LCS

for higher-strength steels. The steels tested by Lundin et al. had higher CEs than those tested by Ito et al.; according to the proposed correlation, the critical stress for the given welding parameters and hydrogen content decreases with P_{CM}. This relationship appears to hold true only for the range of P_{CM} tested by Ito et al. Lundin et al. [47] reported a positive correlation between their work and the work by Matsuda et al. [234] and Christenson and Simonsen [235] on medium-strength ship plate, structural and pipeline grade steel and high-strength quench and tempered steels.

Table 12: Steel elemental compositional range tested by Ito et al. [233].

C	Ni	Cu	B	Mn	Cr	V	Si	Mo	Nb
0.04-0.17	0-1	0-0.24	0-0.001	0.81-1.59	0-048	0-0.04	0.24-0.42	0-0.44	0-0.02

Inagaki's Formula

Following the study by Ito et al. [233], Inagaki et al. [236] proposed the following formula for steels with a P_{CM} range of 0.16–0.282 and a hydrogen content varying from 1–21 ml/100g (JIS method) and a cooling time, $t_{8/5}$, of 5–20 seconds.

Equation 2-21: Relationship proposed by Inagaki et al. [236] used to estimate the LCS for the onset of HACC.

$$LCS\ (kg/mm^2) = 68.9 - 121P_{CM} - 24log([H]+1) + 1.75t_{8/5} + 1.65\times10^2 t_{100}$$

Inagaki et al. [236] used the implant test and the same geometry that Ito et al. [233] used; however Inagaki et al. took into account the critical cooling times $t_{8/5}$ and t_{100}. The authors concluded that a better correlation could be achieved with $Log([H]+1)$ in contrast to $Log\ ([H])$. However, Lundin et al. [47] demonstrated that, as with Ito's formula, Inagaki's formula underestimates the LCS and provides poor experimental correlation.

Matsuda's Formula

Matsuda et al. [234] compared the applicability of Ito's [233], and Inagaki's [236] formulae for a range of steels, including high-yield, cast and Cr-Mo steels with a P_{CM} range of 0.196–0.308 and a hydrogen content range of 1.1–28.5 ml/100g (JIS method). The chemical composition of all the steels tested is listed in Table 13 below. Matsuda et al. [234] conducted implant tests with no preheat and thus proposed a formula that does not take t_{100} into account:

Equation 2-22: Relationship proposed by Matsuda et al. [234] used to estimate the LCS for the onset of HACC.

$$LCS\ (kg/mm^2) = -268P_{CM} - 23.3log([H]) + 138$$

The authors [234] suggested that both formulae underestimated the LCS of the tested steels, though this could be attributed to the fact that Matsuda et al. employed a helical notch, whereas Ito et al. [233] and Ingaki et al. [236] used a circular notch in the implant test specimen.

Table 13: Steel elemental compositional range tested by Matsuda et al. [234].

C	Ni	Cu	Mn	Cr	V	Si	Mo
0.04-0.15	0.03-8.76	0.01-0.23	0.5-0.84	0.04-2.25	0-0.06	0.23-0.06	0.01-0.96

Terasaki's Formula

Terasaki and Satoh [237] took a similar approach to Ito et al. [233], Inagaki et al. [236] and Matsuda et al. [234], using the implant test to establish an LCS above which hydrogen cracking may initiate. However, Terasaki and Satoh did not consider CE as a variable. The authors took an alternative approach by considering the maximum HAZ hardness as a parameter and a thermal factor, $(\sum D\Delta t)_{100}$, proportional to the amount of hydrogen remaining in the weldment at 100 °C. Terasaki and Satoh proposed the following formula to estimate the LCS in implant cracking tests with circular notch geometry for steels with chemical composition in the range in Table 14.

Table 14: Steel elemental compositional range tested by Terasaki and Satoh [237].

C	Ni	Cu	Al	Mn	Cr	V	B	Si	Mo	Nb
0.07-0.42	0.02-9.35	0-0.39	0-0.58	0.42-1.47	0.02-2.3	0-0.059	0-0.014	0.06-0.48	0.01-1	0-0.042

Equation 2-23: Relationship proposed by Terasaki and Satoh [237] to estimate the LCS for the onset of HACC in cases where the residual hydrogen concentration $(H_R)_{100} \geq 2$ ppm.

$$LCS\left(\frac{kg}{mm^2}\right) = -20\log(H_R)_{100} - 0.20H_{max} + 125$$

Equation 2-24: Relationship proposed by Terasaki and Satoh [237] to estimate the LCS for the onset of HACC in cases where the residual hydrogen concentration $(H_R)_{100}$ < 2 ppm.

$$LCS\left(\frac{kg}{mm^2}\right) = -75\log(H_R)_{100} - 0.20H_{max} + 145,$$

where

H_R = retained hydrogen content in ppm at 100 °C.

H_o = diffusible hydrogen content in fused metal just after solidification.

H_F = diffusible hydrogen content measured by the JIS method.

$(\sum D\Delta t)_{100}$ = thermal factor for hydrogen diffusion summed from solidification temperature to 100 °C.

H_{max} = hardness in the course grain HAZ in diamond pyramid hardness.

The residual hydrogen content can be related to the diffusible hydrogen content and thermal factor using the following relationship:

Equation 2-25: Relationship proposed by Terasaki and Satoh [237] between diffusible and residual hydrogen.

$$(H_R)_{100} = H_0 exp\{-75(\sum D\Delta t)_{100}\}, \text{ where } H_0 = 1.26H_F.$$

Karppi's Formula

Karppi and Satoh [152] tested the relationship that Terasaki and Satoh derived using the implant test and the RRC test, demonstrated a positive correlation between the data sets. However, Karppi et al. proposed that the thermal factor introduced by Terasaki and Satoh was in fact influenced by the type of steel being tested. Karppi et al. suggested a modification to the thermal factor $(H_R)_{100} = H_0 exp[-A(\sum D\Delta t)_{100}]$, where A is dependent on the type of steel being tested. Using this formula, A = 75 for Terasaki and Satoh's work and ranged from 41–83 for the steels tested by Karppi et al. (Table 15).

Table 15: Thermal correction factor for different grades of steels introduced by Karppi et al. [152].

Steel Grade	UTS	A
HT 60	85 ksi	83
HT 80	115 ksi	69
HY 130	145 ksi	46
HY 180	200 ksi	41

Karppi et al. suggested the dependence of A on the type of steel; when welded with matching consumable and under similar welding conditions including the hydrogen content, a greater

amount of diffusible hydrogen is retained in the weldments of higher-strength steels than in lower-strength steels.

Karppi et al. tested two groups of steels: C-Mn steels (up to 50 ksi) and low-alloy steels (up to 115 ksi) with a range of compositions (listed in Table 16), proposing the following equation to calculate the LCS:

Equation 2-26: Relationship proposed by Karppi et al. [152] to estimate the LCS for the onset of HACC.

$$LSC\left(\frac{N}{mm^2}\right) = 785 - 1.2H_{max} - 250\log(H_R)_{100}$$

Table 16: Steel elemental compositional range tested by Karppi et al. [152].

C	Mn	Si	Cr	Ni	Mo	Cu	V	Al	B
0.06-0.19	0.56-1.5	0.26-0.43	0.02-0.8	0.017-8.92	0.03-0.63	0.013-0.17	0-0.04	0-0.06	0.0009

2.10.5 Selection of Conventional Control Criterion

Numerous methods have been developed with the aim of predicting the onset of HACC and help define a strategy to prevent it. The critical stress control method is based on the assumption that if the LCS threshold defined during testing can be avoided, the onset of cracking may be avoided. This, however, requires detailed and accurate knowledge of the stresses and strains involved during the deposition of each weld, which is unachievable in most cases.

When considering the suitability of the hardness criterion versus the hydrogen criterion approach, Graville [34] proposed that hardness control is appropriate for steels with a limited alloy content, because such steels have steep hardening curves and the HAZ hardness can be determined with relatively good accuracy by measuring the critical cooling rate. Conversely, for low-carbon, alloyed and microalloyed steels, the hydrogen control method is more suitable, as the hardness profiles of these steels are not drastically influenced by the cooling rate. This is evident when considering the hardening curves, which are significantly flatter. Based on empirical evidence, Graville [34] proposed a system that compartmentalises steels based on their carbon content and their CEs. This system, commonly referred to as the Graville diagram (Figure 70), can be used as a means of determining the more appropriate criterion between hardness or hydrogen to employ in order to minimise the risk of HACC.

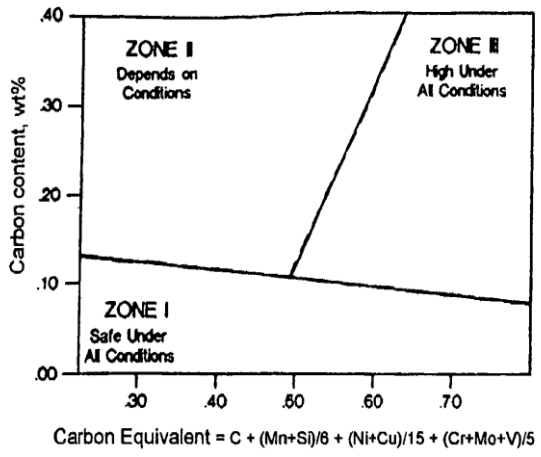

Figure 70: Graville diagram [34] illustrating the classification of steel weldability based on carbon content and alloy composition, as described by CEs.

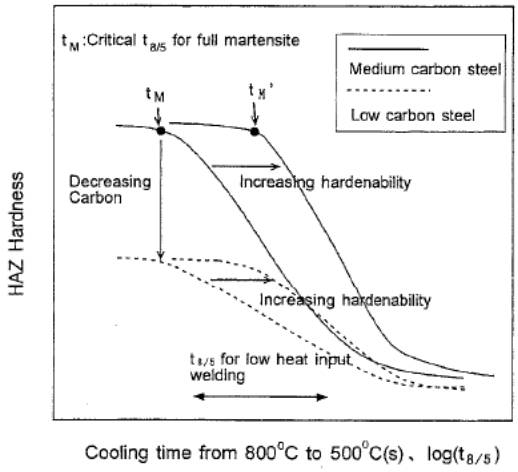

Figure 71: Schematic representation of hardenability curves for low- and medium-carbon steels [238]. HAZ hardness of medium-carbon steels changes significantly in the $t_{8/5}$ region, corresponding to low heat-input welding or when the CE changes (CE_{IIW}). Effect of steel composition on change in HAZ hardness against $t_{8/5}$.

Zone I steels are characterised by having a low carbon content and a relatively low risk of succumbing to HACC unless welded under high restraint and under conditions that result in a high concentration of residual hydrogen. Graville [34] suggested that the hydrogen criterion should be used to determine the preheat levels for steels in this zone. Zone II steels are characterised by having a higher carbon content than Zone I steels and thus have steeper hardening curves. Graville therefore suggested that hardness control is best suited for limiting the risk of HACC for these steels. Steels in Zone III are characterised by higher carbon content than Zone I steels and higher CEs than Zone II steels. Steels in Zone III have higher hardenability and flat hardening curves, for which hydrogen control is more appropriate.

Hydrogen content, microstructure and stress are taken into account in both hardness and hydrogen control approaches when estimating the level of preheat required to ensure crack-free welds can be deposited. However, the degree of emphasis is different in each approach. As expected, in the hydrogen control approach emphasis is placed on hydrogen diffusion and restraint, whereas in the hardness control approach these factors are not as significant as the chemical factors that influence the resulting microstructure and critical hardness. The validity of these two approaches has come under increasing scrutiny as new, microalloyed thermomechanically controlled processed steels are being introduced into the industry; there is little empirical data to test these experimentally derived criteria. Moreover, the conditions under which the traditional safe welding limits were established have been known to yield

results which are overly conservative. Graville [34] suggests that this conservative nature of the results may be due to one or more of the following factors:

- Inadequate characterisation of hardenability by the existing CEs;
- A lower threshold, above which cracking may occur, than in conventional steels;
- The effect of austenite grain size on the hardenability of steels is not included;
- The effect of NMIs on the hardenability of clean steels is not rigorously defined.

To date, there is no clear guideline regarding which approach to apply when considering low-carbon alloyed (Zone I) steels. Compared to Zone II steels, Zone I steels have a flatter hardness versus cooling time behaviour, so the hardness rate of change is rapid and the critical cooling rate will not vary significantly with hardness. Graville [34] suggested that for steels with shallow hardness behaviour like Zone III steels, the hydrogen criterion would yield the best results for preventing cracking. He also indicated that Zone I steels have fairly flat hardening curves, and that even the hardest microstructure that can be produced during welding is not very susceptible to cracking (Figure 71). Based on these insights, it is reasonable to suggest that the hydrogen approach should be used over the hardness control approach. However, there is sufficient anecdotal evidence to suggest that over the past five decades [47] the hardness approach has been successfully used to predict the weldability of HSLA steels. This can in part be attributed to improvements in hardness measurement and prediction techniques upon which this method is formulated.

2.10.6 Micromechanical Characterisation

With the limitations of the traditional means of characterising and quantifying weld metal susceptibility to HACC now identified, it follows that an alternative means of quantifying susceptibility must be sought. It has been established that the elemental chemistry of the parent plate and consumables, the welding process and the amount of hydrogen introduced into the weld as a result of the welding process and conditions can all affect the resulting weld metal properties and thus susceptibility to WMHACC. Of particular concern is the inhomogeneity that exists in the weld metal microstructure. The formation of complex microstructures within the fusion zone and the consequence of the formation of narrow bands within all three heat affected zones (coarse grain HAZ, fine grain HAZ, inter-critical HAZ) as a result of the weld thermal cycle make using the traditional characterisation methods ineffective. This is because classic investigation techniques cannot differentiate between micro grains and give average values of the material components. In addition, the bands

within the HAZ are narrow, so it is difficult to determine the mechanical properties on a micro scale using traditional methods [239].

Instrumented indentation [240-249] (or nanoindentation when applied on a nanoscale), is a relatively new technique that has been used in a range of fields to characterise the mechanical behaviour of materials. It is gaining particular popularity in the characterisation of welded structures [195, 250-254], as the methodology allows for the isolation of both the elastic and plastic components of deformation, potentially giving a comprehensive quantitative description of the effects of both chemistry and processing on the resulting material properties. Traditionally, indentation is used to measure a material's resistance to deformation. A prescribed load is applied to an indenter in contact with a specimen and the area of the residual impression is measured by optical means. The hardness of a material is then obtained by dividing the load by the area of residual impression [243, 247]. Instrumented indentation allows for a load-depth curve to be derived from sensing indentation techniques without the need to measure a contact area, so the hardness and elastic modulus of a material can be measured. Investigations can be carried out not only on a micro scale but even on a nanoscale using ultra-low loads (typically just a few μN, with a limit of 5 mN), making this technique ideal for determining the elastic modulus, hardness creep resistance, residual strain and fatigue properties of small structural features within single grains and at grain boundaries [241-243, 245, 253-256].

2.10.6.1 The Nanoindentation Method

Classic hardness measurements use a test body to make an indentation into a material surface. The indentation is then measured microscopically, limiting the measurement to only the plastic component of the deformation. Nanoindentation employs a dynamic process whereby the depth of penetration is measured as the loading force is increased incrementally, up to some maximum force. The known geometry of the indenter allows the size of the area of contact to be determined. The penetration depth is measured while the load on the indenter is deceased incrementally, resulting in a load-depth curve (Figure 72 and Figure 73). From this curve the elastic and plastic components of deformation can be extracted and allow for the elasticity modulus of the specimen material to be obtained from a measurement of the 'stiffness' of the contact, a term coined for the rate of change of load and depth. Numerous geometries have been used for indenters, each with its own merits and applications. Typically, hardness tests use either spherical or pyramidal indenters. The Berkovich indenter, which has the advantage that edges of a pyramid are more easily constructed to meet at a single point, is

generally used in small-scale indentation studies such as the characterisation of weld metal [247]. The face angle of the Berkovich indenter is 65.27°, which gives the same projected area-to-depth ratio as the Vickers indenter and has a tip radius in the order of 50–100 nm that may increase to 200 nm over time.

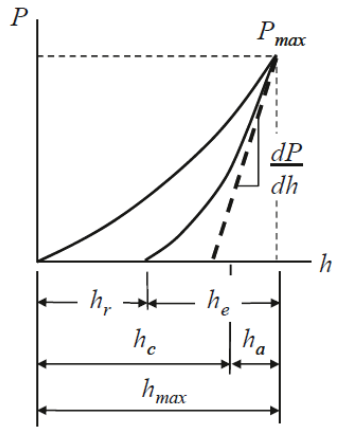

Figure 72: Schematic illustration of typical load-displacement data [255]. The maximum load is denoted by P_{max} and depth beneath the specimen free surface h_{max}. The depth of the contact circle h_c and slope of the elastic unloading dP/dh allow specimen modulus and hardness to be calculated, while h_r is the depth of the residual impression, and h_e is the displacement associated with the elastic recovery during unloading.

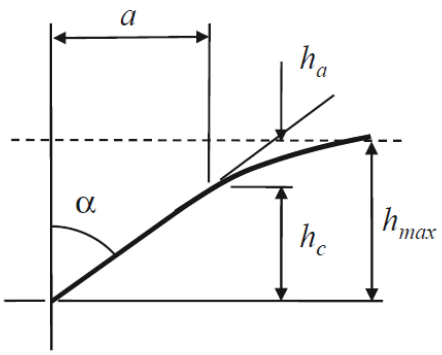

Figure 73: Schematic of indentation deformation at peak load and after unloading [255].

2.10.6.2 Elastic Modulus and Hardness

One of the primary advantages of instrumented indentation over classic measurements is the ability to extract the elastic modulus and hardness of the specimen from experimental readings of the indenter load and the depth of penetration. Typically, force and depth are measured as a load is applied from zero to some maximum and then back down to zero. Using the relationship between the indenter area and load and depth, the mean contact pressure and hardness can be calculated. As noted above, the indenter is loaded incrementally to a maximum predetermined load and subsequently unloaded; as the indenter is unloaded the material will attempt to regain its original shape. The extent to which it can return to that shape will be determined by the degree of plastic deformation that occurred during the indentation process. There will always be some degree of recovery as a result of the relaxation of the elastic strains within the material. It is the analysis of this elastic unloading that gives an estimate of the elastic modulus of the indented martial. For a Berkovich indenter, the relationship between load and depth for elastic-plastic contact is given by Equation 2-27 and on elastic unloading by Equation 2-28.

Equation 2-27: Relationship between load and depth for an elastic-plastic contact for a Berkovich indenter.

$$h = \sqrt{P}\left[(3\sqrt{3}Htan^2\theta)^{-\frac{1}{2}} + \left[\frac{2(\pi-2)}{\pi}\right]\frac{\sqrt{H\pi}}{2\beta E^*}\right]$$

Equation 2-28: Relationship between elastic unloading and depth for an elastic-plastic contact for a Berkovich indenter.

$$h = \sqrt{P}\left(\frac{\pi}{2E^*}\right)^{\frac{1}{2}}\left(\frac{\pi}{3\sqrt{3}}\right)^{\frac{1}{4}}\frac{1}{tan\theta'}$$

In Equation 2-29, R′ and θ′ are the combined radii and angles of the indenter and the shape of the residual impression in the specimen surface. The measurement and analysis of the data relies on the assumption that no reverse plasticity occurs during unloading. The indentation modulus is determined from the slope of the loading and unloading curve. Equation 2-29 shows the indentation modulus as a function of dP/dh.

Equation 2-29: Indentation modulus.

$$E^* = \frac{1}{2}\frac{\sqrt{\pi}}{\sqrt{A}}\frac{dP}{dH}$$

The indentation hardness (H), (Equation 2-30) is calculated from the indentation load (P) divided by the projected contact area (A):

Equation 2-30: Indentation hardness.

$$H = \frac{P}{A}$$

The mean contact pressure is derived from a measure of the contact depth penetration h_c in Figure 73, such that the projected area of the contact (A) is given by Equation 2-31.

Equation 2-31: Projected area.

$$A = 3\sqrt{3}\,{h_c}^2 tan^2\theta.$$

For a Berkovich indenter, θ = 65.72°, so $A = 24.494{h_c}^2$, $\approx 24.5\,{h_c}^2$ and the mean contact pressure or hardness is given by Equation 2-32:

Equation 2-32: Mean contact pressure for a Berkovich indenter (θ = 65.72°).

$$H = \frac{P}{24.5\ {h_c}^2}$$

It is important to note that 'indentation modulus' has precisely the same meaning as the term 'elastic modulus' or 'Young's modulus' in many cases, but that this is not the case for some materials. Particular material behaviour such as dislocation pile up affects the indentation modulus, so care has to be taken when comparing the modulus for materials generated by different testing techniques and on different types of specimens. However, there was no evidence found in the literature to suggest that this was an issue in the analysis of weld metal microstructure. The contact area is determined from the value of h_c (Figure 73) and the known geometry of the indenter. The value for h_c is found by an analysis of the load-displacement data above. As with all experimental measurements, calibration is essential. It is generally accepted that for penetration depths greater than 320 nm, area function has been approximated by a standard calibration procedure with fused quartz material of a known Young's modulus [243, 253, 257, 258].

2.10.6.3 Applications and Limitations of Nanoindentation

Nanoindentation has been demonstrated to be an excellent method for the characterisation of mechanical properties of small regions of materials with complex structures [259-264] . From micromechanical characterisation of individual grains [265] to examining the effect of segregation on the mechanical properties of grain boundaries [254], nanoindentation has been increasingly useful in empirically defining the effects of welding conditions and variables on weld metal integrity. Nanoindentation has also been used to investigate the effects of hydrogen on the micromechanical properties of materials [266-270], especially the effect of hydrogen on the elastic modulus of steel [22, 249, 251, 271]. Their investigations conclude that electrolytic charging significantly affects the elasticity of the material under investigation.

Maier et al. [253] investigated the suitability of nanoindentation as a means of characterising weld metal. For C-Mn welds made using the SAW process, Maier et al. [253] suggested that there was sufficient evidence to suggest that nanoindentation was a superior characterisation technique. The samples investigated by Maier et al. consisted of fine- and coarse-grained structures consistent with a typically welded structure. In addition, Maier's samples were subject to HE.

One of the key advantages of nanoindentation is the ability to characterise properties of single grains. As demonstrated by Maier et al. [253], the traditional Vickers micro indentations, which have diagonal lengths in the range of 15-20 µm, are much larger than the grain sizes in nanoindentation; these were typically less than < 30 µm, with grain boundaries having a width on the order of 10 µm. It is therefore impossible to measure the hardness of one single grain or a small region of a type of grain structure using classic methods. Maier et al. demonstrated the significance of measuring the universal hardness of specific weld metal microstructures.

Maier et al. [253] reported a universal hardness value of 2.58 GPa for fine ferrite grains and a hardness value of 1.21 GPa for large GBF. The differences in hardness are expected and can be attributed to refining effects. When compared to traditional hardness values, Maier et al. showed that all microhardness values for coarse-grained structures are bigger than the microhardness values for fine-grained structures of the same materials; however, the variation in microhardness values of all microstructures is not as large as for nanoscale hardness measurements, since microhardness indentations employ averages across grains and grain boundaries.

Maier et al. concluded that a better understanding of the nanoscale mechanical properties of steels using nanoindentation could be achieved because single phases could be characterised by this technique. In addition, the authors provided evidence to suggest that a correlation exists between nanoscale hardness and manganese concentration distribution in the microstructure, which results in grain boundary segregation.

This is of critical importance when considering the suitability of using instrumented indentation to study and characterise the susceptibility of weld metal to HACC. There are numerous studies which suggest that grain boundary segregation causes embrittlement and that this may lead to material failure; therefore, the science of the grain boundary behaviour of weld materials on the micro scale and on the nanoscale is the basis for an enhanced understanding of material properties and the possible mitigation of WMHACC.

The use of nanoindentation is not without its limitations. The size and scale of the indentation being applied and analysed raises a number of issues that are not normally considered when indenting on a micro or macro scale. These issues revolve around the sensitivity of the measurements taken. Vibration, thermal drift and an inappropriately prepared surface can all significantly affect the measured value of hardness and Young’s modulus obtained during nanoindentation [255]. The International Organization for Standardization (ISO) is one of the

only international bodies that has issued guidelines in depth-sensing indentation testing for indentations in the macro, micro and nano depth ranges. ISO14577 [272] outlines the methodology and precautions and industrially accepted analytical methods that have to be applied when using instrumented indentation. Nevertheless, given the relative infancy of the technique and the fact that at the time when the present study was being carried out, the ISO standard was still in its draft from, with the precautions and guidelines employed derived from published research.

To minimise scatter and reduce interference between successive indentations, the load and spacing of successive indentations need to be determined on a case-by-case basis. For steel welds, Maier et al. [253] concluded that indentations had to be applied with a force on the order of 300 µN to avoid significant scatter in the data. Maier et al. also concluded that for loading forces between 300 and 500 µN, the accuracy of the data has to be checked with care, especially regarding surface profiles and roughness [257].

Numerous studies have concluded that, in order to obtain reliable indentation data, the penetration depth should be larger than the surface roughness by a factor of about four [253, 273]. It is accepted that the roughness of the surface depends on the size of the area being investigated. Maier et al. investigated an area of 2 μm^2 with a sharp silicon tip to measure the surface roughness of both fine and coarse grains to arrive at an average R_a = 8.5 nm. The dependence of loading forces on the hardness was also investigated. Maier et al. [253] concluded that the loading curves were similar for loading forces from 0.3–2 mN. The greatest variation was reported at extremely low loads (up to 0.8 mN). At loads of 1.5 mN and higher the force-hardness curves reach a plateau and hardness values become independent of the loading force [243]. This variability may be explained by densification in the material directly under the tip during indentation. Strain location theory using a model of geometrically necessary dislocations can be employed to describe the depth dependence of crystalline materials [243, 274] or the work hardening effect, which is expected to be larger for smaller indentations. The thin deformed layer left behind after mechanically polishing the surface could also affect hardness value when the load is extremely low [275, 276].

The advantage of nanoindentation over classic investigation methods is the ability to isolate and measure the material properties of a single microstructural morphology. This is a critical aspect to consider when investigating a phenomenon such as WMHACC, as cracks will initiate and propagate preferentially though susceptible microstructures. In order to define what constitutes a susceptible microstructure, it is necessary to identify the mechanical

properties that influence susceptibility, such as the elastic modulus; hardness becomes a pivotal factor. It has already been established that welding parameters, conditions and chemistry will affect the type and properties of the microstructure that evolves during the weld thermal cycle. It has also been established that hydrogen will influence the resultant properties, especially its susceptibility to embrittlement. It is therefore reasonable to suggest that if the micromechanical properties can be empirically determined from samples that have cracked and from samples that have not cracked, they would provide evidence to suggest the role that the various measured parameters play in cracking susceptibility; ideally, measurement of the elastic modulus and hardness can be used as the basis for an empirical predictor for WMHACC.

CHAPTER 3

Research Gaps

3 Research Gaps

From the literature review, it has been established that hydrogen cracks manifest themselves in welds when a critical concentration of hydrogen is trapped within a susceptible microstructure and subject to a critical stress threshold. Although the phenomenon has been studied extensively for the past five decades, there remains no universal consensus as to the exact mechanism that governs the formation of hydrogen cracks, which this makes the prediction and prevention of the phenomenon difficult. HACC is considered to pose a significant threat to pipeline integrity in the oil and gas industry. Its prevalence in pipeline weldments is compounded by the industry's use of high-hydrogen cellulosic electrodes, by the reluctance of industry to employ high levels of preheat and by the transverse stresses that weldments are subject to in the pipeline construction process. The use of higher-strength steels in the pipeline industry is driven by the ever-growing need to lower pipeline construction costs. The increases in yield strength, improved toughness and homogenised microstructures all allow for higher-capacity pipelines to be built with thinner wall thicknesses, resulting in an overall reduction in the tonnage of steel used and a net reduction in construction costs. However, improvements in the steelmaking process have led to a shift in HACC susceptibility from the HAZ to the weld metal, for which there is little guidance, both in terms of scientific literature and codified standards, on how to avoid cracking. To address this limitation, the manifestation of WMHACC in line pipe steels must be investigated.

A critical review of the literature associated with this topic highlighted the following conclusions:

WMHACC

It was established that there is no universally accepted proxy that has been adopted by industry as a means of quantifying weld susceptibility to WMHACC. Although hardness thresholds have been established for the avoidance of HAZHACC, they have been shown to be an ineffective proxy for WMHACC. Additionally, there are limited guidelines as to the critical levels of preheat to be applied to minimise the risk of the onset of WMHACC on HSLA line pipe steels. To develop a suitable proxy, empirical testing has been historically shown to be the most effective and reliable approach.

Weldability Testing

A diverse array of weldability tests—small scale and large scale, intrinsic and extrinsic—were reviewed and established that small-scale intrinsic weldability tests are the best type of test for delineating safe welding conditions, creating a sample set that adequately replicates field conditions and applying to further mechanical, metallurgical and micromechanical analysis. From the intrinsic weldability tests reviewed, the WIC test was identified as the best weldability test for reproducing the restraint conditions experienced by a single-pass root run girth weld. However, the WIC test has been acknowledged to be conservative and not reliable at low heat inputs. In particular, no successful weldability testing has been conducted below a heat input of 1 kJ/mm.

Extensive testing using the WIC test has established empirical boundaries for HSLA steels when welded with E8010 and E9010 electrodes. However, notable differences in the critical preheat required to minimise the risk of cracking have been noted. Limited testing has been conducted using E6010 electrodes. It is also important to note that the design of the traditional WIC test does not allow for the recording of critical welding parameters needed to establish a proxy that can be used to quantify susceptibility to WMHACC.

The Australian Context

The WIC test has been employed in multiple studies that have investigated the susceptibility of several steel-electrode combinations for different thicknesses. However, as these studies have been commissioned by North American and European research institutions, they have primarily replicated industrial practices common in the Northern Hemisphere. Of particular concern is the absence of weldability testing carried out at low heat inputs (< 1 kJ/mm), which is a common practice in Australia.

3.1 Research Aims

To address these limitations identified in the literature and to provide an empirical basis upon which guidance, useful for industry, can be formulated, the overarching aim of the present study is to identify the thermomechanical factors influencing weld metal HACC. To achieve this aim, the role of plate thickness and restraint in influencing the susceptibility of transverse hydrogen cracking in single-pass butt welds deposited at low heat inputs is investigated. This forms the basis on which an empirical proxy to estimate the susceptibility of the root pass of a girth weld involving low heat input and offering high restraint to WMHACC is proposed.

The specific aims of this thesis are intended to address the limitations identified in the literature review. This thesis aims to achieve the following:

[1] Define a weldability test criterion that is representative of typical pipeline construction conditions in Australia;

[2] Develop a means of testing the susceptibility of butt welds deposited at low heat inputs under high restraint to WMHACC when welded on steels typically employed in the construction of oil and gas transmission pipelines in the Australian context;

[3] Empirically define a weldability test envelope within which a safe welding boundary can be delineated;

[4] Investigate the thermomechanical factors influencing weldability of samples across the derived safe welding boundary;

[5] Identify the critical welding parameters and conditions that affect the position of the derived empirical boundary.

3.2 **Research Deliverables**

To achieve these aims, the following research deliverables have been identified; they form the foundation on which the research methodology in the next chapter is presented. The research deliverables include:

[1] Developing a weldability test that will enable the quantitative measurement of the thermomechanical factors influencing the formation of WMHACC;

[2] Developing a system to implement the weldability test to extract critical welding data including essential welding parameters: welding voltage, current and travel speed; critical cooling data ($t_{8/5}$, t_{100}); and local weld metal displacement;

[3] Experimentally determining the critical preheat required to avoid WMHACC for single-pass butt welds deposited at low heat input (< 1 kJ/mm) at high restraint for thick and thin plates of HSLA line pipe steel;

[4] Identifying the impact of plate thickness and restraint on the susceptibility of single-pass butt welds deposited at low heat input, high restraint and at various thicknesses on susceptibility to WMHACC;

[5] Extracting a sample set of weld metal macros from across the derived cracking boundary that can be analysed to determine the influence of welding essential variables on their metallurgical and micromechanical properties;

[6] Identifying the key microstructural features across the derived cracking boundary and along the crack paths for welds that have succumbed to WMHACC;

[7] Identifying the key micromechanical properties of hardness and elastic modulus from across the derived cracking boundary;

[8] Proposing an empirical predictor based on the micromechanical properties that could be used as a proxy to quantify the risk of a weld's succumbing to WMHACC.

3.3 Outcomes and Significance

This thesis aims to enhance the understanding of the factors that influence the formation of weld metal hydrogen cracks in oil and gas transmission pipelines welded in the Australian context by addressing the five research aims detailed in Section 3.1. The fundamental significance of this thesis is its contribution to a better understanding of the mechanisms governing HACC in weldments. It is envisaged as a necessary step in understating the broader phenomenon of HE in ferritic materials. The significance of this thesis to industry is the development of an empirical envelope that maps out the welding parameters within which crack-free welds can be deposited. This will allow for optimisation of welding procedures and provide an industry-useful strategy to improve pipeline integrity.

CHAPTER 4

Methodology

4 Methodology

To delineate the safe welding boundary across which samples can be isolated and analysed to meet the objectives outlined in Chapter 3, a series of controlled weldability tests are conducted. The process and sequence of these weldability tests are detailed in this chapter, as are the procedures used to analyse the samples generated from these weldability tests.

4.1 Experimental Approach

A schematic outline of the four-tiered systematic investigatory approach employed in this thesis to address the research gaps identified in Chapter 2 and highlighted in Chapter 3 is shown in Figure 74. The control of welding parameters and the development of an instrumentation system central to data acquisition and analysis are detailed in Section 4.2 and are the foundation upon which the controlled weldability testing is conducted.

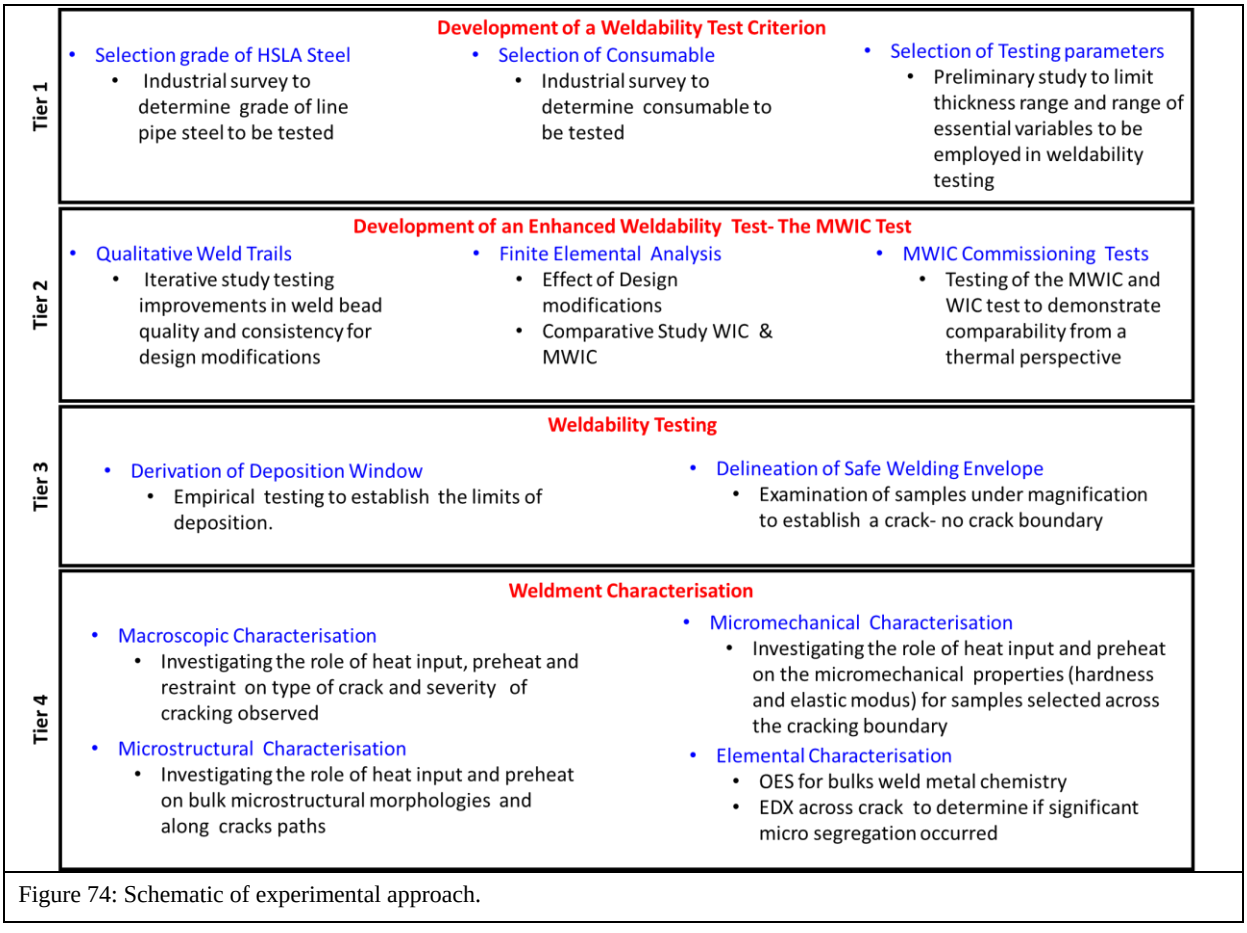

Figure 74: Schematic of experimental approach.

Preparatory Stages

Tier 1 and Tier 2 are the preparatory stages aimed at facilitating the deposition of a weldability test envelope within which the influence of the thermomechanical properties on the susceptibility to WMHACC can be investigated. In Tier 1 (Section 4.5), a weldability test criterion is established that reflects the Australian context through a series of qualitative and quantitative surveys that determine the grade of steel and brand of consumable. Additionally, the results of theoretical calculations to determine the thickness range to be tested are presented. Collectively, these sections address research gap 3.1 [1].

In Tier 2 the design (Section 5.3) and validation (Section 5.5) of the modified WIC (MWIC) test are presented. The development of this enhanced weldability test is aimed at allowing repeatable, reliable deposition of welds at low heat inputs (< 1 kJ/mm). This was identified through the literature review as a welding parameter range within which limited successful weldability testing has been conducted. The influence of the design modification on the thermal and mechanical properties of the specimen is investigated using finite element analysis. These sections directly address aim 3.1 [2] and facilitate the investigation needed to address aim 3.1 [3].

Exploratory Stages

In Tier 3 (Section 6.2), a series of controlled weldability tests are executed with the aim of establishing a deposition window, based on the criteria identified as part of aim 3.1 [1] and intending to validate the parameters within which successful deposition is possible and delineate a CNC boundary. The results of this testing address aim 3.1 [3].

In Tier 4 a range of analytical techniques are applied to the samples generated in Tier 3. Macroscopic characterisation techniques are used to map out the role of heat input, preheat and restraint on the type of cracking observed (Section 6.3) and severity (Section 6.4). Microstructural characterisation techniques are used to investigate the role of welding parameters and conditions on the observed morphologies in the bulk of the sample and along crack paths (Section 6.5). Additionally, spectrographic techniques such as optical emission spectroscopy and energy-dispersive X-ray spectroscopy are used to measure the elemental composition of the bulk samples and the changes in the local elemental intensities across cracks (Section 6.6). Instrumented indentation is used to measure the local weld metal micromechanical properties for samples across the derived cracking boundaries (Section 6.7).

Collectively, these empirical data from these sections are discussed and address research gaps 3.1 [4] and [5].

4.2 **Mechanised Deposition**

In order to investigate the effects of welding parameters on the susceptibility of a weld to WMHACC, repeatable, reliable, defect-free welds have to be deposited within a parameter range that can be closely controlled and recorded. Manual metal arc welding intrinsically introduces a degree of variability, as the welding process is inherently unstable. Minor variations, such as fit-up, eccentricity of the electrode flux and interactions of the arc with the atmosphere require a degree of welder compensation to manipulate the molten weld pool's being deposited so as to produce a weld of sufficient quality to pass inspection. Welder compensation may be direct, which implies a physical change made by the welder during the welding process itself, or indirect, such as a change in a control parameter.

Direct changes include variations in:

- Lead angle (pitch of the electrode)

A change in the lead or contact angle of the electrode alters not only the extent to which the deposited weld metal will penetrate the prepared root but also the angle at which the molten droplets are released from the core of the electrode and hence the wetting capacity. This affects the overall geometry of the deposited weld bead, which influences the cooling rates of the bead and the residual stress levels in the pass.

- Travel speed

A variation in travel speed is one of the most significant tools that the welder can use when manipulating the weld pool to achieve the desired weld bead. A reduction in travel speed will not only increase the heat input and thus the phase and texture of the microstructure, but will also influence the mechanical properties like toughness and yield strength. In addition, the geometry of the bead is significantly affected.

- Force

The force with which the electrode is pushed into the work piece affects the depth of penetration. The primary objective of using a heavy force is to ensure that there is sufficient penetration and a low chance of suck-back that would result in a stress concentrator. The

contact force is indirectly proportional to the resulting arc voltage. As the electrode is pushed into the root, the arc height is shorted, resulting in lower arc voltage. Beyond affecting the depth of penetration, a higher arc force results in a narrow bead. Once again, the force with which the electrode is pushed into the plate is a tool that the welder uses to manipulate the resulting bead.

- Current

The only other control outside physical manipulation of the welding rod by the welder is a change in current. This can be considered to be an indirect control as changes to this parameter are made at the welding power source and not through physical or biometric manipulation by the welder. The change in current will change the deposition or burn-off rate and the cooling rate, as it directly affects the heat input and thus the resulting weld microstructure and geometry. In addition, a change in the applied current has an effect on the applied voltage as illustrated in the constant current curve [277].

Any change in a single parameter or combination of parameters affects the resulting welding parameters, sometimes as much as 0.5 kJ/mm [193]. This variability affects the resulting microstructure and mechanical and micromechanical properties and makes the comparison of weldability results ineffective. Moreover, the variations may be random and occur along different sections of the weld within the test section, effectively giving one test section multiple parameters. This introduces an inconsistency within the test section that cannot be reliably quantified or controlled.

In order to reduce the variability within each test section and ensure consistency across the test range, a degree of control of the welding parameters has to be introduced into the welding process. In the present study, the control of parameters was done by the use of a mechanised welding system known as the AutoRon.

4.2.1 Mechanised Welding System

The mechanised welding system, nicknamed the AutoRon (Figure 75), can be viewed as the integration of three independent systems: the electrode feeder system, the work table and the welding power source. These systems allow for the control of the fundamental welding parameters of welding voltage, welding travel speed and welding current respectively.

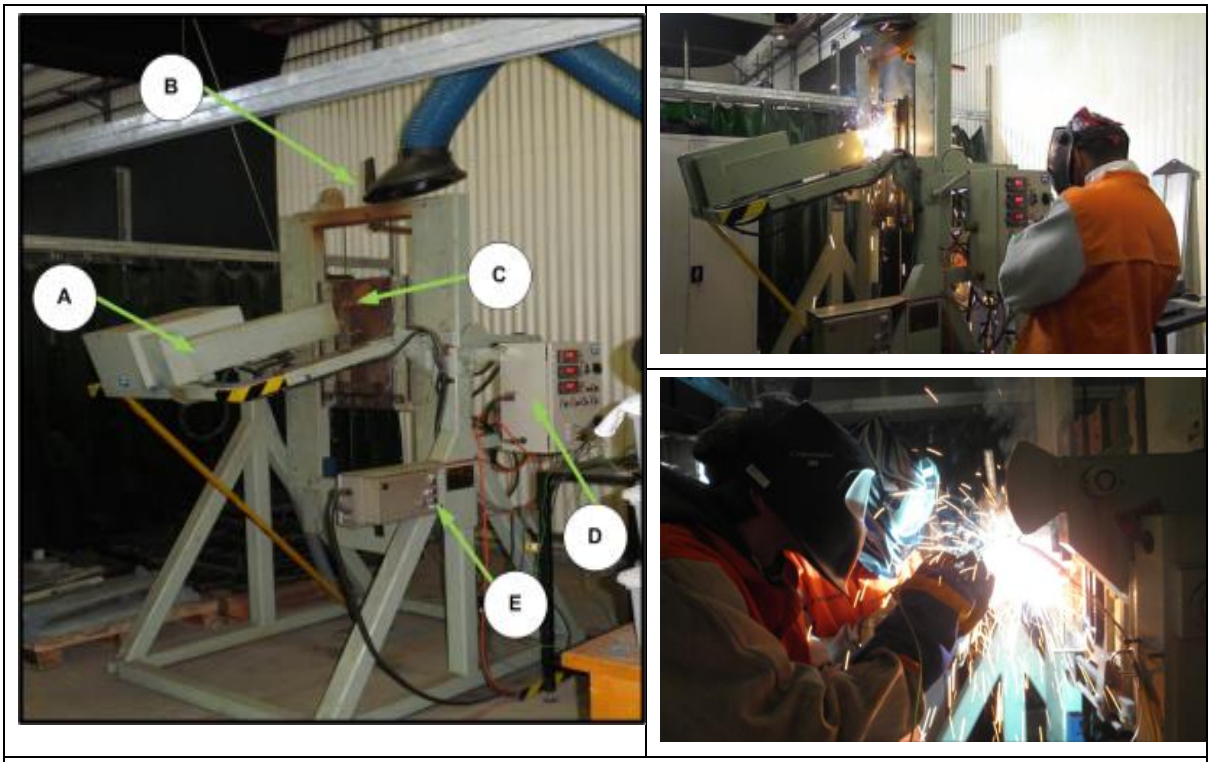

Figure 75: The AutoRon integrates a welding power source, an electrode feeder arm to control the force and voltage and a work table to control the travel speed. Collectively the system consists of: A) an electrode feeder system B) a fume extractor C) a work table D) a system control panel and (E) a work table control panel.

Welding Power Source

The welding power source used in this study is the Lincoln Electric Invertec 350V Pro (Figure 76) with the Advanced Process Module (K1728-7), an inverter-type model that allows for an accurate selection of output current, as the system is digitally controlled. It has an output range of 5–425A and has an open current voltage of 80V DC.

Figure 76: Lincoln Electric Invertec 350V Pro (K1728-7), with the Advanced Process Module.

Electrode Feeder System

The electrode feeder system (Figure 77) consists of an insulated electrode holder guided and driven by means of a re-circulating ball bearing screw system. In essence, it substitutes for the arm of a human welder. The screw is driven by a rubber belt powered by a DC servo motor and is capable of feed rates of up to 360 mm/min. The screw feeder is protected from overload by an internal limit switch and by a mechanical torque-limiting element in the drive. Figure 77 shows the overall mechanism in place so that it can be used to drive the electrode into the work piece.

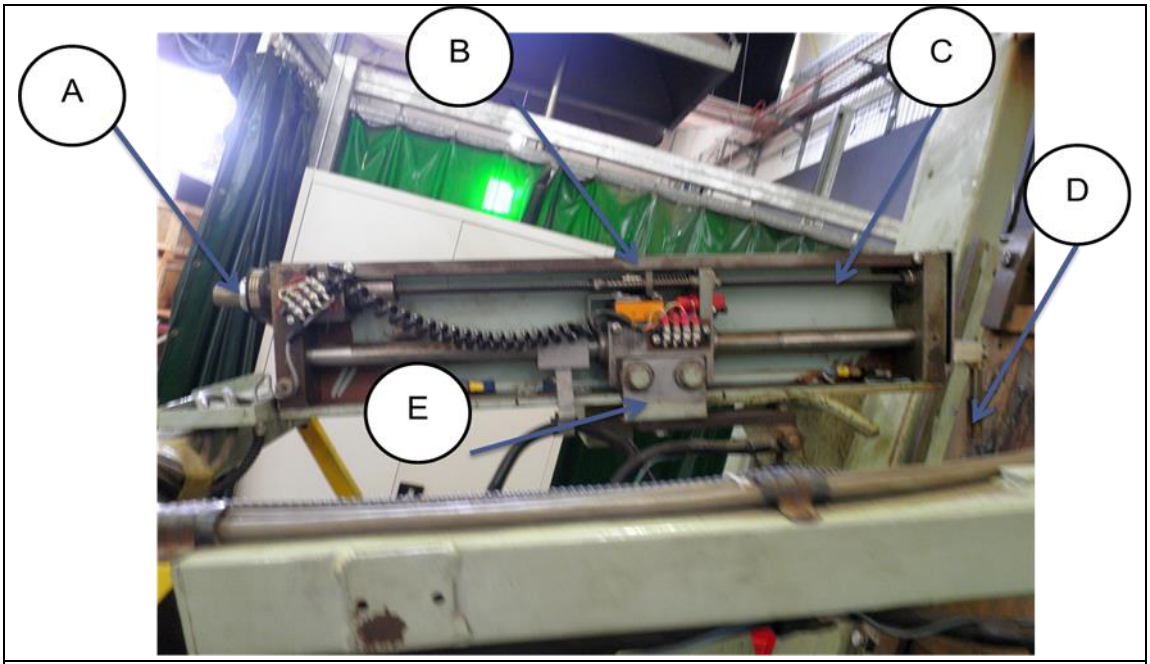

Figure 77: Electrode feeder mechanism: A) belt drive connection; B) compensation spring system; C) driving screw; D) electrode stabilizer; and E) electrode holder.

Detection of welding force and welding voltage are incorporated into the electrode feeder system, while electrode force is sensed by a linear potentiometer that detects the degree of compression of a series of springs between the feeder driver and the electrode holder. The potentiometer is connected directly to the input terminals of the force digital panel meter. Welding voltage is sensed between the electrode holder and the instrument shunt in the work return lead, which permits the system to be operated in a force control mode, when force between the electrode tip and the work piece is maintained, or a voltage control mode, in which the arc voltage control between the work piece and electrode is maintained.

The Work Table

The work table provides a platform upon which a work piece of up to 450 mm in length and 200 mm in width can be attached and positioned to be welded in the horizontal down hand (3G) position through the vertical to the horizontal overhead (4G) position. The work table is

supported by a pair of guides and driven by a ¼-HP (0.19 KW) electric motor and variable-speed gearbox through a steel cable and drum. The travel speed can be adjusted from 140 mm/min (2.3 mm/s) to 690 mm/min (11.5 mm/s).

AutoRon Control Modes

The AutoRon can be operated in three distinct modes, two of which are mechanised—force control mode (FCM) and voltage control mode (VCM)—and one manual control, semi-mechanised mode.

Force Control Mode (FCM)

In FCM, the force with which the electrode is pushed into the work piece is the driving parameter of the welding process, with welding voltage simply a result of the other input variables. The stove pipe, or drag type, welding process used in field production of pipeline root pass girth welds relies on the field welder's physically pushing the electrode into the work piece, so making use of the FCM is most representative of actual field conditions.

Voltage Control Mode (VCM)

The AutoRon can also operate in VCM, in which the voltage between the electrode and work piece is maintained and thus drives the welding process. The force recoded when working in VCM will be a result of the arc pressure's pushing back on the electrode.

Manual Control Mode (MCM)

To allow for a degree of welder manipulation, the third operational mode is manual control mode (MCM) in which the electrode feeder arm is disabled and replaced with a qualified welder. All welding parameters with the exception of voltage (which is proportional to arc height) and electrode angle are controlled by the AutoRon. This mode allows the welder to respond to changes in the keyhole by manipulating the angle of the electrode and the force with which the electrode is pushed into the work piece. The primary advantage of this quick response capacity is the ability to maintain consistency in key welding parameters whilst being able to deposit welds at significantly higher travel speeds than are possible with VCM and FCM.

Figure 78: Initiation in FCM and VCM (steel wool ball).

Figure 79: Initiation in MCM, traditional scratch start.

Sample Mounting

The weldability test sample is secured to the work table by a series of clamps which do not allow for movement in any axis (Figure 80 and Figure 81). There are four earth return cables placed symmetrically to avoid any adverse effects for current return such as blow arc (magnetic deviation of the arc) (Figure 82 and Figure 83).

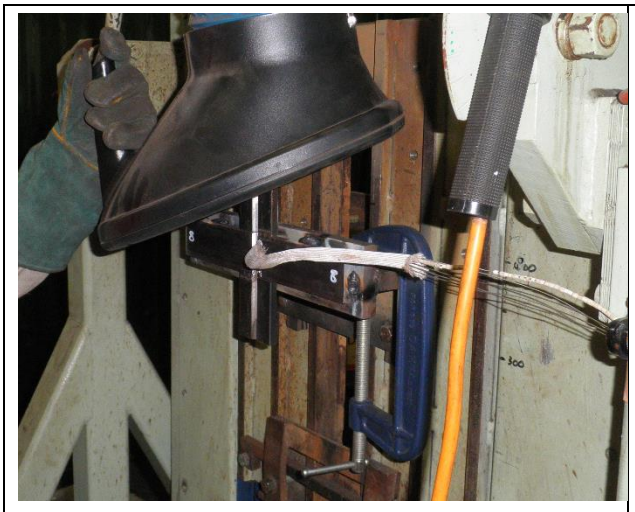

Figure 80: Forward mount when using MCM; the sample is clamped to the work table and the face is free-facing.

Figure 81: Rear mount when using FCM or VCM; tabs are used to secure the sample to the table.

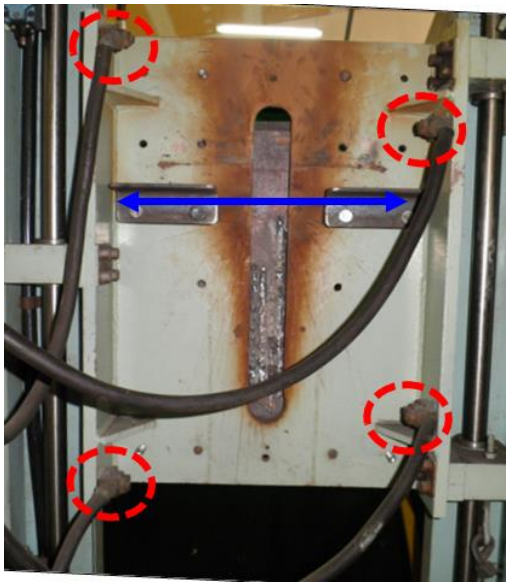

Figure 82: Positon of earth return leads and rear mounting bracket.

Figure 83: Electrode guide designed to assist with deposition in this thesis.

4.2.2 Instrumentation and Data Acquisition

Instrumentation

Type K Thermocouples

To evaluate the temperature field of the sample in the vicinity of the weld's centreline and to verify that applied preheat is uniform, the weldability test was instrumented with standard Type K thermocouples. The position of the Type K thermocouples are detailed in Chapter 5. Type K thermocouples (nickel-chromium/nickel-alumel) were selected as they are inexpensive, accurate (the greater of either ± 2.2C° or ± 0.75%), reliable and operate well within the temperature range anticipated for their intended function.

Type R Thermocouples

To evaluate the centreline temperature of the deposited test welds and especially to measure the critical cooling rates $t_{8/5}$ and t_{100}, a Type R thermocouple was selected to be lanced or harpooned into the molten weld pool behind the welding arc. Lancing would only be expected on samples where sections are not being isolated for delineation of the safe welding envelope or metallurgical analysis, as it has been shown that lancing can contaminate the weld pool and adversely affect the accuracy of weldability tests [195].

Type R thermocouples (platinum/rhodium-13%/platinum) were selected as a result of their suitability in very high temperature environments of up to 1480 °C. Their accuracy (the

greater of either ± 1.5 °C or ± 0.25%) and their stability when compared to Type S thermocouples make them an ideal solution. Type B thermocouples (platinum rhodium 30%/platinum rhodium 6%) were considered, but their marginal improvements for the stated function given their significant cost disqualified their selection.

Extensometer

To measure the displacement of the weld during cooling the weldability test sample was instrumented with the Epsilon 3448-10-50 high temperature extensometer. Details of the attachment onto the MWIC specimen are provided in Chapter 5. The Epsilon 3448-10-50 has a 10 mm gauge length and a measuring range of +50%/-10% of the gauge length (Figure 84). The extensometer is supplied with 200 mm high-purity alumina ceramic rods and eight glass fibre cords of 620 mm in length to allow for multiple attachment configurations between the extensometer and the sample. The extensometer is rated for use in environments where the temperature may reach 1200 °C and meets existing ASTM Class B-1 requirements for accuracy.

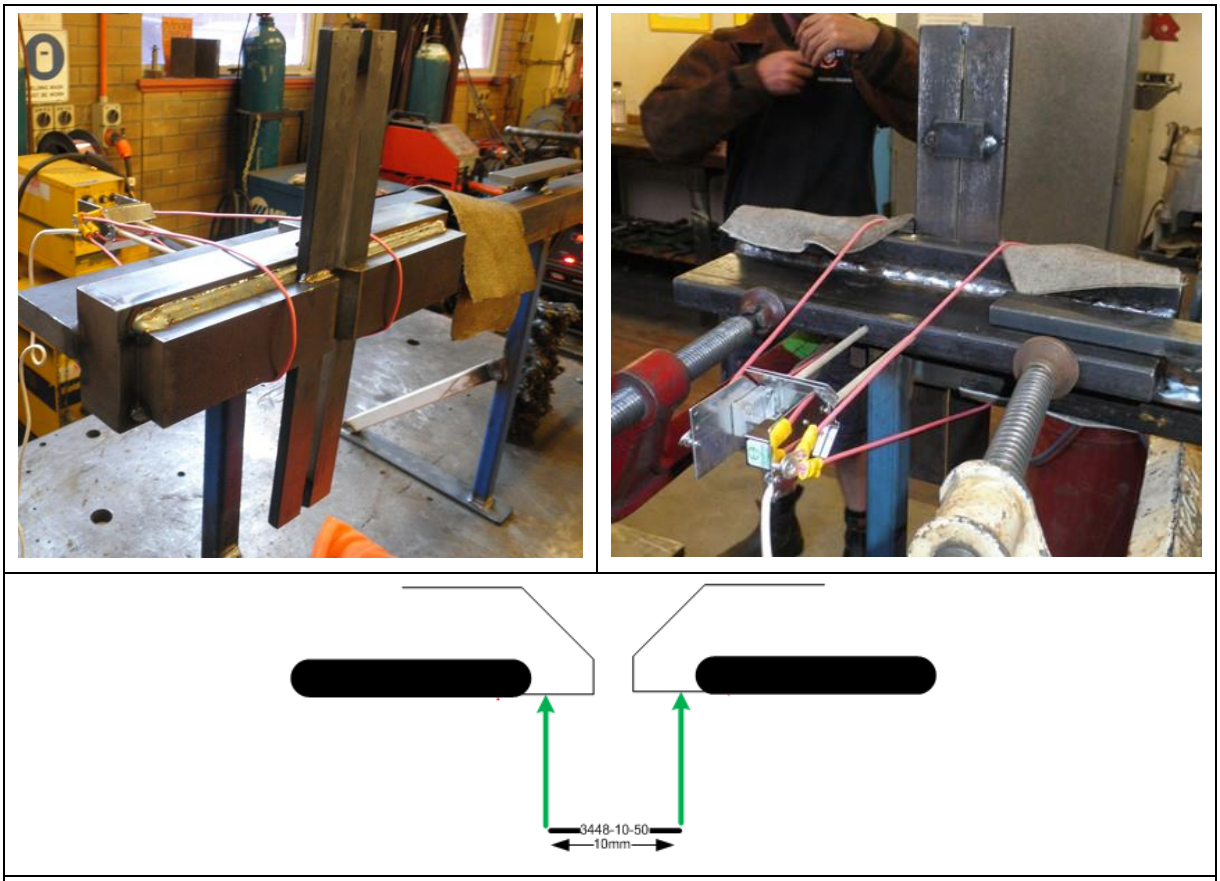

Figure 84: Set-up of the Epsilon 3448-10-50 extensometer during verification trials. The image on the top left shows the set-up of the extensometer when viewed from the front of the specimen, whereas the image on the top right shows the set-up from the rear. The image on the bottom of the figure shows the positon of the extensometer's arms relative to the MWIC specimen's test plates. The bold lines represent the restraint welds. Note that the extensometer is positioned as close to the weld centreline as possible and not in an area restrained by the anchor welds.

High-Speed Camera

A high-speed camera was selected for verification and troubleshooting purposes, especially to verify the position of the welder's arm during deposition testing using MCM and to ensure that the welder did not make significant changes to the angle of the electrode or inadvertently drag the electrode and modify the travel speed during deposition (Figure 85-87).

Figure 85: Typical image extracted of the electrode positon from a video recorded during pre-deposition instrumentation checks.

Figure 86: Typical detailed image extracted from video recording during travel speed verification checks.

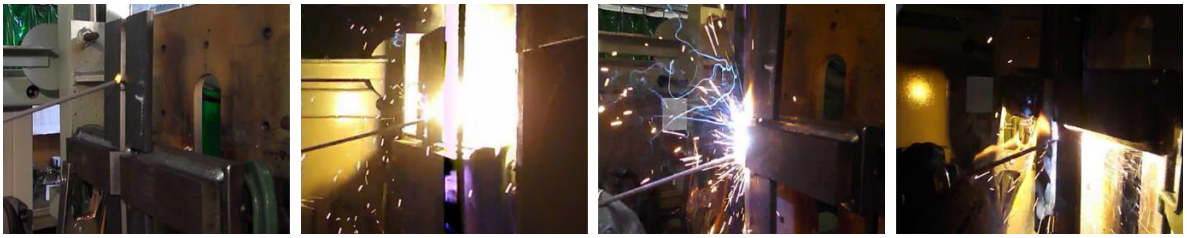

Figure 87: Typical overview image extracted from video recording during electrode position checks.

The camera (Panasonic Lumix DMC FZ200) was set to record at 240 fps in either VGA (640 x 480 format) or at 100 fps in 720p (1280 x 720 format), depending on the verification task being executed. For verifying the position of the electrode and travel speed verification a variable polarising filter was used to reduce arc glare. The camera was set up using -3EV exposure compensation and the Inca Filter 55 mm Variable ND (4-256x) at a + ¾ turn (equivalent to four stops or -8 Ev). These settings allowed for a measurement of the welding speed in each of the four sections of the MWIC weldability test (Figure 88).

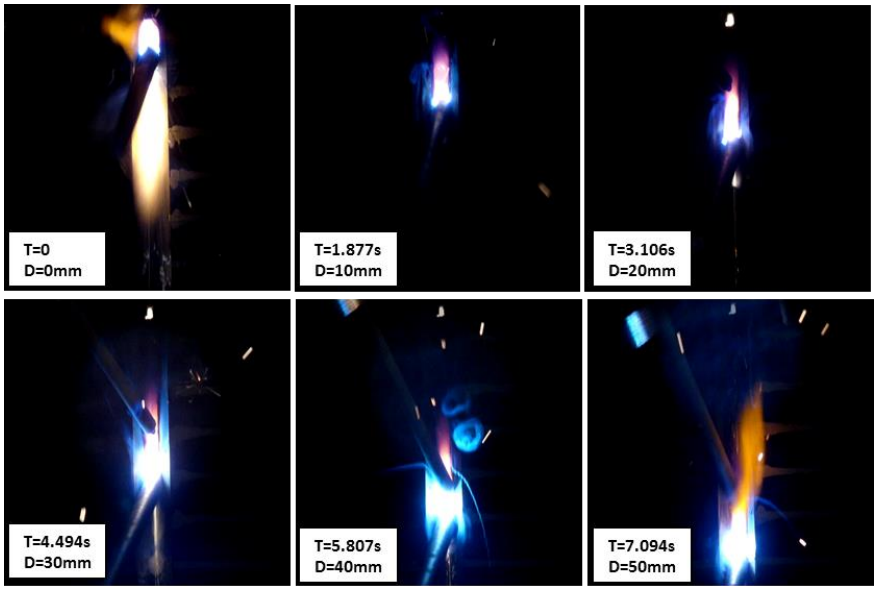

Figure 88: Typical travel speed verification data extracted from the video files.

Data Acquisitions System

A National Instruments® (NI) NI-CDAQ-9188 chassis was used in conjunction with two NI 9219, 4-channel 24-bit analogue input modules and one 16-bit National Instruments® (NI) 9215 voltage modules to acquire temperature and local weld metal displacement (Figure 89). Welding voltage and current data were acquired using Lincoln Electric's proprietary software, LE Power Wave Manager. Temperature and displacement data could be recorded at a frequency ranging from 1 Hz to 100 Hz, with the only limitation being the workstation to which the chassis was connected, while voltage and current data were collected at a frequency of 10Hz.

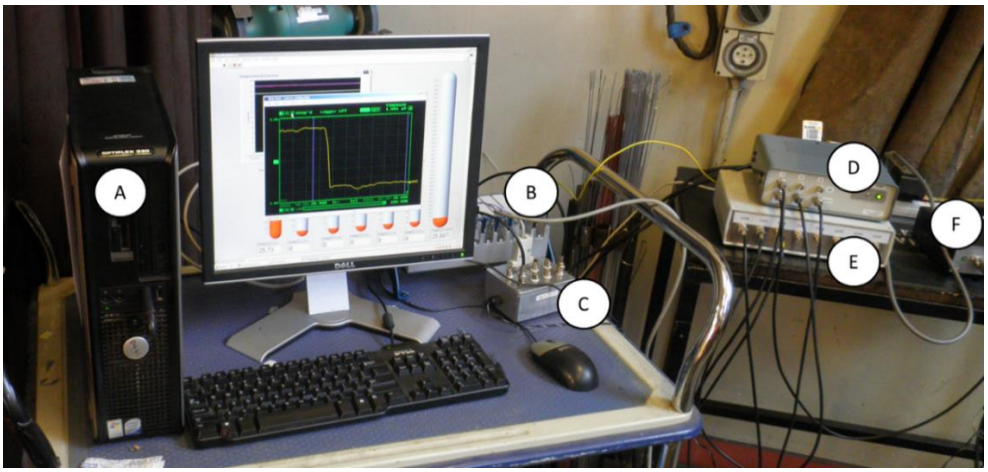

Figure 89: DAQ system layout: (A) workstation; (B) NI-CDAQ-9188 chassis with modules attached; (C) isolation amplifier for thermocouples; (D) amplifier for AutoRon signal; (E) optical isolator for thermocouples to protect the DAQ in the event of current leakage; (F) amplifier for extensometer signal.

A custom virtual instrument for temperature strain acquisition was written in NI LabVIEW® (Laboratory Virtual Instrument Engineering Workbench), which integrated signals from the Type K and Type R thermocouples with the displacement data from the high-temperature extensometer (Figure 90). The virtual instrument was designed to allow for the temperature signals to be recorded in both their raw (mV) and calibrated formats (either as °C or µm). The virtual instrument also included a low-band filter to isolate any electrical interference caused by noise from the welding process.

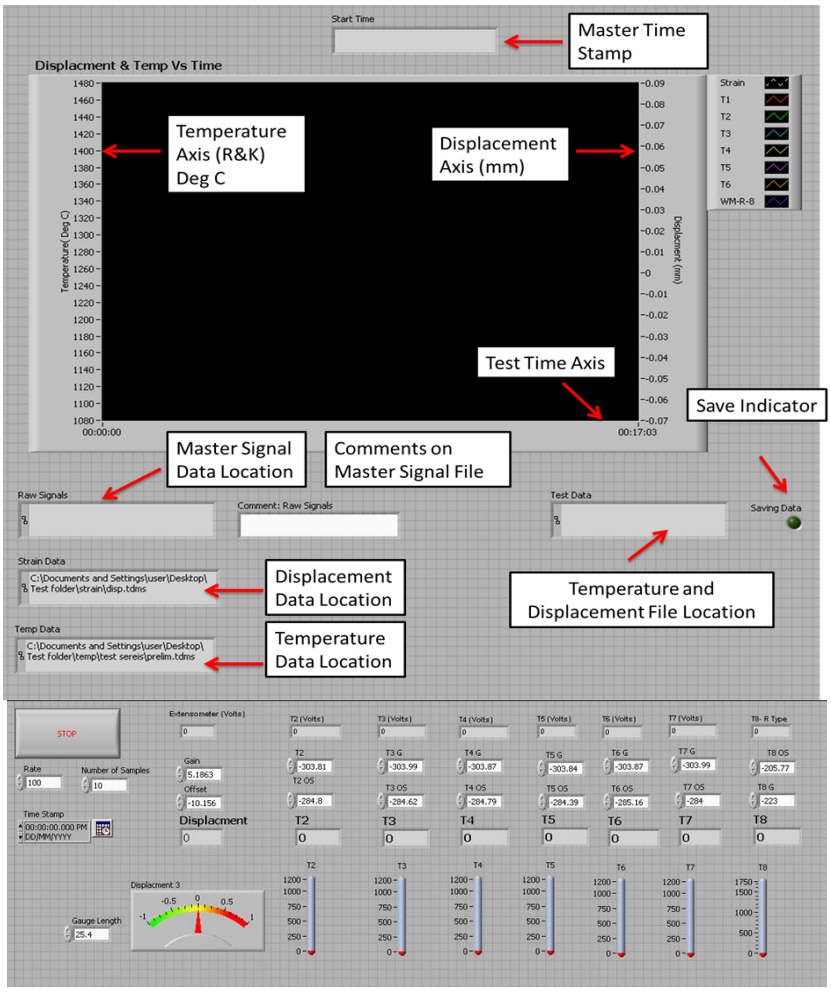

Figure 90: Graphical user interface of the custom-built virtual instrument, which integrates signals from the Type K and Type R thermocouples with the displacement data from the high-temperature extensometer.

The virtual instrument and individual components were tested and calibrated to ensure the accuracy of the parameters being tested and recorded. The thermocouples were calibrated using a Fluke 714 thermocouple calibrator, which allows for a -10 mV–75 mV range at a resolution of 0.01mV with an error of (± 0.025% + 1 count). The R channel was calibrated from 50 °C to 1750 °C and the K channels from 50 °C to 1,350 °C. The thermocouples were calibrated to an accuracy resolution of 1 °C with an error of ± 0.3 °C + 10 mV and a reference junction error of ± 0.2 °C.

4.3 Weldability Test

In the literature review, it was established that the WIC test is the most appropriate weldability test to investigate the susceptibility of single-pass girth welds to HACC. However, the WIC test was identified as having limitations that restricted its applicability for research purposes. These limitations are addresses in Chapter 5.

4.4 Analysis Methods

4.4.1 Sample Extraction and Preparation

The welded joint was removed from the MWIC specimen 24 hours after weld completion by milling the test assembly just inside the restraint length. The anchor welds were sawed off using a water-cooled precision metallographic saw and the test sample was divided into six sections (Figure 91). To prepare the sections for metallographic analysis and indentation, each section was hot-mounted in a conductive epoxy and polished using a semi-automatic Struers LaboForce polishing machine. Final polishing was achieved using a porous neoprene disc with a colloidal silica suspension (0.04 μm). The samples were then observed at 400x magnification for the presence of cracking with a Zeiss Axio Imager 2 optical microscope. Selected samples were then etched using a 2% Nital solution to reveal the weld metal microstructure.

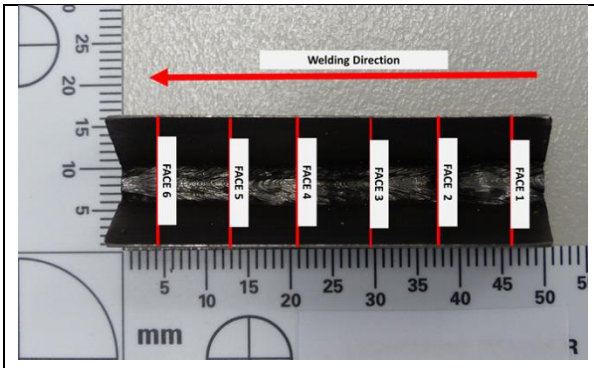

Figure 91: Weldability test piece with the location of the six faces to be examined under an optical microscope at 400x magnification highlighted.

Figure 92: Typical face of a test section mounted on a conductive base to facilitate examination by electron microscope. The test sample is etched with a 2% Nital solution.

4.4.2 Cold Cracking Evaluation

Each of the six sections (Figure 91) from a single test piece was examined at a magnification of 400x and classified as cracked when the vertical length of the defect observed in a single section (t_c) was greater than 5% of the height of the weld bead (t_w) of the test section under

analysis (Figure 93). Cracking severity was defined as the arithmetic sum of the observed percentage cracking over the entire test piece.

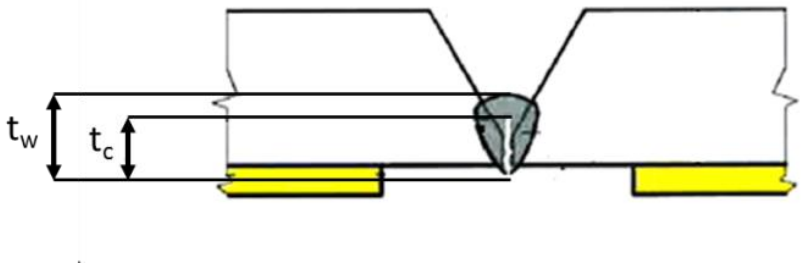

Figure 93: Schematic of a face of a test section. A sample was defined as cracked when a linear defect whose vertical length (t_c) was greater than 5 % of the bead height (t_w).

4.4.3 Metallurgical Analysis

Optical microscopy was used to identify the dominant microstructural morphologies in the weld metal of samples across the derived cracking boundary. That technique was also used to identify the microstructural morphologies along the path through which hydrogen cracks have propagated.

The key purpose of microstructural characterisation is to ascertain if there are major differences in the microstructural morphologies across the derived cracking boundary. If present, these differences may be used to explain the existence and position of the boundary. Additionally, identifying the morphologies along crack path serves as a critical input into a regression analysis to ascertain the dependence of crack path on microstructural morphologies, especially features such as grain boundary misorientation.

4.4.4 Elemental Analysis

The chemical composition of the weld metal was measured by glow discharge optical emission spectrometry (GD-OES), using a Horiba GD-Profiler 2™ instrument calibrated to normalize the composition of all elements present in the alloy from values of 1–100% by wt%. The fourth sections of selected samples across the boundary were selected for analysis. Quantification was made with a 4 mm anode, with the signal acquired as an average over the surface and in volume. Four measurements were taken at 10-second increments per sample.

To extract the weld metal, the mounted test section was removed from its epoxy mounting by making several cuts through the disk and physically prying the mounting apart. The sample was cleaned and washed in an ethanol bath, then mounted on a Struers Secotom 15 precision

metallographic saw. Two cuts were made within the pre-marked lines inside the fusion boundary (Figure 94).

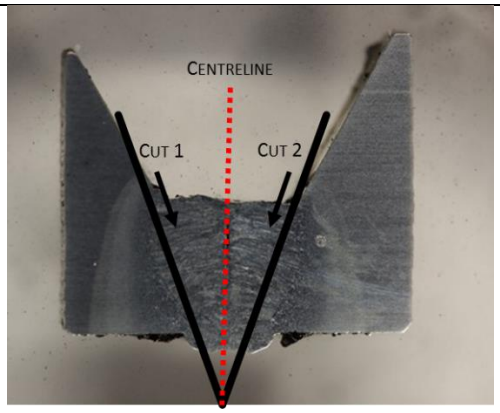

Figure 94: Typical sample used for weld metal chemical analysis extracted from its epoxy mount. The image highlights the location of cuts made to extract the weld metal.

Figure 95: Mounting apparatus with weld metal sample attached (Image courtesy of Horiba).

The extracted weld metal was flattened using a 30-tonne press into a circular disk of approximately 10–12 mm in diameter and 2 mm in thickness. The disk was then ground and polished down with ISO P500 grit paper (30.2 µm), before being immersed in an acetone ultrasonic bath for several minutes, removed and hand dried. The dried samples were then packed in a hermetically sealed container before being shipped to Horiba Laboratories in France for analysis. The samples were cleaned and mounted on custom built mounts by operators at Horiba (Figure 95).

4.4.5 **Micromechanical Analysis**

For micromechanical characterisation, the fourth sections of selected test samples were prepared by mounting the metallographically prepared sample onto a sturdy test stage. The samples were attached to the stage using an adhesive to ensure that no lateral movement was possible during the stage motion whilst guaranteeing that the test section remained perpendicular to the indenter during testing.

Indentation testing was carried out using the Fischer Cripps IBIS Nanoindentation System. Symmetric indentation maps (Figure 96), consisting of 480 indentations (60 columns and eight rows) with an 80-µm space between the centre points of each indentation, were made using a Berkovich diamond tip indenter. The initial column was located at the approximate centreline of the weld, so the maps spanned outwards towards the HAZ. Testing was conducted at a load of 250 mN to achieve a sufficient penetration of the indenter tip into the

material (approximately 2 μm). This depth ensured that the tested material volume is representative of the microstructure volume under consideration. The area function was approximated by a standard calibration procedure with fused quartz material of known Young's modulus and hardness. High-magnification images of selected cracks, indentations and microstructures were taken using the FEI Quanta 450 FEG Environmental Scanning Electron Microscope.

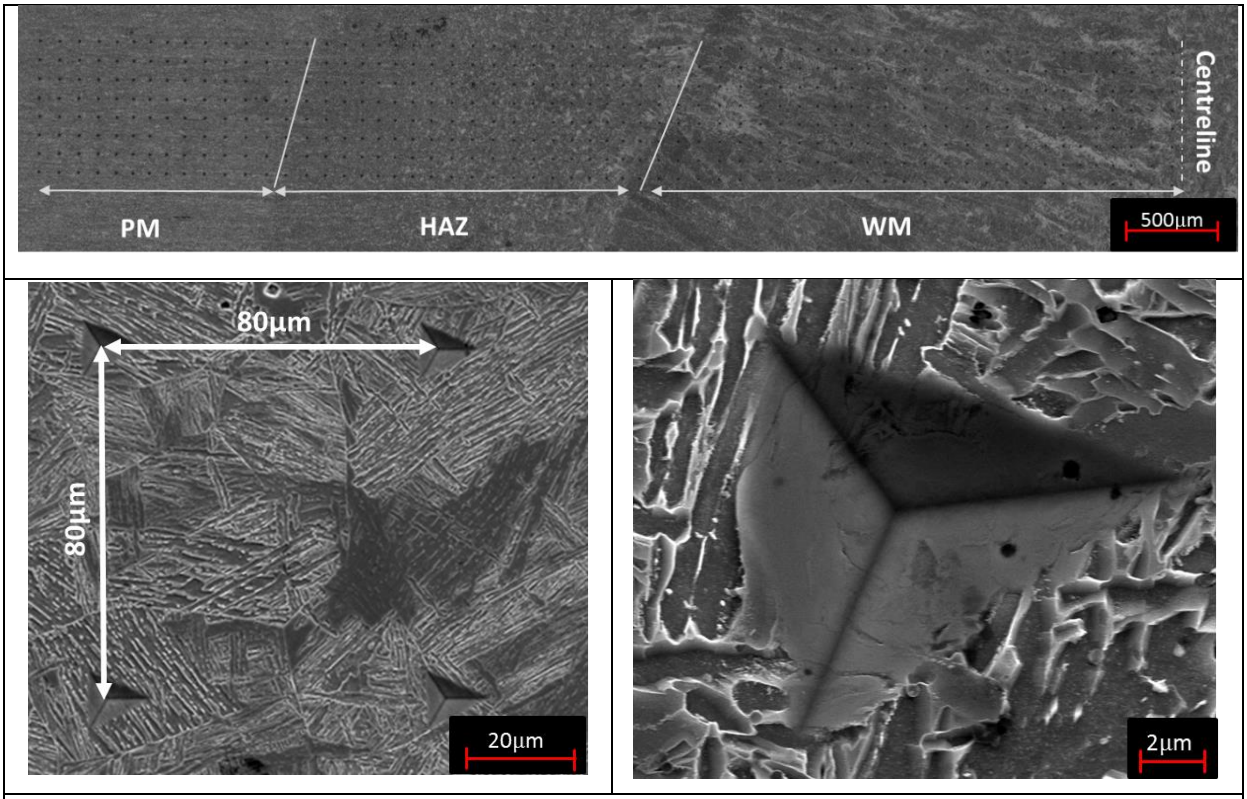

Figure 96: (top) Indentation map; (bottom left) spacing between successive indentations; (bottom right) high-magnification image of individual indentation.

4.5 Development of a Weldability Test Criterion

4.5.1 Selection of Test Thickness and Test Grade

As was reported in Chapter 2, the literature review, plate thickness plays an instrumental role in influencing the critical cooling rates $t_{8/5}$ and t_{100}, which in turn affect not only the resulting microstructure and residual hydrogen content, but also the welding parameters that can be used to deposit a viable weld bead. Consequently, pipe wall thickness is an essential variable not merely in the Australian pipeline welding code (AS2885.2) [23], but also in international pipeline construction codes such as API 1104 [30].

In delineating a safe welding envelope, defining the thickness range within which testing is to be conducted is of primary importance. The selection of the parent plate thickness in this thesis was based on two factors: what is considered the norm in the Australian context and the need to define the theoretical maximum thickness above which a change in thickness would lead to a negligible change in cooling rates. Defining the minimum and maximum thicknesses by integrating these two demands should lead to results that can be applied directly into the Australian context, while also providing empirical boundaries that can be applied universally.

4.5.2 **Industrial Survey**

4.5.2.1 Qualitative Survey Results

An exhaustive qualitative and quantitative survey of the Australian pipeline industry is beyond the scope of this thesis. However, as setting the limits of thickness necessitated a snapshot of the Australian industrial context, data was sourced through a literature survey and through a commercial, in-confidence, industry-specific survey whose results are detailed below.

From the literature review, it was established that line pipe steel used for transmission lines were chosen by primarily API or ASTM specification, with API 5L X65 and X70 common in the Australian context. Williams and Kilmore [278] reported that over 70,000 metric tonnes of X70 had been introduced into Australia between 1992 and 1995 ‘with no particular problem’ and implied that its likelihood of becoming the industry norm was high. In addition, Barbaro et al. [279] identified X70 and X80 as suitable alternatives for the ageing network of the primarily X52 network. In addition, the common diameters have been identified as 14 inch and 15 inch [280] with a maximum allowable operating pressure (MAOP) in the vicinity of 15.3 MPa. According to Norrish and Caprice [280], even though pipe diameters and wall thicknesses vary considerably, ‘Australian practice favours small diameter, thin wall pipes’.

The industrial survey used a stratified sample set of 86 assets (thin-walled small diameter pipes) qualified to AS 2885.2 and commissioned between 1985 and 2010. The assets were delinked from their contactors and the following elements were recorded: grade of line pipe steel, year of commissioning, wall thickness, diameter, MAOP and length.

The cumulative length of the assets was calculated to be 358 km, which is less than 0.01% of the current estimated 30,000-km length of entire oil and natural gas pipeline networks in Australia. However, the survey was not intended to describe the depth or breath of the

industry but rather to give a general insight into the trends of the industry and serve as a platform to discuss the data identified in the literature.

4.5.2.2 Quantitative Survey Results

From the data collected, pipe grades ranged from API 5L X42 to API 5L X70, with lengths from 5 m to 48.5 km (Figure 97). The minimum diameter was 88.90 mm and the maximum 323.90 mm (Figure 98). The mean and median diameters were 131.22 and 114.30 mm respectively. Wall thicknesses ranged from 3 mm to 9.27 mm (Figure 99) with a median thickness of 4 mm. MAOPs ranged from 1.96 to 18.9 MPa with a median of 10 MPa (Figure 100). From the data reviewed, it is clear that API 5L X42 has had a strong presence in the industry and relatively significant sections in the context of the data set were still being commissioned after 2005. However, what is clear is that for MAOPs above 10 MPa, X70 line pipe was the preferred steel; even though the data range ends in 2011, X70 steel has had a presence in the industry from 2005 onwards.

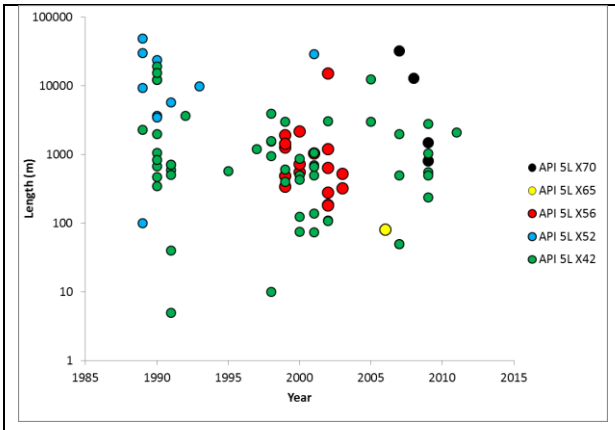

Figure 97: Historical construction trends of pipeline length (m) and grade of line pipe steel in the Australian context.

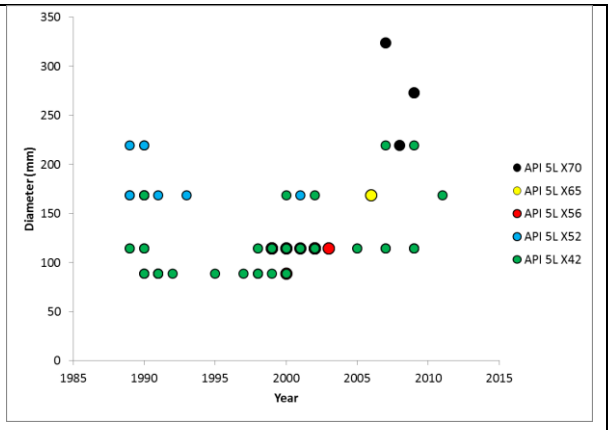

Figure 98: Historical construction trends of pipeline dimeter (mm) and grade of line pipe steel in the Australian context.

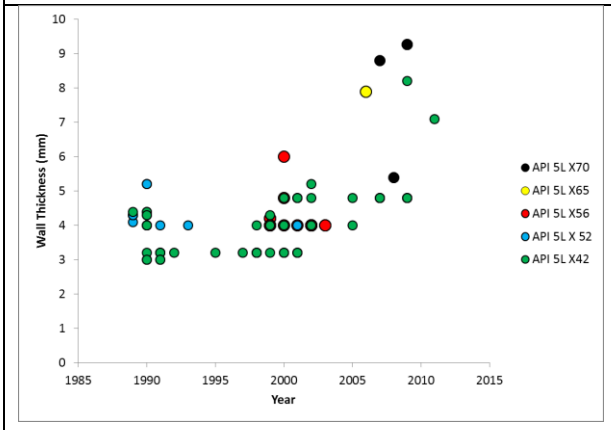

Figure 99: Historical construction trends of pipeline wall thickness (mm) and grade of line pipe steel in the Australian context.

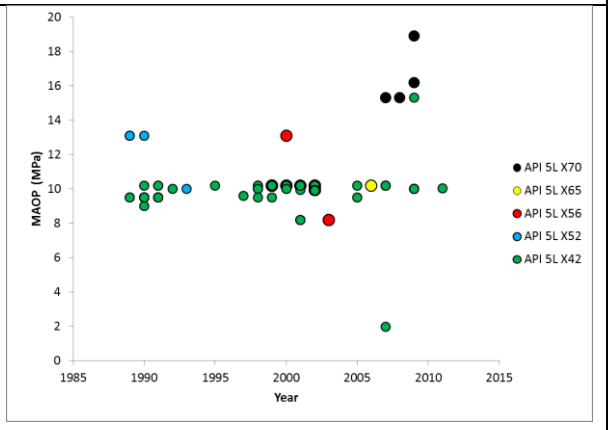

Figure 100: Historical construction trends of pipeline MAOP (MPa) and grade of line pipe steel in the Australian context.

If the years 2000 to 2010 are taken as a precursor to the anticipated trajectory of the industry, it is reasonable to suggest that X70 line pipe steel will have an even greater role to play in the oil and gas pipeline industry.

In terms of wall thickness, acknowledging that there are a number of factors which may affect the final selection, it is still clear that X70 line pipe is being employed for thicknesses above the median thickness recorded in the sample set. This corresponds to the MAOP under which X70 operates. When considering the general trends in the energy industry, this conforms well to the trend that the assets being commissioned recently have a greater capacity, given the growing energy needs of Australia. Thicker-walled, higher-strength steels offer greater capacity at a significantly lower weight penalty.

From the literature review and from the representative sample of pipelines examined, it can thus be said with confidence that API 5L X70 line pipe steel will have a continued presence in the Australian oil and gas industry in the coming decades. Moreover, it is reasonable to suggest that for future transmission, gathering and flow lines a wall thickness of 10 mm will still be prominent in the Australian context, so 10 mm wall thickness API 5L X70 grade pipeline was selected as the foundation of the study, based on the fact that it meets current industry requirements and that it served as an intermediary between what is extensively used by industry at the moment (API 5L X52), what is currently being introduced and what is anticipated to be dominant in the future.

Nevertheless, there is still the need to establish the maximum thickness to be investigated as part of this study, for which a theoretical approach was employed. The critical cooling rate $t_{8/5}$ can be used as a proxy for the microstructure being evolved. A lower $t_{8/5}$ implies a harder microstructure, which is generally more susceptible to cracking. Hence, the variation in $t_{8/5}$ with thickness is a critical measure of the microstructure being developed and of susceptibility to cracking. The critical cooling time t_{100} can be used as a proxy for the residual hydrogen content retained in the weld. A shorter t_{100} suggests a higher residual concentration of hydrogen in the weld and therefore a greater susceptibility to hydrogen cracking.

It was established in the literature review that thickness plays a very significant role in influencing both the $t_{8/5}$ and t_{100}, and that a critical thickness can be established where an increase in thickness above the critical thickness will have an insignificant effect on $t_{8/5}$ or t_{100}.

As the delineation of the safe welding envelope relies on establishing the critical preheat, which in turn has a significant influence on $t_{100,}$ the variation in t_{100} is considered a cause or

driver rather than a consequence. Therefore, it is the variation in $t_{8/5}$ with thickness which is the critical condition in determining the maximum thickness employed in this study.

4.5.3 Theoretical Maximum Thickness

To establish the maximum thickness of the test plate in the study, two well established and widely accepted analytical models were considered: Yurioka et al. [6]and Radaj [135]. These models were used simply to calculate the transitional thicknesses beyond which any positive increment in thickness will have a negligible effect on weld cooling rate. These values are then used as the basis for setting the maximum thickness to be tested. The two models are used for the sake of comparison.

4.5.3.1 Yurioka Model

Yurioka et al. [6] proposed an analytical solution in three dimensions to a point heat source moving on a preheated plate with a finite thickness. The transient temperature can be calculated as per the equation embedded in Figure 101 and carried out without neglecting heat transfer at the plate surfaces and the welded part.

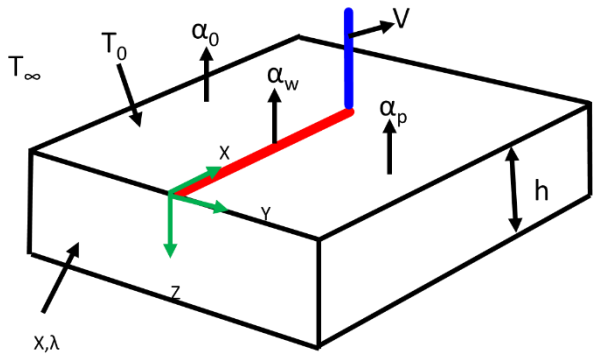

$$T_w(x,y,z,t) = T_\infty + \frac{Q_p}{\pi\lambda h}\sum_{n=0}^{\infty} A_{wn}\left(cos\frac{U_{wn^z}}{h} + \frac{hd_w}{U_{wn}}sin\frac{U_{wn^z}}{h}\right)\times f\left(\frac{r}{h}\sqrt{U_{wn}^2 + \left(\frac{vh}{2k}\right)^2} - \frac{vw}{2k}\right)$$
$$+ 2(T_0$$
$$- T_\infty)\sum_{n=0}^{\infty} A_{pn}\left(cos\frac{U_{pn^z}}{h} + \frac{hd_p}{U_{pn}}sin\frac{U_{pn^z}}{h}\right)\times\left(\left[\frac{\sin U_{pn}}{U_{pn}} - \frac{hd_p(\cos U_{pn} - 1)}{U_{pn}^2}\right]\right)\exp\left(-\frac{kU_{pn}^2}{h^2}t\right)$$

Q_p = Net heat input (kJ/mm)	T_0= Initial or preheat temperature (°C)
η = Arc efficiency	h = Plate thickness (mm)
U = Welding Voltage (V)	λ= Thermal conductivity (w/mm °C)
T_w = Point temperature at a given point in time (°C)	T_∞= Ambient temperature (°C)

Figure 101: 3D thermal analytical solution proposed by Yurioka [6].

The analytical solution provides estimates of the temperature distribution from which $t_{8/5}$ and t_{100} can be extracted. Work by Yurioka et al. has been extensity validated though empirical studies [4, 6, 32].

4.5.3.2 Radaj's Model

Radaj proposed a computationally inexpensive method of calculating critical thickness by considering $t_{8/5}$. Radaj's solution estimates the cooling time by using a point heat source moving through a semi-infinite solid (Equation 4-1) and a line heat source on an infinitely thin plate (Equation 4-2).The critical thickness is derived as (Equation 4-3):

Equation 4-1: Estimated critical cooling time ($t_{8/5}$) using a point heat source through a semi-infinite solid.

$$\Delta t_{8/5} = \frac{q_w}{2\pi\lambda}\left(\frac{1}{500 - T_0} - \frac{1}{800 - T_0}\right)$$

Equation 4-2: Estimated critical cooling time ($t_{8/5}$) using a point heat source on an infinitely thin plate.

$$\Delta t_{8/5} = \frac{q_w^2}{4\pi\lambda\rho c h^2}\left[\left(\frac{1}{500 - T_0}\right)^2 - \left(\frac{1}{800 - T_0}\right)^2\right]$$

Equation 4-3: Estimated critical thickness.

$$h_c = \sqrt{\frac{q_w}{2c\rho}\left(\frac{1}{500 - T_0} + \frac{1}{800 - T_0}\right)}$$

q_w = Net heat input (J/mm)	T_0 = Initial or preheat temperature (°C)
c = Specific heat capacity (J/kg °C)	h = Plate thickness (mm)
ρ = Material density (kg/mm^3)	λ = Thermal conductivity (w/mm °C)

Using the thermal and mechanical constants for API 5L X70 line pipe steel, the theoretical critical cooling time $t_{8/5}$ can be estimated using Yurioka et al.'s and Radaj's analytical solutions, as illustrated by Figure 102 and Figure 103.

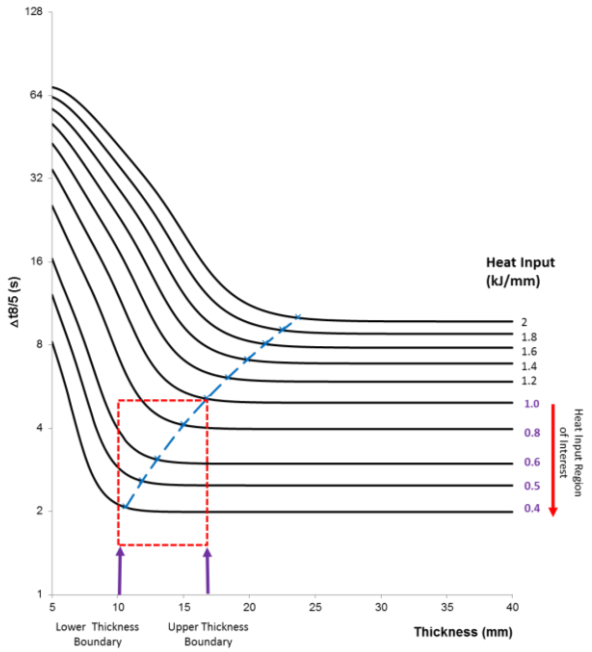

Figure 102: Welding cooling time ($\Delta t_{8/5}$) vs. plate thickness; Yurioka et al. model (critical thickness plotted in blue).

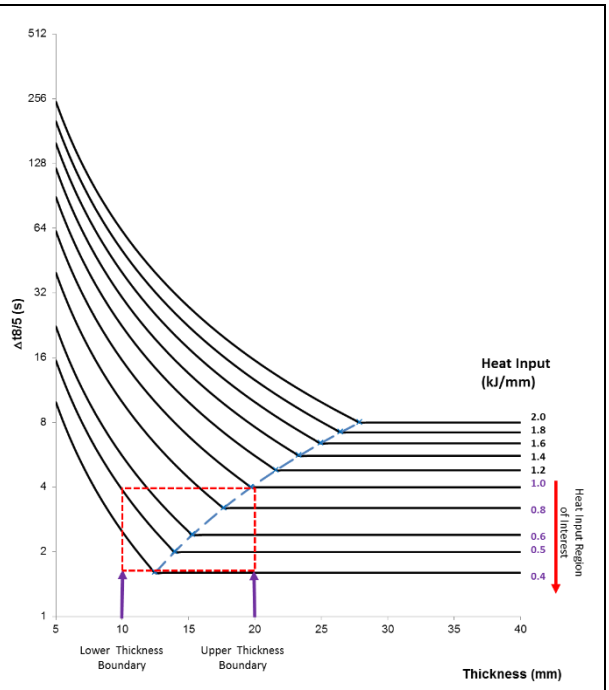

Figure 103: Welding cooling time ($\Delta t_{8/5}$) vs plate thickness: Radaj model (critical thickness plotted in blue).

The initial temperature is assumed to be 20 °C for both models. From the analytical results it can be concluded that for the heat input ROI, < 1 kJ/mmm, Yurioka et al.'s model predicts a transitional thickness to be less than approximately 16 mm and Radaj's model estimates the critical thickness to be less than approximately 20 mm. The analysis does not take into account the effect of preheat or environmental conditions such as wind or rain.

It is clear from both models that above 20 mm and for heat inputs less than 1 kJ/mm, there is no significant difference in the critical cooling rate, so using an upper testing limit of 20 mm sets a reasonable window within which weldability testing can be carried out. In summary, the material grade to be used for weldability testing in this thesis is API 5L X70, with a lower bound thickness of 10 mm and upper bound thickness of 20 mm.

Sixteen 20 mm-thick sample plates of API 5L X70 steel from the same heat were supplied by Baosteel, China; the chemical composition is given in Table 17 below. The CE was calculated as 0.38 and the P_{CM} was calculated as 0.175. The plates were thermomechanically controlled roll processed, yielding a fine microstructure consisting of mainly ferrite with some pearlite. The yield strength of the plate was reported as 458 MPa, with tensile strengths ranging from 600–750 MPa.

Table 17: Chemical composition of line pipe steel (wt%) (from manufacturer)

C	Mn	Si	S	P	Nb	Ti	Cu	Ni	Mo	Cr	Ca	Al	V
0.052	1.55	0.21	0.0011	0.0097	0.041	0.012	0.15	0.19	0.18	0.026	0.0016	0.039	0.029

In preparation for assembly of the MWIC samples, the plates were cut using an abrasive water jet. The Techni INTEC- G2 1612 was employed. A 55,000-psi water jet laced with garnet as an abrasive was used to section the plates with an effective kerf of 1.016 mm. The plates were cut at a mean speed of 85 mm/min. The temperature of the plates and cutting fluid was maintained at 25 ± 2ºC for the entire operation. The orientation of cut ensured that when the test coupons were assembled, the landing of the prepared welding joint would remain perpendicular to the rolling direction of the plate, emulating field conditions.

The parent plate sections were sandblasted in the ToolTec Sandblast SB-350 using glass beads with a diameter range of 106–305 µm to remove any mill scale or surface contaminates. The plates were then wiped down with acetone to dissolve any organic content and stored in a hermetically sealed container with bags of silica gel desiccant to absorb moisture and avoid rusting.

4.5.4 Selection of Welding Consumable

The literature review identified cellulosic electrodes as the favoured consumable for onshore pipe production as a result of their high deposition rates and excellent penetration. With the grade of steel for weldability testing identified as API 5L X70 and the two wall thicknesses identified as 20 mm and 10 mm, a suitable electrode had to be identified. Electrode suitability is based on two key criteria: technical suitability and conformance with current Australian practices.

4.5.4.1 Technical Suitability

Girth weld integrity requires the weld metal to have sufficient strength given, the inherent risk of inhomogeneities in the weld metal as a result of the welding process itself. This is especially true in cases where planar initiation sites such as NMIs are present in the weld. In the event the ligament is loaded beyond its capacity, the weld is theoretically expected to be strong enough to cause plastic strain in the adjacent parent material. In addition, the weld should have sufficient strength and work hardening characteristics to ensure that if fracture were to occur, it would be a result of a gross section yielding in the parent pipe, rather than a net section yielding in the weld [279].

It is understood that weld metal yield strength matching with the pipe will provide the maximum defect tolerance. There are arguments to suggest that strength matching is more appropriate than yield strength matching when designing a weld, as strength matching takes into account factors such as work hardening characteristics, defect limits and pipe wall thickness. Nevertheless, the prevalence and ease of the notched tensile test makes yield strength matching the dominant criterion in the selection of consumables.

Section 2, clause 2.2.1 (b) of AS2885.2-2007 [23] states that lower-strength electrodes should be used for the first pass when welding pipe and components of material greater than grade API 5L X60. Appendix C of those same standards reiterates this point by stating in clause C5 (b), 'on the basis of longstanding satisfactory experience, E6010 electrodes are suitable for use in circumstances where their application is warranted without supplementary requirements'. The use of electrodes with a yield strength of 60 ksi (413 MPa) is therefore ideal for use with the API 5L X70 line pipe steel, which has a yield strength of 70 ksi (482 MPa).

Considering the pipe laying process as detailed in the literature review, especially the lifting and lowering processes, the rationale behind selecting a more ductile electrode is evident. The loads to which the ligament is subjected before the joint is completed in the fill and capping passes may result in some degree of plastic deformation. If this deformation were to occur in the parent plate, the effective wall thickness would be reduced, theoretically decreasing the strength and capacity of the ligament. However, if the deformation were to occur primarily in the weld metal itself, then subsequent passes would accommodate this yielding. Moreover, once the lifting and lowering process is complete, additional passes are added in which higher-strength electrodes are used, bringing the net yield strength to that of the parent plate or greater.

Therefore, as this thesis focuses on the root pass of a girth weld, it is reasonable to conclude that electrode selection should be based on retaining a degree of ductility to accommodate these loads without fracture; the use of E6010 electrodes was thus commissioned for this study.

4.5.4.2 Industrial Survey

With the grade of electrode selected, a confidential commercial survey was sent to the industrial partners supporting this thesis to determine an appropriate brand of consumable. The rationale behind the industrial survey was to select a brand of consumable which was

widely used in the Australian context and one for which anecdotal evidence as to reliability and suitability exists. The individual responses of the survey remain in commercial confidence and thus are not available in the public domain.

After reviewing the survey results, the AWS A5.1: E6010 (ISO 2560-A: E423c25) Lincoln Electric Pipeliner 6P+ was selected. The Pipeliner 6P+ is a cellulosic pipe electrode designed for all position pipe welding, including vertical down root pass welding. The manufacturer asserts and respondents confirmed its suitability for root pass welding of pipe up to and including X80 and fill and cap pass welding up to and including X60. The electrode is renowned for having light slag with little slag interference for easy arc control. The deep penetration gives high dilution ratios. The electrodes produce a weld metal with a typical yield strength of 450 MPa, a tensile strength of 570 MPa, a 27% elongation and an impact ISO-V of 70J at -30 °C.

For the weldability testing carried out in this thesis a single batch (Q2 Lot 968M) of 4 mm Ø Pipeliner 6P+ electrodes was sourced directly from Lincoln Electric USA. The electrodes were issued with a lot control certificate, as each Pipeliner 6P+ batch is individually tested. When tested in accordance with AWS A5.01:2004, the following results were reported by the manufacturer. The deposition composition in wt% is summarised in Table 18.

Table 18: Electrode batch chemical composition (wt%) (from manufacturer)

C	Mn	Si	P	S	Ni	Cr	Mo	V
0.16	0.62	0.19	0.009	0.009	0.02	0.02	0.01	< 0.01

The weld metal when deposited at 140A (DCEP) and 24V with a preheat temperature of 107 °C and an inter-pass temperature of 149 °C had a reported yield strength of 425 MPa (0.2% offset method), a tensile strength of 522 MPa and an elongation of 28%. The average impact energy at -29 °C was 75 J.

4.5.5 Selection of Heat Input Test Range

From the industrial questionnaire results, it was established that contractors in the Australian context were operating at heat inputs lower than 0.7 kJ/mm for the root pass of girth welds. Those results also made clear that weldability testing at heat inputs lower than 0.7 kJ/mm was uncommon and that the WIC test in particular had not been used to map out susceptibility to HACC at extremely low heat inputs. In addition, it was established that, although it is

generally accepted for SMAW, an electrode should not be run at speeds greater than its length per minute (in this case, 350 mm/min); the manufacturers' literature for the electrode chosen specified that the operators should maintain a travel speed of approximately 300 mm/min. However, contractors in Australia favour higher deposition rates to minimize costs. From a review of welding procedure specification data supplied in commercial confidence, it was evident that travel speeds of 400 mm/min and above were not uncommon. With the travel speeds in excess of what was stipulated in the manufacturers' literature, establishing the limits of deposition and consequently the parameters needed to target the test heat input, had to be established.

The conventional approach to establishing deposition limits requires the development of a preliminary welding procedure specification based on the examination of the essential variables as defined by the working code. A test coupon is welded while the essential variable data is recorded in a procedure qualification record. The coupons are then tested destructively and non-destructively for compliance. A range that is usually a percentage of variance on the qualified essential variable is added to the welding procedure specifications to establish the limits within which a defect-free weld can be obtained.

However, given that the objective is to establish the limits at which critical welding defects appear, by finding the boundary of the safe welding envelope, the degree of conservatism displayed by the conventional approach would render the results ineffective for that objective. Moreover, the use of the AutoRon allowed for unique control of the way in which the electrode was driven into the work piece. As discussed in Section 4.2.1, the AutoRon can be operated in two distinct modes: mechanised (FCM and VCM) and semi-mechanised, in which the travel speed is controlled but there is manual manipulation of the electrode. To circumvent this degree of conservatism and capitalise on the unique potential of the AutoRon a variation of the conventional approach was employed.

Three series of experiments were derived and conducted to establish the limits of welding parameters that could be used to delineate a safe welding envelope. The acceptance criterion is based solely on an adaptation of AS3978-2003 [281], a weld bead profile that appears to be compliant by visual examination. These parameters then form the basis of weldability testing on the WIC test. The objectives are summarised in Table 20.

Table 19: Experimental designation and objectives for the development of the weldability criterion to be employed in weldability testing.

Experimental Series	Designation	Objective
Force Control Experiments	FCAL	Determine the force and current range required for successful deposition for a fixed travel speed of 420 mm/min.
Voltage Control Experiments	VCAL	Determine the voltage and current range required for successful deposition for a fixed travel speed of 420 mm/min.
Manual Control Experiments	MCAL	Determine the current range required for successful deposition for a fixed travel speed of 420 mm/min.

Although force cannot be measured in the field and is a consequence of the degree of biometric compensation introduced by the welder, by controlling the force with which an electrode is being driven into the work piece, the human element is effectively eliminated, reducing variability in parameters and consequently increasing the accuracy of the derived envelope.

4.5.5.1 Force Control Results

The force control potentiometer was cycled to give a force range of 0.5–4.5N in current range 150–165A. The testing results are summarised in Table 20.

Table 20: Deposition results under FCM.

Force Control Mode Results						
Test	Force (N)	Voltage (V)	Current (A)	Travel Speeds (mm/min)	Heat Input (kJ/mm)	Defect
FCAL 01	0.5	23.5	155	420	0.52	Lack of Penetration
FCAL 02	0.5	23.5	155	420	0.52	Lack of Penetration
FCAL 03	1	24	155	420	0.53	Lack of Penetration
FCAL 04	1.5	23.2	155	420	0.51	Undercut
FCAL 05	2	24.6	155	420	0.54	Undercut
FCAL 06	2.5	23.7	156	420	0.53	Undercut
FCAL 07	2.5	25	155	420	0.55	Undercut
FCAL 08	3	25.2	158	420	0.57	Undercut
FCAL 09	3	25.2	155	420	0.56	Undercut
FCAL 10	3.5	25	155	420	0.55	Wagon Tracks
FCAL 11	3.5	26	158	420	0.59	Wagon Tracks

FCAL 12	4	26	158	420	0.59	Wagon Tracks
FCAL 13	4	26	160	420	0.59	Wagon Tracks
FCAL 14	4.5	26	155	420	0.58	Pass
FCAL 15	4.5	25.6	160	420	0.59	Pass
FCAL 16	4	25.7	165	420	0.61	Pass

Below 150A and above 165A using FCM, an arc could not be established and maintained. Within the range of 150–165A and below 0.5N, the arc ignited but was extinguished within a couple of seconds, as the distance between the electrode tip and the work piece was too great for the arc to be maintained. Above 4.5N, the arc ignited but the electrode was driven into the work piece, resulting in the arc's being extinguished.

A change in force corresponded to a change in arc height and thus a change in arc voltage. For the FCAL test series, a force of 0.5N corresponded to 23.5V ± 0.5V and a force of 4N corresponded to 26.0V ± 0.5V within a current range of 155–165A ± 2. Consequently, using FCM the physical limits of deposition were recorded at a lower heat input of 0.51 kJ/mm and a maximum heat input of 0.61 kJ/mm, giving a range of 0.1 kJ/mm. This is an extremely limited deposition test window, rendering impossible its adaptation for the development of a practical safe welding envelope that could be used in the field.

The effect of electrode force and heat input on welding defects are illustrated in Figure 104. It is immediately apparent that without sufficient force pushing the electrode into the work piece there is not enough penetration to ensure a sound root bead. Weak penetration not only skews test results, as it would introduce a stress concentrator that could not be removed in practice, but it would also introduce a defect which would disqualify the weld in the field. As the force of the electrode increased from 1.5N to 2N, there was sufficient force to 'punch' the electrode into the groove and form the keyhole, but undercut was prevalent in these samples. Between 4–4.5N at a heat input 0.6 kJ/mm, welds of acceptable quality by visual inspection were produced.

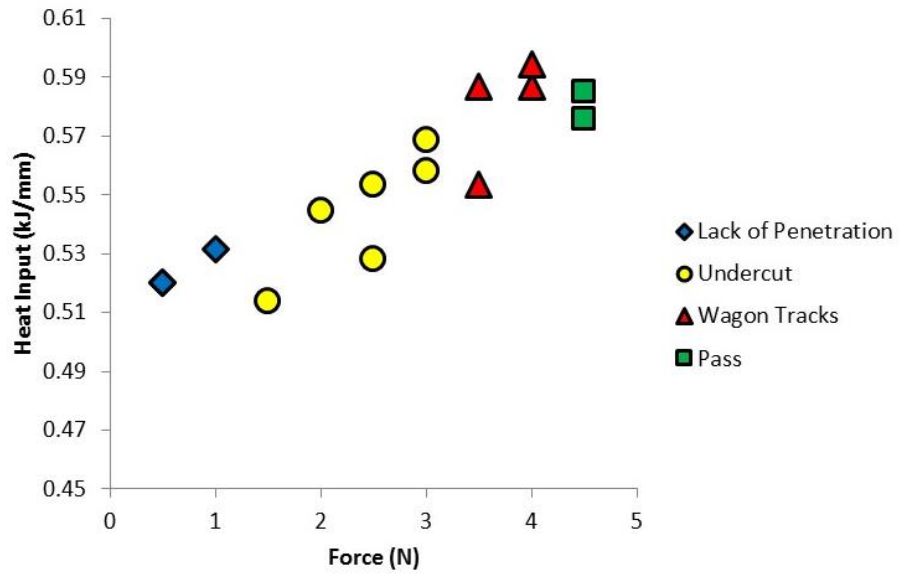

Figure 104: Observed defects for welds deposited under FCM as a function of heat input (kJ/mm) and electrode force (N).

When disqualifying defects were taken into account for the deposition window, it was further reduced to what can be considered to be a single heat input of 0.6 ± 0.2 kJ/mm, making the use of the FCM simply unacceptable as a control mode for deposition when trying to map out cracking susceptibility.

4.5.5.2 Voltage Control Results

The voltage control potentiometer was cycled to give a voltage range of 20–30.5V in the current range 126–167A. The testing results are summarised in Table 21.

Table 21: Deposition results in VCM

Voltage Control Mode Results						
Test	Force (N)	Voltage (V)	Current (A)	Travel Speeds (mm/min)	Heat Input (kJ/mm)	Defect
VCAL 01	-	20	166.5	420	0.48	Lack of Penetration
VCAL 02	-	22	159.2	420	0.50	Lack of Penetration
VCAL 03	-	23	154.8	420	0.51	Pass
VCAL 04	-	24.7	150	420	0.53	Pass
VCAL 05	-	27.5	140.1	420	0.55	Pass
VCAL 06	-	30.5	125.9	420	0.55	Pass

Using VCM to drive deposition, the deposition window increased marginally. Below 20 ± 0.5V and 166.5 ± 0.2A for a travel speed of 420 mm/min, an arc could not be established and above 30.5 ± 0.5V at 125.9 ± 0.2A the arc could not be maintained for more than a couple of seconds. The effect of voltage and consequently heat input of defects present when using VCM is illustrated in Figure 105.

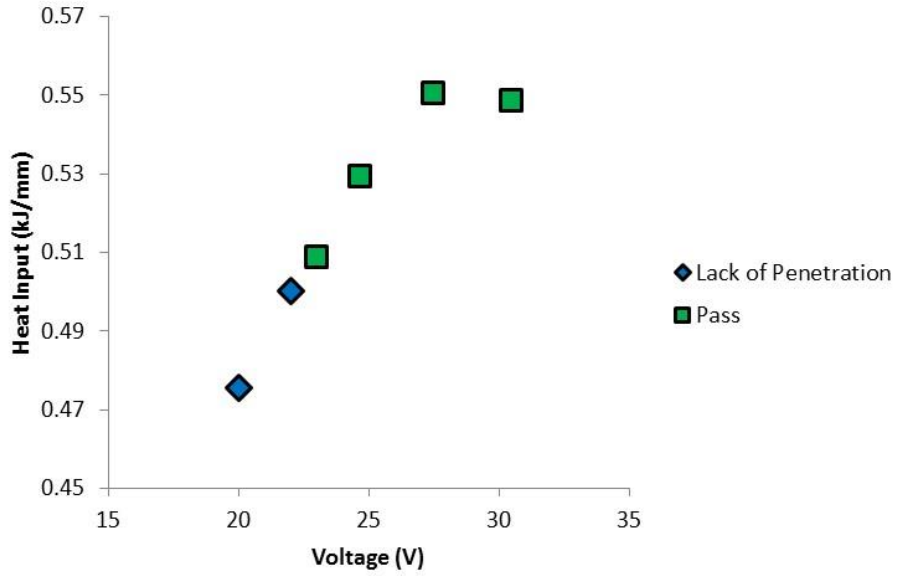

Figure 105: Observed defects for welds deposited under VCM as a function of heat input (kJ/mm) and electrode voltage (V).

Although these parameters correspond to a lower heat input of 0.48 kJ/mm and an upper heat input of 0.55 kJ/mm, there was a significantly larger range of currents within which VCM could operate: 125.9A–166.5A. Theoretically the combinations within this range of attainable parameters would suggest a larger heat input range within which deposition could be tested.

However, eliminating the force with which an electrode is pushed into the work piece to initiate and sustain the keyhole and ensure sufficient penetration and substituting higher voltages and currents for it detracts from the ability to integrate the results directly into industry practice. Moreover, increasing the currents and voltages to artificially high levels to provide a viable weld profile introduces a variability in expected dilution ratios and cooling rates and introduces microstructures and hydrogen concentrations that may not necessarily replicate field conditions.

It is therefore concluded that in order to best replicate field conditions, semi-mechanised welding using the AutoRon must be employed; this allows a close control of welding parameters, especially travel speed, and permits a degree of biometric compensation seen in the field in the force with which an electrode is pushed into the work piece. This approach

provides similar profiles for a given speed without an artificially unrealistic variation in parameters.

4.5.5.3 Manual Control Mode Results

As described earlier under the introduction of MCM, the electrode is manipulated by a certified welder, which allows for a variation of the force with which an electrode is driven into the work piece and the angular orientation of the electrode and permits the welder to adjust the characteristics of the keyhole in real time, effectively manipulating the molten pool to ensure desirable geometric characteristics of the deposited weld bead. The travel speed is maintained by the moving work table and the current is dialled into the power source. Variations in voltage will occur as a result of a change in arc height as a result of the force with which the electrode is driven into the plate, but the fixed current and the autonomously maintained travel speed mean that variations are minimal.

Manual control mode offered a lower heat input of 0.35 kJ/mm and an upper heat input of 0.65 kJ/mm for a current range of 100-170A at a fixed travel speed of 420 mm/min. Below 100A, the arc could be initiated but not sustained over the length of the test piece, while above 170A initiating and maintaining a stable arc was only intermittently possible. Table 22 summarises the testing results.

Table 22: Deposition results under MCM

Manual Control Mode Results						
Test	Force (N)	Voltage (V)	Current (A)	Travel Speeds (mm/min)	Heat Input (kJ/mm)	Defect
MCAL 01	N/A	24.4	100	420	0.35	Lack of Penetration
MCAL 02	N/A	25.5	100	420	0.36	Lack of Penetration
MCAL 03	N/A	23	105	420	0.35	Lack of Penetration
MCAL 04	N/A	24.7	105	420	0.37	Wagon Tracks
MCAL 05	N/A	24	110	420	0.38	Wagon Tracks
MCAL 06	N/A	23	110	420	0.36	Wagon Tracks
MCAL 07	N/A	22.2	115	420	0.36	Pass
MCAL 08	N/A	21.9	115	420	0.36	Pass
MCAL 09	N/A	23.1	120	420	0.40	Pass
MCAL 10	N/A	22.5	120	420	0.39	Pass

MCAL 11	N/A	22.5	130	420	0.42	Pass
MCAL 12	N/A	22.4	130	420	0.42	Pass
MCAL 13	N/A	24.6	140	420	0.49	Pass
MCAL 14	N/A	23.3	140	420	0.47	Pass
MCAL 15	N/A	26	150	420	0.56	Pass
MCAL 16	N/A	25.8	150	420	0.55	Pass
MCAL 17	N/A	21.5	160	420	0.49	Pass
MCAL 18	N/A	26.1	160	420	0.60	Burn Through
MCAL 19	N/A	27	170	420	0.66	Burn Through
MCAL 20	N/A	26.8	170	420	0.65	Burn Through

The results demonstrate that the heat input range is larger than either of the mechanised forms of deposition, FCM and VCM. Moreover, by introducing a degree of biometric compensation while maintaining travel speed through mechanisation, the objective of having lower variability in a targeted heat input while maintaining a degree of field realism can be achieved.

The results also show that the window in which the welds would pass visual inspection was larger, introducing a degree of confidence in the belief that a safe welding envelope could be developed. Lack of penetration was evident for welds deposited at low heat input and burn through occurred when the current exceeded the level recommended by the manufacturer.

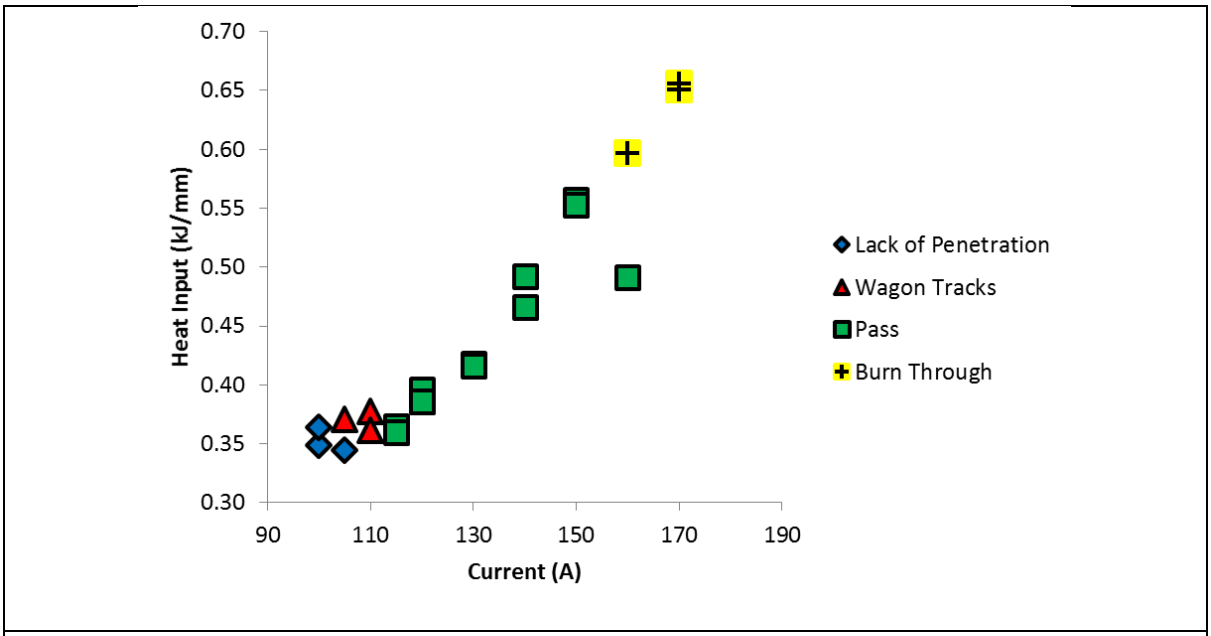

Figure 106: Observed defects for welds deposited under MCM as a function of heat input (kJ/mm) and welding current (A).

The effective heat input achievable corresponded to what was identified in the research gaps as being the area of interest for the overarching objective. However, from a review of the

achievable heat input and defects present at a fixed speed of 420 mm/min, it was readily apparent that having the speed fixed at 420 mm/min (7 mm/s) significantly limits the heat input range that can be tested.

In order to identify a clear safe welding zone, the travel speed would have to be reduced, so it was concluded that to realise the research objectives, weldability testing would be carried out in a semi-mechanised fashion with the travel speed fixed and controlled per test.

4.5.6 Testing Sequence

In Chapter 3, six specific goals were identified to meet the two primary aims of this thesis. These six goals depended primarily on the ability to deposit welds under the required conditions and delineate a safe welding boundary. The experimental methodology employed to meet these goals is summarised in Figure 107.

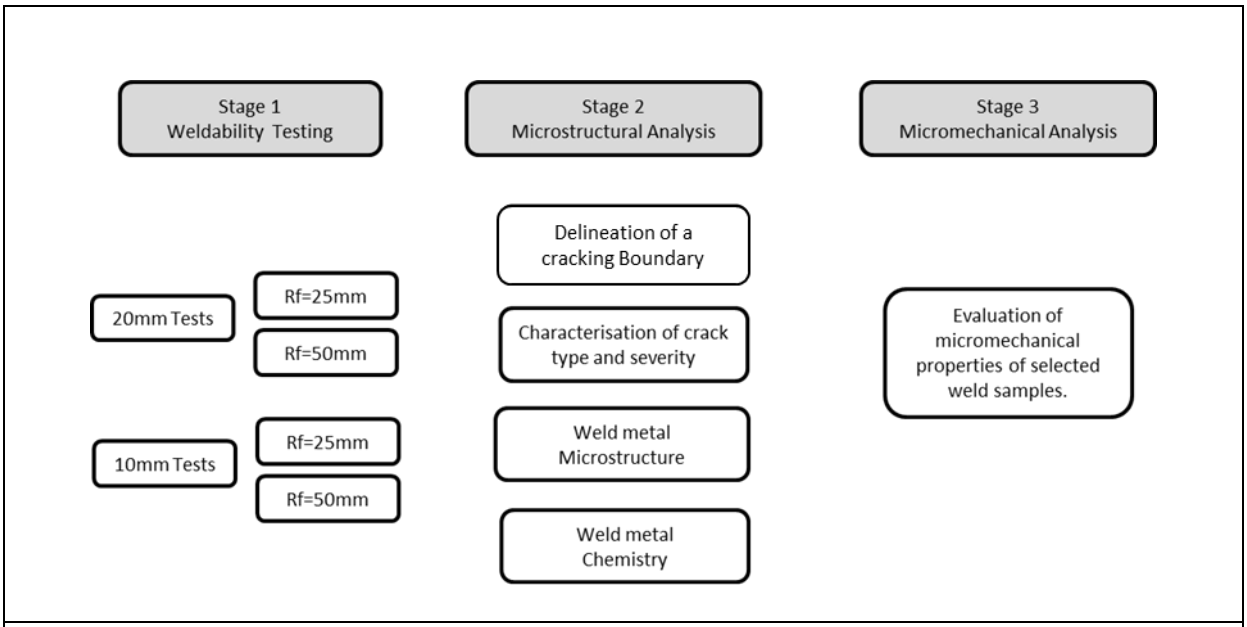

Figure 107: Summary of the methodology employed in this thesis to meet its overarching objective.

Stage 1

Stage 1 involves the creation of the data set that will be used for analysis in subsequent stages of the experimental program. Weldability tests were conducted with the MWIC weldability test on 20 mm- and 10 mm-thick API 5L X70 plate using a single batch of 4 mm Ø E6010 electrodes. To prepare the sample for weldability testing, the groove surfaces of the test specimen and 25 mm on either side of the weld centreline were polished down with ISO 80 grit (201 μm) emery paper and degreased with acetone to minimise the probability of introducing contaminants like surface oil and grease that might dissociate in the welding arc

and alter the cracking results. The entire specimen was degaussed prior to welding to eliminate any residual magnetic fields introduced during fabrication of the weldability specimen. Samples that required preheat were preheated in an industrial electric oven to 10 °C degrees above the specified preheat. The samples were mounted onto the AutoRon and allowed to cool to the required test temperature before testing commenced. The testing parameters are detailed in Table 23. During the 24-hour incubation period, samples were allowed to cool in still air.

Table 23: Testing parameters.

Welding Specifications		**Welding Parameters**	
Direction	Vertical Down (5G)	**Current**	130–170A
Size of Electrode	4.0 mm	**Voltage**	25–30V
AWS Class	A5.1	**Travel Speed**	250–470 mm/min
Specification	E6010	**Heat Input Range (Targeted)**	0.41–1.00 kJ/mm
Polarity	DC+	**Preheat Range (Targeted)**	25 °C–100 °C

To optimise the test sequence in terms of efficiency, weldability tests were conducted in the order of anticipated severity. Therefore, 20 mm tests under high restraint were conducted first, followed by 20 mm tests under lower restraint. The 10 mm tests followed in the same testing sequence. Each test was examined for compliance with adaptation of the weld acceptance criteria in AS/NZS 2885.2. In particular, the weld was examined for the presence of severe welding defects, such as undercut, lack of penetration, porosity and burn through that would disqualify the weld from consideration.

Stage 2

Once weldability tests were conducted and the 24-hour incubation period expired, the sample was disassembled and test sections extracted as described before. Each extracted sample was divided into six sections that were individually prepared for metallurgical analysis, and then analysed for the presence of cracks to create the data set from which the safe welding boundary was delineated. The samples were then repolished and etched for microstructural analysis.

Stage 3

A select number of samples from stage two were selected for micromechanical analysis. The selection was based on the results and is detailed later in this thesis. These samples were repolished and mounted for analysis as detailed above.

CHAPTER 5

Development of an Enhanced Weldability Test

5 Development of an Enhanced Weldability Test

5.1 Modification Criteria

From the weldability tests reviewed in Chapter 2, it was concluded that the traditional WIC test was the best weldability test for the assessment of pipeline materials, welding consumables and welding procedures and processes. Its highly representative nature combines with its low fabrication costs and the inherent degree of conservatism intrinsic to its design, make it the most effective industrial assessment tool. However, the literature review also revealed its limitations as a research tool, which is outlined in the following section.

(a) Difficult to instrument

Instrumentation for measuring the temperature field in the HAZ and the strain across the welded joint need to be attached to the underside of the restrained test plates to avoid high arc temperatures. On a standard WIC sample, access is limited to the 3 mm gap provided by the spacer.

(b) Not representative of the pipeline girth weld process

Stove pipe welding using cellulosic electrodes is commonly used for the root pass of pipeline welds. The flux on cellulosic electrodes produces large volumes of hydrogen and carbon monoxide around the arc; these gases have high ionisation potentials [95], giving the arc high energy that enables deep penetration. This makes them suitable for welding line pipe where welding is possible from one side only and deep penetration is required. During the root pass of a pipeline weld, a keyhole is formed and copious quantities of the gases produced from the flux as well as any dross formed flows into the pipe bore. The evolution of the gases and dross during the welding of two-bevelled plate is shown in Figure 108. However, with a standard WIC sample the void is restricted to the height of the 3 mm spacer and the gases and dross cannot as readily escape, producing a back pressure and reduced arc stability.

Figure 108: Gas and dross escaping from the spacing at the back of the traditional WIC specimen. A restricted gap creates an impingement that forces gases to escape through the front of the work piece, which destabilises the molten weld pool and is not representative of line pipe welding in the field.

(c) Consistency

The back pressure on the molten weld metal resulting from the gases produced by the flux reduces the consistency of the weld bead profile and can result in welding defects like windows. The elimination of such defects requires great skill on the part of the welder. If the region behind the weld better represented the situation in pipeline welding, more consistent welds would be possible with less intervention or manipulation required from the operator.

As the primary research objective required the successful deposition of repeatable and reliable samples in the heat input range of 1 kJ/mm and below, the primary task undertaken was the evaluation and subsequent modification of the well-established WIC test to address these specific limitations.

The traditional WIC geometry is altered in this section so that it is more suitable for research and better represents the situation applicable to the girth welding of oil and gas transmission pipelines with cellulosic electrodes. It was imperative that any alteration to the sample design would not change the thermal field or the restraint conditions around the weld so that the results obtained from samples with the altered design could be compared with those from the original design and with results from other laboratories.

5.2 Modification Strategy

The modified WIC sample (MWIC) includes four significant changes to the test specimen geometry to improve the consistency of the deposited weld bead profile, the quality of the deposited weld at lower heat inputs and the ability to instrument the test specimen. The MWIC weldability test incorporates a gas tunnel, V-grooves, run-on and run-off tabs and

instrumentation access, including a weld centreline access port and an extensometer access port. The design, development and integration of the design changes were achieved through the successful implementation of a three-stage program.

Stage 1 *(Conceptual Study)***:** A conceptual study identifying and introducing elements to improve the quality and consistency of the deposited weld bead in addition to facilitating the measurement of critical cooling times and local weld metal displacement.

Stage 2 *(Finite Element Analysis)***:** Verification of thermal and structural similitude with the traditional WIC weldability test to demonstrate the ability to compare and integrate results from various sources.

Stage 3 *(Commissioning Study)***:** Empirical testing to demonstrate an enhanced testing window and improved bead profile characteristics.

5.3 Design Modifications

5.3.1 Gas Tunnel

Large quantities of gas and fume developed by the welding process are forced through a very narrow gap created by the spacer between the parent plate and the backing plate. The only other egress for the gas and fume is the root gap itself. The pressure built up by the escaping gases acts on the keyhole and requires varying degrees of compensation by the welder to counter the force created by the escaping gas. This can be achieved by altering the arc height by changing the voltage, by changing the force with which the electrode is driven into the plate or by modifying the travel speed. This variability in welding parameters results in an inconsistency in the deposited weld bead geometry. A gas tunnel was introduced to enhance the flow of the weld-generated gas and fume and thus improve the consistency and symmetry of the deposited weld. The inability of gases to escape as a result of the limited space between the strong back and the parent plate was identified as a potential reason for inconsistency in bead profiles. The aim of introducing the gas tunnel is to improve the egress of the shielding gases.

A parametric study examining the improvement in weld quality with increased distance between the parent plate and the strong back formed the basis of the introduction of the gas tunnel. Based on the weldability test envelope identified when developing the weldability criteria, welds were deposited manually with a mean heat input and travel speed of 0.55 ± 0.1 kJ/mm and 450 ± 5 mm/min respectively, no preheat and under ambient conditions (25 ± 5

°C). Mild steel plate (AS/NZS 3678 – 250 [118]) was used for preliminary testing to keep costs to a minimum, with the final tests being conducted on API 5L X70 plate, in specifications mirroring those that would be encountered when carrying out the final weldability testing.

Preliminary testing involved systematically increasing the space between the parent plate and strong back using 5 mm spacers. As restraint was not a parameter of concern, a series of G clamps were used to hold the parent plate onto the strong back. A visual examination of the weld was carried out to quantify the improvement of weld quality. The qualitative examination was carried out by a certified welding inspector to AS 3978-2003 standards [281]. The final test results are tabulated in Table 24 and illustrated in Figure 109.

Table 24: Relationship between weld qualities as assessed to AS 3978-2003 standards with increasing spacer height on prototype MWIC test

Samples	Current (Amps)	Voltage (Volts)	Travel Speed (mm/min)	HI (kJ/mm)	Spacer Height (mm)	Visual Inspection (AS-3978-2003) [281].
GT-1	168	25	439	0.57	3	Fail
GT-2	168	25	500	0.50	3	Fail
GT-3	168	25	405	0.62	10	Pass
GT-4	168	25	500	0.50	10	Fail
GT-5	168	25	503	0.50	20	Pass
GT-6	168	25	475	0.53	20	Pass
GT-7	168	25	461	0.55	20	Pass

From the qualitative test results it was evident that the ideal weld bead consistency (profile and penetration) based on an examination against AS 3978-2003 standards was achieved when the spacer height was 10 mm or greater. With a higher heat input, a 10 mm spacer would have sufficed, but as the envelope was being developed for high travel speeds and consequently lower heat inputs, it was prudent to use a greater spacer height. Tests carried out using mild steel did not show any macroscopic differences under visual inspection when compared to the tests carried out using X70 steel. In addition, the preliminary tests were carried out to a spacer height of 30 mm; there was no observable improvement in weld quality above a 20 mm spacer height.

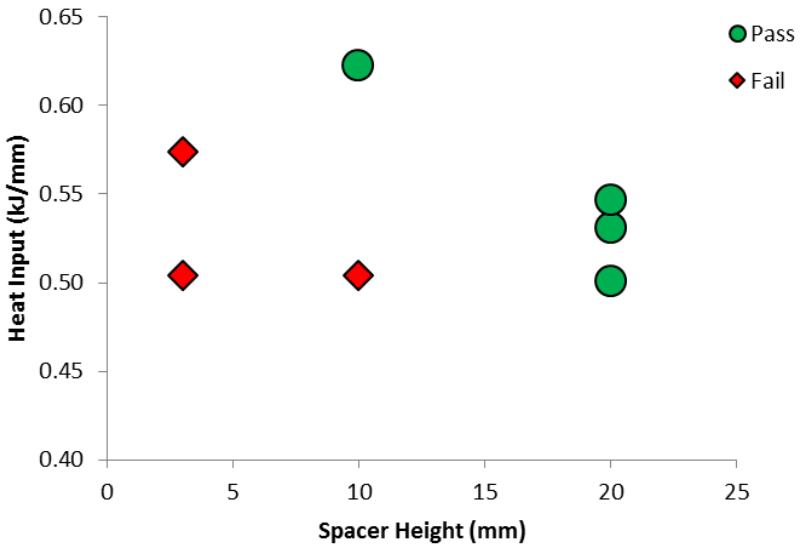

Figure 109: Relationship between weld qualities as assessed to AS 3978-2003 [281] with increasing spacer height and heat input on prototype MWIC test.

With a qualitative improvement in weld quality established, the effects of introducing the introduction spacer had to be examined in relation to the rigidity of the weldability test.

5.3.1.1 Optimisation of Gas Tunnel

As detailed earlier, a gas tunnel was introduced into the WIC test to improve the quality of the weld deposited. The results demonstrated an improvement in the weld bead profile and the ability to deposit welds in a semi-mechanised fashion at high travel speeds. However, the integration of the gas tunnel into the traditional WIC specimen introduced a change in the geometric profile of the specimen. A key criterion to be satisfied as part of the enhancement of the WIC test is maintaining the original test's structural properties and thermal characteristics so as to ensure that the enhancements do not affect the cracking susceptibility when compared to the traditional WIC test.

An optimisation study was carried out to determine the effects of the gas tunnel on the displacement response of the specimens and to quantify the effect of changing the base plate thickness so as to optimise MWIC test design. A preliminary model was used to compare the deflection response to pressure loads for both the WIC and MWIC designs. This in turn was used to validate, mesh and load independence before a high-fidelity optimisation was performed using DesignXplorer®. Finally, the deformation distributions of the original unmodified specimen and the optimised modified specimen were compared. As the introduction of the gas tunnel is a key feature of the developed MWIC test, the following section discusses the optimisation of the gas tunnel and it integration into the MWIC design.

5.3.1.2 Conceptualisation

The primary purpose of the optimisation is to ensure that the introduction of the gas tunnel was integrated into the design of the MWIC test geometry in such a way that the deformation of the modified specimen mimics the deformation behaviour of the original specimen, when subject to similar loading conditions, both thermal and mechanical. To execute the optimisation in a computationally efficient manner, four key simplifying assumptions were made. The first assumption related to the modelling of the geometry in order to minimise computational time and complexity only one half of the specimen was modelled (axial symmetry). This is a safe assumption, given the fact that the response of the specimen is symmetric across the weld centreline.

Secondly, as only the macroscopic response of the specimen is being taken into consideration, the specimens are assumed to be fused throughout the thickness, rather than employing contact elements between the top plate, the connecting plate and the base plate. The use of contact elements is computationally inefficient when considering the optimisation objective.

The third assumption relates to the mechanical response of the specimen. Deflections are assumed to be small and elastic, so a static structural anisotropic elastic model is employed. The heat is dissipated relatively quickly in each specimen in an identical manner, and as such the loads would be more transient; however it is demonstrated below that the relative deflections of the specimens are independent of the applied load, so a static structure is applicable.

The fourth assumption involves the loading conditions. It is assumed that loading acts as a pressure load on the edge of the specimen in the X direction, as shown in Figure 110. This load is present due to the thermal expansion of the specimen near the weld as each side advances towards each other. This expansion is assumed to be identical for both specimens since the hole present in the modified specimen should have no influence over the heating profile of the top of the specimen and the pressure applied should be the same in both cases. Furthermore, expansion in the Y and Z directions were ignored, as they are also insensitive to the presence of the tunnel. Torsion was also ignored for the purposes of this study due to simplicity; including a torsional analysis would require a full 3D model. However, it must be noted that torsional loads will be present due to the weld path's providing a transient heating distribution, although their magnitude would be secondary to the compressive loads experienced.

5.3.1.3 Pre-Processing

The cross-section was modelled in two dimensions using ANSYS Mechanical version 14.5. The material properties of structural steel, Young's modulus of 200 GPa and Poisson's ratio of 0.3 were employed in the analysis. Initially a coarse mesh of 8-node quad elements with removal of the mid-nodes in areas of low loading or interest was applied to the models of each specimen, with face-sizing controls to ensure similar mesh profiles. The coarse mesh was applied at this stage to reduce the computational time of the dimensional optimisation, while a face split was applied along the solution path to increase the accuracy of the results. A finer mesh was applied later, once a suitable candidate was selected. A mesh convergence study, shown in Table 25, was conducted to determine the allowable mesh size. An element size of 7 mm was found to be highly accurate, maintaining computational efficiency with less than 0.5% error.

Table 25: Mesh convergence study of element size against ratio of maximum deflections.

Maximum element size (mm)	$Y_{modified}/Y_{original}$ (Max)	Deviation from 2 mm element size
2	1.1333	+0.0000%
3	1.1362	+0.2600%
4	1.1330	-0.0265%
7	1.1296	-0.3270%

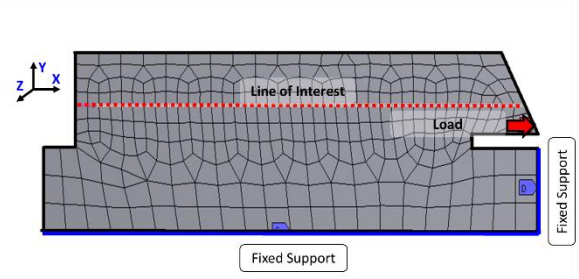

Figure 110: Low-fidelity mesh, solution path and loading and constraint positions for the WIC test geometry.

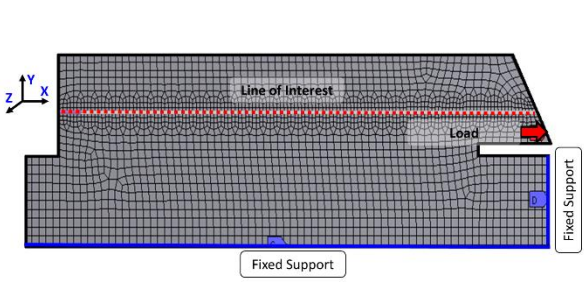

Figure 111: High-fidelity mesh, solution path and loading and constraint positions for the WIC test geometry.

5.3.1.4 Solution

Loads and boundary conditions were applied as shown in Figure 110. The base was fixed along the bottom edge, while the line of symmetry was represented by the other fixed support. A load of 100 MPa was applied along the bottom part of the tapered section in the X

direction. This line segment was selected for the load as it is approximately the height that the weld reaches. The value of the pressure load was chosen arbitrarily.

5.3.1.5 Initial results

The initial deflection profiles of the modified specimen and the original specimen showed 13% greater deflection for the modified specimen, which was consistent with results seen in experiments. The applied pressure was then parameterised and varied to show that the percentage increase in Y deflection is independent of the applied load, as shown in Table 26. This implied that a thicker base plate or a smaller tunnel diameter would be required to give the modified specimen an equivalent stiffness. As a larger gas tunnel diameter reduces weld defects, it is preferable to increase the base height rather than reducing the tunnel diameter.

Table 26: Maximum deflection for applied pressure loads.

Pressure (MPa)	$Y_{modified}/Y_{original}$ (Max)
100	1.1296
150	1.1296
200	1.1296

5.3.1.6 Design optimisation

The height of the base plate and the radius of the hole were both parameterised to find a combination of the two which satisfies the following constraints:

1. Tunnel diameter must be between 40 and 45 mm;
2. The ratio of the modified specimen's Y deflection to the original specimen's Y deflection must be unity ± 1%;
3. Volume and thus mass must be minimised.

This was achieved using the DesignXplorer® package of ANSYS Mechanical 14.5. A response surface was generated based on a sampled matrix with tunnel diameter and base plate height as inputs and ratios of displacements and volume as outputs. Taking the 2D slice at a diameter of 40 mm demonstrated the inverse relationship between deflection ratio and base height, as shown in Figure 112.

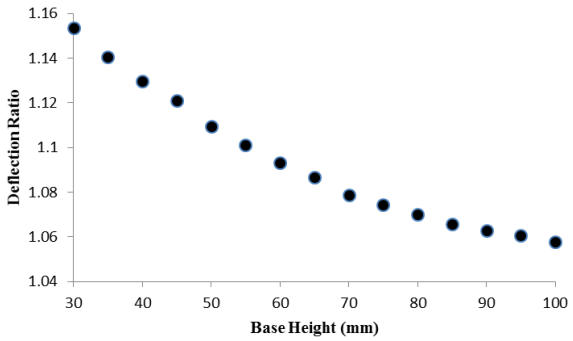

Figure 112: Ratio of maximum deflection of the specimens when the base height is varied for a hole with a diameter of 40 mm.

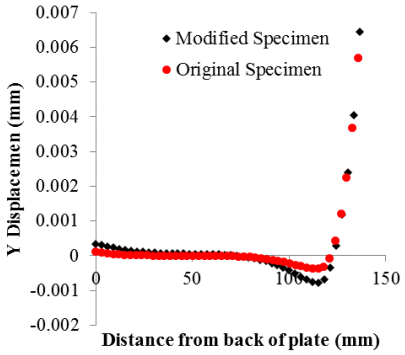

Figure 113: Vertical deformation of a path through the top plate comparing the optimised and original specimens.

The specimens were then remodelled with a finer mesh (see Figure 111), and the displacement paths compared, as illustrated in Figure 113. A finite element parametric study revealed that an increase in the thickness of the base plate of the MWIC test to 40 mm reduced the difference in deflection between the two specimens to 13%, effectively compensating for the introduction of the gas tunnel.

5.3.2 Run-On and Run-Off Tabs

The use of run-on and run-off tabs limit start and end effects [177, 178, 193]; they are particularly helpful in minimising unwanted residual stresses [282] in a test section. In addition, as the test section is supposed to be representative of an interference-free run, extinguishing the arc in the test section would result in an abnormal deposition profile and an increase in the net heat input, altering the test's representative nature. However, when taken in the context of multi-pass welding, the bead profile may be corrected by grinding and subsequent passes may minimise the distribution of the net heat input over the test section. Given that this thesis is concerned only with the root pass of a girth weld, a conscientious effort had to be made to ensure that the test section was welded in a representative manner to ensure the validity and fidelity of the empirical cracking boundary to be derived. To mitigate for these effects, the use of run-on and run-off tabs is required.

The traditional WIC test specification did not specify the use of run-on and run-off tabs, but individual laboratories may have employed of tabs to limit start and end effects. Coniglio [193] specified tabs of 50 mm in length, 25 mm in width and 7 mm in thickness on the entry section and 5 mm in thickness on the exit section. This configuration was employed when using a mechanised form of deposition.

However, preliminary trials demonstrated that using this configuration of tabs when depositing welds in a mechanised or semi-mechanised fashion negatively impacted the reliability of the deposited weld. When transitioning from the run-on tabs to the weld test section, the characteristic of the weld changed; the change in thermal mass and from a flat to a grooved surface led to a different degree of compensation required to keep the arc stable and maintain the integrity of the weld bead. In the field, this can be achieved through either a reduction in travel speed or a reduction in current. However, as the net heat flux had to be maintained within ± 0.05 kJ/mm and the travel speed could not be changed in the test setting, the consequence would have been a defective weld, invalidating the results.

To compensate, run-on and run-off tabs with the same groove preparation were used (Figure 114). The tabs were long enough to establish a stable arc and wide enough to dissipate any heat generated that may have adversely affected the test section. The tabs tapered into a 25 mm-wide shoulder, allowing the tabs to be positioned clear of the anchor welds. One shoulder of each tab was welded using the TIG process autogenously to the parent plate to prevent mechanical interference with the test section and to allow movement of the tab with the parent plate. The tabs were aligned to ensure a smooth transition between the tabs and the test section. To avoid contraction of the root gap in the centre of the tab, the run-on and run-off tabs were tacked with a v-shaped restraint.

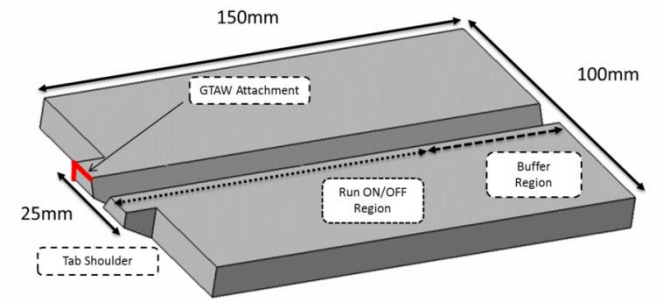

Figure 114: Prototype MWIC run-on and run-off tabs; the tabs are designed to minimise start and end effects.

5.3.3 Instrumentation Access

5.3.3.1 Weld Centreline Temperature

As discussed in the literature review, the weld thermal cycle plays a pivotal role in the mechanical properties of the weld. In particular $t_{8/5}$ is a critical thermal measurement, as it is influenced by the essential variables of thickness and heat input and can be used to predict microstructure and estimate hardness [32, 214].

Traditional weld centreline temperature measurements on the WIC test are made by lancing or harpooning a thermocouple into the trail of molten metal behind the welding arc. This has the potential not only to disrupt the welding process but also to increase the possibility of contamination of the weld pool if the thermocouple tip comes into contact with the welding arc. To avoid these issues, measurement of the weld centreline temperature for the root pass of the weld should be taken from the rear of the specimen. However, in the traditional WIC test the stiffener is attached to the base plate, making access to the rear of the weld impractical. To address this limitation, a thermocouple access port (T_0) was designed for the MWIC test. The port's centre is located at the geometrical centre of the specimen, corresponding to the weld centreline. The 8 ± 0.5 mm-diameter access port was drilled from the rear of the backing plate.

5.3.3.2 Local Weld Metal Displacement

The measurement of local weld metal displacement has two distinct applications. First and foremost, if the instrumentation is sensitive enough, it can be used to measure the onset of cracking. Time to failure has the potential to serve as a means of quantifying cracking susceptibility. Secondly, as discussed in the literature review, measurement of the local weld metal contraction is a critical component in calculating the resultant contraction stresses, which could be used as a means of quantifying susceptibility. Extrinsic tests such as the instrumented restraint cracking and TRC tests have successfully extracted and implemented such measurements through the integration of linear variable differential transformers in the body of the test to measure displacement through the weld thermal cycle accurately.

The integration of sensitive instrumentation to measure local weld metal displacement during the root pass of the weld is not possible with the geometric configuration of the WIC test. As was the case with the thermocouple, the strong back and base plate configuration render the back of the weld inaccessible. In instances where the local weld metal contraction have been measured on the WIC test, the test has been instrumented from the front. Alam [20] used a clip-on gauge to measure the contraction of the edge of the bevel (Figure 115), which was taken to be representative of the displacement of the entire parent plate.

This option not only results in a delay in measurements and does not allow for an extraction of the entre contraction profile, but as the measurement is taken on the edge of the bevel, it also does not truly represent the contraction down at the root pass, especially in cases where the root pass has defects like wagon tracks.

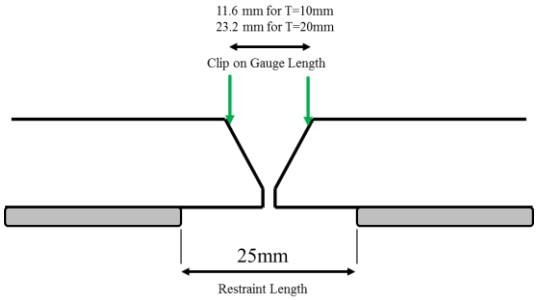

Figure 115: Gauge length for clip-on gauges for 20 mm- and 10 mm-thick parent plates on the WIC and MWIC test specimens.

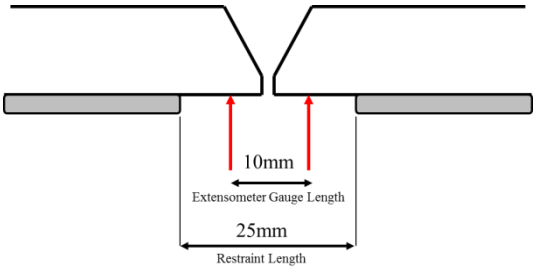

Figure 116: Gauge length for an extensometer on the MWIC test specimen. Regardless of the thickness of the parent plate, a gauge length of 10 mm can be maintained to provide real-time displacement values at the local weld metal scale.

To address this limitation, an extensometer access port was designed for the MWIC test (Figure 116). This port allows a sensitive extensometer to be placed into contact with the parent plate in the rear of the weld, the area of greatest interest. Small indentations or dimples can be punched into the rear of the plate to ensure sufficient contact and minimise the chance of the extensometer's slipping during the welding and subsequent cooling processes. The gauge and sensitivity of the extensometer can be varied to the task at hand.

Ports inserted to access the weld region to measure local weld metal contraction (S) and the weld centreline temperature are detailed in Figure 117.

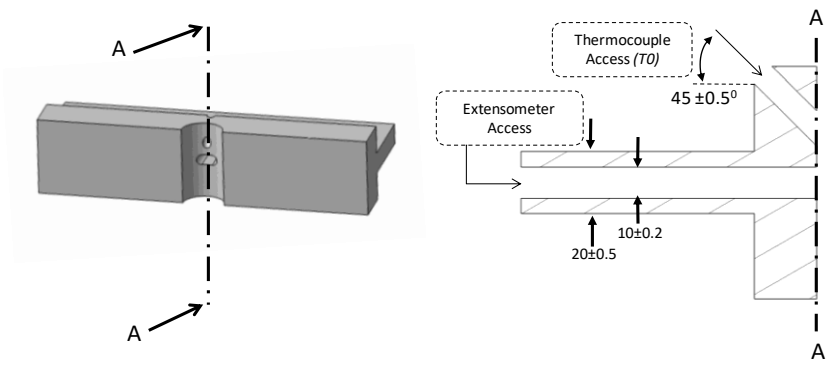

Figure 117: Isometric and cross-sectional view of instrumentation access for weld centreline temperature and local weld metal displacement.

For the purpose of this study, in order to compare the thermal field, especially the degree of homogeneity of the thermal field of the parent plate, thermocouple access was absolutely mandatory. The parent plate's thermal history was measured by drilling three 1.2 mm Ø holes to 1 mm off the bottom of the parent plate 6, 9 and 12 mm away from the weld centreline (Figure 118), giving access to measure the temperature near the HAZ and in the parent metal during welding.

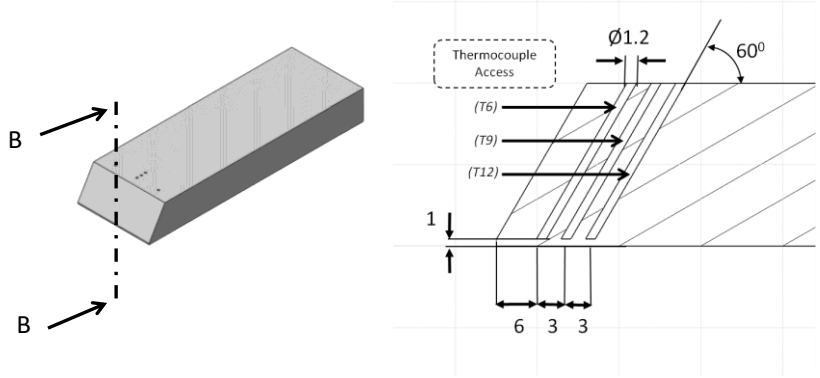

Figure 118: Isometric and cross-sectional views of thermocouple access to the MWIC parent plate.

In addition to the thermocouple access at the centreline, two tracking thermocouple access ports were drilled into the edges of the parent plate. The top tracker was drilled 5 mm off the top datum of the parent plate and 6 mm off the geometric centre of the test specimen and the bottom tracker was drilled 5 mm off the bottom datum of the parent plate and 6 mm off geometric centre.

The positon of the top tracker and bottom tracker allow for a comparison of the entry and exit temperature fields and can be used to compare temperature fluctuations as the electrodes run through the test section.

5.3.4 Tolerance Adjustment

In addition to the gas tunnel and instrumentation access, the joint preparation tolerances were adjusted to accommodate the lack of biometric compensation that accompanied the mechanisation of the welding process (Figure 119 & 120). The inability to vary travel speed in response to a closing gap as the electrode runs through the test section requires the root gap and root face to be adjusted and maintained to allow for sufficient penetration and minimise the probability of lack of fusion at travel speeds above 400 mm/min. To ensure the edges of the parent plate liquefied and that there was adequate wetting of the parent plate, the root gap and root face were minimised to just below the generally accepted minimum dimensions to a root gap and root height of 0.8 ± 0.2 mm[23]. Additionally, the tolerances and limits on misalignment were narrowed to ensure that no artificial stress raiser was introduced into the test specimen and to improve the consistency and symmetry of the deposited weld bead.

However, as was the case with Lazor [31] and Cola [197] with the WIC test, the MWIC test can also be used to test the effect of misalignment, a variation in root gap and root height on cracking susceptibility, distribution of residual stresses or any other aspect of weldability. The tolerance adjustments are necessary when depositing welds at high travel speeds in a semi-

mechanised fashion where biometric compensation is restricted to control the accuracy of the net heat input.

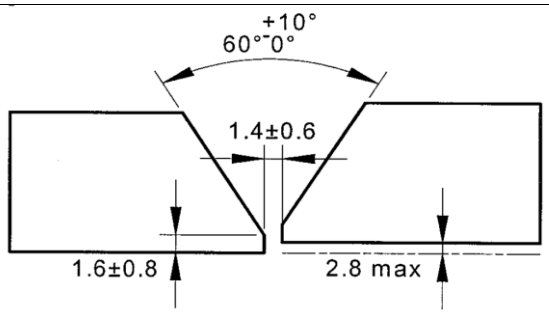

Figure 119: Geometric dimensions and tolerances of a typical single-V butt weld preparation.

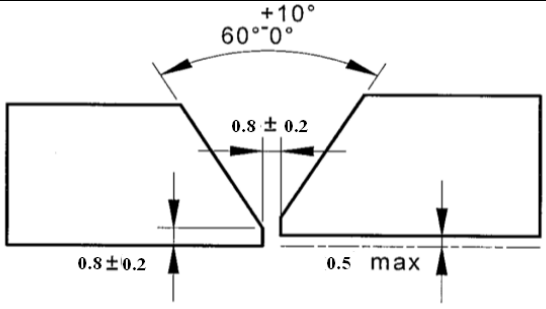

Figure 120: Geometric dimensions and tolerances for a single-V butt weld prep for the MWIC test specimen.

5.4 **Final Design**

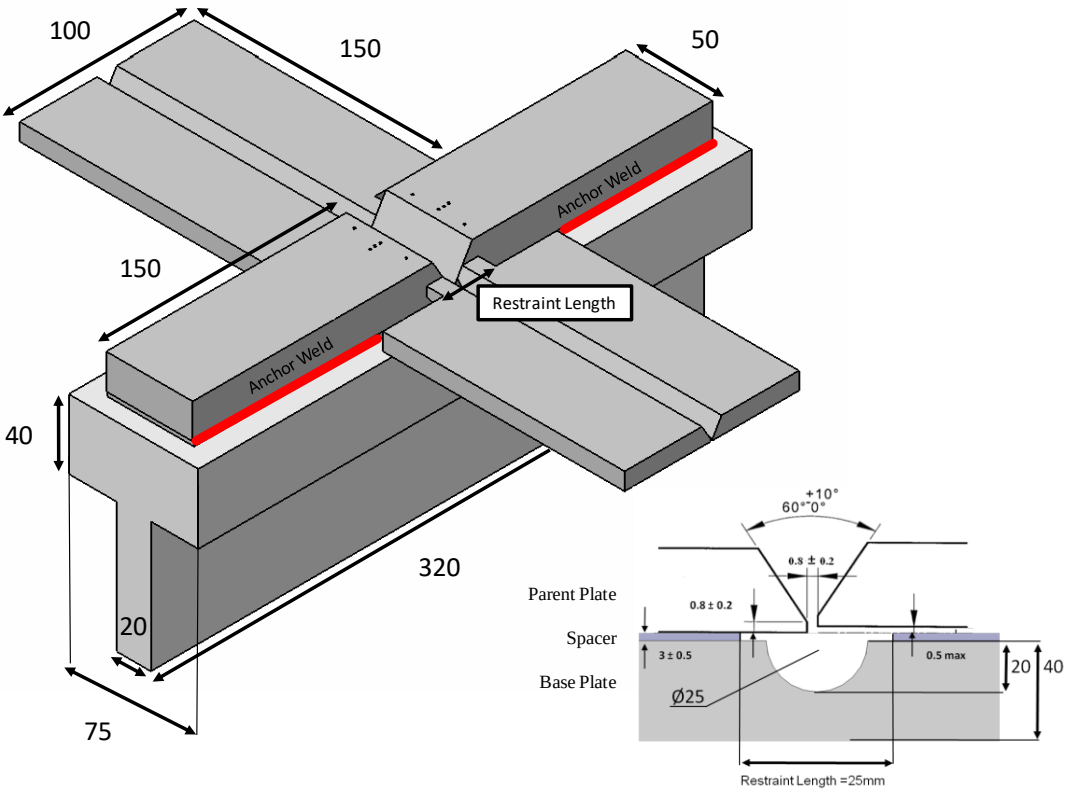

Figure 121: MWIC design: (1) parent plate; (2) run-on and run-off tabs; (3) spacer ;(4) tunnelled backing plate; (5) stiffener. All dimensions in mm.

Figure 121 illustrates the final design of the MWIC test. The base plate, stiffener and spacer are all manufactured from AS/NZS 3678-250 steel. Fillet welds (8 mm actual leg length) were used to join the base plate to the stiffener and for the anchor welds. The preparation of the parent plate and application of the restraint welds and the assembly instructions for the MWIC

test specimen, including degaussing and degreasing prior to use, are similar to those used for the traditional WIC test, as detailed in Section 4.3.

5.5 Validation of the MWIC test

The conceptual stage of the study identified changes that were introduced into the traditional WIC specimen to improve the repeatability and reliability of the test welds' being deposited within the niche requirements identified in Section 5.1, without altering the design principles of the test, given that it has clearly been benchmarked as the most effective weldability test. To investigate the influence of the design modifications, a two-tier validation protocol used.

Tier 1: Validation of structural and thermal similarity using finite element analysis

To limit experimental costs, finite element analysis was used to compare the structural and thermal similitude of the WIC and MWIC tests. Geometrically representative models of the two tests were created using the finite element modelling package ANSYS Mechanical version 14.5 and subjected to expected thermal and structural loading; the results were compared. To limit computation costs, where 3D models were required, only half the structure was modelled because of the symmetric nature of the specimen.

Tier 2: Validation by thermal similarity using experimental methodology

As the thermal field critically affects the residual hydrogen content, resulting microstructure and residual stress distribution, factors that directly affect susceptibility to hydrogen cracking, Tier 2 of the validation protocol experimentally compared the thermal field of the parent plate in both tests in order to account for the simplified nature of the simulation and to provide comprehensive empirical data to demonstrate the tests' similarity.

5.5.1 Tier 1: Finite Element Analysis

5.5.1.1 Structural Analysis

Having already established the necessary increase in base plate thickness to compensate for the addition of the gas tunnel, the structural analysis of the MWIC and WIC test was limited to comparing the maximum displacement between nodes on the surfaces of the prepared edges.

A dimensionally accurate model of half of the WIC and MWIC test was modelled in ANSYS Solid 186; a 3D, multi-node element with three degrees of freedom for each of the 20 nodes

was used as part of the simulation (Figure 122 and Figure 123). Mesh selection and refinement were carried out to ensure a symmetric uniform mesh with a greater density in areas of interest. The material properties of structural steel from

Table 27 were used for both MWIC and WIC tests. The anchor welds were modelled as fixed supports and contact between the spacer, parent and backing plates was modelled through the use of contact elements. Symmetric zero displacement boundary conditions were applied to simulate the sample's being held in place on a flat surface.

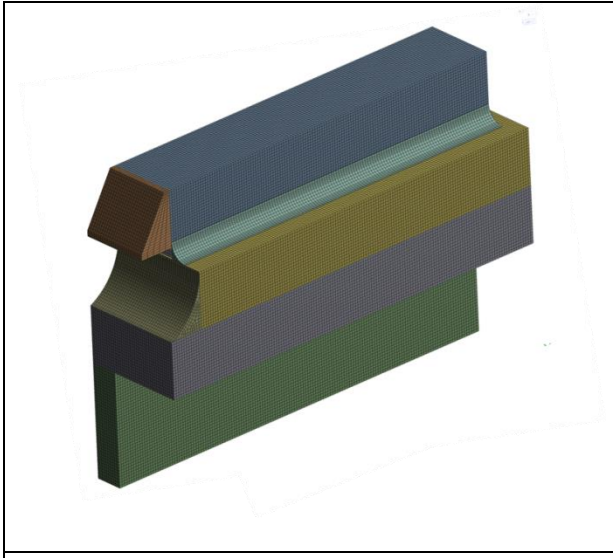

Figure 122: Finite element model of the MWIC test specimen.

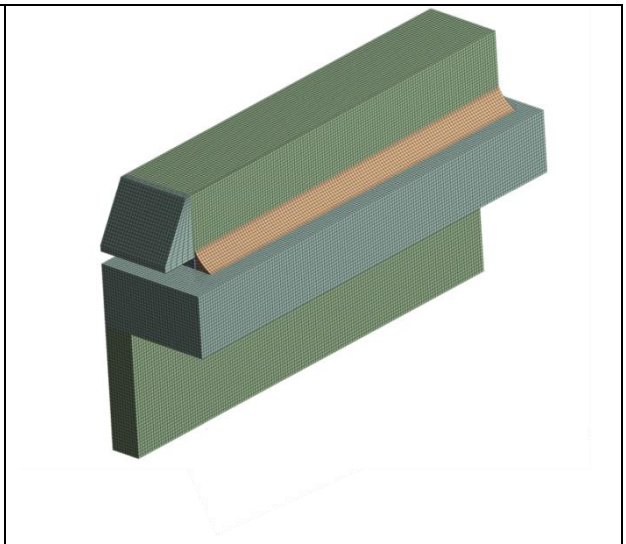

Figure 123: Finite element model of the traditional WIC test specimen.

Table 27: Material properties applied to the finite element simulation.

Compressive yield strength	250 MPa	Young's modulus	200 GPa
Tensile yield strength	250 MPa	Poisson's ratio	0.3
Tensile ultimate strength	460 MPa	Bulk modulus	167 GPa

A load of 300 MPa was applied on the surface of the root landing, and the displacement of three nodes was compared, as illustrated in Figure 124.

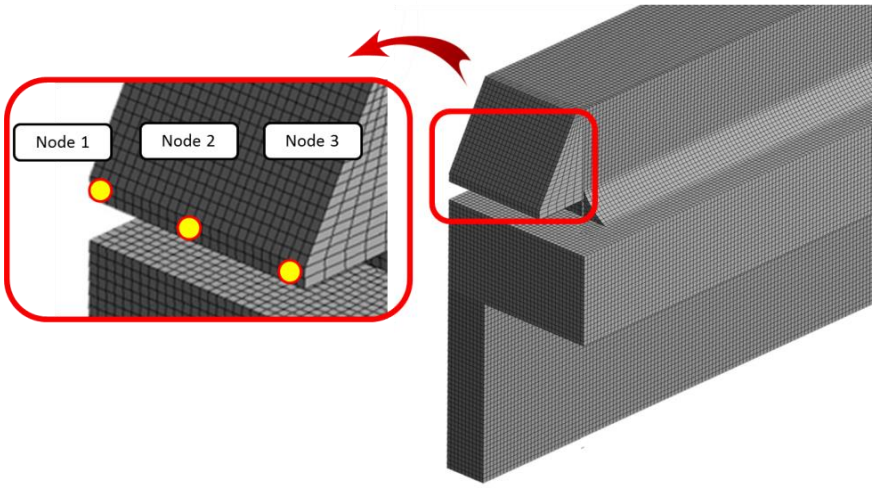

Figure 124: Schematic of relative position of nodes isolated for the analysis of displacement. The image highlights the positon of the nodes isolated on the WIC test. For the MWIC test, nodes located in the sample positon were used for the analysis.

The measured displacements for the three different nodes in similar geometrical locations in weld areas of both original and MWIC specimens are shown in Table 28.

Table 28: Comparison of displacements for the selected nodes in both WIC and MWIC samples.

Coordinates	Nodes	Displacement µm		Comparison (%)
		WIC	MWIC	
X	1	-0.122	-0.133	9.63
	2	-1.31	-1.42	8.45
	3	-2.86	-3.12	8.9
Y	1	28.4	30.3	6.74
	2	25.9	28	8.1
	3	23.1	25.2	8.86
Z	1	44.4	51.9	17
	2	43.1	50.9	18.1
	3	42.1	50	18.7

As expected, the maximum displacements occurred in the Z direction for both test specimens, due to the fact that tensile pressure is applied in the Z direction in the V-groove (weld area). By comparing the results of the displacements for corresponding nodes in both samples (Table 28), a maximum increase of 18.7% in displacement in the MWIC sample occurred in the Z direction. This suggests that the original and MWIC tests provide very similar restraint conditions.

5.5.1.2 Thermal Analysis

A thermal model of the two specimens was required to determine if the thermal response of the top plate of the modified specimen was significantly different from the WIC test. The geometric configuration of the model remained the same, although tetrahedral solid heat transfer elements were used for the thermal analysis.

The expectation was that there would be little difference, as the removed mass of the modified plate has a long conductive path from the weld surface. A transient 3D thermal analysis was performed for each specimen with a moving Gaussian heat source that would mimic temperatures seen for the duration they are seen during actual welding. A coarse mesh was applied to reduce computational time due to the complexity of 3D transient thermal analyses with surface-surface radiation. The heat input was calculated in 0.1s intervals for 8 seconds and distributed with a standard deviation of 1 mm and a mean that moved from one side to the other at a speed of 7 mm/s along the weld surface. The typical thermal response of the WIC and MWIC test are illustrated in Figure 125 and Figure 126.

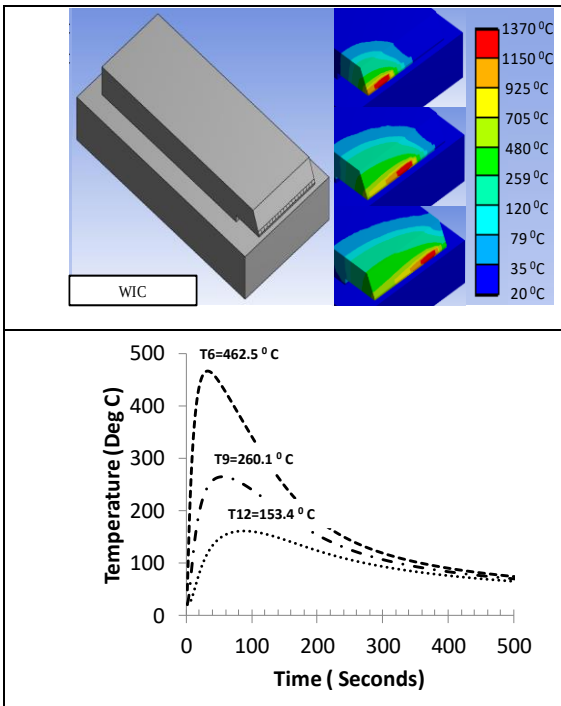

Figure 125: Thermal response of the standard WIC samples to local heating.

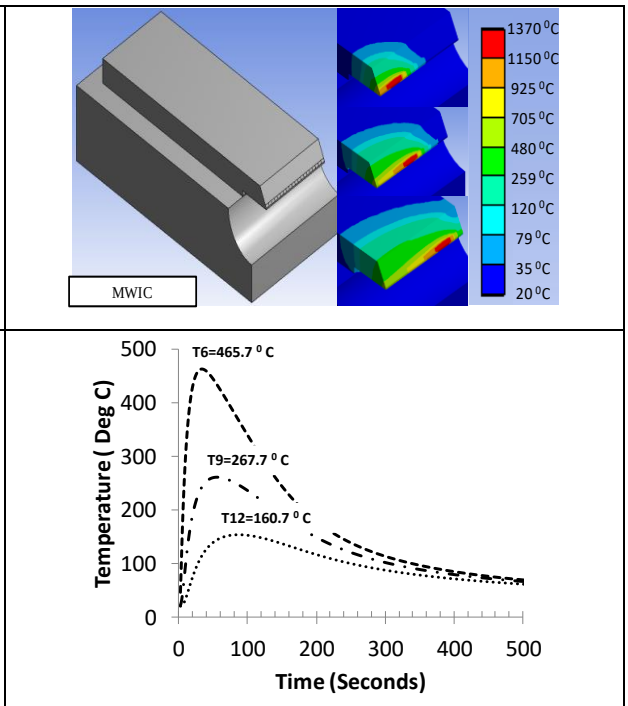

Figure 126: Thermal response of the MWIC samples to local heating.

The comparison tests were undertaken for parent plate thicknesses of both 10 mm and 20 mm. For each pair of tests, a single-pass weld was deposited with a heat input of 0.65 kJ/mm. To compare the two specimens, temperature probes were used to ascertain the peak temperatures and cooling rates at the T6, T9 and T12 positions. For the comparisons made on 10 mm-thick

plates, the peak temperature difference between the WIC and MWIC tests was less than 7.5 °C, while for the 20 mm-thick plate it was less than 5 °C. This nearly negligible difference in recorded peak temperature and a correlation coefficient of unity for the cooling rates suggested that the specimens are comparable from a thermal perspective. From the simulation results, it can be concluded that the MWIC test specimen is comparable thermally and in terms of physical rigidity to the traditional WIC test specimen.

5.5.2 Tier 2: Experimental Analysis

Experimental comparisons of the traditional WIC test and the enhanced MWIC test are limited by the ability to deposit viable welds on the WIC test specimen design across the range of parameters that can be used on the MWIC design. Hence, the comparison of thermal characteristics between the WIC and MWIC test are limited to the test plates' thermal homogeneity for heat inputs with which viable welds can be deposited in both tests.

Comparability with respect to the test specimen designs' influence on the cooling rate of the parent plate of the prototype MWIC and WIC configurations were experimentally tested by depositing single-pass welds on serval instrumented samples. Experimental cooling rates and peak temperature data showed a high degree of correlation with simulated results in both tests, serving to validate the accuracy of the simulation results. It is important to recall that the simulation results showed a difference of less than 10 °C in peak temperature and a near identical critical cooling rate. The experimental temperature difference between the WIC and MWIC parent plates was less than 8.5%, as detailed in Table 29. This evidence suggests that the cooling rates of both the test specimens are comparable.

Table 29: Comparison of the mean peak temperatures for welds deposited in 20 mm-thick test plates on the MWIC and WIC tests at 0.85 ± 0.02 kJ/mm under ambient conditions (25 °C) and maximum restraint (R_F = 25 mm).

Peak Temp	TT	T6	T9	T12	BT
MWIC	402^{0}C	384^{0}C	251^{0}C	175^{0}C	375^{0}C
WIC	425^{0}C	416^{0}C	266^{0}C	184^{0}C	401^{0}C
% Diff	*5.7%*	*8.3%*	*5.9%*	*5.1%*	*6.9%*

Temperature measurements taken from the top-tracking and bottom-tracking thermocouples on the MWIC showed similar cooling rates, indicating a high degree of thermal homogeneity within the test section and providing evidence to verify that that the run-on tabs had no effect on the cooling rates at the edge of the test section. Figure 127 illustrates the mean temperature

profile of MWIC tests carried out at 0.85 ± 0.02 kJ/mm under ambient conditions (25 ± 5 ˚C) and maximum restraint. Across the entire range of experiments, there was less than 10% difference in the peak temperatures recorded. This variance was random and could be attributed to experimental error introduced as a result of contact and the response time of the thermocouple with the parent plate.

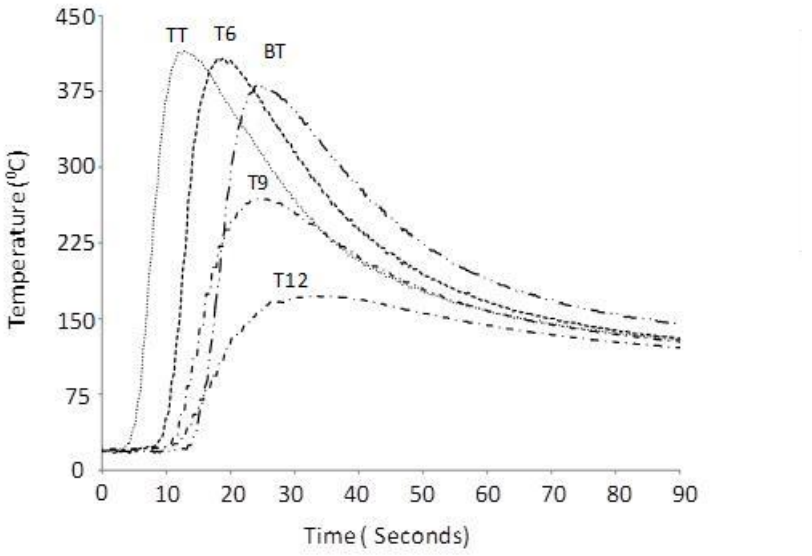

Figure 127: Mean thermal profile of 20 mm-thick plates at 0.85 ± 0.02 kJ/mm under ambient conditions (25 ± 5 ˚C) and maximum restraint in the MWIC test.

With the high degree of correlation between empirical testing results and simulation results, less than 8.5% difference in peak temperatures and the comparable cooling rates of the WIC and MWIC test specimens, there is sufficient evidence to suggest that the test specimens are comparable from a thermal perspective.

5.6 **Commissioning of the MWIC Test**

To quantify the improvements of the MWIC specimen in terms of the enhanced deposition window and the improvement in the consistency of the weld bead deposited, deposition trials were run within the heat input range of interest. Deposition trials were limited to 20 mm-thick parent plates. Welding trials showed that for 20 mm-thick plates under ambient conditions at heat inputs lower than 0.45 kJ/mm, both tests produced defective welds that exhibited lack of fusion and penetration. Testing results also showed that the MWIC specimen could be used to deposit defect-free welds between 0.5 kJ/mm and 1.0 kJ/mm, whereas the standard WIC test was limited to a heat input range of above 0.8 kJ/mm (Figure 128). Welds deposited on the WIC specimen below this range resulted in the formation of windows to the point where the

weld did not represent field weld quality and would generate excessive stress concentration that would prevent accurate determination of the onset of HACC (Figure 129).

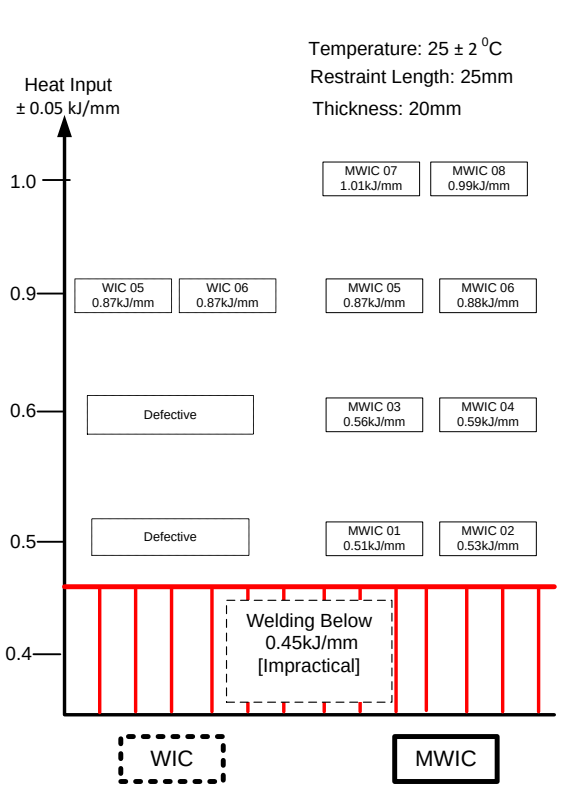

Figure 128: Weldability test range for the WIC and MWIC specimens across the root pass heat input range.

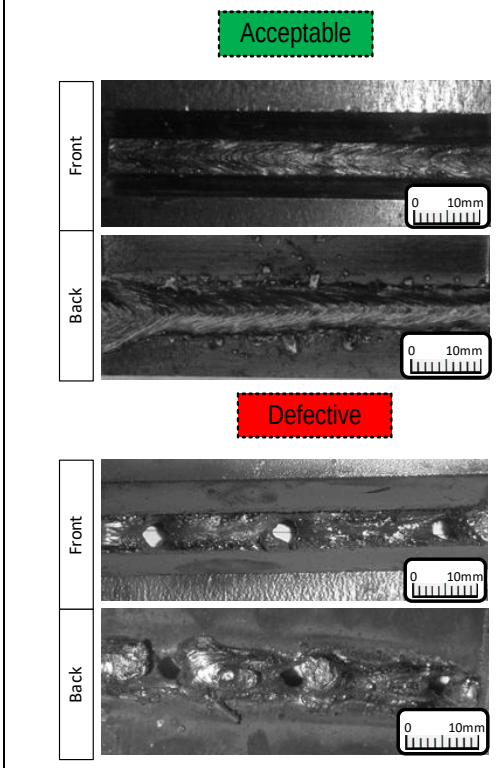

Figure 129: Defective welds highlighting the defective welding window on the WIC test at low heat input and high travel speed.

Weld Profile Consistency

The weld profiles for the WIC and the MWIC were compared in the heat input range at which both tests could successfully deposit a defect-free weld. The mean throat thickness for the 12 examined sections of the WIC test ranged from 4.5 mm to 6 mm; for the MWIC test they ranged from 5.5 mm to 5.7 mm (Figure 130). The MWIC tests showed less than a 10% variation in mean throat thickness across the range of heat inputs tested (0.5–1.0 kJ/mm).

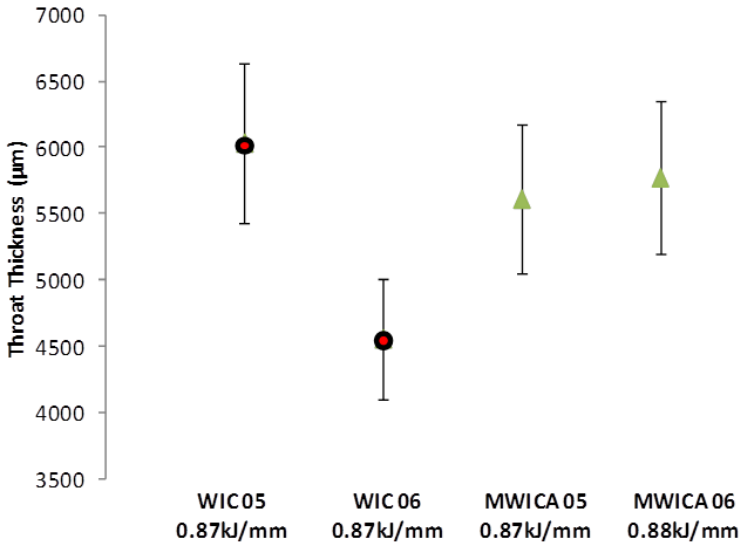

Figure 130: Measured throat thicknesses for the deposition tests executed on the MWIC and WIC test specimens. The MWIC tests generated weld beards with greater consistency of mean throat thickness.

Weldability Test Repeatability

From the deposition testing results, there is sufficient evidence to conclude that the enhancements introduced into the traditional WIC specimen, i.e. MWIC test specimen, have not only enlarged the deposition window, thus facilitating the execution of weldability testing in the heat input range of interest identified in the literature review, but have also improved the geometrical consistency of the deposited weld bead. In addition to the bead's improved symmetry, which improves the reliability of the results generated during weldability testing, deposition testing also revealed an improvement in the repeatability of testing results.

Figure 131 illustrates the point; MWIC_01 and MWIC_02 were welded within ± 0.05 kJ/mm of each other. Both showed similar cracking characteristics in the location and size of the crack across the sections examined, suggesting an enhancement in the reliability of the test.

Sample & Section	MWIC_01 0.51kJ/mm Overall % Cracked 35.72%	MWIC_02 0.53kJ/mm Overall % Cracked 24.52%	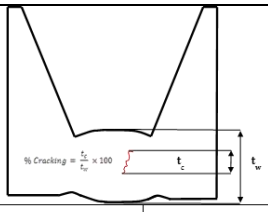	
Face1	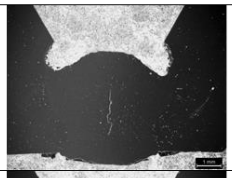	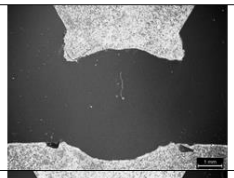	MWIC 1 t_w=4.620 µm t_c=1.896 µm %C=41.04 %	MWIC 2 t_w =4.539µm t_c =1.157 µm % C=25.49%
Face 4	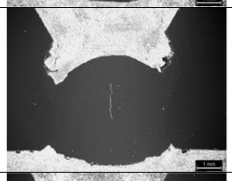	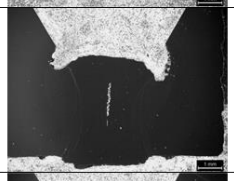	MWIC 1 t_w=4.565µm t_c=1.496 µm %C=32.77%	MWIC 2 t_w =4.470µm t_c =1.783 µm %C=39.89%
Face 6	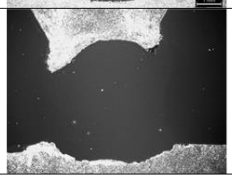	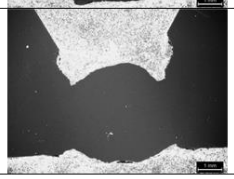	MWIC 1 t_w=4.939µm t_c =0 µm % C=0 %	MWIC 2 t_w =4.017µm t_c=0.323 µm % C=8.04%

Figure 131: MWIC cracking results for tests carried out at 0.5 ± 0.05 kJ/mm on 20 mm X70 plate: Percentage cracking (%C) = throat thickness (t_w) ÷ crack length (t_c).

5.7 **Concluding Remarks**

The MWIC test was designed to improve the consistency of the traditional WIC pipeline weldability test. The MWIC tests allow for 5G (horizontal pipe welding) positional welding with simple alterations to the test rig design, making it more representative of actual field welding. The addition of a gas tunnel improved the consistency of the weld and the reproducibility of the test over a larger range of welding parameters. The extraction of critical parameters through accurate instrumentation provides assurance in ranking the susceptibility of a deposited weld to HACC.

Experimental data has shown that the MWIC test excels for the reasons and explanations outlined below.

1. It allows for defect-free welds to be deposited at high travel speed in a heat input range representative of the root pass conditions encountered on a pipeline spread.

Yurioka's review [283] of the predictive methods for the prevention and control of HACC cracking highlighted the need for a simple, universal qualitative test that could be employed with confidence to establish safe welding envelopes in various conditions. The WIC test, which has been cited extensively in the literature as a tool to prescribe the critical preheat

required to avoid cracking, was modified to enhance its suitability at low heat inputs and high travel speeds. Experimental results demonstrated that the MWIC test can be employed with confidence in the 0.5–1 kJ/mm heat input range, while the traditional WIC test cannot.

2. It produces welds with a consistent throat thickness, improving the reliability and repeatability of the test.

The WIC and by extension the MWIC both allow for a variation in restraint through the variation in the length of the anchor welds, and thus for the quantification of the critical restraint needed to initiate cracking. However, the weld profile asymmetry and throat thickness inconsistency the common with the traditional WIC test promote scatter in identification of the CNC boundary. The modifications of the WIC test reduced the variation in throat thickness and improved the sensitivity of the test.

3. It allows for instrumentation of the test specimen to extract the critical data required to quantify the susceptibility of a weld to HACC.

The extensometer access port allows for the measurement of local weld metal displacement, while plunging the thermocouple into the molten weld pool gives access to the complete thermal history of the weld metal. Extraction of the $t_{8/5}$ can be linked to the resulting microstructure, t_{100} to the diffusible hydrogen content and local weld metal displacement to the resulting strain. Collectively, this data can be used as a proxy to quantify the three critical factors driving HACC.

These justifications provide confidence that the enhanced MWIC weldability test can be used to generate an empirical safe boundary in the heat input range of interest, which was identified as a research gap.

CHAPTER 6

Weldability Testing

6 Weldability Testing

The development of a safe welding envelope, particularly the delineation of the safe welding boundary when welding HSLA steels at high travel speeds, hinges on the ability to deposit consistent welds repeatedly. The development of the MWIC test allowed for a range of high-restraint weldability tests to be carried out on both thick and thin plate sections at high travel speeds. The commissioning of the test demonstrated that the enhanced design allowed for not only a better consistency in the weld bead profile being deposited, and thus greater confidence in comparing cracking data, but also the extraction of critical cooling and displacement data that can be used to characterise weldability and facilitate the development of a universal predictor.

This section presents and discusses the results obtained from the weldability testing conducted. A total of 51 weldability tests were conducted on both 20 mm- and 10 mm-thick API 5L X70 line pipe steel using a single batch of 4 mm E6010 electrodes. Each test length was divided into six sections, yielding 306 faces for analysis, which were then subdivided into three regions of interest (ROIs), yielding 918 sites for microstructural and micromechanical analysis. These samples formed the basis within which the CNC envelope was derived and from which the analysis was undertaken. The analysis of the samples was divided into three tiers. The three-tiered approach allows for a selection of samples for extended analysis based on conclusions drawn from earlier analytical stages.

Tier 1: Macroscopic Characterisation

As outlined in the methodology, macroscopic characterisation involves the following:

- Discussing the role of welding parameters on the cracking susceptibility of the deposited weld. In stage one of the first tier of analysis, the key criterion taken into consideration was whether or not the sample has cracked. Based on previous work discussed in the literature review, cracking in the WIC samples and thus in the MWIC samples was set at 5% of the maximum throat thickness.

- Once the cracked samples were identified, stage two focused on quantifying what type of cracking was observed, based on the distinctly observable features of each crack identified.

- Stage three of Tier 1 presents and discusses the role of welding parameters within the test envelope and testing conditions, especially the relationship between restraint and plate thickness and the severity of observed cracking.

The Tier 1 analysis concludes by identifying a select number of samples from the entire data set to be used for microstructural characterisation in Tier 2 analysis.

Tier 2: Microscopic Characterisation

The Tier 2 analysis focuses on presenting and discussing the observed microstructural features from samples across the CNC boundary, with a focus on the role of weld metal microstructure in the type and severity of cracking observed in the niche region tested.

The microscopic characterisation involves the following:

- Presenting and discussing the role of welding parameters within the test envelope in the general trend of microstructural features formed in the deposited weld bead.

- Identifying particular microstructural features along the crack paths and correlating these features with the type of cracking observed.

- Briefly discussing the elemental composition and consequent bulk weld metal chemistry, as identified through glow discharge optical emission spectroscopy (GD-OES).

The Tier 2 analysis concludes by discussing the role of microstructural features on WMHACC susceptibility, as observed within the welding parameter range tested.

Tier 3: Micromechanical Characterisation

Tier 3 of the analysis focuses on a few select samples derived from the CNC boundary. Using nanoindentation as a means of deriving the micromechanical properties of the deposited weld metal, Tier 3 focuses on the following:

- Empirically deriving the universal hardness and Young's modulus of the weld metal from samples across the boundaries.

- Discussing the role of welding parameters and conditions on the observed micromechanical properties.

- Discussing the correlation between micromechanical properties and microstructural features derived in Tier 2.

Tier 3 analysis concludes by discussing the role of micromechanical properties in the derived CNC boundary and the adaptability of Young's modulus and hardness as WMHACC predictors, as observed within the welding parameter range tested.

This chapter concludes by discussing the influence of the observed thermomechanical properties on WMHACC susceptibility.

6.1 MWIC Weldability Test Parameters

Section 2.7 lists the weldability tests considered in the derivation of the safe welding envelope and the delineation of the safe welding boundary for the steel and conditions within the scope of this thesis. The MWIC test was used for all weldability testing reported in this chapter. The weldability test's dimensions and tolerances are detailed in Chapter 5 and description of the custom-built DAQ system is detailed in Chapter 4.

6.1.1 Welding Conditions

Testing was conducted over a 12-month period and divided into seven series of experiments, which was required by the availability of resources only. In each test series, multiple thicknesses, restraints, preheats and heat inputs were tested. To ensure results were comparable, environmental conditions were recorded at the start of testing, at two points during testing and once after testing was completed. Testing was conducted between 9:00 am and 3:00 pm in an enclosed laboratory with temperature and humidity controlled by an evaporative air conditioning system. Testing was halted if the ambient temperature dropped

below 15 °C or rose above 40 °C. Table 30 lists the mean temperatures and relative humidity of the testing site for each testing series.

Table 30: Mean temperature and relative humidity during weldability testing.

Test Series	Tests	Ambient Temperature	Relative Humidity
Series 1	MWIC 01–12	27.3 °C	62%
Series 2	MWIC 13–20	23.4 °C	67%
Series 3	MWIC 21–26	22.6 °C	61%
Series 4	MWIC27–33	25.1 °C	52%
Series 5	MWIC 34–39	28.3 °C	38%
Series 6	MWIC 40–45	25.4 °C	47%
Series 7	MWIC 46–51	23.9 °C	52%

Over the testing period, average temperatures and the relative humidity of the test site remained relatively constant; this was not only important because ambient temperature may affect the cooling rate of the test weld, but also because humidity is known to influence the amount of moisture absorbed by the welding electrodes' coating, given its hydroscopic nature. This in turn may influence the amount of hydrogen introduced into the test weld. As illustrated in Figure 132, the ambient temperature (bar graph, left ordinate) varied from a minimum of 22.6 °C to a maximum of 28.3 °C, with a mean temperature of 25.1 °C and a standard deviation of 1.9 °C. The relative humidity (right ordinate) of the site varied between 38% and 67%, with a mean relative humidity of 54.1% and a standard deviation of 9.2 %.

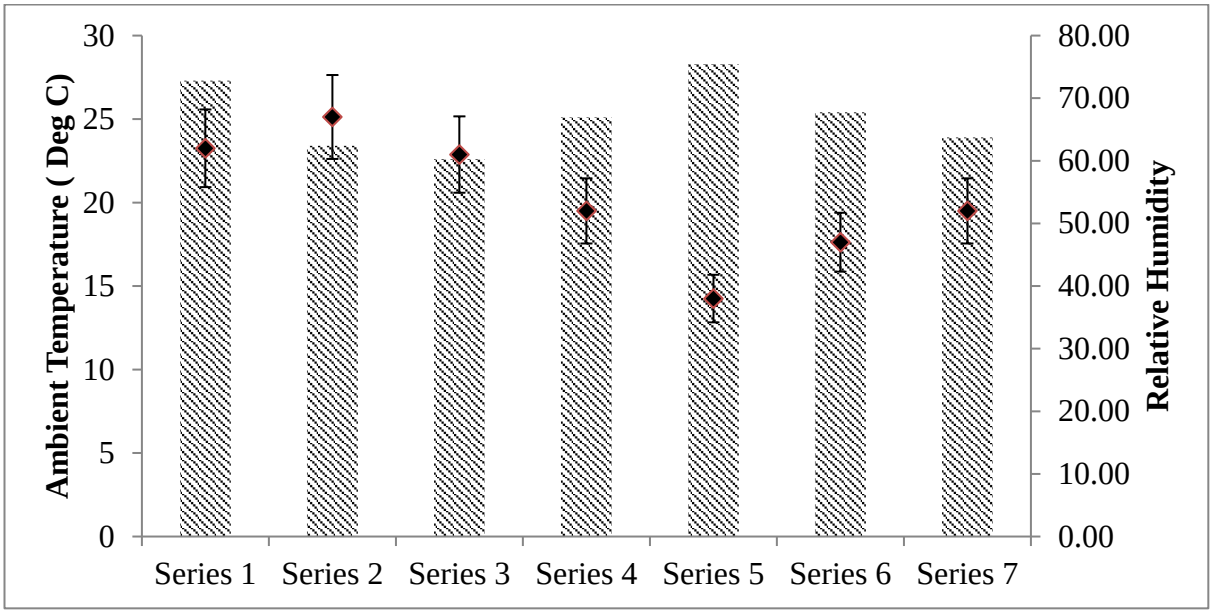

Figure 132: Mean temperature (bar graph) and relative humidity (data points) during MWIC weldability testing.

As identified in the literature review, the moisture content of the electrode flux can have a significant impact on the residual hydrogen content within a weld deposit. Kurji et al. [203] demonstrated that, for this brand and batch of electrodes, significant increases in the moisture content of the flux moisture only occurred after 36 hours at 100% RH at 25 °C and significant decreases in moisture content after 12 hours at 0% RH at 40 °C. The testing conditions were well inside the boundaries within which the moisture content of the flux remains relatively stable and hence had minimal influence on the residual hydrogen content within the weld. This allows for a strong degree of confidence in the assumption that the only factors influencing the residual hydrogen content in the tests conducted were the preheat and heat input.

6.1.2 **Welding Parameters**

As outlined in the methodology, the use of the AutoRon in its MCM allowed for rigid control of travel speed. Initial weldability tests were carried out at a fixed travel speed of 450 mm/min (7.5 mm/s), while final testing was carried out at test speeds greater than 330 mm/min (5.5mm/s). The initial test speed was established after consultation with a board of independent industrial advisors, but preliminary testing established that the degree of welder compensation in angle, force and travel speed required to maintain the mean desired travel speed was unattainable when welding in a semi-mechanised fashion. Although deposition was possible, multiple attempts were required to initiate and maintain an arc, decreasing the

degree of confidence that repeatable welds were being produced. There is anecdotal evidence to suggest that for cellulosic and rutile electrodes less than 5 mm in diameter, the travel speed should be limited to less than the length of the electrode per minute. Within the current range tested for this thesis, this equated to a travel speed < 400 mm/min.

Testing was conducted systematically, with the conditions expected to result in cracking tested and analysed first. This order of priority was based on testing examined in the literature review and detailed in Chapter 2. The order of testing priority and number of tests are listed in Table 31 below.

Table 31: Testing prioritisation by parameter

Group	Priority	Thickness	Restraint	Likelihood of cracking
Group 1	Priority 1	20 mm	High (R_F = 25 mm)	Most Likely ↓ Least Likely
Group 2	Priority 2	20 mm	Low (R_F = 50 mm)	
Group 3	Priority 3	10 mm	High (R_F = 25 mm)	
Group 4	Priority 4	10 mm	Low (R_F = 50 mm)	

Using the Lincoln Electric Invertec 350V Pro, welding currents were dialled in between 105A and 170A, which resulted in a measured current range of 119–178A and a voltage range of 19.1–29.9V as illustrated in Figure 133 and Figure 134. For all testing conducted under ambient conditions, the term ‘preheat’ does not refer to that day’s temperature, but rather a temperature of 25 °C. Temperature measurements of the sample were taken from thermocouple T12. Preheats were controlled to within ± 2 °C, as described in the experimental methodology.

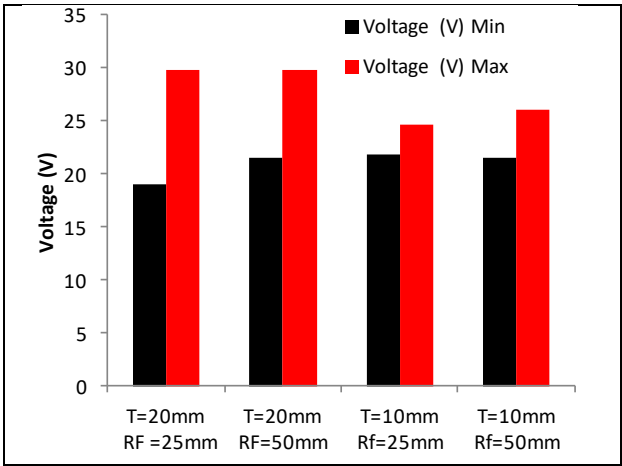

Figure 133: Voltage ranges recorded for each testing series.

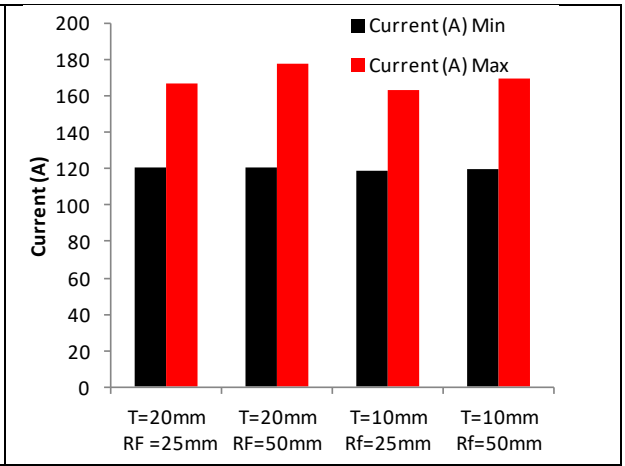

Figure 134: Current ranges recorded for each testing series.

The key welding parameters tested within each test priority group (referred to as simply 'group' below) are summarised in Table 33 and illustrated in Figure 135. Figure 136 illustrates the distribution of weldability tests according to the primary test variables.

Table 32: MWIC weldability test parameter ranges.

Priority Group	Number of Tests	Voltage Range	Current Range	Heat Input Range	Preheats Tested
		V	A	kJ/mm	°C
T = 20 mm & R_F = 25 mm	22	19.1–29.9	121–167	0.37–1.11	25,50,100
T = 20 mm & R_F = 50 mm	13	21.5–29.9	121–178	0.44–0.70	25,50,100
T = 10 mm & R_F = 25 mm	10	21.9–24.6	119–163	0.48–0.82	25,40,50
T = 10 mm & R_F = 50 mm	10	21.5–26.1	120–170	0.33–0.65	25,40,50

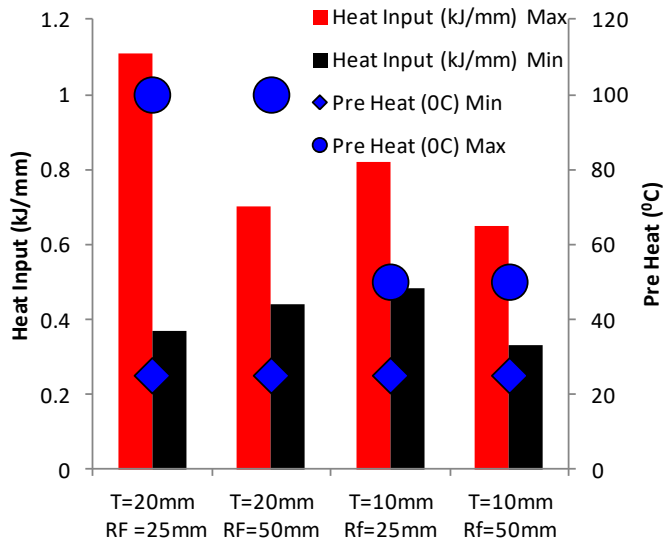

Figure 135: Weldability test preheat and heat input combinations.

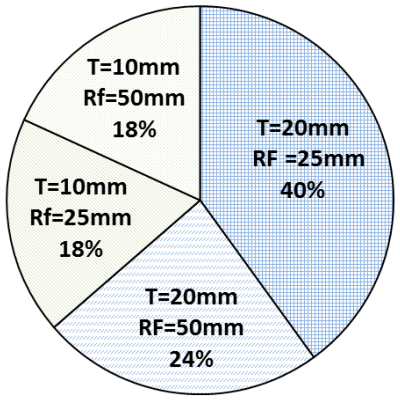

Figure 136: Distribution of weldability tests.

6.2 Delineation of a Safe Welding Envelope

6.2.1 Identification of Safe Welding Conditions

This section presents and discusses the macroscopic weldability test results, focusing on whether cracking was detected in the MWIC test section. As detailed in Chapter 4, a sample is defined as cracked if a planar defect is visually identified on the sample surface when magnified at 400x and the defect's vertical length is greater than 5% of the height of the weld

bead (h_w). The next section presents and discusses the type of cracking present as defined by its visual characteristics and its interrelationship to the microstructure in which it has manifested and propagated.

Testing was conducted in a systematic fashion in terms of identifying the critical (or threshold) preheat at which no cracking was detected. The initial preheat levels were identified from a review of the literature, as detailed in Chapter 4 (Methodology). The applied preheats were incrementally increased at nominal intervals for subsequent weldability tests until cracking was not detected per the predefined criteria. In cases where verification of a result was required, especially when determining limits of deposition, the use of dummy samples was employed to minimise the cost associated with the experimental program; this procedure is outlined below.

6.2.1.1 High Thickness (T = 20 mm) and High Restraint (R_F = 25 mm)

A total of 25 tests were conducted for 20 mm-thick plates under high restraint (R_F = 25 mm), of which 22 were used for crack analysis and three were used to defined the lower limit of weld deposition. In the tests used for crack analysis, the recorded current ranged from 121–167A, recorded voltage from 19.1–29.9V and the calculated heat input from 0.37–1.11 kJ/mm. Tests were conducted with preheats of 25 °C, 50 °C and 100 °C.

Testing demonstrated that deposition was not possible below a heat input of 0.3 kJ/mm for 20 mm-thick plates. Three tests were conducted on fully prepared and instrumented samples at a current of 75 ± 5A and a travel speed of 330 ± 5 mm/min to establish this lower limit. For each of the three tests conducted, there was evidence through visual examination to suggest that there was insufficient current for the chosen electrode's diameter at the desired travel speed to maintain fusion and that there was insufficient penetration in the 50 mm MWIC test section. In addition to a lack of fusion and penetration, it was established that maintaining the arc at low current required a variation in travel speed to levels below the desired range.

To validate the lower boundary of 0.3 kJ/mm for 20 mm-thick plates, several tests were conducted on MWIC dummy samples. In these tests, numerous combinations of current, travel speeds and preheats were tested to verify that (a) an arc could be established and maintained, (b) a weld could be deposited with sufficient penetration of the root pass and (c) the proposed boundary applied to preheats tested within the scope of this thesis. Travel speeds

were decreased to 200 mm/min with currents ranging from 60–80A and preheats increased up to 120 °C, with limited success. All tests for the dummy samples exhibited poor root penetration and arc instability.

Therefore, it is suggested that for 20 mm plates, the lower boundary for deposition is 0.3 kJ/mm for plates within the temperate range 25 °C < P_t < 120 °C when welded at room temperature. Below this heat input, the welds suffer from a lack of penetration and fusion in addition to arc instability. The lower limit for deposition is represented by the shaded areas in Figure 137 below.

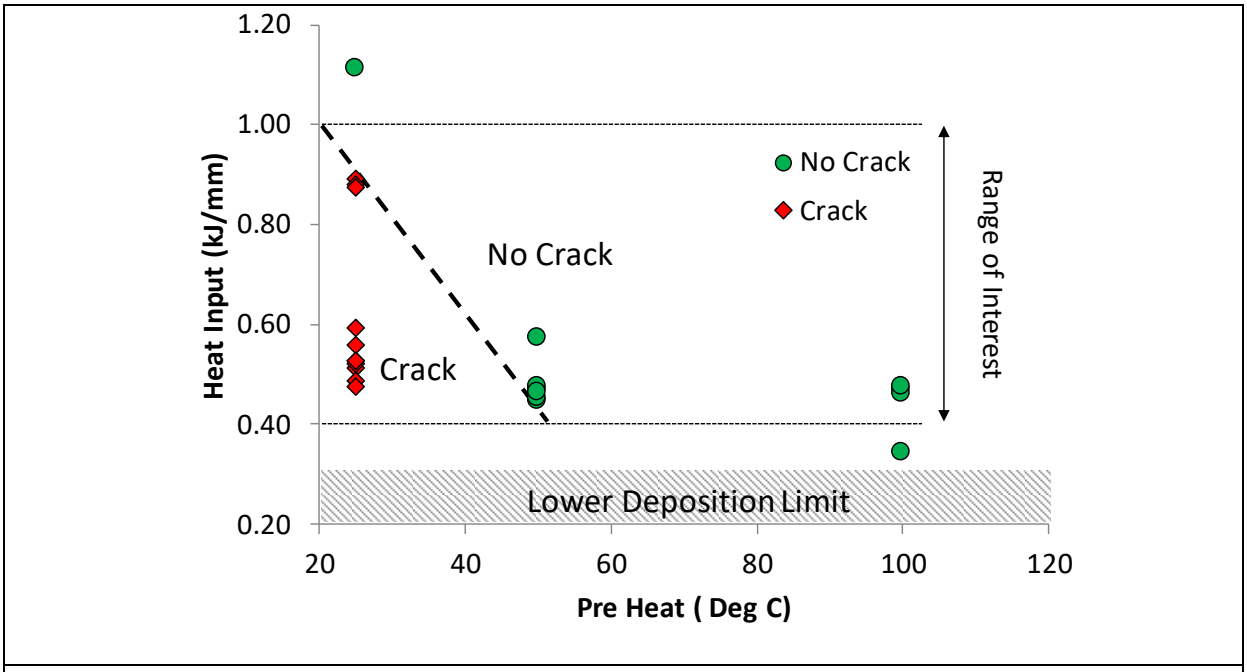

Figure 137: Distribution of cracked and uncracked MWIC samples for welds deposited at T = 20 mm and R_F = 25 mm for various preheats within the heat input range of interest.

Weldability testing results also demonstrated that cracking was present for welds deposited with heat inputs below 1.1 kJ/mm under ambient conditions in which the plate temperature was recorded as 25 °C. However, when the plate temperature was doubled to 50 °C, no cracking was observed for heat inputs as low as 0.45 kJ/mm. When the plate temperature was doubled again to 100 °C, no cracking was observed at heat inputs in the vicinity of 0.4 kJ/mm.

One weldability test was conducted below the heat input range of interest to validate the positive effect of preheating on reducing WMHACC susceptibility. The test was conducted with a net heat input of 0.37 kJ/mm and, although there was evidence of lack of penetration in

sections of the test weld, which introduced a stress concentrator, there was no evidence of HACC.

It is therefore suggested that for 20 mm-thick sections of the steel tested under high restraint, no cracking will occur for single-pass welds deposited with a mean heat input greater than 1 kJ/mm when the mean temperature of the plate is 25 °C and when the welding occurs in conditions with an ambient temperature in the vicinity of 25 °C and a relative humidity in the vicinity of 55%. When a preheat is applied and the temperature of the test plate is raised to approximately 50 °C, no cracking will occur for welds which are deposited at heat inputs as low as 0.45 kJ/mm under similar temperature and humidity conditions.

Using this data set, it is suggested that for 20 mm-thick API 5L X70 line pipe steel under high restraint, welded with 4 mm E6010 electrodes for heat inputs lower than 1 kJ/mm and greater than 0.35 kJ/mm, the minimum preheat required as a function of the heat input used to deposit the root pass of a girth weld can be defined as $PH(C^0) = 70 - 50HI(kJ/mm)$, where PH is the preheat and HI is the heat input. The relationship is derived as an empirical line of best fit from the data generated by weldability testing.

6.2.1.2 High Thickness (T = 20 mm) and Low Restraint (R_F = 50 mm)

A total of 13 tests (Figure 138) were conducted for 20 mm-thick plates under lower restraint (R_F = 50 mm). The recorded current ranged from 121A to 178A, with the recorded voltage varying between 21.5V and 29.9V and the calculated heat input ranging from 0.44 kJ/mm to 0.87 kJ/mm. Tests were conducted with the same preheats as the 20 mm-thick high-restraint tests.

Under ambient conditions within the heat input range of interest, cracking was observed from 0.43 kJ/mm to 0.87 kJ/mm. As no cracking was observed under comparable ambient conditions for heat inputs greater than 1 kJ/mm for the same thickness but more severe restraint conditions, it is reasonable to assume that no cracking would occur above this pre-established limit; therefore, no testing was conducted at or above 1.0 kJ/mm.

With a preheat applied that effectively doubled the plate temperature to 50 °C, no cracking was observed within the heat input range of interest. An ancillary test was run below the

primary ROI at 0.37 kJ/mm, within which cracking was observed. The final tests within this group were conducted at a preheat of 100 °C; as expected, no cracking was observed.

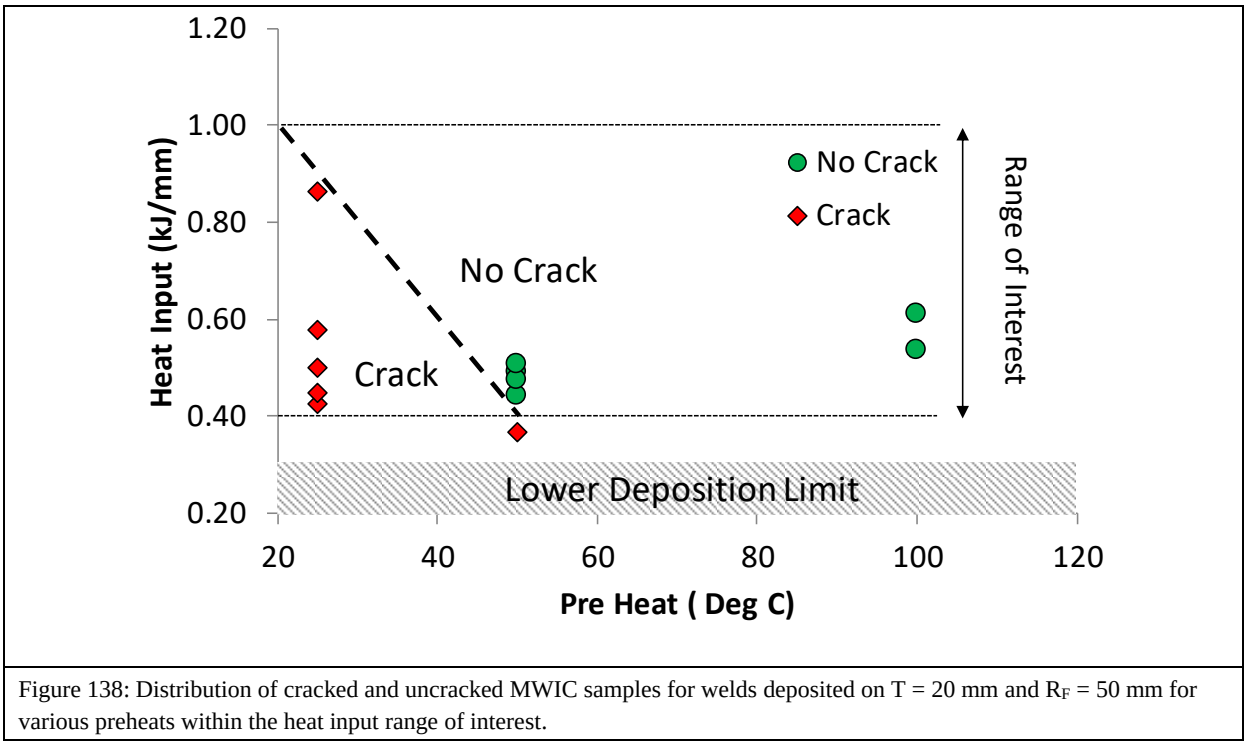

Figure 138: Distribution of cracked and uncracked MWIC samples for welds deposited on T = 20 mm and R_F = 50 mm for various preheats within the heat input range of interest.

The cracking results for weldability tests conducted on 20 mm-thick plates under lower restraint (R_F = 50 mm) suggest that for the plate thickness and level of restraint conditions tested within the heat input range of interest, the minimum preheat required to avoid cracking as a function of the heat input can be defined as $PH(C^0) = 70 - 50HI(kJ/mm)$, where PH is the preheat and HI is the heat input.

At a lower R_F than the tests conducted with a restraint length of R_F = 25 mm, it was expected that the cracking boundary would shift to the left, effectively allowing for welds to be deposited with a lower heat input and preheat without any cracking. However, the results demonstrated that for both high- and low-restraint tests, the thick plate sections shared nearly identical CNC boundaries. Superimposing the data from both the high-restraint and low-restraint tests, Figure 139 illustrates the elegance of applying the derived linear relationship between preheat and heat input for crack avoidance in 20 mm-thick plates.

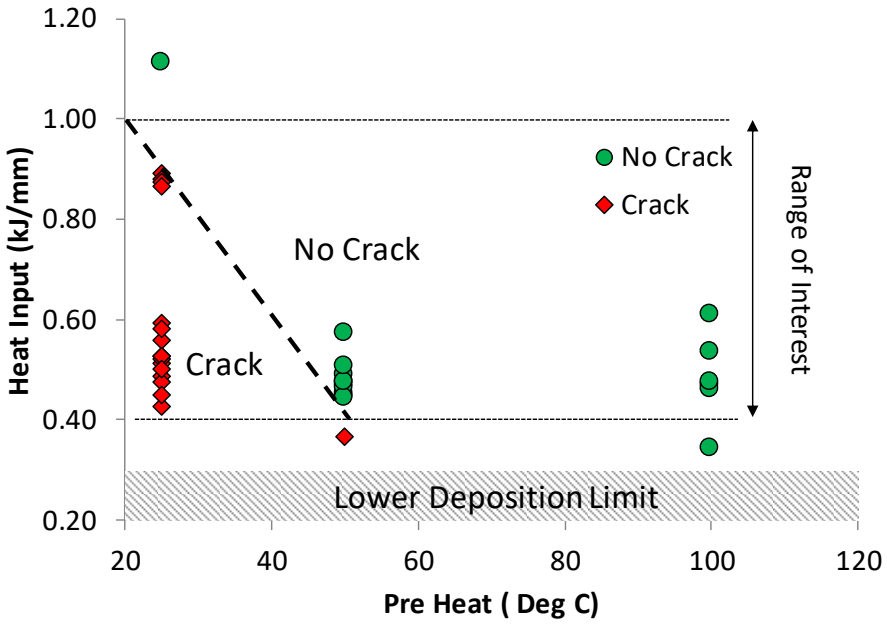

Figure 139: Distribution of cracked and uncracked MWIC samples for welds deposited on T = 20 mm for both high- (R_F = 25 mm) and low-restraint conditions (R_F = 50 mm) for various preheats within the heat input range of interest. Superimposing cracking data from both tests' data sets suggests that changing the restraint length from 25 mm to 50 mm does not change the positon of the proposed cracking boundary.

Nevertheless, it is important to note that although the empirical CNC boundary was defined for simply the presence of cracking as indicated by the presence of planar defects, the type and extent of cracking observed was markedly different for the 20 mm- and 10 mm-thick plates. These differences are detailed in the following sections.

6.2.1.3 Low Thickness (T = 10 mm) and High Restraint (R_F = 25 mm)

A total of 14 tests were conducted for 10 mm-thick plates under high restraint (R_F = 25 mm), with 10 tests instrumented and analysed for cracking results (Figure 140). The recorded current ranged from 119A to 163A, the recorded voltage from 21.9V to 24.6V and the calculated heat input from 0.48 kJ/mm to 0.82 kJ/mm. As detailed in the literature review, the critical preheat to avoid cracking, all else being equal, depends on the test plate thickness, with thinner plates requiring lower preheats than thicker plates. Hence, initial tests were carried out with a preheat of 25 °C and 40 °C with subsequent testing carried out with a preheat of 50 °C.

Using the previously established deposition limit of 0.3 kJ/mm for 20 mm-thick plates, testing was conducted on dummy MWIC samples to validate whether or not this limit applied to 10 mm-thick plates. One test was conducted for each of the following preheats: 25 °C, 50 °C, 80

°C and 100 °C. Testing was conducted on non-instrumented dummy samples at a current of 75 ± 5A and a travel speed of 330 ± 5 mm/min to validate the lower limit of deposition. For the tests conducted at 25 °C and 50 °C there was sufficient evidence through visual examination to suggest a lack of root penetration, which may be attributable to insufficient current for the chosen electrode's diameter at the desired travel speed. However, the results were inconclusive at a preheat of 100 °C. An additional test was conducted at 80 °C, which gave evidence to conclude that there was insufficient penetration of the root pass. Hence, it is suggested that for 10 mm-thick plates the lower limit of heat input for successful deposition is 0.3 kJ/mm within the temperate range 25 °C < P_t < 80 °C when welded at room temperature.

Empirical testing demonstrated that on 10 mm-thick plates under high restraint (R_F = 25 mm), single-pass welds did not crack for heat inputs above 0.8 kJ/mm when welded under ambient conditions (Figure 139). At a preheat of 40 °C cracking was observed at heat inputs below 0.69 kJ/mm. A single test was conducted at a preheat of 50 °C with a heat input of 0.55 kJ/mm; no cracking was observed. It must be noted, however, that the bead profiles deposited for 10 mm-thick plates were asymmetric in some cases, which may have influenced the cracking that resulted. Of particular interest was the bead profile observed for the sample deposited at 0.54 kJ/mm at a preheat of 40 °C. The role of bead symmetry and its influence on the derived CNC boundary is discussed below.

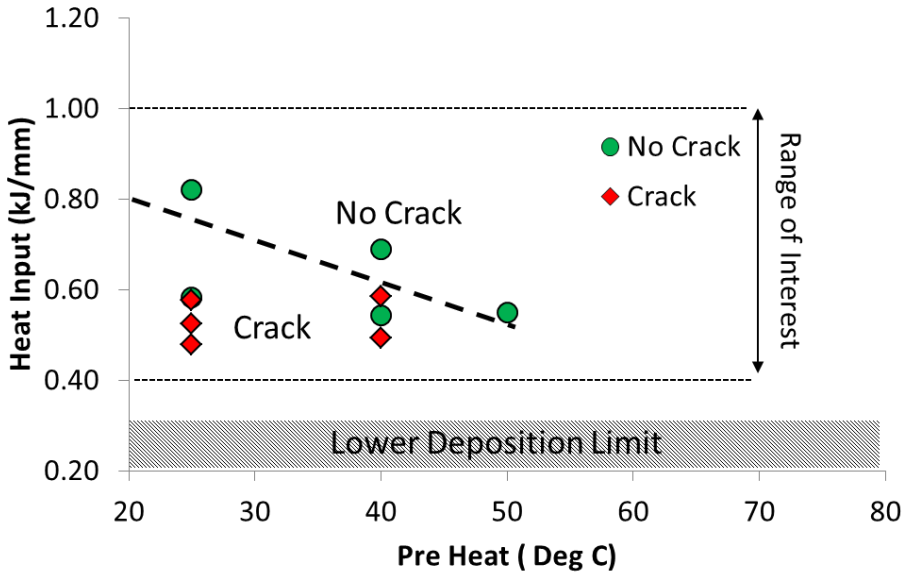

Figure 140: Distribution of cracked and uncracked MWIC samples for welds deposited on T = 10 mm and R_F = 25 mm for various preheats within the heat input range of interest.

For the weldability testing conducted, it is suggested that for 10 mm-thick plates welded under high restraint within a heat input range of 0.5 ≤ HI < 1.0 kJ/mm, the relationship between the critical preheat required to avoid cracking as a function of heat input can be defined as $PH(C^0) = 100 - 100HI(kJ/mm)$. The heat input range was limited to heat inputs greater than 0.5 kJ/mm for preheats above 40 °C, as no testing was conducted below this heat input range at preheats of 50 °C and above.

6.2.1.4 Low Thickness (T = 10 mm) and Low Restraint (R_F = 50 mm)

A total of 10 tests were conducted on 10 mm-thick plate under lower restraint (R_F = 50 mm). The recorded current ranged from 120A to 171A, the recorded voltage from 21.5V to 26.1V and the calculated heat input from 0.33 kJ/mm to 0.65 kJ/mm (Figure 141). The lower limit of deposition established for 10 mm plates at high restraint was transposed for testing at lower restraint.

Empirical testing results demonstrated that under ambient conditions, cracking was not observed at a heat input of 0.65 kJ/mm. With the application of preheat and the temperature of the plate increased to 40 °C, cracking was not observed for heat inputs above 0.51 kJ/mm. However, cracking was observed at a heat input of 0.42 kJ/mm for a sample with a preheat of 48 °C. Although the test was scheduled to run with a preheat of 50 °C, a failure in the custom-built DAQ system required a reboot. The temperature at location T12 was recorded as 48 °C prior to execution of the test protocol. During post-processing it was verified that the temperature recorded fell within the specified acceptable test range, was not decreasing at an accelerated rate and that there was less than 5 °C difference between the thermocouple top tracker, T12 and the bottom tracker. From the review of post-processed temperature data, there is sufficient evidence to suggest that the temperature field in the test section and indeed the test geometry was relatively homogenous, so the test was accepted.

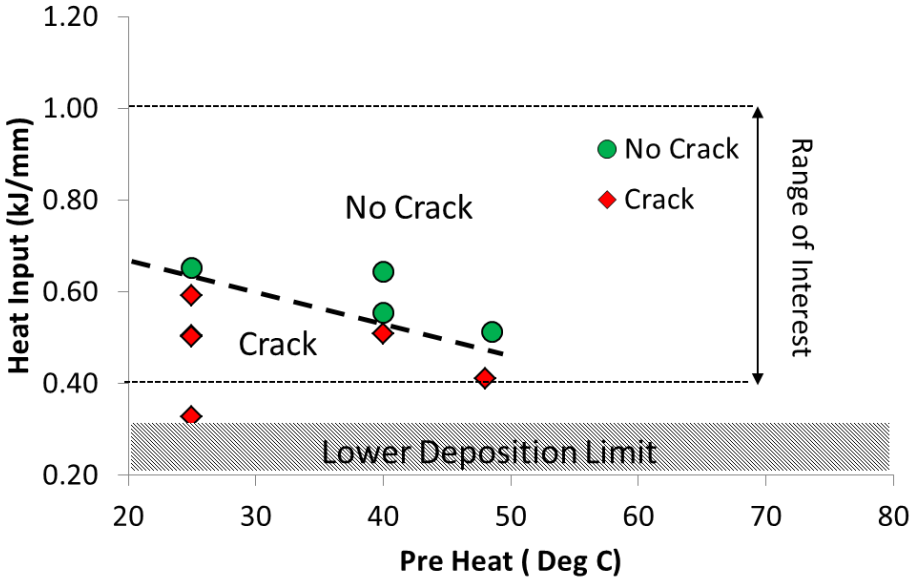

Figure 141: Distribution of cracked and uncracked MWIC samples for welds deposited on T = 10 mm and R_F = 50 mm for various preheats within the heat input range of interest.

For the weldability testing conducted, it is suggested that for 10 mm-thick plates welded under low restraint within the heat input range of $0.5 \leq HI < 1.0$ kJ/mm, the relationship between critical preheat required to avoid cracking as a function of heat input can be defined as $PH(C^0) = 125 - 150HI(kJ/mm)$. This relationship is slightly different than what was obtained for 10 mm plates welded under high restraint.

Superimposing the data from the high- and low-restraint tests yields results similar to those observed when testing the 20 mm tests; the boundaries are almost identical. Figure 142 below illustrates the 10 mm cracking data of both the high- and low-restraint tests with the boundary derived from the high-restraint tests highlighted.

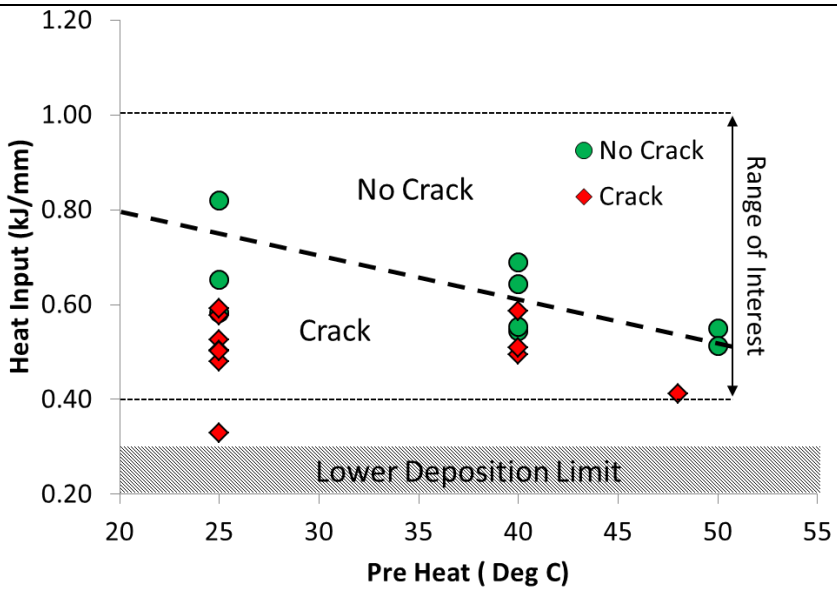

Figure 142: Distribution of cracked and uncracked MWIC samples for welds deposited on T = 10 mm for both high- (R_F = 25 mm) and low-restraint (R_F = 25 mm) conditions for various preheats within the heat input range of interest.

The rationale behind selecting the high-restraint boundary as representative of the 10 mm-thick test plates is twofold. First, testing minute increments in heat inputs is counterproductive, given the inherent degree of variability when welding within the selected range of parameters. In laboratory conditions, such as those in which the MWIC weldability tests were conducted, travel speed was controlled with a mechanised welder. This degree of precision is not available in the field, nor is it ever prescribed when writing a welding procedure specification. Second, as it is anticipated that the boundary derived during laboratory testing will be assimilated and used by industry as the basis upon which welding preheats are selected to avoid WMHACC, it was prudent to select the more conservative mitigating measure.

6.2.2 Delineation of a Crack-No Crack (CNC) Boundary

The empirical evidence gathered though weldability testing can be integrated into a single envelope within which the deposition of a single-pass root weld deposited using high hydrogen cellulosic electrodes can be executed with a low risk of succumbing to WMHACC.

Figure 143 illustrates the boundary for both thick (20 mm) and thin (10 mm) API-5L-X70 steel plates, welded using E6010 electrodes on the MWIC test with no misalignment, under both high and low restraints, for a heat input range of 0.4 kJ/mm to 1 kJ/mm. The tests used to derive this boundary were all conducted at travel speeds in excess of 330 mm/min in

laboratory conditions with temperature regulated at 25 °C and a relativity humidity of 65%. Any combination of preheat and heat inputs to the right of a respective boundary represents an area in which the risk of cracking exists. Cracking in the case of this boundary is defined as the presence of a planar defect visible under an optical microscope at a maximum magnification of 400x and whose vertical length represents more than 5% of the throat thickness of the deposited weld bead including reinforcement and without grinding.

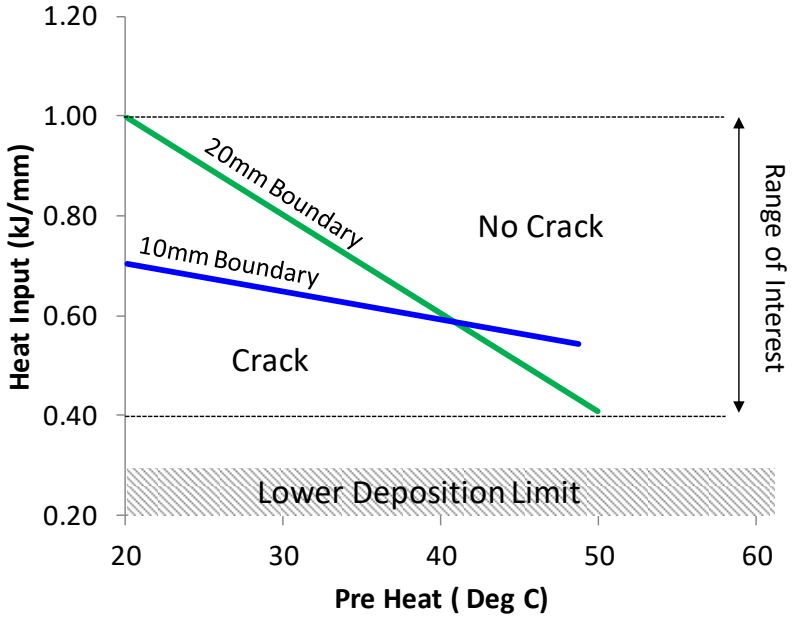

Figure 143: Empirically derived CNC boundary for 20 mm- and 10 mm-thick API-5L-X70 steel plates, welded using E6010 electrodes on the MWIC test with no misalignment, under high (R_F = 25 mm) and low (R_F = 50 mm) restraint, for a heat input range of 0.4 kJ/mm to 1 kJ/mm. The boundaries represent the minimum critical preheats needed to deposit a hydrogen crack-free weld.

6.3 Crack Characterisation

The previous section described and discussed the derived empirical cracking boundary based on the presence of a planar defect whose vertical length was greater than or equal to 5% of the total throat thickness. This measure did not take into account the type of cracking that was observed or the severity of cracking in relation to the welding parameters or conditions within which the test was conducted. In this section of the results, the system used to characterise observed cracking is presented, followed by a discussion correlating the weld parameters and test conditions with which the test welds were deposited to the type and severity of cracking observed.

It is important to note that the results demonstrated that multiple modes of cracking existed in the test welds. In some cases, multi-mode cracking was observed in a single test section, whereas in other cases the mode of cracking changed between sections. The observed cracking is presented first for each section with the dominant mode of cracking, expressed as a percentage of the throat thickness described and discussed in Chapter 4. The crack classification assigned to the test weld is based on the dominant cracking observed throughout all six test sections. The classification system introduced in Chapter 4 is expounded on in this section of the results. The effect of test section on the type of cracking is explored before an examination and discussion of the general microstructural trends through which the cracks propagated is presented and discussed.

6.3.1 Classification of Observed Cracking

A range of geometrically differentiable planar defects were identified in the analysis of the test sections of the MWIC samples (Figure 144). To facilitate the correlation between the role of welding parameters and conditions on the type of cracking identified, a classification system based on the visual appearance of the observed defect was employed in conjunction with the quantification of severity of cracking, as described in Chapter 4. In this thesis, a defect is classified in one of the three categories if it is the dominant imperfection observed in the sample. However, multiple types of imperfections were observed in a select number of samples, which is discussed in Section 6.3.

In addition to the three planar defects observed, there was evidence of hollow bead cracking in a select number of samples. These samples were accounted for in a fourth, independent defect group.

Centreline

The centreline classification referred to any planar cracking that was observed in the geometrical centre of the etched sample. Given the location of the cracking and its characteristics as observed in 2D and based on the literature review, there is sufficient evidence to suggest that the centreline cracking occurred during coalescence of the weld pool and therefore is solidification related cracking.

Hydrogen

The hydrogen classification was assigned to hydrogen cracks that bore a resemblance to the classic hydrogen crack, as described in the literature review. The cracks in this category were either individual isolated micro-cracks or micro-cracks that had joined up in the classic staircase pattern to form larger macro-cracks. Hydrogen cracks that branched off from solidification cracks were not placed in this classification, nor were cracks that originated from a stress concentrator, as these were classified separately to account for the dominant influence of stress concentrators as a result of irregularities in the weld bead geometry.

Cracks in this category were classic hydrogen cracks that initiated within the body of the weld. The actual initiation site- void, inclusion or other microscopic imperfection—was inconsequential. The only restriction in this classification were cracks that were either solidification cracks or hydrogen cracks that had a clear macroscopic initiation site such as an irregularity in the weld bead deposit, such as a wagon track.

Geometric

The geometric classification was assigned to hydrogen cracking that originated specifically from a macroscopic stress concentrator. This category was assigned specifically to highlight the role of bead symmetry and its influence on cracking susceptibility. The formation of a stress concentrator arises as a result of a combination of the welding techniques applied and the welding parameters. The stress concentrator may have manifested as a wagon track or

undercut in the root or toe of the weld. Microscopic stress concentrators were not included in this classification.

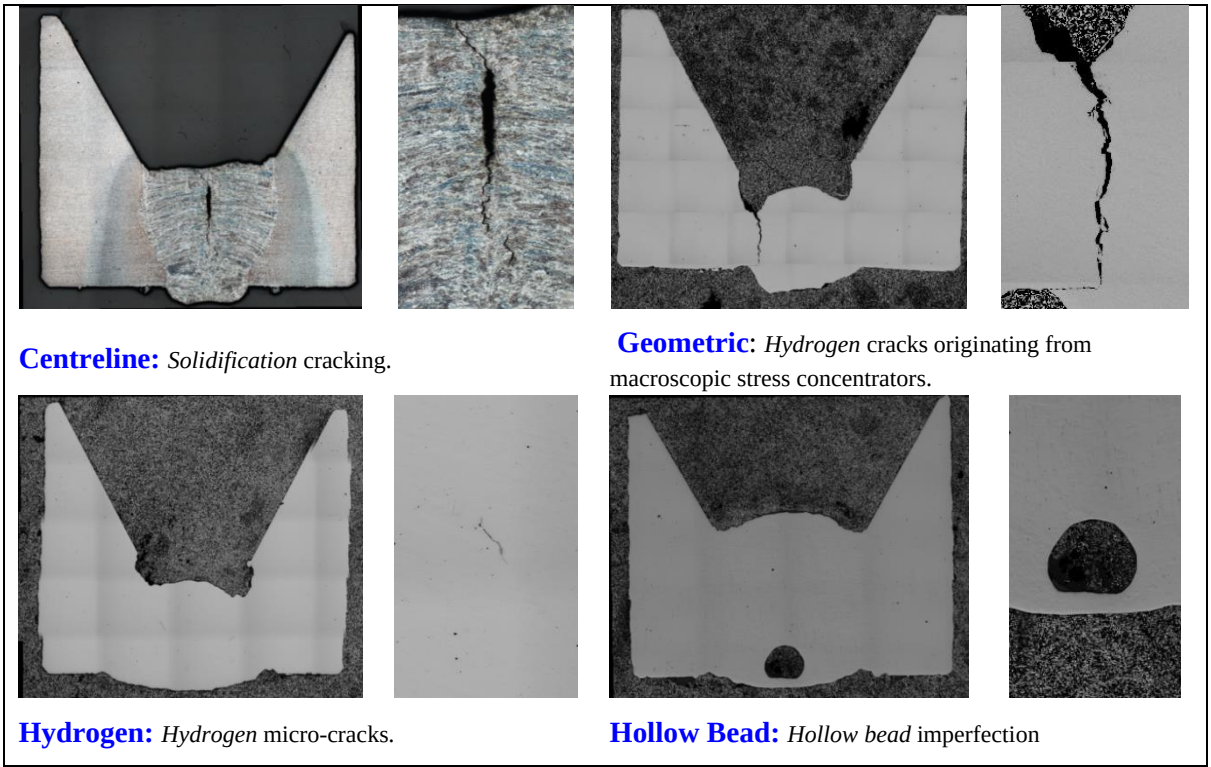

Figure 144: Crack classification system used to differentiate observed cracking in the MWIC samples. The assigned categories reflect the visual characteristics of the observed cracking. It is critical to note, however, that although the designation for hydrogen cracks originating from a macroscopic stress concentrator (such as a pronounced weld toe) and hydrogen cracks originating from microscopic concentrators (such as NMI's) are different, they are both still considered hydrogen cracks.

6.3.2 Crack Characterisation in 20 mm-thick Plates

T = 20 mm, R_F = 25 mm

For the 20 mm-thick plates under high restraint there was evidence to suggest that all three categories of cracking were present in multiple sections of the test samples, as illustrated in Figure 145. To normalise the extent of cracking, crack lengths are described as a percentage of the maximum throat thickness (see Chapter 4). Centreline cracks ranged from 3% to 88% with an average length of 50%, while hydrogen cracks ranged from 3% to 61% with an average length of 27%. Hydrogen cracks that resulted from geometric stress concentrators ranged from 8% to 151%; where the cracking ratio exceeded 1 (or 100%), the cracks ran diagonally though the weld bead profile. The average length of the geometric cracks was 80%.

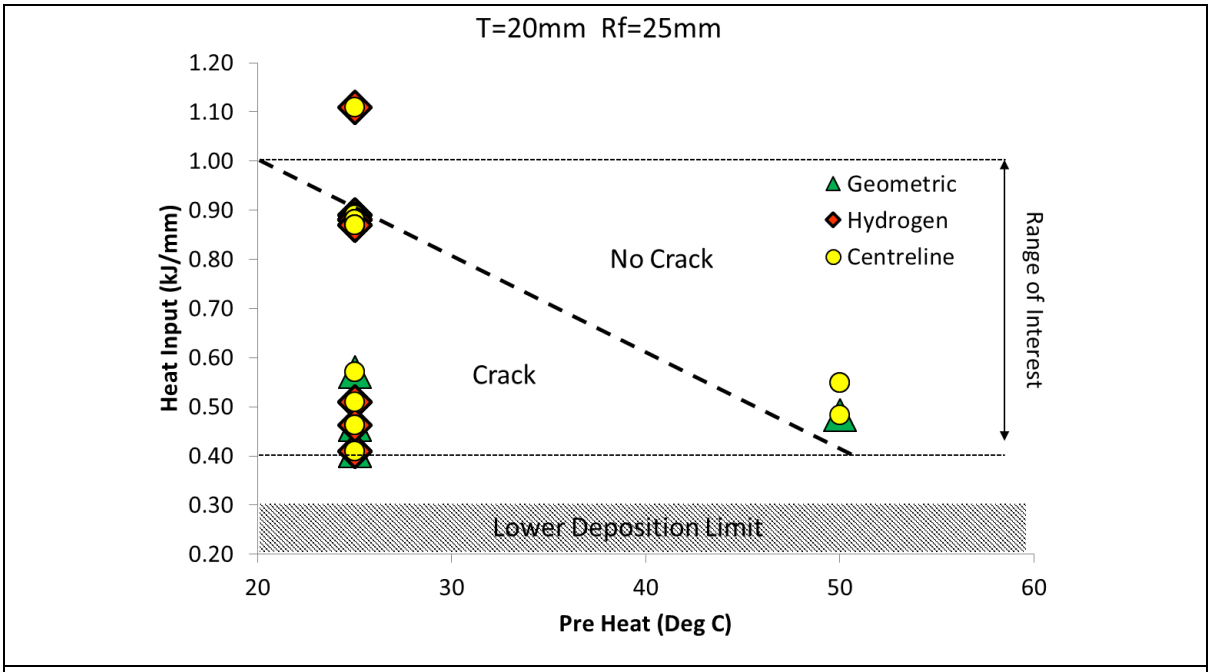

Figure 145: Observed cracking in MWIC test plates at T = 20 mm and R_F = 25 mm.

The collated cracking data suggests that for 20 mm-thick plates under high restraint, regardless of the heat input with which the weld was deposited within the heat input range of interest, centreline cracking was evident. Where imperfections were identified, their location and length were recorded, but the imperfection was only classified as a defect if its length were greater than 5% of the recorded throat thickness of the section under review or if its presence posed an immediate risk to weld integrity and was not caused as a result of a defective weld that would have been disqualified as requiring repair.

Where the imperfections were not of sufficient length to be classified as a defects, they were discounted from the CNC boundary, though they were recorded in the crack classification diagram (Figure 145). Two ROIs are highlighted in Figure 146 below. In these regions imperfections were identified but did not meet the criteria to be classified as defects.

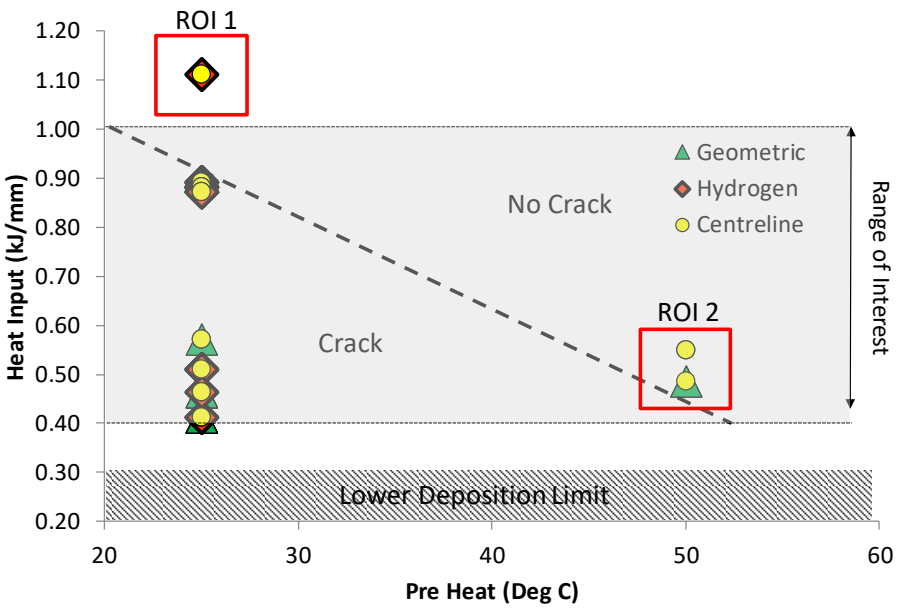

Figure 146: Observed cracking in MWIC test plates at T = 20 mm and R_F = 25 mm with ROIs highlighted. ROI 1 corresponds to cracking observed in welds deposited at a heat input of 1.1 kJ/mm under ambient conditions; ROI 2 corresponds to cracking observed in welds deposited at heat inputs of 0.48 and 0.55 kJ/mm at a preheat of 50 °C.

In ROI 1, the test welds were deposited with a heat input of 1.1 kJ/mm. Both a centreline and hydrogen micro-crack were observed in the sample, but neither satisfied the predefined criteria to be classified as a defect, as they were less than 1% of the throat thickness in both cases. In ROI 2, two test welds were deposited with heat inputs of 0.48 kJ/mm and 0.55 kJ/mm. With the former, a centreline crack was measured at 10% and a geometric defect at 11%. In the second case a centreline defect was measured at 57%. Considering the ratio of crack length to throat thickness, both the observed flaws satisfied the crack length criteria to be classified as defects.

However, in both cases the adjacent sections had a window defect. Figure 147 illustrates a typical example of the observed window defect. It is reasonable to suggest that a defect in an adjacent section influences the integrity of the weld section being examined, particularly when it is a window defect (Figure 148 and Figure 149). To verify the assumption that the adjacent window defect had in fact influenced the formation of the centreline defect, the tests were repeated at a comparable heat input of 0.48 and 0.52 kJ/mm where no cracking was observed in any of the six sections examined for each test. The influence of window defects on the formation of centreline cracks is discussed below.

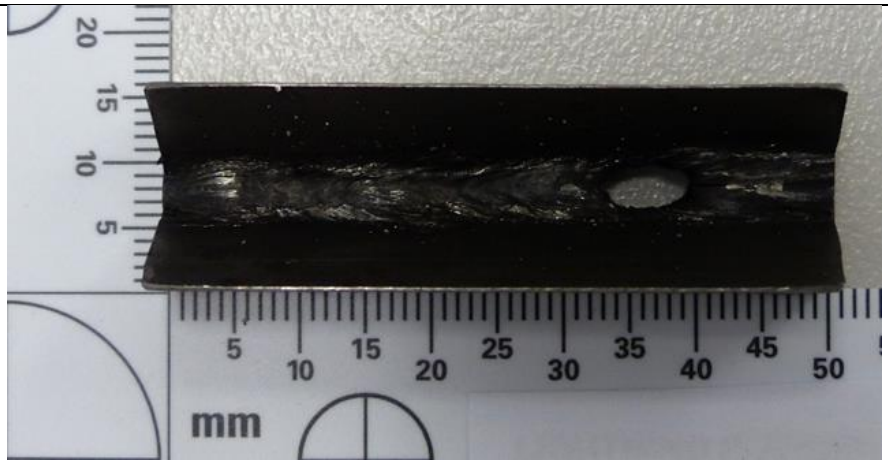

Figure 147: Weld test sample from ROI 2 prior to sample sectioning. A window defect is clearly seen in the region where the fifth section is to be extracted.

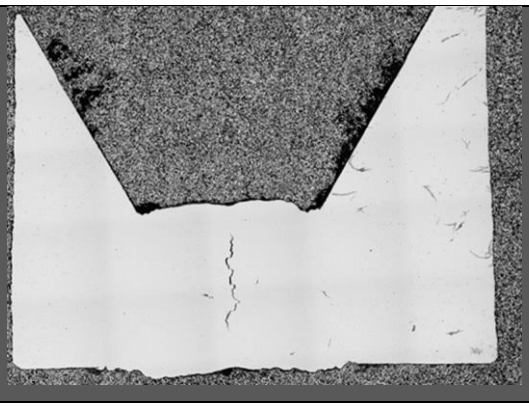

Figure 148: Optical micrograph showing a centreline crack observed in the section adjacent to the sample in which the window defect was observed. The centreline crack propagated along the longitudinal axis through the length of the section and was just observable on the opposite face of the section.

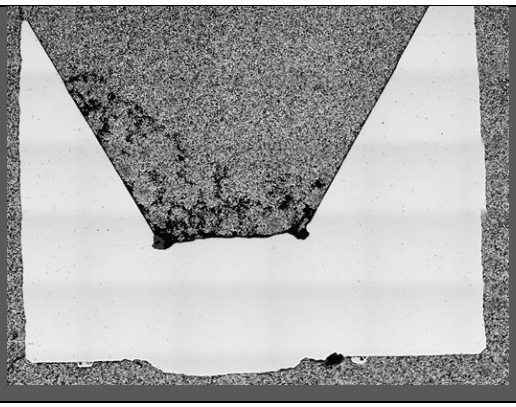

Figure 149: Optical micrographs representative of samples deposited under similar conditions, but where no window defect was present. No cracking was observed under examination using an optical microscope at 400x magnification.

T = 20 mm, R_F = 50 mm

For 20 mm-thick plates under lower restraint (R_F = 50 mm), the empirical cracking boundary shared the same limits as the 20 mm-thick plates under high restraint (R_F = 25 mm), but none of the samples exhibited evidence of centreline cracking (Figure 150). Cracking was dominated by classic hydrogen micro-cracks and originated from a geometrical stress concentrator.

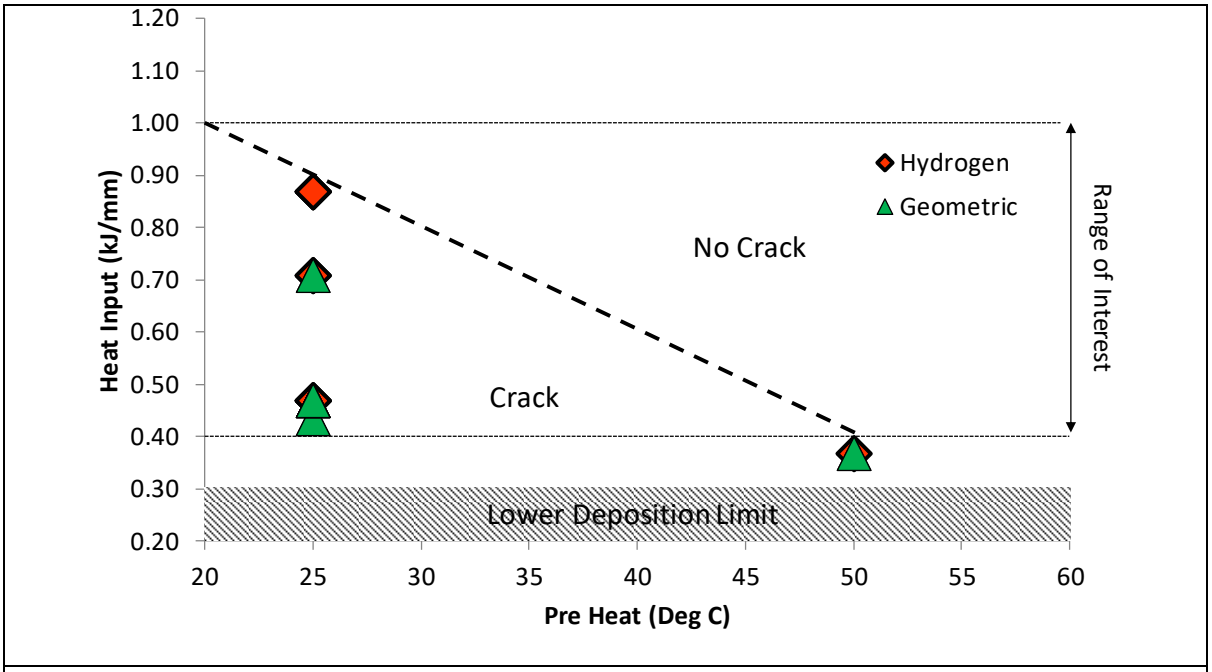

Figure 150: Observed cracking in MWIC test plates at T = 20 mm and R_F = 50 mm.

The possible effects of heat input on the type of cracking observed in the 20 mm-thick plate series can be highlighted by examining Figure 151 and Figure 152. The cracking results from the 20 mm-thick plates under high restraint are replotted in Figure 151 with the hydrogen micro-cracking data and in Figure 152 with the hydrogen cracks that originated from stress concentrators.

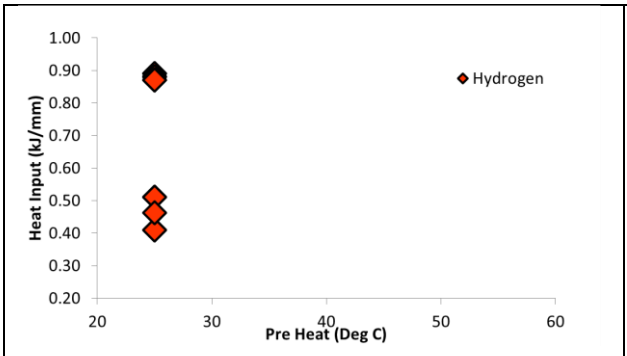

Figure 151: Distribution of hydrogen micro-cracks in MWIC test plates at T = 20 mm and R_F = 25 mm.

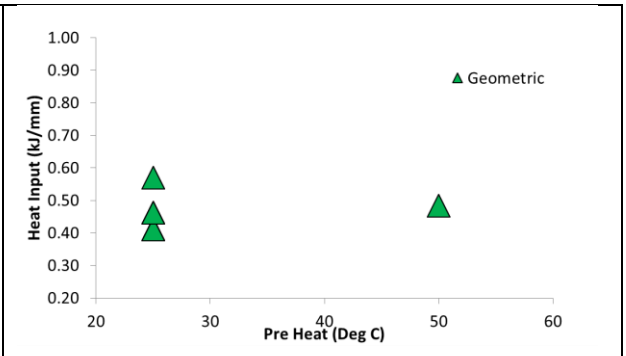

Figure 152: Classification of observed cracking in MWIC test plates at T = 20 mm and R_F = 25 mm.

It was observed that, as was the case with the 20 mm-thick plates welded under high restraint (T = 20 mm, R_F = 25 mm), when the heat input was lowered the prevalence of cracking originating from the weld toe increased. This may be attributable to an increase in the eccentricity of the weld bead profile's increasing the intensity of local stresses at the weld toe and thus serving as a preferential initiation site for hydrogen cracking.

Similarly, the figures below display the cracking data for the 20 mm-thick plates under lower restraint (R_F = 50 mm), with Figure 153 showing the classic hydrogen micro-cracking data and Figure 154 showing the hydrogen cracks that originated from stress concentrators. There is thus evidence to suggest that the trend for plates welded under higher restraint is similar to plates welded under low restraint.

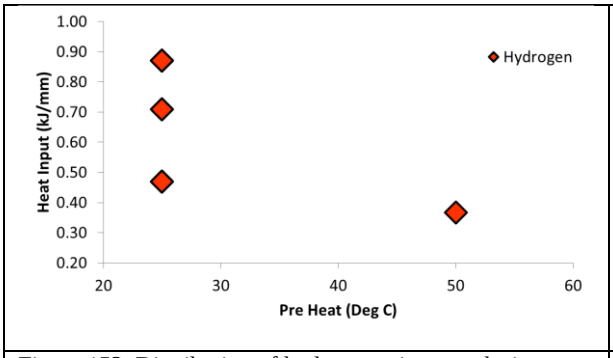

Figure 153: Distribution of hydrogen micro-cracks in MWIC test plates at T = 20 mm and R_F = 50 mm.

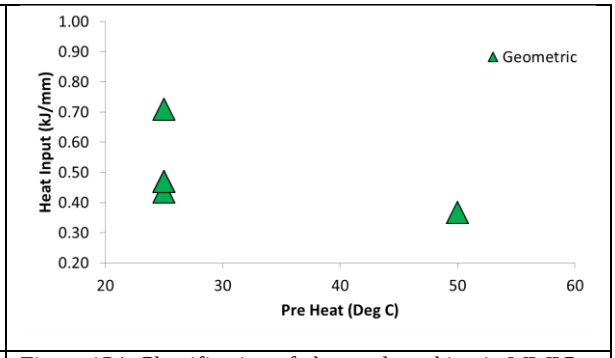

Figure 154: Classification of observed cracking in MWIC test plates at T = 20 mm and R_F = 50 mm.

However, caution must be applied when drawing a conclusion on the effect of heat input on crack type, as testing was restricted to a single plate-electrode chemistry combination.

What can be concluded with a higher degree of confidence is that, as the heat input is lowered, the profile of the weld bead deposited becomes less symmetric (Figure 155 and Figure 156), which influences the distribution of local weld stresses that increase the propensity for cracking. This conclusion accords with published work in which the weld has been shown to influence the distribution of stresses within the weld bead profile [31]. It is important to note that, at a preheat of 100 °C, the effect of the weld bead profile was inconsequential in terms of increasing the risk of cracking propensity. As seen in Figure 157, at a high preheat and even with extreme bread eccentricity in the weld bead profile, the weld did not crack compared; see Figure 156 by contrast, in which a slight eccentricity in the weld bead has resulted in cracking at a comparable heat input.

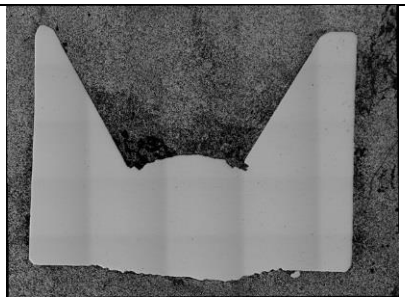

Figure 155: Typical weld bead geometry for sample deposited with a heat input in the upper quartile of the heat input range of interest. The deposited bead appears symmetric with no pronounced eccentricity in the weld toe.

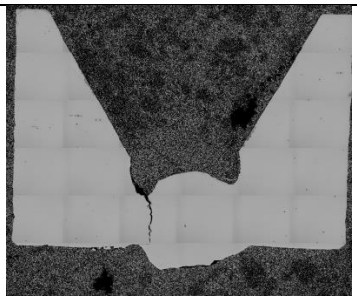

Figure 156: Typical weld bead geometry for sample deposited with a heat input in the lower quartile of the heat input range of interest. Deposition with a low preheat resulted in the formation of a weld with a produced weld toe and a consequent hydrogen crack.

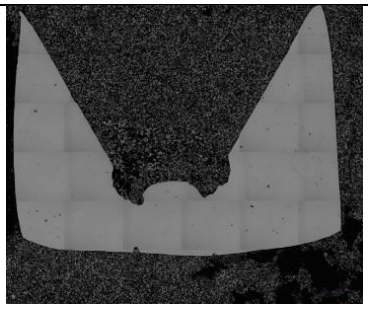

Figure 157: Typical weld bead geometry for sample deposited with a heat input in the lower quartile of the heat input range of interest, at a heat input of 50°. Despite the irregularity of the weld bead and the eccentric weld toe, no hydrogen cracking was observed in the weld bead.

6.3.3 Crack Characterisation in 10 mm-Thick Plates

T = 10 mm, R_F = 25 mm

For the weldability tests conducted on 10 mm-thick plates under high restraint, there was evidence of all three categories of cracking (Figure 158). Under ambient conditions, centreline cracking was observed at all but one of the heat inputs tested. Centreline cracks ranged from a minimum of 38% to a maximum of 81% with an average length of 67%. Conversely, geometric cracks were only observed at lower heat inputs when tested under ambient conditions. These cracks ranged in length from 15% to 81% with an average length of 51%. With the preheat level raised to 40 °C, only geometric cracks were observed. Analysis of the welded samples provided evidence to suggest that like centreline cracks, classic hydrogen micro-cracks were predominantly found in samples welded under ambient conditions. Classic hydrogen micro-cracks ranged from 6% to 48% with the average length calculated at 27%.

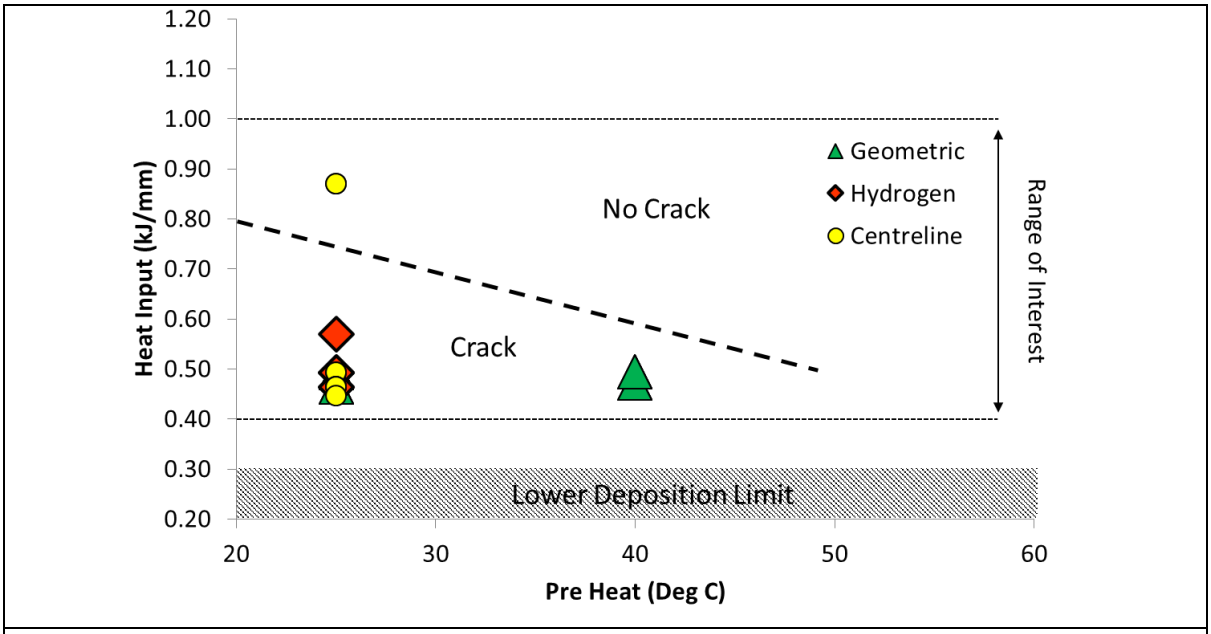

Figure 158: Observed cracking in MWIC test plates at T = 10 mm and R_F = 25 mm.

Like the welds deposited on 20 mm-thick plates, the presence of the window defect introduced a centreline crack in adjacent sections that would otherwise be classified as crack-free. As highlighted in ROI 3 in Figure 159, an initial test weld deposited at 0.82 kJ/mm on a 10 mm-thick plate under high restraint in ambient conditions was classified as cracked and defective as a result of the observed centreline crack. However, the sample had a window defect in between the first and second test sections (Figure 160). This resulted in centreline cracks in the third and fourth sections measuring 73% and 72% respectively. The fifth and sixth sections had no evidence of cracking. A validation test was run under similar conditions; a weld sample was deposited with no window defect and no cracking was observed in the six sections when analysed under an optical microscope.

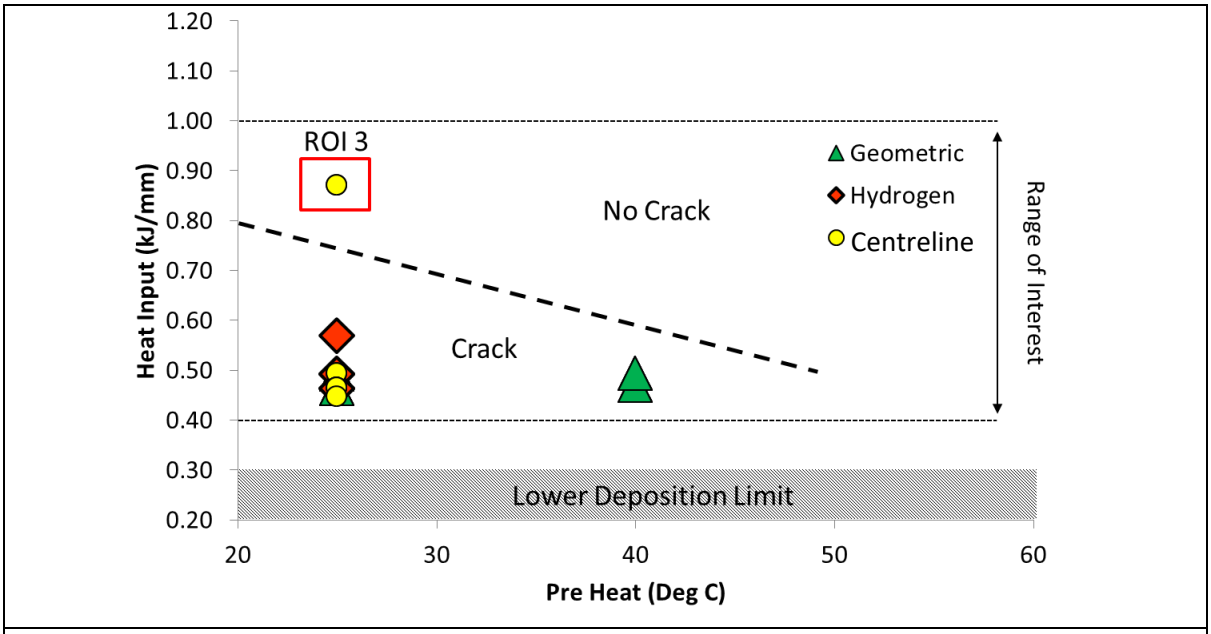

Figure 159: Observed cracking in MWIC test plates at T = 10 mm and R_F = 25 mm with ROIs highlighted. ROI 3 corresponds to cracking observed in welds deposited at a heat input of 0.82 kJ/mm under ambient conditions.

This observation supports the hypothesis, which was initially presented based on the observation made in the 20 mm data set that the presence of a window defect has the potential to create conditions in which a centreline crack may propagate longitudinally through the welded joint. Current field practice in Australia dictates that if a window defect originates during the deposition of the root pass of a girth weld, no remedial measure must be applied, as it is generally accepted that the subsequent hot pass should fill the void created by the window.

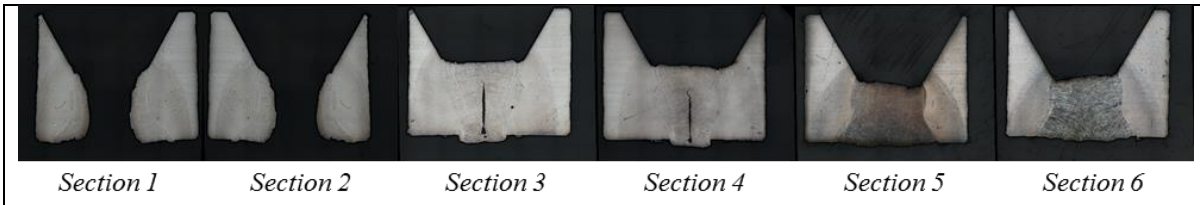

Figure 160: Optical micrographs highlighting the interrelationship between window defects and centreline cracking.

The results generated in this thesis have provided evidence to suggest that this Australian practice may indeed jeopardise the integrity of the deposited weld, as the presence of the window defect provides conditions in which a centreline crack may initiate and propagate longitudinally through the weld. In both the 20 mm and 10 mm data sets, centreline cracks that could be directly attributed to the presence of a window defect extended longitudinally to a maximum of 16 mm. As this thesis focuses on cracking susceptibility investigated in single-pass welds, no data was collected to validate or repudiate this preposition.

T = 10 mm, R_F = 50 mm

Weldability tests conducted on 10 mm-thick plates under lower restraint (R_F = 50 mm) produced samples in which the dominant type of cracking observed was geometric hydrogen cracks with isolated cases of hydrogen micro-cracks and centreline cracking, as illustrated in Figure 161. There was insufficient data in this series to test the hypothesis that classic hydrogen micro-cracks occurred at higher heat inputs than the geometric hydrogen cracks.

The observed geometric cracks ranged in length from 2% to 66% with an average length of 29%. The observed hydrogen cracking ranged from 1% to 24% and the centreline cracks ranged from 11% to 16%.

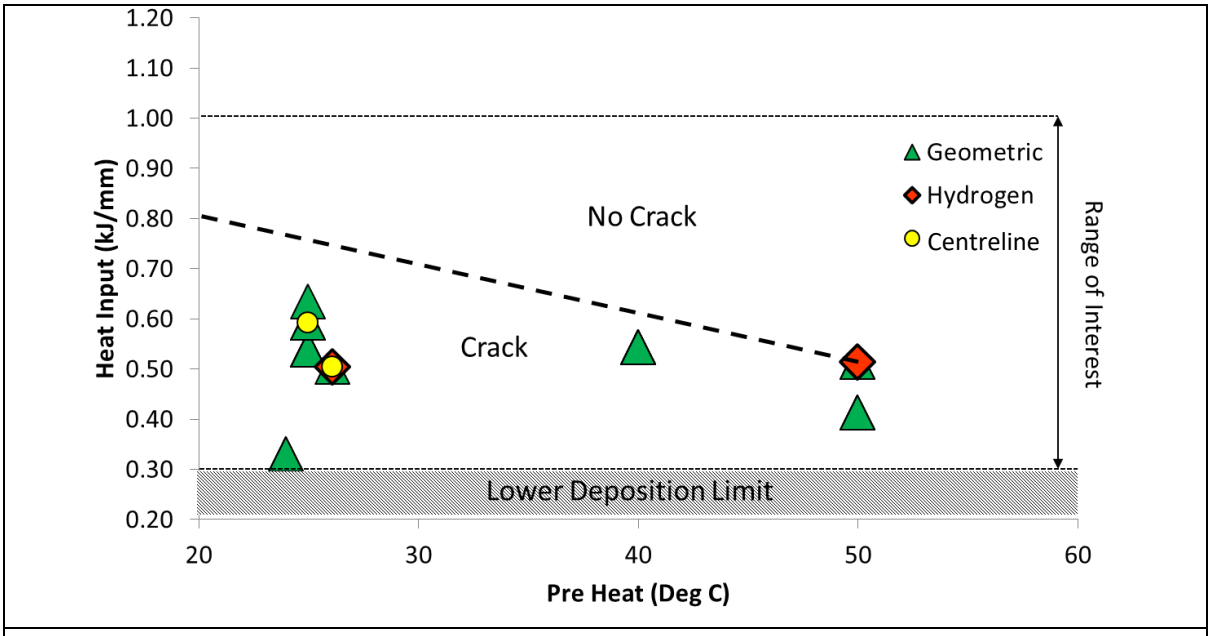

Figure 161: Observed cracking in MWIC test plates at T = 10 mm and R_F = 50 mm.

Given that classic hydrogen micro-cracks were noticeably absent from the examined surfaces, particular attention was devoted to the two regions where classic hydrogen cracking *was* observed. Figure 162 highlights the positon of the observed cracking in relation to the preheat-heat input combination for the test series.

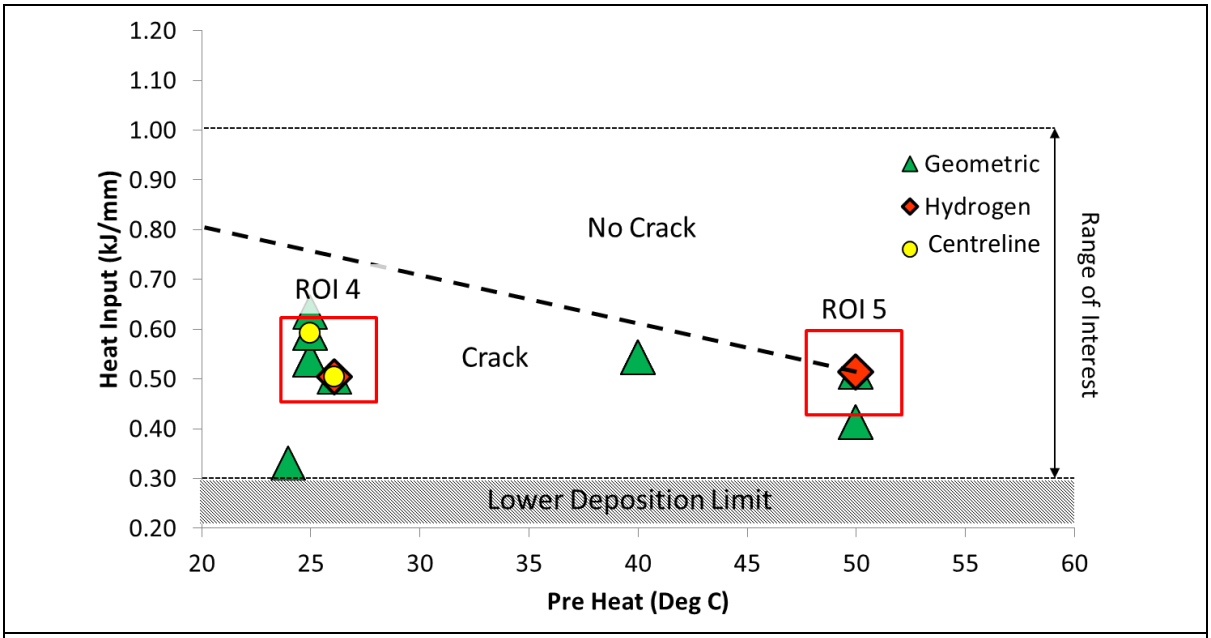

Figure 162: Observed cracking in MWIC test plates T = 10 mm and R_F = 50 mm with ROIs highlighted. ROI 4 and ROI 5 correspond to areas where hydrogen micro-cracks were observed.

In ROI 4 test welds were deposited with a heat input of 0.5 kJ/mm and 0.6 kJ/mm respectively under ambient conditions. Hydrogen cracks measuring a total of 24% of the measured throat length were observed in the third-section weld sample deposited at 0.5 kJ/mm. When examined in the context of adjacent sections, there was evidence of a hollow bead defect in the fourth section, which may have altered the stress state of the adjacent weld metal and created preferential conditions for the formation of the hydrogen crack.

The second weld examined in ROI 4 was deposited at a heat input of 0.6 kJ/mm. A range of centreline cracking was observed in the third test section. However, there was a window defect present in the section adjacent to where the centreline cracking was observed, which again may explain the difference in the type of cracking observed.

In ROI 5, the observed hydrogen crack was 1% of the measured throat thickness in the third section of the weld sample. Although the crack was identified and quantified, its length was well within the limits of what is considered a permissible imperfection, so its presence was discounted from the overall derived CNC boundary. However, a geometric crack 24% long was also present in the section under review and to a lesser extent in adjacent sections. The presence of geometric cracks in ROI 5 supports the derived safe welding limits within the experimental deposition envelope.

6.3.4 Initiation site versus crack classification

As introduced in Section 6.3.1 the 'Geometric' classification was assigned to hydrogen cracking that initiate at geometric discontinuities, which act as macroscopic stress concentrators. This category was assigned specifically to highlight the role of bead symmetry and its subsequent influence on cracking susceptibility. The formation of a stress concentrator arises as a result of a combination of the applied welding technique and welding parameters. The stress concentrator may have manifested as wagon tracks or undercut in the root or toe of the weld. Most of these geometric cracks appear at very low heat inputs. Indeed, geometric HACC formation initiates at the weld metal-base metal interface and usually at the top surface when a lack of deposited metal creates a sharp transition. Geometric cracking has been observed to be inversely linked to the heat input. In the tests carried out in this work, a minimum heat input of 0.7 kJ/mm was required to avoid the geometric-type of HACC for both 20mm and 10mm thick plates. The geometric cracks are therefore avoidable by selecting welding parameters that ensure smooth weldment geometrical features avoiding stress concentrators at the surface [4].

In addition to the observed hydrogen cracking, multiple incidences of solidification cracks were observed in the empirical data set generated during weldability testing. In contrast to HACC, solidification cracking, which is a subset of solidification type defects, develops during the freezing of weld metal as indicated in reviews on the subject [284-288]. During the liquid-to-solid transition most metals undergo a certain amount of volume contraction, which generates strain (usually about 5%). The latter can be reinforced by thermal contractions in the solid. If this contraction is hindered or cannot be freely accommodated by mechanisms such as plastic deformation and movement of solid or liquid, the solidifying mass may be subjected to strains. Since during the final stages of solidification the solidifying material has poor mechanical properties, the generated tensile strain is sufficient to crack the hot weld metal. Furthermore, the solid and liquid at the final stages of solidification can no longer move freely to compensate shrinkage and therefore are unable to heal the cracks generated by tensile strain.

The relative absence of solidification cracking in completed production girth welds [289] is considered to be due in part to the deposition of subsequent passes in quick succession. Nevertheless, a significant risk exists to pipeline integrity when the elimination of a

solidification crack in a girth weld depends on grinding down the face of the root pass and depositing of the hot pass to fill and fuse any existing cracks. In particular, incomplete merging may leave a residual defect that can act as a powerful stress concentrator and initiate cold cracking [290].Therefore to minimise the risk of hydrogen cracking in the root pass of girth welds, delineating the conditions within which hydrogen cracks form from solidification cracks is critical. In this body of work, only single pass welds were investigated as the root pass is considered to be the critical pass in pipeline construction. However, from the empirical data generated, it is evident that the basis of the preposition that hydrogen cracks can indeed initiate from solidification type cracks was shown to be plausible. Figure 163 and Figure 164 highlight typical centreline cracks which served as initiation sites for hydrogen cracks. The meandering hydrogen crack appears to initiate from the blunt crack tip typically associated with solidification type cracks [63, 284, 287]. Further fractographic studies, which is beyond the scope of this body of work would be needed to validate and quantify cases where a hydrogen crack is suspected to initiate from a centreline crack.

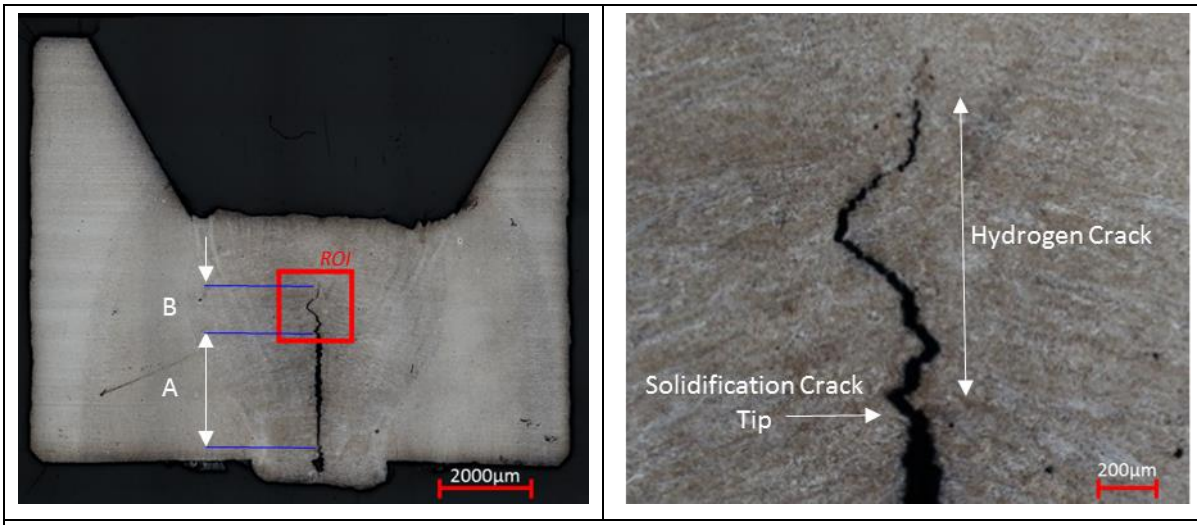

Figure 163: Typical centreline crack observed in the test section of weld deposited in the upper quartile heat input range of interest under low magnification *(left)*. The length demarcated 'A' outlines the centreline crack, whereas 'B' demarcates the length associated with a hydrogen crack that has initiated form the blunt crack tip of the solidification crack. The higher magnification image *(right)* highlights the point where the solidification crack ends and the hydrogen crack initiates

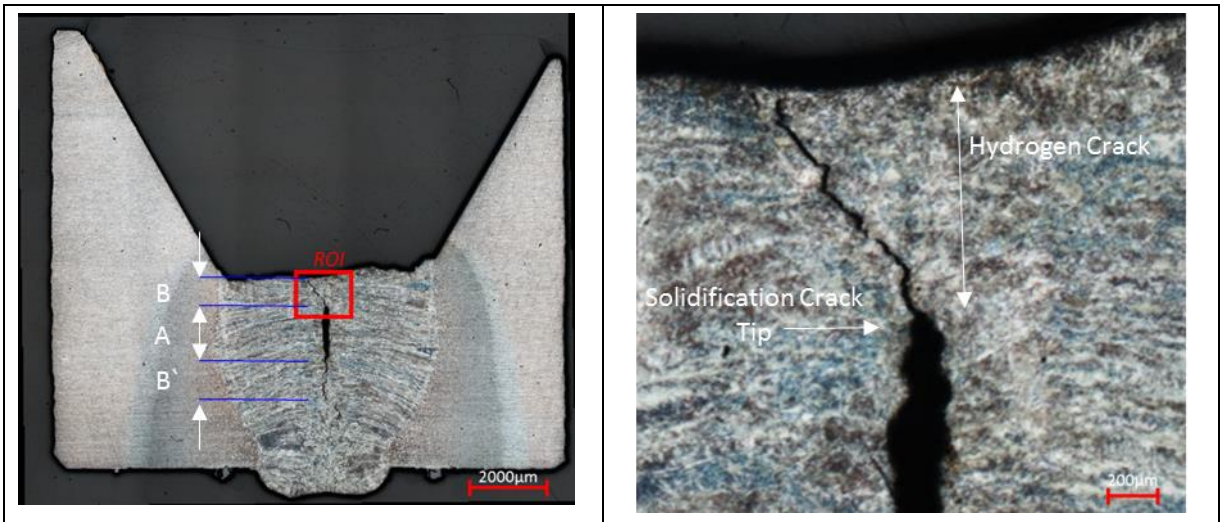

Figure 164: Typical centreline crack observed in the test section of weld deposited in the lower quartile heat input range of interest under low magnification *(left)*. The length demarcated 'A' outlines the centreline crack, whereas B and B^{I} demarcates the length associated with a hydrogen crack that has initiated form the blunt crack tip of the solidification crack. The higher magnification image *(right)* highlights the point where the solidification crack ends and the hydrogen crack initiate for crack B

6.3.5 Prevalence of Centreline type cracks

When comparing, the empirical data generated from studies commissioned to investigate the susceptibility of weldments deposited using cellulosic electrodes on HSLA line pipe steel to solidification cracking and HACC, there is evidence to suggest that both defects have the potential to manifest under similar welding conditions. Moreover, strategies employed to minimise the risk of solidification cracking (i.e. the use of low heat inputs and high strength electrodes [289, 290]) increased the susceptibility of weldments to HACC [3-5, 101]. Although weldability testing, commissioned to investigate the susceptibility of weldment to HACC has been conducted for a range of electrode-steel combinations, most studies have been conducted at travel speeds around or below 300mm/min resulting in heat inputs at or above 1kJ/mm.

Multiple studies have investigated the susceptibility of pipeline girth welds to solidification type defects. Work by Nolan et al. [290] and Nolan and Hutchings [289], conducted on full-scale sections of pipe, concluded that the root pass of pipeline girth welds deposited with cellulosic electrodes are particularly sensitive to solidification cracking. The studies attributed this sensitivity to the characteristics of cellulosic consumables (high arc force, full penetration welding and high welding speeds) and the geometry of the weld configuration which provided

more favourable conditions for the development of solidification cracking than for other Manual Metal Arc Welding (MMAW) processes and conditions.

Bailey [291] and Amend and Jarvis [292] suggested that increasing travel speeds result in an increased risk of solidification cracking and attributed this to the effect of the weld depth to width ratio. An increase in travel speed, necessitating the use of higher currents and voltages, altering the weld bead profile, making it deeper [91, 95], consequently increasing the susceptibility to solidification cracking. Similarly, Nolan [290] concluded solidification cracking was observed at the lower welding speed of 300mm/min, but susceptibility was enhanced by an increase in welding speed to 500mm/min. These findings are consistent with those of Oshita et al. [293], who have concluded that for MMAW of pipe girth welds using cellulosic electrodes, a critical travel speeds (330 mm/min) exists below which cracking does not occur. The empirical results generated in this study concurs with the works of Oshita et al. [293] and Nolan [290].

It is generally accepted that welding at the upper end of the recommended range of electrode currents for a given consumable is a major factor which influencing susceptibility of a weldment to solidification cracking [294, 295]. Nolan [289] went on to conclude that when comparing a range of consumable tensile strengths, solidification cracking occurred predominantly in welds deposited with the low strength (E6010) electrodes. As detailed in Section 6.4.1 Nolan's observation were confirmed with the severity of centerline cracking increasing with increasing heat input. These results can be related to the observations of Bailey [291] and Amend and Jarvis [292] where increases in heat input, increased the depth to width ratio of root bead profile, effectively creating a narrow weld bead which is more susceptible to cracking given the propensity for the tensile loads to act in the geometric centre of the bead.

6.4 **Cracking Severity**

Section 6.3 focused on analysing the raw cracking results generated during weldability testing using the metallographic techniques described in Chapter 4 and the defect acceptance criteria proposed in this thesis (Section 6.3.1) to characterise the type of cracking observed. This section extends the analysis presented in the previous section to take into account the severity of cracking. Its primary aim is to describe and discuss how the combination of preheat and heat input affected the severity of the dominant type of cracking observed in each section of

the test samples produced. Additionally the ROIs identified in Section 6.3 are reviewed in terms of the severity of the cracking observed.

In the previous section, it was suggested that for both 20 mm and 10 mm plates, the level of restraint influenced the prevalence of centreline cracking. Additionally, it was suggested that the prevalence of geometric cracking was inversely proportional to the heat input with which the weld was deposited. In this section these arguments are extended to encapsulate the severity of cracking, with the conclusions that at high levels of restraint the severity of centreline cracking will increase and that the degree of restraint does not affect the degree of geometric cracking, where it is the heat input that plays the dominant role in influencing the severity of cracking.

Once again, to normalise the extent of cracking, crack lengths are stated as a percentage of the measured throat thickness for the particular section under review. Cracking anomalies manifested as a result of the presence of window defects identified in the previous sections are presented in this section to serve as a preamble to the discussion on the role of window defects on influencing cracking in adjacent plate sections.

6.4.1 Cracking Severity in 20 mm-thick Plates

T = 20 mm, R_F = 25 and 50 mm (Centreline Cracking)

When analysing the centreline cracking results for the 20 mm-thick plates under both the 25 mm and 50 mm restraint conditions, it is immediately apparent that the greater the restraint level, the greater the prevalence and severity of observed centreline cracking, as illustrated in Figure 165.

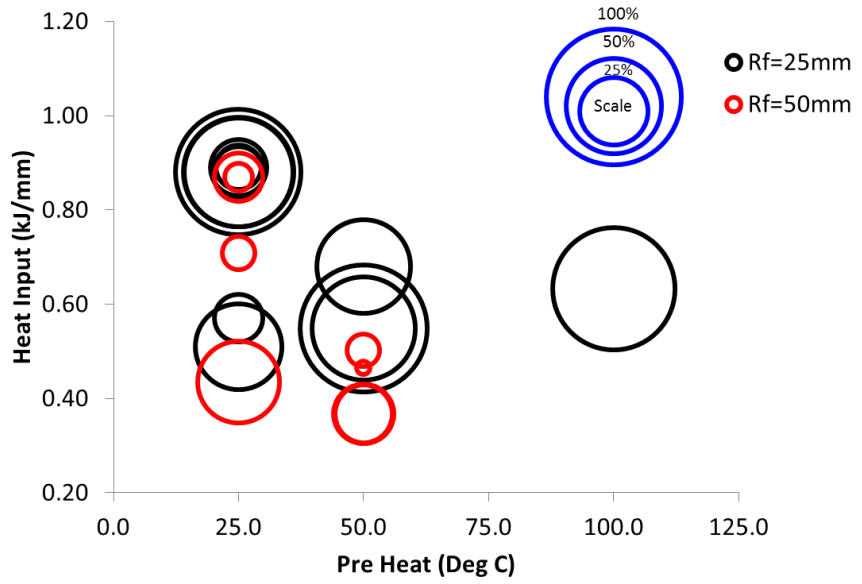

Figure 165: Centreline cracking severity diagram welds deposited in 20 mm-thick plates (T = 20 mm) under high (R = 25 mm) and low restraint (R_F = 50 mm) within the heat input range of interest for various preheat levels.

When considering the number of cracking incidents observed in the weld metal samples, it is important to note that under high restraint (R_F = 25 mm) and ambient conditions the number of cracking incidents detected is higher at the upper end of the heat inputs tested. In these conditions, the severity of cracking is also greatest at heat inputs above 0.8 kJ/mm.

When the preheat is increased to 50 °C, no cracking is detected above 0.8 kJ/mm, but the severity of cracking observed at 0.5 kJ/mm is comparable to what was observed under ambient conditions. This suggests that for welds deposited under conditions of high restraint, when centreline cracking occurs, its severity will remain similar regardless of the heat input with which the weld is deposited.

The results also suggested that under ambient conditions, as the heat input is lowered, the severity of centreline cracking is reduced. As was reported in the previous section, when the heat input is lowered for 20 mm-thick plates under high restraint, the prevalence of geometric cracking increases. Given the role that tensile loads play in the initiation and propagation of centreline cracks, it may be suggested that the preferential formation of geometric cracks at a lower heat input reduce the net tensile loads acting on the initiation sites of centreline cracks, effectively reducing the prevalence and severity of centreline cracks as the heat input is lowered (for concurrent sections of the deposited bead). This hypothesis accords with the observations reported in Section 6.3.2 and the literature cited in Chapter 2.

As discussed in the literature review, an increase in the preheat levels reduces the residual hydrogen content in the weld metal. Consequently, the deposited weld bead is significantly more tolerant to asymmetry in the bead profile and less sensitive to any stress concentrators arising from an asymmetric bead profile, which under ambient conditions would have served as an initiation site for a hydrogen crack. Without the formation of geometric hydrogen cracks and the consequent reduction in the net tensile load section on the bead, a centreline crack eventuates. To have definitive evidence to support this hypothesis, a measure of the instance when each type of crack initiates would be required. The use of acoustic emission to determine the onset of hydrogen cracking has been shown to be successful in the literature, but was beyond the scope of this thesis.

For the 20 mm plate data set two ROIs were identified, initially in Figure 146 and used again in Figure 166.

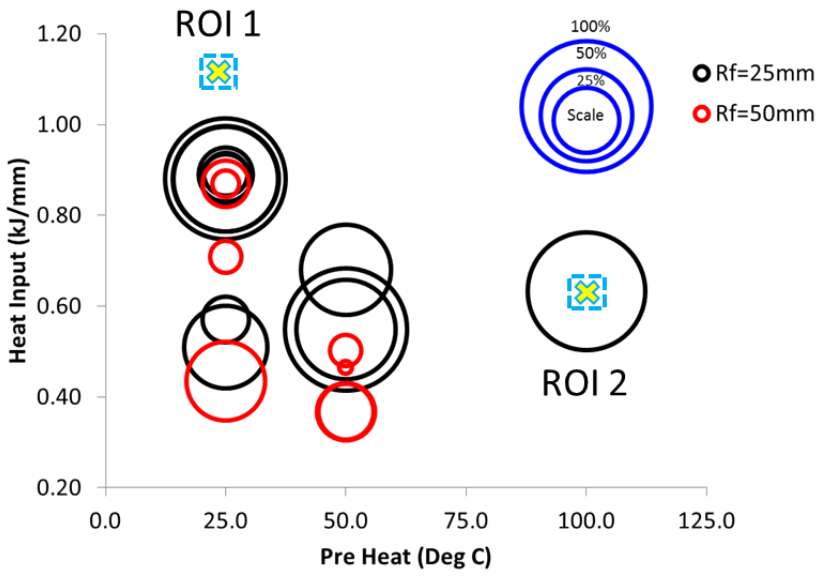

Figure 166: Centreline cracking severity diagram welds deposited in 20 mm-thick plates (T = 20 mm) under high (R_F = 25 mm) and low (R_F = 50 mm) restraint within the heat input range of interest for various preheats, with ROIs highlighted.

Of particular interest is the pronounced centreline cracking identified in ROI 2. Its severity relative to other centreline cracking observed in 20 mm plates is significant, but as discussed above the presence of a window defect may be responsible for the formation of the centreline crack. As the number of window defects was limited, proposing a correlation between the dimension of the defects and the severity of centreline cracking is not possible. What can however be deduced from the observations, in particular from ROI 2, is that the presence of a window defect can lead to significant centreline cracking, even at high preheat levels.

What is of greater importance is that the presence of the defect can in fact influence the propensity for a centreline defect to initiate and propagate at some distance away from the origin of the window defect. In the case of ROI 2, a window defect in section one of the test sample led to centreline cracking being identified in sections two and three, whose faces were over 16 mm away from the initiation of the window.

T = 20 mm, R_F = 25 and 50 mm (Geometric Cracking)

When analysing the geometric cracking results for 20 mm-thick plates under both 25 mm and 50 mm restraint conditions, the results suggest that the level of restraint influences the severity but not the prevalence of cracking, unlike centreline cracking, as illustrated in Figure 167. Moreover, the results support the hypothesis that the presence of geometric defects reduces the prevalence of centreline defects. Examining Figure 166 and Figure 167 makes clear that where geometric defects exist, there is a lower prevalence of centreline cracking.

This same data does however support an alternative interpretation. A contrary argument may be applied to the relationship between the prevalence and severity of centreline cracking and geometric hydrogen cracks. It is possible that the presence of centreline cracking reduced the prevalence of geometric cracking, and it may thus be argued that tensile loads during solidification were high enough to initiate centreline cracking, which results in a lower net tensile load on the ligament after solidification that is insufficient to facilitate the propagation of a hydrogen crack.

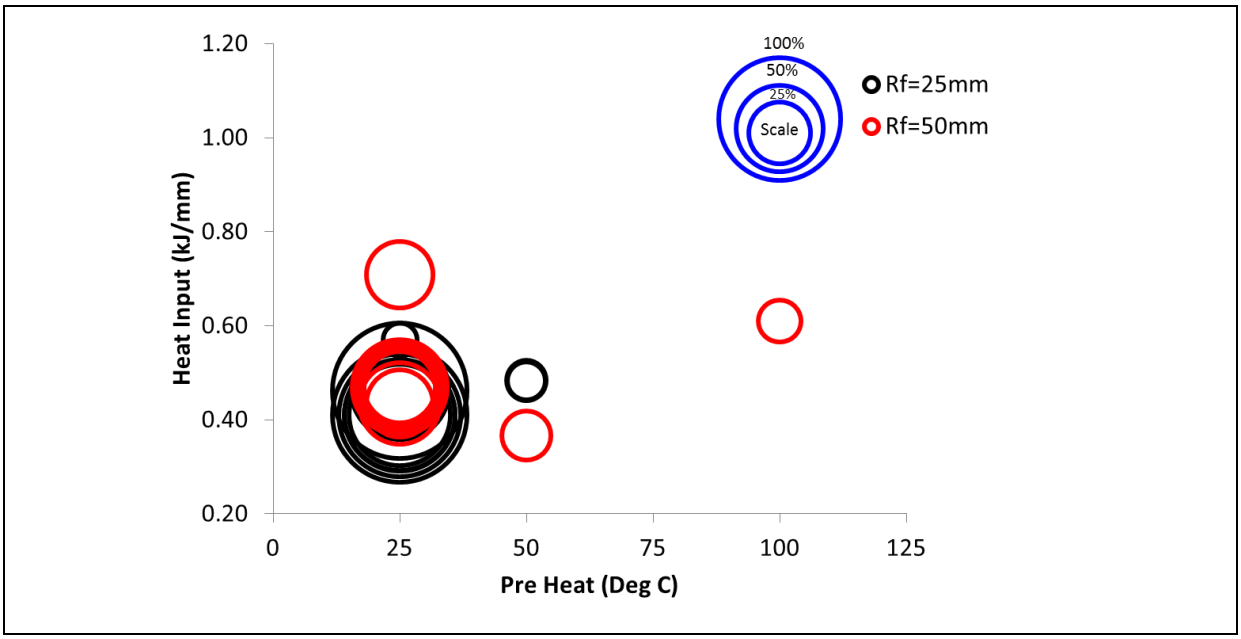

Figure 167: Geometric hydrogen crack severity diagram of welds deposited on 20 mm-thick plates (T = 20 mm) under high (R_F = 25 mm) and low (R_F = 50 mm) restraint within the heat input range of interest using various preheats.

When subjected to the presented analytical techniques the experimental data collected can be interpreted either way. In order to establish which type of cracking occurred first, techniques involving the use of acoustic emission testing would be needed and are beyond the scope of this thesis.

T = 20 mm, R_F = 25 and 50 mm (Classic Hydrogen Micro-cracking)

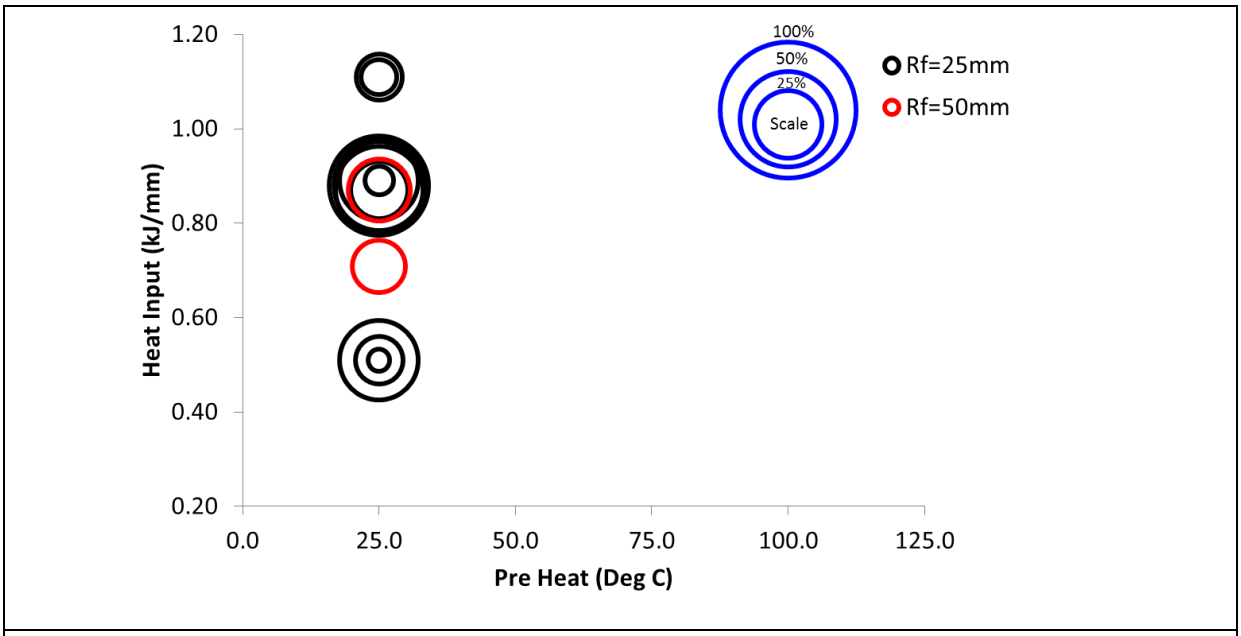

Figure 168: Hydrogen micro-crack severity diagram of welds deposited on 20 mm-thick plates (T = 20 mm) under high (R_F = 25 mm) and low (R_F = 50 mm) restraint within the heat input range of interest using various preheats.

An analysis of the empirical results from classic hydrogen cracks for 20 mm-thick plates suggests that the prevalence, and to some degree the severity of classic hydrogen cracks decreases as the level of restraint is eased by increasing the restraint length from 25 mm to 50 mm in the MWIC test.

The literature review made clear that a critical threshold of stress is required for a hydrogen crack to initiate and propagate. A reduction in the level of restraint reduces the magnitude of the mechanical driving force responsible for the initiation and propagation; as the restraint level is lowered, it follows from Equation 2-7 and Equation 2-9 that there will be a reduction in the stress acting on a weld bead. Therefore, it follows that an increase in the restraint length effectively lowers the stress intensity and the level of stress acting on a weld bead, which supports the observation that easing the restraint level leads to a decrease in the number and

severity of observed classic hydrogen cracks. Conversely, the number and severity of cracks observed for welds deposited under high restraint increases as the heat input is increased. This observation applied to the empirical results, with the exception of the cracking anomalies identified in ROI 1. Between 0.8 kJ/mm and 1 kJ/mm, approximately twice as many cracks were observed than in tests conducted between 0.4 kJ/mm and 0.6 kJ/mm. On average, the severity of cracks was 30% greater at the higher heat input.

When considering the conclusions drawn from the literature review, the observed cracking results may appear to be contradictory. However, when considering the hypothesised relationship between bead eccentricity, heat input and the prevalence of geometric hydrogen cracks introduced earlier in this section and consolidating the cracking data, the observations actually support the notion that the lower the heat input with which the test welds are deposited, the greater the prevalence of hydrogen cracking. It is therefore important to reiterate that the classification system introduced in this thesis was employed to differentiate between types of hydrogen cracking observed, as both geometric cracks and classic hydrogen micro-cracks are both examples of HACC. At a lower heat input the weld bead eccentricity is a dominating factor (Figure 169); the resulting weld bead profile has geometric stress concentrators introduced as a result of this eccentricity. This was suggested as increasing the prevalence of geometric hydrogen cracks. As the heat input is increased the symmetry of the bead improves significantly (Figure 170).

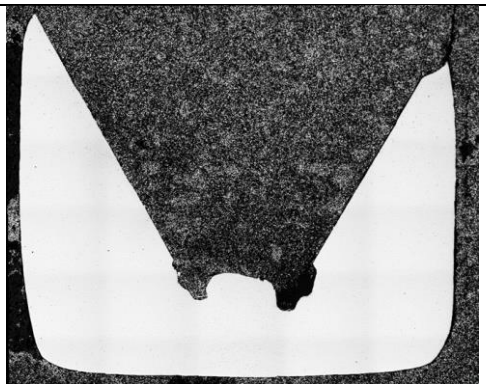

Figure 169: Typical weld bead profile for weld deposited in the lower quartile heat input of interest. The deposited bead's geometry had a greater degree of eccentricity observed in the weld toe.

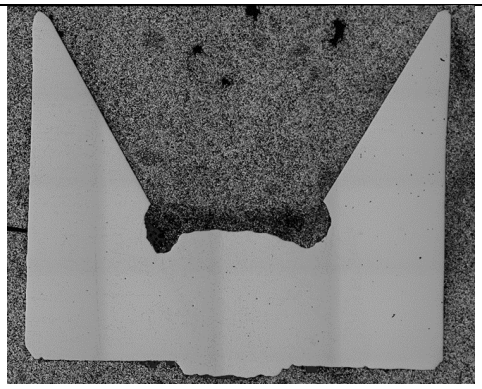

Figure 170: Typical weld bead profile for weld deposited in the upper quartile heat input of interest. The deposited bead's geometry generally appeared to be more symmetric and less pronounced than observed in the weld toe.

Without the presence of geometric stress concentrators, it is hypothesised that hydrogen migrates to microscopic stress concentrators such as NMIs (Figure 171), which create areas of high triaxial stress; hydrogen migrates preferentially to these regions. Moreover, authors such

as [85, 213], among others, have shown a positive correlation between the presence of NMIs and the formation of hydrogen cracks. Several micro-cracks were examined to validate this hypothesis. From the cracks examined there was evidence to support the claim; the role of NMIs relative to the formation of hydrogen cracks is discussed in more detail in the next section in the context of the weld metal microstructure.

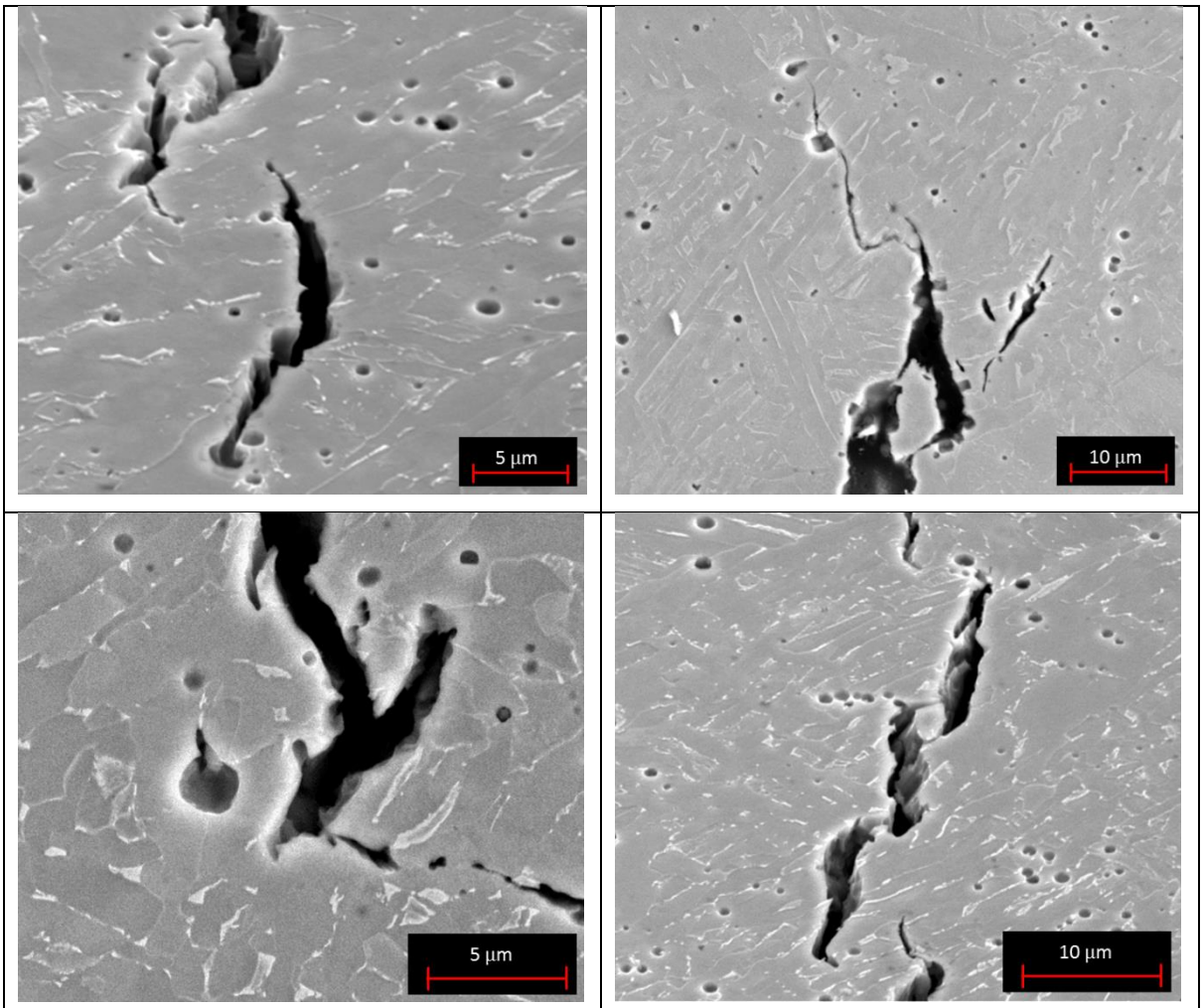

Figure 171: High-magnification micrographs acquired using a scanning electron microscope. The micrographs highlight typical microscopic hydrogen cracks. A large proportion of the observed micro-cracks appear to originate from NMIs and propagate through paths aligned with NMIs.

6.4.2 Cracking Severity, 10 mm-Thick Plates

T = 10 mm, R_F = 25 and 50 mm (Centreline Cracking)

Analysing the centreline cracking results for the 10 mm-thick plates under both 25 mm and 50 mm restraint conditions showed that the effect of restraint level on the prevalence and severity of centreline cracking is not as apparent as it was for welds deposited on 20 mm plates. As

expected from the analysis of the 20 mm plates, the number and severity of observed centreline cracking decreased as the level of restraint was reduced (Figure 172).

However, the number of centreline cracks observed in 10 mm plates was significantly lower than in 20 mm plates, which may be due to the fact that the restraint levels are inversely proportional to plate thickness, as discussed in the literature review. A statistically significant relationship cannot be established, given the limitations of the data points collected.

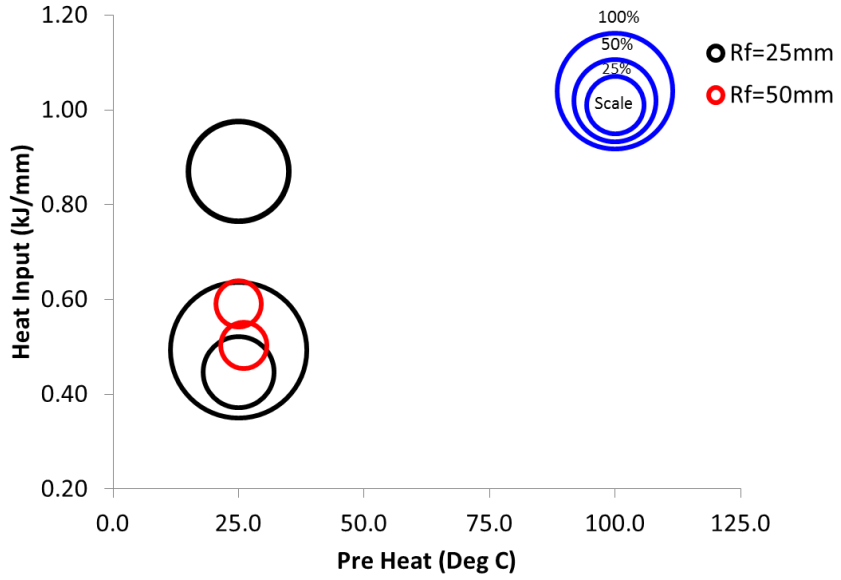

Figure 172: Centreline cracking severity diagram of welds deposited in 10 mm-thick plates (T = 20 mm) under high (R_F = 25 mm) and low (R_F = 50 mm) restraint within the heat input range of interest for various preheats.

Particular attention must be paid to ROI 3 and ROI 4, identified earlier in the section discussing crack characterisation and superimposed on the crack severity diagram below (Figure 173), in which cracking anomalies were identified. These anomalies were suggested in the previous section to be as a result of the presence of window defects, which discounted the sample from use in the overarching CNC boundary. The cracking severity measurements support the proposition that that the samples were in fact anomalies; they are discussed more fully below.

ROI 3 is positioned on the no-crack side of the CNC boundary. The clear presence of a defective weld disqualified the sample from the data set used to delineate the CNC boundary. Its presence and severity are inconsequential, so the sample was disregarded in the analysis. However, none of the other welds deposited in ROI 3 had any evidence of cracking.

The severity of the observed centreline cracking ROI 4 was disproportionately high when compared with centreline cracking observed in samples deposited with similar heat inputs, and the severity of cracking was comparable to what was seen in the 20 mm plates. Noting the presence of the window defect in the adjacent section and reiterating the disproportionate severity of the cracking observed, in addition to the lack of evidence of any additional factor that may have influenced the severity of the centreline crack, it is reasonable to suggest that the crack identified in ROI 4 is in fact a cracking anomaly resulting from the presence of the adjacent window defect.

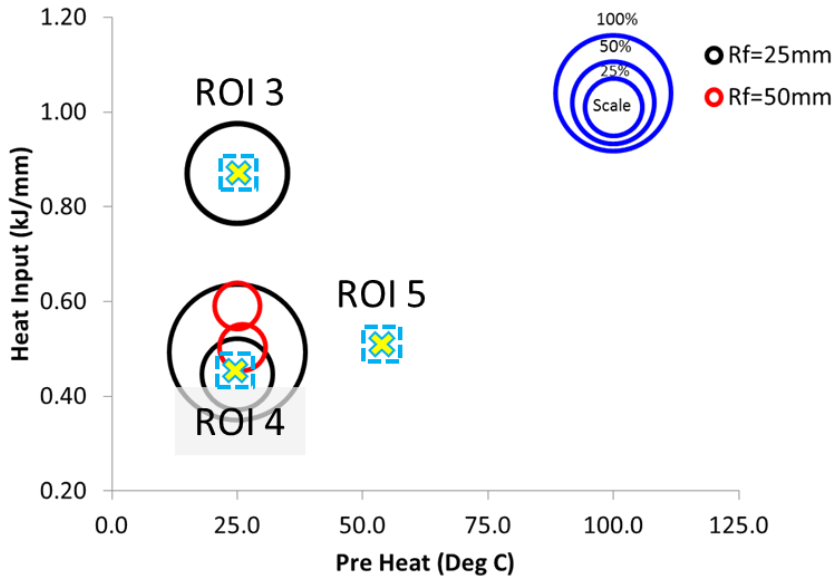

Figure 173 Centreline cracking severity diagram of welds deposited in 10 mm-thick plates (T = 20 mm) under high (R_F = 25 mm) and low (R_F = 50 mm) restraint within the heat input range of interest for various preheats, with ROIs highlighted.

T = 10 mm, R_F = 25 and 50 mm (Classic Hydrogen Micro-cracking)

The presence of micro-cracking was minimal in 10 mm-thick plates in both high and low restraint cases. From the data collected, it appeared that the level of restraint did not affect the number or severity of micro-cracking in 10 mm plates (Figure 174), which may be interpreted as a direct result of the presence of other forms of hydrogen cracks, especially geometric cracking.

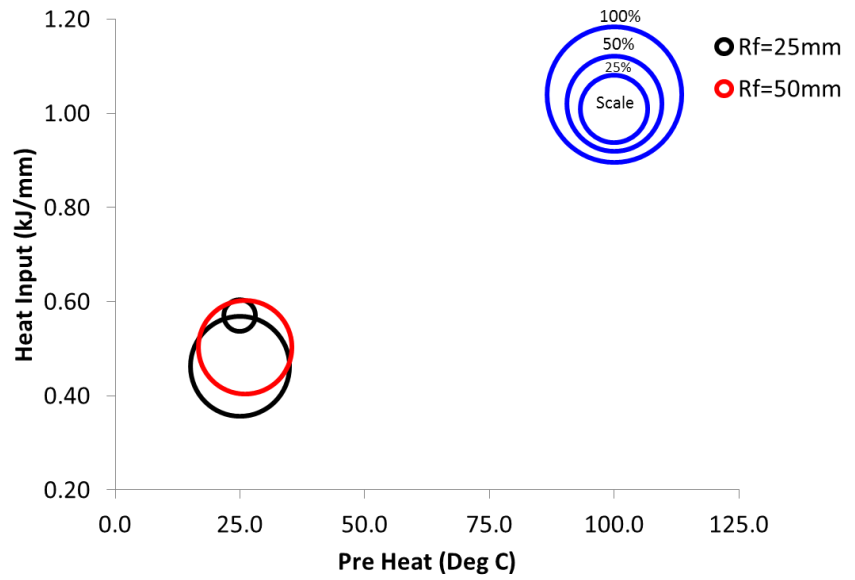

Figure 174: Hydrogen micro-crack severity diagram of welds deposited on 10 mm-thick plates (T = 20 mm) under high (R_F = 25 mm) and low (R_F = 50 mm) restraint within the heat input range of interest for various preheats.

T = 10 mm, R_F = 25 and 50 mm (Geometric Cracking)

For 10 mm plates, the most dominant classification of hydrogen cracking observed was geometric for both high (R_F = 25 mm) and low (R_F = 50 mm) restraint conditions (Figure 175). The empirical data suggested that a reduction in the level of restraint did not significantly affect the number of geometric cracks observed, but there was a marginal decrease in the measured severity of the observed cracking.

As discussed above, a reduction in restraint was expected to result in an overall decrease in the observed severity of cracking. This notion is supported not only by the literature but also by the cracking results observed and reported above for the 20 mm plates and here for the 10 mm plates.

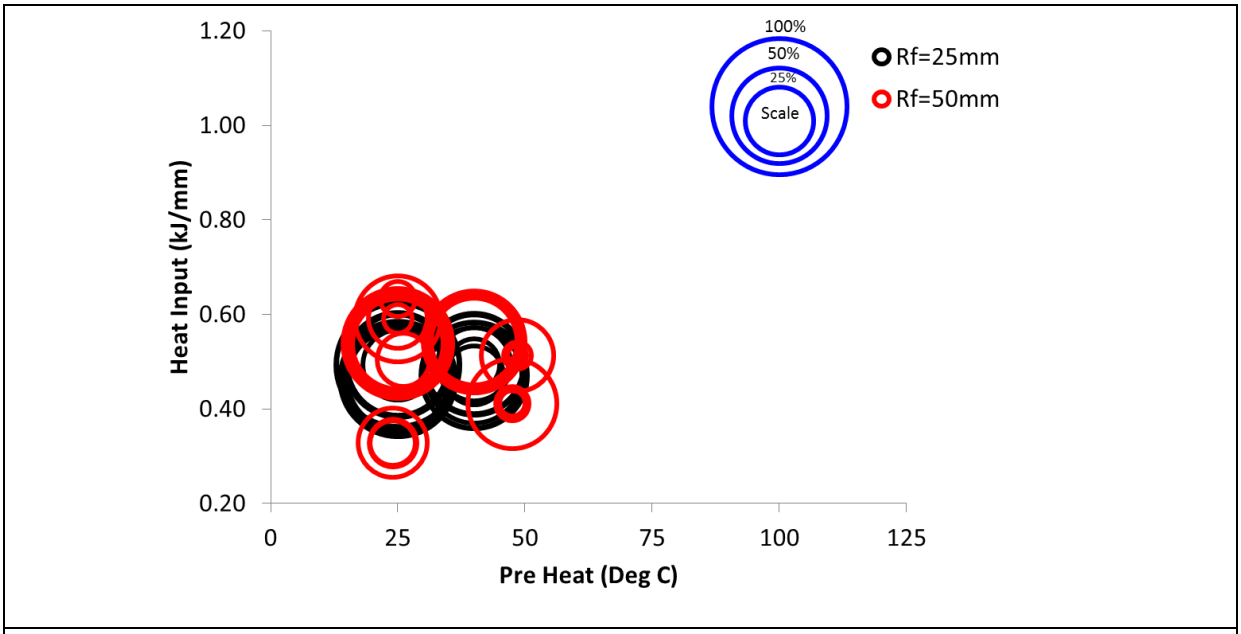

Figure 175: Geometric hydrogen crack severity diagram of welds deposited on 10 mm-thick plates (T = 20 mm) under high (R_F = 25 mm) and low (R_F = 50 mm) restraint within the heat input range of interest for various preheats.

Unlike centreline cracking and hydrogen micro-cracks, geometrical hydrogen cracking was observed both under ambient conditions and when the preheat of the plate was raised to 40 °C in both high- and low-restraint conditions (Figure 176).

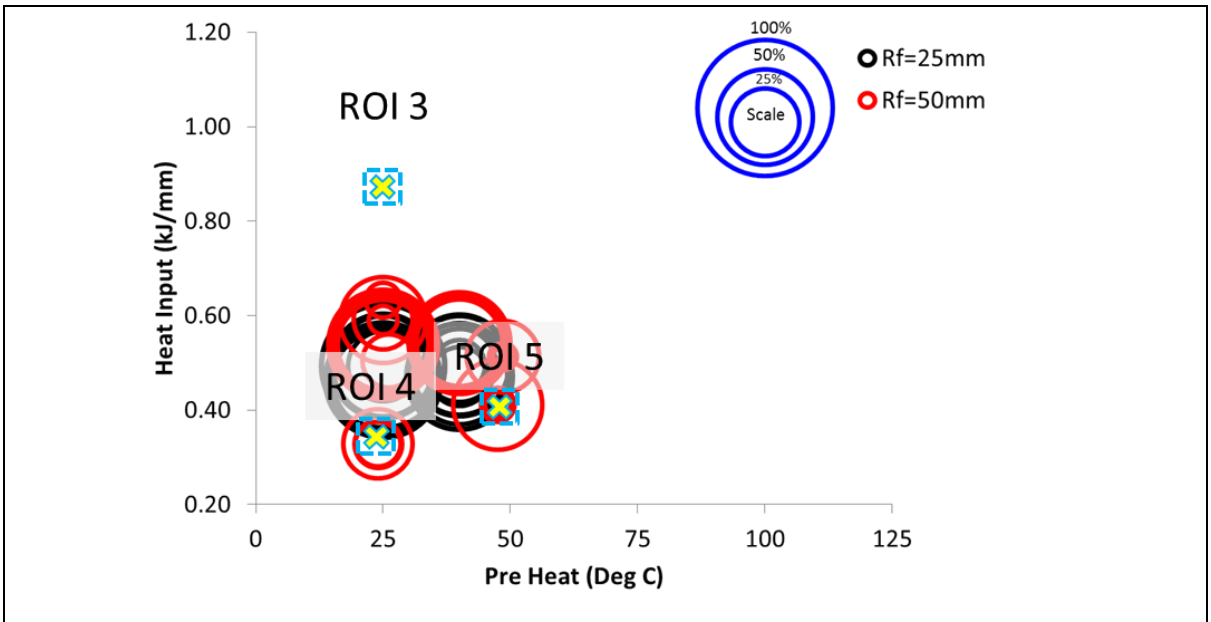

Figure 176: Geometric hydrogen crack severity diagram of welds deposited on 10 mm-thick plates (T = 20 mm) under high (R_F = 25 mm) and low (R_F = 50 mm) restraint within the heat input range of interest for various preheats, with ROIs highlighted.

As discussed and illustrated earlier, cracking in ROI 4 was disqualified from the data set used to delineate the CNC boundary because an adjacent section had a window defect which may have created conditions that would not be expected if the weld quality had been sound.

The geometric cracking in ROI 5 was not discounted, however, as there were no defects in the adjacent section. The bead deposited, although compliant as a permissible weld when visually inspected, did exhibit a degree of eccentricity as illustrated in Figure 177. From the highlighted region and as detailed in Figure 178 it is reasonable to suggest the eccentricity of the bead resulted in a geometric stress concentrator that served as an initiation site for the geometric hydrogen crack.

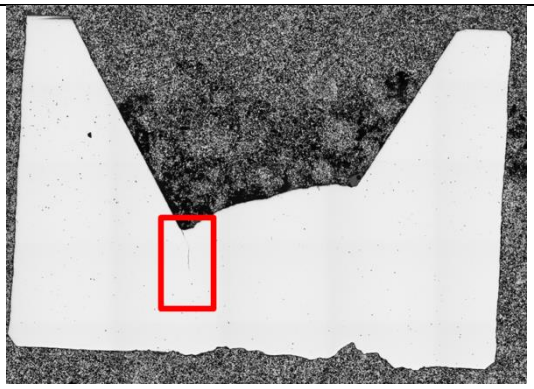

Figure 177: Typical weld bead profile for welds extracted from ROI 5. The profile exhibited a degree of asymmetry, in particular a pronounced weld toe.

Figure 178: Magnified section from Figure 177, highlighting the presence of a geometric hydrogen crack.

What can be surmised from the cracking identified in ROI 5 is that, even with a 50 °C preheat and relatively low restraint (R_F = 50 mm), at low heat inputs (0.4–0.5 kJ/mm) 10 mm-thick plates are still susceptible to hydrogen cracking, especially if a geometrical stress concentrator is present.

The observations in ROI 5 serve as further evidence to support the hypothesis that at low heat inputs the most dominant factor in influencing WMHACC is bead geometry. Moreover, it was established through observation of the 20 mm and 10 mm test series that the symmetry of deposited welds deteriorated as the heat input is lowered. This inverse relationship exemplifies the need to keep a sufficiently low travel speed to maintain a high enough heat input to yield a symmetric bead.

6.5 **Microstructural Analysis**

Section 6.2 presented and discussed the derived empirical CNC boundary based on the presence of planar defects whose vertical length was greater than or equal to 5% of the total throat thickness. Section 6.3 expounded on the results and analysis of Section 6.2 to discuss the type of cracking observed and the extent of cracking in relation to the heat input and

preheat combination with which the welds were deposited. This method of analysis was applied to both 20 mm- and 10 mm-thick plates and subject to both high (R_F = 25 mm) and low (R_F = 50 mm) restraint. The results of both thick and thin plates and high and low restraints were contrasted and compared to highlight the effect of overall restraint, which is a function of both plate thickness and restraint length in the MWIC test.

Section 6.2 suggested that 20 mm-thick plates will not crack under ambient conditions at heat inputs greater than 1 kJ/mm. Similarly, within the heat input range of interest (0.4 kJ/mm ≤ HI ≤ 1 kJ/mm) it was concluded that welds will not crack when a preheat greater than or equal to 50 °C is applied. The results generated in empirical testing suggested that for the 20 mm-thick plates, the level of intrinsic restraint applied by manipulating the MWIC restraint length had no effect on the macroscopic CNC boundary. However, as discussed in Section 6.3, the level of applied restraint influenced the type of cracking observed. In particular it was suggested that for 20 mm-thick plates under low restraint (R_F = 50 mm), although the empirical CNC boundary remained the same, there was no evidence to suggest the presence of the centreline cracks that were observed at higher levels of restraint. Sections 6.3 and 6.4 concluded that at lower heat inputs, bead eccentricity increased the prevalence of geometric cracks. A similar argument was proposed for 10 mm-thick plates, with the key differentiating factor being the empirical limits of the boundary. It was established that for thinner plates, the heat input and preheat combinations within which crack-free welds could be deposited were lower.

With the thesis having established an empirical boundary at which cracking was identified and then examined precisely where different forms of cracking manifested themselves along the CNC boundary as a result of welding conditions and parameters, this section focuses on establishing whether there is a difference in weld metal microstructure of sufficient significance to explain both the existence of the CNC boundary and the type of cracking observed.

6.5.1 Weld Metal Microstructure Analysis Sample Selection

As outlined in the literature review, the microstructure in the fusion zone of a weld is inhomogeneous and complex. Different microstructures and microstructural features influence the welds' resulting mechanical properties and thus susceptibility to cracking. Other than the type of microstructure, one key influential parameter is the grain size of a particular

microstructure. Grain size at room temperature has been reported to have a measurable effect on the mechanical properties of the weld, including, hardness, yield strength, tensile strength, fatigue strength and impact strength. It is generally accepted that these mechanical properties increase with decreasing grain size. Nevertheless, coarse grains in steel are reported to have better resistance to creep and stress rupture because grain boundary shielding which is responsible for creep failure becomes less dominant due to a lower grain boundary area.

To execute an in-depth analysis of the microstructure and its features and properties is beyond the scope of this thesis. However, as the weld metal microstructure is one of the three factors influencing HACC, it is critical to ascertain whether there are significant differences in the type of microstructures or their features observed across the derived CNC boundary.

To account for the complexity and inhomogeneity of the microstructures encountered in the fusion zone, a systematic comparison of representative weld metal samples found at the edges of the deposition envelope is carried out, as detailed in the methodology. It may be argued that given that the degree of variation between each section is minimal because of the narrow heat input range within which the welds were deposited, randomly selecting weld faces to examine would have given a better representation of the developed weld microstructures. This would be justified given that the start and end effects on the weld were minimised by the use of the V-groove run-on and run-off tabs on the MWIC test and the degree of thermal homogeneity in the test sections were verified by the similitude between the peak temperature and cooling rates, as measured by the top tracker and bottom tracker thermocouples at the entrance and exit of the test weld area respectively. Nevertheless, it is equally true that even though the welding process is assumed to be in a steady state through the entire test section, sections four of the test weld would be representative of the weld, as it is in the geometric centre of the test assembly, so analysis of the weld metal microstructure was conducted on the fourth section of each weld deposited.

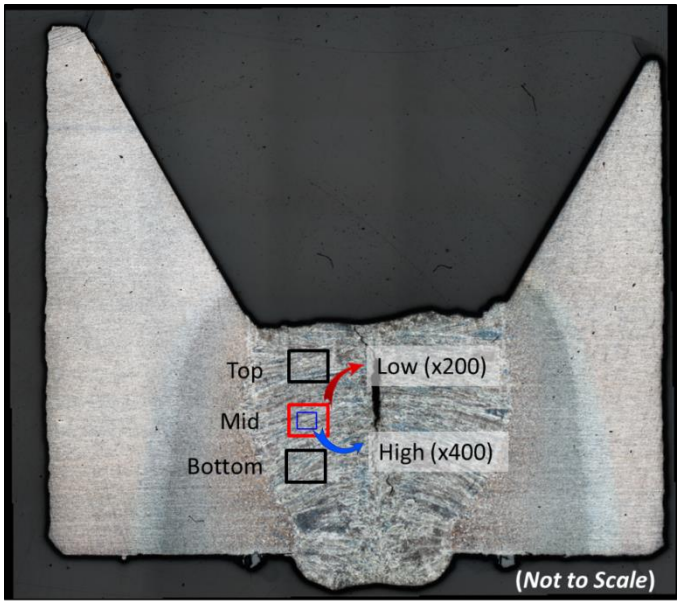

Figure 179: Micrographs with the relative position of the areas used for microstructural analysis highlighted. The microstructural analysis was carried out in three position on the fourth section of each MWIC weld sample. Six high-magnification micrographs were taken of three distinct regions within the weld metal and were used to compare qualitatively the microstructural features from samples across the CNC boundary.

The analysis of the weld metal microstructure was conducted in two stages. For each weld, after an initial examination of the entire weld sample, three representative low-magnification images and corresponding high-magnification images, as detailed in the methodology and illustrated in Figure 179 were taken and analysed to identify differences in observed microstructures. The second part of the analysis focused on identifying the microstructure through which selected cracks propagated.

It is important to recall, for this section of the analysis and discussion that the term ‘microstructural sample’ refers to the image taken mid-location in the fourth section of the each MWIC sample.

20 mm-Thick Plates

To highlight the differences in the observed weld metal microstructure, samples situated on the periphery of the deposition envelope and across the CNC boundary were selected and presented for discussion.

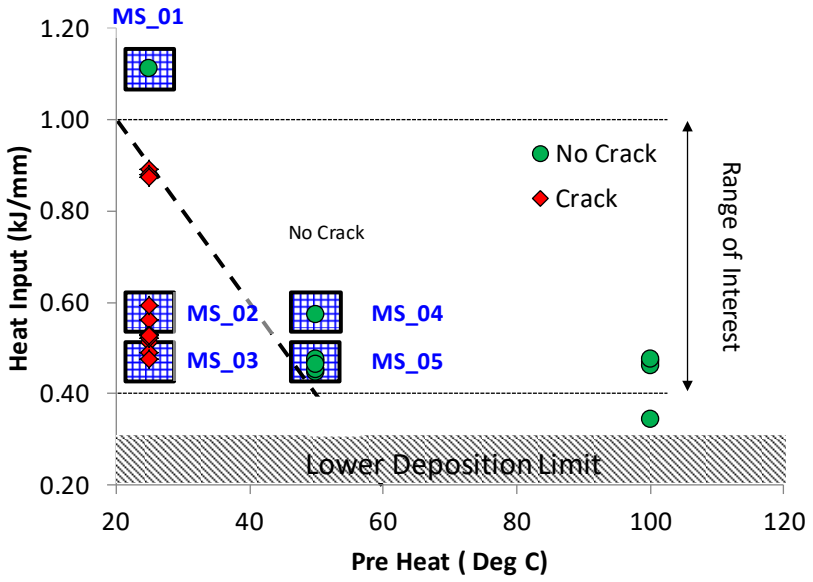

Sample	HI (kJ/mm)	Preheat (°C)
MS_01	1.11	25 °C
MS_02	0.60	25 °C
MS_03	0.51	25 °C
MS_04	0.57	50 °C
MS_05	0.45	50 °C

Figure 180: Samples from the 20 mm test series deposited under high restraint (R_F = 25 mm) selected for micromechanical characterisation.

For the 20 mm-thick plates under high restraint (R_F = 25 mm), five microstructural samples were selected from the heat input-preheat combination (see Figure 180, with parameters detailed in the embedded table). Four of the samples were within the heat input range of interest and of comparable heat input (< 0.1 kJ/mm difference in heat input) but sat on either side of the CNC boundary. MS_01 is a microstructural sample outside the heat input range of interest but was selected for discussion because it comes from the sample deposited with the highest heat input.

For the 20 mm-thick plates under low restraint (R_F = 50 mm), three microstructural samples were selected from the heat input-preheat combination (see Figure 181, with parameters detailed in the embedded table). Although all samples for this test series were within the heat input range of interest, MS_06, deposited at the upper end of range of acceptable heat inputs had no comparable sample across the CNC boundary, as it was established that for samples under lower restraint, crack-free welds could be deposited at a significantly lower heat input with a preheat of 50 °C.

MS_07 and MS_08 were situated on either side of the CNC boundary and were deposited at comparable heat inputs (< 0.1 kJ/mm difference in heat input), though MS_08 was subject to a preheat of 50 °C.

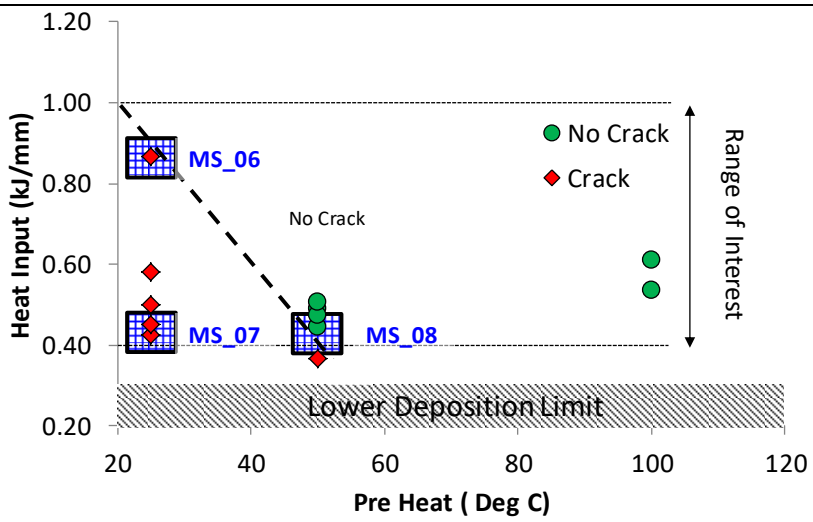

Sample	HI (kJ/mm)	Preheat (°C)
MS_06	0.87	25 °C
MS_07	0.45	25 °C
MS_08	0.49	50 °C

Figure 181: Samples from the 20 mm test series deposited under low restraint (R_F = 50 mm) selected for micromechanical characterisation.

10 mm-Thick Plates

For 10 mm-thick plates under high restraint (R_F = 25 mm), four microstructural samples were selected from the heat input-preheat combination (see Figure 182, with parameters detailed in the embedded table). The samples selected for discussion were extracted from the upper and lower limits of deposition within the heat input range of interest and sat on either side of the CNC boundary. Across the boundary, the samples selected for discussion were deposited at comparable heat inputs (< 0.1 kJ/mm difference in heat input).

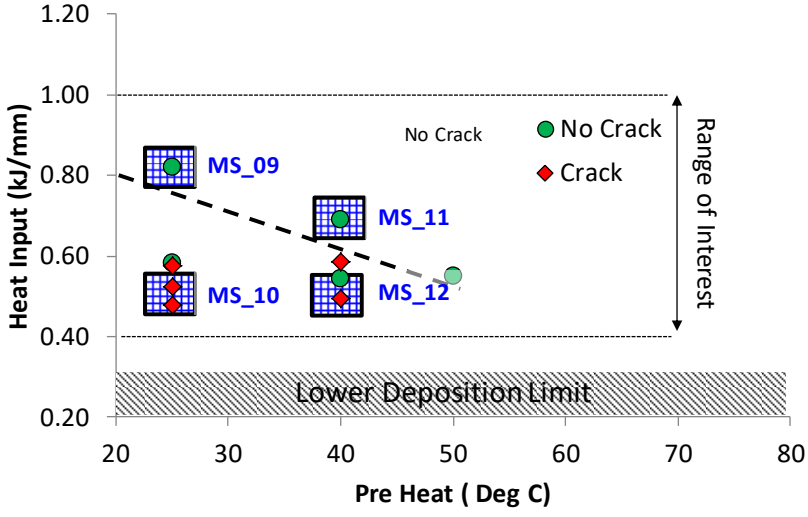

Sample	HI (kJ/mm)	Preheat (°C)
MS_09	0.82	25 °C
MS_10	0.48	25 °C
MS_11	0.69	40 °C
MS_12	0.49	40 °C

Figure 182: Samples from the 10 mm test series deposited under high restraint (R_F = 25 mm) selected for micromechanical characterisation.

As was the case for weldability tests conducted on 10 mm-thick plates under low restraint for (R_F = 50 mm), four samples were extracted from the upper and lower limits of deposition within the heat input range of interest and sat on either side of the CNC boundary (Figure 183). Across the boundary the samples selected for discussion were deposited at comparable heat inputs (0.1 kJ/mm difference in heat input).

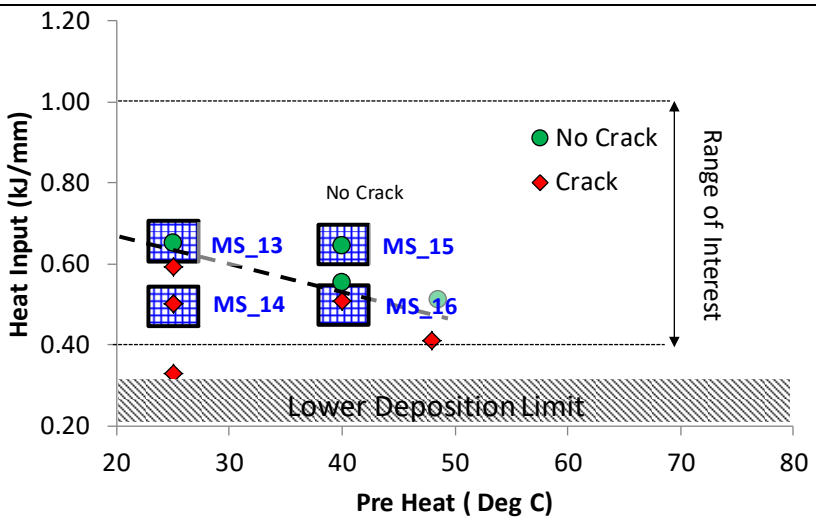

Sample	HI (kJ/mm)	Preheat (°C)
MS_13	0.65	25 °C
MS_14	0.50	25 °C
MS_15	0.64	40 °C
MS_16	0.51	40 °C

Figure 183: Samples from the 10 mm test series deposited under low restraint (R_F = 50 mm) selected for micromechanical characterisation.

6.5.2 Microstructural Trends

6.5.2.1 20 mm Samples

As detailed in Section 6.5.1, to ascertain whether the weld metal microstructure played a definitive role in influencing the characteristics of the derived CNC boundary, sections from weldability tests were prepared and analysed using the procedure detailed in Chapter 4. To highlight the apparently negligible difference in microstructure, samples selected from the edges of the deposition test envelope, as described in the previous section, are presented and discussed in the section below.

High Heat Input

The optical micrographs of MS_02 are considered representative of microstructures observed for welds deposited with heat inputs in the upper quartile of the heat input range of interest for thick plates under high restraint. As identified in Figure 184 and detailed in Figure 185, the weld microstructure consists primarily of AF and what appears to be a lesser proportion of WF and GBF.

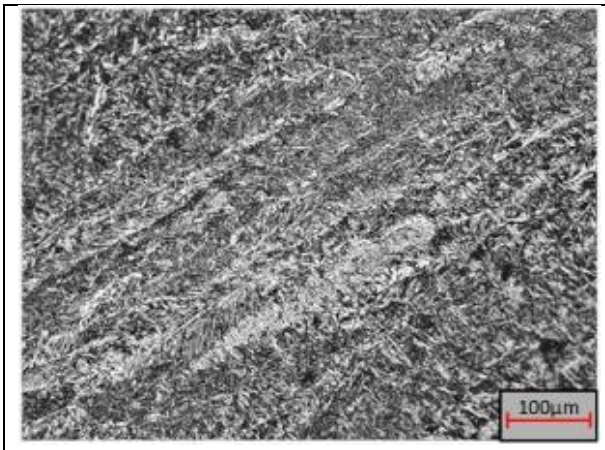

Figure 184: Low-magnification image of weld microstructural sample MS_02. The weld was deposited on a 20 mm-thick plate under high restraint with no preheat in the upper quartile of the heat input range of interest.

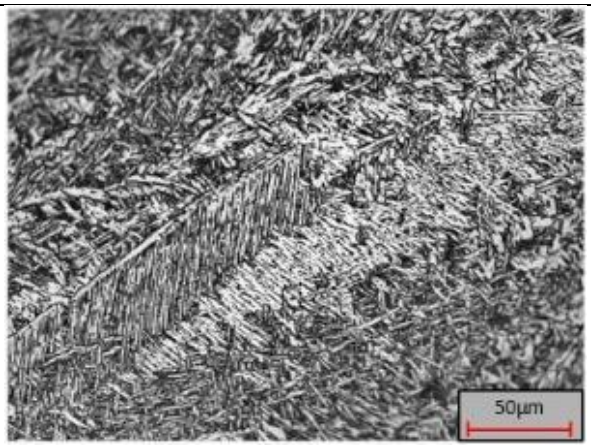

Figure 185: High-magnification image of weld microstructural sample MS_02. The weld microstructure consists primarily of AF and WF.

Figure 186: Low-magnification image of weld microstructural sample MS_04. The weld was deposited on a 20 mm-thick plate under high restraint with 50 °C preheat in the upper quartile of the heat input range of interest.

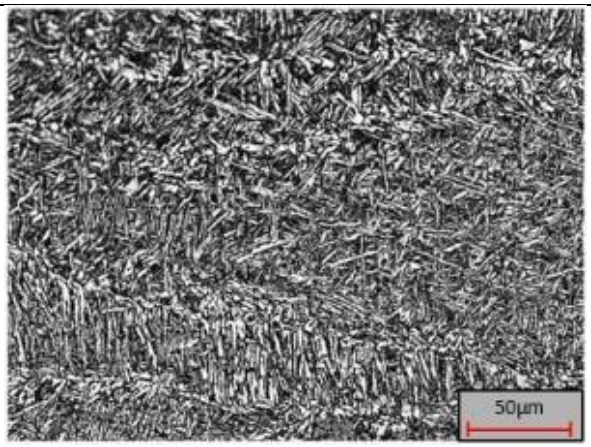

Figure 187: High-magnification image of weld microstructural sample MS_04. The weld microstructure consisted primarily of AF, with evidence of WF and GBF observed.

When compared with the micrographs for microstructural samples MS_04 (Figure 186 and Figure 187), which are considered representative of microstructures observed for welds deposited with heat inputs in the upper quartile of the heat input range of interest but at a preheat of 50 °C, there is little apparent difference in the observed weld metal microstructure. As evident in Figure 187, the weld again consists primarily of AF with little difference in the morphology of the observed grains, especially grain size and aspect ratio.

Low Heat Input

Similar observations are made for weld samples deposited in the lower quartile of the heat input range of interest on either side of the CNC boundary. The optical micrographs of MS_03 are considered representative of microstructures observed for welds deposited with heat inputs in the lower quartile of the heat input range of interest for thick plates under high restraint and in ambient conditions. As identified in Figure 188 and detailed in Figure 189, the weld microstructure consisted primarily of AF, as was observed for welds deposited at a higher heat input.

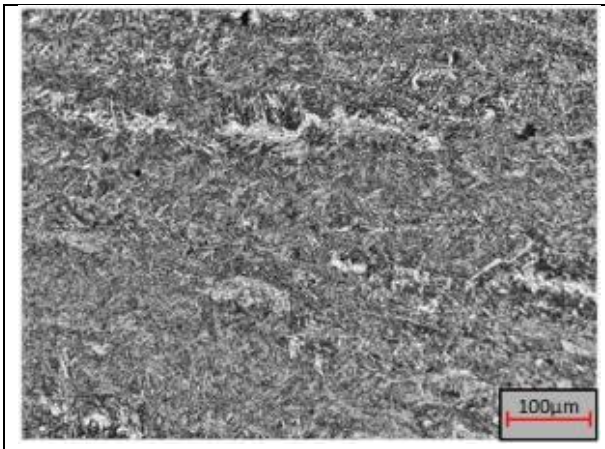

Figure 188: Low-magnification image of weld microstructural sample MS_03. The weld was deposited on a 20 mm-thick plate under high restraint with no preheat in the lower quartile of the heat input range of interest.

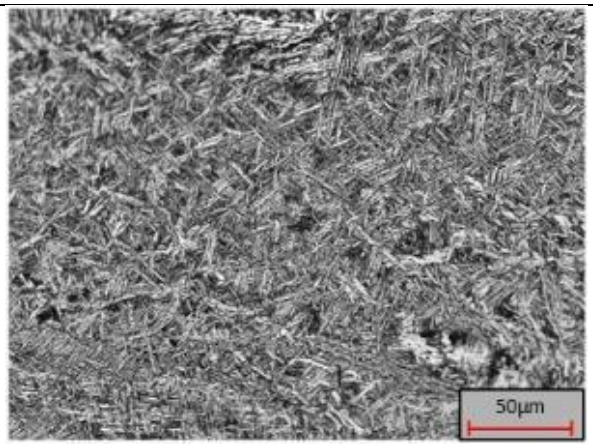

Figure 189: High-magnification image of weld microstructural sample MS_03. The weld microstructure consists primarily of AF, with evidence of WF and GBF observed.

When compared with micrographs from MS_05 (Figure 190 and Figure 191) that are representative of welds deposited under the same conditions as MS_03 except for a preheat of 50 °C, there appears to be no significant difference in the type of the microstructural constituents identified. The arguments applied for similitude between samples deposited in the upper quartile of the heat input range of interest can be extended to welds deposited in the lower quartile.

When compared to the results derived for welds deposited in the upper quartile of the heat input range of interest, the lower-quartile welds appear to have the same type of microstructures with no significant difference in the level of refinement. It may be argued that the proportion of the major microstructural constituents differs when comparing the high-magnification images from MS_03 (Figure 189) and MS_05 (Figure 191). However, the high-magnification images are used to identify the type rather than the content proportion of

microstructures. The suggestion that there is no significant difference in the proportion of major microstructural constituents identified is drawn from an analysis of the entire set of captured images.

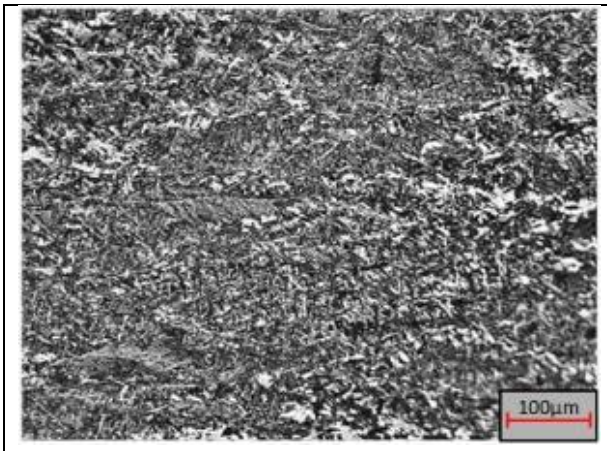

Figure 190: Low-magnification image of weld microstructural sample MS_05. The weld was deposited on a 20 mm-thick plate under high restraint with 50 °C preheat in the lower quartile of the heat input range of interest.

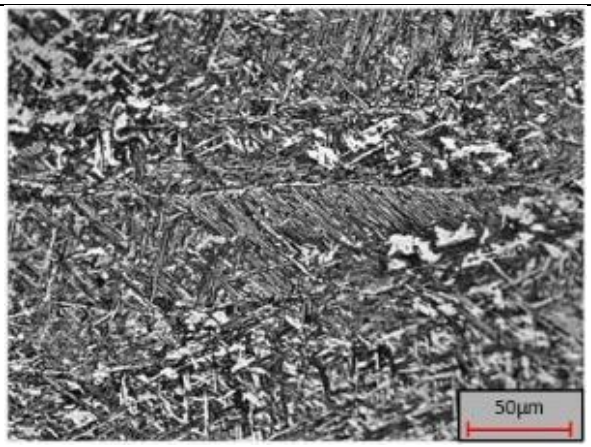

Figure 191: High-magnification image of weld microstructural sample MS_05. The weld microstructure consists primarily of AF, with WF and GBF also observed.

MS_01 represents the sample deposited outside the primary heat input range of interest. At 1.11 kJ/mm, this weld was also deposited with the highest heat input in the entire test series. Figure 192 and Figure 193 make clear that all three microstructures identified in samples deposited in the lower and upper quartiles of the heat input range of interest and under ambient conditions (25 °C) and elevated preheats (50 °C) are present in MS_01. However, a review of the micrographs taken of MS_01 show that the microstructures appear to be coarser. The proportions of AF and WF appear unchanged, though the aspect ratio of the latter's WF suggests a coarser grain structure. The islands of GBF also appear to be marginally larger, suggesting a general coarsening in the observed microstructure. This may be attributed to the welding being deposited at a higher heat input.

However, a review of the thermal data generated from the top tracker, T6 and the bottom tracker of MS_01 compared with MS_02 and MS_03, in which welds were deposited under ambient conditions on 20 mm-thick plates, revealed no discernible difference in cooling curve gradients, which may be attributable to limitations in the thermal data extraction system designed as part of this thesis.

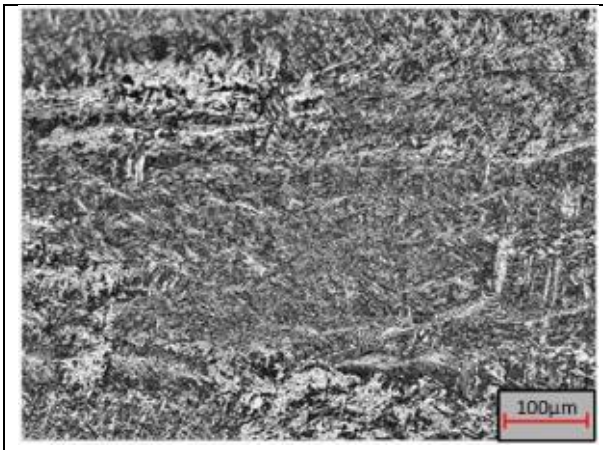

Figure 192: Low-magnification image of weld microstructural sample MS_01. The weld was deposited on a 20 mm-thick plate under high restraint with no preheat at a heat input of 1.11 kJ/mm.

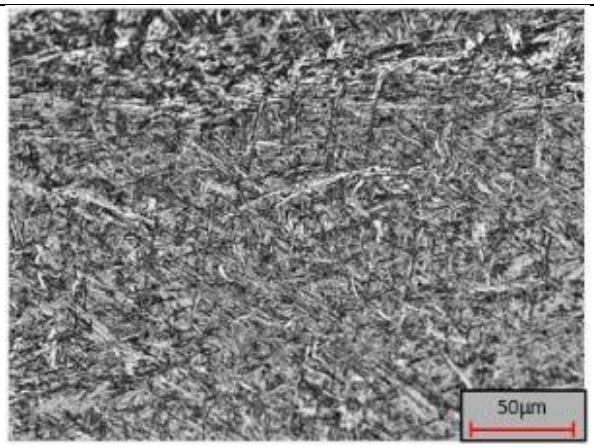

Figure 193: High-magnification image of weld microstructural sample MS_01. The weld microstructure consists primarily of AF and WF and GBF. Microstructures appear to be marginally finer than samples MS_02, MS_03, MS_04 and MS_05.

With the upper heat input limit for crack-free welds established in high restraint (R_F = 25 mm) weldability tests, lower-restraint tests were conducted with the aim of ascertaining if the CNC boundary shifted to the left, as detailed in Section 6.2.2. However, as concluded in that same section, the CNC boundary did not shift to the left as hypothesised. The empirical results generated suggested that the limits of the CNC boundary remained the same, although the type of cracking differed, as detailed in Section 6.3. As suggested above, a change, especially a downward change, in the level of restraint did not change the limits of the CNC boundary but did lead to a lower propensity for centreline cracking to manifest. To assess the role of microstructure in the type of cracking observed, the microstructures along selected cracks were identified; they are assessed later in this chapter, but the dominant microstructural phases observed in the bulk of the sample must be identified first.

For 20 mm-thick plates welded under lower restraint (R_F = 50 mm), only three ROIs were identified for analysis, because as part of the empirical testing sequence, no weldability testing was conducted in the upper quartile of the heat input range of interest at elevated preheats, as crack-free welds were identified in the lower quartile heat input of interest under elevated preheats. As the primary objective was to delineate a boundary within which crack-free welds could be deposited, testing in the upper quartile was deemed to be an unnecessary use of resources.

MS_06 is representative of microstructures observed for welds deposited at heat inputs in the upper quartile of the heat input range of interest for thick plates under low restraint and in

ambient conditions (Figure 194 and Figure 195). As was true of samples deposited under similar welding parameters but high restraint, the welds were observed to consist primarily of AF, with a smaller proportion of WF and GBF.

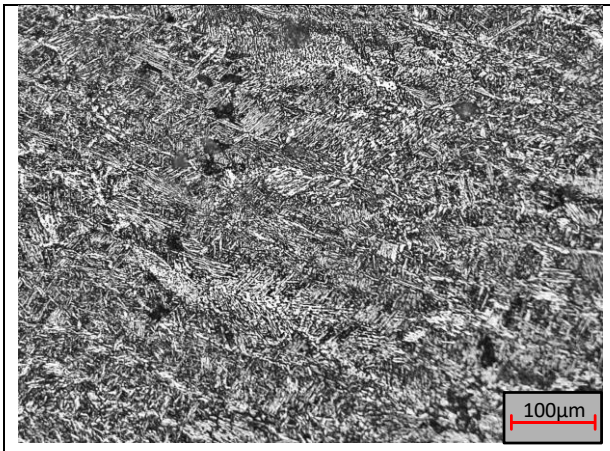

Figure 194: Low-magnification image of weld microstructural sample MS_06. The weld was deposited on a 20 mm-thick plate under low restraint with no preheat in the upper quartile of the heat input range of interest.

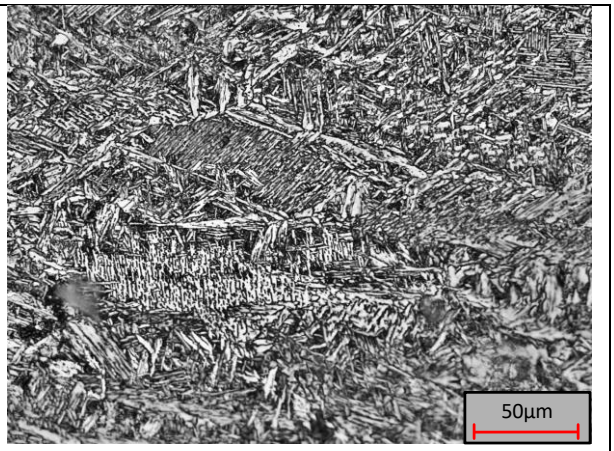

Figure 195: High-magnification image of weld microstructural sample MS_06. The weld microstructure consists primarily of AF, WF and GBF.

However, for samples deposited in the lower quartile of the heat input range of interest (Figure 196 and Figure 197), the welds appear to have a lower proportion of AF and greater proportions of WF and GBF. This is similar to welds deposited in MS_08 (Figure 199 and Figure 200), which is representative of welds deposited in the lower quartile of the heat input range of interest with a preheat of 50°C.

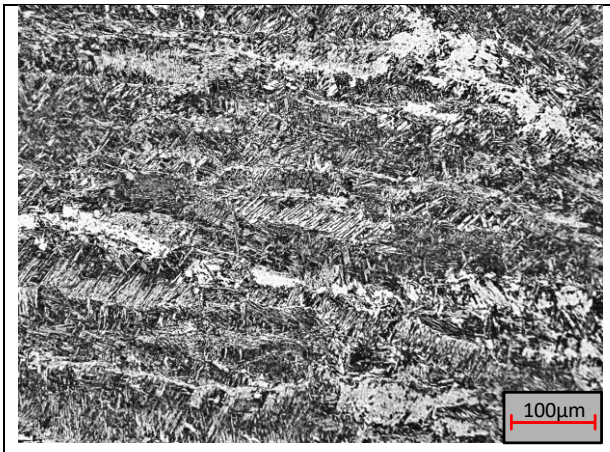

Figure 196: Low-magnification image of weld microstructural sample MS_07. The weld was deposited on a 20 mm-thick plate under low restraint with no preheat in the lower quartile of the heat input range of interest.

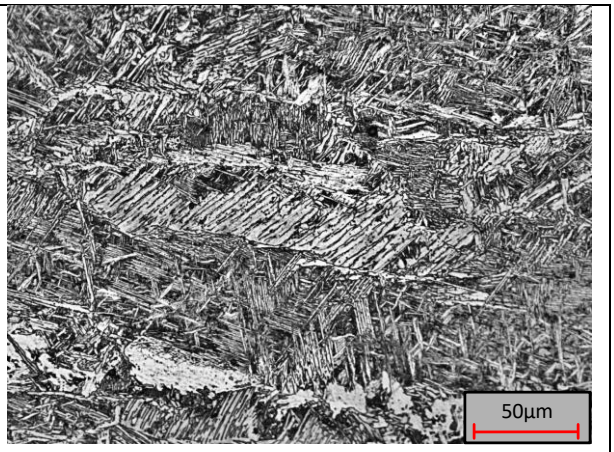

Figure 197: High-magnification image of weld microstructural sample MS_07. The weld microstructure consists primarily of AF, WF and GBF.

It is critical to note that the difference in heat input for samples deposited in the lower quartile of the heat input range of interest between high-restraint (MS_03 and MS_05) and low-restraint samples (MS_07 and MS_08) was 0.06 kJ/mm for samples deposited under ambient conditions and 0.04 kJ/mm for samples deposited with an elevated preheat of 50 °C. This nearly negligible difference in heat input was not expected to result in an appreciable difference in the observed weld metal microstructure.

The change in restraint conditions with the MWIC samples for a given test sample thickness is governed solely by the restraint length, which, as detailed in the literature review, is altered by changing the length of the anchor welds. The effects of a change in the length of the welds on cooling characteristics of the weld sample was determined as being negligible, as detailed in the Chapter 5. Therefore, the nearly negligible change in heat input coupled with the nearly negligible change in thermal characteristics of the MWIC sample under both high and low restraints should not yield any significant changes in the observed microstructures. The differences in those microstructures, especially in their relative content proportions, may simply be attributable to the expected variability as a result of the microstructural section selection.

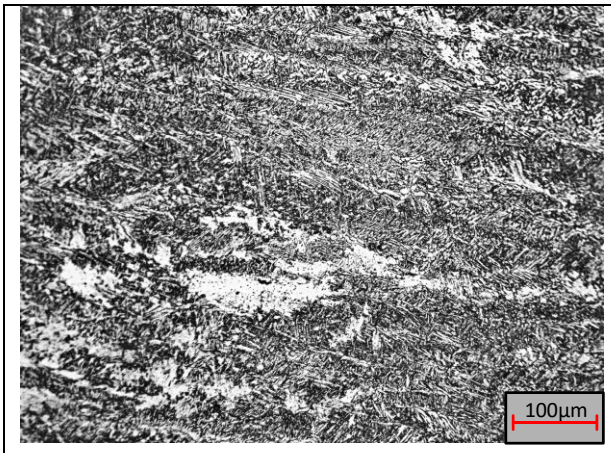

Figure 198: Low-magnification image of weld microstructural sample MS_08. The weld was deposited on a 20 mm-thick plate under low restraint with a preheat of 50 °C in the lower quartile of the heat input range of interest.

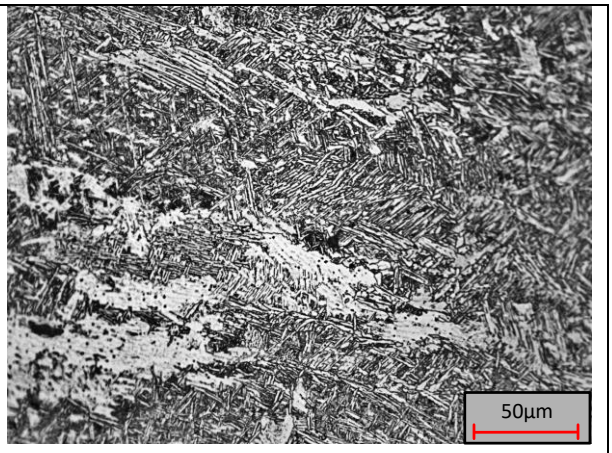

Figure 199: High-magnification image of weld microstructural sample MS_08. The weld microstructure consists primarily of AF, WF and GBF.

6.5.2.2 10 mm Samples

High Heat Input

Optical micrographs of MS_09 and MS_11 are representative of microstructures observed for welds deposited with a heat input in the upper quartile of the heat input range of interest for thin plates (10 mm) under high restraint (R_F = 25 mm) at preheats of 25 °C and 40 °C respectively. As illustrated in Figure 200 and detailed in Figure 201, with a preheat of 25 °C, the weld metal microstructure appears optically similar to MS_02. The samples appear to consist primary of AF and WF.

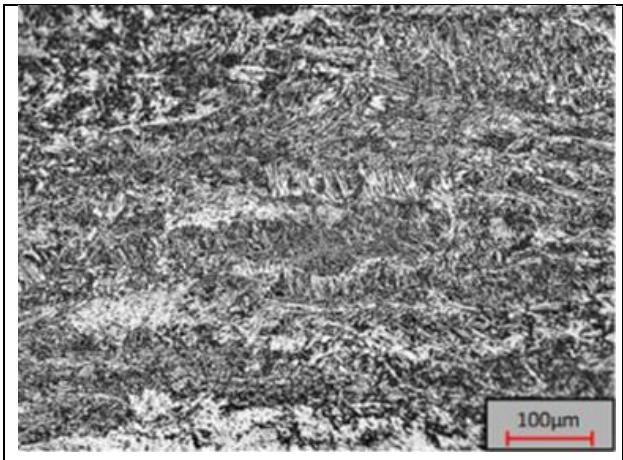

Figure 200: Low-magnification image of weld microstructural sample MS_09. The weld was deposited on a 10 mm-thick plate under high restraint with no preheat in the upper quartile of the heat input range of interest.

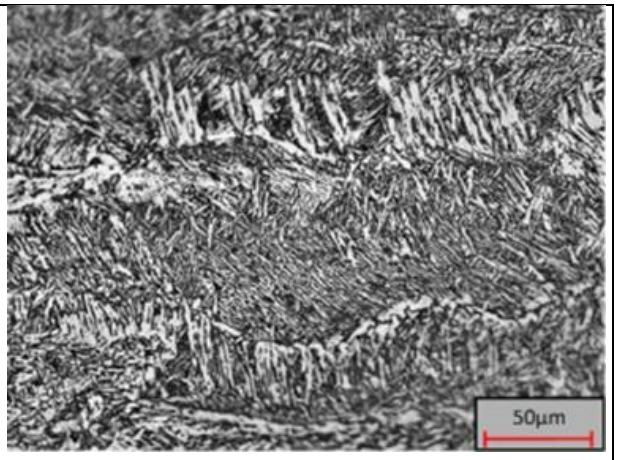

Figure 201: High-magnification image of weld microstructural sample MS_09. The weld microstructure consists primarily of AF and WF.

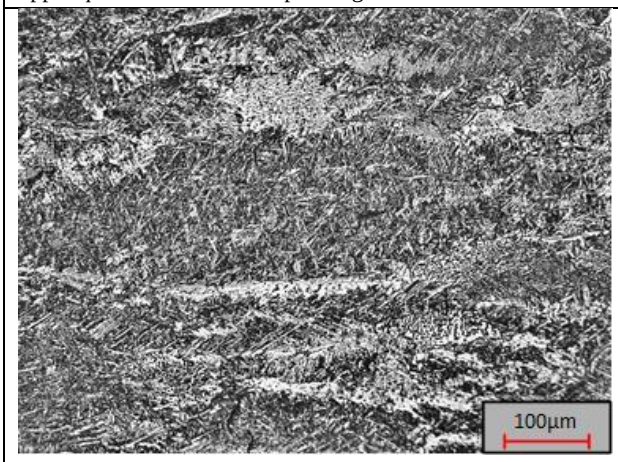

Figure 202: Low-magnification image of weld microstructural sample MS_11. The weld was deposited on a 10 mm-thick plate under high restraint with a preheat of 40 °C in the upper quartile of the heat input range of interest.

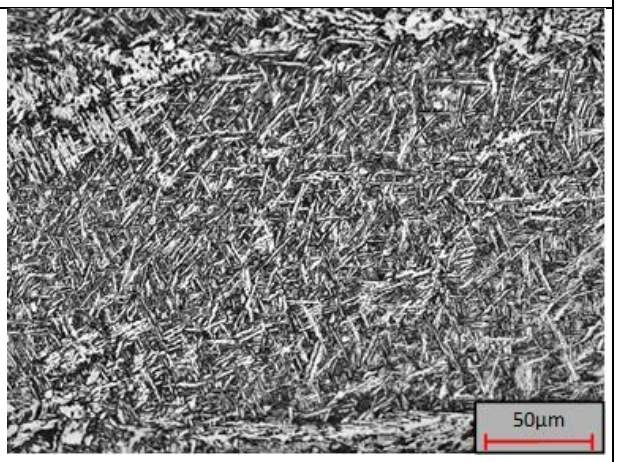

Figure 203: High-magnification image of weld microstructural sample MS_11.

When considering the micrographs from MS_11, which were deposited with a similar heat input but with a preheat of 40 °C (Figure 202 and Figure 203), there appeared to be no significant difference in the observed microstructures. This is similar to the conclusions drawn when observing the samples from various heat inputs of the 20 mm data set. As also

observed in the 20 mm data set, the lower restraint level did not appear to have any effect on the observed microstructure for welds deposited in the upper quartile of the heat input range of interest. Figure 204 and Figure 205 outline and detail the microstructural morphologies representative of welds deposited on the 10 mm samples under low restraint in the upper quartile heat input of interest with a 25 °C preheat, while Figure 206 and Figure 207 are representative of the microstructural morphologies observed for welds deposited under similar conditions but with a 40 °C preheat.

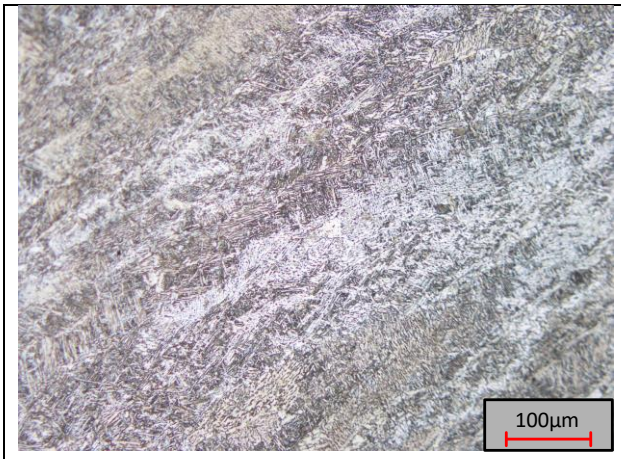

Figure 204: Low-magnification image of weld microstructural sample MS_13. The weld was deposited on a 10 mm-thick plate under low restraint with no preheat in the upper quartile of the heat input range of interest.

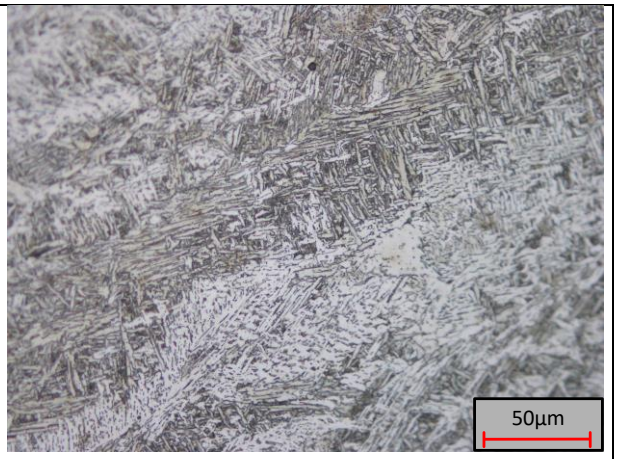

Figure 205: High-magnification image of weld microstructural sample MS_13.

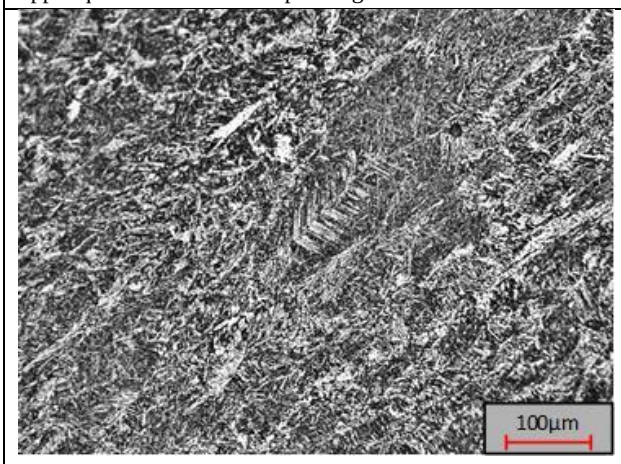

Figure 206: Low-magnification image of weld microstructural sample MS_15. The weld was deposited on a 10 mm-thick plate under low restraint with a preheat of 40 °C in the upper quartile of the heat input range of interest.

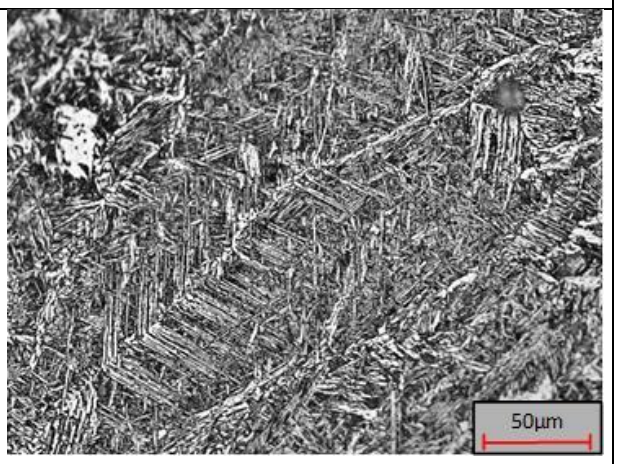

Figure 207: High-magnification image of weld microstructural sample MS_15.

For the 10 mm sample set, microstructural morphologies and features appear to be similar regardless of the level of preheat and restraint level for the welds deposited in the upper quartile of the heat input range of interest.

Low Heat Input

Optical micrographs of MS_10 and MS_12 are representative of microstructures observed for welds deposited with a heat input in the lower quartile of the heat input range of interest for thin plates (10 mm) under high restraint (R_F = 25 mm) at preheats of 25 °C and 40 °C as seen in Figure 208 & 207 and Figure 210 & 209 respectively. Like the samples from the upper quartile of the heat input range of interest, the difference in heat input between the preheated sample and the sample deposited under ambient conditions was less than 0.15 kJ/mm.

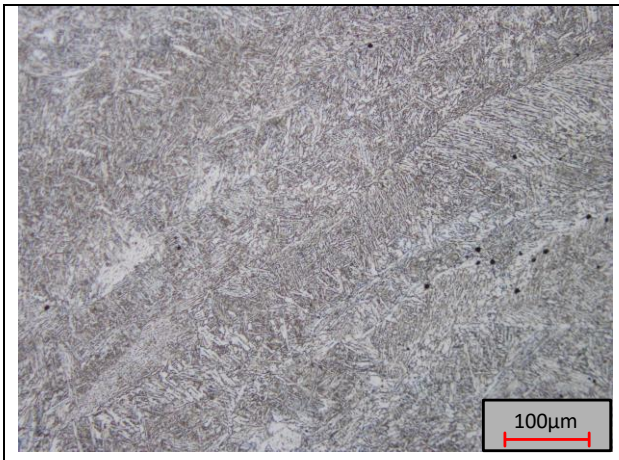

Figure 208: Low-magnification image of weld microstructural sample MS_12. The weld was deposited on a 10 mm-thick plate under high restraint with a 40°C preheat in the lower quartile of the heat input range of interest.

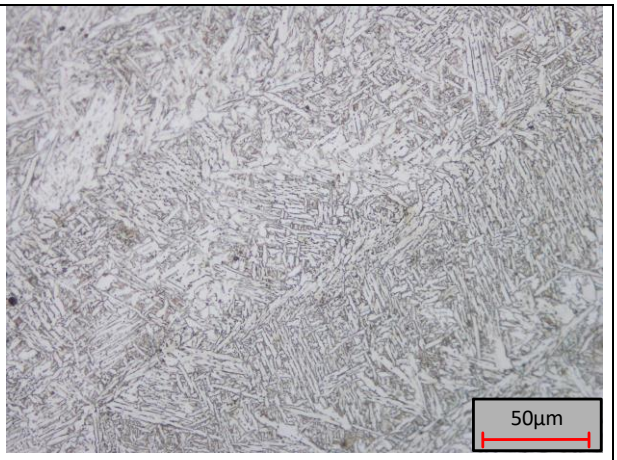

Figure 209: High-magnification image of weld microstructural sample MS_12.

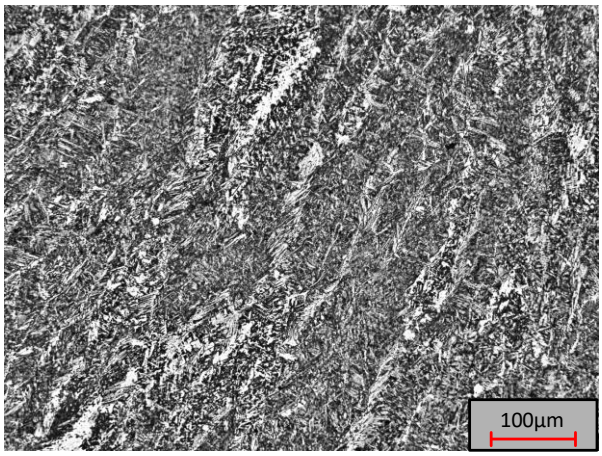

Figure 210: Low-magnification image of weld microstructural sample MS_10. The weld was deposited on a 10- mm-thick plate under high restraint with no preheat in the lower quartile of the heat input range of interest.

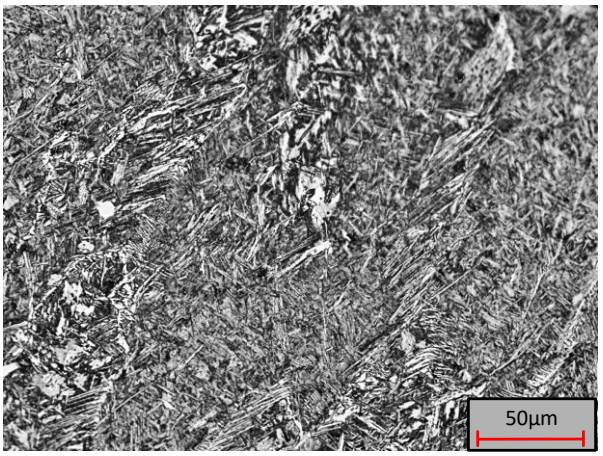

Figure 211: High-magnification image of weld microstructural sample MS_10.

When considering the samples deposited in the lower quartile of the heat input range of interest (MS_14 and MS_16) under ambient conditions (Figure 212 and Figure 213) and with

a preheat of 40 °C (Figure 214 and Figure 215), the micrographs suggest that, as with the 10 mm samples, no significant difference is apparent in the observed microstructural morphologies.

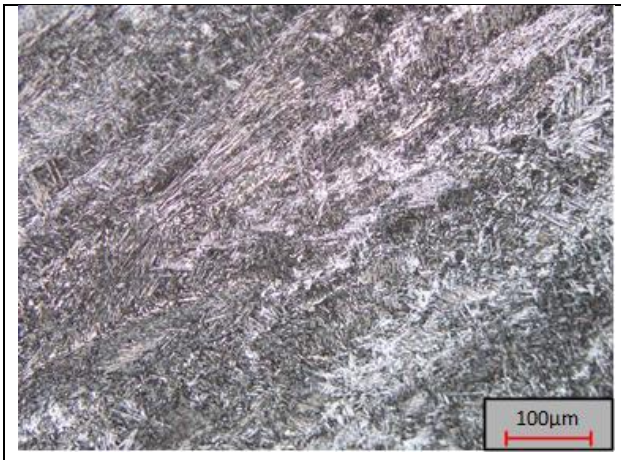

Figure 212: Low-magnification image of weld microstructural sample MS_14. The weld was deposited on a 10 mm-thick plate under low restraint with no preheat in the lower quartile of the heat input range of interest.

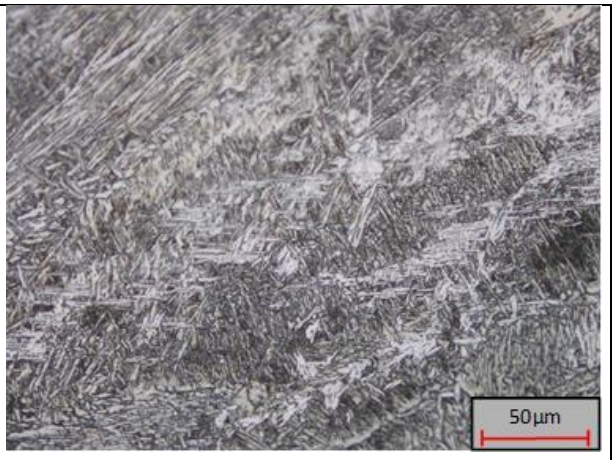

Figure 213: High-magnification image of weld microstructural sample MS_14.

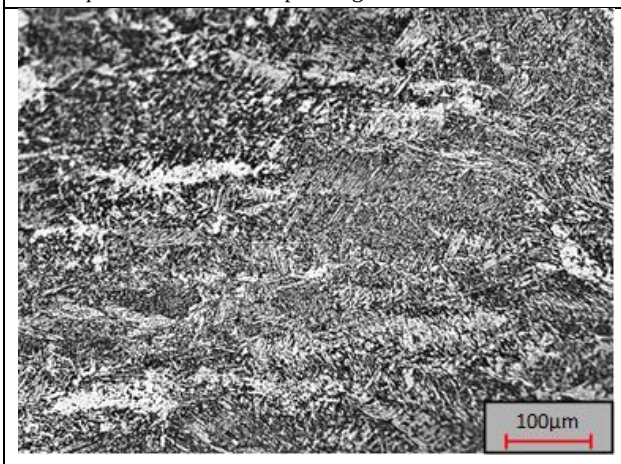

Figure 214: Low-magnification image of weld microstructural sample MS_16. Weld deposited on a 10 mm-thick plate under low restraint with a preheat of 40 °C preheat in the lower quartile of the heat input range of interest.

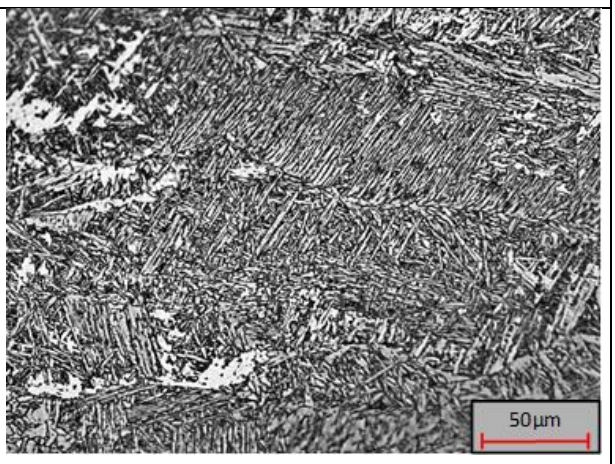

Figure 215: High-magnification image of weld microstructural sample MS_16.

6.5.3 Microstructure along Crack Paths

As highlighted above, a review of the 20 mm and 10 mm samples from both sides of the derived cracking boundary revealed no apparent differences in the observed microstructural constituents, especially the proportions of particular morphologies. Hence, the microstructures were similar across the cracking boundary and did not play any observable role in cracking susceptibility or the position of the CNC.

Given the minimal variation in the heat input range of interest within which testing was conducted and the fact that testing was conducted on single parent plate and electrode chemistry combinations, this conclusion conforms with the expectations laid out in the literature review. Although the bulk microstructures have been shown to be similar, it is important to recall that three distinct crack types were identified in the 20 mm and 10 mm samples and that the literature review identified particular microstructural morphologies as more susceptible to crack propagation than others.

To ascertain if a given microstructure was particularly susceptible one of the three identified crack types—geometric, micro-crack and centreline—the microstructure along cracks paths identified in the 20 mm and 10 mm samples were examined.

Geometric Cracks

Geometric hydrogen cracks originated from stress concentrators introduced by the shape of the deposited weld beads. Typically, these stress concentrators were observed to be predominantly wagon tracks, with some mild undercut. The cracks originating from macroscopic stress concentrators (Figure 216 and Figure 217) were typically wider than the hydrogen micro-cracks but not as wide as the centreline cracks. Additionally, a greater proportion of geometric cracks were observed in the lower quartile of the heat input range of interest. When examining the microstructure along crack paths in both the 20 mm and 10 mm samples, there was qualitative visual evidence to suggest that the crack propagated through all the observed morphologies. From the samples examined there was also no evidence to suggest that a crack path was determined or influenced by the microstructure through which it propagated. For geometric cracks, especially in terms of width (Figure 214 and Figure 215), the crack path appears to be independent of the local microstructure through which it propagates. However the way the crack propagates through each individual phase vary and is beyond the scope of this body of work. The intricacies of hydrogen crack propagation paths are explored in a detailed study by Costin [296].

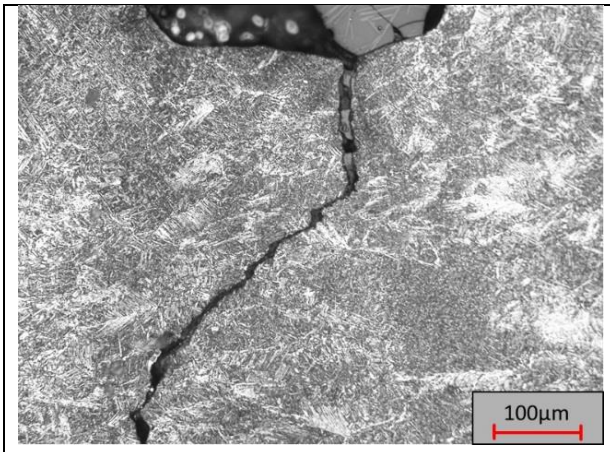

Figure 216: Low-magnification micrograph of a typical geometric hydrogen crack and the observed microstructural morphologies along the crack path.

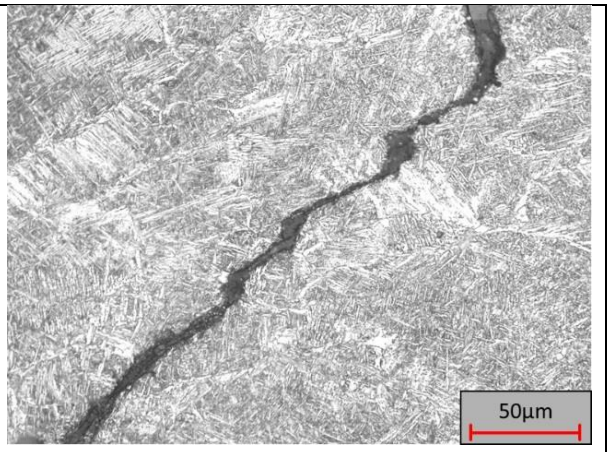

Figure 217: High-magnification micrograph of a geometric hydrogen crack, highlighting the typically observed microstructural morphologies along the crack path.

Micro-cracks

Unlike the geometric cracks, the observed micro-cracks (Figure 218 and Figure 219) were significantly thinner. Moreover, there was no evidence to suggest that the micro-cracks had a common initiation site or condition, whereas the geometric cracks all originated from a geometric defect in the weld toe. However, like geometric cracks, the micro-cracks were transverse in nature. In considering the orientation and the propagation paths of the micro-cracks in relation to the local weld metal microstructure, there is no evidence to suggest a preferential crack path trajectory, though the cracks path can be described as tortuous, unlike geometric cracks that exhibited a more pronounced direct crack path with only the occasional kink.

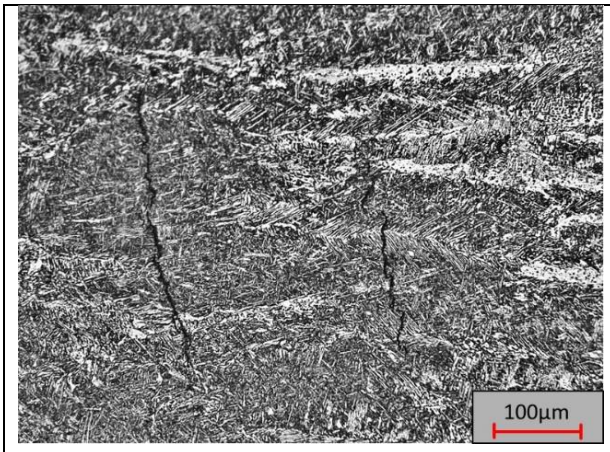

Figure 218: Low-magnification micrograph of a typical hydrogen micro-crack and the observed microstructural morphologies along the crack path.

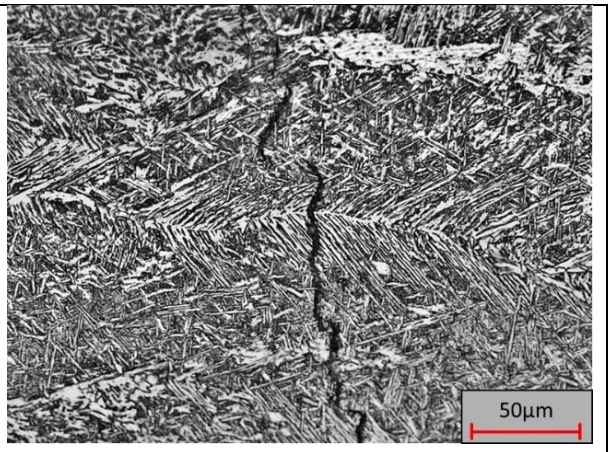

Figure 219: High-magnification micrograph of a hydrogen micro-crack, highlighting the typically observed microstructural morphologies along the crack path.

Centreline Cracks

The observed centreline cracks were manifested in a significantly larger range of widths and lengths than geometric cracks and micro-cracks. Centreline cracks were observed only in close proximity to the geometric centre of the deposited weld bead, but centreline crack paths' (Figure 220 and Figure 221) were observed to be both tortuous and kinked. From a qualitative analysis of the micrographs of both the 20 mm and 10 mm data sets at both high and low restraints, there is no evidence to suggest that the centreline cracks propagated preferentially through a single particular morphology. Figure 220 and Figure 221 are low- and high-magnification images of a typical centreline crack, which propagates through the grain structure in the centre of the bead, regardless of the microstructural constituents.

Figure 220: Low-magnification micrograph of a typical centreline crack and the observed microstructural morphologies along the crack path.

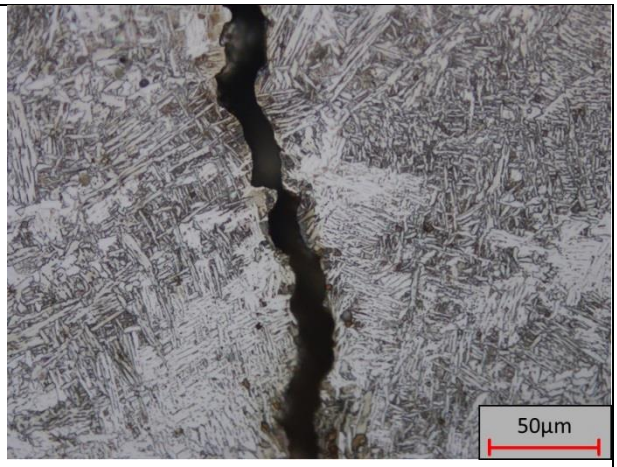

Figure 221: High-magnification micrograph of a centreline crack, highlighting the typically observed microstructural morphologies along the crack path.

The ends of the centreline cracks were in several cases distinctly different from the midsections of those cracks. Crack ends can be differentiated in terms of width and crack progression trajectory, with the ends appearing consistently thinner and much more visually similar to micro-cracks. Examination of the etched images of the crack ends showed that, although the crack path appears in some cases to weave intricately through different microstructural morphologies, there was insufficient qualitative evidence to suggest that the crack path trajectory can be correlated to a particular microstructural morphology.

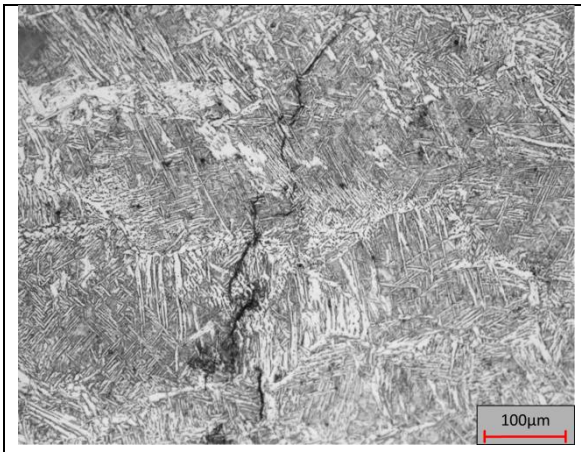

Figure 222: Low-magnification micrograph of the typical microstructure observed at crack tips predominantly in geometric and micro-cracks.

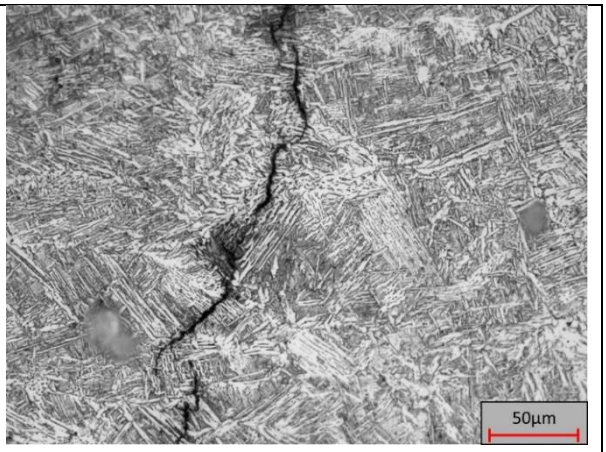

Figure 223: High-magnification micrograph of a typical microstructure observed at crack tips predominantly in geometric and micro-cracks.

6.5.4 Relationship between Crack Path and Weld Metal Microstructure

A qualitative review of the microstructure along crack paths revealed that regardless of the type of cracking observed (geometric, micro-crack or centreline), no definitive correlation could be defined between crack path trajectory and weld metal microstructural morphology. This observation applied to both the 20 mm and 10 mm data sets.

It has been established that AF improves the toughness of the weld metal and thus resistance to cold cracking. A review of the micrographs taken along the crack paths for samples from both the 20 mm and 10 mm data sets established that AF was the most predominant microstructure observed in the samples produced in this study.

A qualitative review of the crack paths suggested that the propagation route in some samples appeared to be influenced locally by the microstructural morphology encountered by the crack tip. Especially when considering the propagation of cracks through AF, which was the most commonly observed morphology in both sample sets, several cracks appeared to blunt during propagation across the fine AF and then branch into multiple micro-cracks in the vicinity of the primary crack. This may be a result of the fine interlocking nature of AF [22]. The scope of this thesis, however, is limited to microstructural analysis along the crack path and a qualitative visual analysis conducted using optical microscopy.

Although these is no conclusive evidence based on the analysis conducted to suggest that either cracking in general or one type of cracking was influenced by a single microstructural morphology, there is some evidence to suggest that the intricacies of the local trajectories of

micro-cracks and the ends of centreline cracks may have been influenced in part by the local weld metal microstructure. It is therefore suggested that a quantitative analysis, measuring the angular displacement of crack paths and the grain boundary misorientation of the local microstructural morphology be undertaken to ascertain if a positive correlation can be derived.

6.5.5 **Concluding Remarks**

6.5.5.1 Observed microstructures

The polished samples etched with 2% Nital and examined under an optical microscope revealed that the observed microstructural constituents consisted primarily of AF with small fractions of ferrite with aligned side plates or WF and GBF. Within the heat input range of interest, a visual review of the optical micrographs provided evidence to suggest that the identified morphologies were comparable on both sides of the deposition boundary.

6.5.5.2 Variation in microstructure along the transverse axis of the sample

As illustrated by Figure 224, several micrographs taken along the transverse axis of the weld highlight the variability in observed microstructures for a single weld. Especially in the case of higher-magnification images that are representative of the weld in question, not all observed micrographs may be presented in the image; for the purposes of brevity, only a select number of images were presented.

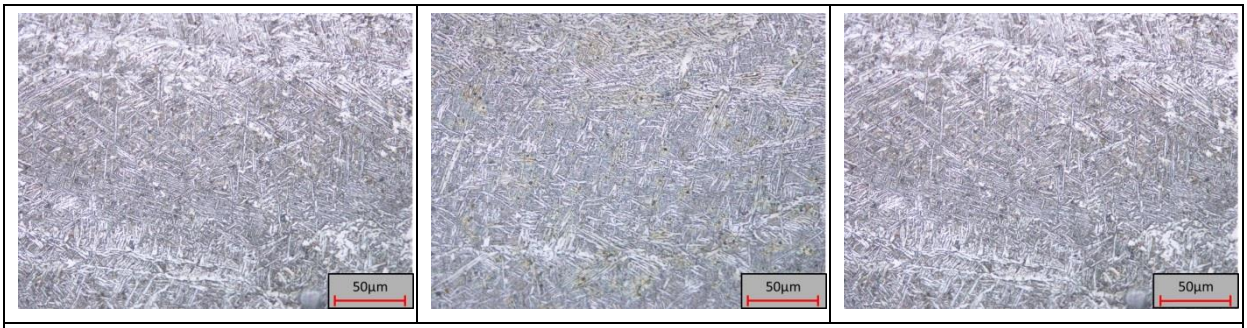

Figure 224: Micrographs of sections 1, 3 and 6 (left to right) taken along the transverse axis of sample MS_02.

For the studies conducted within the scope of this work it is apparent that weld metal microstructure does not change sufficiently to alter the susceptibility to WMHACC.

6.5.5.3 Role of heat input and preheat on observed microstructures

The effect of heat input on the type, morphology and proportion of microstructures within the heat input range of interest across the CNC boundary appears to be insignificant. As expected and as demonstrated by the results, in welds deposited with comparable heat inputs under comparable conditions, the resulting weld microstructures do not differ significantly. In the case of microstructural samples MS_02 and MS_04, the only significant measured difference between the deposition conditions was the addition of a preheat of 50 °C for MS_04. Though it is universally accepted that the application of preheat alters the thermal cycle of a weld, two questions must be addressed: which portions of the weld's thermal cycle will be affected by the addition of preheat and what magnitude of change in the preheat level will result in changes of sufficient significance to the weld's thermal cycle to influence solidification characteristics and solid-state transformations? The preheat levels for the samples in this thesis were 25 °C and 50 °C. Experimentally, welds deposited on parent plates with temperatures of 25 °C, 50 °C and even 100 °C in this study showed no significant difference in the critical cooling time, $t_{8/5}$; the measured difference in cooling time averaged ± 0.5 seconds, and that difference may be attributed to experimental scatter, introduced as a result of limitations of the lancing system used to plunge the thermocouple into the molten pool to extract the weld centreline's thermal cycle.

There is sufficient evidence in the literature to suggest that a change in preheat significantly affects the lower portion of a weld's thermal cycle. This is expected, as it has been shown that the rate of heat loss is proportional to the temperature gradient imposed by the boundary conditions, and preheats are generally restricted to temperatures well below the AC_3 temperature. The reason for that restriction is that preheats are generally applied to increase the t_{100} time and allow sufficient time for hydrogen to effuse out of the weld and mitigate the risk of hydrogen cracking. Therefore, as long as the temperature of the work piece is kept sufficiently high to keep hydrogen mobile, additional energy applied to the work piece is inefficient both economically and from a thermal perspective. Theoretically, then, the application of preheat does not influence the type of microstructure that evolves.

The magnitude of preheat applied in this study changed the plate temperatures by a minimum of 25 °C and a maximum of 50 °C. Cola [197], Lazor [31] and Noble and Pargeter [199] applied similar levels of preheat on traditional WIC specimens, although the steels and heat

inputs used were different. All authors reported no correlation between the $t_{8/5}$ and preheating and a positive correlation between the t_{100} and preheating.

With no significant differences observed in the type of microstructures, nor any substantial difference recorded in the critical cooling rate, it is reasonable to suggest that, based on the level of analysis conducted, samples across the boundary in the upper quartile of the heat input range of interest showed no appreciable difference in the type of microstructures or in their characteristic features. A similar argument can be extended to welds on either side of the CNC boundary for welds deposited in the lower quartile of the heat input range of interest.

6.5.5.4 Role of weld metal microstructure on cracking susceptibility

Generally speaking, the risk of HACC increases with increasing strength or hardness [28, 34, 228]. However, there is no consensus as to what particular aspect of a weld metal microstructure makes it more susceptible to cold cracking. As summarised by Davidson [223], a number of authors have suggested that it is the specific microstructure used to achieve strength which will have a greater influence on HE than on strength level *per se*. Additionally, neither hardness nor strength are reliable indicators of cold cracking susceptibility.

For both the 20 mm and 10 mm MWIC sample sets, the weld metal microstructure consisted primarily of AF, which are known to have superior mechanical properties than steel weld metals containing higher fractions of ferrite side plates or GBF [56, 73, 97, 180, 297]. This can be attributed to the high degree of misorientation between grain boundaries inherent in AF's morphology. AF's microstructure is also known to be ductile and to have a relatively finer grain structure than other morphologies [73]. AF's fine, needle-like structure improves resistance to cleavage-type crack propagation. As a cleavage fracture in ferrite occurs along (100) planes, a fracture must change direction when it crosses a high-angle boundary between adjacent grains of AF. The smaller grain size and consequently intricate fracture path provide a relatively greater resistance to a propagating crack than other weld metal microstructural morphologies.

Qualitatively, the apparent proportion of AF was comparable across the cracking boundary for both the 20 mm and 10 mm sample sets, and the samples from both sets appeared to consist primarily of AF across both sides of the CNC boundary. Hence, from a

microstructural perspective there is evidence to suggest that all the samples shared a similar degree of inherent resistance to hydrogen cracking.

The samples were also observed to have GBF, which has been associated with hydrogen cracking by numerous authors, as summarised in a review by Davidson [100]. Allen et al. [298] hypothesised that cracking along the prior austenite grain boundaries initiated at GBF. Allen et al. [298] postulated that the ductility of GBF is reduced by hydrogen, but did not offer any description of the mechanism by which this occurs. Matsuda et al. [299], on the other hand, suggested that carbon expelled from pro-eutectoid ferrite during the phase transformation from austenite segregates to the grain boundaries, making them more susceptible to cold cracking. It has been suggested that segregated carbon generally increases the strength of the grain boundaries, though high levels can weaken the boundary [55]. For both the 20 mm and 10 mm data sets, the cracked samples did not appear to have a greater proportion of GBF or evidence to suggest that observed hydrogen cracks propagated preferentially thought GBF.

6.5.5.5 Non-Metallic Inclusions

In addition to the major observed microstructural morphologies, there was evidence to suggest the presence of micro-constituents like NMIs and retained austenite. NMIs play a dichotomous role in a weld susceptibility to HACC. On the one hand, they serve as hydrogen traps, and their presence and distribution serve as a means of reducing the net hydrogen content available for diffusion into a potential initiation site. On the other, NMIs may actually serve as hydrogen crack initiation sites themselves. Large, acutely shaped NMIs create an interface in which hydrogen can be trapped and the particle itself serves as a stress concentrator and consequently a potential initiation site for a hydrogen crack [65, 123, 300].

Several samples from the 20 mm data set were examined under an electron microscope. Backscatter electron micrographs revealed that the NMIs ranged in size from 200 nm to 2 µm, as shown in Figure 225. The distribution of NMIs ranged from random to aligned, as demonstrated in Figure 226, Figure 227 and Figure 228.

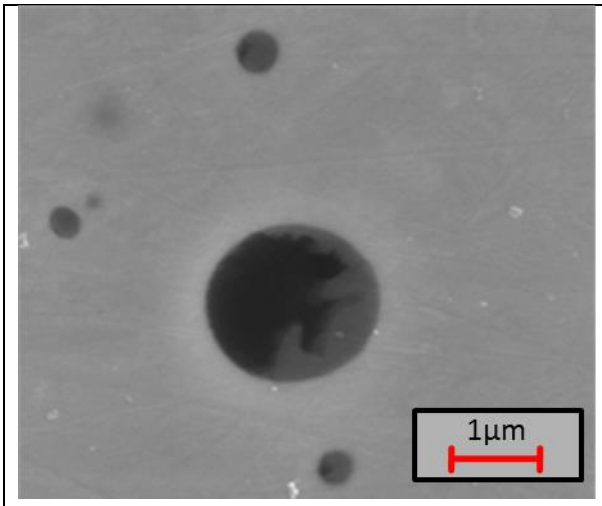

Figure 225: Range of NMI diameters found in the MWIC specimen.

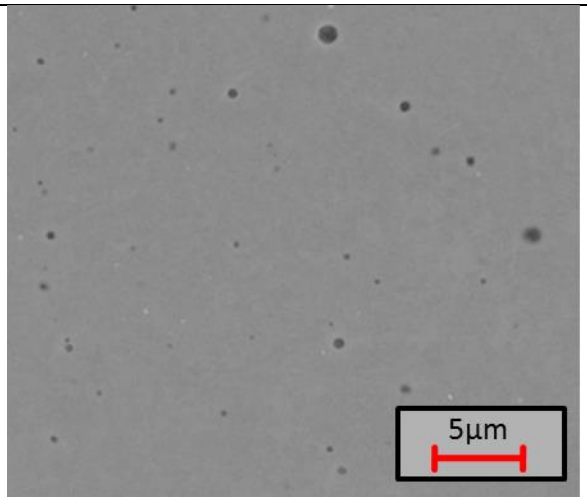

Figure 226: Random distribution of NMIs.

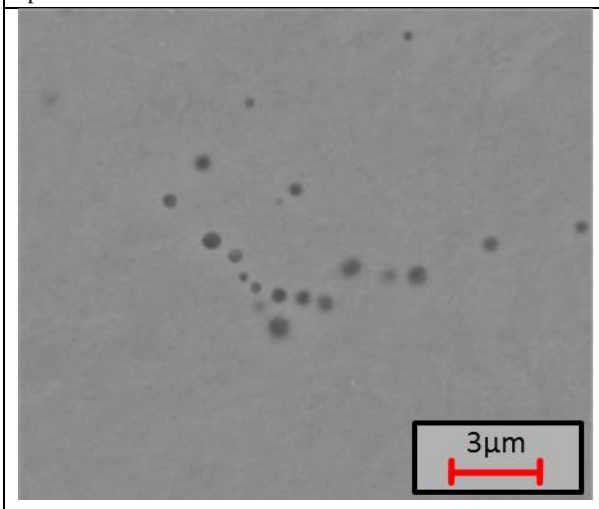

Figure 227: Agglomeration of NMIs.

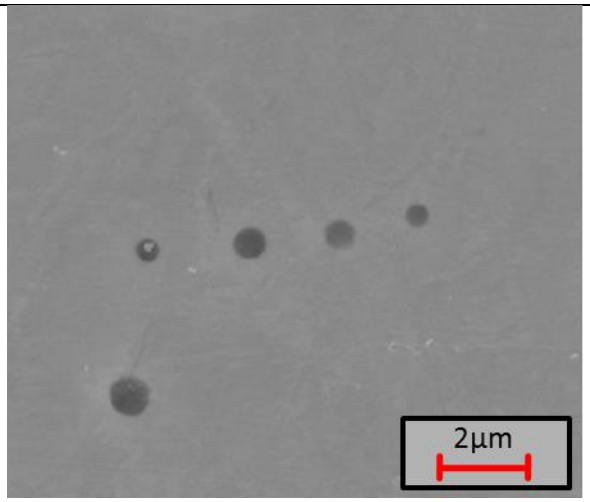

Figure 228: Aligned distribution of NMIs.

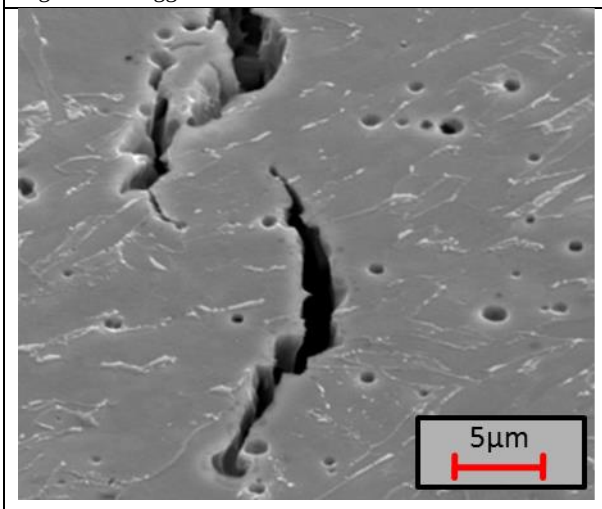

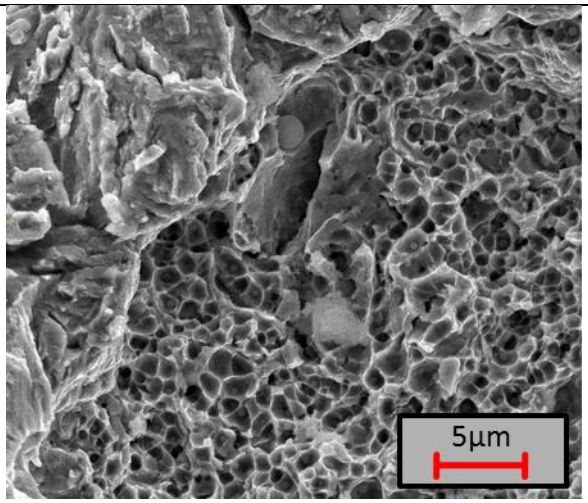

Figure 229: Micro-cracks propagating along aligned distribution of NMIs.

Additionally, numerous micro-cracks were observed in close proximity to NMIs distributed in an aligned fashion. This suggests that the NMIs may have served as initiation sites or as

guides along which the crack propagated. It is important to recall, however, that preparation of the samples for analysis, especially the final stage of polishing with colloidal silica, stripped the samples surfaces of some of their inclusions. Figure 229 shows holes that represent the sites at which inclusions would have been embedded in the weld metal.

Although it is generally agreed that the size, distribution and morphology of NMIs influence the role that NMIs play in a weld's susceptibility to HACC, the specific role played by these factors remain a matter of debate [174]. The size and distribution of NMIs will not only affect the net distribution of hydrogen across the weld metal, but also may influence diffusion paths and the local distribution of stress, which can influence a weld's susceptibility to cracking. Additionally, the chemistry of an NMI and its cohesion to the matrix will play a role in the initiation of HACC above a critical local hydrogen content by fracturing in QC or interfacial de-cohesion respectively.

Investigating in detail the role of NMIs in cracking initiation and propagation is beyond the scope of this thesis. However, in reviewing the microstructural trends for the 20 mm and 10 mm sample sets, there is evidence to suggest that NMIs may have influenced the positions of derived cracking boundaries and should be investigated further.

In summary, from the examination of the micrographs generated from the MWIC weldability tests carried out on API 5L X70 steel within the heat input range of interest, no significant difference in microstructure was observed across the CNC boundary. It is therefore reasonable to suggest that, within the limits of the examination carried out, the type of microstructure did not play a significant role in influencing the position of the cracking boundary. However, the weld metal chemistry and micromechanical properties of the samples across the cracking boundary need to be examined to so as to characterise fully the differences across the boundary and suggest a reason for the existence of the boundary, especially its limits. These factors are discussed in the next section.

6.6 Weld Metal Chemistry

6.6.1 Bulk Weld Metal Chemistry

As discussed in the literature review, the chemical composition of steel plays a pivotal role in influencing the resulting microstructure and micromechanical properties of the weld metal and the HAZ. The resulting weld metal elemental composition is a combination of the base metal and electrode compositions, in a ratio determined by geometry of the joint and influenced by the heat input at which the weld is deposited. As the weld cools through the austenitic temperature range, the weld metal composition influences the transformation kinetics which in turn influences the microstructure developed. Acknowledging that the weld metal microstructure is largely influenced by the weld metal chemistry and is a key variable in the three factors influencing the susceptibility of a weld to HACC, it is therefore essential to measure the elemental composition of the deposited welds across the derived cracking boundary. This will help determine if a significant difference can be detected across the derived welding boundary that would serve as a possible explanation for the boundary's existence.

6.6.2 Sample Selection for Elemental Analysis

Samples for chemical analysis were selected from the edges of the deposition window to give a representative snapshot of the elemental composition across the derived cracking boundary. Table 33 lists the welding parameters for the samples selected for analysis by GD-OES.

Table 33: Sample section bulk weld metal chemical analysis using GD-OES.

Sample	HI (kJ/mm)	Preheat (°C)	Thickness (mm)	Restraint (R_F)	Cracked?
MS_01	1.11	25	20	25	No Crack
MS_03	0.51	25	20	25	Crack
MS_04	0.57	50	20	25	No Crack
MS_05	0.45	50	20	25	No Crack
MS_09	0.82	25	10	25	No Crack
MS_10	0.48	25	10	25	Crack
MS_11	0.69	40	10	25	No Crack
MS_12	0.49	40	10	25	Crack

6.6.3 **Bulk Weld Metal Composition**

The detector was calibrated to detect 49 elements, of which 26 were detected at measurable intensities. Figure 230 illustrates the wt% and relative standard deviation (RSD) of nine of the key elements, as discussed in the literature review, for the samples selected for analysis.

<table>
<tr><td> 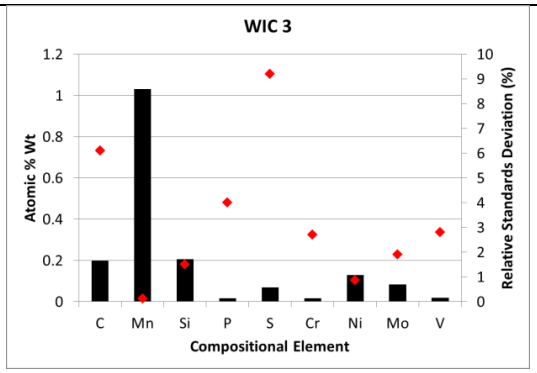
</td><td> 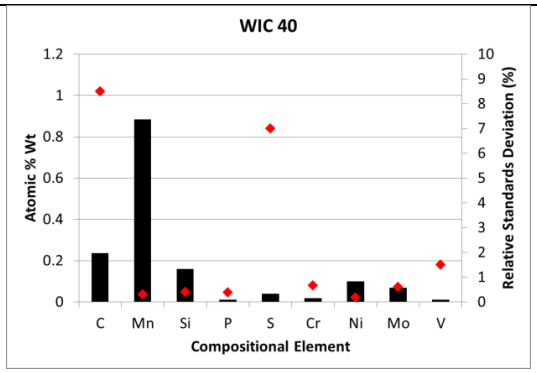
</td></tr>
<tr><td>MS_03: PH 25 °C, HI 0.51 kJ/mm, T 20 mm</td><td>MS_09: PH 25 °C, HI 0.82 kJ/mm, T 10 mm</td></tr>
<tr><td> 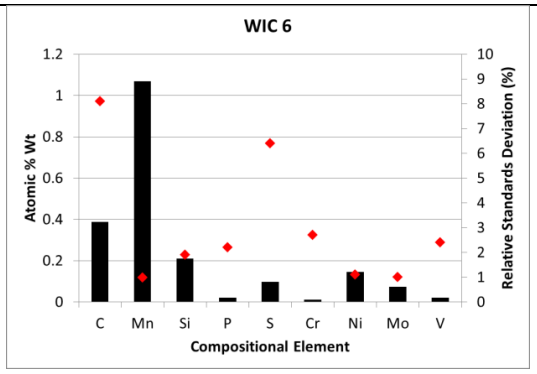
</td><td> 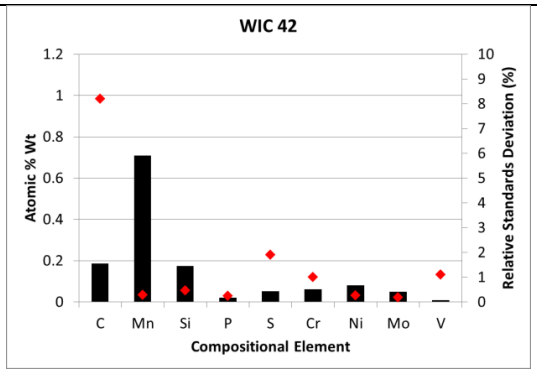
</td></tr>
<tr><td>MS_01: PH 25 °C, HI 1.11 kJ/mm, T 20 mm</td><td>MS_10: PH 25 °C, HI 0.48 kJ/mm, T 10 mm</td></tr>
<tr><td> 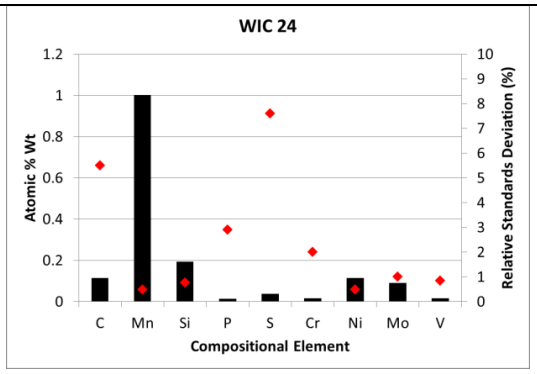
</td><td> 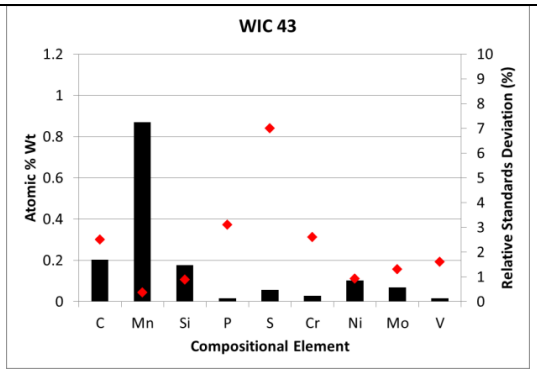
</td></tr>
<tr><td>MS_05: PH 50 °C, HI 0.45 kJ/mm, T 20 mm</td><td>MS_12: PH 40 °C, HI 0.49 kJ/mm, T 10 mm</td></tr>
</table>

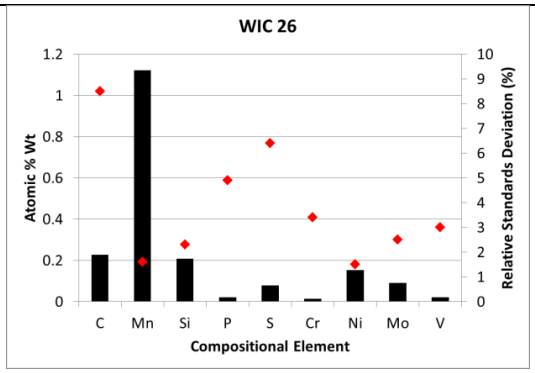

MS_04: PH 50 °C, HI 0.57 kJ/mm, T 20 mm

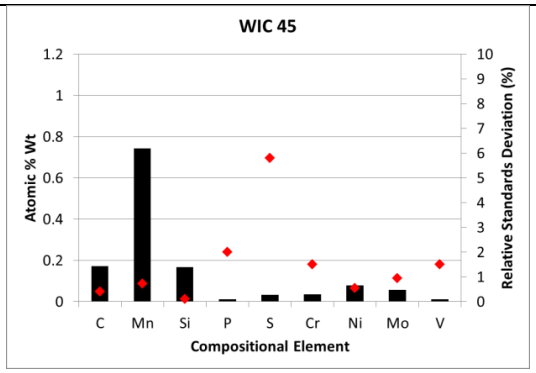

MS_11: PH 40 °C, HI 0.69 kJ/mm, T 10 mm

Figure 230: Bulk elemental composition for 20 mm and 10 mm samples selected from across the derived cracking boundary. The bar graph indicates the atomic % Wt for the key elemental constituents (*left axis*). The '◊' symbol indicates the relative standard deviation (%) for the key elemental constituents (*right axis*).

Only a relative measurement of residual hydrogen was taken, as an absolute measure of the residual hydrogen concentration was not possible, given the inability of Horiba Laboratories to calibrate the detector. Section 6.6.6 discusses the results derived for hydrogen concentration.

6.6.3.1 20 mm Samples

In the 20 mm samples there was a nearly negligible variation in wt% for manganese, silicon and phosphorus for the samples analysed. There is thus evidence to support the theoretical preposition that within the testing parameters, neither heat input nor preheat levels had a significant effect on the resulting wt% of these elements in the 20 mm data set.

This was also true for carbon content, but an anomalous result was detected for the carbon content measured in MS_01. The average carbon content for the samples excluding MS_01 was 0.18 wt%, with a standard deviation of 0.005 wt%, while MS_01 was reported as having a carbon content of 0.388 wt% with an RSD of 8.1. This result was significantly higher than both the parent metal and the electrode. The unusually high carbon concentration may be a result of contamination during sample preparation for analysis. Theoretically, weldability test conditions and especially welding parameters could not be responsible for the elevated levels of carbon detected. In addition to the anomalous level of carbon detected in MS_01, its sulphur and titanium content were also recorded as being higher than the other samples in the 20 mm data set.

6.6.3.2 10 mm Samples

The samples in the 10 mm data set demonstrated a greater degree of inconsistency in composition variation across samples with changes in heat input and preheat levels. However, this scatter is considered insignificant when examining the variations in wt% and RSD. The narrow heat input range of interest and the variation in preheat did not provide the conditions necessary for a significant change in the observed weld metal chemistry. The theoretical expectation of nearly negligible change in the bulk weld metal chemistry was satisfied for the results derived for the 10 mm data set.

6.6.4 Composition Differences between 20 mm and 10 mm Data Sets

In the entire suite of elements detected by GD-OES, including trace elements, no significant appreciable differences were detected in elemental concentration by wt% between the 20 mm and 10 mm data sets.

6.6.5 Composition across the Crack No Crack (CNC) Boundary

The bulk weld metal chemistry was examined for samples across the derived cracking boundary. The motivation behind analysing the elemental data across the boundaries for both the 10 mm and 20 mm data sets was to verify if a significant difference in elemental chemistry could be detected across the cracking boundary, and whether any such difference might account for the existence of the derived boundary. The arithmetic averages of the elemental composition were calculated for both the cracked and uncracked samples; they is presented in Figure 231 (20 mm data set) and Figure 232 (10 mm data set).

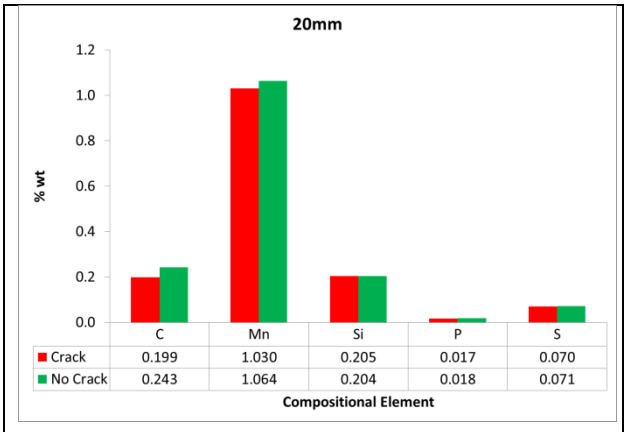

Figure 231: Key elemental composition for 20 mm samples (cracked and uncracked).

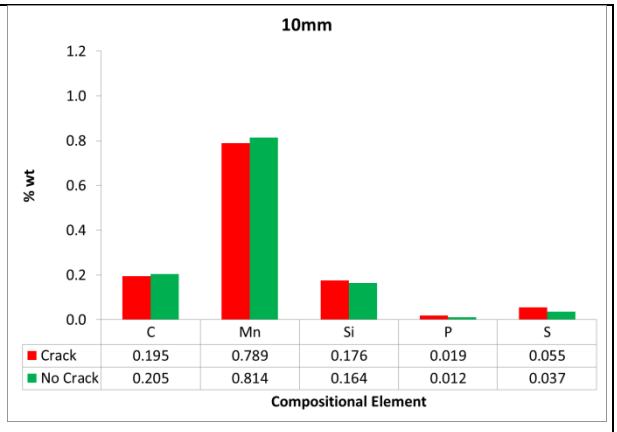

Figure 232: Key elemental composition for 10 mm samples (cracked and uncracked).

Across the cracking boundary, no significant difference was noted in the wt% of manganese, silicon, phosphorus or sulphur. However, a significant difference was detected in the carbon content in the uncracked sample, which, as discussed in section 6.6.3.1, was suggested to be a result of a potential anomaly in the chemical analysis.

An increase in the carbon content of low- and medium-strength weld deposits leads to an increase in both yield and tensile strengths along with a reduction in ductility [301]. When compared to steels with low carbon content, high-carbon steels have been shown to be more susceptible to HACC. However, in the case of MS_01, although the carbon content was reported as significantly higher than in other samples, no cracking—a defect greater than 5%—was detected in the sample.

Similarly for the 10 mm data set, no significant difference was recorded for the manganese, silicon, phosphorus and sulphur content between cracked and uncracked samples. Unlike the 20 mm data set, the carbon content for cracked and uncracked samples was similar.

6.6.6 Hydrogen Concentration

A relative measure of the residual hydrogen content can be made by considering the intensity of the signal captured during analysis by GD-OES (Figure 233). However, an absolute measure cannot be taken, as there was no sample with which the intensities could be calibrated. Additionally, unlike the other elements, the risk of contamination by air for hydrogen was reported as being high by Horiba, so the results must be regarded with a degree of caution and conservatism.

In the 20 mm data set, an increase in preheat from 25 °C to 50 °C reduced the average signal for hydrogen in arbitrary units from 48.35 to 39.6. For the 10 mm data set. The intensity of the signal resulting from the residual hydrogen content dropped from 28.94 to 27.86 as the preheat level increased from 25 °C to 40 °C.

What is clear from the data is that an increase in the preheat reduces the residual hydrogen content; these results accord with the principles of hydrogen diffusion, which have been extensively explored and discussed in the literature. A clear trend cannot, however, be extrapolated or defined for the relationship between heat input and residual hydrogen content as estimated by signal intensity.

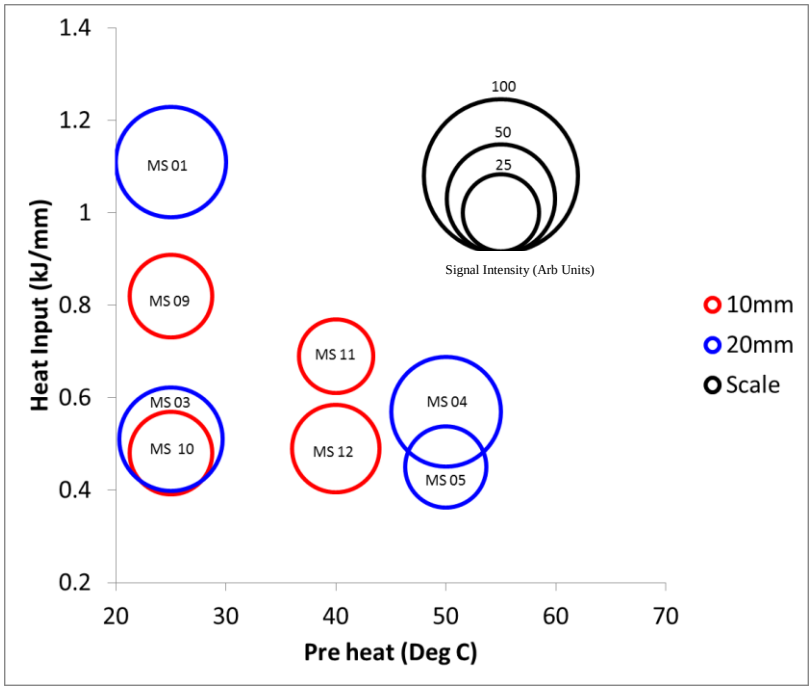

Figure 233: Measured hydrogen intensity in arbitrary units from analysis by GD-OES.

6.6.7 Effect of Elemental Composition on Susceptibility To WMHACC

The elemental composition of a given steel as captured by the CE is a commonly adopted and codified measure of the weldability of that steel. As discussed in the literature review, CE has been adopted as an empirical factor in predicting HACC in the HAZ, as it can be correlated to the hardenability of the parent metal, which indicates that the likelihood of forming hard martensitic microstructures that are typically associated with a relatively high susceptibility to HACC [4, 99, 215, 224]. However, CE has not been proven to be a reliable indicator for HACC in the weld metal [4, 42, 99, 215, 224, 227]. The results derived in this thesis are in accord with these results.

Extending the concept of the CE equivalent to welds deposited across the derived cracking boundary, the data suggests that for both the 20 mm and 10 mm data sets, a correlation could not be derived linking the CE, as expressed by P_{cm} and CE_{IIW}, to WMHACC cracking susceptibility as shown in Figure 234.

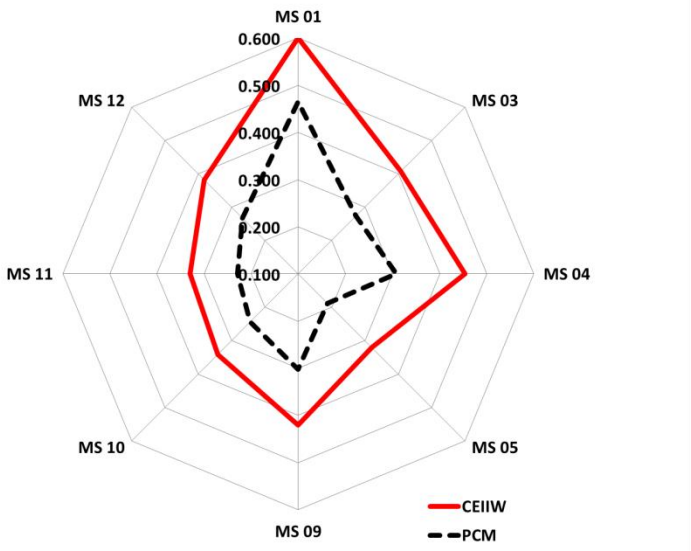

Figure 234:The calculated CEs, CE_{IIW} and P_{CM} for samples across the derived cracking boundary. With the exception of sample MS-01, the CE for the samples are comparable. This conforms to expectations, as major factors which would influence the bulk elemental composition, such as base metal and electrode composition were the same for all samples tested. Factors such as the effect of heat input had a minimal effect on the resulting composition as the heat input range of interest was narrow. Similarly, the effects of dilution were minimal given the singular joint configuration and narrow heat input range of interest.

Additionally, when considering the variation in individual elemental constituents across the cracking boundary, it can be concluded that no single element can be associated with increased cracking susceptibility. This conclusion aligns with the published results in the literature that suggest that, although changes in elemental composition may influence the resulting microstructure, there is no consistent evidence that proves the role of specific elements in influencing the susceptibility of a weld to WMHACC.

It is important, however, to consider the role of individual elements. The role played by different alloying elements in the resulting susceptibility of a weld to HACC is quite complex as a result of the interaction between elements in different concentrations with one another.

It is generally agreed that carbon is the most influential elemental constituent on the mechanical, microstructural and micromechanical properties of a deposited steel weld. For a constant grain size, the ratio between yield strength and ultimate tensile strength is reduced with increasing carbon content. Additionally, as carbon content increases, fracture toughness changes. An increase in the carbon content shifts the Charpy V-notch curve, reducing the energy in the upper shelf and extending the transition temperature between ductile and brittle fractures. Although it is widely acknowledged that carbon plays a pivotal role in defining a weld's hardness in the HAZ and in combination with other elements determines hardenability,

attempts to define the effects of specific elements or combinations of elements on the susceptibility of weld metal to HACC have proved to be unsuccessful. This can be attributed to the inconsistent and in some cases contradictory results published in various studies.

As discussed in the literature review, microalloying elements influence not only the microstructure but also micromechanical properties, which affect susceptibility to cold cracking. Alloying additions are known to restrain grain growth by the Zener pinning effect, which is known to improve toughness and reduce susceptibility to HACC, because the transformation kinetics of austenite to non-martensitic constituents in a fine-grained structure is comparatively rapid. Additionally, the critical cooling times below which 100% martensite forms decreases almost linearly with austenite grain size [302]. Easterling [303] advises that the hardenability of steels can be fully represented by a composition involving parameter and austenite grain size. For the HAZ in conventional steels the effect of austenite gran size is not discernible, hardenability in the HAZ is dictated solely by the steel's chemical composition. This however has not been demonstrated for the weld metal itself.

Minor changes in alloying additions may influence the size, morphology and prevalence of NMIs that could influence the existence and position of the cracking boundary, as NMIs serve as initiation sites for hydrogen cracking. However, a detailed study into the role of inclusions in the formation of hydrogen cracks is beyond the scope of this thesis.

6.6.8 Effect of Local Elemental Composition on WMHACC Susceptibility

Some studies, such as Brown [206] and Powell [304], have suggested that that hydrogen cracking susceptibility is related to the local weld metal compositional differences arising as a result of micro-segregation during solidification. Brown suggested that micro-segregation leads to a change in the local weld metal chemistry and thus the local micromechanical properties without manifesting as a change in the bulk weld metal chemistry as encapsulated by the CE. Similarly, Powell's study [304] of multi-pass welding on quenched and tempered steels showed that intercellular-dendritic segregation of manganese and nickel resulted in compositional differences up to 1.4 times higher than the nominal composition of the weld metal. Brown [206] extended that finding to show that micro-segregated regions were found to be 100 HV higher than in the weld metal. Brown also postulated that the hydrogen cracks propagated through micro-segregated regions that were harder. This thesis does not delve into determining the relationship between particular microstructures or elemental compositions

and WMHACC susceptibility, but to determine whether there was compelling evidence that further work needs to be directed at investigating the prevalence and consequence of micro-segregation on WMHACC susceptibility, the local weld metal chemistry was analysed for samples extracted from region MS_02.

To reveal intercellular-dendritic segregation, the sample was repolished and etched with Le Pera's reagent (Figure 235) as the initial Nital etching cannot be used to reveal such characteristics. Powell [304] reported that the segregation which occurs during solidification of the liquid phase to the δ phase persists to room temperature, regardless of the solid-state allotropic changes that occur with decreasing temperature.

Figure 235: Overview of weld metal after etching with Le Pera's reagent.

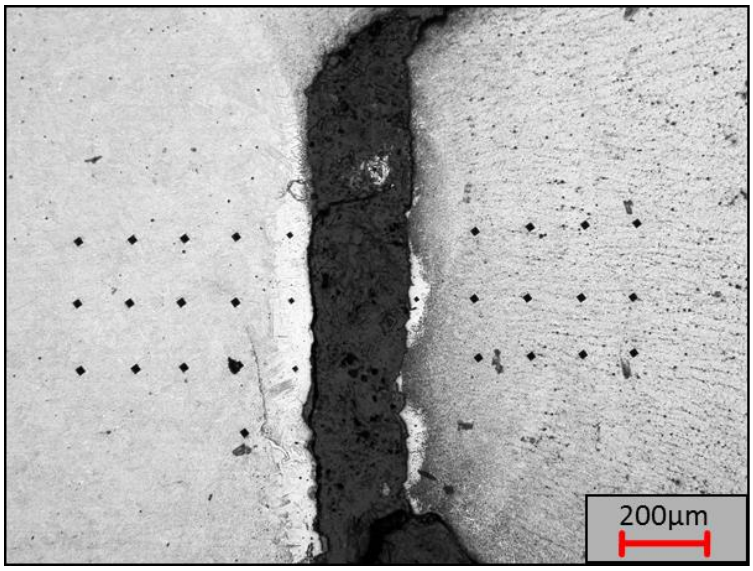

Figure 236: Detailed micrograph with micro-hardness traverses.

The contrast as a result of the etching with Le Pera's reagent suggests the presence of segregation, but does not indicate which elements have segregated or to what extent. The etching reveals the presence of bainite that appears black and ferrite which appears tan in the optical micrograph. A microhardness survey in the region showed that the hardness in the ROI was higher in the vicinity of the crack than in the area further away from the crack. To identify and quantify the degree of segregation and explore whether the elevated hardness could be attributed to a potential change in elemental composition along the edge of the crack, a scan using electron probe microanalysis with wavelength dispersive x-ray analysis was employed to provide a high-resolution analysis in the ROI. The line scan was conducted over a length of 50 µm, with a column potential of 20keV and a current of 50nA. The line

consisted of 50 spot scans, with a spacing of 1 µm between each point. The scans were conducted three times over each region; the average of the line scans are presented in Figure 237.

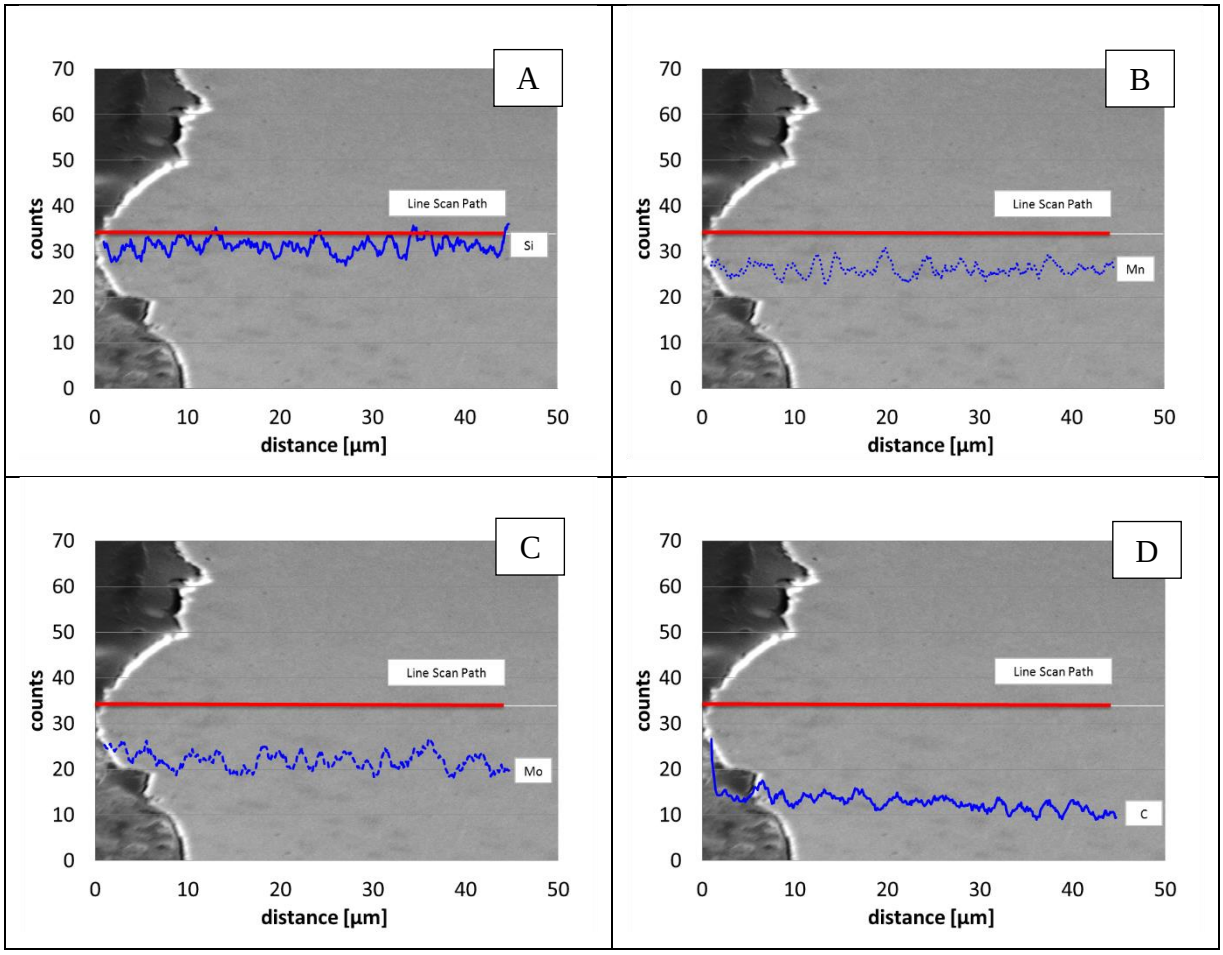

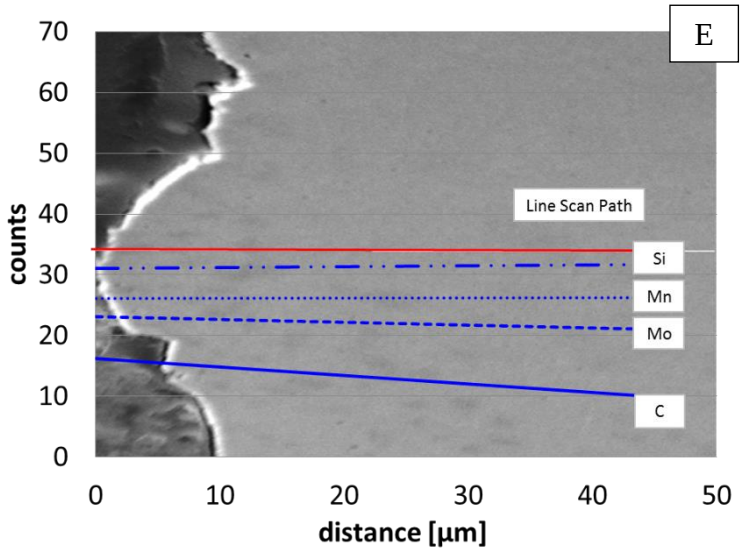

Figure 237: X-ray spectroscopy line scan along the red line of the selected area in the figure showed no significant compositional differences in chemical constituents. Figure A-D plots the signal count for Si, Mn, Mo and C versus the distance from the edge of the crack respectively. Figure E plots, the linear trend line for the elemental constituents.

The X-ray spectroscopy revealed no significant difference in the elemental constituents across the crack that was analysed, so there is evidence to suggest that, in that context at least, micro-segregation did not play a definitive role in WMHACC susceptibility. However, substantial additional work would be required to verify this hypothesis, including additional testing of cracks and exploring multiple scan methods at various resolutions. While that effort is beyond the scope of this thesis, it is nonetheless a recommendation for future work in this field.

6.6.9 Effect of Bulk Weld Metal Chemistry on Hardenability

As discussed in the literature review, changes in the weld metal chemistry influence the resulting microstructure and mechanical properties. These properties have been used to define empirical predictors which have been assimilate by industry and used as a means of quantifying the risk of the onset of cold cracking.

The simplest proxy used to define microstructural susceptibility to HAZ hydrogen cracking is hardness [28, 32, 224, 228]. It is therefore not surprising that hardness control criteria have been extensively codified [23, 25, 30]. A discussed in Section 2.10.5, Graville [34] compared the suitability of the hardness versus the hydrogen control criteria, suggesting that the use of hardness control is better for steels with limited alloy content. His hypothesis was based on

the observation that steels with a limited alloy content have steep hardening curves and the hardness of the HAZ can be determined with a high degree of accuracy by measuring the critical cooling time ($t_{8/5}$; Figure 71). For low carbon and microalloyed steels, in which the hardness profile of the weld is not influenced significantly by the critical cooling time ($t_{8/5}$), Graville suggested that the hydrogen control approach would be more appropriate.

A discussed in Section 2.10.5, this system simplifies the selection of the most appropriate criterion to employ to minimise the risk of hydrogen cracking. Zone 1 steels are typically considered steels at low risk of cracking, unless welded under high restraint and with high-hydrogen electrodes like cellulosic electrodes. When considering HACC control strategies to implement, steels in Zone I are typically subject to the hydrogen control criterion. Zone 2 steels are characterised by significantly higher carbon content and consequently have much steeper hardening curves than steels in Zone 1. Steels in Zone 2 are therefore subject to hardness control criteria. Zone 3 steels are typically subject to a combination of both criteria, given their elevated risk of cold cracking.

The hydrogen and hardness control criteria have different areas of emphasis. Unsurprisingly, the emphasis is on hydrogen diffusion and restraint in the hydrogen control criterion, whereas in the hardness control criterion the emphasises in on chemistry, which is the primary factor that influences the microstructure. However, when estimating the level of preheat required to ensure crack-free welds can be deposited, both control criteria take into consideration that HACC is the consequence of the interaction of trapped hydrogen in a susceptible microstructure subject to stress.

The introduction of new microalloyed, thermomechanically controlled processed steels has raised the question of the suitability of the empirically derived control criteria, which are based on older-generation steels. Limited data on the suitability of these traditional criteria on newer grades of steels and studies such as Davidson et al.'s [305] demonstrate the need to reassess the control criteria. This need is compounded by the development of novel methods, such as instrumented indentation, that can be used to extract the mechanical properties of materials.

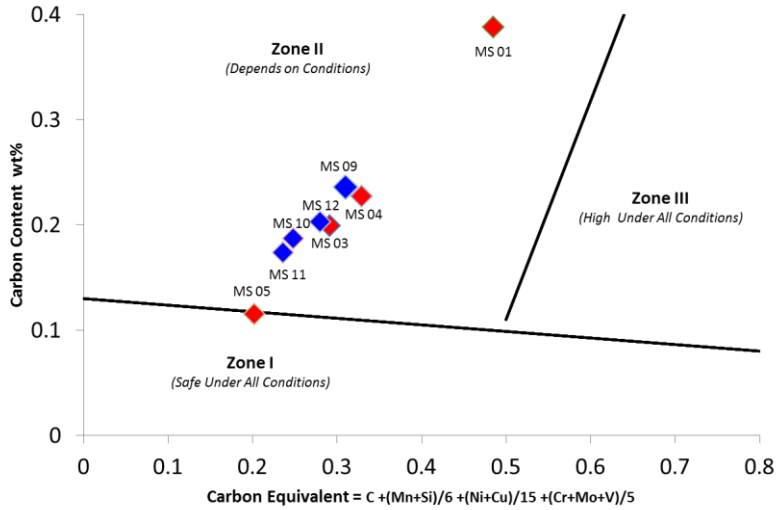

Figure 238: Positon of 20 mm and 10 mm samples superimposed on Graville's diagram.

Figure 238 shows that the samples in this study clearly fall into Zone 2 of Graville's diagram. Given the high carbon Zone 2 steels are characterised by a steep hardening curve and should therefore be subject to hardness control criteria, Section 6.7 will assess the samples' mechanical and micromechanical properties.

6.6.10 **Concluding Remarks**

Having established that the measured elemental composition across the derived cracking boundary does not appear to vary significantly, that there is insufficient evidence to correlate a single element or combination of elements with an increase in cold cracking susceptibility and that there is no apparent difference in observed weld metal microstructure, the micromechanical properties across the cracking boundary need to be assessed to ascertain if the combined effect of minute changes in chemistry and microstructure that are not observable by conventional analysis techniques, has manifested itself as a change in the micromechanical properties that can be quantified and used to assess cracking susceptibility.

6.7 Micromechanical Characterisation

Section 6.6 described and discussed the microstructural trends observed for samples across the empirically derived deposition envelope, concluding that, within the heat input range of interest, there were no significant observable differences in microstructural morphologies identified. Moreover, for the observed morphologies and within the limits of the techniques employed during the analysis of the samples, there were no significant apparent differences in the characteristics of the typically observed morphologies. It was therefore concluded that within the test envelope for this thesis, the cracking boundary could not be attributed to a particular microstructural or any physical characteristics of a particular morphology.

The bulk weld metal chemistry was also measured using GD-OES and, for the results generated, no significant difference in elemental chemistry was noted for samples across the cracking boundary. As with the observed microstructure, little difference was expected in terms of bulk elemental chemistry given the narrow heat input range within which testing was conducted, in addition to the fact that this thesis focused on a single electrode-steel combination.

With elemental chemistry and weld metal microstructural characteristics as examined by optical examination rendered ineffective as a means of differentiating differences in samples across the CNC boundary, the welds' micromechanical properties were assessed to determine whether the derived cracking boundary can be attributed to a difference in those properties.

The underlying objective behind the investigation of the thermomechanical properties influencing WMHACC is to facilitate the ability to predict and thus mitigate the onset of WMHACC. In order to predict the susceptibility of a welded joint to HACC, it is necessary to have sufficient information of the three parameters that are pivotal to its onset: the residual hydrogen content, the weld metal microstructure and the stresses experienced by the welded joint.

6.7.1 Sample Selection

To assess the suitability of micromechanical characterisation as a means of ranking the susceptibility of deposited welds to WMHACC, several samples were selected from across the derived safe welding boundary, as indicated in Figure 239 and Figure 240.

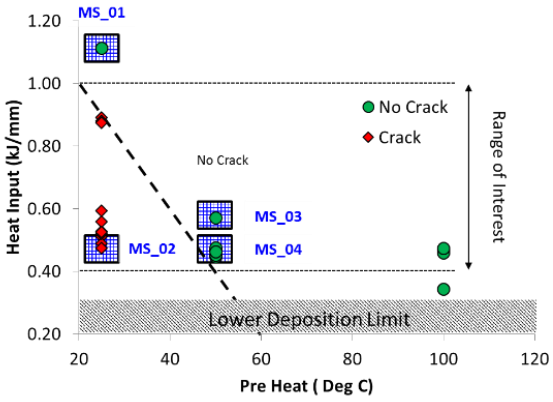

Figure 239: Samples from the 20 mm test series (grid regions) selected for micromechanical characterisation.

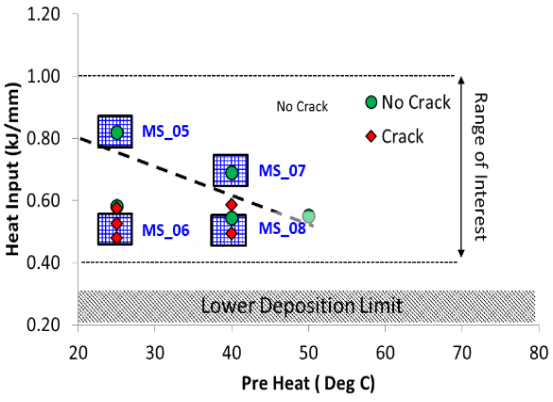

Figure 240: Samples from the 10 mm test series (grid regions) selected for micromechanical characterisation.

6.7.2 Weld Metal Hardness

The universal hardness values for 20 mm- and 10 mm-thick tests welded at multiple preheats are illustrated in Figure 243 and Figure 244 respectively.

Table 34 summarises the significant statistical measures derived from empirical testing, which offer evidence to suggest that the hardness distribution for both HAZ and weld metals have similar trends regardless of the welding parameters with which the welds were deposited. HAZ hardness increased from the parent metal towards the weld metal fusion zone, while the weld metal displayed a relatively constant hardness value across the entire weld. The continuous increase of hardness within HAZ may be attributable to the formation of more bainitic structures towards the fusion zone. This observation is supported by Young and Bhadeshia [306], who suggested that carbon partitioning into the remnant austenite from which the bainite forms is a plausible explanation for the higher hardness of the fine-grained region of the HAZ.

Decreasing heat inputs appear to have increased the weld metal hardness for both 10 mm and 20 mm plates (283 to 300 HV and 242 to 277 HV respectively) at ambient temperatures (Figure 241) and the reverse trend for preheated plates (294 to 275 HV and 265 to 253 HV) (Figure 242). Additionally, when the heat input is relatively constant, an increase in the level of preheat decrease hardness was observed in samples MS_06 and MS_08 and samples MS_02 and MS_04. The observations support previous reports [31, 197, 199] and were expected, since a lower heat input increases the cooling rate and preheating reduces residual hydrogen. The former should generate more residual stresses with finer grains and so increase

hardness, while the latter should result in fewer obstacles to dislocation movements and thus lower hardness. As for plate thickness, the trend was expected to be lower hardness for thinner plates due to their smaller heat sink, but that was not the case in the samples chosen (MS_02 and MS_06 or MS_04 and MS_08), which may be attributable to the MWIC test's geometry, especially the large heat sink effect of the strengthened back. In sum, the effect of a change in plate thickness is insignificant with regard to the cooling rate.

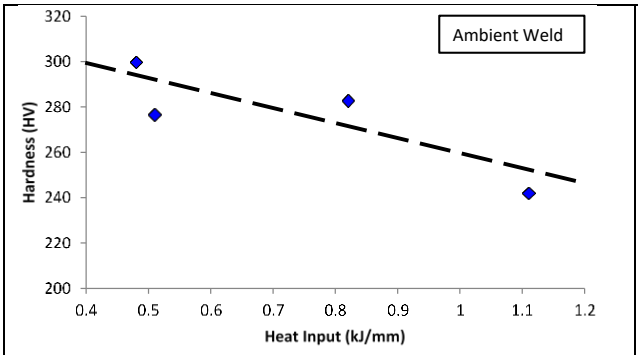

Figure 241: Measured hardness for samples deposited at various heat inputs under ambient conditions.

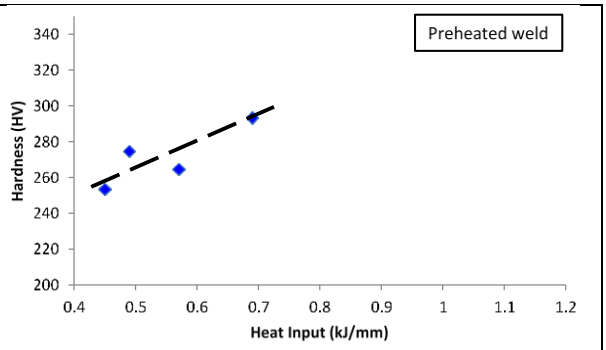

Figure 242: Measured hardness for samples deposited at various heat inputs under preheated conditions.

The measured peak hardness through the weld metal and the HAZ did not exceed the generally accepted hardness threshold of 350HV [23, 25, 30] above which hydrogen cracking is expected. However, weld hydrogen cracks were observed in samples with a peak hardness value as low as 300HV. These observations support the proposition in the literature [28, 177] that the traditional empirical hardness limits cannot be used as a universally infallible proxy for hydrogen cracking.

A change in heat input affects not only the thermal cycle of the deposited weld bead, but has a profound effect on the bead's geometry, especially the eccentricity of the bead's weld toe. One potential consequence of a change in bead eccentricity is the distribution of local stresses in the weld bead, which may in turn affect the position and severity of hydrogen cracks, given the affinity of atomic hydrogen for areas of high triaxial stress. It was observed that for the both the 20 mm but especially the 10 mm sample sets, a reduction in the heat input with which a weld was deposited increased the asymmetry of the deposited weld bead. This in turn increased the prevalence of cracking in the weld toe, which may be attributable to an increase in the eccentricity of the weld bead profile. The eccentricity of the weld bead increases the intensity of the local stresses at the weld toe, which then serves as a preferential initiation site for hydrogen cracking. However, as preheat levels were increased, the degree of eccentricity did not affect the prevalence of cracking (see Figure 157). It is therefore be suggested that the

local weld stresses resulting from bead eccentricity is a critical fact in influencing the susceptibility of a single-pass weld to hydrogen cracking.

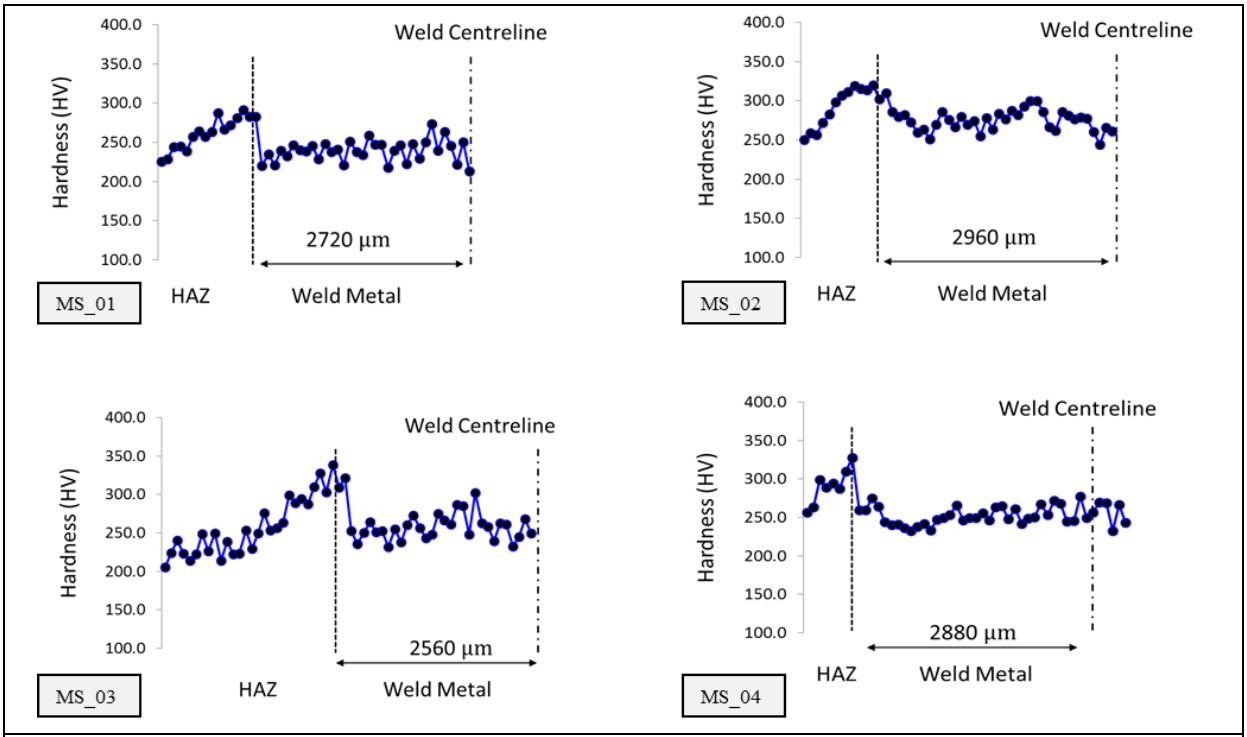

Figure 243: Measured hardness values for 20 mm-thick plates taken from the HAZ to the weld metal for samples deposited within the heat input range of interest under ambient conditions and with preheating applied.

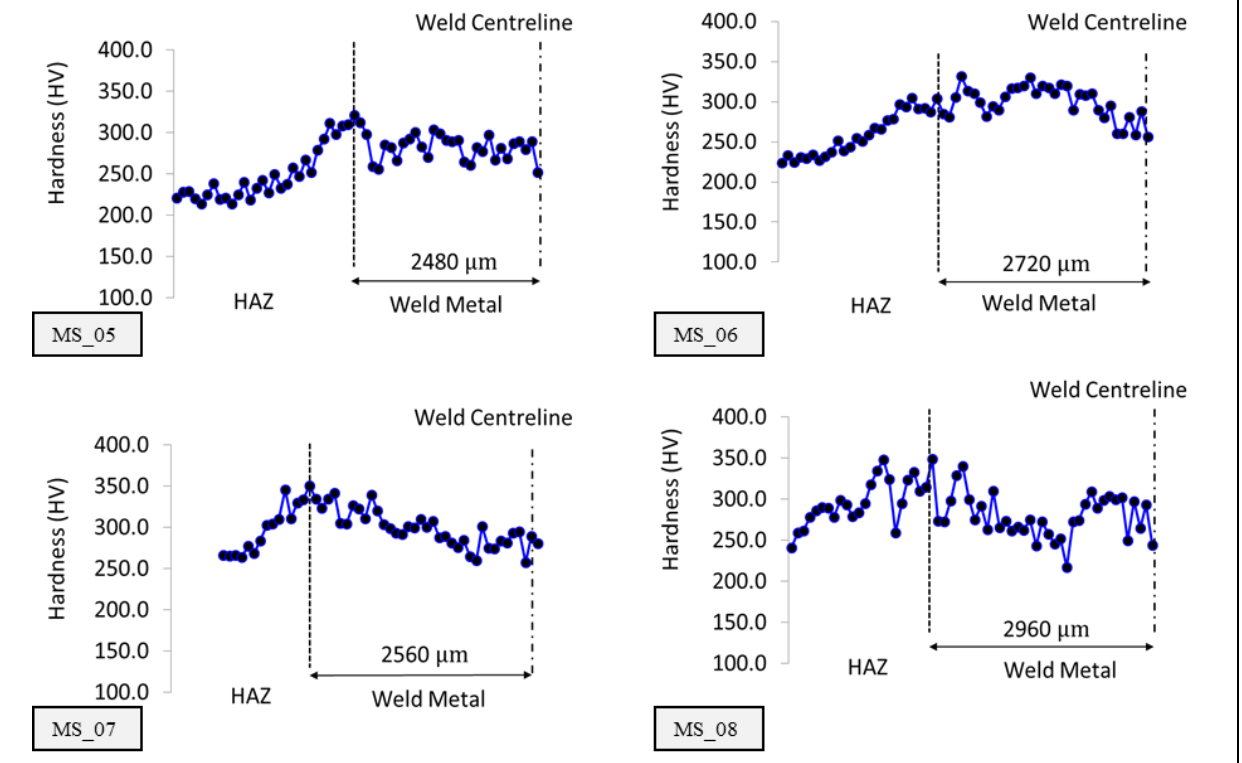

Figure 244: Measured hardness values for 10 mm-thick plates taken from the HAZ to the weld metal for samples deposited within the heat input range of interest under ambient conditions and with preheating applied.

6.7.3 Weld Metal Elastic Modulus

The measured modulus of elasticity for 20 mm- and 10 mm-thick tests welded at multiple preheats are illustrated in Figure 247 and Figure 248 respectively.

Table 34 summarises the significant statistical measures derived from empirical testing, which suggest that although there was a slight increase in the elastic modulus along the HAZ towards the weld metal fusion zone, the weld metal displayed an almost constant value across the weld cross-section. There are, however, some changes related to heat inputs and preheats. The geometry of the MWIC weldability test influences the cooling rate as a consequence of its base, which is used to ensure rigidity of the specimen and replicate the restraint conditions experienced in the field.

It is clear that when the heat input was almost constant, the elastic modulus increased with application of preheat. This observation accords well with the proposition that the application of a preheat reduces the residual hydrogen content of the weld metal because it encourages the diffusion of hydrogen. The modulus of elasticity is determined by the binding energy between the atoms as represented by the cohesive energy of the iron lattice. It is expected that hydrogen atoms will interfere with the binding energy when dissolved interstitially within the iron crystal lattice. Less hydrogen to interfere with interatomic binding energy limits the reducing effect on the modulus, so a preheated weld will have a higher modulus. There was, however, an anomaly for 10 mm-thick plates, as shown in Table 34, in which the modulus decreases with application of preheat in MS_06 and MS_08. This could be attributable to experimental error. A greater modulus means smaller elastic strain resulting from the application of a given stress with materials that are more brittle due to higher rigidity and stiffness.

The results on the effect of heat input on the modulus is such that increasing the magnitude of heat input appears to have reduced the modulus, regardless of preheat, although the trend was less distinct for preheated welds. A larger heat input was expected to generate slower cooling rates, resulting in a longer time for phase transformation to impart some effects on the microstructure scale to have slightly coarser ferritic phases. The hydrogen atom diffusion was expected to be more dependent on the level of preheat, whereas Figure 246 shows that when preheat was applied, the slope changes for the modulus line were very limited. This observation is supported by previous reports [55, 134].

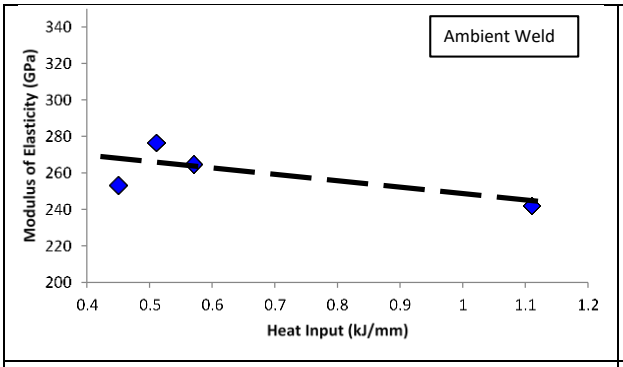

Figure 245: Measured elastic modulus for all samples deposited at various heat inputs under ambient conditions.

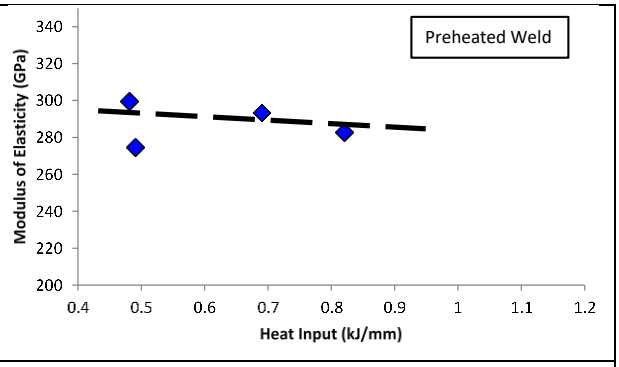

Figure 246: Measured elastic modulus for all samples deposited at various heat inputs under preheated conditions.

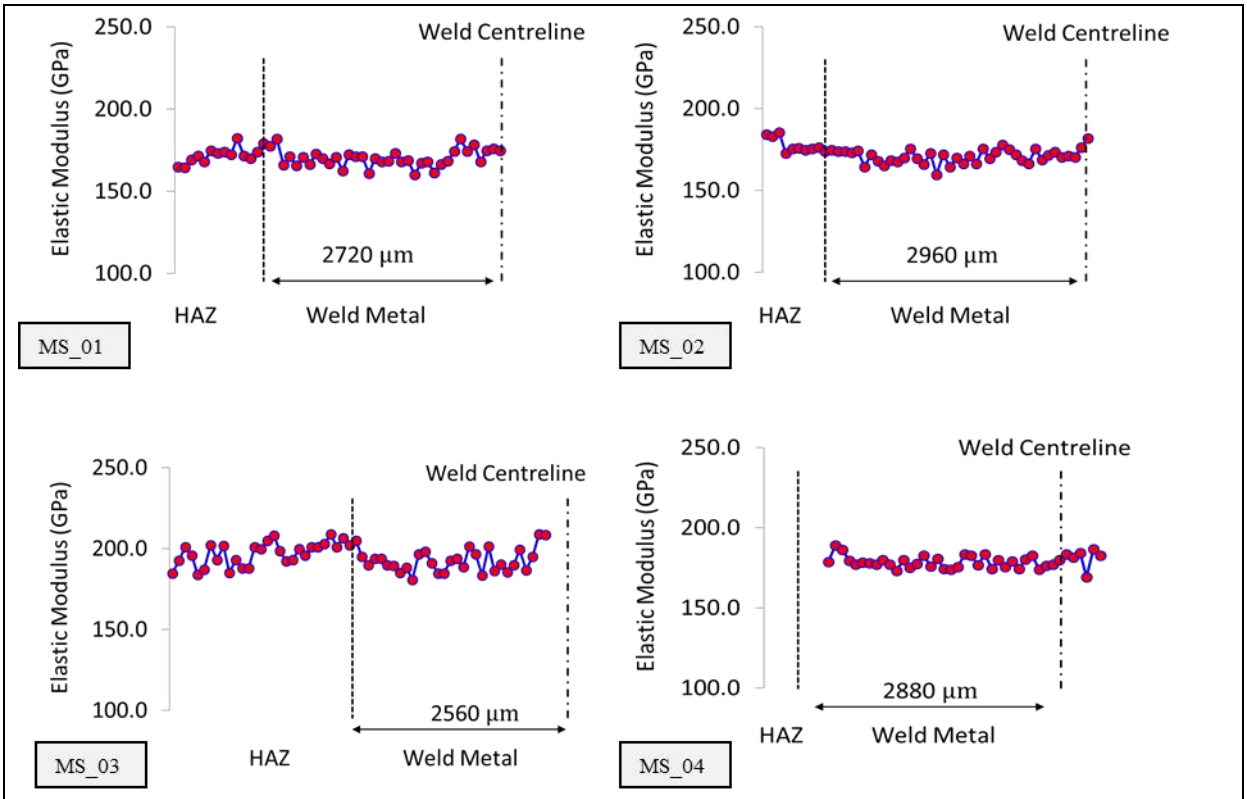

Figure 247: Measured elastic modulus for 20 mm-thick plates taken from the HAZ to the weld metal for samples deposited within the heat input range of interest under ambient conditions and with preheating applied.

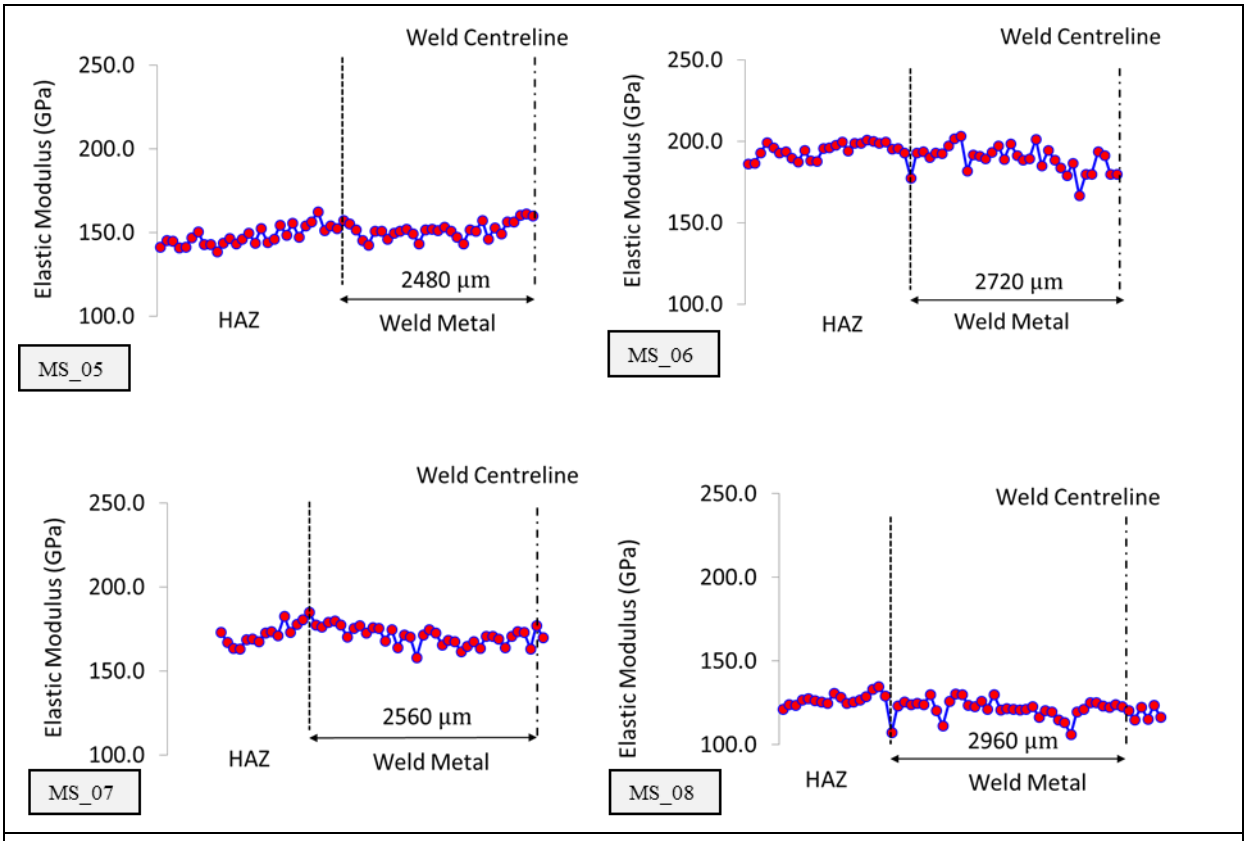

Figure 248: Measured elastic modulus for 10 mm-thick plates taken from the HAZ to the weld metal for samples deposited within the heat input range of interest under ambient conditions and with preheating applied.

Table 34: Welding parameters and cracking conditions for samples selected for micromechanical characterisation.

	Sample Parameters				Hardness (HV)				Elastic Modulus (GPa)				Analysis	
Sample	Heat Input (kJ/mm)	Pre-heat (°C)	Thick-ness (mm)	CNC?	Max	Min	Mean	Stdev	Max	Min	Mean	Std ev	H^3/E^2	$(E/H)^{1/2}$
MS_01	1.11	25	20	No Crack	273.4	213.3	242	15.1	182.1	160	170.1	5.4	489.82	0.8384
MS_02	0.51	25	20	Crack	300	244.3	276.7	13.7	181.9	164.4	171.7	4.1	718.60	0.7877
MS_03	0.57	50	20	No Crack	338.3	231.7	264.8	21	208.8	180.8	193.5	7.4	495.9	0.8548
MS_04	0.45	50	20	No Crack	277.3	232.5	253.4	11.8	186.5	169	178.7	4	509.53	0.8398
MS_05	0.82	25	10	No Crack	320.8	251.6	282.9	16.9	161.3	142.5	151.7	4.7	983.85	0.7323
MS_06	0.48	25	10	Crack	331.8	256.7	299.9	20.6	203.5	166.8	189.7	7.6	749.54	0.7953
MS_07	0.69	40	10	No Crack	339.4	257.2	293.5	18.4	177.5	158	170.1	4.9	873.81	0.7613
MS_08	0.49	40	10	Crack	340.2	217.1	274.9	26.1	130.4	106.3	121.3	4.9	1411.9	0.6643

6.7.4 Proposal of a New Proxy for WMHACC Susceptibility Assessment

Phenomenologically, in order for a hydrogen crack to manifest, a critical concentration of hydrogen must be trapped in a susceptible microstructure and subjected to a critical level of stress. The exact mechanism by which the process of embrittlement takes place is still a matter of debate.

It is well established that failure occurs in materials embrittled by hydrogen at significantly lower load levels than hydrogen-free materials [307]. Of the numerous theories proposed to explain the mechanism governing HE, the HELP mechanism is based on experimental observations [308-313] and theoretical calculations [139, 140]. The HELP mechanism suggests that hydrogen solutes assist the elastic interactions between dislocations and obstacles [139, 308, 314], resulting in enhanced dislocation mobility [309-311, 315]. The presence of hydrogen induces shear localisation of the plastic flow [310, 311, 316-318] which results in a highly localised ductile rupture process [310-313]. A study by Sofronis et al. [142] demonstrated that the presence of hydrogen induced shear banding bifurcation at macroscopic strains. The degree of local material softening [240] was suggested to be directly dependent on the corresponding local hydrogen concentration. Birnbaum and co-workers [138, 140, 165], in discussing local material softening and hydrogen concentration, suggested that the experimental evidence pointed to hydrogen's inducing material softening at the microscale by enhancing dislocation mobility. It was therefore expected that for samples across an empirically generated cracking boundary, a difference in the elastoplastic properties would be measurable.

For an empirical cracking boundary produced where the only significant difference is the residual hydrogen content in the weld, as influenced by the level of preheat with which the samples were produced [28, 32], it was suggested that there should be some inherent differences in the resulting material properties across the boundary that allowed for the propagation of a hydrogen crack at a given preheat.

From the results presented in this thesis, it appears that the preheat and heat input affect the hardness and the elastic modulus of the cracked and non-cracked samples to almost the same extent. However, as the samples were situated across an empirical boundary within narrow heat input ranges, hardness and elastic modulus did not necessarily vary as expected. Table 34 shows for example that the cracked sample MS_08 had a lower hardness value than the non-

cracked sample MS_07A, which was welded at the same preheat level but with a lower heat input. Moreover, it was shown that all cracked samples presented hardness values below the defined threshold of 350 HV, below which cracking is not normally expected [223]. As the propagation of hydrogen cracks depends on the elastoplastic properties of the material within which a crack has initiated [319], it is proposed that the hardness proxy can be refined by combining the material's hardness with its measured elastic modulus.

Assuming that that the process of embrittlement is in fact governed by HELP, samples predisposed to cracking should display a lower resistance to plastic deformation. The yield pressure (P_y) (Equation 6-1), which is an indication of resistance to plastic deformation, is reported to change with H^3/E^2 [320].

Equation 6-1: Yield pressure [320].

$$P_y = 0.78r^2\left(\frac{H^3}{E^2}\right)$$

The geometry of the MWIC test, especially the large thermal sink that results from the strong back used to ensure the rigidity of the sample, renders a change in test plate thickness with respect to cooling rates inconsequential. Therefore, consolidating the 20 mm and 10 mm data sets and examining the effects of preheat and heat input levels on the potential resistance to plastic deformation, there is evidence to suggest that for welds deposited under conditions that would promote the onset of WMHACC—low heat input and low preheat—the welds had a relatively higher resistance to plastic deformation (Figure 249 and Figure 250). In conclusion, as preheat and heat input increase, the resistance to plastic deformation falls.

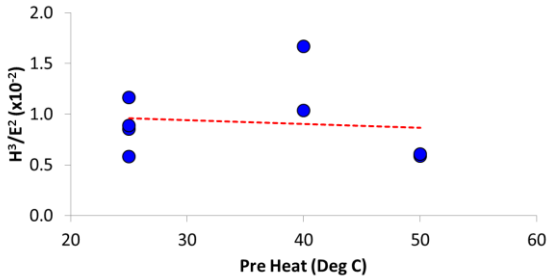

Figure 249: Ratio of H^3/E^2 for all MWIC samples deposited at various heat inputs. From the data generated during testing, *ceteris paribus*, there is evidence to suggest that as the level of applied preheat increased, the samples exhibited less resistance to plastic deformation.

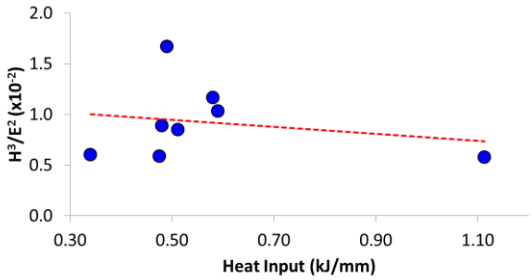

Figure 250: Ratio of H^3/E^2 for all MWIC samples deposited at various heat inputs. From the data generated during testing, *ceteris paribus*, there is evidence to suggest that as the level of applied heat input increased, the samples exhibited less resistance to plastic deformation.

The other parameter that provides indication of brittleness or ductile failure, including the susceptibility to crack propagation, is fracture toughness (K_C) (Equation 6-2), which varies directly with $(E/H)^{1/2}$ [321].

Equation 6-2: Fracture toughness as a function of (E/H) [321].

$$K_c = \alpha_1 \left(\frac{E}{H}\right)^{1/2} \left(\frac{P}{C^{3/2}}\right)$$

Consolidating the 20 mm and 10 mm data sets and examining the effect of preheat and heat input levels on the potential change in fracture toughness, there is evidence to suggest that for welds deposited under conditions that would promote the onset of WMHACC—low heat input and low preheat—fracture toughness decreases.

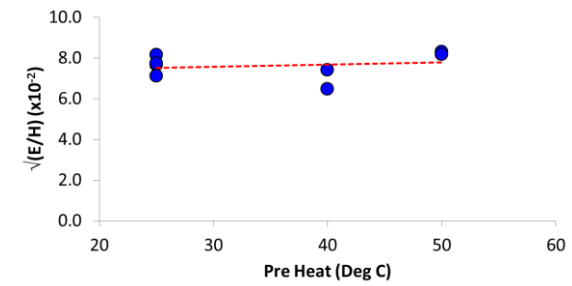

Figure 251: Ratio of √ (E/H) for all MWIC samples deposited at various preheats. From the data generated during testing, there is evidence based on Equation 6.2 to suggest that as the level of applied preheat increased, the samples exhibited a higher fracture toughness.

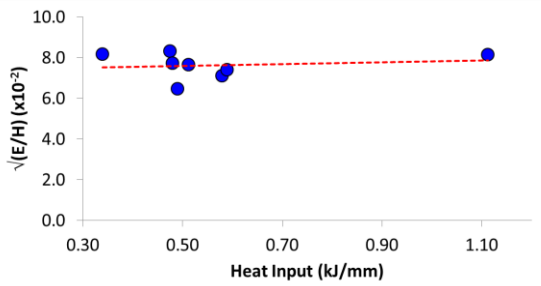

Figure 252: Ratio of √ (E/H) for all MWIC samples deposited at multiple heat inputs. From the data generated during testing, there is evidence based on Equation 6.2 to suggest that as the heat input with which the welds are deposited increased, the samples exhibited a higher fracture toughness.

Although the trends derived when considering the aforementioned proxies for cracking agreed with theoretical expectation, neither proxy could account for the actual cracking observed. This is likely a direct result of the limited sample size and the effect of weld bead eccentricity, as discussed earlier.

However, the H/E ratio can be used as a more accurate proxy for assessing the susceptibility of weld metal to HACC. Traditionally the H/E ratio is used to rank materials in terms of wear resistance [322-324]; it also appears in the so-called plasticity index [322, 325] , which is widely quoted as a valuable measure in determining the limit of elastic behaviour in surface contact. Higher H/E values result in higher critical loads for the onset of yield (non-elastic

deformation) in indentation [325]. Early works related the H/E ratio of a material to its yield strength [323, 324], and it has been well established in the literature that an increase in yield strength decreases the stress intensity threshold for HACC to occur [230, 326-328]. It is thus expected that higher H/E ratios would imply higher HACC susceptibility for a given material.

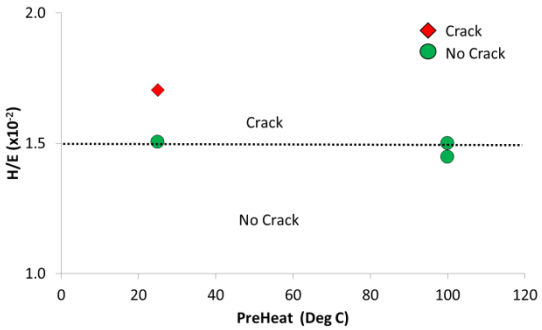

Figure 253: H/E ratios for samples from the 20 mm data set. No samples with an H/E ratio ≤ 1.5 x 10^{-2} cracked.

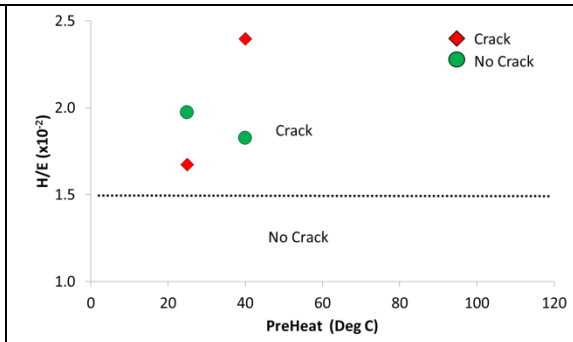

Figure 254: H/E ratios for samples from the 10 mm data set. A cracking anomaly detected with an H/E ratio = 1.6 x 10^{-2}. Uncracked samples had ratios as high as H/E = 2 x 10^{-2}.

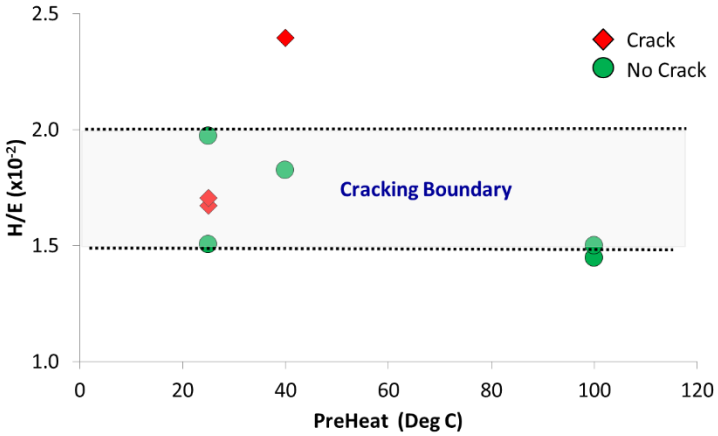

Figure 255: H/E ratios for both 20 mm and 10 mm data sets. Combining the data sets presents a hypothesised boundary within which cracking is uncertain. However, as the yield strain increases, it is postulated that there will be a higher prevalence of WMHACC.

Examining the ratio of the universal hardness (H in GPa) and elastic modulus (E in GPa) for both the 20 mm and 10 mm data sets, there is evidence to suggest that there is the possibility of delineating a boundary that would serve as an indicator of potential susceptibility to WMHACC. The data suggests that with an H/E ratio > 2 x 10^{-2}, the weld is susceptible to WMHACC. Conversely, if the H/E ratio < 1.5 x 10^{-2}, the weld is not susceptible to WMHACC. These experimental outcomes support the hypothesis that materials with higher H/E ratios are more susceptible to HACC. Moreover, it can be seen that the cracked sample

MS_08, which could be classified as safe if considering only its hardness (which is lower than the uncracked sample MS_07 for the same preheat but a lower heat input), becomes unsafe when considering its H/E ratio (2.3×10^{-2}). The use of the H/E ratio as a refined hardness proxy could be thus a more suitable parameter to predict WMHACC susceptibility for HSLA steels than hardness alone.

6.7.5 Concluding Remarks

The increased prevalence of WMHACC in higher grades of line pipe steel has raised the question of the reliability of traditional cracking proxies such as hardness. Historically, a limit of 350 HV has been established through extensive empirical testing and has been widely codified.

Empirical testing conducted in this thesis provides data to suggest that the limit of 350 HV does not apply to welds deposited under high restraint, such as those experienced in the pipeline industry during the fabrication of oil and gas transmission and gathering lines. Welds deposited using E6010 electrodes on two thicknesses (20 mm and 10 mm) of API 5L X70 steel at heat inputs ranging from 0.4–1.1 kJ/mm were established as having hydrogen cracks in samples with weld metal hardness values as low as 273.4 HV for 20 mm samples and 331.8 HV for 10 mm samples.

Given that using traditional hardness as a proxy to determine the susceptibility of weld metal to HACC has proven to be fallible and that the propagation of hydrogen cracks is dependent on the elastoplastic properties of the material, it is proposed to refine this proxy by combining the material's hardness with its elastic modulus as the H/E ratio. From the data collected, this ratio, which is directly related to the yield strength of the material, was shown to be a better indicator of WMHACC susceptibility than hardness alone. It is also proposed that the cracking boundary for API 5L X70 steel welded with cellulosic electrodes is $1.5 \times 10^{-2} < H/E < 2 \times 10^{-2}$. Nevertheless the introduction of the weld metals micromechanical properties as a proxy to quantify the susceptibility of a weldment to WMHACC, in particular the ratio of H/E, is a novel concept still in its infancy. One of the key limitations of such an approach is the assumption of limited eccentricity of the weld bead profile. Traditional proxies as hardness make the similar assumptions, and are based on the foundation that a symmetric weld bead profile is an essential element of compliance in the acceptance criteria of weld quality. This implies that if the deposited weld bead had an adversely irregular profile it

would not comply and therefore would have to be removed and replaced before additional mechanical tests were carried out to quantify susceptibility to a delayed phenomenon such as hydrogen cracking

.

CHAPTER 7

Conclusions & Future Work

7 Conclusions and Future Work

It is universally acknowledged that, for a weld metal hydrogen crack to form, a critical concentration of hydrogen needs to be trapped in a susceptible microstructure that is subjected to a threshold level of stress. Nevertheless, no consensus has been established to date as to the exact mechanism governing the initiation and propagation of hydrogen cracking. Moreover, there is no universal, infallible proxy that can be used to predict the onset of hydrogen assisted cold cracking. This has in part been attributed to the complex interaction of the three primary variables—hydrogen, microstructure and stress—that govern the propagation of hydrogen cracks. Additionally, newer-generation steels have markedly different chemistries and are thermomechanically processed, which has resulted in a shift from traditional HAZHACC to WMHACC. Consequently, there is a growing need to identify a cracking parameter that can be used to quantify and assess the risk of WMHACC for newer generation of steels.

To understand the interaction of these variables better and therefore predict the onset of WMHACC, the overarching objective of this thesis was to investigate the thermomechanical factors that influence the onset of the phenomenon. As this thesis was commissioned and funded by the Energy Pipeline Cooperative Research Centre, the underlying objective of this study was the empirical identification of a safe welding envelope for the welding of oil and gas transmission pipelines under typical Australian field conditions with the line pipe steels that Australia is expected to employ over the next decade.

In order to meet these objectives, a three-tiered system was establish:

- Tier 1: Deposition Window

The primary objective of this thesis was to identify the typical field welding conditions, especially the welding parameters, with which oil and gas transmission pipelines are manufactured in Australia. Based on these conditions, multiple weldability tests were conducted to explore the limits of deposition, to create a sample space within which hydrogen cracking could be investigated.

- Tier 2: Delineation of a CNC Boundary

The secondary objective of this thesis was to delineate a boundary within which hydrogen crack-free welds can be deposited within the previously established deposition window. The effect of welding parameters on crack type and severity were explored and discussed.

- Tier 3: Characterisation of the CNC Boundary

The tertiary objective of this thesis was to characterise the thermomechanical properties from samples within the developed deposition window across the derived safe CNC boundary, with the aim of identifying a means to differentiate the micromechanical proprieties of the samples.

A quantitative and qualitative industry survey established the parameter range, grade of steel and type of electrode to be used for weldability testing. Theoretical calculations were used to establish the thickness range and restraint levels that were to be tested to replicate Australian field conditions most faithfully. Weldability tests were carried out based on these essential variables. The following significant conclusions were drawn from the weldability testing and microstructural and micromechanical analysis carried out in this thesis.

7.1 Development of the MWIC test

The traditional Welding Institute of Canada test was identified after an extensive literature review as an appropriate weldability test to replicate field conditions when depositing a single-pass girth weld. However, preliminary testing established that the traditional WIC test configuration could not be used to investigate successfully weldability at the fast travel speeds and low heat inputs (< 1 kJ/mm) used extensively in Australia. The issues surrounding the repeatability and reliability of the test were exacerbated when depositing welds in a semi-mechanised fashion (or MCM) that is used to control heat inputs with greater accuracy. The WIC test was found to be particularly ineffective when investigating weldability for welds deposited at heat inputs lower than 0.8 kJ/mm. Below this heat input, more than 80% of the welds deposited exhibited window defects that would invalidate the test results. An enhanced version of the test, the Modified Welding Institute of Canada (MWIC) weldability test, was introduced to facilitate the successful and reliable deposition of welds at heat inputs less than 0.8 kJ/mm. The MWIC test was designed so that its thermal and restraint characteristics are comparable to the traditional WIC test, but it could also be extensively instrumented and provide critical cooling and displacement data without jeopardising the integrity of the test. The MWIC test can be used on deposited welds at heat inputs as low as 0.4 kJ/mm with no

restrictions on the upper limit of the heat input. The development of the MWIC test therefore facilitated the execution of the weldability tests needed to meet the primary objective.

7.2 Derivation of a Safe Welding Envelope

Weldability testing was conducted on API 5L X70 line pipe steel using E6010 electrodes at multiple preheats and heat inputs on 20 mm- and 10 mm-thick plates. For both thicknesses it was established that single-pass welds could not be deposited successfully at heat inputs lower than 0.4 kJ/mm; welds deposited below that level exhibited consistent evidence of insufficient penetration, lack of side wall fusion and weld bead asymmetry. The lack of penetration was correlated to the rapid travel speed and consequent small volume of electrode metal deposited per unit length of weld, while eccentricity at the weld bead toe caused a geometrical feature favouring hydrogen crack initiation.

7.3 Delineation of a Crack-No Crack (CNC) Boundary

An empirical CNC boundary was established from weldability testing results generated using both 20 mm- and 10 mm-thick plates welded under high (R_F = 25 mm) and low (R_F = 50 mm) restraint lengths (Figure 256). For 20 mm-thick API 5L X70 line pipe steel welded under high and low restraint conditions using a 4 mm-diameter E6010 electrode and heat inputs in the 0.35–1.00 kJ/mm range, the critical preheat required to ensure hydrogen crack-free welds was defined as a function of preheat temperature PH and heat input HI: $PH(C^0) = 70 - 50HI(kJ/mm)$. The relationship was derived as an empirical line of best fit from the data generated during weldability testing. For 10 mm-thick plates welded under high and low restraints the critical preheat was determined by $PH(C^0) = 100 - 100HI(kJ/mm)$.

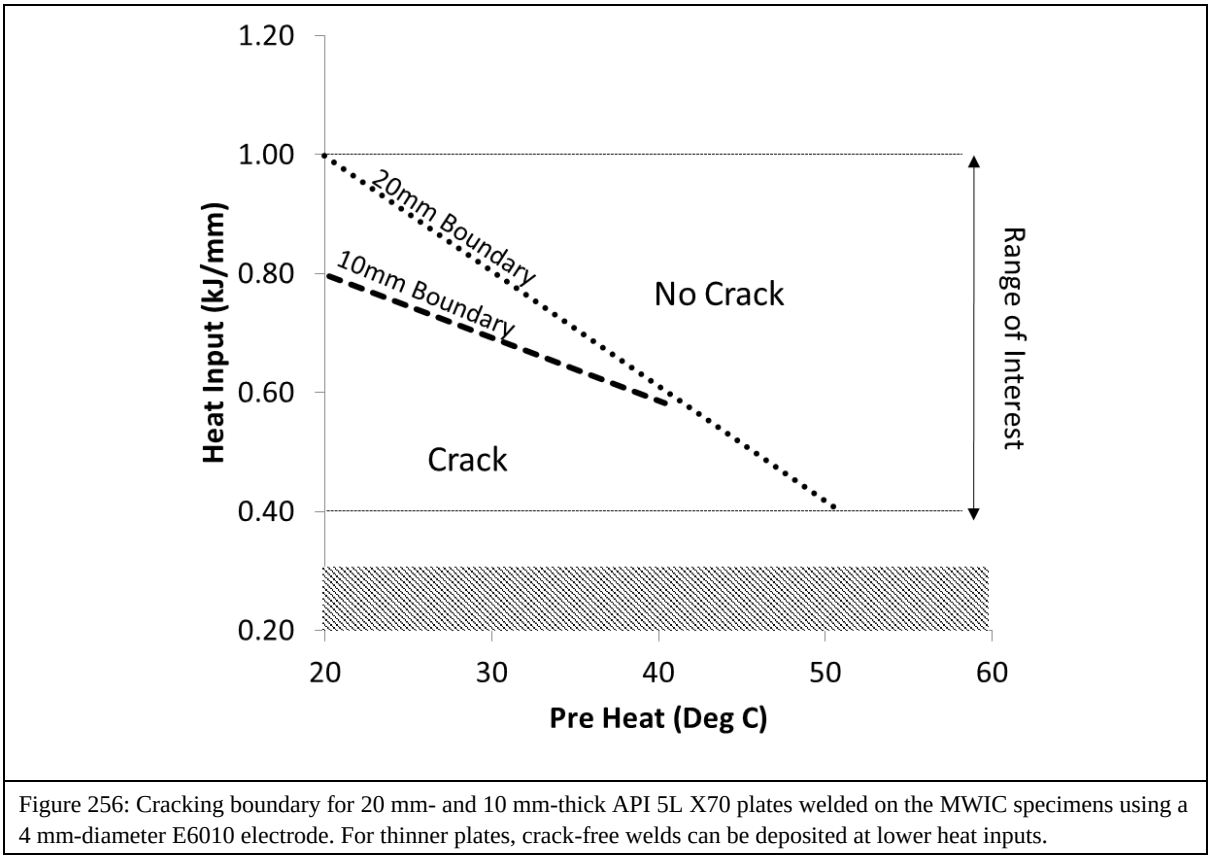

Figure 256: Cracking boundary for 20 mm- and 10 mm-thick API 5L X70 plates welded on the MWIC specimens using a 4 mm-diameter E6010 electrode. For thinner plates, crack-free welds can be deposited at lower heat inputs.

Three distinct crack morphologies were observed for samples deposited within the heat input range of interest: centreline cracks, geometric hydrogen cracks and classic hydrogen micro-cracks. This classification system was introduced to differentiate the distinct features of the hydrogen cracks observed. There was sufficient evidence to suggest that these distinctions could be connected to the welding parameters within which the welds were deposited. The MWIC test results indicated that the welding parameters with which a test weld was deposited had a pronounced effect on the length, width and location of initiation of the observed cracking.

In particular the restraint level affects the type of cracking. For both 20 mm and 10 mm plates at lower heat inputs, there was a greater prevalence of geometric hydrogen cracks. Changes in restraint level did not change the prevalence or severity of the observed morphology for welds deposited below 0.55 kJ/mm heat inputs. When the restraint levels were lowered, for 20 mm plates (Figure 257 and Figure 258) in the upper quartile of the heat input range of interest, hydrogen micro-cracks were observed in the place of centreline cracks. This can be attributed to a change in restraint levels which reduces the transverse stresses on the weld bead, creating

conditions that are more favourable to the formation of hydrogen micro-cracks than solidification cracks. However, in the lower quartile of the heat input range of interest, the dominant cracking type was still geometric hydrogen cracks.

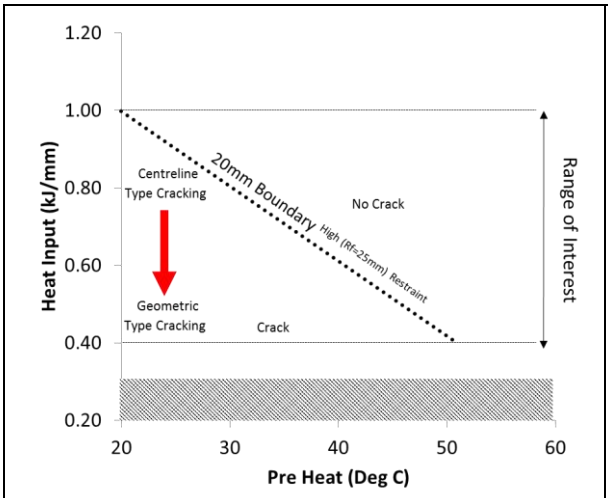

Figure 257: Types of cracking observed for 20 mm-thick plates under high restraint welded on the MWIC specimen. At heat inputs in the upper quartile of the heat input range of interest, a greater number of centreline cracks were observed than geometric and micro-cracks.

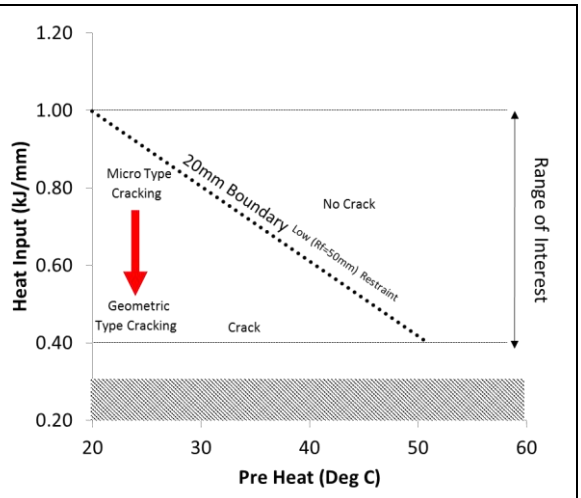

Figure 258: Types of cracking observed for 20 mm-thick plates under low restraint welded on the MWIC specimen. At heat inputs in the lower quartile of the heat input range of interest, a greater number of micro-cracks were observed than centreline and geometric cracks.

For the 10 mm-thick plates (Figure 259 and Figure 260), a reduction in heat input increased the prevalence of geometric hydrogen cracks. A reduction in the level of restraint resulted in only geometric hydrogen cracks' being observed in both the upper and lower quartiles of the range of heat inputs tested. It was established that the rationale governing the observed crack morphologies was applicable to both 20 mm- and 10 mm-thick plates.

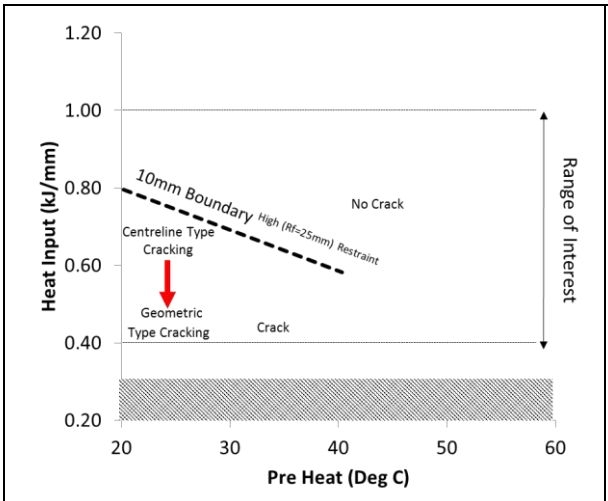

Figure 259: Type of cracking observed for 10 mm-thick plates under high restraint welded on the MWIC

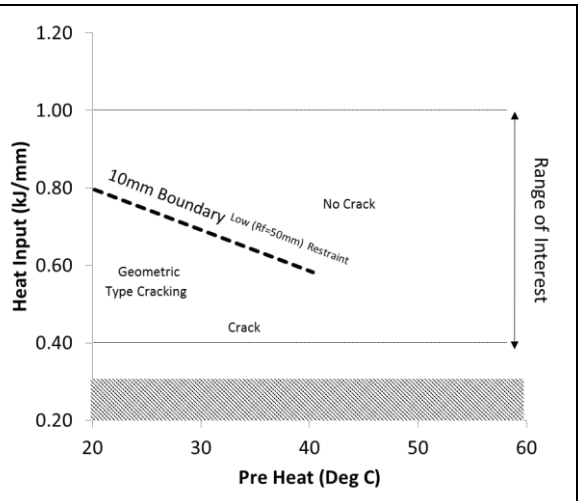

Figure 260: Type of cracking observed for 10 mm-thick plates under low restraint welded on the MWIC specimens.

specimens. At heat inputs in the upper quartile of the heat input range of interest, a greater number of centreline cracks were observed than geometric and classic micro-cracks.	At heat inputs in the lower quartile of the heat input range of interest, only geometric hydrogen cracks were observed.

The proposed relationship between welding parameters and crack morphology is summarised in Figure 261 and Figure 262. However, these relationships do not take into account the observed interrelation between crack types, especially centreline and micro-cracks. From a review of the observed cracking morphology there was evidence to suggest that the micro-cracks may have originated from the tips of centreline cracks previously formed during weld metal solidification. This conclusion was drawn by comparing the features, especially the orientation of propagation, the width and the size, of the crack tips of cracks that branched off primary centreline cracks. This hypothesis can only be verified by confirming the morphology of the crack surface between the primary centreline cracks and the cracks that branched off the primary crack. The use of acoustic emission to characterise the cracks, the type of cracking formed and the time of initiation would be an invaluable asset in assessing the validity of the hypothesis.

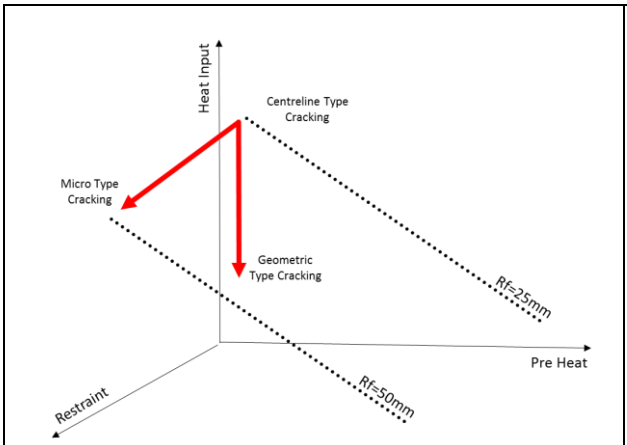

Figure 261: Schematic of the variation of observed crack morphologies for 20 mm-thick plates in relation to the established cracking boundary for the range of welding parameters tested.

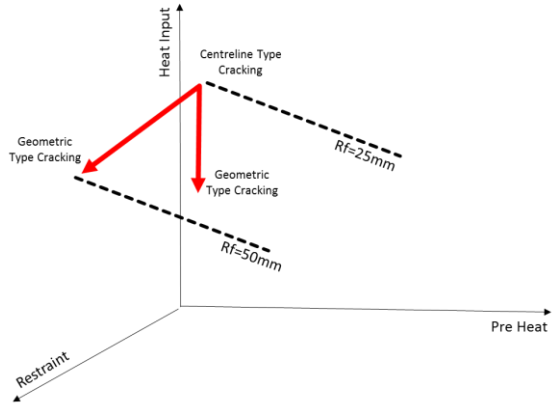

Figure 262: Schematic of the variation of observed crack morphologies for 10 mm-thick plates in relation to the established cracking boundary for the range of welding parameters tested.

For the derivation of the safe welding envelope and especially the delineation of the CNC boundary, weldability tests that had evidence of defects such as lack of side wall fusion, lack of penetration, severe undercut, burn through, porosity, etc. were discounted from the sample set used for analysis. Nevertheless at the high travel speeds tested, there was consistent evidence of window defects. Anecdotal evidence from consultations carried out on several site visits suggested that the presence of this type of defect was not uncommon when

depositing the root pass of a girth weld at high travel speeds. Additionally, common field practice in Australia is simply to deposit the hot pass of the defective section to seal the window and provide sufficient penetration to pass non-destructive examination. However, through empirical testing it was established that the presence of the window defects created a centreline defect that could extend up to 16 mm away from the approximate centre of the window, which could create conditions that lead to failure of the weld centimetres away from the initial site of the defect. It is therefore concluded that, in the circumstances in which a window is observed, the section of the root pass must be repaired in accordance with the specified repair weld procedure to ensure integrity of the root pass.

7.4 **Microstructural Characterisation**

For both the 20 mm and 10 mm data sets, no appreciable difference was noted in the observed microstructural morphologies at the heat inputs with which the welds were deposited. The investigated heat input range was selected by the institutions funding this thesis as representative of Australian practices. Within this limited heat input range, the welds consisted primarily of AF, with evidence of WF, GBF and bainite. There was no evidence to suggest that cracking occurred with greater prevalence in any particular microstructural morphology.

When examining the microstructure along the crack paths, there was no definitive evidence to suggest that hydrogen cracks propagated preferentially through a particular microstructure or altered their paths in relation to the particular morphology through which they propagated. Therefore, it was concluded that within the heat input range tested, the weld metal microstructure did not influence the initiation or propagation paths of hydrogen cracks. Nevertheless, most hydrogen micro-cracks appeared to initiate in the vicinity of NMIs, and there was some evidence to suggest that some micro-cracks propagated along an NMI-containing path. A thorough analysis of the size, morphology and distribution of NMIs would be necessary to draw any definitive conclusions as to the specific role played by NMIs and the susceptibility of a weld to WMHACC.

7.5 **Micromechanical Characterisation**

Two key micromechanical properties were extracted from the weld metal samples: hardness and elastic modulus. It was concluded from the samples tested that the traditional hardness threshold of 350HV, below which hydrogen cracking is not expected, did not apply to the electrode-steel combination tested within the heat input range of interest. This observation supports the hypothesis that weld metal hardness is not an infallible proxy that can be used to quantify the risk of WMHACC for all grades and generation of lines pipe steels, including line pipe steels such as API 5L X70, on which this thesis is based and which is currently used in the Australian pipeline network. Additionally, based on these results, it is suggested that caution should be employed when applying the current codified standards (AS2885.2), which do rely on hardness, to assess the risk of hydrogen cracking.

Having discounted the use of weld metal hardness as a reliable proxy to determine the susceptibility of a weld to hydrogen cracking and acknowledging the role of elasticity in hydrogen crack propagation, the modulus of elasticity at a grain scale for samples across the C-NC boundary was extracted and analysed. For both the 20 mm and 10 mm samples an increase in the heat input resulted in a decrease in the elastic modulus of the weld metal for samples deposited under ambient and preheated conditions. From the observed variations in elastic modulus and welding parameters, it was concluded that there was evidence to suggest that the elasticity of the weld metal may be useful in assessing the susceptibility of a weld to HACC.

However, when considering the actual samples that cracked and the number of samples generated during testing, there was insufficient evidence to conclude that a statistically sound relationship can be drawn between the weld metal elastic modulus and susceptibility to HACC. When considering the entire data set, there was sufficient evidence to suggest that the H/E plasticity ratio may serve as a suitable proxy assess the susceptibility of newer-generation line pipe steels to WMHACC.

For API 5L X70 steels welded with E6010 electors, it is proposed that a plasticity ratio $1.5 \times 10^2 < H/E < 2.0 \times 10^2$ can be used to delineate a safe welding boundary. Although the use of the plasticity ratio and its suitability can be related to the current theories governing hydrogen embrittlement, the exact limits of the boundary as proposed by this thesis are empirically

defined. It is therefore imperative that in order to validate the hypothesis that the plasticity ratio can indeed be used as a proxy to assess the risk of WMHACC, further testing on a greater range of steels and wider parameters is required. Additionally, the empirical limits proposed by this thesis need to be validated and refined through further testing.

To summarise the thesis, a weldability test was developed to facilitate the deposition of test welds under conditions similar to those experienced during field construction in Australia. From a series of weldability tests, a deposition boundary was established within which a safe welding envelope was defined. The interrelationship between crack morphology and welding parameters was identified and explained. The role of weld metal microstructure was analysed in relation to the derived cracking boundary and found to be inconsequential. Traditional proxies for HACC were examined and found to be ineffective. A new proxy based on the local weld metal properties was proposed after empirical testing.

7.6 Future Work

This thesis aimed to enhance the understanding of the thermo mechanical factors influencing the formation of Weld Metal Hydrogen Assisted Cold Cracks. To achieve this objective, an enhanced weldability test, the MWIC test, was designed and a suite of weldability tests were conducted on a single grade of HSLA (API 5L X70) steel and electrode (E6010) which was shown to be representative of the Australian context. From these tests an empirical safe welding boundary was delineated and the samples generated were analysed, in terms of the macroscopic, microstructural and micromechanical characteristics. Based on the results presented in this thesis the following areas are provided as a frame work for future research to expand our understanding of weld metal hydrogen assisted cold cracking.

The MWIC Test: An Enhanced Weldability Test

The development of the MWIC test, allowed for reliable and repeatable tests welds to be deposited at heat inputs lower than 1kJ/mm; a heat input not previously tested. Additionally, the instrumentation access designed into the weldability test, allowed for extraction of critical cooling times ($t_{8/5}$, and t_{100}) as well as the local weld metal displacement the bead experienced during solidification and cooling to room temperate. However limitations in the data acquisition system and the instrumentation, in particular the extensometer, limited the resolution of displacement data obtained. Additionally, the experimental procedure did not

facilitate the accurate recording of the time at which cracking initiated. To ensure accurate characterisation of crack types and isolate the strain rates at which hydrogen cracks initiate, which as discussed is pivotal when discussing the mechanisms which govern the hydrogen cracking phenomena, significant improvements need to be made to the data acquisition system and the instrumentation used on the MWIC test. Additionally, it is suggested that the use of acoustic emission as a tool for crack characterisation be explored.

Safe Welding Envelopes

In this thesis, a cracking boundary was delineated for root pass of a girth weld deposited on X70 line pipe steel using a 4mm E6010 electrode at heat inputs which mirror conditions experienced in the field. Testing was conducted on high and low restraint for thin (10mm) and thick (20mm) sections of steel. This allowed for the development of a comprehensive safe welding envelope for the most contentions electrode steel combinations in the Australian industrial context. Nevertheless as discussed in the literature review, grades of line pipe steel such as X70 and above can be welded with higher grade electrodes such as E8010 and E9010. Although studies have been carried out using these electrode steel combinations as discussed in Section 2.9 weldability testing has not been conducted at low heat inputs. With the introduction of the MWIC test, weldability testing in this space is now possible. To complete the cracking boundaries, as was done in the case of E6010 electrodes in this body of work and to better understand the position of cracking boundaries, it is suggested that weldability testing should be extended to multiple steel and electrodes combinations. In particular to reflect the conditions in the Australian oil and gas industry, the susceptibility of X70 steel to WMHACC should be investigated when welded with E9010 electrodes. Ideally this would be eventually extended to other grades of HSLA to give an insight into the weldability and susceptibility of these new generation steel slated to be introduced into Australia market in the future. Additionally this would generate a samples sets which can be analysed in a similar fashion to that introduced in this body of work which would allow for the development of robust regulatory and statutory standards to minimise the risk of WMHACC.

Crack Characterisation

In this thesis, a range of characterisation techniques were employed to differentiate macroscopic and microstructural features of samples across the derived cracking boundary. Within the parameter range tested, characteristically different types of hydrogen cracks were

identified and a classification system based on the initiation site of these crack was introduced. Within this classification system, the relationship between welding parameters and different classifications of hydrogen crack were explored. The relationship between bead eccentricity, base plate thickness, welding parameters and heat inputs were discussed for geometric and micro hydrogen cracks. However, as discussed when exploring the microstructural features along crack paths, a strong dependence on the path of hydrogen micro cracks and non-metallic inclusions were noted. The size, morphology and distribution of NMI's were notes as being potentially influential on the cracks propagation path. To establish this relationship, a quantitative study mapping out the characteristics of NMI's across the derived cracking boundary is suggested.

Micromechanical Characterisation

The use of instrumented indention, in particular the use of micromechanical parameters as a tool to map out the susceptibly of welds to WMHACC, is a novel technique proposed by this body of work. This technique is in its infancy and has only been used on the samples generated for the weldability test envelopes derived in this body of work. To validate its use, it is suggested that the techniques be applied to a range electrode –steel combinations and be extended to a range of welding processes.

The interrelationship between Solidification Cracking and Hydrogen cracking

However the most important future investigation suggested by this body of work regards investigating the interrelationship between solidification cracking and weld metal hydrogen assisted cold cracking. Experimental results demonstrated that within the empirical boundaries generated, there was a region where both modes of cracking were observed.

Solidification cracking, which is a subset of solidification defects develop during the freezing of weld metal. Solidification cracks form when a partially solidified weld bead is subject to a tensile strain, as a result of shrinkage or imposed deformation; the remaining liquid weld metal has no strength and is therefore unable to accommodate the strain. In such circumstances the liquid may rupture resulting in the formation of cavities in the weld metal region where the last solidified weld metal was located. The relative absence of solidification cracking in completed production girth welds is considered to be due in part to the deposition of subsequent passes in quick succession. Nevertheless a significant risk exists to pipeline integrity

when the elimination of a solidification crack in a girth weld depends on grinding the down face of the root pass and depositing of the hot pass to fill and fuse the existing crack. In particular, incomplete coalescence may leave residual defect that can act as a powerful stress concentrator which may initiate cold cracking. Therefore to minimise the risk of hydrogen cracking in the root pass of girth welds, delineating the conditions within which hydrogen cracks form from solidification cracks is critical.

CHAPTER 8

References

8 References

1. Alam, N., et al., *Weldment Cold Cracking - The Effect of Hydrogen and Other Factors*, in *Joint Seminar Hydrogen Management in Steel Weldments*. 1996: Melbourne, Australia. p. 46-90.

2. Barbaro, F.J., *Types of Hydrogen Cracking in Pipeline Girth Welds*, in *First International Conference on Weld Metal Hydrogen Cracking in Pipeline Girth Welds*. 1999, WTIA: Wollongong, Australia. p. 11.1-11.15.

3. Fletcher, L. and N. Yurioka, *A Holistic Model of Hydrogen Cracking in Pipline Girth Welds*, in *First International Conference on Weld Metal Hydrogen Cracking in Pipeline Girth Welds*. 1999: Wollongong, Australia.

4. Yurioka, N., *Predictive methods for prevention and control of hydrogen assisted cold cracking*, in *First International Conference on Weld Metal Hydrogen Cracking in Pipeline Grith Welds*. 1999: Wollongong, Australia.

5. Yurioka, N., *Weldability of modem high strength steels*, in *1st US-Japan Symposium on Advances in Welding Metallurgy*. 1990: San Francisco, CA. p. 79 - 100.

6. Yurioka, N., et al., *Welding Note 3rd Edition*. 1985, Kanagawa Japan: Nippon Steel.

7. Yurioka, N., S. Yamasaki, and H. Morimoto, *Hydrogen effusion from high strength weld metal.* Science and Technology of Welding and Joining, 2005. **10**(4): p. 497-502.

8. Revie, R.W., *Oil and gas pipelines: Integrity and safety handbook*. 2015: John Wiley & Sons.

9. Papadakis, G.A., *Major hazard pipelines: a comparative study of onshore transmission accidents.* Journal of Loss Prevention in the Process Industries, 1999. **12**(1): p. 91-107.

10. Montiel, H., et al., *Historical analysis of accidents in the transportation of natural gas.* Journal of Hazardous Materials, 1996. **51**(1): p. 77-92.

11. Roshan, W., et al. *Welding of Small Diameter Pipelines in Australia*. in *APIA / EPRG / PRCI 19th Joint Technical Meeting*. 2013. Sydney, Australia.

12. Rampaul, H., *Pipe welding procedures*. 2003: Industrial Press.

13. McAllister, E., *Pipeline rules of thumb handbook: a manual of quick, accurate solutions to everyday pipeline engineering problems*. 2013: Gulf Professional Publishing.

14. Smart, R. and K. Bilston. *Stresss upon Partially Completed Girth Welds During Line Up*. in *Joint Research Seminar, Research WTIA/APIA Panel 7*. 1995. Wollangong, Australia.

15. Linnert, G.E., *Welding Metallurgy*. 4th ed. Vol. 1. 1994, Miami, Florida: AWS.

16. Quigley, M.B.C., *The Physics of Welding*, in *High Power Density Welding*. 1986, IIW Abington Publishing: UK. p. 306-323.

17. Suban, R., J. Tusek, and M. Uran, *Use of Hydrogen in Welding Engineering in Former Times and Today.* Journal of Material Processing Technology, 2001. **119**: p. 193-198.

18. Zhou, J. and H. Tsai, *Effects of Electromagnetic Force on Melt Flow and Porosity Prevention in Pulsed Laser Keyhole Welding.* International Journal of Heat and Mass Transfer, 2007. **50**: p. 2217-2235.

19. *Welding Pressure Pipelines and Piping Systems*. 1993: Lincoln Electric.

20. Alam, N., D. Dunne, and F.J. Barbaro, *Weld Metal Crack Testing for High Strength Cellulosic Electrodes*, in *First International Conference on Weld Metal Hydrogen Cracking in Pipeline Girth Welds*. 1999, WTIA: Wollongong, Australia. p. 9.1-9.23.

21. Costin, W., et al. *Micromechanical examination of the relationship between weld metal microstructure and hydrogen assisted cold cracking*. in *6th International Pipeline Technology Conference (06 Oct 2013-09 Oct 2013: Ostend, Belgium)*. 2013.

22. Costin, W.L., et al., *Investigation of hydrogen assisted cracking in acicular ferrite using site-specific micro-fracture tests.* Materials Science and Engineering: A, 2016. **651**: p. 859-868.

23. *ASNZS 2885.2-2008 Pipelines- Gas and liquid petroleum Part 2- Welding*. 2007: Australia.

24. Kumar, P.G. and K. Yu-ichi, *Diffusible hydrogen in steel weldments.* Transactions of JWRI, 2013. **42**: p. 39-62.

25. *CSA-Z662-99 Oil and gas pipeline systems*. 1999.

26. Pargeter, R.J., *Effects of arc energy, plate thickness and preheat on C-Mn steel weld metal hydrogen cracking*, in *TWI Research Report (CRP)*. 1992: UK.

27. Kuebler, R., M. Pitrun, and I. Pitrun, *The effect of welding parameters and hydrogen levels on the weldability of high strength Q&T steel welded with FCAW consumables.* Australian Welding Journal, 2000. **45**: p. 38-47.

28. Kurji, R. and N. Coniglio, *Towards the establishment of weldability test standards for hydrogen-assisted cold cracking.* The International Journal of Advanced Manufacturing Technology, 2015. **77**(9-12): p. 1581-1597.

29. (AWS), A.W.S., *Structural Welding Code-Steel*, in *AWS D1.1-2010*. 2010, American Welding Society.

30. *API 1104- Welding of pipelines and related facilities*, in *American Petroleum Institute*. 1999.

31. Lazor, R.B., *Examination of Pipeline Welding Procedural Variables*. 1984, Pipeline Research Council International: Texas, USA.

32. Yurioka, N. and H. Suzuki, *Hydrogen assisted cracking in C-Mn and low alloy steel weldments.* International Materials Reviews, 1990. **35**(4): p. 217 - 249.

33. Granjon, H. *Cold Cracking in Welding of Steels*. in *International Symposium on Cracking and Fracture in Welds (Conference Proceedings)*. 1971. Tokyo: Japan Welding Society.

34. Graville, B.A., *Interpretive report on weldability tests for hydrogen cracking of higher strength steels and their potential for standardization*. 1995, Welding Research Council, New York: New York, NY.

35. Graville, B.A. *Hydrogen cracking sensitivity of HSLA steels*. in *The Metallurgy, Welding and Qualification of Microalloyed (HLSA) Steel Weldments*. 1990. Miami, Florida.

36. Graville, B.A., *The Principles of Cold Cracking Control in Welds*. 1975, Quebec, Canada: Dominion Bridge Company.

37. Graville, B.A., *Cold Cracking in Welds in HSLA Steels*, in *International Conference on Welding on HSLA (Microalloyed) Structural Steels*. 1976: Rome, Italy. p. 85 - 101.

38. Graville, B.A., *A Survey Review of Weld Metal Hydrogen Cracking.* Welding in the World, 1986. **24**(9/10): p. 190-198.

39. Graville, B.A. and M. McParlan, *Weld metal cold cracking.* Metal Construction and British Welding Journal, 1974. **62**(2): p. 62 - 63.

40. Kotousov, A., et al. *A Model of Hydrogen Assisted Cold Cracking in Weld Metal*. in *9th International Pipeline Conference*. 2012. Calgary, Alberta, Canada: ASME.

41. Kuo, S., *Welding Metallurgy*. 2003, USA: John Wiley & Sons, Inc.

42. McParlan, M. and B.A. Graville, *Hydrogen cracking in weld metals.* Welding Research Supplement, 1976. **55**(4): p. 95 - 102.

43. Olson, D.L., et al. *Hydrogen management in high strength steel weldments*. in *Joint seminar of Defence Science and Technology Association (Australia), Welding Technology Institute of Australia, and US Army Research Office*. 1997. Melbourne, Victoria.

44. Savage, W.F., E.F. Nippes, and E.S. Szekers, *Hydrogen Induced Cold Cracking in a Low Alloy Steel.* Welding Journal Research Supplement, 1976. **57**: p. 276s - 283s.

45. Signes, E.G. and P. Howe, *Hydrogen-Assisted Cracking in High-Strength Pipeline Steels.* Welding Journal, 1988. **67**(8): p. 163s-170s.

46. Suzuki, H., *Cold Cracking and its Prevention in Steel Welding (III), Effects of Heat Input and Restraint*. 1980.

47. Lundin, C.D., et al., *Carbon Equivalence and Weldability of Microalloyed Steels*. 1989, Welding Research and Engineering Group, The University of Tennessee: USA.

48. Trevisan, R.d.E. and H.C. Fals, *Fracture modes and acoustic emission characteristics of hydrogen-assisted cracking in high-strength low-alloy steel weldment.* Journal of the Brazilian Society of Mechanical Sciences, 1999. **21**: p. 675-682.

49. Vuik, J., *An update of the state-of-the-art of weld metal hydrogen cracking.* Welding in the World, 1993. **31**(5): p. 23 - 32.

50. Vigilante, G., et al., *Hydrogen induced cracking tests of high strength steels and nickel-iron base alloys using the bolt-loaded specimen*, in *Fatigue and Fracture Mechanics: 28th Volume*. 1997, ASTM International.

51. Gladman, T., *The Physical Metallurgy of Microalloyed Steels*. 2002, UK: IOM, Maney Publishing.

52. Vishnu, R., *Solid State Transformation in Weldments*. 10th Edition ed. Welding, Brazing, and Soldering, Metals Handbook. 1993, USA: ASM International.

53. Thewlis, G., *Classification and quantification of microstructures in steels.* Materials Science and Technology, 2004. **20**(2): p. 143 - 160.

54. IIW, *Guide to the Light Microscope Examination of Ferritic Steel Weld Metals*, in *IIW- Doc. IX-1533-88*. 1988.

55. Bhadeshia, H. and R. Honeycombe, *Steels: microstructure and properties: microstructure and properties*. 2011: Butterworth-Heinemann.

56. Honeycombe, R.W.K. and H.K.D.H. Bhadeshia, *Steels. Microstructure and Properties*. 1995, UK: Edward Arnold.

57. Bhadeshia, H.K.D.H. and L.E. Svensson, *Modelling the evolution of microstructure in steel weld metal*, in *Mathematical modelling of weld phenomena*, H. Cerjak and K.E. Easterling, Editors. 1993, Institute of Materials: London, UK. p. 109 - 182.

58. Lehmann, J., P. Rocabois, and H. Gaye, *Kinetic model of non-metallic inclusions' precipitation during steel solidification.* Journal of Non-Crystalline Solids, 2001. **282**: p. 61-71.

59. David, G.J. and J.G. Garland, *Solidication Structures and Properties of Fusion Weld.* International Materials Reviews, 1975. **20**: p. 83 - 106.

60. Grong, O. and D.K. Matlock, *Microstructural development in mild and low-alloy steel weld metals.* International Metal Review, 1986. **31**(1): p. 27-48.

61. David, S.A. and S.S. Babu, *Microstructure modelling in weld metal*, in *Mathematical Modelling of Weld Phenomena 3*, H. Cerjak, Editor. 1997, The Institute of Materials: UK. p. 151 - 180.

62. Grong, O., *Metallurgical Modelling of Welding*. 2nd Edition ed. 1997, UK: The Institute of Materials.

63. Solomon, H.D., *Fundamentals of weld solidification*, in *Welding, Brazing, and Soldering, Metals Handbook*. 1993, ASM International: USA. p. 45 - 54.

64. Jokl, M.L., et al., *Solute segregation and intergranular brittle fracture in steels.* Metal Science Journal, 1980. **14**: p. 375 - 384.

65. Jin, T.Y., Z.Y. Liu, and Y.F. Cheng, *Effect of non-metallic inclusions on hydrogen-induced cracking of API5L X100 steel.* International Journal of Hydrogen Energy, 2010. **35**(15): p. 8014-8021.

66. Lee, T.K., et al., *Effect of inclusion size on the nucleation of acicular ferrite in welds.* ISIJ International, 2000. **40**(12): p. 1260 - 1268.

67. Basu, B. and R. Raman, *Microstructural variations in a high-strength structural steel weld under isoheat input conditions.* Welding Research Supplement, 2002. **81**(11): p. 239 - 248.

68. Suito, H., H. Ohta, and S. Morioka, *Refinement of solidification microstructure and austenite grain by fine inclusion particles.* ISIJ International, 2006. **46**(6): p. 840 - 846.

69. Babu, S.S. and H.K.D.H. Bhadeshia, *Mechanism of the transition from bainite to acicular ferrite materials.* Materials Transactions, 1991. **32**(8): p. 679 - 688.

70. Bhadeshia, H.K.D.H., *Models for the elementary mechanical properties of steel welds*, in *Mathematical modelling of weld phenomena III*, H. Cerjak and H.K.D.H. Bhadeshia, Editors. 1997, Institute of Materials: London, UK. p. 229 - 284.

71. Bhadeshia, H.K.D.H., *Bainite in Steels*. 2nd ed. 2001, London, UK: Institute of Materials.

72. Jones, S.J. and H.K.D.H. Bhadeshia, *Kinetics of the Widmanstatten ferrite transformation in steels*, in *Displacive phase transformations and their applications in materials engineering*, K. Inoue, et al., Editors. 1998: Warrendale, PA. p. 419-426.

73. Bhadeshia, H.K.D.H., *Reliability of Weld Microstructure and Property Calculations.* Welding Journal, 2004. **83**(9): p. 237 - 243.

74. Strangwood, M. and H.K.D.H. Bhadeshia. *The Mechanism of Acicular Ferrite Formation in Steel Weld Deposits*. in *Advances in Welding Technology and Science, ASM*. 1987. Metals Park, Ohio.

75. Babu, S.S., *The mechanism of acicular ferrite in weld deposits.* Current Opinion in Solid State & Materials Science, 2002. **8**(3-4): p. 267-278.

76. Gregg, J.M. and H.K.D.H. Bhadeshia, *Solid-state nucleation of acicular ferrite on minerals added to molten steel.* Acta Materialia, 1997. **45**(2): p. 739 - 748.

77. Kang, B.Y., H.J. Kim, and S.H. Hwang, *Effect of Mn and Ni on the variation of microstructure and mechanical properties of low-carbon weld metals.* ISIJ International, 2000. **40**(12): p. 1237 - 1245.

78. Abson, D.J. and R.J. Pargeter, *Factor influencing as-deposited strength microstructure, and toughness of manual metal arc welds suitable for C-Mn steel fabrications.* International Metal Review, 1986. **31**(4): p. 141-194.

79. Hsieh, K.C., et al., *Calculation of inclusion formation in low alloy steel welds.* Materials Science & Engineering, 1996. **A215**: p. 84 - 91.

80. Kluken, A.O. and O. Grong, *Mechanisms of Inclusion formation in Al-Ti-Si-Mn deoxidized steel weld metals.* Metallurgical and Material Transactions, 1989. **20A**: p. 1335-1349.

81. Akselsen, O.M., O. Grong, and J.K. Solberg, *Structure-property relationships in intercritical heat affected zone of low-carbon microalloyed steels.* Materials Science and Technology, 1987. **3**: p. 649 - 655.

82. Babu, S.S., et al., *Development of macro- and microstructures of carbon-manganese low alloy steel welds: inclusion formation.* Materials Science and Technology, 1995. **11**: p. 186 - 199.

83. Babu, S., et al. *Modeling the formation of oxide inclusions in low alloy steel welds*. in *Trends in Welding Research. 4 th International Conference*. 1995.

84. Hong, T., et al., *Modeling of inclusion growth and dissolution in the weld pool.* Metallurgical and Material Transactions B, 2000. **31B**: p. 161 - 169.

85. Barbaro, F.J., P. Krauklis, and K.E. Easterling, *Formation of acicular ferrite at oxide particles in steels.* Materials Science and Technology, 1989. **5**(11): p. 1057 - 1068.

86. Ricks, R.A., P.R. Howell, and G.S. Barritte, *The nature of acicular ferrite in HSLA steel weld metals.* Journal of Materials Science, 1982. **17**(3): p. 732 - 740.

87. Cochrane, R.C., Welding in the World, 1983. **21**(1/2): p. 16 - 24.

88. Choi, C.L. and D.C. Hill, Welding Journal, 1978. **57**(8): p. 232s - 236s.

89. Koseki, T. and G. Thewlis, *Inclusion assisted microstructure control in C-Mn and low allow steel welds.* Materials Science and Technology, 2005. **21**(8): p. 867 - 879.

90. Evans, G.M. and N. Bailey, *Metallurgy of Basic Weld Metal*. 1997, UK: Abington Publishing.

91. Lancaster, J.F., *Metallurgy of welding*. 1999, Abington, UK: Woodhead Publishing.

92. Evans, G.M., *The effect of carbon on the microstructure and properties of C-Mn all-weld metal deposits.* Welding Journal, 1983. **62**(11): p. 313s - 320s.

93. Ohkita, S. and Y. Horii, *Recent Development in Controlling the Microstructure and Properties of Low Alloy Steel Weld Metals.* ISIJ International, 1995. **35**(10): p. 1170-1182.

94. Potapov, N., *Oxygen effect on Low alloy steel weld metal properties.* Welding Journal, 1993. **78**(8): p. 367s-370s.

95. Kou, S., *Welding metallurgy.* New York, 1987.

96. Yang, H.S. and H.K.D.H. Bhadeshia, *Austenite grain size and the martensite-start temperature.* Scripta Materialia, 2009. **60**: p. 492 - 495.

97. Lee, S.J. and Y.K. Lee, *Effect of austenite grain size on martensitic transformation of a low alloy steel.* Materials Science Form, 2005. **475**: p. 3169 - 3172.

98. Bollinghaus, T., H. Hoffmeister, and C. Middel, *Scatterbands for hydrogen diffusion coefficients in steels having a ferritic or martensitic microstructure and steels having an austensitic microstructure at room temperature.* Welding in the World, 1996. **37**(1): p. 16 - 23.

99. Olson, D.L., et al., *Hydrogen Management in High Strength Steel Weldments*, in *Hydrogen Management in Steel Weldments*, J.L. Davidson and D.L. Olson, Editors. 1996, Defense Science and Technology Organization (DSTO): Melbourne Australia. p. 1-19.

100. Davidson, J.L., S.P. Lynch, and A. Majumdar, *The relationship between hydrogen-induced cracking resistance, microstructure and toughness in high strength weld metal*, in *Joint Seminar of Defence Science and Technology Organisation / Welding Technology Institute of Australia*, J.L. Davidson and D.L. Olson, Editors. 1996: Melbourne, Australia. p. 21 - 34.

101. Yurioka, N., et al., *Determination of necessary preheat temperature in steel welding.* Welding Journal, 1983. **62**(6): p. 147 - 153.

102. Oriani, R.A., *A brief survey of useful information about hydrogen in metals*, in *International Symposium on Cold Fusion and Advanced Eneregy Sources*, H. Fox, Editor. 1994, Fusion Information Centre: Minsk, Belarus. p. 125 - 128.

103. Oriani, R., *Hydrogen degradation of ferrous alloys.* Noyes Publications, Mill Rd. at Grand Ave, Park Ridge, New Jersey 7656, USA, 1985. 886, 1985.

104. Oriani, R.A., *The diffusion and trapping of hydrogen in steel.* Acta Materialia, 1970. **18**(1): p. 147 - 157.

105. Oriani, R.A., *A mechanistic theory of hydrogen embrittlement of steels.* Berichte der Bunsen-Gesellschafft fur Physikalische Chemie, 1972. **76**(8): p. 848 - 856.

106. Sasse, A.G.B.M. and V.J. Gadgil, *The Kinetics of Hydrogen Assisted Cracking of Metals*, in *Hydrogen Effects in Materials*. 2013, John Wiley & Sons, Inc. p. 497-504.

107. Carter, T.J. and L.A. Cornish, *Hydrogen in metals.* Engineering Failure Analysis, 2001. **8**(2): p. 113 - 121.

108. Oriani, R.A. *The physical and metallurgical aspects of hydrogen in metals*. in *4th International Conference on Cold Fusion*. 1993. Lahaina, Maui, HI: Electric Power Research Institute.

109. Troiano, A.R., *The role of hydrogen and other interstitials in the mechanical behaviour of metals.* Metallurgical and Materials Transactions A, 1960. **52**: p. 54-80.

110. Li, J., R. Oriani, and L. Darken, *The thermodynamics of stressed solids.* Zeitschrift für Physikalische Chemie, 1966. **49**(3_5): p. 271-290.

111. Gedeon, S.A. and T.W. Eagar, *Assessing Hydrogen-Assisted Cracking Fracture Modes in High-Strength Steel Weldments.* Welding Journal, 1990. **69**(6): p. 213s-220s.

112. Gedeon, S. and T. Eagar, *Thermochemical analysis of hydrogen absorption in welding.* Welding Journal, 1990. **69**(7).

113. Ćwiek, J., *Hydrogen degradation of high-strength steels.* Journal of Achievements in Materials and Manufacturing Engineering, 2009. **37**(2): p. 193-212.

114. Mundra, K. and T. Debroy, *A general model for partitioning of gases between a metal and its plasma environment.* Metallurgical and Materials Transactions B, 1995. **26**(1): p. 149-157.

115. Bhadeshia, H.K.D.H., *Modelling of steel welds.* Materials Science and Technology, 1992. **8**: p. 123 - 133.

116. Eliaz, N., et al., *Characteristics of hydrogen embrittlement, stress corrosion cracking and tempered martensite embrittlement in high-strength steels.* Engineering Failure Analysis, 2002. **9**(2): p. 167-184.

117. Liu, Q. and A. Atrens, *A critical review of the influence of hydrogen on the mechanical properties of medium-strength steels.* Corrosion Reviews, 2013. **31**(3-6): p. 85-103.

118. Maroef, I., et al., *Hydrogen trapping in ferritic steel weld metal.* International Materials Reviews, 2002. **47**(4): p. 191-223.

119. Pressouyre, G.M., *Trap theory of hydrogen embrittlement.* Acta Materialia, 1980. **28**(7): p. 895 - 911.

120. Pundt, A. and R. Kirchheim, *Hydrogen in Metals: Microstructural Aspects.* Annual Review of Materials Research, 2006. **36**(1): p. 555-608.

121. Bhadeshia, H.K.D.H., *Prevention of Hydrogen Embrittlement in Steels.* ISIJ International, 2016. **56**(1): p. 24-36.

122. Gibala, R. and D.S. DeMiglio, *Hydrogen in iron and steels: interactions, traps and crack paths*, in *Hydrogen in Metals*. 1980.

123. Garet, M., et al., *Hydrogen trapping on non metallic inclusions in cr-mo low alloy steels.* Corrosion Science, 1998. **40**(7): p. 1073-1086.

124. Krom, A.H.M. and A. Bakker, *Hydrogen trapping models in steel.* Metallurgical and Material Transactions, 2000. **31**(6): p. 1475 - 1482.

125. Asahi, H., D. Hirakami, and S. Yamasaki, *Hydrogen Trapping Behavior in Vanadium-added Steel.* ISIJ International, 2003. **43**(4): p. 527-533.

126. Davidson, J.L., *Hydrogen induced cracking of low carbon - low alloy steel weldments.* Materials Forum, 1995. **19**: p. 35 - 51.

127. Choo, W.Y., et al., *Hydrogen solubility in pure iron and effects of allying elements on the solubility in the temperature range of 20 to 500^{o}C.* Journal of Materials Science, 1981. **16**(5): p. 1285.

128. Lee, H.G. and J.A. Lee, *Hydrogen trapping by TiC particles in iron.* Acta Metallurgica, 1984. **32**(1): p. 131 - 136.

129. Oriani, R.A., *The diffusion and trapping of hydrogen in steel.* Acta Metallurgica, 1970. **18**(1): p. 147-157.

130. Pressouyre, G., *Trap theory of hydrogen embrittlement.* Acta Metallurgica, 1980. **28**(7): p. 895-911.

131. Katano, G., K. Ueyama, and M. Mori, *Observation of hydrogen distribution in high-strength steel.* Journal of Materials Science, 2001. **36**(9): p. 2227 - 2286.

132. Olson, D.L., *Hydrogen and preheat management in welded high strength steel for difence applications*. 1999, US Army Research Office.

133. Oriani, R.A., *Hydrogen embrittlement of steels.* Ann. Rev. Mater. Scie., 1978. **8**: p. 327 - 357.

134. Alipooramirabad, H., et al., *Residual stress-microstructure-mechanical property interrelationships in multipass HSLA steel welds.* Journal of Materials Processing Technology, 2016. **231**: p. 456-467.

135. Radaj, D., *Heat Effects of Welding; Temperature Field, Residual Stresses, Distortion*. 1992, Springer, Berlin.

136. Satoh, K., Y. Ueda, and H. Kihara, *Recent trends of research into restraint stresses and strains in relation to weld cracking.* Welding in the World, 1973. **11**(11S (11W-425-73)).

137. Niwa, M., T. Shikama, and A. Yonezu, *Mechanism of hydrogen embrittlement cracking produced by residual stress from indentation impression.* Materials Science and Engineering: A, 2015. **624**: p. 52-61.

138. Birnbaum, H., et al. *Mechanisms of hydrogen related fracture--a review*. in *Second International Conference on Corrosion-Deformation Interactions. CDI'96*. 1996.

139. Sofronis, P., *The influence of mobility of dissolved hydrogen on the elastic response of a metal.* Journal of the Mechanics and Physics of Solids, 1995. **43**(9): p. 1385-1407.

140. Sofronis, P. and H.K. Birnbaum, *Mechanics of the hydrogendashdislocationdashimpurity interactions—I. Increasing shear modulus.* Journal of the Mechanics and Physics of Solids, 1995. **43**(1): p. 49-90.

141. Sofronis, P. and J. Lufrano, *Interaction of local elastoplasticity with hydrogen: embrittlement effect.* Materials Science & Engineering, 1999. **260**: p. 41 - 47.

142. Sofronis, P.t., Y. Liang, and N. Aravas, *Hydrogen induced shear localization of the plastic flow in metals and alloys.* European Journal of Mechanics-A/Solids, 2001. **20**(6): p. 857-872.

143. Beachem, C., *A new model for hydrogen-assisted cracking (hydrogen "embrittlement").* Metallurgical transactions, 1972. **3**(2): p. 441-455.

144. Toribio, J. and V. Kharin, *Fractographic and numerical study of hydrogen-plasticity interactions near a crack tip.* Journal of Materials Science, 2006. **41**(18): p. 6015 - 6025.

145. Karppi, R., M. Toyoda, and K. Nohara, *Mechanical controlling factor of weld hydrogen cracking.* Trans. Jpn. Weld. Soc., 1981. **12**(2): p. 14-23.

146. Gao, H. and W. Cao, *Effects of stress-strain conditions on hydrogen-induced fracture.* Fatigue & Fracture of Engineering Materials & Structures, 1998. **21**(11): p. 1351 - 1360.

147. Liang, Y., P. Sofronis, and R.H. Dodds Jr, *Interaction of hydrogen with crack-tip plasticity: effects of constraint on void growth.* Materials Science and Engineering: A, 2004. **366**(2): p. 397-411.

148. Kuipers, J., *Nanomechanical testing of in situ hydrogen charged high strength steel.* 2013.

149. Sofronis, P., I.M. Robertson, and D.D. Johnson, *Hydrogen embrittlement of pipline steels: causes and remediation*. 2005, US Department of Energy.

150. Satoh, K., et al., *Effect of intensity of bending restraint on weld cracking in multipass weld.* Transactions of the Japan Welding Society, 1977. **8**(1): p. 42 - 49.

151. Sato, K., et al., *Restraint Intensity of Weld Joints in Structural Elements.* Transactions of JWRI, 1972.

152. Karppi, R.A.J., et al., *Predicitng safe welding conditions with hydrogen cracking parameters.* Scandinavian Journal of Metallurgy, 1984. **13**(2): p. 66-74.

153. TERASAKI, T., R. KARPPI, and K. SATOH, *Relationship between critical stress of HAZ cracking and residual diffusible hydrogen content.* Transactions of the Japan Welding Society, 1979. **10**(1): p. 53-57.

154. Oriani, R.A., *Hydrogen embrittlement of steels.* Annual Review Material Science, 1978: p. 327-357.

155. Beachem, *A New Model for Hydrogen Assisted Cracking.* Metallurgical Transactions 1972. **3**.

156. Hirth, J.P., *Effects of Hydrogen on the Properties of Iron and Steel.* METALLURGICAL TRANSACTIONS A, 1980. **11 A**.

157. Zapfe, C.A. and G. Sims, *Hydrogen embrittlement in engineering materials, internal stress and defects in steel.* Transactions of the ASME, 1941(145): p. 225 - 261.

158. Garofalo, F., Y.T. Chou, and V. Ambegaokar, *Effect of hydrogen on stability of micro cracks in iron and steel.* Acta Metallurgica, 1960. **8**(8): p. 504-512.

159. Bilby, B.A. and J. Hewitt, *Hydrogen in steel--the stability of micro-cracks.* Acta Metallurgica, 1962. **10**(6): p. 587-600.

160. Eliaz, N., *Hydrogen-assisted processing of materials.* Materials Science and Engineering A289 2000: p. 41–53.

161. Hirth, J.P., *Effects of hydrogen on the properties of iron and steel.* Metallurgical and Material Transactions, 1980. **11**(6): p. 861 - 890.

162. Smialowski, M., *Hydrogen in Steel*. 1962, Oxford: Pergamon Press Ltd.

163. Beachem, C.D., *A new model for hydrogen-assisted cracking (hydrogen "embrittlement").* Metallurgical Transactions, 1972. **3**(2): p. 441 - 455.

164. Lynch, S.P., *Environmentally assisted cracking: overview of evidence for an adsorption-induced localised slip process.* Acta Materialia, 1988. **36**(10): p. 2639 - 2661.

165. Birnbaum, H.K.D.H. and P. Sofronis, *Hydrogen-enhanced localized plasticity - a mechanism for hydrogen-related fracture.* Materials Science & Engineering, 1994. **176**(1-2): p. 191 - 202.

166. Kolachev, B.A., *General aspects of the interaction of metals with hydrogen*, in *Hydrogen Embrittlement of Nonferrous Metals*, I.P.f.S. Translations, Editor. 1968.

167. Petch, N.J. and P. Stables, *A decohesion theory for hydrogen-induced crack propagation.* Nature (London), 1952. **169**: p. 842 - 843.

168. Pokhodnya, I.P. *Hydrogen Behaviour in Welded Joints*. in *Joint Seminar Hydrogen Management in Steel Weldments*. 1996. Melbourne, Australia: Defence Science Techonoloy Center (DSTO).

169. Wert, C.A. and R.C. Frank, *Trapping of interstitials in metals.* Annual Review of Materials Science, 1983. **13**(1): p. 139-172.

170. Song, J. and W.A. Curtin, *Atomic mechanism and prediction of hydrogen embrittlement in iron.* Nat Mater, 2013. **12**(2): p. 145-151.

171. Petch, N.J., *Delayed Fracture of Metals under Static Load.* Nature, 1952. **169**(4307).

172. Tien, J., et al., *Hydrogen transport by dislocations.* Metallurgical Transactions A. **7**(6): p. 821-829.

173. Konstantarakis, C., *Hydrogen Degradation of High Strength Steel Weldments*. 1993, Massachusetts Institute of Technology.

174. Pressouyre, G.M., *Trap theory of hydrogen embrittlement: experimental investigations*, in *Hydrogen in Metals*. 1980.

175. Graville, B.A. *Determining Preheat Requirements for Structural Steels*. in *67th AWS Annual Convention*. 1986. Atlanta.

176. Kannengiesser, T. and T. Boellinghaus, *Cold cracking tests—an overview of present technologies and applications.* Welding in the World, 2013. **57**(1): p. 3-37.

177. Glover, A. and B. Rothwell, *Specifications and Practices for Hydrogen Crack Avoidance in Pipeline Girth Welds*, in *First International Conference on Weld Metal Hydrogen Cracking in Pipeline Girth Welds*. 1999, WTIA: Wollongong, Australia. p. 13.1-13.18.

178. North, T.H., et al., *Weldability of High Strength Line Pipe Steels.* Welding Journal, 1982: p. 243s-257s.

179. Vasudevan, R., R.D. Stout, and A.W. Pense, *Hydrogen-assisted cracking in HSLA pipeline steels.* Welding Research Supplement, 1981. **60**(9): p. 155 - 168.

180. Magudeeswaran, G., V. Balasubramanian, and G. Madhusudhan Reddy, *Effect of welding consumables on fatigue performance of shielded metal arc welded high strength, Q&T steel joints.* Journal of Materials Engineering and Performance, 2009. **18**(1): p. 49 - 56.

181. Lazor, R.B. and B. Graville, *Effect of Microalloying on Weld Cracking in Low Carbon Steels.* Canadian Welder and Fabricator, 1983: p. 21-23.

182. Sawhill, J.M., A.W. Dix, and W.F. Savage, *Modified Implant Test for Studying Delayed Cracking.* Welding Journal, 1974. **53**(13): p. 554s-560s.

183. Law, M., R. Holdstock, and D. Nolan, *Method for the quantitative assessment of transverse weld metal hydrogen cracking.* Materials Characterization, 2008. **59**(8): p. 991 - 997.

184. Perteneder, E. and H. Königshofer, *Capabilities and Limitations of Cellulosic Electrodes - A Producer's Perspective*, in *First International Conference on Weld Metal Hydrogen Cracking in Pipeline Girth Welds*. 1999, WTIA: Wollongong, Australia. p. 17.1-17.7.

185. Sarrafan, S., F.M. Ghaini, and E. Rahimi, *Weld Metal Hydrogen Cracking in Transmission Pipelines Construction*, in *Proceedings of the 8th International Pipeline Conference IPC2010*. 2010: Calgary, Canada.

186. Cottrell, C.L.N. and B.J. Bradstreet, *Weldability of Twelve Low Alloy Steels Containing Vanadium*. 1953, Directorate of Weapon Research: USA.

187. Bradstreet, B.J., *Methods to Establish Procedures for Welding Low Alloy Steels.* The Engineering Journal, 1963: p. 37-41.

188. Kinsey, A.J., *The Welding of Structural Steels Without Preheat.* Welding Journal, 2000. **79**(4): p. 79s-88s.

189. Sterjovski, Z., *Investigation of postweld heat treatment of quenched and tempered pressure vessel steels*. 2003, University of Woolongong: Wollongong, NSW, Australia.

190. Hart, P.H., *The Influence of Steel Cleanliness on HAZ Hydrogen Cracking: The Present Position*. 1984.

191. Sterjovski, Z., et al., *Artificial Neural Networks for Predicting Diffusible Hydrogen Content and Cracking Susceptibility in Rutile Flux-Cored Arc Welds.* Journal of Materials Processing Technology, 2007. **184**: p. 420-427.

192. Suzuki, H., *Revised Cold Cracking Parameter PHA and its Applications*. 1984.

193. Coniglio, N., et al., *Hydrogen Assisted Cold Cracking Susceptibility of Weld Metal Deposited by Cellulosic Shielded Metal Arc Welding Consumables*, in *International Pipeline Conference, IPC2010*. 2010: Calgary, Canada.

194. Ushio, M., et al., *Cracking in GMAW Pipeline Girth Welds Based on Experiences in Pipeline Construction in Japan*, in *First International Conference on Weld Metal Hydrogen Cracking in Pipeline Girth Welds*. 1999, WTIA: Wollongong, Australia. p. 10.1-10.9.

195. Kurji, R., et al., *An improved welding institute of Canada test for evaluation of high-strength pipeline steel weldability*, in *6th International Pipeline Technology Conference*. 2013: Ostend, Belgium.

196. Coniglio, N., V.M. Linton, and E. Gamboa, *Mechanised WIC Testing of Boron Containing SMAW Consumables*. 2010.

197. Cola, M.J., *Investigation of WIC Test Variables*. 1991, Edison Welding Institute: Texas, USA.

198. Noble, R.J., R.J. Pargeter, and A.G. Association, *Final Report on Field Weldability of High Strength Pipeline Steels: To American Gas Association*. 1988: Edison Welding Institute.

199. Noble, D.N. and R.J. Pargeter, *Field Weldability of High Strength Pipeline Steels*. 1988, Edison Welding Institute: Texas, USA.

200. Fletcher, L. and N. Yurioka, *A Holistic Model of Hydrogen Cracking in pipeline Girth Wleding.* Welding in the World, 2000. **44**(2): p. 29-36.

201. Wong, R., et al., *Welding Induced Hydrogen in US Navy Structural Steel*, in *Joint Seminar Hydrogen Management in Steel Weldments*. 1996: Melbourne, Australia. p. 35-48.

202. Kurji, R., *Thermo Mechanical Factors Influencing Weld Metal Hydrogen Assisted Cold Cracking*, in *School of Mechanical Engineering*. 2016, The University of Adelaide: Adelaide, Australia.

203. Kurji, R., et al., *Weld Metal HACC Susceptibility Under Controlled Welding Conditions and Restraint Levels*. 2011, Energy Pipeline CRC: Adelaide, Australia.

204. North, T., et al., *Weldability of High Strength Line Pipe Steels.* WELDING J., 1982. **61**(8): p. 243-257.

205. Pargeter, R.J., *Field Weldability of High Strength Pipline Steels*. 1986: Abington, Cambridge.

206. Brown, I.H., et al. *The role of microsegregation in centreline cold cracking of high strength low alloy steel weldments.* in *50th WTIA Annual Conference and the 12th International TWI Computer Technology in Welding and Manufacturing Conference*. 2002. Sydney, Australia.

207. Abson, D.J. and R.J. Pargeter, *Factors influencing as-deposited strength, microstructure, and toughness of manual metal arc welds suitable for C-Mn steel fabrications.* International Metals Reviews, 1986. **31**(1): p. 141-196.

208. Adonyi, Y., *Weldability of high performance steels*, in *Conference on Steel Bridge Design and Construction for the New Millennium with Emphasis on High Performance Steel*. 2000: Baltimore, MD.

209. Archer, G.L., P.H. Hart, and A.Q. Stalker, *An assessment of pipeline girth welds*, in *WRC Symposium at 57th AWS Annual Meeting*. 1976, Welding Research Council: St Louis, MO. p. 147 - 175.

210. Bailey, N., et al., *Welding steels without hydrogen cracking*. 1973, UK: ASM, International, Abington Publishing.

211. Coe, F.R., *Welding Steels without Hydrogen Cracking*. 1973, Abington: The Welding Institute Report.

212. Datta, R., et al., *Weldability characteristics of shieled metal arc welded high strength quenched and tempered plates.* Journal of Materials Engineering and Performance, 2002. **11**(1): p. 5 - 10.

213. du Plessis, J. and M. du Toit, *Reducing diffusible hydrogen contents of shielded metal arc welds through addition of flux-oxidizing ingredients.* Journal of Materials Engineering and Performance, 2008. **17**(1): p. 50 - 56.

214. Glover, A. and B. Graville, *The Risk of Hydrogen Cracking in Multipass Welds and its Effect Upon Procedure Design*, in *First International Conference on Weld Metal Hydrogen Cracking in Pipeline Girth Welds*. 1999, Wollongong, Australia. p. 9.1-9.23.

215. Talaş, Ş., *The assessment of carbon equivalent formulas in predicting the properties of steel weld metals.* Materials & Design, 2010. **31**(5): p. 2649-2653.

216. Dearden. J and O'Neil. H, *A guide to the selection and welding of low alloy structural steels.* Trans Int Weld, 1940. **3**(10): p. 203-214.

217. Suzuki, H. and H. Tamura, *Weldability of high strength steels evaluated by synthetic HAZ ductility test.* Trans. National Res. Inst. Metals, 1961. **3**(1).

218. Hannerz. N, *The influence of silicon on the weldability of mild and high tensile structural steels*. 1980, IIW: IIW Doc. IX-1169-80.

219. Uwer, D. and H. Hohne, *Determination of suitable minimum preheating temperatures for the cold-crack-free welding of steels*, in *IIW Doc. IX-1631-9*. 1991, IIW.

220. Ito, Y. and K. Bessayo, *Weldability Formula of High Strength Steels Related to Heat Affected Zone Cracking*. 1968.

221. Duren, C., *Equations for the prediction of cold cracking in field welding large diameter pipes*, in *IIW Doc. IX-1356-85*. 1985.

222. Yurioka, N., S. Ohshita, and H. Tamehiro, *Study on Carbon Equivalents to Assess Cold Cracking Tendency and Hardness in Steel Welding*, in *Conference on Pipeline Welding in 80's*. 1981: Melbourne.

223. Davidson, J.L. and D.L.R. Olson, *Hydrogen management in steel weldments: joint seminar, Melbourne, Australia, 23rd October 1996 : proceedings of the seminar*. 1997: Published by the Organising Committee of the Joint Seminar on behalf of Defence Science and Technology Association and Welding Technology Institute of Australia.

224. Graville B., *A Survey Review of Weld Metal Hydrogen Cracking.* Welding in the World, 1986(24): p. 190-198.

225. McParlan M. and Graville B.A., Welding Journal, 1976. **55**(4): p. 95-102.

226. Talas, *The assessment of carbon equivalent formulas in predicting the properties of steel weld metals.* Materials and Design, 2010. **35**(5).

227. Watkinson F., Welding Journal, 1969. **48**(9): p. 417-424.

228. Yurioka, N. *Predictive Methods for Prevention and Control of Hydrogen Assisted Cold Cracking*. in *Weld Metal Hydrogen Cracking in Girth Welds* 1999. Wollongong.

229. Gangloff, R.P., *Hydrogen assisted cracking of high strength alloys*, in *Comprehensive structural integrity*, J. Petit and P. Scott, Editors. 2003, Elsevier Science: New York, NY. p. 31-101.

230. Homrossukon, S., S. Mostovoy, and J.A. Todd, *Investigation of Hydrogen Assisted Cracking in High and Low Strength Steels.* Journal of Pressure Vessel Technology, 2009. **131**(4): p. 041405-041405.

231. Ito, Y. and K. Bessayo, *A Prediction of Welding Procedure to Avoid Heat Affected Zone Cracking*. 1969.

232. Suzuki, H. and T. Terasaki, *Estimating Critical Stress and Preheat Temperature to Avoid Cold Cracking in Implant and JIS-Y (Tekken) Tests*. 1986.

233. Ito, Y., M. Ikeda, and M. Nakanishi, *Study on Estimation of Lower Critical Stress for Cold Cracking at Welds by Implant Test Method.* Journal of the Japan Welding Society, 1976. **45**(12): p. 1029-1036.

234. Matsuda, F., H. Nakagawa, and K. Shinozaki, *The LB-TRC test for cold crack susceptibility of weld metal for high-strength steels.* Transactions of the JWRI, 1979. **8**(1): p. 113 - 119.

235. Christensen, N. and T. Simonsen, Scandinavian Journal of Metallurgy, 1981. **10**: p. 120-126.

236. Inagaki, M., et al., *Application of Implant Test on Cold Cracking*. 1978.

237. Terasaki, T. and K. Satoh, ISIJ International, 1982. **68**(1): p. 140-146.

238. Yurioka, N., *Predictive Methods for Prevention and Control of Hydrogen Assisted Cold Cracking*, in *First International Conference on Weld Metal Hydrogen Cracking in Pipeline Girth Welds*. 1999, WTIA: Wollongong, Australia. p. 2.1-2.16.

239. Pham, T.-H., J.J. Kim, and S.-E. Kim, *Estimation of microstructural compositions in the weld zone of structural steel using nanoindentation.* Journal of Constructional Steel Research, 2014. **99**(0): p. 121-128.

240. Cheng, Y.-T. and C.-M. Cheng, *Relationships between hardness, elastic modulus, and the work of indentation.* Applied Physics Letters, 1998. **73**(5): p. 614-616.

241. Lucca, D.A., K. Herrmann, and M.J. Klopfstein, *Nanoindentation: Measuring methods and applications.* CIRP Annals - Manufacturing Technology, 2010. **59**(2): p. 803-819.

242. VanLandingham, M.R., *Review of instrumented indentation.* Journal of Research of the National Institute of Standards and Technology, 2003. **108**(4): p. 249-265.

243. Oliver, W.C. and G.M. Pharr, *Measurement of hardness and elastic modulus by instrumented indentation: Advances in understanding and refinements to methodology.* Journal of Materials Research, 2004. **19**(01): p. 3-20.

244. Chudoba, T., *Measurement of Hardness and Young's Modulus by Nanoindentation*, in *Nanostructured Coatings*, A. Cavaleiro and J.T.M. De Hosson, Editors. 2006, Springer New York: New York, NY. p. 216-260.

245. Schuh, C.A., *Nanoindentation studies of materials.* Materials Today, 2006. **9**(5): p. 32-40.

246. Johnson, K.L., *Contact Mechanics*. 1985: Cambridge University Press.

247. Fischer-Cripps. A, C., *Introduction to Contact Mechanics*. Mechanical Engineering Series. 2007, USA: Springer US.

248. Bao, Y., W. Wang, and Y. Zhou, *Investigation of the relationship between elastic modulus and hardness based on depth-sensing indentation measurements.* Acta Materialia, 2004. **52**(18): p. 5397-5404.

249. Barnoush, H. and H. Vehoff, *In situ electrochemical nanoindentation: a nanochemical approach to rank hydrogen embrittlement in extremely small specimens*, in *International Hydrogen Conference, Effects of Hydrogen on Materials*. 2008: Moran, WY.

250. Ye, D., et al., *Use of instrumented indentation testing to study local mechanical properties of 304L SS welded joints subjected to low-cycle fatigue loadings.* Materials Science and Engineering: A, 2013. **564**: p. 76-84.

251. Fang, J. and H. Yuan. *The local concept to assess weldment with help of nano-indentation and FEM simulation*. in *13th International Conference on Fracture 2013, ICF 2013, June 16, 2013 - June 21, 2013*. 2013. Beijing, China: Chinese Society of Theoretical and Applied Mechanics.

252. Baltazar Hernandez, V.H., et al., *Nanoindentation and microstructure analysis of resistance spot welded dual phase steel.* Materials Letters, 2010. **64**(2): p. 207-210.

253. Maier, P., et al., *Application of nanoindentation technique for structural characterisation of weld materials.* Materials Characterization, 2002. **48**(4): p. 329-339.

254. Mukhopadhyay, N.K. and P. Paufler, *Micro- and nanoindentation techniques for mechanical characterisation of materials.* International Materials Reviews, 2006. **51**(4): p. 209-245.

255. Fischer-Cripps, A.C., *Nanoindentation testing*, in *Nanoindentation*. 2011, Springer. p. 21-37.

256. Oyen, M.L. and R.F. Cook, *A practical guide for analysis of nanoindentation data.* Journal of the Mechanical Behavior of Biomedical Materials, 2009. **2**(4): p. 396-407.

257. Gerberich, W., et al., *Nanoindentation-induced defect–interface interactions: phenomena, methods and limitations.* Acta Materialia, 1999. **47**(15): p. 4115-4123.

258. Elmustafa, A.A. and D.S. Stone, *Nanoindentation and the indentation size effect: Kinetics of deformation and strain gradient plasticity.* Journal of the Mechanics and Physics of Solids, 2003. **51**(2): p. 357-381.

259. Ortiz, M. and J. Ovejero-Garcia, *Effect of hydrogen on Young's modulus of AISI 1005 and 1070 steels.* Journal of materials science, 1992. **27**(24): p. 6777-6781.

260. Hardiman, M. and C.T. McCarthy. *Experimentation and numerical modelling of nanoindentation of fibrous composites*. in *15th European Conference on Composite Materials: Composites at Venice, ECCM 2012, June 24, 2012 - June 28, 2012*. 2012. Venice, Italy: European Conference on Composite Materials, ECCM.

261. Gibson, R.F., *A review of recent research on nanoindentation of polymer composites and their constituents.* Composites Science and Technology, 2014. **105**: p. 51-65.

262. Pulla, S.S. and Y.C. Lu, *Effective interfacial thickness in dissimilar materials through nanoindentation.* Computers, Materials and Continua, 2012. **29**(3): p. 263-278.

263. Babu, J.S.S. and C.G. Kang, *Nanoindentation behaviour of aluminium based hybrid composites with graphite nanofiber/alumina short fiber.* Materials and Design, 2010. **31**(10): p. 4881-4885.

264. Ferencz, R., et al., *AFM nanoindentation to determine Young's modulus for different EPDM elastomers.* Polymer Testing, 2012. **31**(3): p. 425-432.

265. Choi, J.-K. and S.-I. Pyun, *A new theory describing the hydrogen-assisted intergranular cracking of high-strength steels.* Journal of Materials Science, 1999. **25**: p. 246 - 252.

266. Barnoush, A. and H. Vehoff, *In situ electrochemical nanoindentation of a nickel (111) single crystal: Hydrogen effect on pop-in behaviour.* International Journal of Materials Research, 2006. **97**(9): p. 1224-1229.

267. Barnoush, A., C. Bies, and H. Vehoff, *In situ electrochemical nanoindentation of FeAl (100) single crystal: Hydrogen effect on dislocation nucleation.* Journal of Materials Research, 2009. **24**(3): p. 1105-1113.

268. Barnoush, A. and H. Vehoff, *Electrochemical nanoindentation: A new approach to probe hydrogen/deformation interaction.* Scripta Materialia, 2006. **55**(2): p. 195-198.

269. Gao, X., *Displacement burst and hydrogen effect during loading and holding in nanoindentation of an iron single crystal.* Scripta Materialia, 2005. **53**(11): p. 1315-1320.

270. Tal-Gutelmacher, E., et al., *Hydrogen effect on dislocation nucleation in a vanadium (1 0 0) single crystal as observed during nanoindentation.* Scripta Materialia, 2010. **63**(10): p. 1032-1035.

271. Barnoush, A., et al. *Examination of hydrogen embrittlement in FeAl by means of in situ electrochemical micropillar compression and nanoindentation techniques*. 2010. Elsevier Ltd.

272. ISO, *Metallic materials -- Instrumented indentation test for hardness and materials parameters*, in *14577-1 Part 1: Test method*. 2015.

273. Bobji, M. and S. Biswas, *Deconvolution of hardness from data obtained from nanoindentation of rough surfaces.* Journal of materials research, 1999. **14**(06): p. 2259-2268.

274. Nix, W.D. and H. Gao, *Indentation size effects in crystalline materials: a law for strain gradient plasticity.* Journal of the Mechanics and Physics of Solids, 1998. **46**(3): p. 411-425.

275. Göken, M., M. Kempf, and W. Nix, *Hardness and modulus of the lamellar microstructure in PST-TiAl studied by nanoindentations and AFM.* Acta materialia, 2001. **49**(5): p. 903-911.

276. Liu, Y. and A. Ngan, *Depth dependence of hardness in copper single crystals measured by nanoindentation.* Scripta Materialia, 2001. **44**(2): p. 237-241.

277. Jeffus, L., *Welding: principles and applications*. 2011: Nelson Education.

278. Williams, J.G. and C.R. Killmore. *High Strength ERW Pipeline Steels with Improved Weldability*. in *WTIA/APIA Panel 7 Research Seminar*. 1995. Wollongong.

279. Barbaro, F.J., et al., *Weldability of High Strength EWR X80 Grade Pipe*, in *Pipeline Technology Conference*. 1995: Ostend, Belgium.

280. Norrish, J. and M. Carapic, *The Feasibility of Mechanized Girth Welding for the Installation of Land Based Transmission Pipelines in Australia*, in *Mechanized Girth Welding of Thin Wall, High Strength Pipelines*. 2002, Cooperative Research Center - Welded Structures.

281. *AS/NZS 3978-2003 Non-destructive testing - Visual inspection of metal products and components*. 2003.

282. Mochizuki, M., et al., *Analytical study on effects of strain distribution in welding start/end on welding distortion.* Welding International, 2009. **23**(9): p. 654-661.

283. Yurioka, N., *Predictive Methods for Prevention and Control of Hydrogen Assisted Cold Cracking*, in *First International Conference on Weld Metal Hydrogen Cracking in Pipeline Girth Welds*. 1999, WTIA: Wollongong, Australia.

284. Coniglio, N. and C. Cross, *Initiation and growth mechanisms for weld solidification cracking.* International Materials Reviews, 2013. **58**(7): p. 375-397.

285. Eskin, D. and L. Katgerman, *A quest for a new hot tearing criterion.* Metallurgical and Materials Transactions A, 2007. **38**(7): p. 1511-1519.

286. Suyitno, W.K. and L. Katgerman, *Hot tearing criteria evaluation for direct-chill casting of an Al-4.5 Pct Cu alloy.* Metall Mater Trans A, 2005. **36**(6): p. 1537-1546.

287. Cross, C., *On the origin of weld solidification cracking*, in *Hot cracking phenomena in welds*. 2005, Springer. p. 3-18.

288. Eskin, D. and L. Katgerman, *Mechanical properties in the semi-solid state and hot tearing of aluminium alloys.* Progress in Materials Science, 2004. **49**(5): p. 629-711.

289. Nolan, D. and R. Hutchings, *Hot Cracking in Cellulosic Pipeline Girth Welds*. 1998, CRC-WS: Wollongong, Australia.

290. Nolan, D., D. Dunne, and J. Norrish, *Root pass solidification cracking in low carbon pipeline girth welds deposited via cellulosic manual metal arc welding.* Science and Technology of Welding and Joining, 2003. **8**(2): p. 102-112.

291. Bailey, N., *Weldability of ferritic steels*. 1994, Abington, UK: Woodhead Publishing Ltd.

292. Ahmed, N. and B. Jarvis, *The effect of welding conditions on the thermal cycles in single electrode submerged arc welding.* Australasian Welding Journal, 1998. **43**(3).

293. Ohshita, S., et al., *Prevention of solidification cracking in very low carbon steel welds.* WELDING J., 1983. **62**(5): p. 129.

294. Olson, D.L., *ASM handbook: welding, brazing, and soldering*. Vol. 6. 1993: Asm Intl.

295. Connor, L.P. and R. O'Brien, *Welding handbook: welding processes*. Vol. 2. 1991: Amer Welding Society.

296. Costin, W., *On the relationship between microstructure mechanical properties and weld metal hydrogen assisted cold cracking*, in *School of Mechanical Engineering*. 2016, The University of Adelaide: Adelaide.

297. Yayla, P., E. Kaluc, and K. Ural, *Effects of welding processes on the mechanical properties of HY 80 steel weldments.* Materials & Design, 2007. **28**(6): p. 1898-1906.

298. Allen, D., B. Chew, and P. Harris, *Formation of Chevron cracks in submerged arc weld metal.* WELDING J., 1982. **61**(7): p. 212.

299. Matsuda, F., et al., *Evaluation of transformation expansion and its beneficial effects on cold crack susceptibly using y-slit crack test instrumented with strain gauge.* Transactions of JWRI (Japanese Welding Research Institute), 1984. **13**(1): p. 47-55.

300. Elboujdaini, M. and W. Revie, *Effect of Non-Metallic Inclusions on Hydrogen Induced Cracking*, in *Damage and Fracture Mechanics*, T. Boukharouba, M. Elboujdaini, and G. Pluvinage, Editors. 2009, Springer Netherlands. p. 11-18.

301. Surian, E., et al., *Influence of chromium on the mechanical properties and microstructure of weld metal from a high-strength SMA electrode.* WELDING JOURNAL-NEW YORK-, 1994. **73**: p. 45-s.

302. Kirkwood, P., *A viewpoint on the weldability of modern structural steels.* The Metallurgical Society/AIME, 1987: p. 21-44.

303. Easterling, K., *Introduction to the Physical Metallurgy of Welding*. 2nd Edition ed. 1992, UK: Butterworth-Heinemann Ltd.

304. Powell, G., et al. *Cold cracking and segregation in multipass welds of a quenched and tempered steel*. in *International Conference on Trends in Welding Research (6th: 2002: Phoenix, Ariz. USA.)*. 2002.

305. Davidson, J.A., P.J. Konkol, and J.F. Sovak, *Assessing fracture toughness and cracking susceptibility of steel weldments. A review.* Welding Research Council Bulletin, 1989(345).

306. Young, C.H. and H.K.D.H. Bhadeshia, *Strength of mixtures of bainite and martensite.* Materials Science and Technology, 1994. **10**: p. 209 - 214.

307. Symons, D.M., *Effect of carbide precipitation on the hydrogen-enhanced fracture behavior of alloy 690.* Metallurgical and Materials Transactions A: Physical Metallurgy and Materials Science, 1998. **29 A**(4): p. 1265-1277.

308. Sirois, E. and H. Birnbaum, *Effects of hydrogen and carbon on thermally activated deformation in nickel.* Acta metallurgica et materialia, 1992. **40**(6): p. 1377-1385.

309. Shih, D., I. Robertson, and H. Birnbaum, *Hydrogen embrittlement of α titanium: in situ TEM studies.* Acta Metallurgica, 1988. **36**(1): p. 111-124.

310. Robertson, I. and H. Birnbaum, *An HVEM study of hydrogen effects on the deformation and fracture of nickel.* Acta Metallurgica, 1986. **34**(3): p. 353-366.

311. Tabata, T. and H. Birnbaum, *Direct observations of hydrogen enhanced crack propagation in iron.* Scripta metallurgica, 1984. **18**(3): p. 231-236.

312. Lynch, S., *Environmentally assisted cracking: overview of evidence for an adsorption-induced localised-slip process.* Acta Metallurgica, 1988. **36**(10): p. 2639-2661.

313. Lynch, S., *Metallographic contributions to understanding mechanisms of environmentally assisted cracking.* Metallography, 1989. **23**(2): p. 147-171.

314. Birnbaum, H.K. and P. Sofronis, *Hydrogen-enhanced localized plasticity—a mechanism for hydrogen-related fracture.* Materials Science and Engineering: A, 1994. **176**(1-2): p. 191-202.

315. Bond, G., I. Robertson, and H. Birnbaum, *Effects of hydrogen on deformation and fracture processes in high-ourity aluminium.* Acta Metallurgica, 1988. **36**(8): p. 2193-2197.

316. Tabata, T. and H. Birnbaum, *Direct observations of the effect of hydrogen on the behavior of dislocations in iron.* Scripta Metallurgica, 1983. **17**(7): p. 947-950.

317. Lee, T.-D., T. Goldenberg, and J. Hirth, *Effect of hydrogen on fracture of U-notched bend specimens of spheroidized AISI 1095 steel.* Metallurgical Transactions A, 1979. **10**(2): p. 199-208.

318. Onyewuenyi, O. and J. Hirth, *Effects of hydrogen on notch ductility and fracture in spheroidized AISI 1090 steel.* Metallurgical Transactions A, 1983. **14**(1): p. 259-269.

319. Di Leo, C.V. and L. Anand, *Hydrogen in metals: A coupled theory for species diffusion and large elastic–plastic deformations.* International Journal of Plasticity, 2013. **43**: p. 42-69.

320. Tsui, T., et al. *Nanoindentation and nanoscratching of hard carbon coatings for magnetic disks*. in *MRS Proceedings*. 1995. Cambridge Univ Press.

321. Pharr, G., *Measurement of mechanical properties by ultra-low load indentation.* Materials Science and Engineering: A, 1998. **253**(1): p. 151-159.

322. Leyland, A. and A. Matthews, *On the significance of the H/E ratio in wear control: A nanocomposite coating approach to optimised tribological behaviour.* Wear, 2000. **246**(1-2): p. 1-11.

323. Oberle, T.L., *Properties influencing wear of metals.* American Institute of Mining and Metallurgical Engineers -- Journal of Metals, 1951. **3**(6): p. 438-439.

324. Finkin, E.F., *Examination of Abrasion Resistance Criteria for Some Ductile Metals.* Journal of Lubrication Technology-Transactions of the Asme, 1974. **96**(2): p. 210-214.

325. Zhang, S., *Thin Films and Coatings-Toughening and Toughness Characterization*, ed. S. Zhang. 2015, Boca Raton, FL: CRC Press, Taylor and Francis Group.

326. Gerberich, W.W. and Y.T. Chen, *A threshold stress intensity concept for environmental cracking.* International Journal of Fracture, 1973. **9**(3): p. 369-371.

327. Yamaguchi, Y., H. Nonaka, and K. Yamakawa, *Effect of Hydrogen Content on Threshold Stress Intensity Factor in Carbon Steel in Hydrogen-Assisted Cracking Environments.* Corrosion, 1997. **53**(2): p. 147-155.

328. Loginow, A.W. and E.H. Phelps, *Steels for seamless hydrogen pressure vessels.* Journal of Engineering for Industry, Transactions of the ASME, 1975. **97 Ser B**(1): p. 274-282.

CHAPTER 9

Publications

9 Publications

The following journal publications are of close relevance to the present work and are attached to this thesis

1. Kurji, R., Coniglio, N., Griggs, J. and R. Ghomashchi, Modified WIC test: an efficient and effective tool for evaluating pipeline girth weldability. Science and Technology of Welding and Joining- Accepted 25th Aug 2016

2. Kurji, R., O. Lavigne, and R. Ghomashchi, Micromechanical characterisation of weld metal susceptibility to hydrogen-assisted cold cracking using instrumented indentation. Welding in the World, 2016. 60(5): p. 883-897

3. Ghomashchi, R., W. Costin, and R. Kurji, Evolution of weld metal microstructure in shielded metal arc welding of X70 HSLA steel with cellulosic electrodes: A case study. Materials Characterization, 2015. 107: p. 317-326.

4. Kurji, R. and N. Coniglio, Towards the establishment of weldability test standards for hydrogen-assisted cold cracking. The International Journal of Advanced Manufacturing Technology, 2015. 77(9-12): p. 1581-1597.

SCIENCE AND TECHNOLOGY OF WELDING AND JOINING, 2016
http://dx.doi.org/10.1080/13621718.2016.1232674

The Institute of Materials, Minerals and Mining

Taylor & Francis
Taylor & Francis Group

Modified WIC test: an efficient and effective tool for evaluating pipeline girth weldability

R. Kurji[a], N. Coniglio[b], J. Griggs[a] and R. Ghomashchi[a]

[a]School of Mechanical Engineering, The University of Adelaide, Adelaide, Australia; [b]Ecole Nationale Supérieure d'Arts et Métiers ParisTech, Laboratory MSMP, Aix en Provence, France

ABSTRACT

The Welding Institute of Canada (WIC) test is a simple and standardised weldability test for hydrogen assisted cold cracking that was developed in the 80s. It has been extensively utilised by the industry to qualify safe welding envelopes but the difficult access to the weldment by instrumentation hinders its use for scientific research. Moreover the lack of repeatability arising from the traditional manual deposit and the short weld length causes industrial trials to have a low success rate. The present work proposes a modified geometry, referred to as the modified WIC (MWIC) test that shows: (1) an improved success rate of weld deposition, (2) an enhancement to instrument the weldment and (3) welding conditions in better accordance with the field pipeline girth welding conditions. The design is validated under a mechanised, shielded metal arc welding process with the cellulosic electrodes used for in-field pipeline construction.

ARTICLE HISTORY
Received 16 June 2016
Accepted 25 August 2016

KEYWORDS
Hydrogen assisted cold cracking; weldability testing; shielded metal arc welding; modified welding institute of canada

Introduction

The pipeline industry has long desired the establishment of standardised weldability tests in order to quantify the susceptibility to hydrogen assisted cold cracking (HACC) of pipeline girth welds [1–3], a significant threat to pipeline weld integrity. The predominant advantage of such standardisation is the ability to compare weldability test data across a range of sources reliably and with confidence. This is becoming ever more important as the prevalence of weld metal HACC (WMHACC) is increasing [4–7] and major standards such as the Australian Standards AS2885.2:2007 [8] and the European Standard EN 1011-2:2001 [9] do not provide guidelines on specific procedures such as preheating to minimise the risk of cracking.

HACC is a defect likely to occur in hydrogenated weldments subjected to high residual tensile stresses. HACC is complex in nature, involving interplay between hydrogen and thermal, mechanical and metallurgical factors. A number of theories and criteria have been proposed to describe and characterise HACC formation, as indicated in reviews on the subject [2,5,10–15]. However, since the underlying mechanism governing this phenomenon is not well understood, it is still a contentious subject today.

Hydrogen may be introduced into the weld, during welding, from several sources including contaminants such as oil and grease present on the surface of the weld preps and atmospheric moisture. However, the dominant source of hydrogen when welding is the electrode flux itself. In the root pass of pipeline girth welds where high deposition rates and deep penetration welds are required the use of cellulosic electrodes is common place [16–19]. The disassociation of the cellulosic $(C_6H_{10}O_5)_n$ flux and the moisture it contains during welding introduces into the weld metal larger amounts of diffusible hydrogen (10^1–10^2 mL H_2/100 g Fe) [20]. The development of the tensile residual stress during weld metal cooling provides the complementary driving force for HACC formation [20–23].

Technological advancements in the steel making process have led to the development of higher strength line pipe steel. The economic benefits, including higher capacity and a net cost saving following a reduction in the raw tonnage of steel used, have accelerated its adoption by industry. The use of higher strength steels has necessitated the use of higher strength electrodes for pipeline construction. The richer chemistry of high strength electrodes delays the weld metal austenite-to-ferrite transformation in such a way that the transformation occurs after the austenite-to-ferrite transformation of the HAZ of high strength low alloy (HSLA) steel pipes. As the solubility of hydrogen is lower in ferrite than austenite, hydrogen is rejected during cooling from the ferritic HAZ to the adjacent austenitic weld metal [20]. The subsequent high levels of hydrogen in the weld metal favours the formation of cold cracking into the weld metal.

CONTACT R. Kurji rahim.kurji@adelaide.edu.au; R. Ghomashchi reza.ghomashchi@adelaide.edu.au

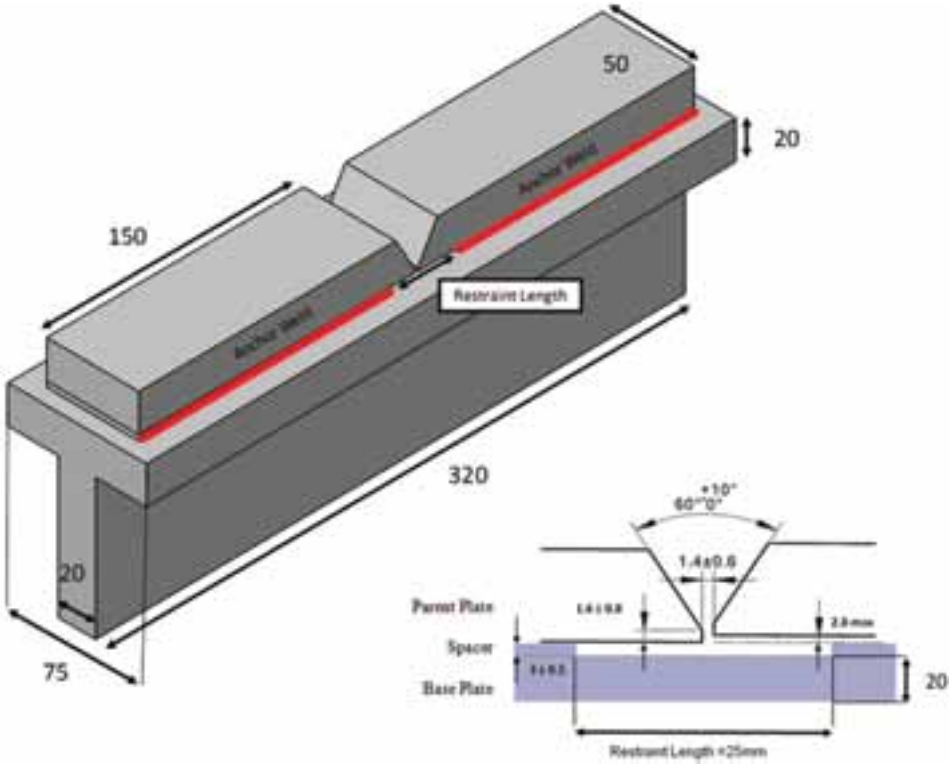

Figure 1. Schematic of experimental setup for WIC test.

In such cases (i.e. where HSLA steels are welded with cellulosic electrodes) there is an elevated risk of WMHACC. A variety of weldability tests have been developed over the years and are specifically designed to generate HACC by promoting special restraint conditions in the weld metal region [2,3,24,25]. Each test design develops specific restraint conditions and loading configurations so that their suitability to represent full-scale welding is not universal. A weldability test representative of pipeline girth welding for small diameter thin walled pipes, such as those typically found in the Australian context, must subject a girth weld deposited into a V-prep groove to high restraint conditions. Among the numerous weldability tests developed to date [3] the Welding Institute of Canada (WIC) test has proven to reproduce the restraint conditions during in-field pipeline girth welding. Nevertheless its short welding length and the traditionally deposited weld in a horizontal manual manner hinders the comparison between the weldability test result and the in-field conditions (vertical down 5G deposition).

The present work proposes an improved conception of the original WIC test into a novel geometry referred to as the 'Modified WIC' (MWIC) test. The improvement of the novel sample geometry is asserted by investigating girth welding conditions of gas transmission pipeline steel with cellulosic electrodes. It was considered imperative that any alteration to the sample design would not change the thermal field or the restraint conditions around the weld so that results obtained from samples with the altered design could be compared with those from the original design and with results from other laboratories.

The traditional WIC weldability test

The WIC test [4,25–28] consists of depositing a single pass weld metal into a V-prep groove separating two restraint test plates. These plates are clamped with anchor welds to a stiffener tee with the restraint intensity controlled by the free-weld length (referred to as the restraint length) between the anchor welds (Figure 1). The welded joint is removed from the WIC specimen usually 24 h after welding completion by sawing the test assembly just inside the restraint length avoiding the ends of the anchor welds. The weld zone is then assessed for cracking.

Traditionally, the weld metal in the WIC test groove was deposited manually in the flat position. But this procedure has limited repeatability, originating from the variations in heat input inherent to manual welding. Moreover a vertical-down welding direction should be more representative of the in-field pipeline conditions. To reduce variations in the weld bead shape and heat input inherent with manual welding, a recent development of the WIC test procedure has included the mechanised vertical-down deposition of the weld metal to improve the consistency and repeatability of the tests [26].

In the WIC testing, the critical preheat temperature to avoid cracking depends on the welding conditions and weld metal chemistry, but also on the misalignment of the two welded plates [2]. This test has been

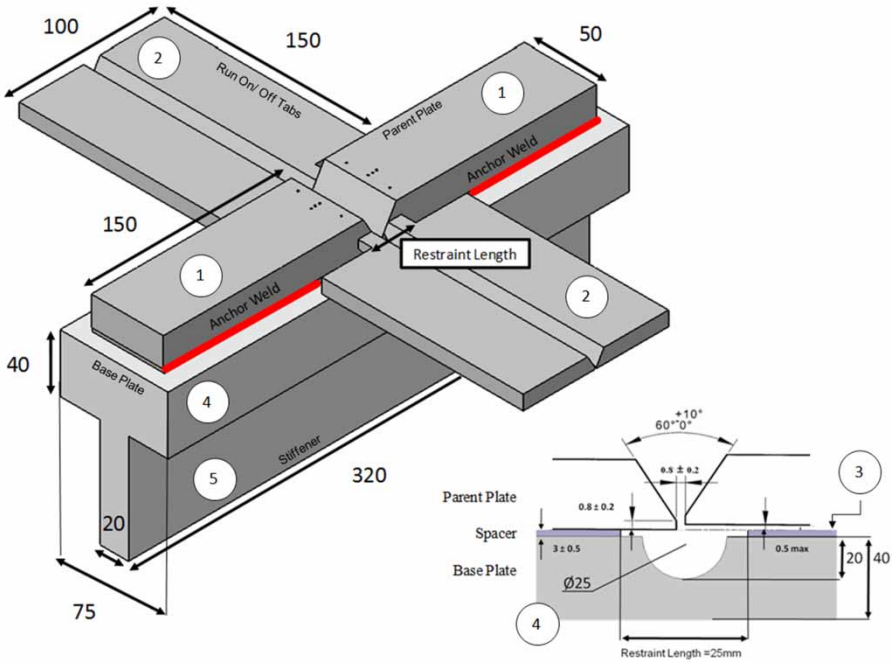

Figure 2. MWIC design. (1) Parent plate, (2) run on/off tab, (3) spacer, (4) tunnelled backing plate, (5) stiffener.

successful in comparing the HACC susceptibility of weld metals deposited by cellulosic Shielded metal arc welding (SMAW) consumables [4,27,29–33] and the critical preheat values to avoid cracking in the WIC test are similar to those obtained in full-scale weldability testing of pipe welding [27]. The WIC test has been benchmarked as a procedure for developing in-field pipeline welding requirements [34]. As both the critical preheat temperature and the restraint intensity affect crack formation, the critical restraint intensity-preheat temperature mapping concept was proposed to determine the thermo-mechanical conditions for cracking in the WIC test [4].

The traditional WIC test geometry has two major drawbacks in its geometry design: a short length for depositing the weld metal and the small gap between the backside of the groove root and the T-shaped support. The tests short test section (welding length) makes it difficult for a weld to be deposited under steady-state thermal conditions, leading to a strong influence of start and end conditions making the results difficult to interpret.

The small gap between the backside of the groove root and the T-shaped support which is provided by a 3 mm-thick spacer limits the access to the root of the weld. Such access is required for thermal analysis and local displacement measurement if the WIC test is to be instrumented. Moreover, this small gap hinders the venting of the gases produced during the decomposition of the electrode flux during SMAW. During in-field girth welding, large volumes of carbon monoxide and other shielding gases produced during welding flow through the weld keyhole into the pipe bore. The small back-space in the WIC test produces high back-pressures and causes the apparition of through-thickness holes in the weld metal. To compensate, a higher degree of welder compensation, in terms of lead angle, lateral weave and force with which the electrode is pushed into the weld prep to sustain the key hole, is required. Such a compensation results in a higher variation of heat input and is less representative of in-field welding conditions.

The MWIC weldability test

The proposed geometric configuration of the MWIC Test was introduced after a series of iterative simulation and experimental studies aimed at improving the quality and consistency of the deposited weld bead [35]. The MWIC test has been designed (Figure 2) from the original geometric features of the WIC test. A 20 mm-diameter scoop is machined out below the welded joint to allow for the egress of the gases and dross. A change in the thickness of the backing plate from 20 to 40 mm ensures maintenance of the stiffness of the strong back. Run on and run off tabs, with the same V groove preparation as the test section, are TIG welded to the test plates (on one side) so as to follow the restraining movements of the test plates and not affect the restraint conditions. Access for instrumentation is also incorporated into the design (Figures 6 and 7).

Finite element analysis

Simulation parameters

To investigate the influence of the design modifications, geometrically representative models of the WIC and MWIC were created in a finite element modelling package; ANSYS® 14. Material properties of structural steel

Table 1. Material properties applied to the finite element simulation.

Compressive yield strength	250 MPa	Young's modulus	200 GPa
Tensile yield strength	250 MPa	Poisson's ratio	0.3
Tensile ultimate strength	460 MPa	Bulk modulus	167 GPa

(Table 1) were applied to both specimens. Quad node shell elements were used for the structural analysis and tetrahedral solid heat transfer elements were used for the thermal analysis. The anchor welds were modelled as fixed supports and contact between the spacer, parent and backing plate was modelled though the use of contact elements. A coarse mesh was applied through the bulk of the geometry with a finer mesh applied in the region of interest.

Restraint conditions

It is desirable for the MWIC test to have a similar deformation response under load to that of the WIC test, as this allows for cracking test results to be compared between the test specimens. Therefore, to compare the maximum displacement between nodes on the surfaces of the prepared edges of the WIC and MWIC tests a dimensionally accurate model of half of the tests were implemented. Symmetrical zero displacement boundary conditions were applied to simulate the sample being held in place on a flat surface. The restraint conditions of the MWIC and WIC specimens were investigated by applying a constant pressure to the weld area.

A stress of 300 MPa was applied on the surface of the root landing and the displacement of three nodes for WIC and MWIC, as illustrated in Figure 3, compared.

The calculated displacements for the three different nodes (in similar geometrical locations) in weld area for both original WIC and MWIC specimens are shown in Table 2. As expected the maximum displacements occurred in the *Z*-direction for both test specimens and this is due to the fact there is a tensile load applied in the *Z*-direction in the V groove (weld area). By comparing the results of the displacements for both samples (Table 2), for corresponding nodes, an increase of maximum 18.7% in displacement in the MWIC sample occurred in *Z*-direction. This suggests that the original WIC and the MWIC tests provide very similar restraint conditions.

Table 2. Comparison of displacements for the selected nodes in both WIC specimens (original and MWIC samples).

		Displacement µm		
Coordinates	Nodes	WIC	MWIC	Comparison (%)
X	1	−0.12	−0.13	9.6
	2	−1.3	−1.42	8.5
	3	−2.7	−3.12	8.9
Y	1	28.4	30.3	6.7
	2	25.9	28.0	8.1
	3	23.1	25.2	8.9
Z	1	44.4	51.9	17.0
	2	43.1	50.9	18.1
	3	42.1	50.0	18.7

Thermal analysis

A 3D transient thermal analysis was conducted using a moving Gaussian heat source to compare the thermal response of the parent plate in the WIC and MWIC tests. The analysis methodology was similar to those employed by Darmadi et al. [36], Iacobescu [37], Teixeria et al. [38] and Alipooramirabad et al. [39]. The heat input was calculated in 0.1 s intervals for 8 s and distributed with a standard deviation of 1 mm and a mean that moved from one side to the other at a speed of 7 mm s^{-1} along the weld surface. A coarse mesh was applied to reduce computational time due to the complexity of 3D transient thermal analyses with surface-surface radiation.

Simulation cases were run for single pass welds deposited at a heat input of 0.65 kJ mm^{-1} on both 10

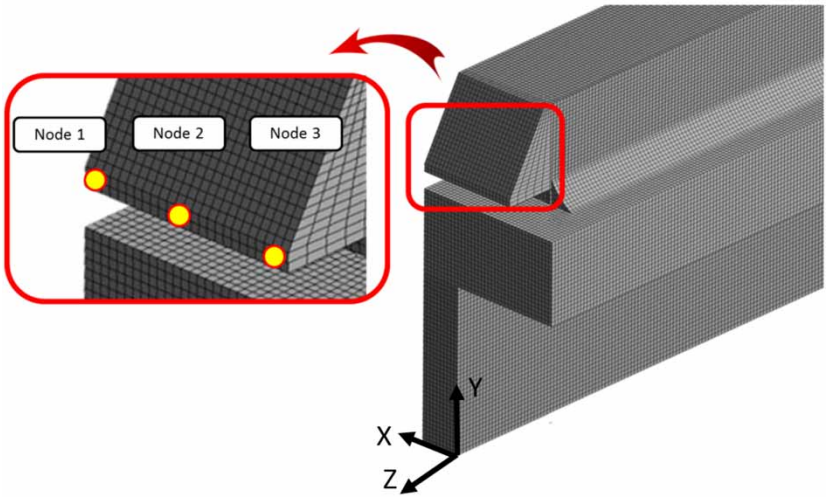

Figure 3. Schematic of relative position of nodes isolated for the analysis of displacement. The image highlights the position of the nodes isolated on the WIC test. For the MWIC test, nodes located in the sample position were used for the analysis.

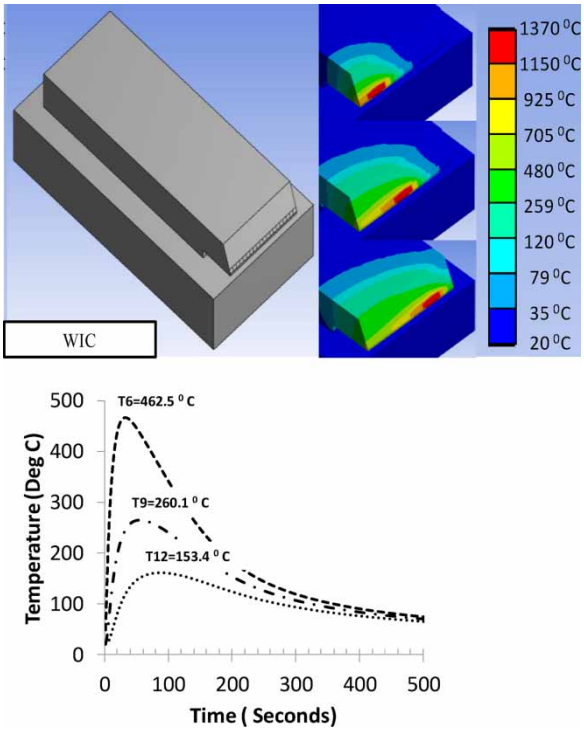

Figure 4. Thermal response of the standard WIC samples to local heating.

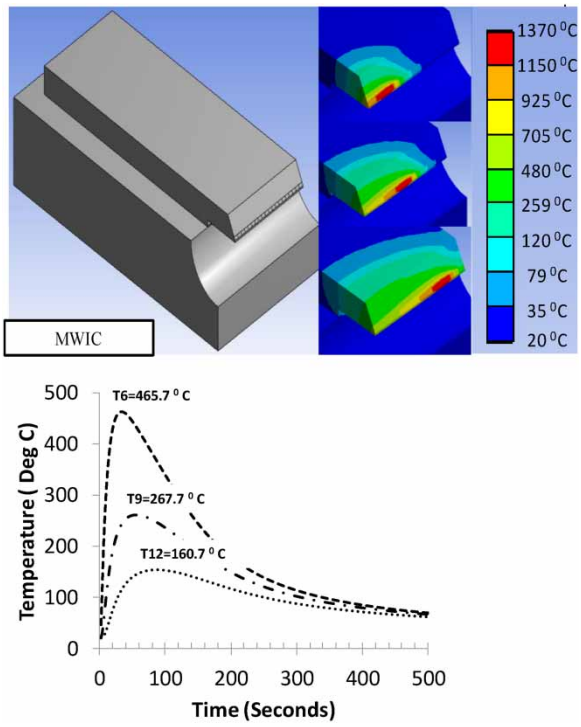

Figure 5. Thermal response of the MWIC samples to local heating.

and 20 mm thick parent plate. The heat input for the simulation case was selected as it is suggested to be representative of field conditions [40] and can be experimentally replicated for validation on both the WIC and MWIC tests. To compare the two specimens temperature probes are used to ascertain the peak temperature and cooling rates at 6, 9 and 12 mm away from the weld centreline. These positions correspond to the T6, T9 and T12 positions on the MWIC physical test specimen (Figure 6).

Figures 4 and 5 shows a typical temperature history during the welding cycle for the two designs at various distances from the weld axis. In the finite element calculations the typical temperature-dependent properties of steel were used and the local heating was modelled by an increase of the initial temperature in the weld location. The adopted simplifications are justified by the main objective of the modelling, which is to compare the thermal response of the two specimen geometries to the local intensive heating simulating to some extent the welding conditions. The accurate modelling of welding requires much greater computational effort and an extensive validation, which are outside of the scope of this paper.

The temperature fields presented in Figures 4 and 5 show a near negligible difference of the thermal responses to the local heating of the WIC and MWIC samples. For simulations run on 10 mm thick plate, the peak temperature difference between the WIC and MWIC tests was less than 7.5°C and for the 20 mm thick plate less than 5°C. The near negligible difference in recorded peak temperature and an approximate correlation coefficient of unity for all the positions (T6, T9 and T12) with regards of the cooling rates suggests the specimens are comparable from a thermal perspective.

Weldability testing

To establish the performance of the MWIC test a two tier experimental programme was employed as summarised in Table 3.

Testing parameters

Weldability testing was carried out on a uni-directional, mechanised SMA welding machine with a specimen-holding plate moving vertically upwards during welding at a controlled velocity, thus simulating vertical-down welding conditions. Welding parameters are

Table 3. Divisions of the experimental programme.

Tier 1	***Experimental validation of simulation results and design modifications*** A series of weldability tests were conducted on the WIC and MWIC test specimen, replicating conditions that were simulated using FEA. The primary objective of Tier 1 testing is to validate the comparability of the thermal response of the two test specimens
Tier 2	***Comparative weldability envelope evaluation*** Weldability tests were conducted for a broad range of parameters on the WIC and MWIC test to provide a sample set with which the deposition window can be compared. Additionally the sample set provides the basis to compare repeatability and reliability of the test specimens.

Table 4. Welding parameters.

Welding specifications		Welding parameters	
Direction	Vertical down (5G)	Current	130–170 A
Size of electrode	4.0 mm	Voltage	25–30 V
AWS class	A5.1	Travel speed	250–470 mm min^{-1}
Specification	E6010	Heat input range	0.41–1.00 kJ mm^{-1}
Polarity	DC+	Preheat range	25–100°C

summarised in Table 4. A constant force and an angle of 20° normal to the plate were maintained between the electrode and the workpiece. The Lincoln Electric Invertec 350V Pro was used as the welding power source. The groove surfaces of the test specimen and 25 mm either side of the weld centreline was polished down with ISO 80 grit (201 µm) emery paper and degreased with acetone. The entire specimen was degaussed prior to welding. The WIC and MWIC specimen designs were tested across a heat input range (0.4–1.0 kJ mm^{-1}), using commonly encountered welding parameters when laying the root pass of a girth weld (Table 4).

Material

The WIC and MWIC tests were fabricated using API 5L grade X70 line pipe steel for test plate. The weld deposition was performed with a 4 mm-diameter E6010 electrodes. The test plate chemical composition is given in Table 5 and the electrodes batch chemistry is given in Table 6.

Thermal analysis

Test plate thermal data was obtained by fitting three electrically-grounded K-type thermocouples (1 mm outer diameter) coated with thermal paste into the parent plate. The three 1.2 mm diameter holes are 1 mm off the bottom of the parent plate and 6 (T6), 9 (T9) and 12 (T12) mm away from the weld centreline, respectively (Figure 6). This allows for measurement of the thermal cycle from HAZ through to the unaffected base metal. Two additional thermocouple access holes, the top tracker (TT) and bottom tracker (BT) were drilled 5 mm from the edge of test section (1 mm off the bottom surface) to measure the entry and exit temperature of the test section to verify relative thermal homogeneity in the test weld.

The weld metal centreline temperature was measured through an access port drilled through the tunnelled backing plate (Figure 7). An R-type thermocouple was plunged into the molten weld pool through the centreline access port at the specimens' back, behind the welding arc without interfering with the welding process (Figure 7).

Local strain measurement

Ideally, what is most pertinent to cracking is the strain experienced by the weld metal from its deposition and during its solidification and cooling. In this study, the strain was measured using an extensometer in the local vicinity of the weld. The deformation of the weld metal will capture the local displacement (at the weld metal

Table 5. Chemical composition of line pipe steel (% weight) (from manufacturer).

C	Mn	Si	S	P	Nb	Ti	Cu	Ni	Mo	Cr	Ca	Al	V
0.052	1.55	0.21	0.0011	0.0097	0.041	0.012	0.15	0.19	0.18	0.026	0.0016	0.039	0.029

Table 6. Electrode batch chemical composition (% weight) (from manufacturer).

C	Mn	Si	S	P	Ni	Mo	Cr	V
0.16	0.62	0.19	0.009	0.009	0.2	0.01	0.02	< 0.01

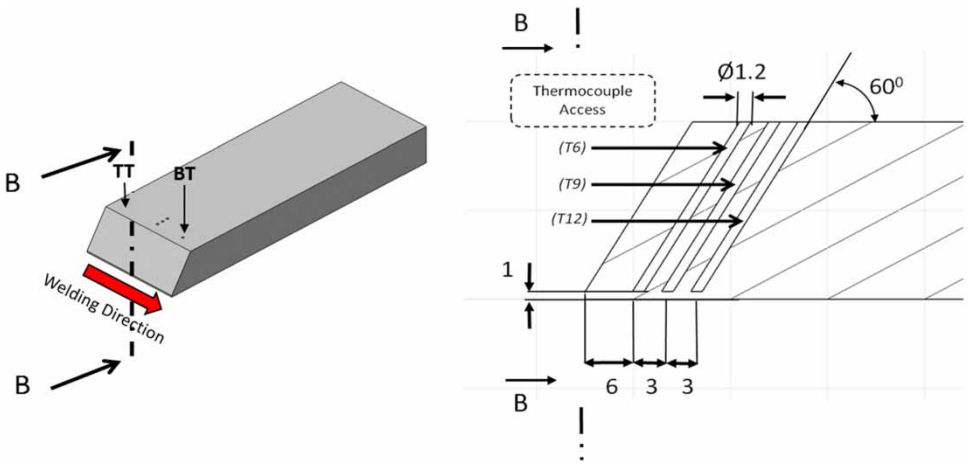

Figure 6. Isometric and cross-sectional view of thermocouple access for parent plate.

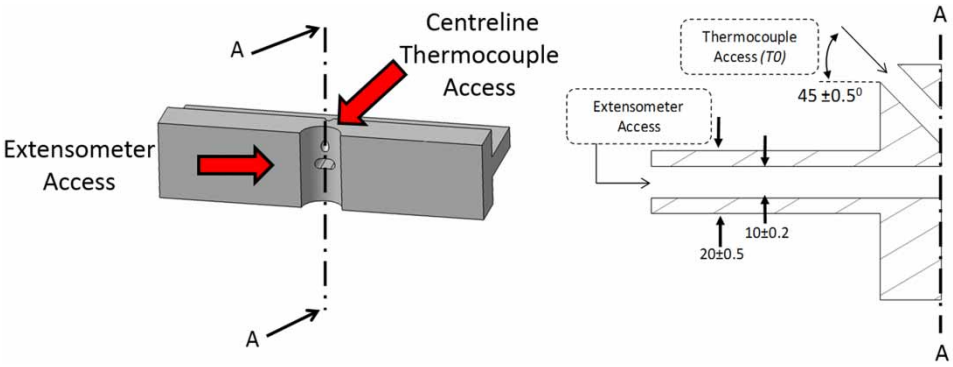

Figure 7. Isometric and cross-sectional view of instrumentation access for weld centreline temperature and local weld metal displacement.

scale) and allow for a measure of the residual stress that builds up until the attainment of the room temperature by the weldment. A high temperature extensometer (Epsilon 3448-10-50) was attached underneath the weld coupon, through the drilled access shown in Figure 7, in the path of the weld at mid-length, to measure the local transverse strain across the weld pool during and after the welding process. The gauge length of the extensometer is 10 mm spanning across a 6 mm-wide weld bead.

Data acquisition

The extensometer and thermocouples outputs were filtered and recorded at a 10 Hz frequency during the entire test using a Virtual Instrument built using Lab View®-2010. The data signals are acquired through a NI-CDAQ-9188 analog-to-digital converter and channelled through an optical isolation system into several 16bit National Instruments® (NI) 9215 voltage modules embedded in a NI-CDAQ-9188 chassis. Welding voltage and current was recorded at 2 Hz using Lincoln Electrics® (LE) proprietary software; LE Power Wave Manager.

Weld analysis

The welded joint was removed from the WIC and MWIC specimens 24 h after weld completion by milling the test assembly just inside the restraint length. The anchor welds were sawed off using a water-cooled precision metallographic saw. The weld zone was assessed for cracking by examining six weld metal transverse cross-sections prepared for metallurgical inspection (Figure 8). A sample is defined as cracked (Figure 9) if a planner defect is visually identified on a sample surface when magnified at ×400, and the vertical length of the defect is greater than 5% of the height of the weld bead (t_w). The weld metal microstructure was examined using an optical microscope on metallographically prepared weldments cross-sections, (polished to 1 µm diamond paste and etched in a 2% nital solution).

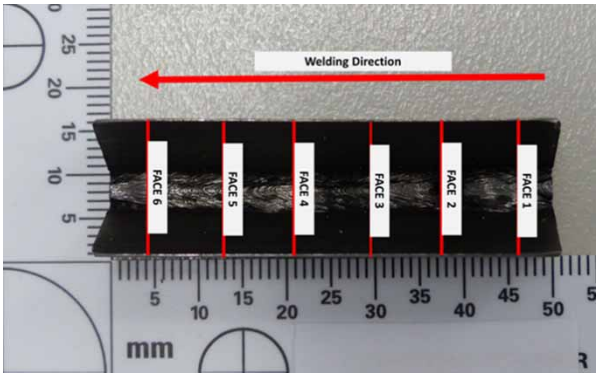

Figure 8. Weldability testpiece with the location of the six faces to be examined under an optical microscope at a magnification of ×400.

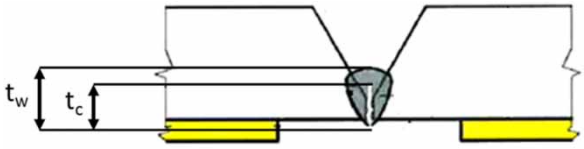

Figure 9. Schematic of a face of a test section. A sample is defined as cracked when a linear defect whose vertical length (t_c) is greater than 5% of the bead height (t_w).

Results

Tier 1: Experimental validation of simulated results and design modifications

Thermal results

Experimental cooling rates and peak temperature data showed a strong positive correlation with simulated results for the WIC and MWIC tests. A maximum difference of 58°C in peak temperature was noted between simulated and experiential results. This difference can be accounted for by the simplifications, including the use of coarse mesh, employed when constructing the

Table 7. Comparison of the peak temperatures for 20 mm thick MWIC and WIC tests at 0.85 ± 0.02 kJ mm^{-1} under ambient conditions and maximum restraint.

	Peak temperature (°C)				
Sample	TT	T6	T9	T12	BT
MWIC	402°C	384°C	251°C	175°C	375°C
WIC	425°C	416°C	266°C	184°C	401°C
% Difference	5.7%	8.3%	5.9%	5.1%	6.9%

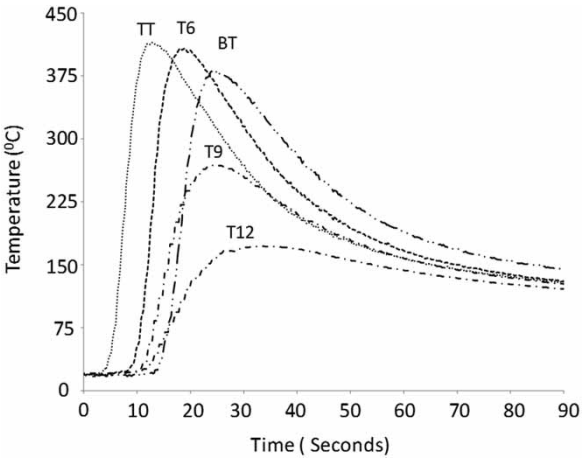

Figure 10. Mean thermal profile of 20 mm thick MWIC at tests at 0.85 ± 0.02 kJ mm^{-1} under ambient conditions (25 ± 5°C) and maximum restraint.

thermal model. Nevertheless the recorded temperature differences between the WIC and MWIC parent was less than 8.5% (Table 7). Temperature measurements taken from the TT and BT thermocouples on the MWIC show similar cooling rates indicating a high degree of thermal homogeneity within the test section and verifying that the run on tabs have no effect on the cooling rates at the edge of the test section. Figure 10 illustrates the mean temperature profile of MWIC tests carried out at 0.85 ± 0.02 kJ mm^{-1} under ambient conditions (25 ± 5°C) and maximum restraint. Across the entire range of experiments there was less than 10% difference in the peak temperatures recorded. This variance was random and could be attributed to experimental error introduced as a result of contact and response time of the thermocouple with the parent plate.

To establish the thermal cracking index, incorporating the critical cooling time $t_{8/5}$ under various welding conditions, an R-type thermocouple was lanced into the molten weld pool behind the arc. Given the intrinsic geometric configuration of the traditional WIC test this was not possible without disturbing the test sequence. However, the rear access port on the MWIC test allowed for successful plunging in. Measurements on weld metals without (Figure 11) and with (Figure 12) plunged thermocouples highlight an increase in hardness values for the latter experimental condition. This hardness increase is possibly related to different cooling conditions and elemental contaminations from the thermocouples. Indeed, EDX scans on weld metal with plunged thermocouples revealed traces of platinum (Pt) and rhodium (Rh) in the weld pool (Figure 13), thus potentially distorting any conclusion drawing when using the MWIC weldability test or for that matter any weldability test that had a thermocouple plunged into the molten weld pool.

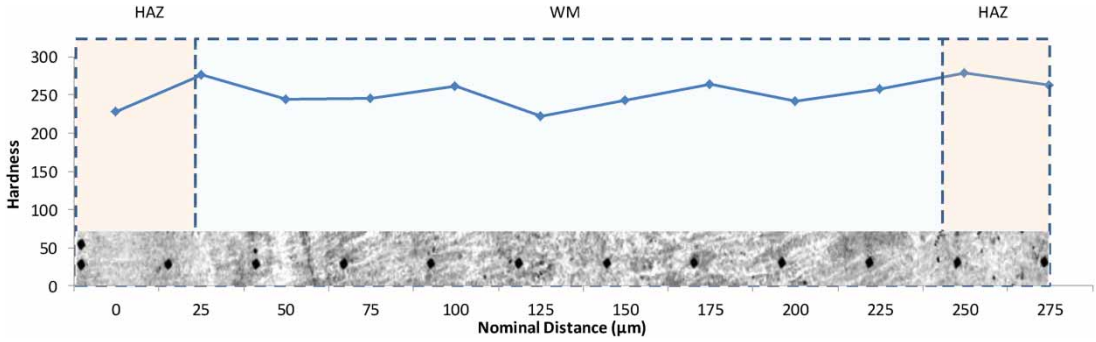

Figure 11. Weld metal harness traverse for MWIC sample without a thermocouple plunge and consequently expected hardness levels.

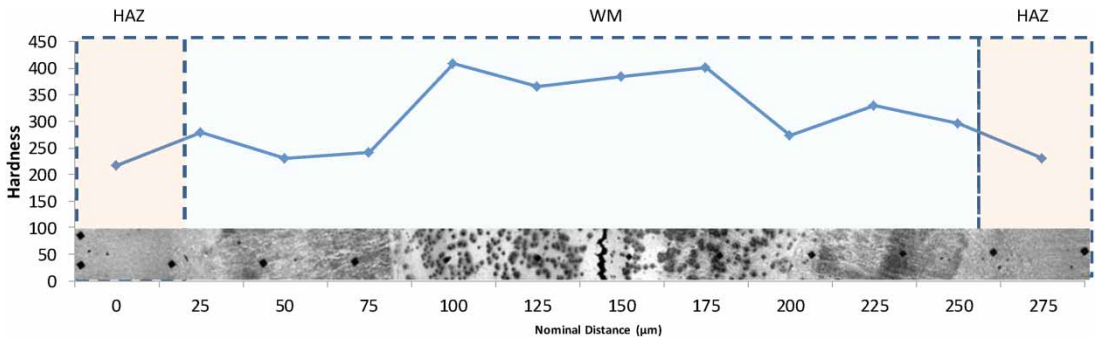

Figure 12. Weld metal hardness traverse for MWIC sample with R-type thermocouple plunged and consequent elevated hardness.

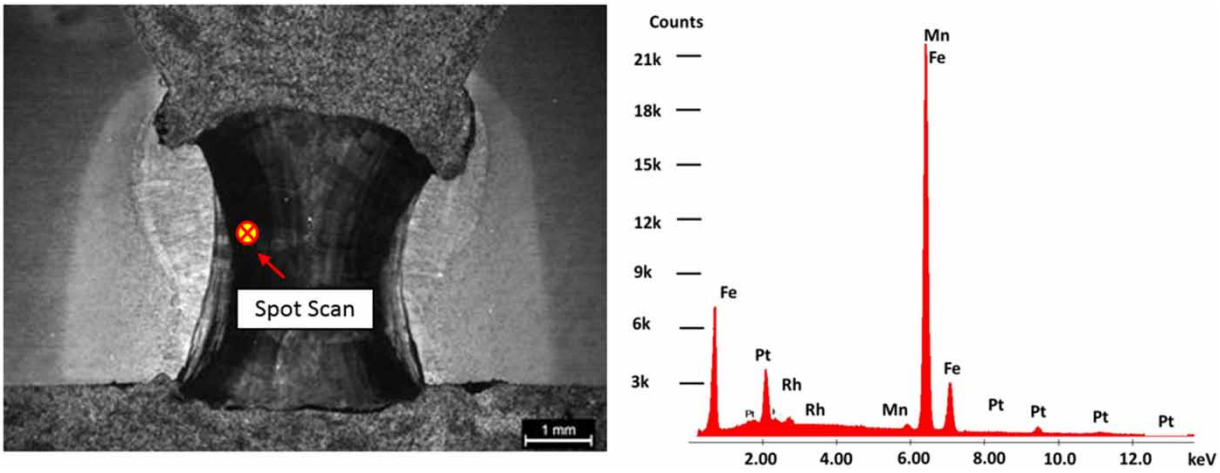

Figure 13. Plunged sample Le Pera's etching macrograph (left). EDX spectrum of spot scan at 20 kV (right).

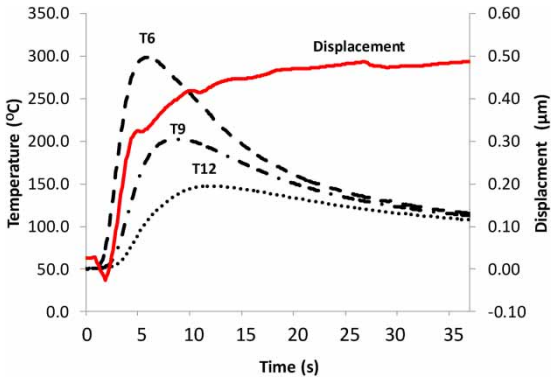

Figure 14. Strain measurement superposed to thermal analyses for a MWIC test under experimental conditions: 20 mm thick baseplates, 0.6 kJ mm^{-1} heat input, 50 ± 5°C preheat, 50 mm restraint length.

Displacement results

An extensometer of 10-mm gauge length is spanned across the groove prior to welding on the root side. An example of strain measurement made during the MWIC test is presented in Figure 14, shown as a function of time with the thermal analysis superimposed. Negative strain represents displacement toward the weld centreline. Note that the strain becomes negative between 1 and 4 s, which is likely due to thermal expansion ahead of the advancing weld electrode [41]. The irregularity of the strain curve likely represents intermittent crack growth, in agreement with the observations of other researchers [4,42]. Restraint length affects local strain even for uncracked welds. This could be due to the lower cooling rate at longer restraint length resulting in lower rates of solidification shrinkage and thermal contraction.

Tier 2: Weldability envelope evaluation

Deposition envelope

Welding trials showed that for 20 mm thick plates under ambient conditions, at heat inputs lower than 0.45 kJ mm^{-1} both tests produced defective welds that exhibited lack of fusion and penetration. Testing results also showed that the MWIC specimen could be used to deposit defect free welds between 0.5 and 1.0 kJ mm^{-1}, whereas the standard WIC test was limited to a heat input range of above 0.8 kJ mm^{-1} (Figure 15). Welds deposited on the WIC specimen below this range resulted in the formation of 'windows' to the point where the weld did not represent field weld quality and would generate undue stress concentration for accurate determination for the onset of HACC (Figure 16).

Welding in the WIC and MWIC test proved the existence of a lower limit in welding heat inputs. However, while defective welds were deposited in the WIC test below 0.9 kJ mm^{-1}, the MWIC test deposited acceptable welds as low as 0.5 kJ mm^{-1}. Figure 16 highlights the considered defective welds.

Weld bead consistency

The weld profile for the WIC and the MWIC were compared at the heat input range where both tests could successfully deposit a defect free weld (Figure 17). The mean throat thickness for the 12 examined sections of the WIC test ranged from 4.5 to 6 mm, whereas for the MWIC test ranged from 5.5 to 5.7 mm. The MWIC tests showed less than 10% variation in mean throat thickness across the range of heat inputs tested (0.5–1.0 kJ mm^{-1}).

Discussion

A weld metal cold cracking is formed if a hydrogenated susceptible microstructure is subjected to a stress greater than a threshold value. The WIC and MWIC test can both be used to rank single pass welds in regards to their susceptibility to cold cracking for a range of welding parameters, preheats, consumable and parent plate chemistries.

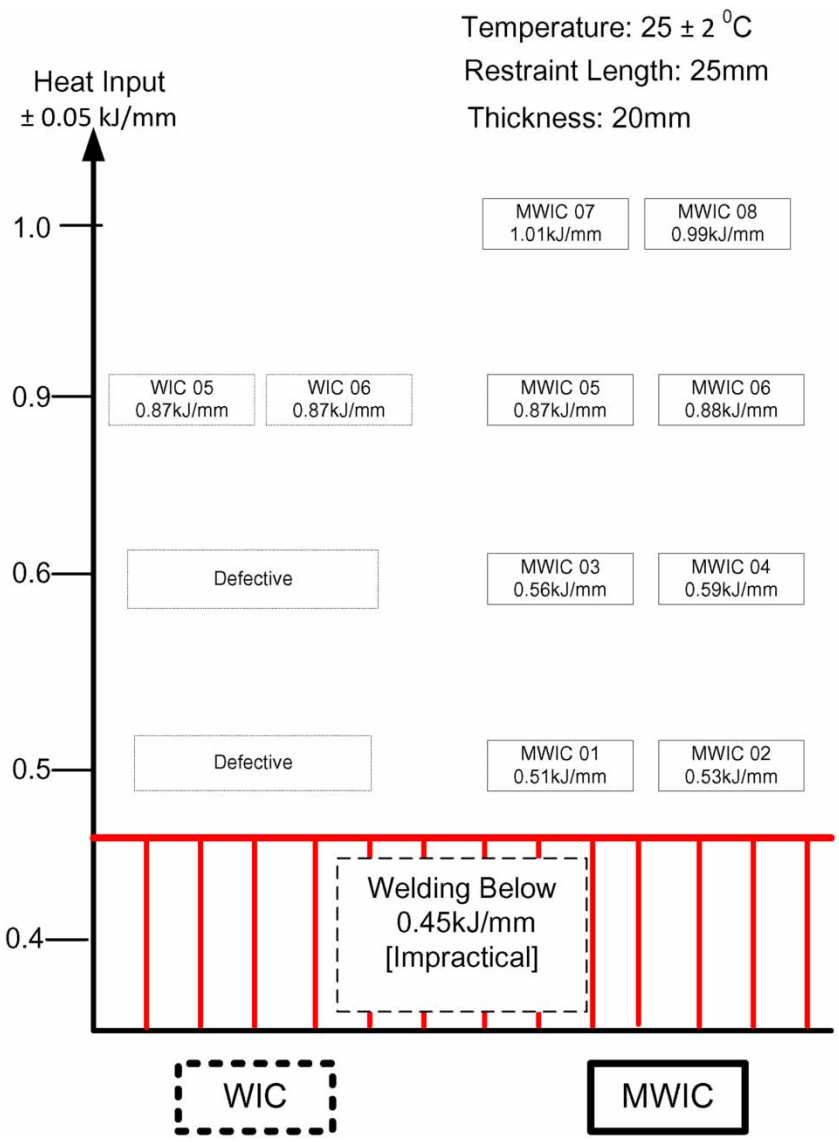

Figure 15. Weldability test range for the WIC and MWIC specimens across the root pass heat input range.

The heat input range representative of the root pass conditions encountered on a pipeline spread corresponds to low heat inputs due to fast welding speeds. While the WIC test has been cited extensively in literature as a tool to prescribe the critical preheat required to avoid cracking [2], the MWIC test possesses modifications of the WIC test that enhance the tests suitability at low heat inputs and high travel speeds. Experimental results demonstrated the MWIC test can be employed with confidence in the heat input range from 0.5 to 1 kJ mm^{-1} where the traditional WIC test cannot (Figure 18).

The MWIC test produces welds with a more consistent throat thickness than the WIC test, improving the reliability and repeatability of the tests. The WIC test and by extension the MWIC test allows for a variation in restraint through the variation in the length of the anchor welds, and thus for the quantification of the critical restraint needed to initiate cracking. However, asymmetry in the weld profile and inconsistency in the throat thickness common with the traditional WIC test promotes scatter in identification of the crack/no crack boundary. The modifications to the WIC test reduced the variation in throat thickness and improved the sensitivity of the test. To illustrate the point consider Figures 19 and 20. MWIC_01 and MWIC_02 were welded within ±0.05 kJ mm^{-1} of each other. Both tests showed similar cracking characteristics in terms of the location of the crack and size of the crack across the sections examined suggesting an enhancement in the reliability of the test.

Finally the MWIC test has been instrumented to give access to the weld metal thermal history and displacement data. Thermal analysis provides the input to estimate the validity of the use of $t_{8/1}$ criteria. The thermocouple access allows for a thermocouple to be plunged into the molten weld pool giving access to the complete thermal history of the weld metal. Extraction of the $t_{8/5}$ can be linked to the resulting microstructure, t_{100} to the diffusible hydrogen content and local weld

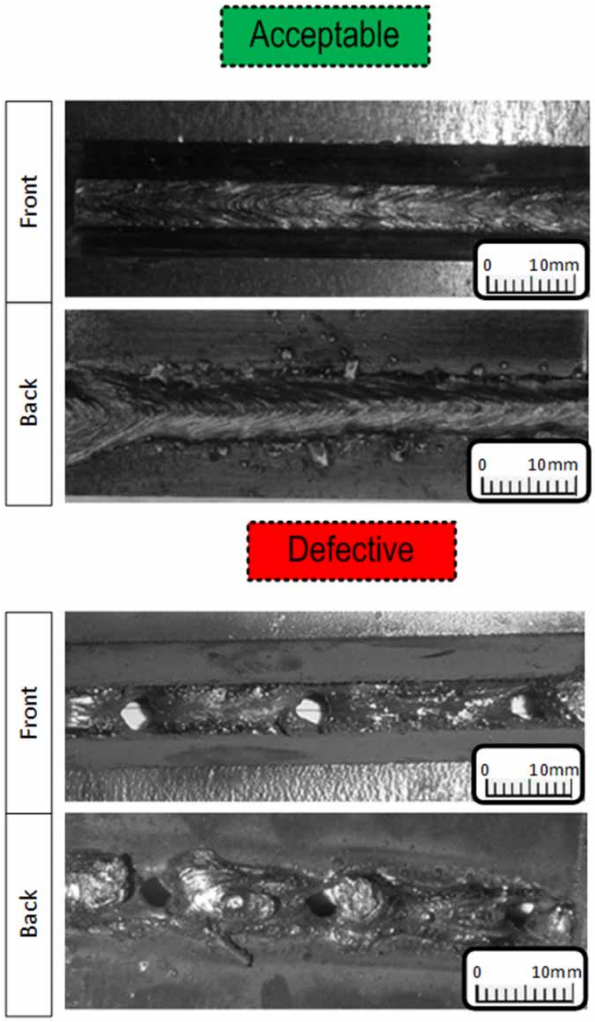

Figure 16. Acceptable and defective welds highlighting the defective welding 'window'/burn through on the WIC test at low heat input and high travel speed.

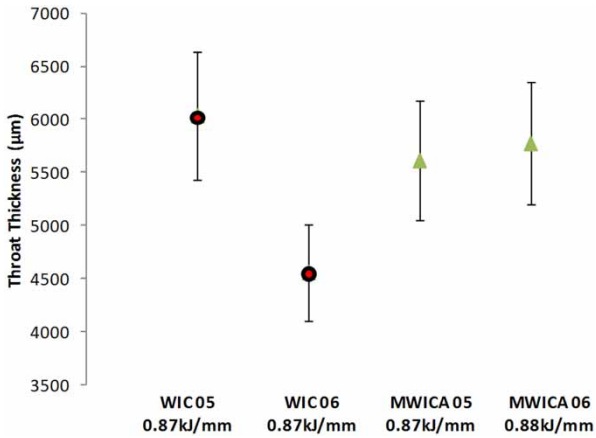

Figure 17. Comparison weld throat thickness for WIC and MWIC tests at 0.85 ± 0.02 kJ mm^{-1}.

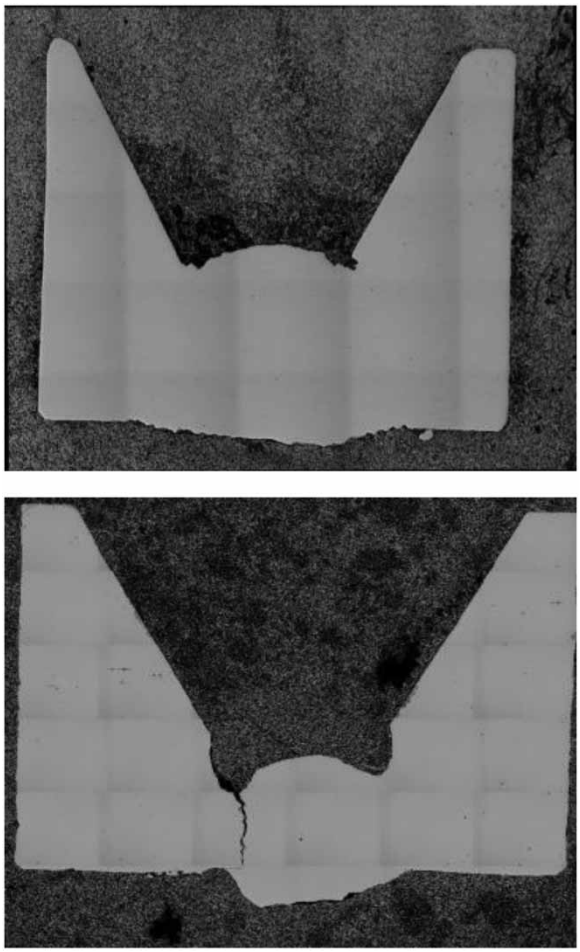

Figure 18. Typical symmetric (top) and asymmetric (bottom) weld bead profile. (*Images not to scale*).

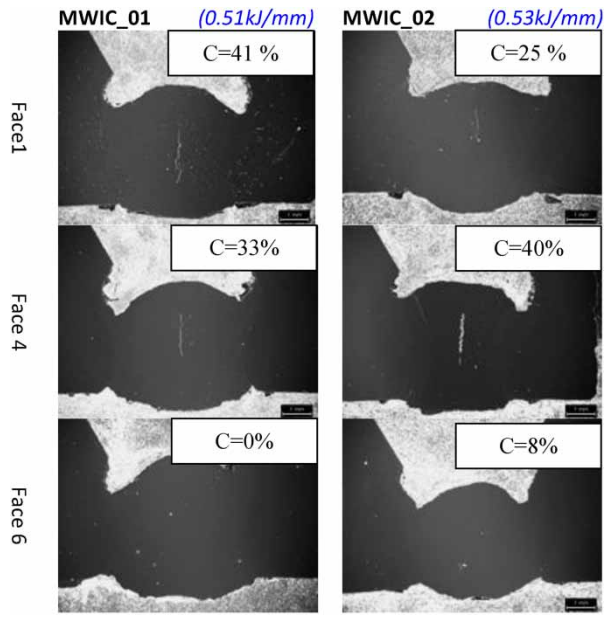

Figure 19. MWIC cracking results for tests carried out at 0.5 ± 0.05 kJ mm^{-1} on 20 mm $\times$70 plate. Percentage cracking is calculated as; (C%) = [Crack length (t_c)/Throat thickness (t_W)] $\times$ 100.

metal displacement to resulting strain. Collectively this data can be used as a proxy to quantify the three critical factors driving HACC.

Assuming that all thermo-metallurgical factors are held constant (e.g. constant alloy composition and cooling rate), it is useful to concentrate on the thermo-mechanical conditions require for crack formation. Measuring local strain in the vicinity of the weld during

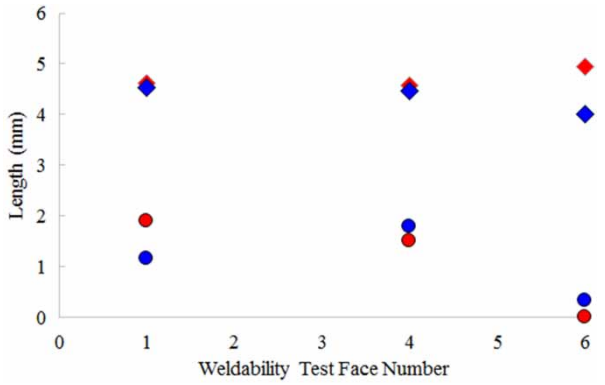

Figure 20. Variation in t_w for MWIC_01 (◆) and MWIC_02 (◆) and t_c for MWIC_01 (●) and MWIC_02 (●).

the whole welding cycle poses some unique challenges such as the high temperatures encountered in welding. The hole drilled through the back of the T-support enables the access of an extensometer and strain measurements that are lacking today.

Conclusions

A new MWIC weldability test and test procedure have been developed that allows for the experimental determination of the critical strain needed for cold cracking formation post-welding. In particular the weldability of API-5L-X70 was examined for E6010 cellulosic SMA weld metal. The modifications allowed obtaining a significant increase in success rate of achieving an industry acceptable weld in the tests. The new designed geometry enables easier access for instrumentation and for the more reproducible production of test specimens facilitating the use of the test specimen as a research tool. To ensure that the modifications did not modify significantly the thermal and restraint conditions of the test and the results are comparable with those achieved in other studies using the WIC test, physical and finite element studies for the original and modified test geometries have been undertaken. The results show that the modifications to the design have little or no influence on the thermal and mechanical properties of the test, but improve the ease with which consistently high quality samples are produced.

Although the MWIC test is in some regards similar to the WIC test in its application of controlled transverse global restraint levels, what is of particular importance in the MWIC test is the measurement of local strain critical to crack formation. The same approach could be accomplished using other established weldability tests including tensile tests (e.g. TRC) or restraint applied in the plane of the test specimen (e.g. RRC, window type cruciform test, H-slit test, Lehigh slot test) [2,3]. Weldability tests that do not lend to themselves to this approach are those involving bending, where the strain is not uniform throughout the test specimen. The disadvantage of the strain analysis is that it adds to test complexity and is time consuming. However, expressing cracking susceptibility in terms of a critical parameter directly related to a cracking mechanism has the advantage of providing a more meaningful representation of weldability. Of particular importance is the possibility to use these data in the modelling of cracking mechanisms, allowing for future prediction. Strain analysis also allows for the identification of the instance of crack formation, thus possibly identifying if solidification cracking has formed prior to HACC formation.

Acknowledgements

The research work was funded by the Energy Pipeline CRC supported through the Australian Government's Cooperative Research Centres Program. The cash and in-kind support from the APIA-RSC is gratefully acknowledged. The authors would like to thank Neville Cornish, Principle Welding Engineer, Australian Welding Solutions (AWS) for access to welding facilities and Pascal Symons, Welding Technician, University of Adelaide. We would also like to thank Prof V Linton of the Energy Pipeline CRC for her continued support and A/Prof A. Kotousov, Dr E. Gamboa, I. Brown and PhD candidates Walter Costin and Houman Alipooramirabad for their comments and discussion. Adelaide Microscopy and Technical team are also gratefully acknowledged.

Disclosure statement

No potential conflict of interest was reported by the authors.

References

[1] Yurioka N. Predictive methods for prevention and control of hydrogen assisted cold cracking. First international conference on 'weld metal hydrogen cracking in pipeline grith welds'; 1999; Wollongong, Australia.
[2] Yurioka N, Suzuki H. Hydrogen assisted cracking in C-Mn and low alloy steel weldments. Int Mater Rev. 1990;35(4):217–249.
[3] Kannengiesser T, Boellinghaus T. Cold cracking tests – an overview of present technologies and applications. Weld World. 2013;57(1):3–37.
[4] Alam N, Dunne D, Barbaro FJ. Weld metal crack testing for high strength cellulosic electrodes. First international conference on 'weld metal hydrogen cracking in pipeline girth welds'; 1999; WTIA, Wollongong, Australia. p 9.1–9.23.
[5] Barbaro FJ. Types of hydrogen cracking in pipeline girth welds. First international conference on 'weld metal hydrogen cracking in pipeline girth welds'; 1999; WTIA, Wollongong, Australia. p. 11.1–11.15.
[6] Costin W, Lavigne O, Linton VM, et al. Micromechanical examination of the relationship between weld metal microstructure and hydrogen assisted cold cracking. 6th International Pipeline Technology Conference; 2013 Oct 6–9; Ostend, Belgium.
[7] Costin WL, Lavigne O, Kotousov A, et al. Investigation of hydrogen assisted cracking in acicular ferrite using site-specific micro-fracture tests. Mater Sci Eng A. 2016;651:859–868.
[8] ASNZS 2885.2-2008 Pipelines – Gas and liquid petroleum Part 2 – Welding; 2007; Australia.

[9] BS EN 1011-2:2001 Welding. Recommendations for welding of metallic materials. Arc welding of ferritic steels.
[10] Eliaz N, Eliezer D, Olson DL. Hydrogen-assisted processing of materials. Mater Sci Eng A. 2000;289(1–2): 41–53.
[11] Bailey N. Weldability of ferritic steels. Abington, UK: Woodhead Publishing Ltd; 1994.
[12] Bailey N, Coe FR, Gooch TG, et al. Welding without hydrogen cracking. 2nd edn. Cambridge: TWI, Abington Publishing; 1995.
[13] Davidson JA, Konkol PJ, Sovak JF. Assessing fracture toughness and cracking susceptibility of steel weldments—a review. Weld Res Coun Bull. 1989;45(345): 1–43.
[14] Lynch S. Hydrogen embrittlement phenomena and mechanisms. Corros Rev. 2012;30:105–123.
[15] Smialowski M. Hydrogen in steel. Oxford: Pergamon Press Ltd; 1962.
[16] Fletcher L. Field weldability of large-diameter thick-walled linepipe. Aust Weld J. 1988;First Quarter(17): 17–21.
[17] Fletcher L, Yurioka N. A holistic model of hydrogen cracking in pipeline girth welds. First international conference on 'weld metal hydrogen cracking in pipeline girth welds'; 1999; Wollongong, Australia.
[18] Kotousov A, Borkowski K, Fletcher L, et al. A model of hydrogen assisted cold cracking in weld metal. 9th international pipeline conference; 2012; Calgary, Alberta, Canada, ASME.
[19] Roshan W, Bumpstead M, Fletcher L, et al. Welding of small diameter pipelines in Australia. APIA/EPRG/PRCI 19th Joint Technical Meeting; 2013; Sydney, Australia.
[20] Kumar PG, Yu-ichi K. Diffusible hydrogen in steel weldments. Trans JWRI. 2013;42:39–62.
[21] Alipooramirabad H, Ghomashchi R, Paradowska A, et al. Residual stress-microstructure-mechanical property interrelationships in multipass HSLA steel welds. J Mater Process Technol. 2016;231:456–467.
[22] Radaj D. Heat effects of welding: temperature field, residual stress, distortion. Berlin: Springer-Verlag; 2012.
[23] Satoh K, Terasaki T, Ohkuma Y. Relationship between critical stress of HAZ cracking and residual diffusible hydrogen content. J Japan Weld Soc. 1979;48(4):248–252.
[24] Graville BA. A survey review of weld metal hydrogen cracking. Weld World. 1986;24(9/10):190–198.
[25] Graville BA. Interpretive report on weldability tests for hydrogen cracking of higher strength steels and their potential for standardization. New York: NY, Welding Research Council, New York; 1995.
[26] Coniglio N, Barbaro FJ, Linton VM, et al. Hydrogen assisted cold cracking susceptibility of weld metal deposited by cellulosic shielded metal arc welding consumables. International pipeline conference, IPC2010; 2010; Calgary, Canada.
[27] North TH, Rothwell B, Glover A, et al. Weldability of high strength line pipe steels. Weld J. 1982;61(8): 243–257.
[28] Signes EG, Howe P. Hydrogen-assisted cracking in high-strength pipeline steels. Weld J. 1988;67(8):163s–170s.
[29] Lazor RB, Graville B. Effect of microalloying on weld cracking in low carbon steels. Canadian Welder Fabricator. 1983;74(21):21–23.
[30] Sarrafan S, Ghaini FM, Rahimi E. Weld metal hydrogen cracking in transmission pipelines construction. Proceedings of the 8th international pipeline conference IPC2010; 2010; Calgary, Canada.
[31] Cola MJ. Investigation of WIC test variables. Houston, TX: Edison Welding Institute; 1991.
[32] Lazor RB. Examination of pipeline welding procedural variables. Houston, TX: Pipeline Research Council International; 1984.
[33] Noble DN, Pargeter RJ. Field weldability of high strength pipeline steels. Houston, TX: Edison Welding Institute; 1988.
[34] Glover A, Rothwell B. Specifications and practices for hydrogen crack avoidance in pipeline girth welds. First international conference on 'weld metal hydrogen cracking in pipeline girth welds'; 1999; WTIA: Wollongong, Australia. p. 13.1–13.18.
[35] Kurji R. Thermo mechanical factors influencing weld metal hydrogen assisted cold cracking. School of Mechanical Engineering. PhD Project, The University of Adelaide: Adelaide, Australia; 2016.
[36] Darmadi D, Norrish J, Tieu AK. Analytic and finite element solutions for temperature profiles in welding using varied heat source models. World Acad Sci Eng Technol. 2011;81:154–162.
[37] Iacobescu G. A theoretical model for welding process with Gaussian heat source – Part 1. Univ 'Politehnica' Bucharest Sci Bull, Series D: Mech Eng. 2006;68(4): 45–50.
[38] Teixeira PRDF, Araújo DBD, Cunda LABD. Study of the Gaussian distribution heat source model applied to numerical thermal simulations of TIG welding processes; 2014.
[39] Alipooramirabad H, Paradowska AM, Ghomashchi R, et al. Prediction of welding stresses in WIC test and its application in pipelines. Mater Sci Technol. 2016;32(14):1462–1470.
[40] Kurji R, Coniglio N, Gamboa E, Ghomashchi R. Weld metal HACC susceptibility under controlled welding conditions and restraint levels. Adelaide, Australia: Energy Pipeline CRC; 2011.
[41] Chihoski RA. The character of stress fields around a weld arc moving on aluminum sheet. Weld J. 1972;51(1):9–18.
[42] Vasudevan R, Stout RD, Pense AW. Hydrogen-assisted cracking in HSLA pipeline steels. Weld Res Suppl. 1981;60(9):155–168.

Weld World
DOI 10.1007/s40194-016-0348-2

RESEARCH PAPER

Micromechanical characterisation of weld metal susceptibility to hydrogen-assisted cold cracking using instrumented indentation

Rahim Kurji[1] · **Olivier Lavigne**[1] · **Reza Ghomashchi**[1]

Received: 1 February 2016 / Accepted: 18 April 2016

Abstract Hydrogen-assisted cold cracking is generally accepted to be the consequence of a critical concentration of hydrogen trapped within a susceptible microstructure and subjected to a threshold level of stress. Traditionally, hardness has been used as a proxy for establishing the critical limits above which the risk of a hydrogen crack propagating is considered significant. However, developments in the steel-making process, in particular thermomechanically controlled processing, has brought into question the suitability of empirical hardness limits developed using older generation steels. In this paper, a safe welding boundary was established for single-pass root runs for API 5 L X70 steel welded with E6010 electrodes. Across this boundary, it was shown that hydrogen cracks were present in welds with hardness's well below the traditionally accepted threshold of 350 HV. This paper explores the use of nanoindentation as means of quantifying the susceptibility of welds deposited on high-strength low-alloy steels, using shielded metal arc welding, to hydrogen-assisted cold cracking. It is suggested that the use of the hardness/elastic modulus (H/E) ratio, which is directly related to the yield strength of a material, is a more suitable parameter to predict weld metal hydrogen-assisted cold cracking (HACC) susceptibility than is the hardness alone.

Keywords (IIW Thesaurus) Pipeline steels · MMA welding · Cold cracking · Hardness · Elasticity

Recommended for publication by Study Group RES - Welding Research Strategy and Collaboration

✉ Olivier Lavigne
Olivier.lavigne@adelaide.edu.au; lavigneolivier@hotmail.com

[1] School of Mechanical Engineering, The University of Adelaide, Adelaide, SA 5005, Australia

1 Introduction

In Australia, the use of hydrogen-rich cellulosic consumables is common place for the construction of oil and gas pipeline networks. Coupled with the high levels of restraint as a result of clamping and the lifting-lowering stresses, the pipeline is subjected to during construction, the root pass is generally accepted as the most vulnerable pass with respect to susceptibly to hydrogen-assisted cold cracking (HACC). Although the exact mechanism governing the initiation and propagation of hydrogen cracks is still in contention, it is generally accepted that hydrogen cracks occur when critical levels of hydrogen interact with a susceptible microstructure when a weld is subjected to a threshold level of stress [1–20]. Preheat can minimise the risk of cracking [2–4]; however, it limits weld productivity and adds costs. To ensure that the risk of HACC is designed out of the weld procedure, evaluation of the conditions for the onset of HACC needs to be established with confidence.

1.1 Weld metal hydrogen-assisted cold cracking

Hydrogen cracking is traditionally associated with crack initiation and propagation through the heat-affected zone (HAZ). However, with the improvements in the steel-making process and a consequent reduction in steel hardenability, an increased tendency for HACC to occur in the weld metal (WM) rather than the HAZ is suggested [3, 17, 21, 22]. The prevalence of weld metal hydrogen-assisted cold cracking (WMHACC) over heat-affected zone hydrogen cracking (HAZ HACC) has been suggested to be the consequence of changes in the alloy content and the as-cast microstructure of the parent plate. Modern alloy designs have raised the austenite (γ) to ferrite (α) transformation temperatures of the heat-affected zone to a point where the ferrite transformation occurs in the heat-

Published online: 25 April 2016

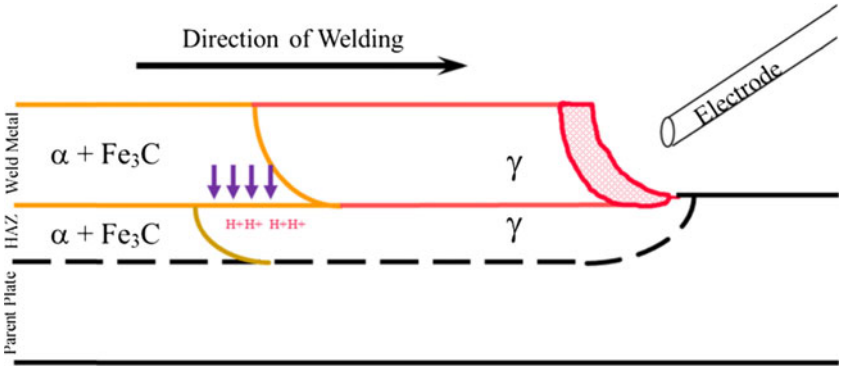

Fig. 1 HAZ-HACC. The austenite (γ) to ferrite (α) transformation is suggested to occur in the WM before the HAZ, leaving the HAZ to effectively acting as a hydrogen sink. Hydrogen accumulates in areas of high tri-axial stress within the HAZ, creating conditions which favour the formation of hydrogen cracks

affected zone before the weld metal [1]. As the solubility of hydrogen in ferrite is lower than in austenite [23], hydrogen is rejected from the HAZ and accumulated in the WM. The higher diffusivity of hydrogen in ferrite [24] also favours this process. The consequence is the preferential accumulation of hydrogen in the weld metal as illustrated in Figs. 1 and 2.

1.2 Predicting the onset of hydrogen-assisted cold cracking—HACC control criterions

The potential catastrophic consequence of hydrogen-assisted cold cracking has seen a significant amount of research focused on deriving methods to predict the onset of the phenomenon. As it universally agreed [1–22, 25–27], that HACC can be summed up as the critical interaction of three factors (hydrogen concentration, susceptible microstructure and stress), empirical predictors have generally focused on identifying thresholds of the three factors above which the risk of HACC is considered to be significant.

Considering that an accurate estimation of stresses evolved during fabrication is difficult to achieve, the most commonly adopted methods by industry and in particular by statutory codes is the control of hydrogen and a control of the resulting microstructure. Unlike residual hydrogen which has a direct correlation to the level of preheat applied [2] and thus makes the hydrogen control criterion the most commonly adopted control criterion, a proxy which defines a 'susceptible' microstructure is much more complex to define. The complexity arises from the inhomogeneity of the weld microstructure [28].

The simplest proxy used to define microstructural susceptibility to hydrogen cracking is hardness [2–4, 17]. It is therefore not surprising that hardness control criterions have been extensively codified [29–31]. Graville [19] compared the suitability of the hardness versus the hydrogen control criterions and suggested that the use of hardness control is best suited to steels with limited alloy content. His hypothesis was based on the observation that steels with a limited alloying content have steep hardening curves and the hardness of the heat-affected zone can be determined with a high degree of accuracy by measuring the critical cooling time ($t_{8/5}$; Fig. 3). Conversely, for low-carbon and microalloyed steels, as the hardness profile of the weld is not influenced significantly by the critical cooling time ($t_{8/5}$), Graville suggested that hydrogen control approach would be more appropriate.

Based on empirical observations, a system commonly known as Graville's diagram (Fig. 4), which classifies steels based on their carbon content and alloying constituents, was proposed. This system simplifies the selection of the most appropriate criterion to employ to minimise the risk of hydrogen cracking.

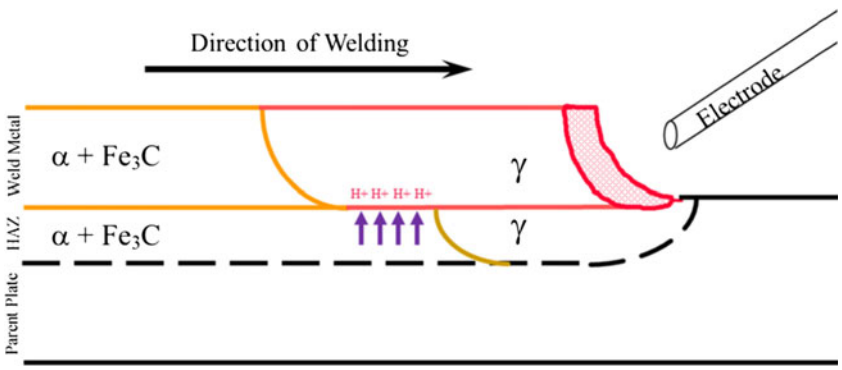

Fig. 2 WM-HACC. Modern alloy designs favour the austenite (γ) to ferrite (α) transformation in the HAZ before the WM. This transforms the WM into an effective hydrogen sink within which hydrogen can accumulate in areas of high tri-axial stress, creating the conditions which favour the formation of hydrogen cracks

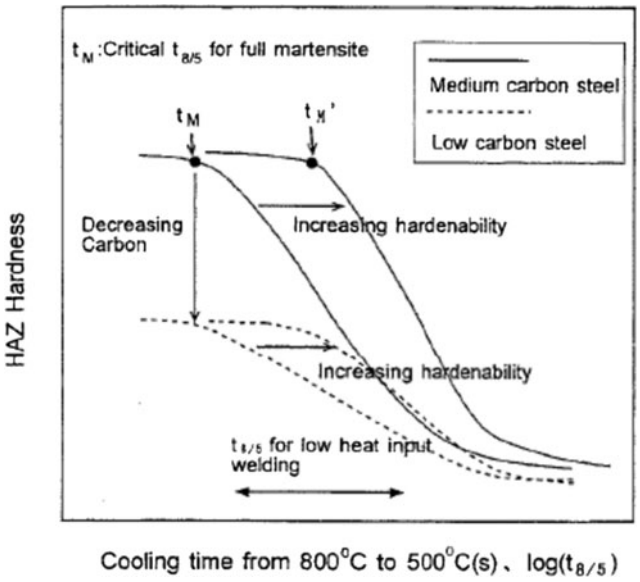

Fig. 3 Schematic representation of hardenability curves for low- and medium-carbon steels [4]. HAZ hardness of medium-carbon steels change significantly in a $t_{8/5}$ region corresponding to low heat input welding or when the carbon equivalent changes (CE_{IIW})

Zone 1 steels are typically considered to be steels at low risk of cracking, unless welded under high restraint and with high-hydrogen electrodes such as cellulosic electrodes. When considering HACC control strategies to implement, steels in zone I are typically subject to the hydrogen control criterions. Zone 2 steels on the other hand are characterised by significantly higher-carbon content and consequently have much steeper hardening curved compared to steels in zone 1. Steels in zone 2 are therefore subject to hardness control criterions. Zone 3 steels are typically subject to a combination of both criterions given the elevated risk of cold cracking.

It is important to note that the hydrogen and the hardness control criterions have different areas of emphasis. As

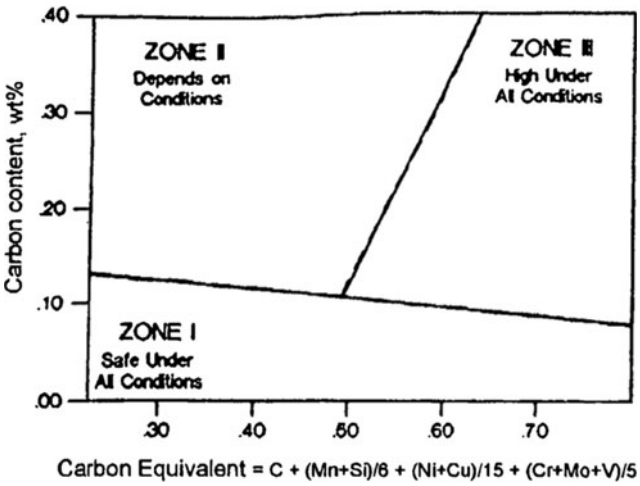

Fig. 4 Graville's diagram [19], illustrating the classification of steel weldability based on their carbon content and alloying composition as described by their carbon equivalent

expected, with hydrogen control criterions, the emphasis is on hydrogen diffusion and restraint, whereas with hardness control criterion, the emphasis is on the primary factor which influences the resulting microstructure, namely chemistry. Nevertheless, both control criterions acknowledge and take into consideration that HACC is the consequence of the interaction of trapped hydrogen in a susceptible microstructure subject to stress when estimating the level of preheat required to ensure that crack-free welds can be deposited.

The introduction of new microalloyed, thermomechanically controlled processed (TMCP) steels has raised the question of the suitability of the empirically derived control criterions, based on older generation steels. Limited data on the suitability of these traditional criterions on newer grades of steels and studies such as those by Davison et al. [32] demonstrate the need to assess the control criterions. This is compounded by the development of novel methods which can be used to extract mechanical properties of materials such as instrumented indentation.

1.3 Instrumented indention

Although indentation has been used to measure hardness for several decades [33], technological advancement in the field of instrumentation and the subsequent advent of instrumented indention, on both at microscale and nanoscale, have facilitated the measurement of material micromechanical properties through the decomposition and analysis of the load versus penetration depth curve. Numerous reviews addressing the fundamental principles of contact mechanics upon which the technique of instrumentation indentation is based have been published in addition to reviews exploring the applications of instrumented indention [33–42].

Unlike classical hardness measurements which use a definite test body to make an indent into the surface of a material, which has to be optically measured, instrumented indentation utilises an accurate measurement of the load applied to the indenter tip and the consequent depth of penetration into the surface. This allows for an accurate measurement of the universal hardness, H, as highlighted in Eq. 1, where F_{max} is the maximum applied load and A_c is the cross-sectional area corresponding to the depth h_c.

$$H = \frac{F_{\max}}{A_C(h_c)} \tag{1}$$

The determination of the contact depth h_c is given by Eq. 2, where S is the contact stiffness obtained from the slope of the upper portion of the unloading force-depth curve (Eq. 3).

$$h_c = h_{\max} - 0.75\frac{F_{\max}}{S} \tag{2}$$

Table 1 Divisions of the experimental program

Tier 1	Weldability tests are conducted to derive an empirical envelope within which a safe welding boundary can be delineated.
Tier 2	Samples selected from across the derived safe weld boundary are characterised using instrumented indentation to determine the elastic modulus and hardness of weld metal microstructure.

$$S = \frac{dF}{dh} \tag{3}$$

The reduced Young's modulus E_r which is a measure of the elastic properties of the sample can be calculated from the force-depth curves according to Eq. 4.

$$E_r = \frac{1}{2}\sqrt{\frac{\pi}{A_c(h_c)}}\frac{dF}{dh} \tag{4}$$

For an elastically deformable indenter, the reduced modulus E_r is related to the actual Young's modulus E by Eq. 5, where ν is Poisson's ratio of the indented material and ν_i and E_i are the Poisson's ratio and Young's modulus of the indenter, respectively.

$$\frac{1}{E_r} = \frac{1-\upsilon^2}{E} + \frac{1-\upsilon_i^2}{E_i} \tag{5}$$

where penetration depths are greater than 320 nm and the area function can be estimated using a standard calibration procedure on a fused silica quartz sample of a known Young's modulus [40].

Therefore, the application of instrumented indention allows for the elastic and plastic contribution to indention to be measured. This allows for the material to be characterised in terms of its elasto-plastic properties and was cited by several authors as an ideal method to characterise microstructures of steels and weld areas [40–42]. This is especially important when quantifying the susceptibility of a weld to HACC, as crack propagation is dependent on the elasto-plastic properties of the material within which a crack has initiated [43].

2 Experimental procedure

In order to establish the viability of micromechanical characterisation as a means of assessing the susceptibility of a weld deposit to HACC, a two-tier experimental program was employed as summarised in Table 1 below.

Using the two-tier approach, the variation in the key micromechanical properties can be used as a means of characterising the susceptibility to WMHACC.

2.1 Weldability testing

Weldability tests were conducted using the Modified Welding Institute of Canada (MWIC) weldability test [44] on two thicknesses (20 and 10 mm) of API 5 L X70 line pipe steel using 4-mm Ø E6010 electrodes. The MWIC test is a variant of the Welding Institute of Canada Test (WIC) which is a widely accepted weldability test used by the pipeline industry to rank the susceptibility of a single-pass weld to HACC. Figure 5 illustrates the dimensions of the test specimen and specifications of the preparation of the single butt V grove joint within which the tests welds are deposited. The elemental compositions of the batch of steel and batch of electrode used for testing are given in Tables 2 and 3, respectively. To replicate conditions found in Australia, in particular the high travel speeds, weldability testing was conducted within the parameters listed in Table 4.

To minimise variability introduced by the manual welding process, the tests welds were deposited using a

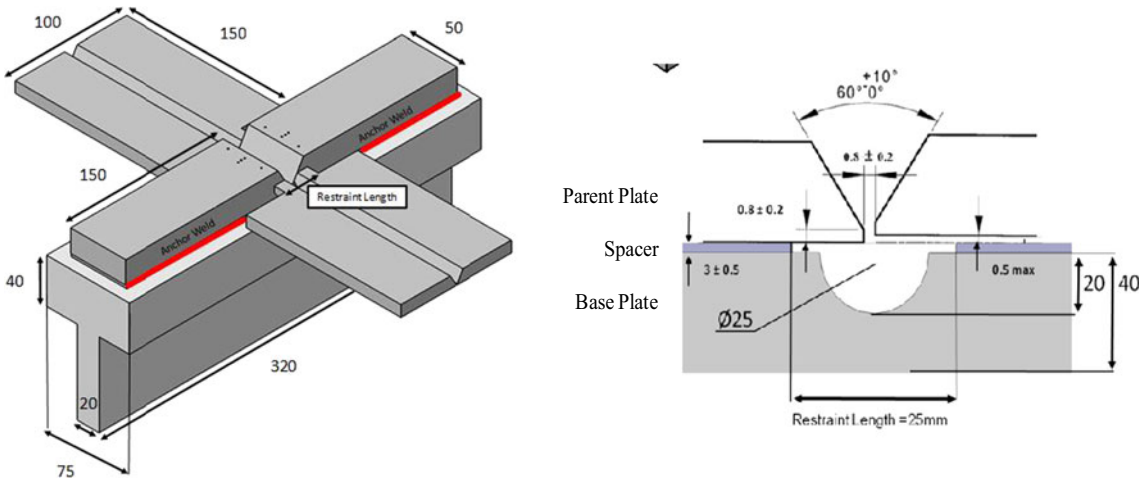

Fig. 5 Dimensions of the MWIC weldability test and single V butt weld preparation used for weldability testing. All dimensions in millimeter

Table 2 Chemical composition of line pipe steel (percent weight; from manufacturer)

C	Mn	Si	S	P	Nb	Ti	Cu	Ni	Mo	Cr	Ca	Al	V
0.052	1.55	0.21	0.0011	0.0097	0.041	0.012	0.15	0.19	0.18	0.026	0.0016	0.039	0.029

Table 3 Electrode batch chemical composition (percent weight; from manufacturer)

C	Mn	Si	S	P	Ni	Mo	Cr	V
0.16	0.62	0.19	0.009	0.009	0.2	0.01	0.02	<0.01

uni-directional, semi-mechanised shielded metal arc welding (SMAW; weld efficiency $\eta \approx 1$) machine with a specimen-holding plate moving vertically upwards during welding at a controlled velocity, thus simulating vertical-down welding conditions. A constant force and an angle of 20° normal to the plate were maintained between the electrode and the workpiece. The Lincoln Electric Invertec 350 V Pro was used as the welding power source. The groove surfaces of the test specimen and 25 mm either side of the weld centreline was polished down with ISO 80-grit (201 μm) emery paper and degreased with acetone, to minimise the probability of introducing contaminants (such as surface oil and grease) which may dissociate in the welding arc and may alter the cracking results. The entire specimen was de-gaussed prior to welding to eliminate any residual magnetic fields introduced during fabrication of the weldability specimen. This was shown to be essential [44] to ensure successful, symmetric deposition when using a semi-mechanised method of deposition on the MWIC test. Weldability testing was conducted over a 12-month period in an indoor facility where the temperature varied from a minimum of 22.6 °C to a maximum of 28.3 °C with a mean temperature of 25.1 °C. The relative humidity on site during testing varied between 38 and 67 % with a mean relative humidity of 54.1 %. The 350-mm-long, 4-mm Ø E6010 electrodes used for testing were stored in a hermetically sealed container and were used in their 'as-received' condition for testing.

2.2 Data acquisition

Welding parameter trace data (voltage and current) was collected at 0.5 Hz directly from the welding power source (Lincoln Invertec 350 V Pro) using a serial interface and the propriety software, Power Wave Manager™ supplied by Lincoln Electric. Travel speed data was derived by measuring the displacement of the specimen holding plate using Sick Laser sensor DT20-P214B (±1 mm) and the internal clock of the data acquisition system. Test plate thermal data was obtained by fitting three electrically grounded K-type thermocouples (1-mm outer diameter) coated with thermal paste into the parent plate MWIC specimen. Data was channelled at 10 Hz through an optical isolation system into several 16-bit National Instruments® (NI) 9215 voltage modules embedded in a NI-CDAQ-9188 chassis. Independent calibration was carried out to ensure signal accuracy and fidelity. A custom program was written in LabVIEW® 2010 to acquire and record data.

2.3 Weld analysis

The welded joint was removed from the MWIC specimen 24 h after weld completion by milling the test assembly just inside the restraint length. The anchor welds were sawed off using a water-cooled precision metallographic saw, and the test sample was divided into six sections. To prepare the sections for metallographic analysis and indentation, each section was hot mounted in a conductive epoxy and polished using a semi-automatic LaboForce polishing machine (Struers). Final polishing was achieved using a porous neoprene disc with a colloidal silica suspension (0.04 μm). The samples were then observed at ×400 magnification for the presence of cracking using an optical microscope (Ziess Axio Imager 2). Selected samples were then etched using a 2 % nital solution to reveal the weld metal microstructure.

Table 4 Testing parameters

Welding specifications		Welding parameters	
Direction	Vertical down (5 G)	Current	130–170 A
Size of electrode	4.0 mm	Voltage	25–30 V
AWS class	5.1 A	Travel speed	250–470 mm/min
Specification	6010 E	Heat input range (targeted)	0.41–1.00 kJ/mm
Polarity	DC+	Preheat range (targeted)	25 °C–100 °C

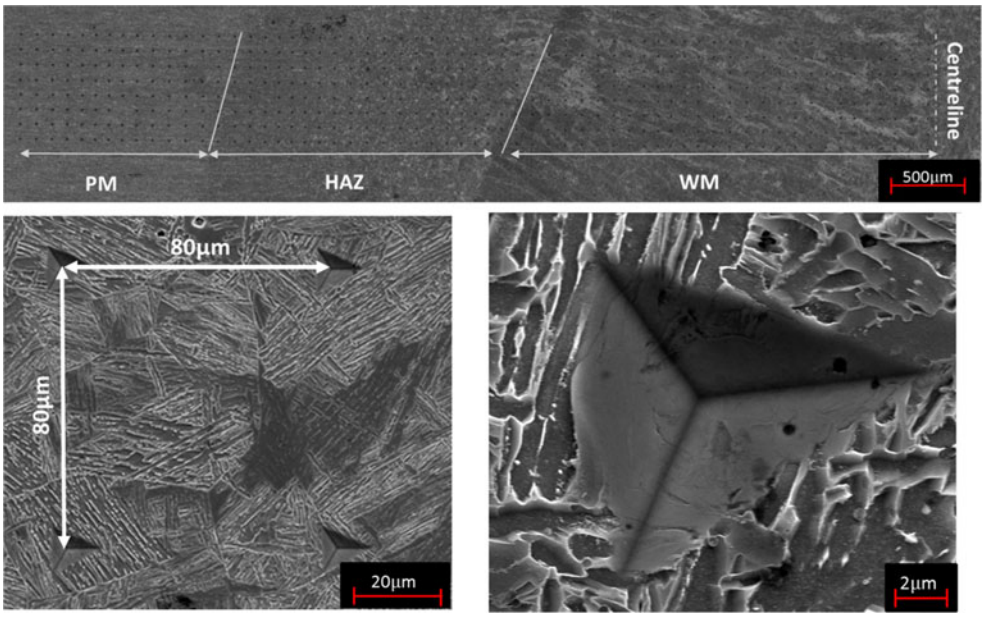

Fig. 6 *top* Indention map. *bottom left* Spacing between successive indents. *bottom right* High-magnification image of individual indent

2.4 Micromechanical analysis

For micromechanical characterisation, the fourth sections of selected test samples were prepared by mounting the metallographically prepared sample onto a sturdy test stage. The samples were attached to the stage using an adhesive to ensure no lateral movement was possible during the stage motion whilst ensuring that the test section remained perpendicular to the indenter during testing.

Indentation testing was carried out using the Fisher-Cripps IBIS Nanoindention System. Symmetric indention maps (Fig. 6), consisting of 480 indents (60 columns and 8 rows) with an 80-µm space between the centre point of each indent, were made using a Berkovich-type diamond tip indenter. The initial column was located at the approximate centreline of the weld, and the maps spanned outwards towards the HAZ. Testing was conducted at a load of 250 mN to achieve a sufficient penetration of the indenter tip into the material (approximately 2 µm). This depth insured that the tested material volume is representative of the considered microstructure volume. The area function was approximated by a standard calibration procedure with fused quartz material of known Young's modulus and hardness. High-magnification images of selected cracks, indents, and microstructure were taken using the FEI Quanta 450 FEG environmental scanning electron microscope (ESEM).

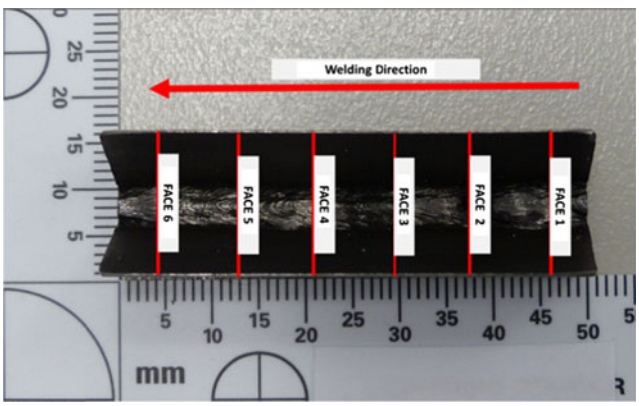

Fig. 7 Weldability test piece with the location of the six faces to be examined under an optical microscope at a magnification of ×400 highlighted

3 Results and discussion

3.1 Delineation of safe welding boundary

Each of the six sections (Fig. 7) from a single test piece was examined at a magnification of ×400 and classified as cracked when the vertical length of the defect observed in a single section (t_c) was greater than 5 % of the height of the weld bead (t_w) of the test section under analysis (Fig. 8). Cracking

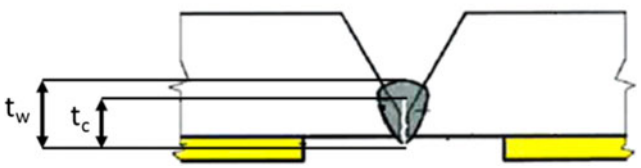

Fig. 8 Schematic of a face of a test section. A sample is defined as cracked when a linear defect whose vertical length (t_c) is greater than 5 % of the bead height (t_w)

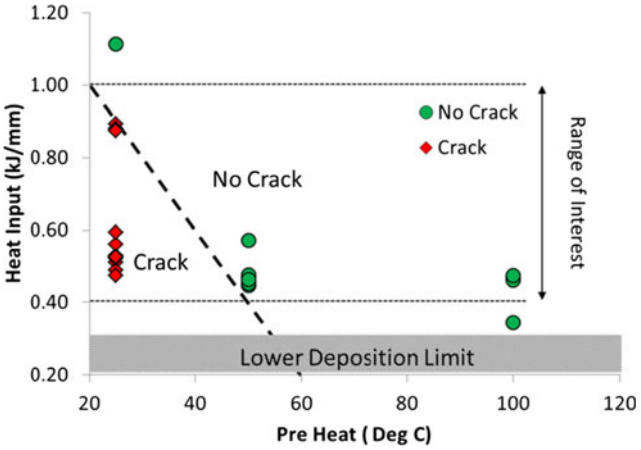

Fig. 9 MWIC weldability testing on the 20-mm-thick API 5 L X70 line pipe steel under high restraint (R_f=25 mm). A *green circle* represents a sample within which no cracking is observed. A *red diamond* represents a sample within which a crack was observed

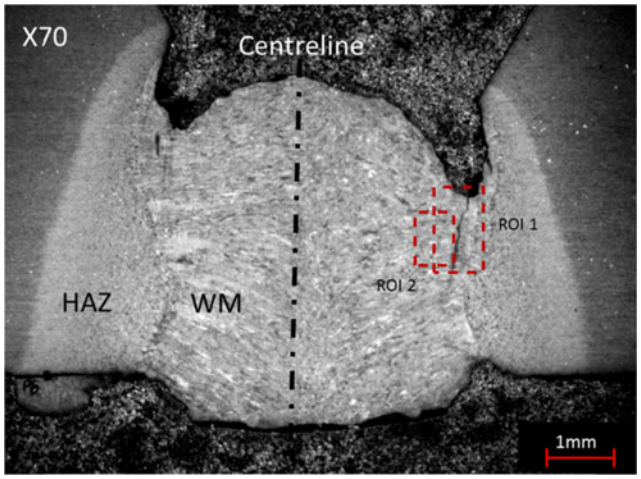

Fig. 11 Overview of weld bead (2 % nital etch) highlighting macrohydrogen (ROI 1) cracks which initiate from macroscopic defects such undercut in the weld toe and microscopic hydrogen cracks (ROI 2) which initiate from microvoids or non-metallic inclusions

severity was defined as the arithmetic sum of the observed percent cracking over the entire test piece.

A total of 25 tests were conducted for 20-mm-thick plates under high restraint (R_f=25 mm), of which 22 were used for crack analysis and 3 were used to defined the lower limit of weld deposition. For the tests used for crack analysis, the recorded current ranged from 121 to 167 A with recorded voltage varying from 19.1 to 29.9 V, and the calculated heat input ranged from 0.37 to 1.11 kJ/mm. Tests were conducted with a preheats of 25, 50, and 100 °C. Similarly, a total of 14 tests were conducted for 10-mm-thick plates under high restraint (R_f=25 mm) with 10 tests instrumented and analysed for cracking results and 4 used to validate the lower limit of weld deposition. The recorded current ranged from 119 to 163 A with the recorded voltage ranging from 21.9 to 24.6 V, and the calculated heat input ranged from 0.48 to 0.82 kJ/mm. Testing was carried out with preheats of 25, 40, and 50 °C.

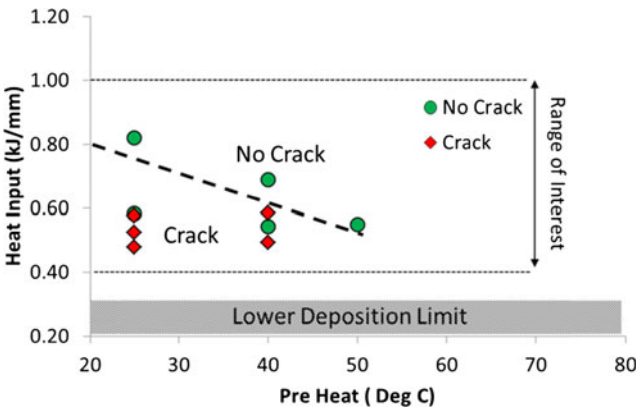

Fig. 10 MWIC weldability testing on the 10-mm-thick API 5 L X70 line pipe steel under high restraint (R_f=25 mm). A *green circle* represents a sample within which no cracking is observed. A *red diamond* represents a sample within which a crack was observed

These weldability tests established a lower heat input (HI) limit of 0.3 kJ/mm for both the 20- and 10-mm tests plates when welded in ambient condition (i.e. $T=25\pm2$ °C and RH <80 %). Below this heat input limit, the welds suffered from insufficient penetration and lack of side wall fusion. Within the heat input range of interest (0.4 kJ/mm < HI < 1 kJ/mm), testing results empirically suggest that for the 20-mm-thick sections of line pipe steel under high restraint (Fig. 9), the minimum (critical) preheat (PH) required to deposit single-pass hydrogen crack-free weld as a function of the heat input can be defined as PH(°C) = 70 − 50 HI(kJ/mm). Similarly, for the 10-mm-thick plates welded under high restraint (Fig. 10), the minimum (critical preheat) required to deposit single-pass hydrogen crack-free welds can be defined as PH(°C) = 100 − 100 HI(kJ/mm).

The observed hydrogen cracks developed on the samples indicated as red triangles in Figs. 9 and 10 can be classified into two distinct categories, macroscopic and microscopic cracks. Macroscopic cracks typically originated from the weld toe and propagated in a transverse fashion though the weld cross section (region of interest (ROI) 1; Figs. 11 and 12). The cracks ranged in length from a tenth of a millimetre to several millimetres. Microcracks, on the other hand, were distributed throughout the weld metal and were generally orientated perpendicular to the forces arising (normal to the weld) as a result of the restraint conditions created by the weldability test specimen. The cracks ranged in length from a fraction of a micrometre to several micrometres. The cracks were also observed to generally initiate from non-metallic inclusion (NMI; Fig. 13). A distinct difference was noted between the number and the severity of the type of cracking observed. For both the

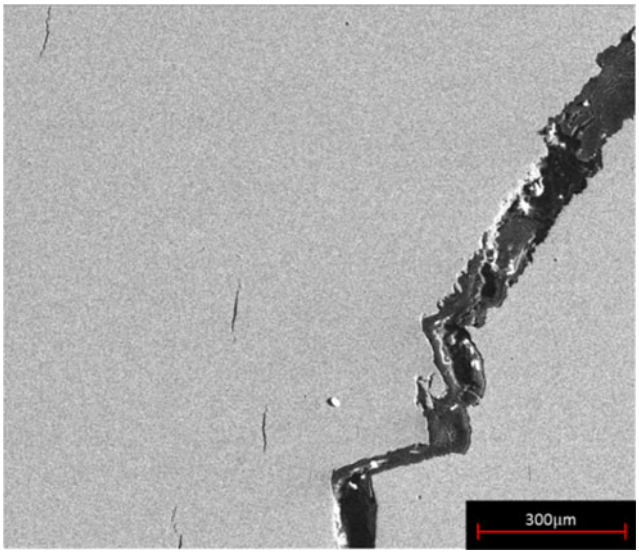

Fig. 12 ROI 1 typical 'macroscopic' hydrogen crack, originating from a stress concentration, typically wagon tracks in the weld toe. The cracks propagate in a transverse fashion towards the weld centreline. 'Microscopic' cracks in the normal direction of the weld can also be observed

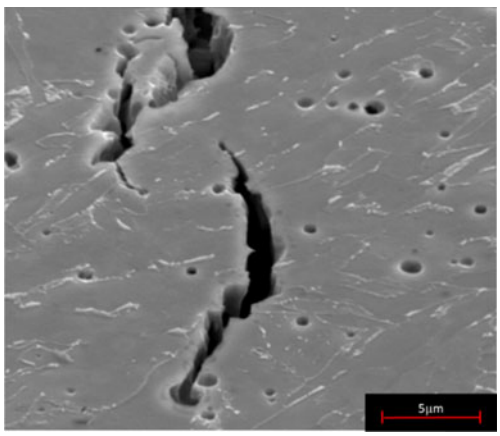

Fig. 13 ROI 2 typical 'microscopic' hydrogen crack. A large proportion of the observed microcracks originated from non-metallic inclusions

20- and 10-mm test plates, there was evidence to suggest than the number of macroscopic cracks increased as the heat input decreased. This could be attributed to the fact that at a lower heat input, the eccentricity of the deposited weld bead increased, creating stress concentrators at the weld toe and thus favourable initiation sites for hydrogen cracks.

At comparable heat input and preheat, the 10-mm plates appeared to have a greater number of microcracks; however, their severity was marginally less than microcracks observed in the 20-mm plates. This may be attributed to the higher overall restraint experienced by the thicker plate.

3.2 Microstructural characterisation

The weld metal samples of both the 10- and 20-mm samples consisted primary of acicular ferrite (Fig. 14a), bainite (Fig. 14b), and Widmanstatten ferrite (Fig. 14c). Some instances of grain boundary ferrite, ferrite with non-aligned second, and ferrite with aligned second phase were also observed. The detailed microstructural analysis of the weld metals is presented in [28]. Given the limited heat input range within which the samples were deposited, it is not surprising that no significant difference was observed in the morphology or fraction of observed microstructures. Additional general review of the microstructure along the macroscopic crack path showed no significant relationship to any particular microstructural morphology [45].

3.3 Micromechanical characterisation

3.3.1 Sample selection

To assess the suitability of micromechanical characterisation as a means of ranking the susceptibility of deposited welds to WMHACC, several samples were selected from across the derived safe welding boundary as highlighted in Figs. 15 and 16.

3.3.2 Weld metal hardness

The weld metal hardness for the 20-mm thick samples ranged from 213.3 to 300 HV for samples welded under

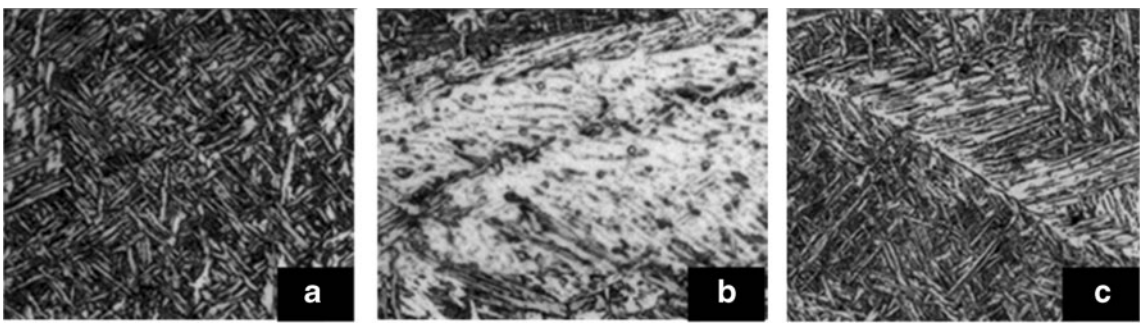

Fig. 14 Micrographs (not scaled) of typical microstructures observed in both the 20- and 10-mm weld metal samples; the samples consisted primarily of acicular ferrite (**a**), bainite (**b**) and Widmanstatten ferrite (**c**)

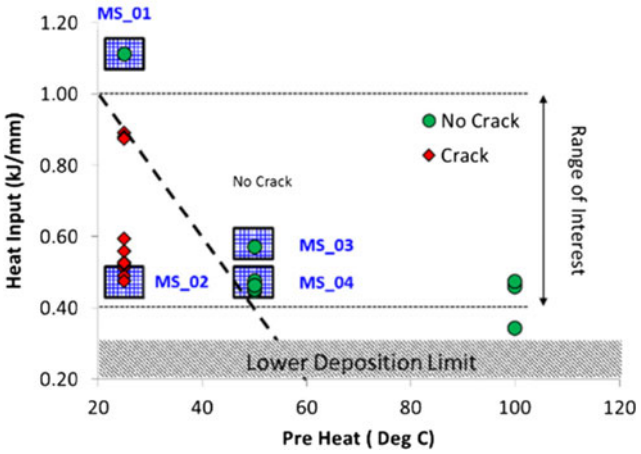

Fig. 15 Samples from the 20-mm test series (grid regions) selected for micromechanical characterisation

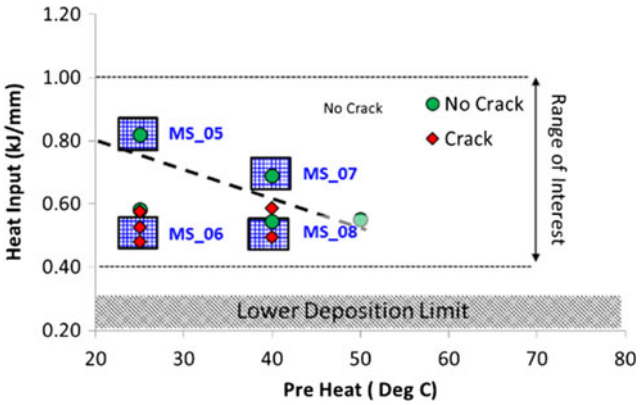

Fig. 16 Samples from the 10-mm test series (grid regions) selected for micromechanical characterisation

ambient conditions and 253.4 to 264.8 HV for samples welded with a preheat of 50 °C (Fig. 17). A maximum standard deviation of 21 HV was recorded across the 20-mm sample set. The variation in the hardness values can be attributed to the different microstructural constituents indented at each test. For 10-mm thick samples (Fig. 18), the measured weld metal hardness ranged from 282.9 to 299.9 HV for samples welded under ambient conditions. The narrow hardness range can be attributed to the narrow heat input range within which the samples were deposited and consequently minimal variation in weld metal microstructure. For samples welded with a preheat of 40 °C, the measured weld metal hardness ranged from 274.9 to 293.5 HV. A maximum standard deviation of 26.1 HV was recorded across the 10-mm sample set.

Considering the measured values of the hardness and their respective standard deviation (Table 5), it can be seen that the preheat and heat input, due to their limited ranges, do not significantly affect the overall hardness values of the weld metals. This is in accordance with the minimal variation of the microstructure observed across the different samples. Nevertheless, two trends can be drawn considering the mean values of the hardness (Table 5). For both the 10- and 20-mm thick samples welded under ambient condition, the hardness tends to decrease with the increase of the heat input due to grain coarsening [46]. At higher preheats, the opposite trend is observed (i.e. the hardness increases with the heat input) for both the 10- and 20-mm samples. This trend, however, may not be significant, considering the experimental scatter of the values

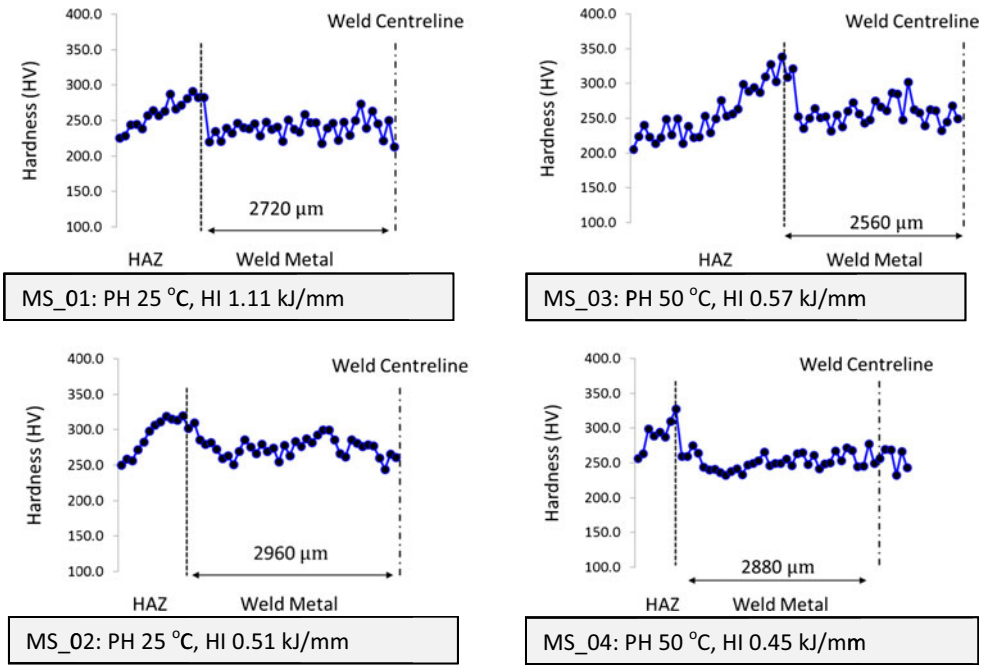

Fig. 17 Hardness traverse for the 20-mm-thick plates

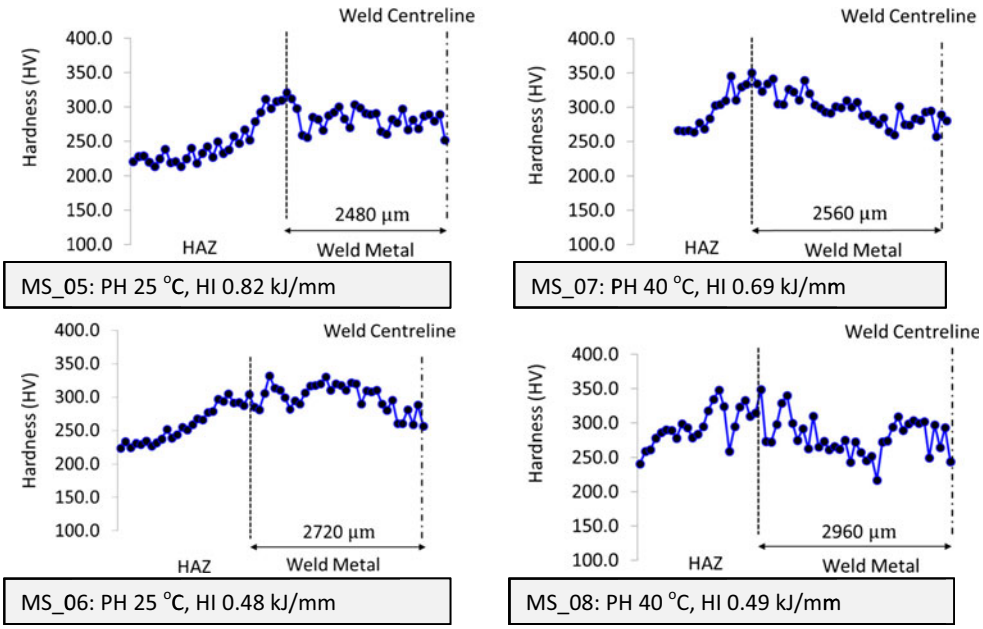

Fig. 18 Hardness traverse for the 10-mm-thick plates

observed within the narrow heat input range used at higher preheats.

Figures 17 and 18 also show that the HAZ hardness increases from the parent metal towards the weld metal fusion zone. The continuous increase of hardness within HAZ may be attributed to the formation of more bainitic structure towards fusion zone as reported for multi-pass welds [47]. In any case, it is important to note that the measured peak hardness through the weld metal and the HAZ did not exceed the generally accepted hardness threshold of 350 HV [29–31], above which hydrogen cracking is expected. Additionally, weld hydrogen cracks were observed in samples with a peak hardness value as low as 300 HV. These observations support the proposition in literature that the traditional empirical hardness limits cannot be used as a universal infallible proxy for hydrogen cracking [3, 4, 14, 16].

3.3.3 Weld metal elastic modulus

The weld metal elastic modulus for the 20-mm thick samples (Fig. 19) ranged from 160 to 182.1 GPa for samples welded under ambient conditions and 169 to 208 GPa for samples welded with a preheat of 50 °C. A maximum standard deviation of 7.4 GPa was noted for the 20-mm data set. The 10-mm data set (Fig. 20) showed a greater degree of variability. For samples welded under ambient conditions, the measured elastic modulus ranged from 142.5 to 203.5 GPa, and for samples welded with a preheat of 40 °C, the measured elastic modulus ranged from 106.3

Table 5 Welding parameters and cracking conditions for samples selected for micromechanical characterisations

	Sample parameters				Hardness (HV)				Elastic modulus (GPa)			
Sample	Heat input (kJ/mm)	Preheat (°C)	Thickness (mm)	Crack/no crack	Maximum	Minimum	Mean	Standard deviation	Maximum	Minimum	Mean	Standard deviation
MS-01	1.11	25	20	No crack	273.4	213.3	242	15.1	182.1	160	170.1	5.4
MS-02	0.51	25	20	Crack	300	244.3	276.7	13.7	181.9	164.4	171.7	4.1
MS-03	0.57	50	20	No crack	338.3	231.7	264.8	21	208.8	180.8	193.5	7.4
MS-04	0.45	50	20	No crack	277.3	232.5	253.4	11.8	186.5	169	178.7	4
MS-05	0.82	25	10	No crack	320.8	251.6	282.9	16.9	161.3	142.5	151.7	4.7
MS-06	0.48	25	10	Crack	331.8	256.7	299.9	20.6	203.5	166.8	189.7	7.6
MS-07	0.69	40	10	No crack	339.4	257.2	293.5	18.4	177.5	158	170.1	4.9
MS-08	0.49	40	10	Crack	340.2	217.1	274.9	26.1	130.4	106.3	121.3	4.9

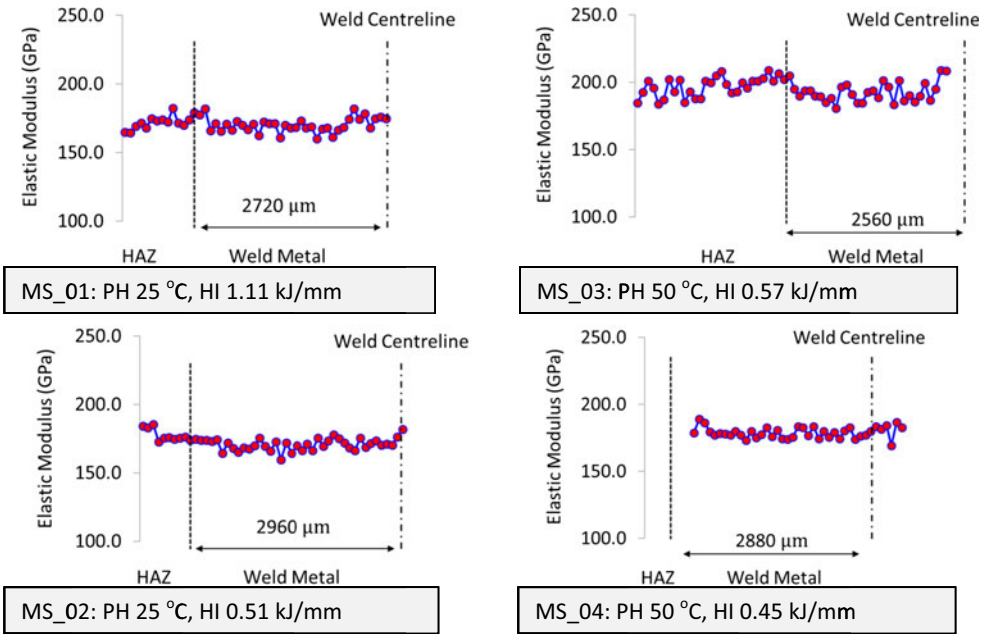

Fig. 19 Elastic modulus traverse for the 20-mm-thick plates

to 177.5 GPa. A maximum standard deviation 7.6 GPa was measured across the 10-mm data set.

The elastic modulus of the considered samples (Table 5) follows the same general trend as the hardness in function of the heat input, i.e. decreases with the increase of the heat input when the samples are welded under ambient condition (that had been observed in [48]) and increases with the increase of the heat input at higher preheat. This latter trend might not be significant though for the reasons evocated in Sect. 3.3.2. Table 5 gathers the welding parameters and the corresponding measured micromechanical properties of the selected samples.

3.4 Proposition of a new proxy for WMHACC susceptibility assessment

Phenomenologically, in order for a hydrogen crack to manifest, a critical concentration of hydrogen needs to be trapped in a susceptible microstructure and subjected to a critical level of stress. For an empirical cracking boundary produced where the only significant difference is the residual hydrogen content in the weld, as influenced by the level of preheat with which the samples were produced [2, 3], it is suggested that this should be some inherent differences in the resulting material

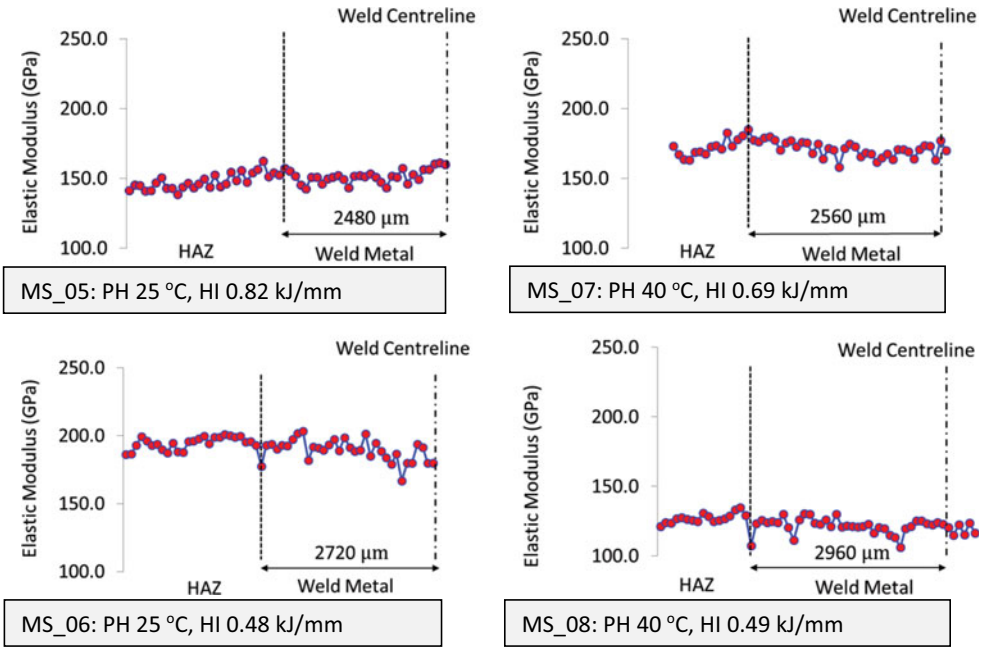

Fig. 20 Elastic modulus for the 10-mm-thick plates

properties across the boundary which allowed for the propagation of a hydrogen crack (for a given preheat).

From the presented results, it seems that the preheat and the heat input affect the hardness and the elastic modulus of the cracked and non-cracked samples in the same directions. However, the samples being situated across an empirical boundary, within narrow heat input ranges, the hardness and elastic modulus do not vary necessarily as expected. Table 5 shows for example that the cracked sample MS-08 has a lower hardness value than the non-cracked sample MS-07 welded at the same preheat but with a lower heat input. Moreover, it has been shown that all cracked samples presented hardness values below the defined threshold of 350 HV below which cracking is not expected. As the propagation of hydrogen cracks is dependent on the elasto-plastic properties of the material within which a crack has initiated [43], it is proposed that the hardness proxy can be refined by combining the hardness with the measured elastic modulus of the material as a ratio hardness/elastic modulus (H/E). This ratio could be used as a more accurate proxy for assessing the susceptibility of a WM to HACC. Moreover, the H/E ratio, traditionally used to rank materials in terms of wear resistance [49–51], appears also in the so-called 'plasticity index' [49, 52], which is widely quoted as a valuable measure in determining the limit of elastic behaviour in a surface contact. Higher H/E values result in higher critical loads for the onset of yield (non-elastic deformation) in indentation [52]. Early works have related the H/E ratio of a material to its yield strength [50, 51], and it has been well established in the literature that the increase of the yield strength decreases the stress intensity threshold for HAC to occur [25–27, 53]. It is thus expected that higher H/E ratio would traduce higher HACC susceptibility of a material.

Examining the ratio of the universal hardness (H in GPa) and elastic modulus (E in GPa) for both the 20- and 10-mm date sets (Figs. 21, 22 and 23), there is evidence to suggest that there is a potential to delineate a boundary which serves as an indicator to the potential susceptibility to WMHACC. The data suggests that if the H/E ratio $>2\times10^{-2}$, the weld is susceptible to WMHACC. Conversely, if the H/E ratio $<1.5\times10^{-2}$, the weld is not susceptible to WMHACC. These experimental outcomes support the hypothesis that materials with higher H/E ratio are more susceptible to HACC. Moreover, it can be seen that the cracked sample MS-08 that could be classified as 'safe' by considering its hardness only (that is lower than the uncracked sample MS-07 for the same preheat but lower heat input) becomes 'unsafe' by considering its H/E ratio (2.3×10^{-2}).The use of the H/E ratio as a refined hardness proxy could be thus a more suitable parameter to predict WMHACC susceptibility than is the hardness alone for HSLA steels.

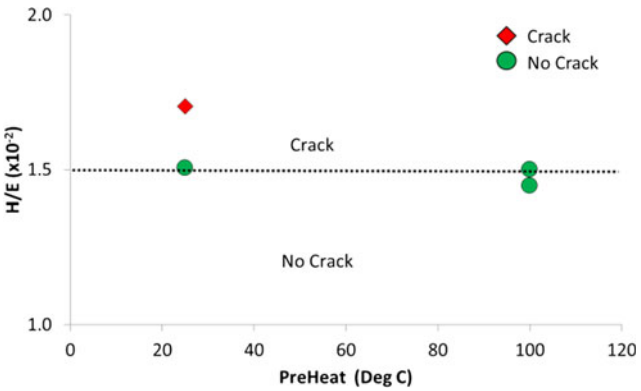

Fig. 21 H/E ratio for samples from the 20-mm data set. No samples with a ratio of $H/E \leq 1.5\times10^{-2}$ cracked

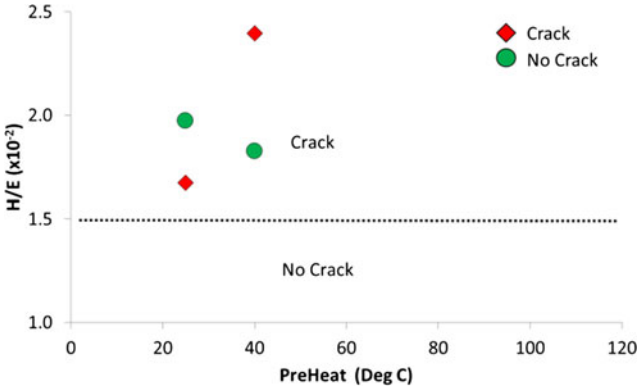

Fig. 22 H/E for samples from the 10-mm data set. A cracking anomaly detected with a ratio of $H/E=1.6\times10^{-2}$. Uncracked sample has ratio as high as $H/E=2\times10^{-2}$

3.5 Role of weld bead eccentricity on WHMACC susceptibility

It is important to note that a change in heat input affects not only the thermal cycle of the deposited weld bead but has a profound effect on the geometry of the deposited weld bead, in particular the eccentricity of the weld toe of the deposited weld bead. One potential consequence of a change in bead eccentricity is the distribution of local stresses in the weld

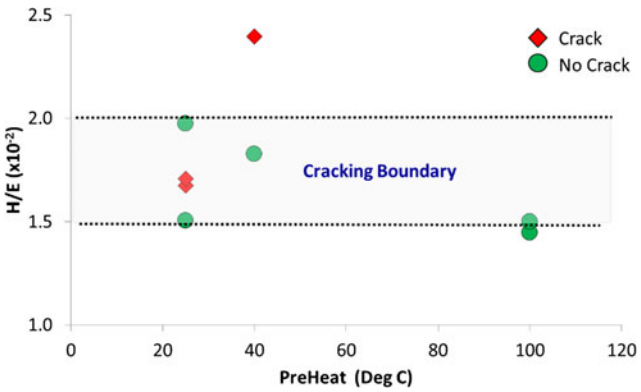

Fig. 23 H/E ratio for both 20 and 10 mm. Combining the data presets a hypothesised boundary within which cracking is uncertain. However, as the yield strain increases, it is postulated that there will be a higher prevalence of WMHACC

bead. This in turn may influence the type and position of hydrogen cracks, given the affinity of atomic hydrogen to areas of high tri-axial stress. It was observed that for the both the 20-mm but especially the 10-mm sample sets, a reduction in the heat input with which a weld was deposited increased the asymmetry of the deposited weld bead. This in turn increased the prevalence cracking in the weld toe. This may be attributed to an increase in the eccentricity of the weld bead profile (Figs. 24 and 25), increasing the intensity of the local stresses at the weld toe, consequently serving as a preferential initiation site for hydrogen cracking.

However, as the preheat levels were increased, the degree of eccentric did not affect the prevalence of cracking as illustrated in Fig. 26. It is therefore suggested that the local weld stresses resulting from bead eccentricity is a critical factor influencing the susceptibility of a single-pass weld to hydrogen cracking.

4 Conclusions

The increased prevalence of WMHACC, as grades of line pipe steel evolve, has raised the question of the reliability of traditional cracking proxies such as hardness. Historically a limit of 350 HV has been established through extensive empirical testing and has been extensively codified.

Empirical testing conducted in this body of work provides data to suggest that the limit of 350 HV does not apply to welds deposited under high restraint, such as those experienced in the pipeline industry during the fabrication of oil and gas transmission and gathering lines.

Welds deposited using E6010 electrodes on two thicknesses (20 and 10 mm) of API 5 L X70 steel at heat inputs ranging from 0.4 to 1.1 kJ/mm were established as having hydrogen cracks in samples with weld metal hardness values as low as 273.4 HV for the 20-mm samples and 331.8 HV for the 10-mm samples.

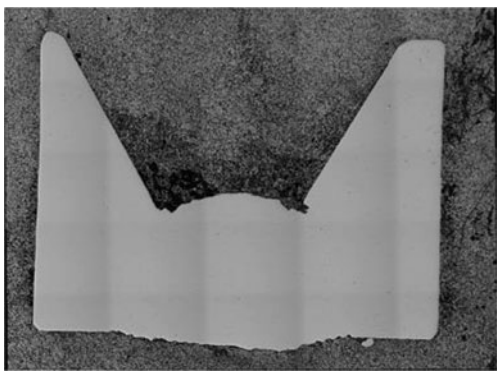

Fig. 24 Typical weld bead geometry for sample deposited with a heat input in the upper quartile of the heat input range of interest. The deposited bead appears symmetrical with no pronounced eccentricity in the weld toe

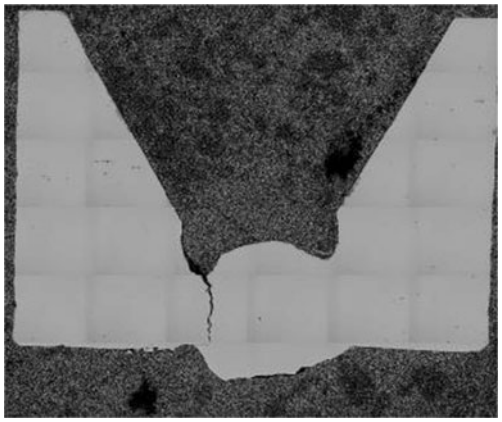

Fig. 25 Typical weld bead geometry for sample deposited with a heat input in the lower quartile of the heat input range of interest. Deposition with a low preheat resulted in the formation of a weld with a produced weld toe and consequently a hydrogen crack

The traditional hardness as a proxy to determine the susceptibility of a WM to HACC proving not to be infallible, and the propagation of hydrogen cracks being dependent on the elasto-plastic properties of the material, it is proposed to refine this proxy by combining the hardness with the elastic modulus of the material as a ratio H/E. From the data collected, this ratio, which is directly related to the yield strength of the material, shows to be a better indicator of the WMHACC susceptibility than is the hardness alone. It is proposed that cracking boundary for API 5 L X70 steel welded with cellulosic electrode is $1.5 \times 10^{-2} < H/E < 2 \times 10^{-2}$.

5 Future work

It is critical to note however that this relationship has been derived based on the empirically testing of one steel composition welded with the same batch of E6010 electrodes for a heat input range typically found in the production of oil and

Fig. 26 Typical weld bead geometry for sample deposited with a heat input in the lower quartile of the heat input range of interest with a heat input of 50°. Despite the irregularity of the weld bead and the eccentric weld toe, no hydrogen cracking was observed in the weld bead

gas pipelines. In order to establish the validity of the predictor for WMHACC in general, it is suggested that a range of steel compositions and electrode combinations are tested for a greater range of heat inputs. This would allow a range of weld metal compositions and microstructural morphologies to be assessed. Although the root pass of a girth weld is accepted as the most vulnerable pass in the welding sequence, to assess the effect of interpass tempering and to ascertain the overall suitability of H/E as a measure of cracking susceptibility, it is also suggested that multi-pass welds be tested.

Acknowledgments The research work was funded by the Energy Pipeline CRC supported through the Australian Government's Cooperative Research Centre Program. The cash and in-kind support from the APGA-RSC is gratefully acknowledged. The authors would also like to thank Neville Cornish from Australian Welding Solutions and Pascal Symons. Walter Costin and Adelaide Microscopy are also acknowledged.

References

1. Barbaro FJ (1999) Types of hydrogen cracking in pipeline girth welds, in: First International Conference on Weld Metal Hydrogen Cracking in Pipeline Girth Welds, Wollongong, Australia, 11.1-11.15. WTIA
2. Yurioka N, Suzuki H (1990) Hydrogen assisted cracking in C-Mn and low alloy steel weldments. Int Mater Rev 35:217–249
3. Kurji R, Coniglio N (2015) Towards the establishment of weldability test standards for hydrogen-assisted cold cracking. Int J Adv Manuf Technol 77:1581–1597
4. Yurioka N (1999) Predictive methods for prevention and control of hydrogen assisted cold cracking. in: First International Conference on Weld Metal Hydrogen Cracking in Pipeline Girth Welds, Wollongong, Australia, 2.1-2.16. WTIA
5. Vasudevan R, Stout RD, Pense AW (1980) A field weldability test for pipeline steels—part II. Weld J 59:76s–84s
6. Signes EG, Howe P (1988) Hydrogen-assisted cracking in high-strength pipeline steels. Weld J 67:163s–170s
7. Fletcher L, Yurioka N (2000) A holistic model of hydrogen cracking in pipeline girth welding. Weld World 44:29–36
8. Beachem CD (1672) A new model for hydrogen-assisted cracking (hydrogen "embrittlement"). Metall Trans 3:437–451
9. Birnbaum HK, Sofronis P (1994) Hydrogen-enhanced localized plasticity—a mechanism for hydrogen-related fracture. Mater Sci Eng A 176:191–202
10. Kinsey AJ (2000) The welding of structural steels without preheat. Weld J 79:79s–88s
11. Fletcher L, Yurioka N (1999) A holistic model of hydrogen cracking in pipeline girth welding. in: First International Conference on Weld Metal Hydrogen Cracking in Pipeline Girth Welds, Wollongong, Australia, 12.1-12.14. WTIA
12. Gedeon SA, Eagar TW (1990) Assessing hydrogen-assisted cracking fracture modes in high-strength steel weldments. Weld J 69: 213s–220s
13. Glover A, Rothwell B (1999) Specifications and practices for hydrogen crack avoidance in pipeline girth welds. in: First International Conference on Weld Metal Hydrogen Cracking in Pipeline Girth Welds, Wollongong, Australia, 13.1-13.18. WTIA
14. Glover A, Graville B (1999) The risk of hydrogen cracking in multipass welds and its effect upon procedure design. in: First International Conference on Weld Metal Hydrogen Cracking in Pipeline Girth Welds, Wollongong, Australia, 9.1-9.23. WTIA
15. Vasudevan R, Stout RD, Pense AW (1981) Hydrogen-assisted cracking in HSLA pipeline steels. Weld J 155s-168s
16. Graville BA, McParlan M (1974) Weld-metal cold cracking. Met Constr Br Weld J 6:62–63
17. Graville BA (1986) A survey review of weld metal hydrogen cracking. Weld World 24:190–198
18. McParlan M, Graville BA (1976) Hydrogen cracking in weld metals. Weld J 55:95s–102s
19. Graville BA (1995) Interpretive report on weldability tests for hydrogen cracking of higher strength steels and their potential for standardization. WRC Bulletin 400
20. Costin WL, Lavigne O, Kotousov A, Ghomashchi R, Linton V (2016) Investigation of hydrogen assisted cracking in acicular ferrite using site-specific micro-fracture tests. Mater Sci Eng A 651C: 859–868
21. Trevisan RE, Fals HC (1999) Fracture modes and acoustic emission characteristics of hydrogen-assisted cracking in high-strength low-alloy steel weldment. J Braz Soc Mech Sci Eng 21:675–682
22. Vuick J (1992) An update of the state-of-the-art of weld metal hydrogen cracking. Weld World 31:308–321
23. Song EJ, Bhadeshia HKDH, Suh DW (2013) Effect of hydrogen on the surface energy of ferrite and austenite. Corros Sci 77:379–384
24. Grabke HJ, Riecke E (2000) Absorption and diffusion of hydrogen in steels. Mater Tehnol 34:331–342
25. Gerberich WW, Chen YT (1973) A threshold stress intensity concept for environmental cracking. Int J Fract 9:369–371
26. Homrossukon S, Mostovoy S, Todd JA (2009) Investigation of hydrogen assisted cracking in high and low strength steels. J Press Vessel Technol-Trans ASME 131:1–11
27. Yamaguchi Y, Nonaka H, Yamakawa K (1997) Effect of hydrogen content on threshold stress intensity factor in carbon steel in hydrogen-assisted cracking environments. Corrosion 53:147–155
28. Ghomashchi R, Costin W, Kurji R (2015) Evolution of weld metal microstructure in shielded metal arc welding of X70 HSLA steel with cellulosic electrodes: a case study. Mater Charact 107:317–326
29. API Standard 1104-Nineteenth Edition (1999) Welding of pipelines and related facilities. American Petroleum Institute, Washington, DC
30. CSA Z662 (2003) Oil and gas pipeline systems, CSA International
31. AS 2885.2-2002 (2002), Pipelines—gas and liquid petroleum, Part 2: welding, Standards Australia
32. Davidson JA, Konkol PJ, Sovak JF (1989) Assessing fracture toughness and cracking susceptibility of steel weldments—a review. WRC Bulletin 345
33. Cheng YT, Cheng CM (1998) Relationships between hardness, elastic modulus, and the work of indentation. Appl Phys Lett 73: 614–616
34. Lucca DA, Herrmann K, Klopfstein MJ (2010) Nanoindentation: measuring methods and applications. CIRP Ann-Manuf Technnol 59:803–819
35. VanLandingham MR (2003) Review of instrumented indentation. J Res Natl Inst Stand Technol 108:249–265
36. Oliver WC, Pharr GM (2004) Measurement of hardness and elastic modulus by instrumented indentation: advances in understanding and refinements to methodology. J Mater Res 19:3–20
37. Chudoba T (2006) Measurement of hardness and Young's modulus by nanoindentation. In: Cavaleiro A, Hosson JT (eds) Nanostructured coatings. Springer, New York
38. Johnson KL (1985) Contact mechanics. Cambridge University Press, Cambridge
39. Fischer-Cripps AC (2000) Introduction to contact mechanics. In: Ling FF (ed) Mechanical engineering series. Springer, New York

40. Maier P, Richter A, Faulkner RG, Ries R (2002) Application of nanoindentation technique for structural characterisation of weld materials. Mater Charact 48:329–339
41. Ye D, Mi F, Liu J, Xu Y, Chen Y, Xiao L (2013) Use of instrumented indentation testing to study local mechanical properties of 304L SS welded joints subjected to low-cycle fatigue loadings. Mater Sci Eng A 564:76–84
42. Fang J, Yuan H (2013) The local concept to assess weldment with help of nano-indentation and FEM simulation, in: 13th International Conference on Fracture. Beijing, China
43. Di Leo CV, Anand L (2013) Hydrogen in metals: a coupled theory for species diffusion and large elastic–plastic deformations. Int J Plasticity 43:42–69
44. Kurji R, et al. (2013) An improved welding institute of Canada test for evaluation of high-strength pipeline steel weldability, Paper no: S11-03, 6th International Pipeline Technology Conference, Ostend, Belgium
45. Costin WL, Lavigne O, Linton V, Brown IH, Kotousov AG, Barbaro FJ, Ghomashchi R (2013) Micromechanical examination of the relationship between weld metal microstructure and hydrogen assisted cold cracking, Paper no: S10-02, 6th International Pipeline Technology Conference, Ostend, Belgium
46. Kumar S, Shahi AS (2011) Effect of heat input on the microstructure and mechanical properties of gas tungsten arc welded AISI 304 stainless steel joints. Mater Des 32:3617–3623
47. Alipooramirabad H, Ghomashchi R, Paradowska A, Reid M (2016) Residual stress-microstructure-mechanical property interrelationships in multipass HSLA steel welds. J Mater Process Technol 231:456–467
48. Rafiqul MI, Ishak M, Rahman MM (2011) Effects of heat input on mechanical properties of metal inert gas welded 1.6 mm thick galvanized steel sheet. IOP Conf Ser: Mater Sci Eng 36:1–8
49. Leyland A, Matthews A (2000) On the significance of the *H*/*E* ratio in wear control: a nanocomposite coating approach to optimised tribological behaviour. Wear 246:1–11
50. Oberle TL (1951) Properties influencing wear of metals. J Metals 3: 438–439
51. Finkin EF (1974) Examination of abrasion resistance criteria for some ductile metals. J Tribol-Trans ASME 96:210–214
52. Zhang S (2016) Thin films and coatings—toughening and toughness characterization. CRC Press, Taylor and Francis Group, Boca Raton
53. Loginow AW, Phelps EH (1975) Steels for seamless hydrogen pressure vessels. Corrosion 31:404–412

Materials Characterization 107 (2015) 317–326

Contents lists available at ScienceDirect

Materials Characterization

journal homepage: www.elsevier.com/locate/matchar

Evolution of weld metal microstructure in shielded metal arc welding of X70 HSLA steel with cellulosic electrodes: A case study

Reza Ghomashchi *, Walter Costin, Rahim Kurji

School of Mechanical Engineering, The University of Adelaide, Adelaide, SA 5005, Australia

ARTICLE INFO

Article history:
Received 23 April 2015
Received in revised form 17 June 2015
Accepted 28 July 2015
Available online 30 July 2015

Keywords:
SMAW
Cellulosic electrode
Pearlite
Bainite
Ferrite
Widmanstätten
Acicular
Inclusion

ABSTRACT

The microstructure of weld joint in X70 line pipe steel resulted from shielded metal arc welding with E6010 cellulosic electrodes is characterized using optical and electron microscopy. A range of ferritic morphologies have been identified ranging from polygonal inter- and intra-prior austenite grains allotriomorphic, idiomorphic ferrites to Widmanstätten, acicular and bainitic ferrites. Electron Backscatter Diffraction (EBSD) analysis using Image Quality (IQ) and Inverse Pole Figure (IPF) maps through superimposition of IQ and IPF maps and measurement of percentages of high and low angle grain boundaries was identified to assist in differentiation of acicular ferrite from Widmanstätten and bainitic ferrite morphologies. In addition two types of pearlitic structures were identified. There was no martensite detected in this weld structure. The morphology, size and chemistry of non-metallic inclusions are also discussed briefly.

1. Introduction

Shielded metal arc welding (SMAW) with cellulosic welding consumables is traditionally used for "stovepipe" welding of steel gas transmission pipelines in Australia. This manual metal arc welding technique, used with cellulosic welding electrodes, offers unique productivity advantages and is therefore part of a well-established process for pipeline girth weld production for small and medium size pipeline diameters. This process involves the use of E6010 electrodes without preheat for the root pass, and E8010 electrodes for subsequent passes [1,2].

The integrity of a welded joint is known to be dependent not only on the symmetry of the deposited weld bead and consequently its ability to transfer load across the ligament but the micromechanical properties and the degree of homogeneity within the constituents of the ligament. This includes weld metal microstructure established during the cooling of the weld cycle that influences the load bearing capacity of the joint dramatically [2,3]. The load bearing capacity however is dependent on the microstructure interaction with its surrounding including the gases generated during welding such as hydrogen [4–6]. It is for this reason that there is a large quantity of research dedicated to determining the ideal thermo-mechano-chemical factors which will produce a desirable microstructure [2–9]. The identification of the desirable microstructure itself is a daunting task since it entails detailed knowledge of mechanical and morphological characteristics of the various microconstituents form during welding either solo or in combination with one another. The knowledge includes the nature of grain boundary (low or high angle, misorientation relationship), crack susceptibility or crack deflectability of various phases and boundaries and of course the morphology (equiaxed, lathes/sheaves, spiked) and mechanical properties of individual phases such as Young's modulus (E), hardness (HV) and fracture resistance (K_{IC}). In order to be confident in identifying the desirable microstructure, the first and most critical stage is to identify individual microconstituents such as bainite or grain boundary ferrites and the mechanism controls their formation. Thewlis and co-workers attempted to characterize the morphology of different phases formed during welding [10–13]. The following classification of weld structure is now well accepted and is followed in this report;

1- *Polygonal primary ferrites*, where they nucleate mainly on the prior austenite grain boundaries and to a lesser degree within austenite grains where there are non-metallic inclusions (NMIs).
2- *Widmanstätten ferrite*, the primary Widmanstätten ferrite plates grow directly from the prior austenite grain boundaries, whereas the secondary Widmanstätten ferrite plates grow from polygonal primary ferrites (allotriomorphic ferrite) at the grain boundaries.Primary Widmanstätten ferrite plates may also grow from inclusions, while secondary Widmanstätten ferrite plates can grow from intragranular primary ferrite (idiomorphic) which is itself NMIs nucleated.

* Corresponding author.
E-mail address: reza.ghomashchi@adelaide.edu.au (R. Ghomashchi).

http://dx.doi.org/10.1016/j.matchar.2015.07.032
1044-5803/

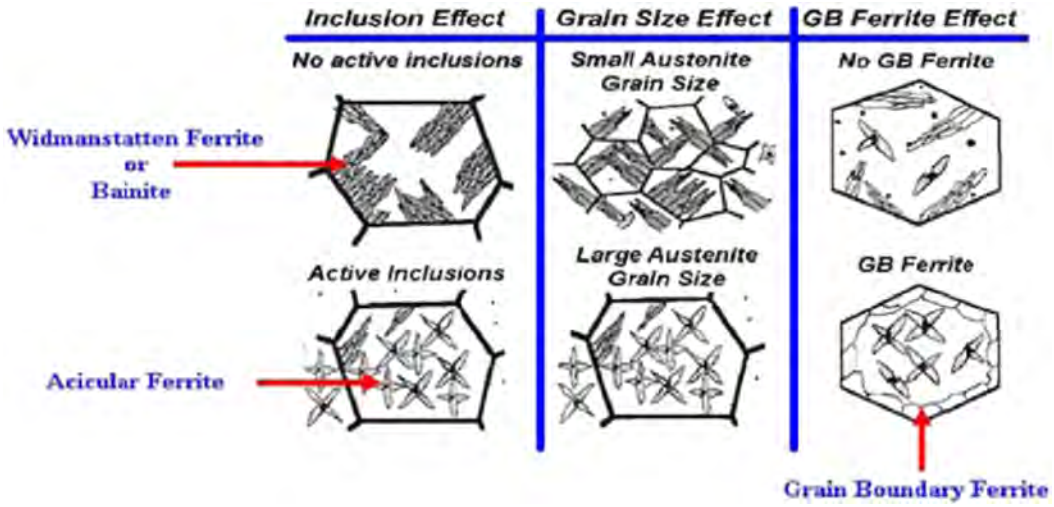

Fig. 1. Schematic diagram adapted from Bhadeshia and Svensson to show the effect of prior austenite grain size and non-metallic inclusions on the nucleation of bainite, Widmanstätten ferrite and acicular ferrite [19].

3- *Acicular ferrite* nucleates intragranularly from inclusions within the prior austenite grains and is characterized by fine ferrite plates (diameter typically <5 μm) that form an interlocking morphology [14]. For a long time acicular ferrite was considered to be a single transformation product. Early studies suggested that it was intragranularly nucleated Widmanstätten ferrite [15]. Later research provided evidence for intragranularly nucleated bainitic acicular ferrite [14]. However, more recent investigations demonstrated that different reaction products may nucleate on intragranular inclusions at reconstructive (diffusion-based) and displacive (diffusionless) transformation temperatures during continuous cooling depending on the nature, size and amount of inclusions [12]. Hence, acicular ferrite may consist of mixtures of different intragranular transformation products such as idiomorphic ferrite, intragranular Widmanstätten ferrite and intragranular bainite [12]. Alternatively, Widmanstätten acicular ferrite or bainitic acicular ferrite may form by itself [14,15].

4- *Bainite* grows as individual plates or sub-units that can form sheaves of parallel ferrite laths which can be categorised as either upper or lower bainite, depending on the transformation temperature [16]. For upper bainite, carbon precipitates as cementite (Fe_3C) between the bainitic ferrite plates (sheaves). In lower bainite, the ferrite becomes supersaturated with carbon and some carbide precipitation occurs within the ferrite sub-units as well as between them [16].

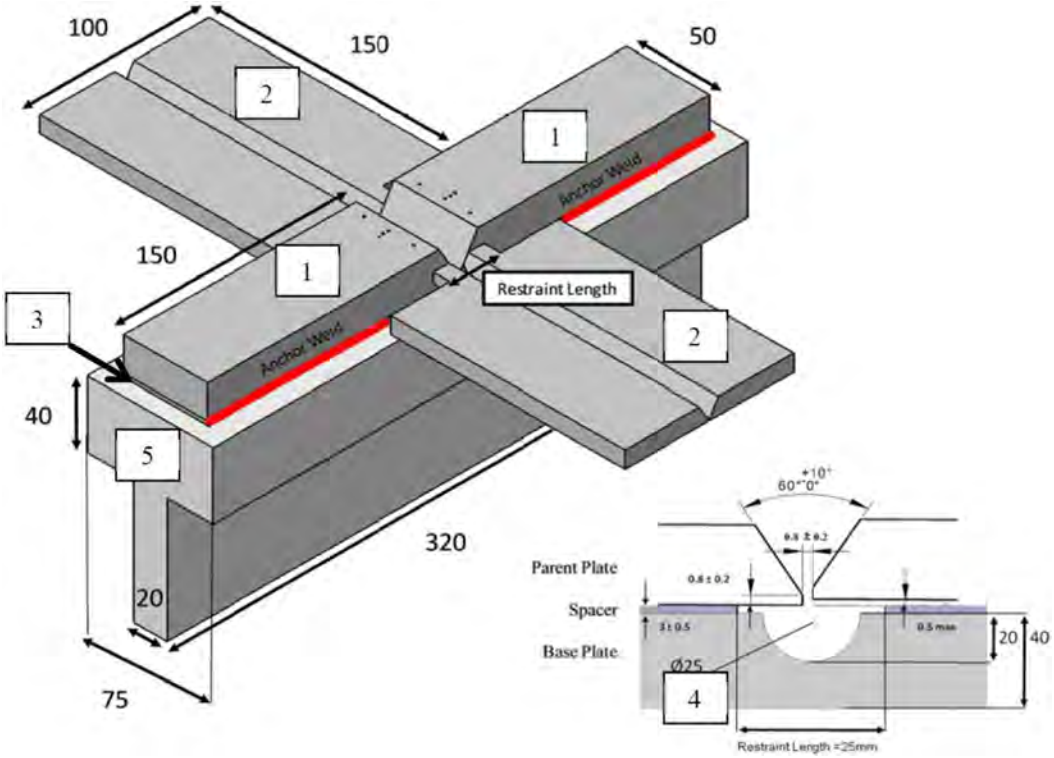

Fig. 2. Modified WIC Design. (1) Parent plate (2) Run-On/Off tab (3) Spacer (4) Tunnelled backing plate (5) Stiffener. All dimensions in mm [20].

Table 1
Welding specifications and parameters used to deposit the weld specimen.

Welding specifications		Welding parameters	
Direction:	Vertical down (5G)	Current:	178 [A]
Size of electrode:	Ø 4.0 [mm]	Voltage:	22.9 [V]
AWS class:	A5.1	Travel speed:	456.7 [mm/min]
Specification:	E6010	Heat input range:	0.61 [kJ/mm]
Polarity:	DC+	Preheat	100 [°C]

5- *Pearlite* transformation may occur at the austenite grain boundaries or at inhomogeneities such as inclusions [16]. At high transformation temperatures, pearlite forms nodules of alternate ferrite and cementite lamellae that may be quite coarse. As the transformation temperature is lowered, the lamellae become increasingly finer until the structure becomes irresolvable under the light microscope [12]. Alternatively, distorted lamellae may appear as virtually irresolvable ferrite/carbide aggregate [12].
6- *Martensite* forms as a result of a rapid and diffusionless transformation where carbon is retained in solution [17]. Martensite can occur in the form of either laths or plates. The sub-structure of lath martensite is characterized by a high density of dislocations arranged in cells where each martensite lath is composed of many dislocation cells. The substructure of plate martensite consists of very fine twins, i.e., twinned martensite [12].

Besides the abovementioned principal microstructural constituents and NMIs, weld metal usually contains microphases like Retained Austenite (RA) and Martensite–Austenite–Carbide constituents (M–A–C) [18].

The conclusion of the above-mentioned classification is that the formation of different microconstituents in weld structure is controlled mainly by the prior austenite gain size and non-metallic inclusions form during solidification. This is well illustrated in the schematic diagram shown in Fig. 1 adapted from the work of Bhadeshia and Svensson [19].

This is the theme of the current article where the microstructure of SMAW welded X70 high strength low alloy (HSLA) steel with E6010 cellulosic consumables are characterized using optical and electron microscopy including the application of EBSD and EDS analyses.

2. Experimental procedures

The SMAW specimens were prepared using the MWIC weldability test developed by our team at the University of Adelaide [20]. The MWIC should enable the study of the effect of restraint, plate thickness, heat input and weldmetal joint geometry on the weldmetal thermo-mechanical characteristics and quality. The Modified WIC sample (MWIC) includes four significant changes to the standard test specimen geometry to improve the consistency of the deposited weld bead profile, the quality of the deposited weld at lower heat inputs and the ability to instrument the test specimen. The MWIC weldability test incorporates: a gas tunnel, V grooved Run-On/Run-Off tabs, and instrumentation access including a weld centreline access port and an extensometer access port (Fig. 2) [20].

The welding procedure involved a unidirectional, mechanized SMA welding machine with a specimen-holding plate moving vertically upwards during welding at a controlled velocity, thus simulating vertical-down (stovepipe) welding conditions. A constant force and an angle of 20° normal to the plate were maintained between the electrode and the work piece. All the specifications and the welding parameters, Table 1, used to fabricate the specimens had the main purpose to replicate the field conditions that may be encountered when laying the root pass of a girth weld during pipeline construction.

Welding was carried out using 4 mm Ø E6010 cellulosic electrodes and API 5L grade X70 line pipe steel. The test plate chemical composition is given in Table 2 and the electrode batch chemistry is given in Table 3.

Table 3
Electrode batch chemical composition (wt.%—from the manufacturer).

C	Mn	Si	S	P	Ni	Mo	Cr	V
0.16	0.62	0.19	0.009	0.009	0.2	0.01	0.02	<0.01

3. Results and discussion

A typical weld overview structure (Root Run) is shown in Fig. 3 with both the heat affected zone (HAZ) and weldmetal regions well clear (arrowed) along with welding defects; undercuts and the resulted hydrogen assisted cold crack (HACC). The HACC is due to stress concentration at the undercut regions. A thorough examination of the etched weld cross sections have revealed that the microstructure basically comprises of mainly ferritic structure (light etched regions) with some regions having some pearlitic structure (dark region) as well. A typical optical micrograph is presented for each of the regions in Fig. 4. However, the ferrite itself shows a wide range of morphologies and that is the aim of this report to try to classify the phases along with their morphologies.

3.1. Ferrites

If the optical micrographs in Fig. 4 are examined closely, the phases are basically forming intergranularly (grain boundary nucleated) or are intragranular (nucleated within the grains).

The application of electron backscattered diffraction (EBSD) enables to better differentiate between the morphologies of the weld microconstituents. The contrast variation in the image quality (IQ) map (Fig. 5a) represents the undisturbed (brighter tone) crystallographic regions and imperfections such as grain boundaries (darker tone) to provide a useful visualisation of the microstructure. A common map to represent the texture of a microstructure is the Inverse Pole Figure (IPF) map. These types of maps show the distribution of crystallographic orientations relative to a selected reference direction, Fig. 5b. Through analysis of IQ and IPF maps it is possible to generate information on different morphologies and the nucleation sites of microconstituents. When an IQ map is superimposed on an IPF map, the result would be a better way of verifying the nucleation sites of different microconstituents. As shown in Fig. 5c, the ferrite phase growing from the prior austenite grain boundaries at the plane of polish are clearly shown against those growing from intragranular regions within the prior austenite grain; such distinction may be used as a tool to help in identification of phases due to their specific nucleation sites.

The ferrite morphology appears in a great number of varieties as can be seen in Figs. 4 and 5 and more specifically identified in Figs. 6–8. There are primary ferrites nucleated at the prior austenite grain boundary to appear as a continuous phase (Fig. 6a) or equiaxed grains which is identified as allotriomorphic ferrite (Fig. 6b). In addition, there is

Table 2
Chemical composition of the X70 test plates (wt.%).

C	Mn	Si	S	P	Nb	Ti	Cu	Ni	Mo	Cr	Ca	Al	V
0.052	1.55	0.21	0.001	0.0097	0.041	0.012	0.15	0.19	0.18	0.026	0.0016	0.039	0.029

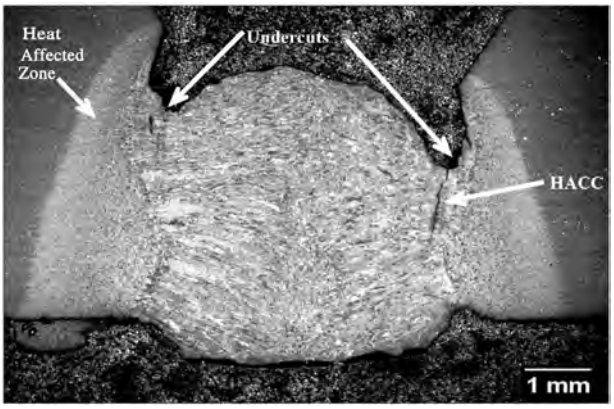

Fig. 3. Typical weldmetal overview structure. The formation of a hydrogen assisted cold crack (HACC) along with weld defect and heat affected zone are identified on the micrograph.

primary ferrite particles nucleated within the prior austenite grains as shown in Fig. 6c, i.e., idiomorphic ferrite nucleated on non-metallic inclusions, NMIs, or intragranular ferrite which is in fact an allotriomorphic ferrite of a grain underneath the plane of polish intersecting it, Fig. 6d. So it may be referred to as pseudo-intragranular ferrite.

As the transformation temperature is depressed, the morphology of ferrite tends to change to Widmanstätten or acicular ferrite. The optical micrographs in Fig. 7 characterize a range of morphologies for Widmanstätten ferrite, depending on the nucleation site;

1- Primary Widmanstätten ferrite nucleating and growing from the prior austenite grain boundaries, Fig. 7a.
2- Secondary Widmanstätten ferrite nucleating and growing off the primary grain boundary ferrite, Fig. 7b
3- It is expected to have primary and secondary Widmanstätten ferrite nucleating intragranularly on inclusions and idiomorphic ferrites within the prior austenite grains as shown in Figs. 7c and d respectively.

The fact that the phases identified in Fig. 7c and d are Widmanstätten ferrite and not acicular ferrite is based on the aspect ratio consideration which is more than 4/1 in confirmation with literature [11].

In addition to the above-mentioned Widmanstätten ferrite phases, there is always the possibility of plane of polish (observation plane) interesting primary or secondary Widmanstätten ferrite growing from prior austenite grain underneath the plane of polish having no specific morphology.

The next major ferrite morphology which is also the most preferred morphology in welded structures is the acicular ferrite. Acicular ferrite is characterized by a chaotic arrangement of fine-grained plates with different orientations that are separated by high angle grain boundaries, Fig. 8. It has to be pointed out that optical metallography after 2% Nital etching is not an easy process to clearly distinguish between Widmanstätten ferrite and acicular ferrite nor bainite and acicular ferrite. The application of SEM and EBSD however is quite helpful in clear distinction of these phases. The EBSD-IQ map and the superimposed IQ and IPF maps in Fig. 8b confirm the acicular ferrites having high angle grain boundaries while for bainite and Widmanstätten ferrites the detection of low angle boundaries should confirm their positive identification.

It has been reported that microstructures containing a high proportion of acicular ferrite seem to have a higher strength and toughness than even bainitic microstructures [2]. This is further supported in a very recent publication where both crack initiation energy and crack propagation energy

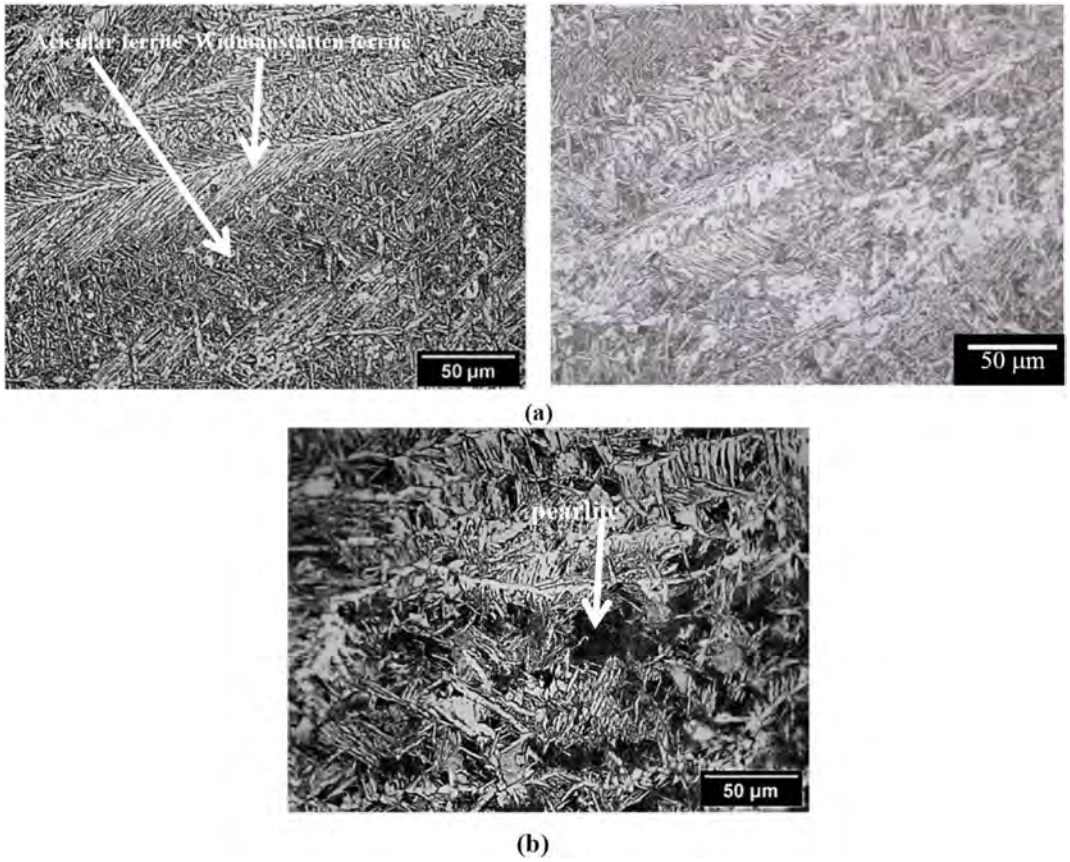

Fig. 4. Optical micrographs of the typical microstructures formed in the WIC test specimens. (a) Mainly ferritic structure. (b) Ferrite with some pearlite.

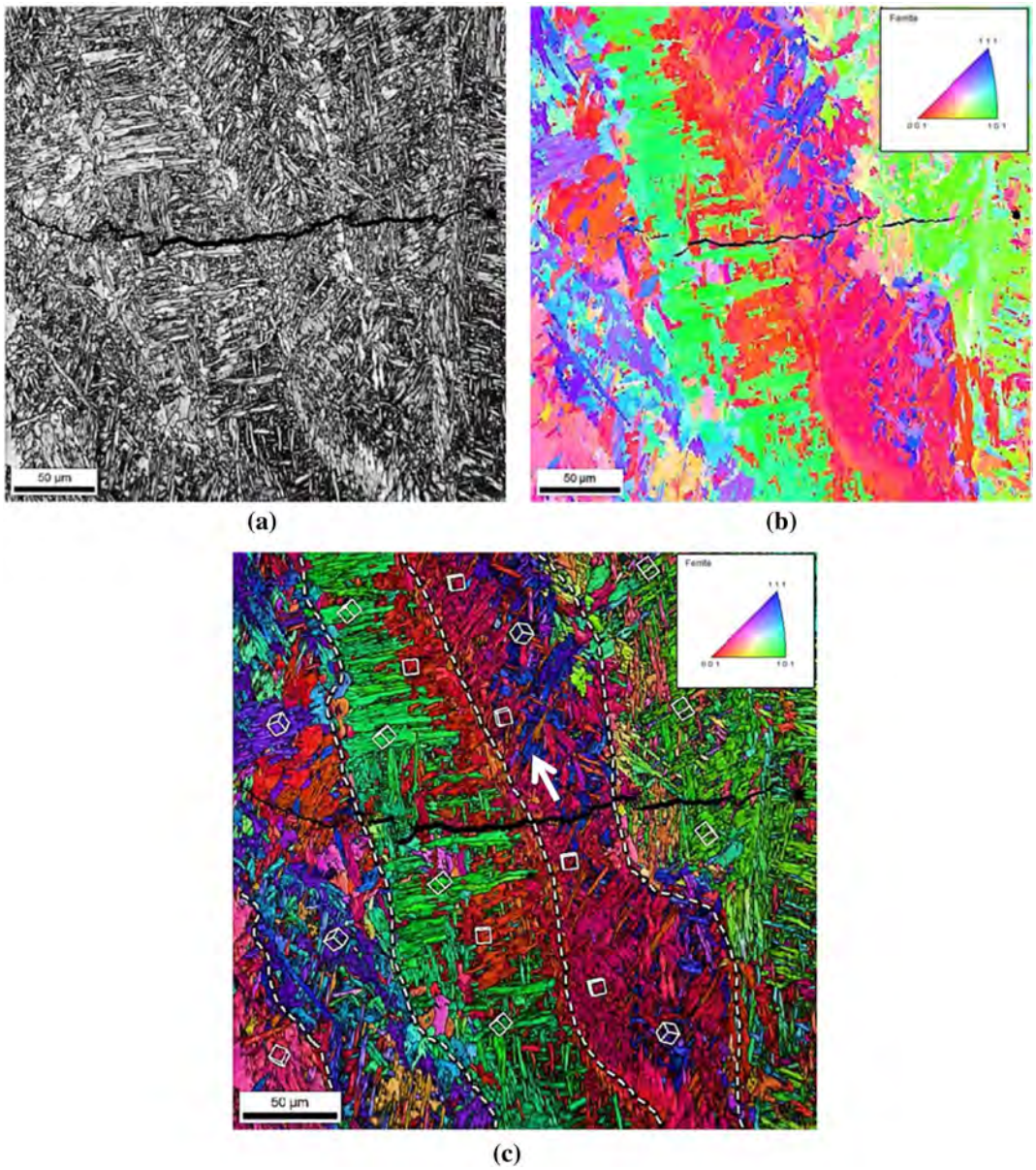

Fig. 5. Application of EBSD analysis to characterize weldmetal microstructure.

a) Image Quality (IQ) map to show undisturbed crystallographic regions in a brighter tone and imperfections such as grain boundaries in a darker tone.
b) Inverse Pole Figure (IPF) map to show the distribution of crystallographic orientations relative to the selected reference direction (normal to the sample surface [001]).
c) Superimposing IQ and IPF maps in (a) and (b). The prior austenite grain boundaries are shown by the broken lines. The different colour contrast helps to differentiate between phases growing from prior austenite grain-boundaries and those within the grain. The blue phase (arrowed) is an intragranularly nucleated phase as discussed later.

(toughness) of the steel in the presence of intragranular acicular ferrite (IAF) were higher than steel without IAF [23]. Also acicular ferrite appears to have a higher resistance to HACC than other high strength phases such as upper bainite [2,21]. This was mainly associated with the high density of high angle grain boundaries in acicular ferrite which apparently increases the resistance to cleavage like fracture [3,21].

3.2. Bainite

As mentioned before, there is both upper and lower bainitic sheaths form within the weld metal structure nucleating mainly at the prior austenite grain boundaries. The morphology of upper bainite as shown in Fig. 9a, b and c comprises of ferrite sheaths with parallel cementite flakes in between the sheaths (Fig. 9c). However, if the plane of polish intersects the bainitic grains below the plane of polish, there may be a misaligned carbide phase in the structure as shown in Fig. 9b.

The superimposed inverse pole figure (IPF) and image quality (IQ) maps (Fig. 9d) illustrates that upper bainite forms crystallographic packets which consist of ferrite laths with largely similar orientations.

As for lower bainite, it is characterized with intra-lath segregation of carbides as shown in Fig. 10.

3.3. Pearlite

As shown by the optical micrograph in Fig. 4b, the weld metal contains some pearlite since the carbon content of the parent metal and the electrode were 0.052 and 0.16 wt.% respectively (Tables 2 and 3). It is also difficult to resolve pearlitic structure using optical microscope

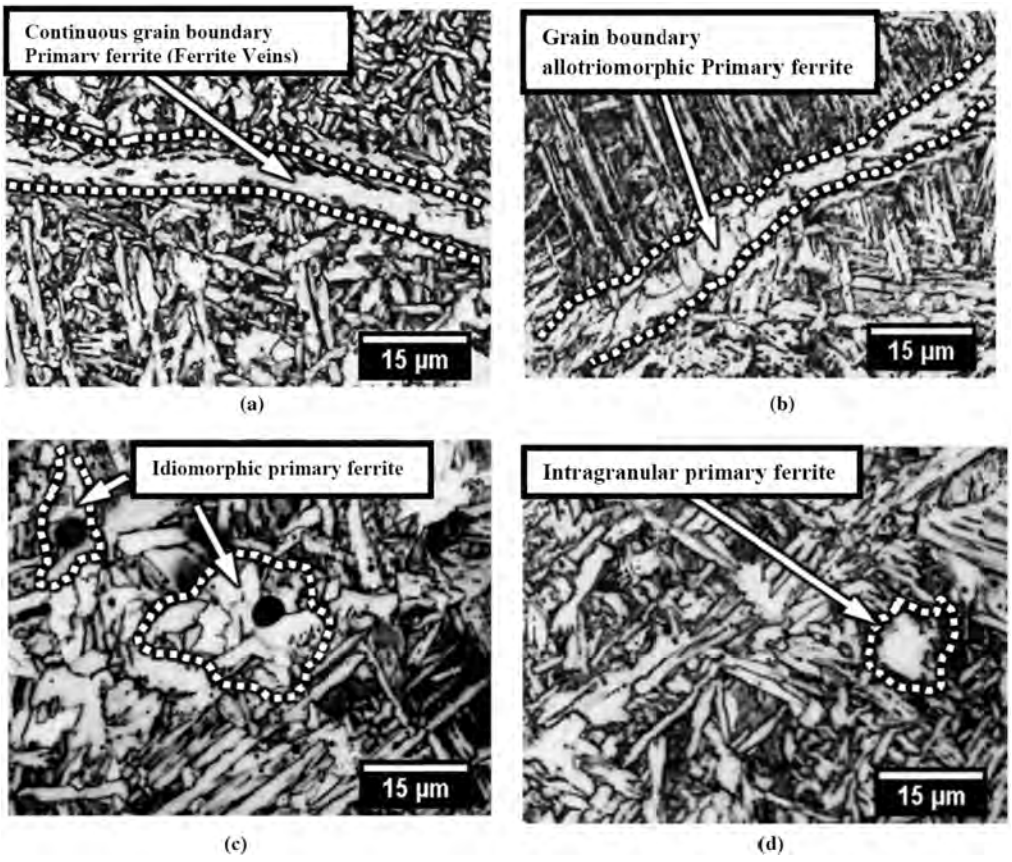

Fig. 6. Optical micrographs to show different primary ferrite morphologies in the weld.

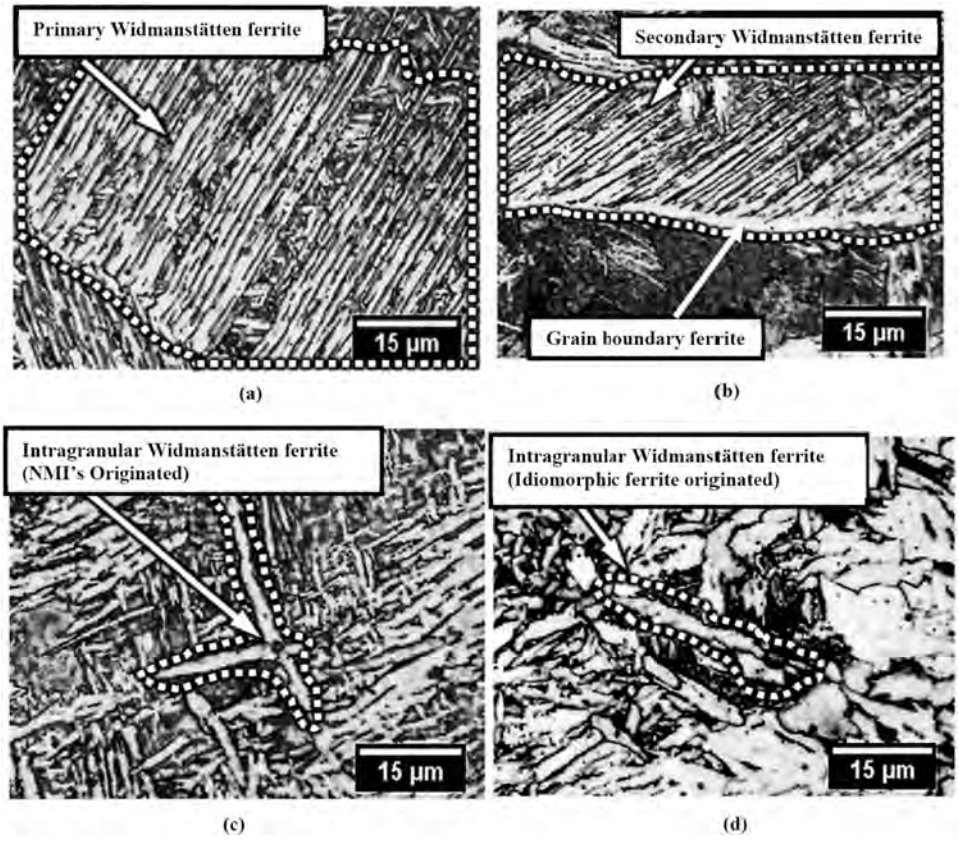

Fig. 7. Optical micrographs to show different morphologies of Widmanstätten ferrite in the weld.

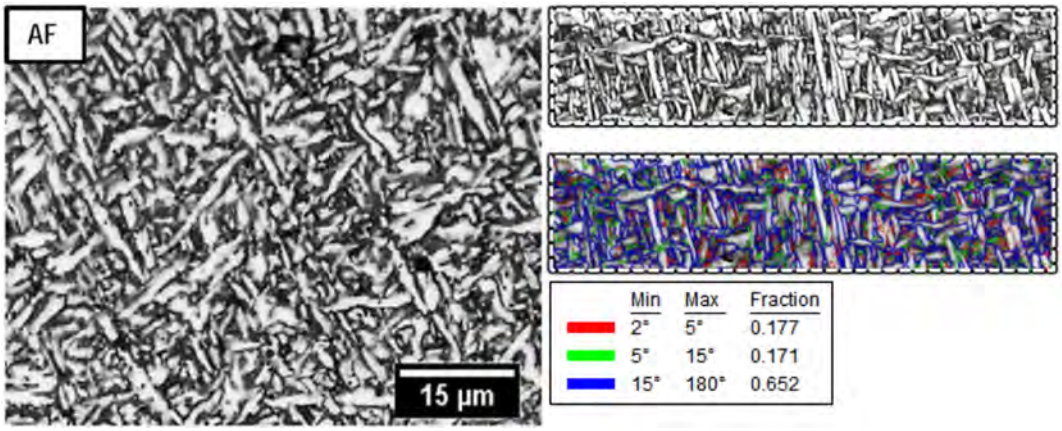

Fig. 8. Acicular ferrite morphology in weldmetal. The IQ map clearly shows the acicular ferrite which is superimposed on IPF to confirm acicular ferrite with their large angle grain boundaries. The Table confirms the structure contains about 65% acicular ferrite.

as it is well clear in Fig. 4b. As reported [12], the pearlite could be of lamellar or degenerated nature or even a ferrite and fine carbide mixture specified as ferrite–carbide aggregate. The SEM micrographs in Fig. 11 clearly specify the pearlite morphology with the distinction proposed by Thewlis [12].

3.4. Martensite

The martensite due to its brittle nature makes the weldmetal susceptible to cracking and therefore regarded as undesirable during SMAW fabrication of energy pipeline. The formation of martensite was not detected when SMAW of X70 steel was carried out on modified WIC (MWIC) test coupons using E6010 electrodes.

3.5. Non-metallic inclusions (NMIs)

As mentioned before, the formation of various ferrite morphologies is dependent on the size of prior austenite grains and the distribution of non-metallic inclusions, see Fig. 1. The types of inclusions may influence the morphology of phases as for instance it is reported that oxide inclusions may encourage the formation of acicular ferrite which itself is a positive contributor towards weld metal toughness [22].

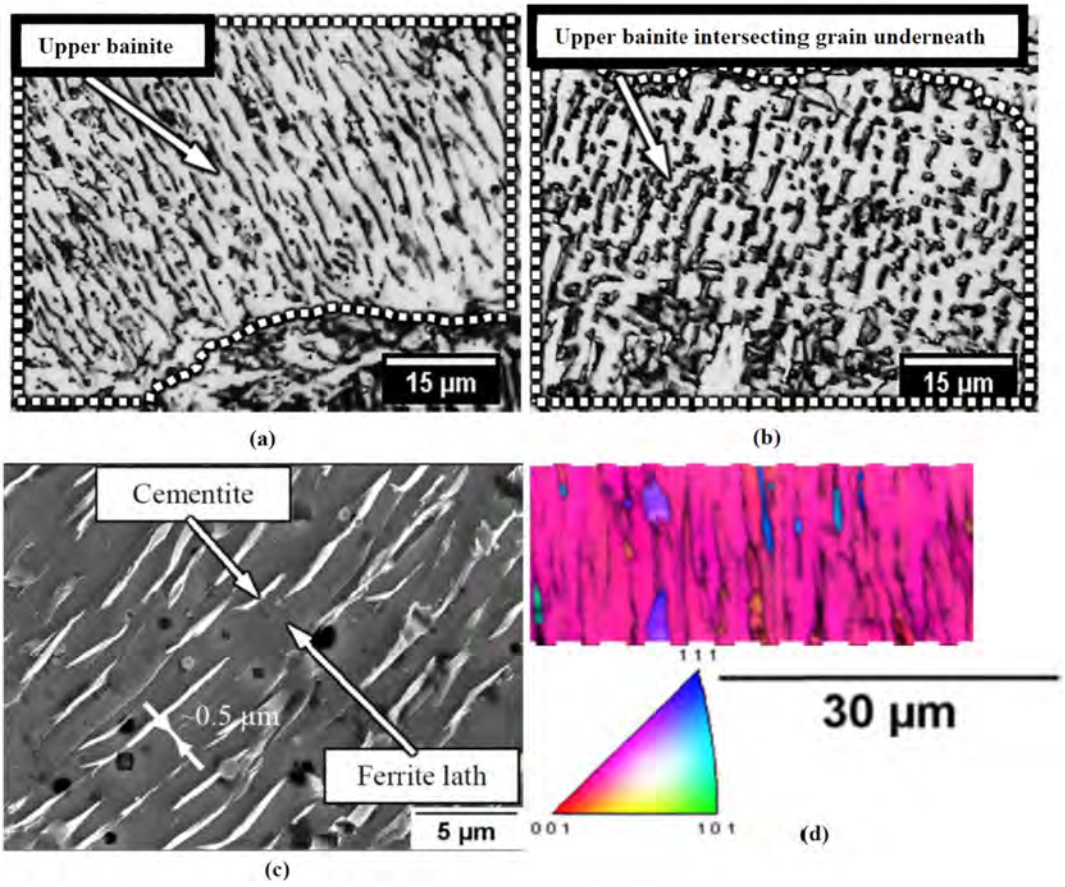

Fig. 9. (a) and (b) are optical micrographs to show upper bainite morphologies in the weld. The SEM micrograph (c) reveals the formation of cementite within upper bainite inter-laths. (d) Superimposed [001] IPF and IQ map.

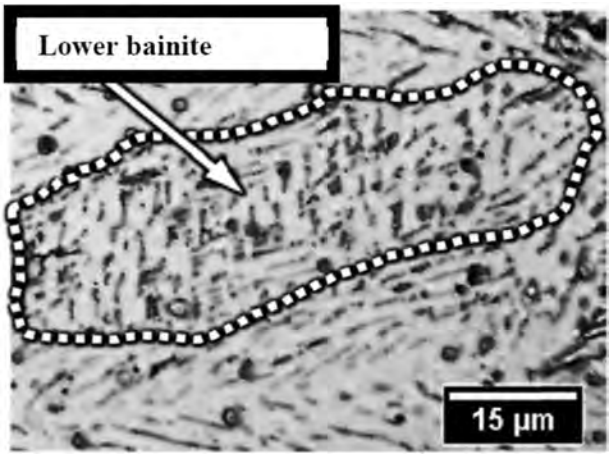

Fig. 10. Lower bainite with intra-lath carbide segregation.

The electrode covering used for SMAW contains cellulose $(C_6H_{10}O_5)_x$ and various chemicals for a range of functions including protection against the environment and also deoxidization of molten pool. The decomposition of cellulose covering of the electrodes produces a gaseous shield rich in H_2, for instance, 41% H_2, 40% CO, 16% H_2O, and 3% CO_2 in the case of E6010 electrodes [22]. Therefore, the interaction amongst the electrode covering, weldmetal molten pool and environment is much expected to be the source of a range of NMIs within the weld structure. A scanning electron microscope in conjunction with energy dispersive spectrometry and back scattered electron imaging was used to identify the morphology, size and chemistry of several inclusions detected during SMAW welding of MWIC samples. The SEM (secondary electron) micrographs in Fig. 12 provide information on the size and shape of NMIs. As it is evident, the fine rounded inclusion may segregate nearly uniformly within the weld (Fig. 12a) or even cluster as shown in Fig. 12b. A typical EDS spectrum (from the inclusion showed by the arrow—Fig. 12a), provides some information on the chemistry of inclusions in X70-E6010 shielded metal arc welding. It is worth mentioning that the Mo peak is an artefact as no Kα-line (E = 17.441 keV) was detected for Mo.

4. Conclusions

The microstructure of weldmetal plays an important role on its integrity. However, recognizing every specific morphology is rather difficult and requires experienced and well trained operator. A thorough analysis of weldmetal microstructure resulted from welding X70 linepipe HSLA steel with E6010 cellulosic electrodes has been carried out using optical and electron microscopy including EDS and EBSD in

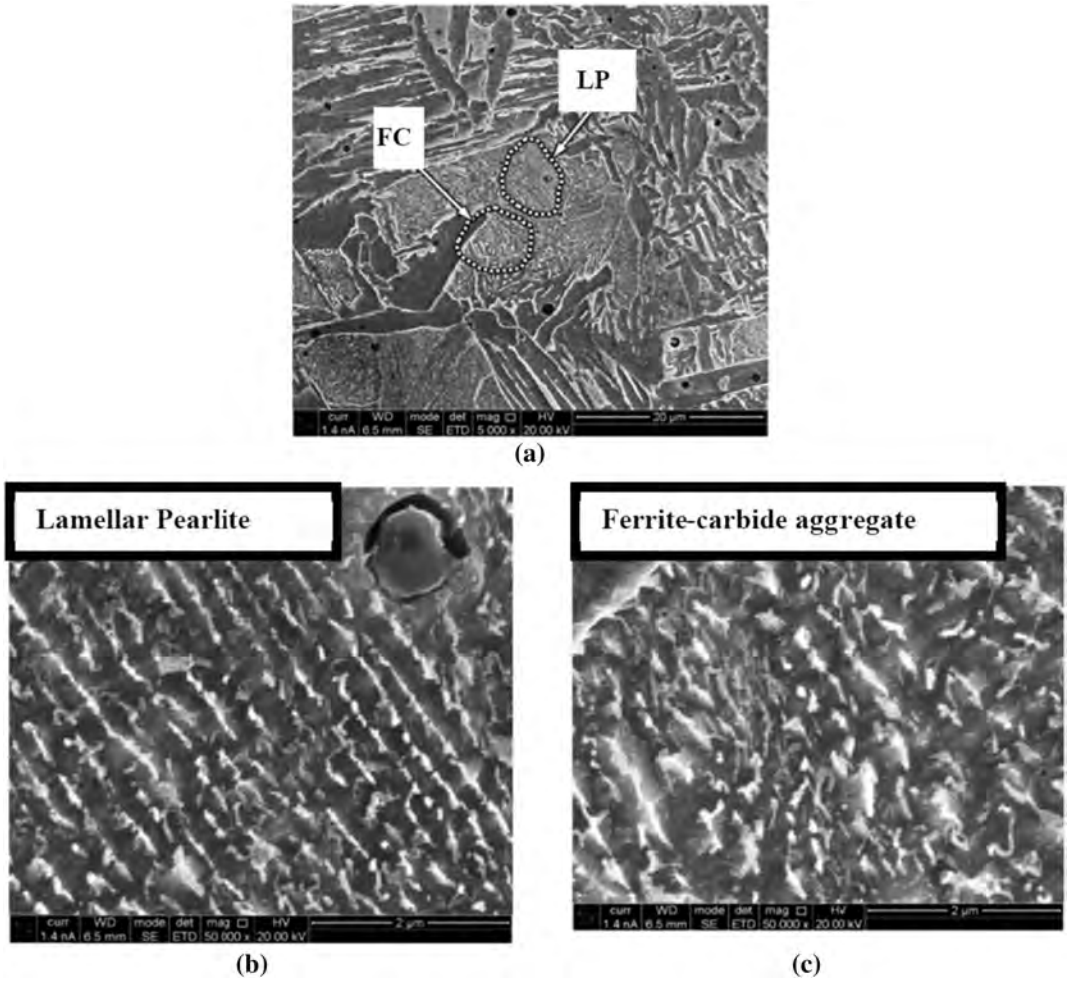

Fig. 11. SEM micrographs to show two distinct pearlitic structures of lamellar pearlite and ferrite-carbide aggregate.

a) As-weld structure showing pearlitic patches with two distinct morphologies.
b) Lamellar pearlite
c) Ferrite-carbide aggregate

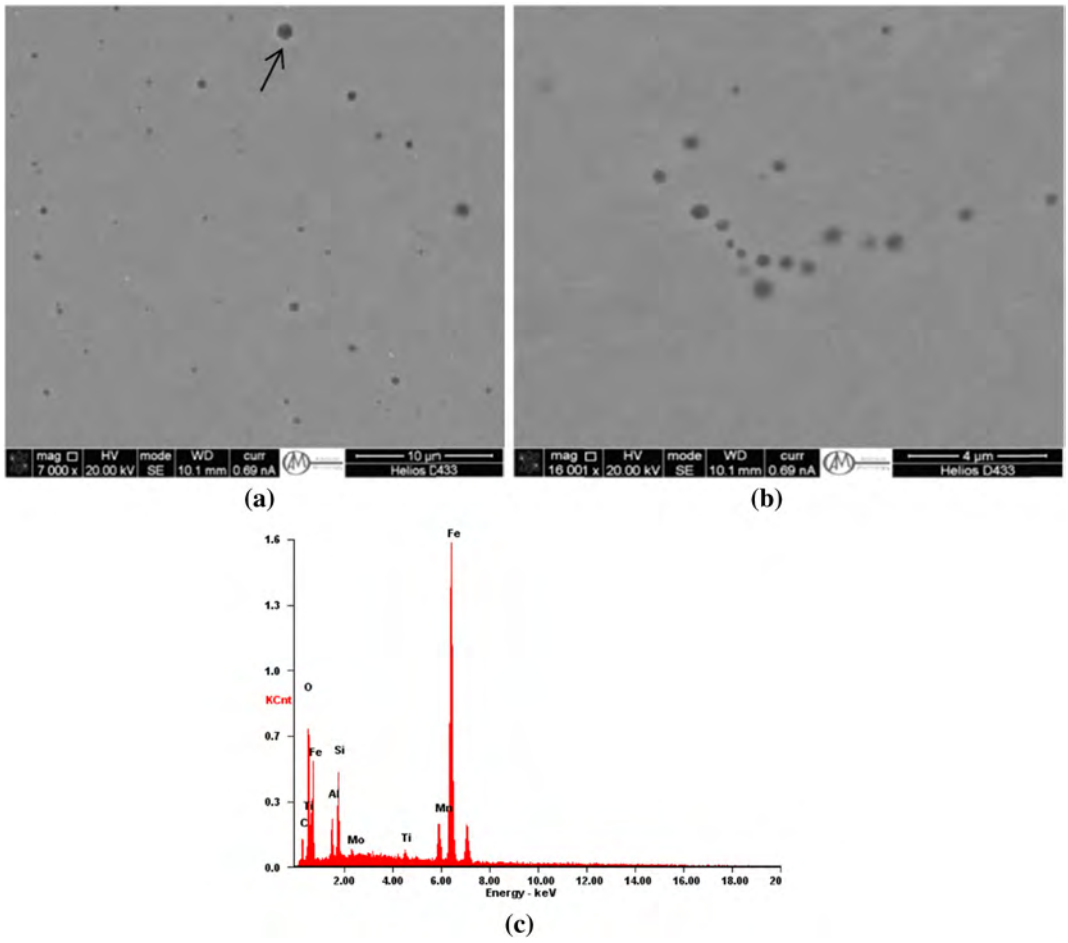

Fig. 12. SEM micrographs of Non-Metallic Inclusions (NMI's) along with a typical EDS spectrum (Arrowed particle in (a)) form during welding of X70 using E6010 electrodes.

a) Uniform distribution of NMI's **b)** clustered NMI's

conjunction with Image Quality (IQ) and Inverse Pole Figure (IPF) maps. A range of polygonal, Widmanstätten and acicular ferrites, lamellar pearlite and ferrite–carbide aggregate and of course upper and lower bainite morphologies were detected and characterized. The morphology, size and chemistry of non-metallic inclusions are also briefly discussed.

Acknowledgements

The authors would like to thank Energy Pipelines-CRC for their financial support (grants RP1-02B, 81107701 and RP1-02D, 81109119). The in-kind support from the APIA-RSC along with the guidance and advice provided by the Projects industrial advisors are also gratefully acknowledged. We also acknowledge with thanks the constructive comments made by Prof. V. Linton, CEO of Energy Pipeline CRC. The provision of X70 HSLA steel by Baosteel-China is gratefully acknowledged.

References

[1] D. Cuiuri, N. Coniglio, Qsn3 Site Visit, EPCRC Report, Mitchell, Queensland, 2010.
[2] N. Alam, D. Dunne, I. Squires, F. Barbaro, B. Feng, Weldment cold cracking—the effect of hydrogen and other factors, Proceedings of Joint Seminar Hydrogen Management in Steel Weldments, Melbourne, Australia 1996, pp. 49–60 (WTIA1996).
[3] W. Costin, et al., Micromechanical examination of the relationship between weld metal microstructure and hydrogen assisted cold cracking, Paper no: S10-02, 6th International Pipeline Technology Conference, Ostend, October 2013.
[4] N. Yurioka, H. Suzuki, Hydrogen assisted cracking in C–Mn and low alloy steel weldments, Int. Mater. Rev. 35 (4) (1990) 217.
[5] L. Fletcher, A holistic model of hydrogen cracking in pipeline girth welding, Welding in the World London, 44(2) 2000, p. 7.
[6] A. Barnoush, H. Vehoff, Recent developments in the study of hydrogen embrittlement: hydrogen effect on dislocation nucleation, Acta Mater. 58 (16) (2010) 5274–5285.
[7] H.K. Birnbaum, P. Sofronis, Hydrogen-enhanced localized plasticity—a mechanism for hydrogen-related fracture, Mater. Sci. Eng. A 176 (1-2) (1994) 191–202.
[8] Talas, The assessment of carbon equivalent formulas in predicting the properties of steel weld metals, Mater. Des. 31 (2010) 2649–2653.
[9] D. Zander, I. Maroefa, D. Olsona, D. Eliezer, P ositive effects of hydrogen on the plasticity of 2 1/4 Cr–1Mo steel, J. Alloys Compd. 356–357 (2003) 809–812.
[10] G. Thewlis, J.A. Whiteman, D.J. Senogles, Dynamics of austenite to ferrite phase transformation in ferrous weld metals, Mater. Sci. Technol. 13 (3) (1997) 257–274.
[11] G. Thewlis, The nature of acicular ferrite in ferrous weld metals and the challenges for microstructure modelling, Materials Science Forum, vol. 426, Trans Tech Publ 2003, pp. 4019–4026.
[12] G. Thewlis, Classifcation and quantification of microstructures in steels, Mater. Sci. Technol. 20 (2004) 143–160.
[13] S.F. DI Martino, G. Thewlis, Transformation characteristics of ferrite/carbide aggregate in continuously cooled, low carbon-manganese steels, Metall. Mater. Trans. A 45A (2014) 579.
[14] H.K.D.H. Bhadeshia, Bainite in Steels: Transformations, Microstructure and Properties, 2nd edn IOM Communications, London, 2001.
[15] R.A. Ricks, P.R. Howell, G.S. Barritte, The nature of acicular ferrite in HSLA steel weld metals, J. Mater. Sci. 17 (3) (1982) 732–740 (1982/03/01).
[16] H.K.D.H. Bhadeshia, R.W.K. Honeycombe, Steels Microstructure and Properties, Butterworth-Heinemann, 2011.
[17] G.R. Speich, W.C. Leslie, Tempering of steel, Metall. Trans. 3 (5) (1972) 1043–1054 (1972/05/01).
[18] C. Wildash, Microstructure Factors Affecting Hydrogen Induced Cold Cracking in High Strength Steel Weld Metal(Ph.D. thesis) University of Leeds, 1999.
[19] H.K.D.H. Bhadeshia, L.E. Svensson, Modelling the evolution of microstructure in steel weld metal, in: H. Cerjak, K.E. Easterling (Eds.), Mathematical Modelling of Weld Phenomena, Institute of Materials, London 1993, pp. 109–182.

[20] R. Kurji, J. Griggs, V. Linton, F. Barbaro, A. Kotousov, E. Gamboa, R. Ghomashchi, N. Coniglio, An improved Welding Institute of Canada test for evaluation of high strength pipeline steel weldability, Paper No: S11-03, 6th International Pipeline Technology Conference, Ostend, Belgium, 7–9 October, 2013.
[21] E. Mazancová, Z. Rucká, K. Mazanec, Comparison of microfractographic behaviour of acicular ferrite and bainite and hydrogen cracking resistance, Arch. Mater. Sci. 28 (1–4) (2007) 95–99.
[22] S. Kou, Welding Metallurgy, Second edition John Wiley & Sons, Inc., 2003 (ISBN: 0-471-43491-4 Copyright).
[23] Z. Xiong, S. Liu, X. Wang, C. Shang, X. Li, R.D.K. Misra, The contribution of intragranular acicular ferrite microstructural constituent on impact toughness and impeding crack initiation and propagation in the heat-affected zone (HAZ) of low-carbon steels, Mater. Sci. Eng. A 636 (2015) 117–123.

Int J Adv Manuf Technol
DOI 10.1007/s00170-014-6555-3

ORIGINAL ARTICLE

Towards the establishment of weldability test standards for hydrogen-assisted cold cracking

R. Kurji · N. Coniglio

Received: 29 July 2014 / Accepted: 27 October 2014

Abstract Industry and research have long desired the establishment of standards for weldability testing in regards to hydrogen-assisted cold cracking formation. This would have the obvious advantage of allowing data to be reliably compared between different research labs. But making decisions regarding standards requires some careful thought and agreement on i) how test parameters affect test results, ii) what exactly needs to be measured, and iii) how test results should be interpreted and reported. Our depth of understanding on these points has matured significantly over time and, while there is not always universal agreement, it is at least possible to start highlighting factors important to standards. This paper examines these factors, including the welding parameters, restraint, hydrogen, and cracking index. When comparing different alloys having different thermal characteristics, the use of constant welding parameters (common practice) will result in variable weld penetration and weld pool shape, which can influence grain shape and microstructural features, which can result in inequitable weldability comparisons. Welding on test coupons having different dimensions can affect restraint, which will influence the residual stresses around the weldment. High restraint usually results in higher crack susceptibility. Also, hydrogen content present in a weldment depends on the thermal history, welding parameters, and surrounding atmosphere humidity, with high hydrogen contents associated to great cracking susceptibility. Finally, the selection of an appropriate cracking index is required for data analysis. Quantifications of crack length and minimum preheat temperature are common indexes used for comparison. Critical stress and hydrogen content are other indexes. But how well these indexes actually represent weldability are contentious issues. This paper will examine and quantify these issues in detail, thus providing the reader with an appreciation of all things that must be considered when preparing a standardized procedure for weldability testing.

Keywords Weldability tests · Restraint · Stress · Welding parameters · Hydrogen-assisted cold cracking

Nomenclature

CTS	Controlled thermal severity
FCAW	Flux-cored arc welding
G-BOP	Gapped bead-on-plate
GMAW	Gas metal arc welding
HACC	Hydrogen-assisted cold cracking
HAZ	Heat-affected zone
IG	Intergranular
IRC	Instrumented restraint cracking
MVC	Macrovoid coalescence
M-WIC	Modified Welding Institute of Canada
QC	Quasi-cleavage
RRC	Rigid restraint cracking
SAW	Submerged arc welding
SMAW	Shielded metal arc welding
TRC	Tensile restraint cracking
WIC	Welding institute of Canada
WM	Weld metal

1 Introduction

The establishment of a standardized weldability test for hydrogen-assisted cold cracking (HACC) is an ongoing topic

R. Kurji
School of Mechanical Engineering, The University of Adelaide, Adelaide, Australia

N. Coniglio (✉)
MSMP Laboratory, Arts et Metiers ParisTech, 2 cours des Arts et Metiers, 13617 Aix en Provence, France
e-mail: nicolas.coniglio@ensam.eu

Published online: 14 November 2014

of interest for the industry. This would have the obvious advantage of enabling a reliable comparison in cracking susceptibility between diverse alloys and welding conditions. Cracking is generally believed to result from the tensile fracture at room temperature of a hydrogenated solid metal.

Significant work has already been devoted to characterize weldability [1–5]. In addition, there is no huge disparity found in alloy rankings between different tests and laboratories [6]. In addition, there does not appear to be a large disparity between test rankings and perceived real-world behaviour [3, 6]. However, even though the numerous existing tests appear to do a reasonable job of providing a rough comparison (i.e. ranking) of alloy weldability, the problem arises in not knowing how variations in testing procedure may affect test rankings and how test results relate to real welding applications. Difficulty may be encountered in deciphering small differences in weldability between similar alloys. There is also the inability to predict, with any certainty, whether or not cracking will occur in a specific application. This has led one to question the validity of these trends, if tests are being performed correctly, or if the correct things are being measured. In essence, this begs a bigger question of how test measurements actually relate to weldability.

Full-scale testing [4, 6] has been adopted in an effort to bypass the difficulties inherent in predicting field behaviour from small-scale laboratory tests. However, due to the complexity and large dimensions of full-scale testing, smaller-scale restraint cracking tests have been developed to evaluate the weldability in laboratories, limiting the full-scale weldability tests to a validation role of in-field welding procedure. Nevertheless, limitations exist in providing an overview of the alloy's weldability. The broad spectrum of loading methods (e.g. load orientation, tension, or bending) and weldability test design (shape, size) bring about inconsistencies in the testing methodology and collected data. These discrepancies highlight a lack of understanding and agreement on the critical variables controlling crack formation.

The goal of the present paper is to provide a perspective on establishing future standards for the weldability testing of different alloys and welding conditions. A review of the status of current weldability testing in the literature is compiled to identify important test parameters and test limitations. The meaning behind weldability data is examined. A checklist summary is provided that facilitates the comparison of weldability data.

2 Alloy composition

When considering weldability, minute details regarding alloy composition and impurities can be of utmost importance. For this reason, it is necessary to accurately measure and document base metal, filler metal, and weld metal compositions. Certain alloy systems are notorious for poor weldability, and so both base metal and filler metal compositions should always be determined and reported. For flux-based welding processes (for example cellulosic SMAW [7] and SAW [8] processes), flux chemistry can likewise have a major effect on weld metal composition and subsequently affect the crack susceptibility of the weld metal [9]. Experimental G-BOP test data have even shown that base metal compositions can also influence the weld metal crack susceptibility for small filler dilutions [10]. Possibilities for inadvertent weld contamination must also be considered, including shielding gas, joint preparation, weld fixtures, and entrained weld spatter. Outlined below are two characteristic features that demonstrate the importance of alloy composition on weldability.

2.1 Carbon equivalent

The steel-based systems that are welded today represent a broad spectrum of steel compositions, rendering a direct comparison difficult. Thus, carbon equivalent formulas have been developed to provide a quantitative value representative of the weldment composition [11, 12]. This value has in turn served as a proxy to cracking susceptibility. Several empirical values have been proposed (Table 1) weighting each element's effect in regards to the reference element carbon [13–20]. Hence, these formulas are usually limited in a range of compositions that are included into the envelope of compositions used for their determination. The P_{cm} value has been estimated as a better crack susceptibility index [11], but this remains a highly contentious subject as high P_{cm} values are not necessarily associated to high crack susceptibility [21]. As none of the existing carbon equivalent formulas seems suitable to evaluate the critical preheat temperature required in weld metal steels to avoid cracking [11], the welding conditions can be converted into CEN increments to account for the welding conditions [22]. Nevertheless, the general trend follows the carbon content–carbon equivalent mapping concept as designed by the Graville diagram (Fig. 1), where maximum crack susceptibility happens for simultaneously high carbon contents and high carbon equivalent values (zone III in Fig. 1).

2.2 Solidification mode

The location of the cracking in high strength low alloy steel weldments has been shown to be controlled partly by the solidification mode (determined by alloy content) [23]. The hydrogen solubility drops during the primary austenite-to-ferrite transformation and diffuses to the adjacent austenitic zones (Fig. 2). As the used base metals have higher strengths, the required strength matching between the weld metal and base metal is achieved by the use of richer electrode chemistries, thus delaying in time the weld metal austenite-to-ferrite transformation and enhancing hydrogen transportation from

Table 1 Carbon equivalent formulas and their applicability

Carbon equivalent formula	Application range according to Talas et al. [11]	Application range according to Yurioka et al. [3]	Reference
Group A			
$CE_{IIW} = C + \frac{Mn}{6} + \frac{Ni+Cu}{15} + \frac{Mo+V}{5}$	C-Mn steels with high CE content	$C \leq 0.08$ %	13
$CE_{WES} = C + \frac{Si}{24} + \frac{Mn}{6} + \frac{Ni}{40} + \frac{Cr}{5} + \frac{Mo}{4} + \frac{V}{14}$			14
Group B			
$CE_{DNV} = C + \frac{Si}{24} + \frac{Mn}{10} + \frac{Ni+Cu}{40} + \frac{Cr}{5} + \frac{Mo}{4} + \frac{V}{10}$	Steels with lower CE contents	0.08 % ≤ C≤0.12 %	15
$CE_T = C + \frac{Mn}{10} + \frac{Cu}{20} + \frac{Ni}{40} + \frac{Cr}{20} + \frac{Mo}{10}$			16
Group C			
$Pcm = C + \frac{Si}{30} + \frac{Mn}{20} + \frac{Cu}{20} + \frac{Ni}{60} + \frac{Cr}{20} + \frac{Mo}{15} + \frac{V}{10} + 5B$	Pipeline steels	C ≤0.12 %	17
$CE_{PLS} = C + \frac{Si}{25} + \frac{Mn}{16} + \frac{Cu}{16} + \frac{Ni}{60} + \frac{Cr}{20} + \frac{Mo}{40} + \frac{V}{15}$			18
$CE_{HSLA} = C + \frac{Mn}{16} - \frac{Ni}{50} + \frac{Cr}{23} + \frac{Mo}{7} + \frac{Nb}{5} + \frac{V}{9}$			19
Group D			
$CE_N = C + f(C) * \left(\frac{Si}{20} + \frac{Mn}{6} + \frac{Cu}{15} + \frac{Ni}{20} + \frac{Cr+Mo+Nb+V}{5}\right)$ $f(C)=0.75+0.25\tanh[20(C-0.12))]$	All steels	C≤0.3 %	20

HAZ to weld metal. This explains the trends towards the greater likelihood of crack formation in the weld metal nowadays.

3 Test selection

Selecting the most appropriate weldability test requires careful consideration of many different aspects including cost, availability, and type of cracking expected. Because tests are typically not available commercially, this requires in-house design and construction, leading to unique test variations from one laboratory to another. Test designs can vary in complexity from a simple turn-table to make a restraint circular weldability test (cost ≈US$1K) to a variable speed tensile restraint cracking test (≈US$100K). Some tests have the restraining support integrated into the specimen design, requiring its fabrication for each test sample.

3.1 Type of tests

A broad variety of weldability tests has been developed over the years. Their designs impose controlled restraint and/or stress–strain after welding in the weldment region [5]. Table 2 lists different weldability tests according to classifications discussed below.

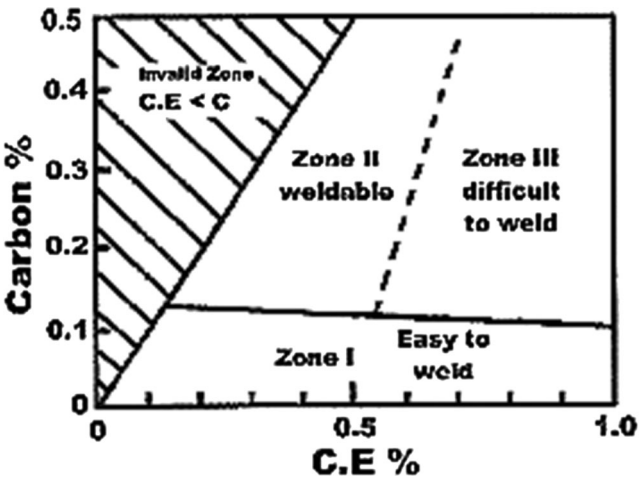

Fig. 1 Graville diagram demarking regions for cracking applied to steels

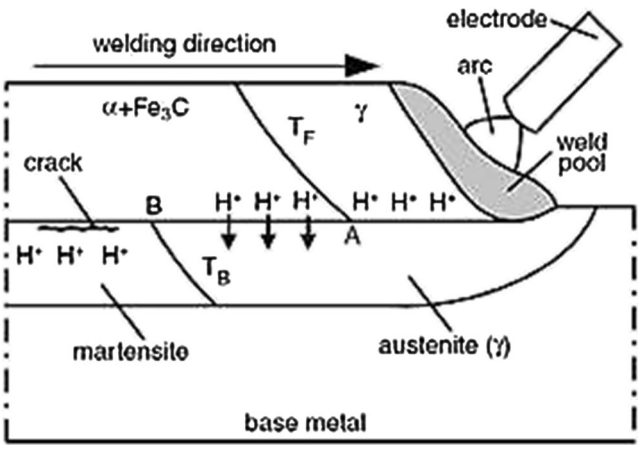

Fig. 2 Schematic illustration of hydrogen diffusion in steels [23]

Table 2 Overview of weldability tests developed for characterizing weld metal susceptibility to HACC

Test	Intrinsic vs extrinsic	Bending vs tensile	Longitudinal vs transverse loading	HACC cracking index	Reference
One-side lifted pipe	Extrinsic	Bending	Transverse	Crack length lifting height	4
Four-point bending pipe	Extrinsic	Bending	Transverse	Crack length bending force	6
Cranfield test	Intrinsic	Tensile	–	Crack length	3
WIC test	Intrinsic	Tensile	Transverse	Restraint preheat	6, 9, 24, 25
M-WIC test	Intrinsic	Tensile	Transverse	Restraint preheat	26
Implant test	Extrinsic	Tensile	Transverse	Stress	21, 25, 27–30
t test	Intrinsic	Tensile	Transverse	Crack length	3
Bending test	Extrinsic	Bending	Transverse	Crack length deflection	31–33
Tensile restraint cracking TRC test	Extrinsic	Tensile	Transverse	Load	3
Rigid restraint cracking RRC test	Extrinsic	Tensile	Transverse	Load strain restraint	34
Window-type cruciform restraint test	Intrinsic	Tensile	–	Crack length	3
Controlled thermal severity CTS test	Intrinsic	Tensile	–	Cooling rate	35
Gapped bead-on-plate G-BOP test	Intrinsic	Tensile	Longitudinal	Crack length	10, 36–38
One-plate self-restraint weldability test	Intrinsic	Tensile	Transverse	Crack length preheat	4
Restraint circular weldability test	Intrinsic	Tensile	Transverse	Crack length	3
Lehigh U-groove, or Stout, test	Intrinsic	Tensile	Transverse	Crack length	4
Lehigh slot test	Intrinsic	Tensile	Transverse	Crack length	29, 39
Tekken test, or y-groove restraint test	Intrinsic	Tensile	Transverse	Hydrogen content preheat	40
Instrumented restraint cracking IRC test	Intrinsic	Tensile	Transverse	Crack length	3
Restraint root cracking test, or Schnadt-Fisco test	Intrinsic	Tensile	Transverse	Crack length	6
H-slit restraint test	Intrinsic	Tensile	Transverse	Crack length	3
Window-type restraint multiple-layer cracking	Intrinsic	Tensile	Transverse	Crack length restraint	41

3.2 Intrinsic vs extrinsic

Intrinsic tests rely upon internally generated stresses and strains to cause cracking. While simple and less expensive to perform, intrinsic tests typically involve complex and non-uniform loading that evolve during cooling and cannot be easily quantified. This limits the collection of information that would help define critical conditions needed for cracking. Even so, these tests provide an easy and inexpensive way to rank alloys, if that is all that is desired. The severity of loading can often be systematically varied, for example, by changing coupon dimensions, slot depths (Lehigh test), restraint distance (WIC and M-WIC tests), or circle diameter (restraint circular weldability test). A detracting aspect of these tests is the difficulty in separating out effects of welding parameters and material properties, since the stress/strain experience is strongly linked to these values.

Extrinsic tests, on the other hand, involve the controlled application of an external stress or strain during welding that enables loading to be more independent of material properties or welding parameters. These tests are more expensive to build, but allow for the quantification of loading and/or straining. The simplest of these tests is the bending test [31–33]. More complicated but popular in the 80s, the implant test [21, 25, 27–30] investigates the cracking characteristics of HAZ region, but its difficult reproducibility (such as implant location) and its unusual load field make it difficult to transfer the data to in-field applications.

Intrinsic and extrinsic tests differentiate in the stress evolution as the crack propagates [29], as indicated in Fig. 3 with

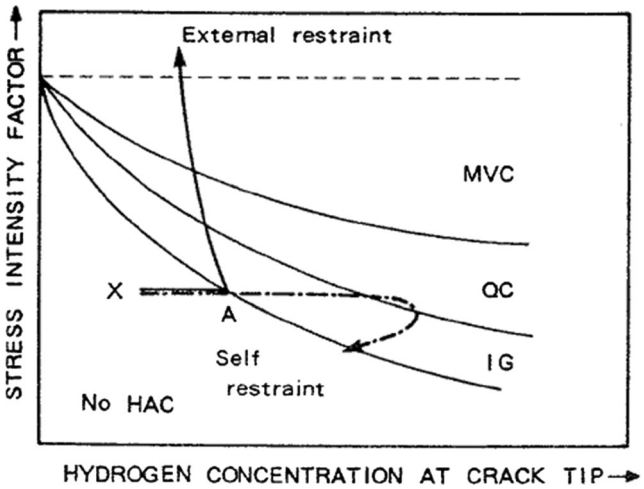

Fig. 3 Superposition on Beachem diagram of stress history at crack tip (indicated by *lines* with *arrows*) for external loading and self-restraint cracking tests [3]

the stress history superimposed on Beachem diagram. While the load drops with crack opening in an intrinsic test, the extrinsic test that maintains a constant loading value generates an increase in stress intensity as the crack size grows. The reduced threshold hydrogen content required for crack growth correlates to the increased stress intensity at the crack tip and subsequent macrovoid coalescence (MVC) fracture mode. Thus, intrinsic tests provide through their stress relief access to critical conditions for crack arrest. With the concept illustrated in Fig. 3, the cracking mode (MVC, QC, IG) provides post-mortem indications on the stress intensity value that induced crack growth.

3.3 Bend vs tensile

Bend-type extrinsic tests [31–33] apply controlled strain to a weld by forcing a specimen to conform to the surface radius of a die block (Fig. 3). Hence, the maximum strain experienced in the vicinity of the weldment (ε in mm mm^{-1}) is determined by the radius of curvature of mandrel (R in mm) and the specimen thickness (t in mm):

$$\varepsilon = \frac{t}{2R} \times 100\% \quad (1)$$

Mandrels having different radii can be exchanged in a series of tests to vary the maximum applied strain. A minimum amount of strain is needed to get cracking depending upon the material and is observed by a sudden drop in the applied force. The weld specimen is either kept at low temperatures to immobilize hydrogen prior to testing [2] or machined from the initial weld 24 h after the weld completion [32, 33]. The former method must be applied with care as microstructural changes may occur at low temperatures. The latter method consists of using the bending test as an opener of pre-existing cracks to facilitate their observation and counting. The bending is carried out at room temperature and slow loading rates to maximize the hydrogen embrittling effects. The formation of a significant number of cracks is indicated by a load drop on the load-deflection curve [2]. The bend-type tests have also been used to open pre-cracked welds to facilitate crack counting (Fig. 4).

While bending tests are easy to perform, they do not lend themselves to the precise determination of critical conditions needed for cracking. The non-uniform distribution of strain and strain rate within the coupon during strain application varies over the duration of the test and throughout the coupon thickness. “Hinging” is another problem that can occur in bend tests, arising from the non-conformity of the specimen with the die block as depicted in Fig. 5, where plastic deformation is concentrated in hot material along the weld seam.

Cross-weld tensile tests in comparison are much better suited for measuring critical values of strain and strain rate needed for cracking. Specifically, it is advantageous to have the direction of loading oriented perpendicular to weld metal centre-line grain boundaries. At any point in time, the load, strain, and strain rate are uniform through the coupon thickness for full-penetration welds.

3.4 Guidance for crack location

Hydrogen-assisted cold cracking may form in the HAZ or weld metal depending on metallurgical features, hydrogen distribution, loading, and groove design. The implant test [21, 25, 27, 28] investigates the cracking susceptibility of the only HAZ by loading a pre-placed implant over which a butt weld was deposited (Fig. 6), but the reproducibility of the implant location within the HAZ is difficult. Other tests control the stress in the vicinity of the weldment in part through the shape of the welding groove. A U-groove (Lehigh U-groove test) favours crack formation at the root of the weld metal rather than in the HAZ while a y-groove (Tekken test) facilitates the cold cracking in the HAZ of the root of the weldment [3, 4].

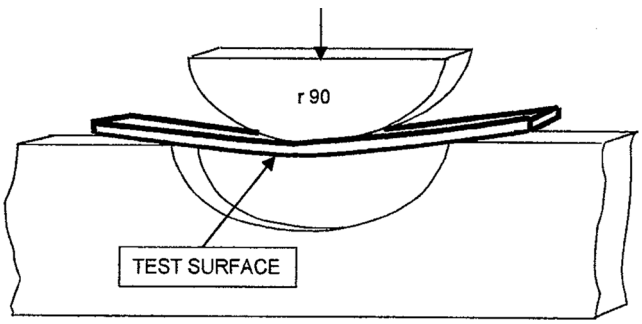

Fig. 4 Experimental setup of bending weldability test [32]

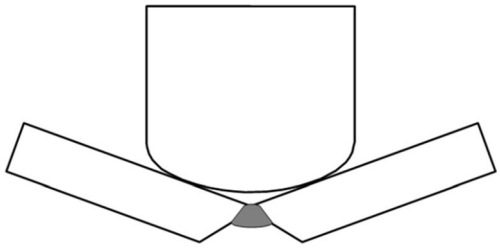

Fig. 5 Schematic illustration showing hinging effect in bend testing

3.5 Embrittlement vs weldability

The cold cracks present in hydrogenated steels are similar in nature to hydrogen-assisted cold cracking observed in weldments. It follows that embrittlement tests developed to produce cold cracks should likewise indicate susceptibility to hydrogen-assisted cold cracking in weldments. Embrittlement evaluations have the advantage of allowing the testing of small parts of the weldment without having to produce numerous welds under different loading conditions. It has the obvious disadvantage, however, of not exactly replicating the same thermo-mechanical or hydrogen diffusion conditions experienced in a weld.

The cooling conditions of temperature gradient, cooling rate, and hydrogen diffusion for embrittlement techniques compared to welds differ significantly. While cooling enables hydrogen diffusion out of the weldment during cooling, the quenching of the weld metal immediately after the welding ends stops the hydrogen movement and solid-state phase transformations. For example, the weldment in preparation for the bending test is first quenched in ice water and then placed in liquid nitrogen for storage until testing [31], which brings out the question of how cold storage modifies the weldment microstructure. Nevertheless, micromechanical embrittlement testing, such as the nano-indentation [42] and micro-cantilever [43] tests, enables the behaviour characterization of local microstructure (Fig. 7) as opposed to the general mean behaviour observed in weldability tests.

4 How test parameters affect test results

4.1 Effect of loading direction and history

The load is additive to the stress field so that greater load magnitudes induce greater local tensile stresses, favouring cracking. The direction in which load is applied to the weld, relative to the welding direction, will tend to favour one type of cold crack over the other. Cracks will preferentially grow in a direction oriented perpendicular to the load. Longitudinal loading, as experienced in G-BOP test, promotes transverse cracking while transverse loading as experienced in the M-WIC, Lehigh, and restraint circular weldability tests promotes cracking parallel to the welding direction.

The loading history will also tend to favour one type of cold crack over the other. As hydrogen diffuses and thermal stress builds up, the weldment susceptibility to cracking changes with time. Hence, the loading rate will generate a specific response for a specific metallurgical condition and subsequently the most susceptible microstructure to crack formation (Fig. 8).

4.2 Effect of stress

Stress has generally been taken to have the primary influence on HACC formation [3, 44]. Extensive weldability test data support this assumption, where higher applied stresses eventually lead to cracking. It has been demonstrated experimentally that a critical stress must be exceeded in order to cause

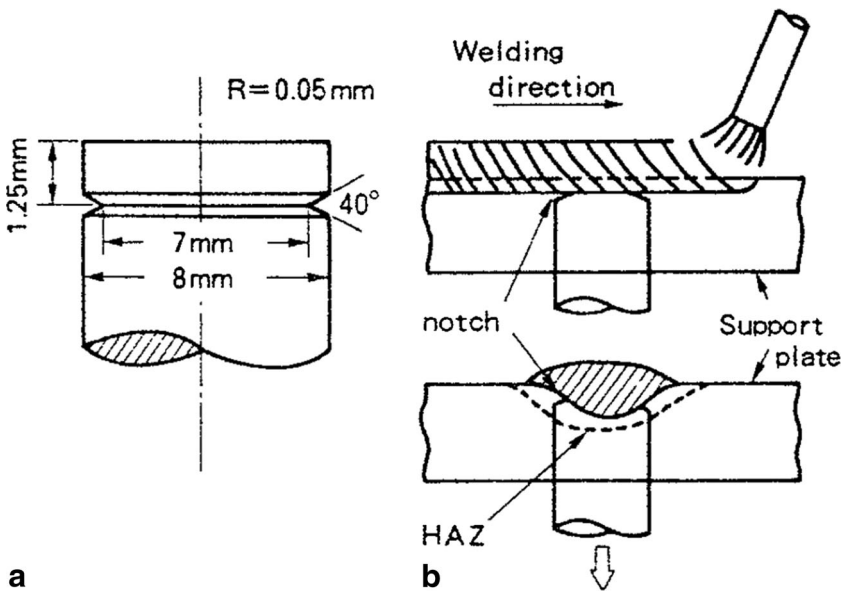

Fig. 6 Experimental set-up of **a** implant and **b** implant test [29]

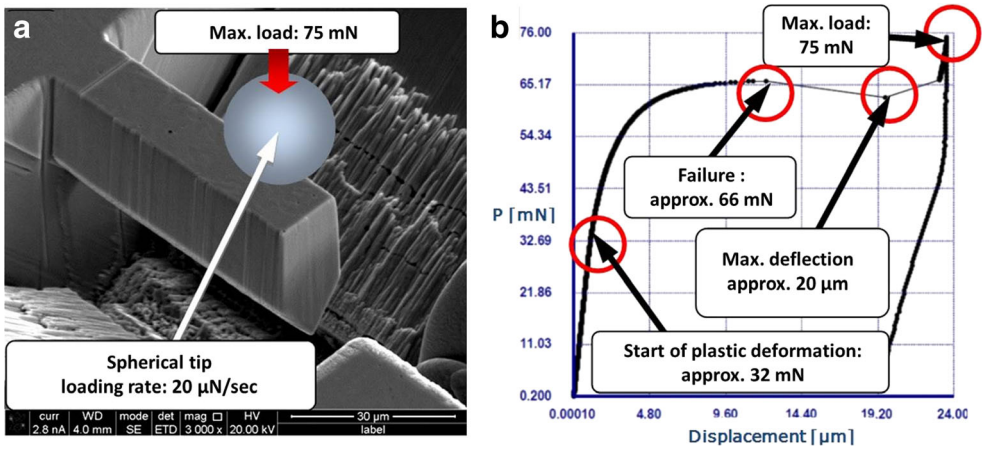

Fig. 7 **a** Micro-cantilever loaded with spherical nano-indent and **b** load–displacement (beam deflection) curve for acicular ferrite test specimen [43]

cracking. An important point to be made here is that, while stress is applied globally in weldability tests, it is actually the local stresses in the vicinity of each microstructural feature that are of primary importance to cracking models, and these stresses cannot be easily measured. Micromechanical tests [42, 43] permit to isolate the individual behaviour of a metallurgical feature contaminated by hydrogen and will help in understanding stress partitioning within the weldment.

When welding complex, multiple joint structures, residual stresses build that influence weldability. The presence of tensile stress formed during welding and cooling aggravates cracking. Along these lines, several weldability tests consist of applying a tensile load immediately after welding completion (e.g. TRC, implant test). This allows crack–no crack comparisons and permits a critical load to be measured, where greater critical loads indicate better weldability. In intrinsic tests, restraint hinders the free contraction of the weldment region, building up greater tensile stresses (Fig. 9). High loads add to the stresses normally associated with welding and result in greater local tensile strains. The upper limit of preload is bounded by the yield stress of the weldment.

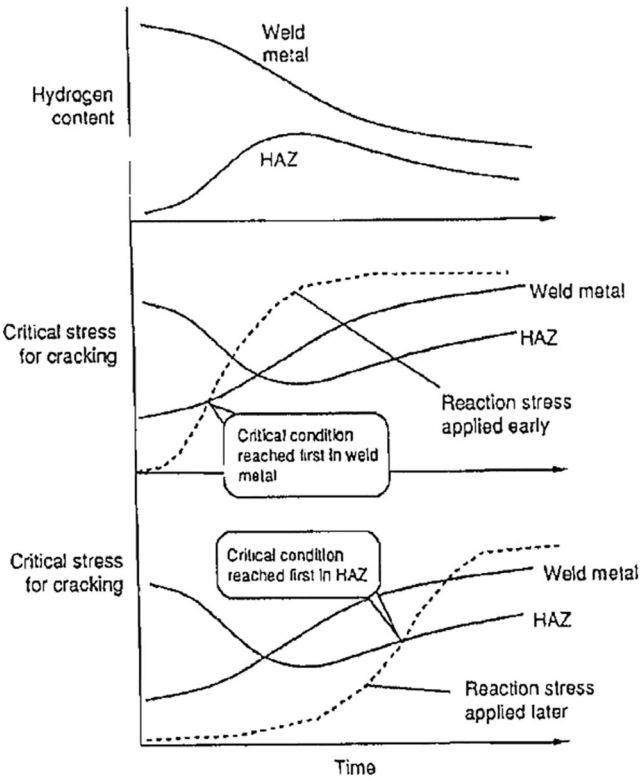

Fig. 8 Weldment response to different loading rates [2]

4.3 Effect of restraint

Restraint intensity is a measure of the resistance to strain after weld completion and can be thought of as a spring constant. It is influenced by the rigidity of the welding fixture as well as the weld coupon size and shape. The thermal and shrinkage stresses generated during and after welding interact with restraining forces to influence strain in the vicinity of the weldment. It is generally the case that high restraint gives high residual stress. Some weldability tests that involve the controlled variation of restraint intensity incorporate slots milled along the sides of the weld coupon (Lehigh U-groove test). Too small restraint levels, such as in the Schnadt-Fisco test, do not enable the HACC ranking of a wide range of weldment chemistries [6].

The H-slit restraint test consists of machining two test plates in a same larger plate and to control the restraint intensity by varying the slit length. The WIC and M-WIC tests have the tested plates welded onto an external fixture, the free-anchor welded lengths of the plates controlling the restraint intensity submitted to the weldment (Fig. 10). Reaction stresses in the weld metal develop earlier and attain a greater magnitude at higher restraint levels (Fig. 9). The restraint stress (σ_R in MPa) is expressed by

$$\sigma_R = \frac{SR_F}{h_w}, \tag{2}$$

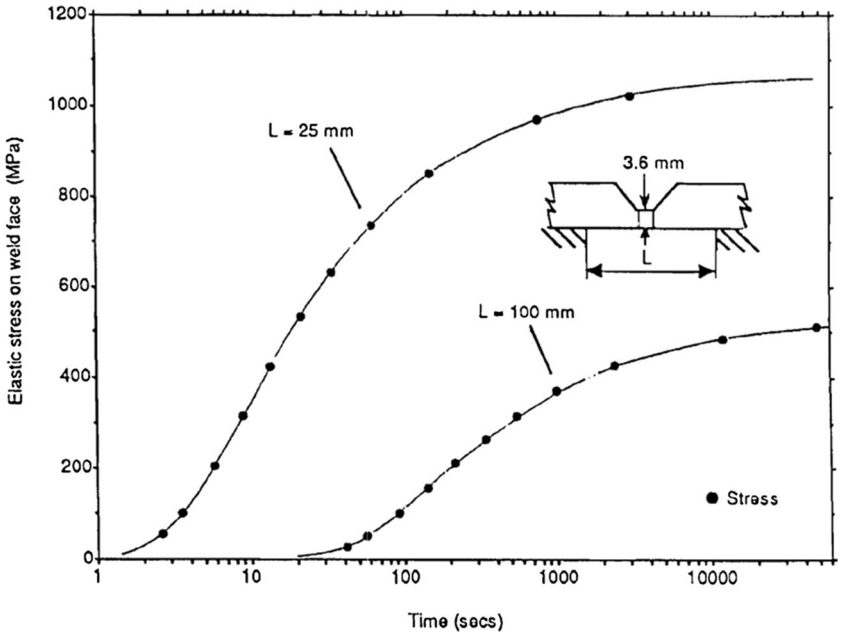

Fig. 9 Reaction stress estimated for two restraint lengths using a one-dimensional analysis [2]

where S is the total contraction (in mm), R_F is the tensile restraint intensity (in N mm^{-1} mm^{-1}), and h_w is the height of the weld metal throat (in mm).

Data from WIC testing [24] indicates that the maximum stress encountered in practice through restraint and bending is unlikely to exceed that imposed by the standard restraint length in the WIC test (16.4 kN mm^{-2} for 8.6-mm thick plate) and that restraint conditions are less critical than weld metal hydrogen content in inducing HACC. The traditionally used 25-mm restraint length provides a much higher restraint than that encountered during pipeline welding in the field. The M-WIC test

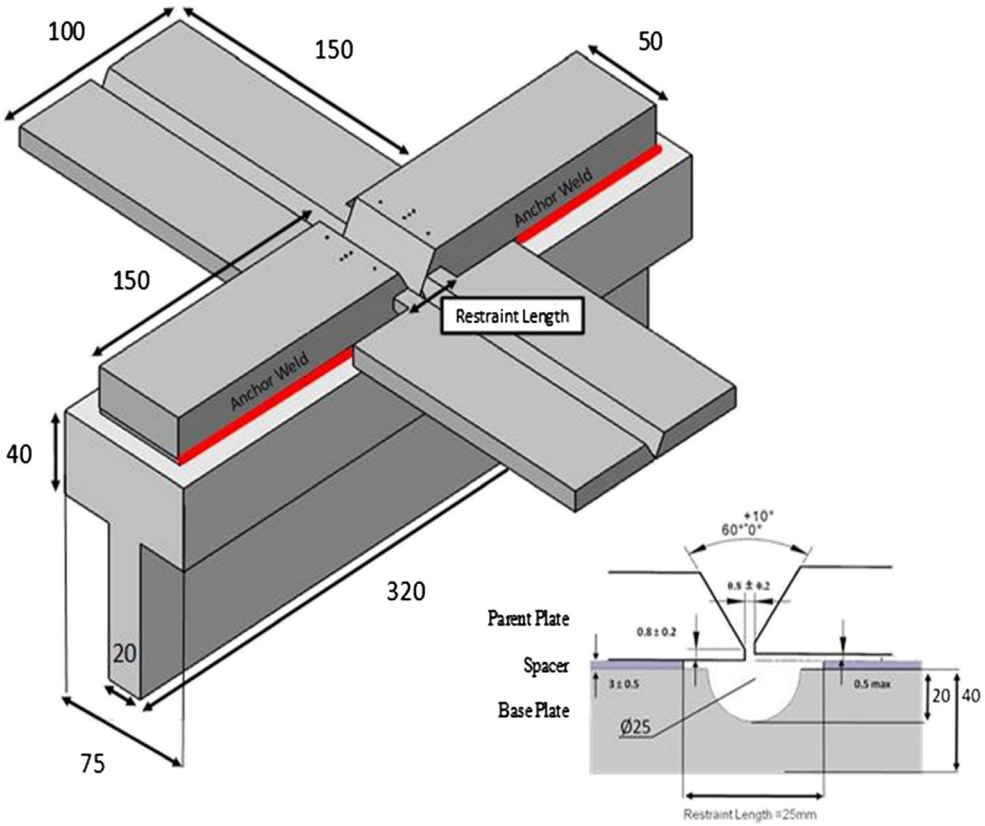

Fig. 10 Schematic illustration of M-WIC test [26]

was designed to conserve the restraint intensity–restraint length relationship while enhancing the evacuation of gases produced during electrode coating decomposition through the underneath 25-mm diameter groove.

It is of interest to note that several cold cracking weldability tests, such as circular patch and *t* tests, have been proven to generate weld solidification cracking too [45]. However, weldments highly susceptible to HACC are usually tested in low restraint conditions, which are known to favour solidification cracking [46]. Therefore, at small restraints, cold crack may possibly grow from pre-existing solidification cracks, which are identified by their dendritic fracture surface.

4.4 Effect of welding parameters

Welding parameters can have a significant impact on the cracking susceptibility of an alloy and hence must be considered when performing weldability tests. Ranking alloys for a given application should be done by using a similar welding process and parameters for both test and application when possible. However, the different thermal properties of some alloys may require higher current to achieve the same penetration. For this reason, it may be argued that alloys should be weldability tested each with unique welding parameters to produce a constant penetration. Whichever approach is chosen, it should be appreciated that any change in weld heat input can modify the size and shape of the weld and HAZ as well as change stress and strain behaviour. It can also change temperature gradients and cooling and solidification rates, which will result in different weld metal grain structures and sub-grain microstructures.

Welding heat input is defined as energy per unit length of weld and is commonly used for a comparative indication between welding conditions. Making welds with similar heat input for a given material provides roughly similar weld pool volumes and cooling rates, but not necessarily similar penetration and weld metal cross-sectional shape. Increasing heat input will increase the weld cross-section and lower the cooling rate. It is generally observed that reduced heat input gives greater susceptibility to cracking. Nevertheless, heat input is not sufficient information on its own as, for similar heat inputs and materials, lower arc voltages during shielded metal arc welding will deposit richer weld metal chemistries [7].

Yurioka and Kasuya [12] proposed a chart method to determine the necessary preheat temperature to avoid cracking in steel weld metals. This method is based upon master curves experimentally obtained for each set of welding conditions. The steel carbon equivalent value CEN is corrected depending on the weld metal hydrogen content (Fig. 11a), heat input, and CEIIW (Fig. 11b). This correction follows the enhancement of cold cracking at greater hydrogen levels and at smaller heat inputs. Once the corrected CEN value is obtained, the plate thickness is accounted for the minimum preheat temperature measured in a y-groove self-restraint cracking test (Fig. 11c). This preheat temperature determined in laboratory is corrected for welding practice in the field depending on steel yield strength (Fig. 11d).

4.5 Effect of preheat

The reduction of cracking by preheating (Fig. 12) has been proven to be of major interest for in-field construction, where restraint conditions are rarely changeable. A high and uniform preheating impacts the cracking susceptibility by slowing the cooling rate and subsequently enabling more hydrogen to diffuse away from the weldment region. Preheating may be performed by electrical resistance and oxy-flames on the joint and its surroundings. Uniform temperature in the joint region requires a certain delay between preheating finish and welding start, a rough estimation being 2-min waiting per 25-mm plate thickness. Combined preheating with low restraint designs is an efficient way in reducing cracking (Fig. 13)

The experimental data suggest a linear or logarithmic effect of hydrogen concentration on the critical preheat temperature to avoid cracking. The minimum preheat temperature T_{P1} has been estimated for preventing cracking in multiple-layer weld metals in GMAW [41] as a function of diffusible hydrogen content measured by the glycerol displacement method (H_{GL} in ml/100 g Fe), weld layer thickness (d_w in mm), and tensile strength of weld metal (σ_w in MPa). For $15<d_w<30$ mm, the equation is [47]

$$T_{P1} = 120 + 120\log\left(\frac{H_{\mathrm{GL}}}{3.5}\right) + 5(d_w{-}20) + 8(\sigma_w{-}83) \quad (3)$$

Okuda et al. proposed the following predictive equation for the necessary preheat temperature T_{P2} and interpass temperature for avoiding transverse weld metal HACC [47]:

$$T_{P2} = 6.03\sigma_{UTS} + 318.6\log(H_{GC}){-}554.3, \quad (4)$$

with σ_{UTS} the ultimate tensile strength of the weld metal (in MPa) and H_{GC} the weld metal hydrogen content measured by the gas chromatography method (in ml/100 g Fe).

The minimum preheat temperature is used to limit the cooling rate to an upper value. Even though the time for weld metal to cool from 800 to 500 °C ($t_{8/5}$) has been an effective indicator, the primary factor controlling weld

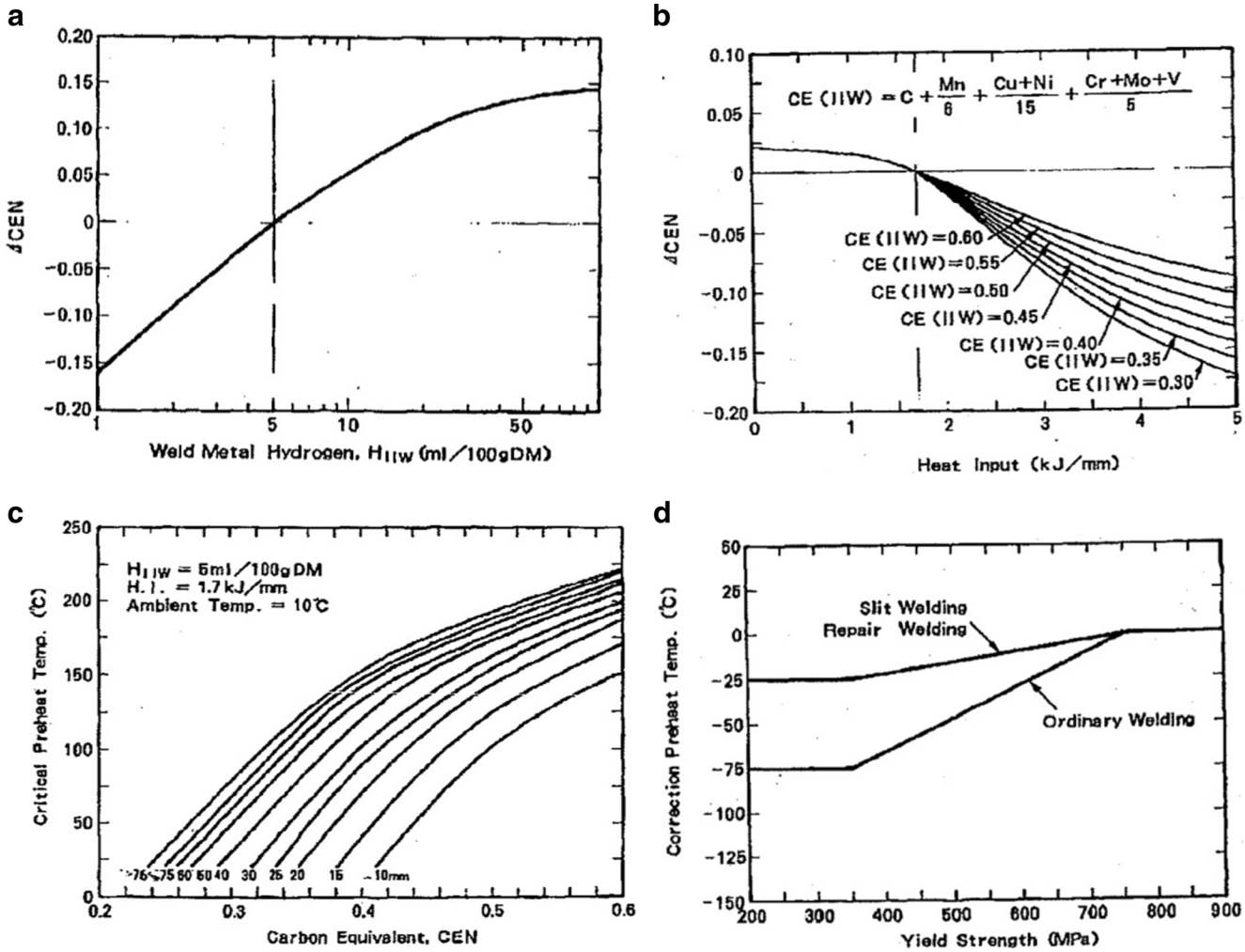

Fig. 11 Maps used in Yurioka's chart method for evaluating critical preheat temperature to avoid cracking for welding practice—**a** carbon equivalent (CEN) value correction as a function of weld metal hydrogen content, **b** CEN value correction as a function of welding heat input and carbon equivalent (CE_{IIW}) value, **c** critical preheat temperature for laboratory y-groove restraint testing as a function of plate thickness and CEN value at indicated test conditions, and **d** critical preheat temperature correction from laboratory test to welding practice as a function of steel yield strength [12]

metal cracking was hydrogen diffusion through control of the cooling time to 100 °C [48]. In WIC and gapped bead-on-plate tests, the cooling time to 100 °C ($t_{100,min}$ in s) depends on the carbon equivalent CEN value and the

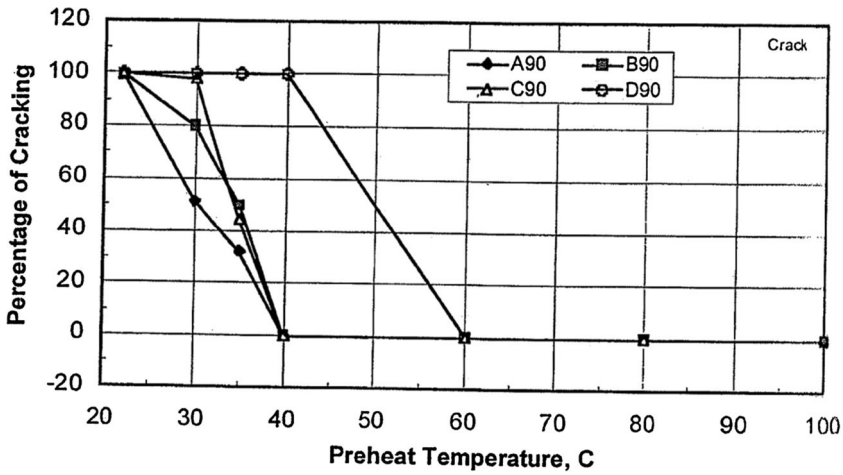

Fig. 12 Percentage of cracking as a function of preheat temperature for E9010 weld metal using WIC test [24]

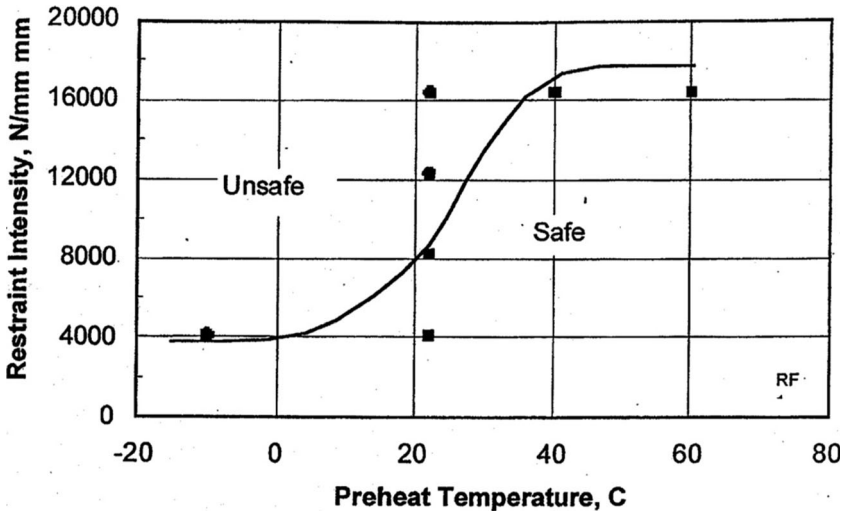

Fig. 13 Critical restraint intensity-preheat temperature map demarking cracking regions using WIC test [24]

diffusible hydrogen content H_d of the weld metal (in ml/100 g Fe):

$$t_{100,\min} = 34.1 \cdot (CEN) + \frac{H_d - 5}{3.5} - 9.1 \quad (5)$$

5 Measurements that uniquely define weldability

The desired outcome of weldability tests is cracking, which is most often quantified in percentage of weld length. It is usually assumed that for fixed testing conditions, an alloy having higher cracking susceptibility should result in a more extensive cracking in weldability tests. However, there are inherent problems when considering only crack length, due to alloy-dependent variations in thermal gradient and weld metal shape. Moreover, cracks may be embedded into the weldment and are thus difficult to characterize. In essence, the comparison of cracking extent becomes difficult for different alloys when all test conditions are not exactly the same.

A more appropriate measure of cracking susceptibility that is more characteristic of a particular alloy is its stress to fracture. Nevertheless, the fracture stress depends on the hydrogen level in the weldment region. Time to

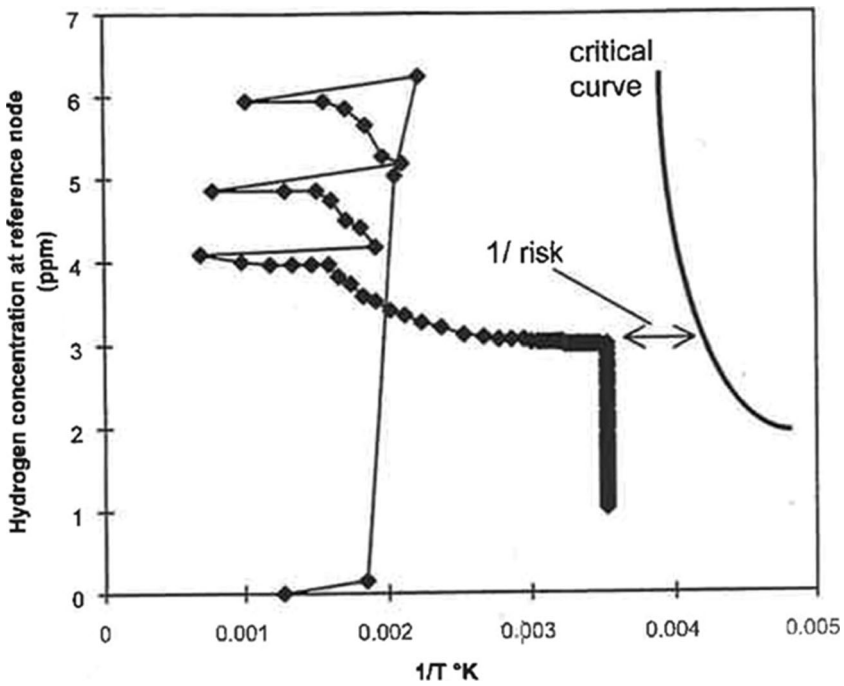

Fig. 14 Critical temperature–hydrogen map demarking region for cracking (*right side of the critical curve*) and compared to history of a multipass weld (*line with dots*) [53]

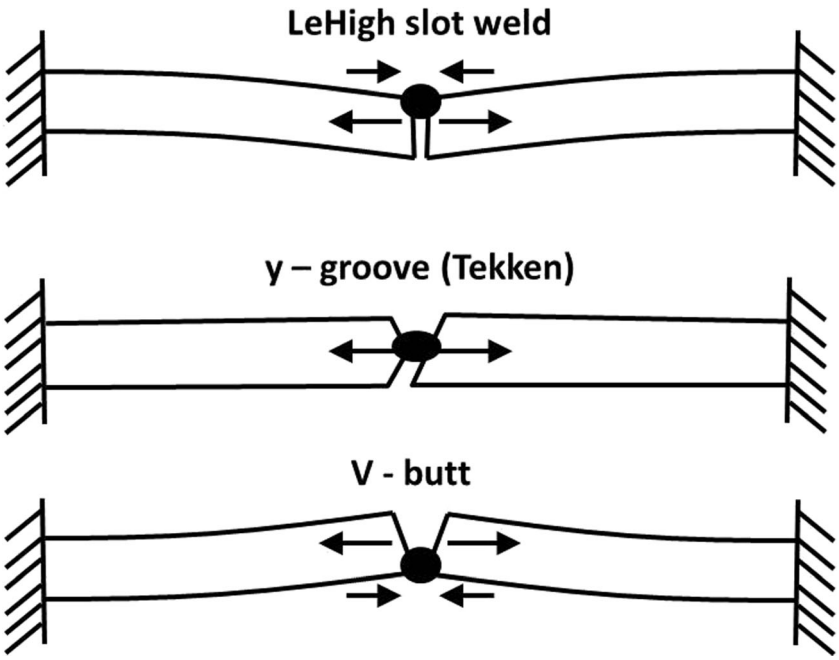

Fig. 15 Effect of weld eccentricity on local stress at weld root in different groove configurations [3]

fracture can also be viewed as a characteristic that defines weldability for a particular alloy, as alloys having higher crack susceptibility should fracture earlier after welding completion.

Cold cracking is caused by residual stresses after welding. Numerous weldability test designs have been developed to measure relative cracking behaviour of various alloys. Nevertheless, a better approach would be to consider weldability testing as experimental setups to identify critical conditions for cold crack initiation and growth mechanism. Mechanisms for both crack initiation and growth show stress and hydrogen to be controlling factors [49].

5.1 Diffusible hydrogen content

Diffusible hydrogen present in steel weldments limits the performance of the material. During arc welding processes, the dissociation of water molecules in the high-temperature arc plasma generates hydrogen ions that are absorbed by the liquid weld pool. In gas metal arc (GMA) welding, the use of

Groove Type	Kt	Groove Type	Kt
Oblique y	4.0	Single bevel-3	6.9
Double Vee	3.7	Single bevel-4	3.5
Single bevel-1	5.8	Symmetric Y	4.2
Single bevel-2	5.4		

Fig. 16 Stress concentration factor (K_t) at root of weld of basic joint geometry [34]

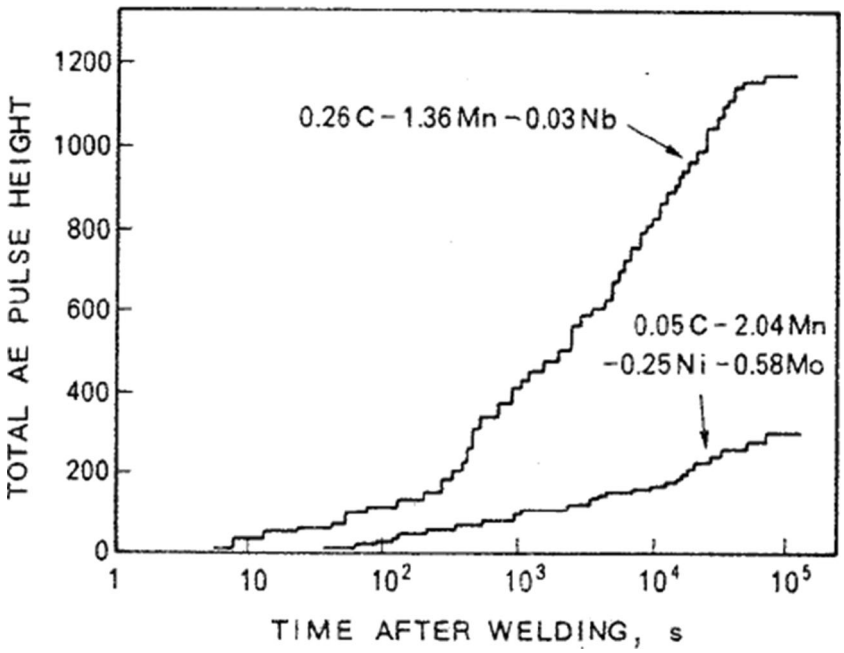

Fig. 17 Intermittent crack growth recorded by acoustic emission in Lehigh slot test [29]

dry inert gases protects the liquid pool from the contamination of atmospheric moisture. In the processes such as shielded metal arc welding (SMAW), flux-cored arc welding (FCAW), and submerged arc welding (SAW), a flux is used to prevent the molten metal from oxidation. Low hydrogen fluxes must be kept in a dry, warm environment to avoid moisture absorption and deposit weld metals with small hydrogen contents after baking the flux. Nevertheless, cellulosic coated electrodes have chemically bonded water ($-H_2O$) in their structure that enables fast deposition rates. In that case, hydrogen contents of the weldments can reach high levels (above 40 ml/100 g Fe) [50].

Despite the importance of hydrogen content in the weldment susceptibility to cracking, the hydrogen content of the weldment is not reported in the literature when performing weldability tests. This fact may be due to the difficulty in

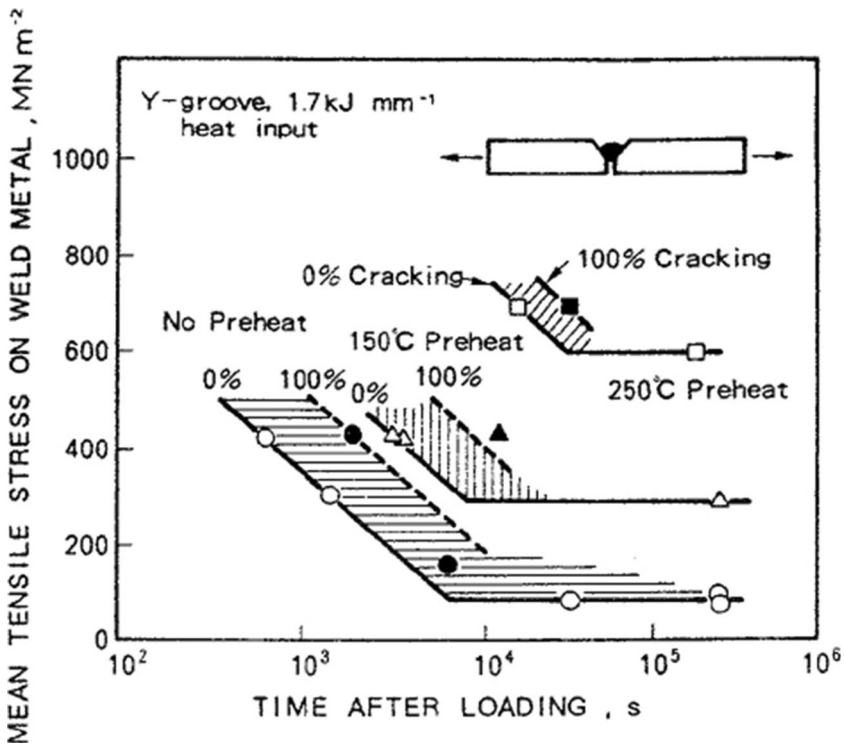

Fig. 18 Stress to fracture–time to failure relationship measured using tensile restraint cracking (TRC) test for a 700 MN.m^{-2} yield strength steel [3]

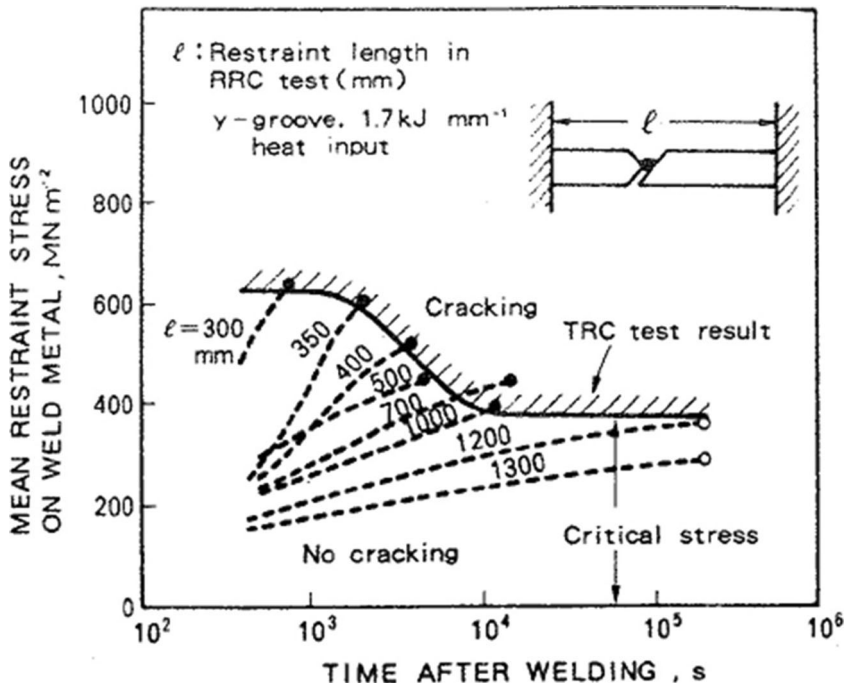

Fig. 19 Comparison RRC and TRC test results with y-groove configuration [3]

measuring diffusible hydrogen amount present in the weldment. Most popular methods include glycerin method, mercury method, and gas chromatography method. Each method gives different hydrogen values for a given weldment due to some absorption of hydrogen by the material of the method (such as glycerin) [50]. Hot extraction methods permit moreover to the total amount of hydrogen present in the weldment, to identify the trapping site by the temperature at which it releases hydrogen.

Statistical data modelling tools, used to evaluate the HACC susceptibility in weld metals, account for the hydrogen content in combination with the thermal history [51–53]. A probabilistic neural network method has been applied to estimate the hydrogen level and crack susceptibility of G-BOP tests of rutile flux-cored arc welds based upon consumable chemistries, welding process parameters, and environmental atmospheric conditions [37]. A holistic time-dependent model compares the crack driving forces at the crack tip with the material crack resistance, taking into account both the weld metal thermal history and hydrogen concentration, and was successfully applied to the pipeline front end welding operation [51, 52]. The local accumulation of hydrogen is quantified into the PHA cracking index as given by [40]:

$$PHA = -\log\left(\frac{[H]_{FB,cr}}{[H]_0}\right), \tag{6}$$

where $[H]_{\mathrm{FB,cr}}$ is the critical hydrogen concentration at the weld fusion line where a root crack initiates against the initial as deposited hydrogen concentration $[H]_0$. The value $[H]_{\mathrm{FB,cr}}$ is function of the weldment chemistry and the restraint level. Both hydrogen concentrations are expressed in ml/100 g Fe.

The weld metal hydrogen content and the thermal history affect the weld metal cracking susceptibility. Therefore, a critical temperature–hydrogen mapping concept was developed [53] to evaluate the risk of HACC formation in a multipass weld in Fig. 14. The left hand curve shows a plot of the local hydrogen content and the temperature during the complete history of welding. The right hand curve represents the critical hydrogen content for cracking and belongs to a family of such curves dependent upon the applied stress. The HACC susceptibility is calculated as the inverse of the distance separating the two curves (double arrow in Fig. 14), i.e. the inverse of the temperature difference between the actual weld metal temperature and the critical temperature for HACC as determined for a weld metal hydrogen content. The critical hydrogen content $[H]_c$ for HACC versus temperature, i.e. the right hand curve, can be represented by the equation

$$\log_{10}[H]_c = \log_{10}A - \frac{803}{T}, \tag{7}$$

where T is the absolute temperature (in K) and A is a constant determined by the external stress. A major drawback of this model is that it ignores the time factor, i.e. the incubation period to initiate a crack when exceeding a critical hydrogen amount.

5.2 Stress

Hydrogen-assisted cold cracking models view stress as important for the initiation and growth of a crack in a hydrogenated

Table 3 Checklist to be considered for each weldability test procedure

Category	Items
Alloy	Base metal – filler metal – dilution
Temperature	Cooling rate - preheat
Crack type	HAZ crack – weld metal crack
Time of cracking	Time after weld completion
Fracture mode	Intergranular – transgranular – cleavage
Test type	Intrinsic – extrinsic – bending – tensile
Load orientation	Longitudinal – transverse
Restraint	Coupon dimensions
Welding process	Process description
Welding parameters	Current – voltage – travel speed
Linear heat input	Heat input
Applied load	Maximum stress – loading rate
Hydrogen	Hydrogen content – atmospheric humidity
Local stress	Maximum strain – strain rate
Crack measurement	Percentage of weld length

microstructure [49]. Stress can be deduced from load and strain measurements. Measuring local strain in the vicinity of the weld during the welding cycle poses some unique challenges such as the high temperatures encountered in welding. The stress can be deduced from the deformation using the concept of restraint. The variation of stress distribution with the weld eccentricity and groove geometry (Fig. 15) has been considered using a concentration factor K_t for the stress calculation (Fig. 16). This multiplicative factor K_t is useful to compare welds deposited in grooves of different geometries.

5.3 Time of cracking

As HACC forms with some delay after welding completion, it is of interest to determine the time of fracture. A temperature-controlled tinting of the cracked areas can indicate the temperature at which the surface formed [6]. The intermittent crack growth has been confirmed experimentally. Acoustic emission sensors located near the weldment enable to follow the growth of the crack size [29] (Fig. 17). These sensors have proven the intermittent growth of cold cracking, suggesting that hydrogen transport to the crack tip is a critical requirement for HACC propagation.

The time of rupture shortens for greater stress, following experimental measurements using the implant test [4], TRC test [3], and RRC test [34]. While the TRC test applies post-welding a constant load transverse to the weld direction, the RRC test adjusts the transverse load to maintain a predefined local strain across the weld during cooling. The TRC and RRC results are in good correlation in terms of fracture stress and time to failure (Figs. 18 and 19). The characteristic delayed formation of cold cracking can be measured using a clip gauge positioned after weld completion across the weld metal [24], with a sudden increase in the strain value relating to the crack formation. Instrumenting the weldment surrounding regions with strain gauges enables to record the stress induced by the thermal contraction and solid phase transformation in the weldment and its sudden release by crack formation [36, 38].

6 Summary

Many weldability tests have been developed to rank cracking susceptibility of different alloys based solely upon relative comparisons of crack length. Although useful in making rough-cut rankings, a better approach is to consider weldability testing as an experimental means to identify critical conditions for hydrogen-assisted cold crack initiation and growth. Mechanisms for both crack initiation and growth show hydrogen and stress to be controlling factors, backed up by considerable experimental evidence. With advancing ideas regarding cracking mechanisms and improved testing methods, welding science is moving towards a point where the likelihood of cracking may someday be predicted for a given alloy and welding application. This paper has examined numerous weldability test approaches in order to identify important distinctions. Standardization of not only weldability test procedures but also defining what needs to be measured will help in the long-term understanding of alloy weldability. Table 3 is a proposed checklist of all the things one should consider and quantify, if possible, when performing weldability tests.

Acknowledgments The research work was funded by the Energy Pipeline CRC supported through the Australian Government's Cooperative Research Centres Program. The cash and in-kind support from the APIA-RSC is gratefully acknowledged.

References

1. Graville B (1986) A survey review of weld metal hydrogen cracking. Weld World 24(9/10):190–198
2. B.A. Graville (1995) Interpretive report on weldability tests for hydrogen cracking of higher strength steels and their potential for standardization. WRC Bull 400
3. Yurioka N, Suzuki H (1990) Hydrogen assisted cracking in c-mn and low alloy steel weldments. Int Mater Rev 35(4):217–249
4. Glover A and Rothwell B (1999) Specifications and practices for hydrogen crack avoidance in pipeline girth welds, In: First International Conference on Weld Metal Hydrogen Cracking in Pipeline Girth Welds, Wollongong, Australia, 13.1-13.18. WTIA
5. Kannengiesser T, Boellinghaus T (2013) Cold cracking tests—an overview of present technologies and applications. Weld World 57:3–37

6. North TH, Rothwell AB, Glover AG, and Pick RJ (1982) Weldability of high strength line pipe steels. Weld J, August, 243s-257s
7. Coniglio N, Linton V, Gamboa E (2010) Coating composition, weld parameter, and consumable conditioning effects on weld metal composition in shielded metal arc welding. Sci Technol Weld Join 15(5): 361–368
8. Natalie CA, Olson DL, Blander M (1986) Physical and chemical behavior of welding fluxes. Annu Rev Mater Sci 16:389–413
9. Coniglio N, Barbaro F, Linton VM, Gamboa E, and Kurji R (2010) Hydrogen assisted cold cracking susceptibility of weld metal deposited by cellulosic shielded metal arc welding consumables. In: Proceedings of the 8th International Pipeline Conference, IPC2010, Calgary, Canada. IPC2010-31680
10. Hart P (1986) Effects of steel inclusions and residual elements on weldability. Met Constr, October, 610–616
11. Talas S (2010) The assessment of carbon-equivalent formulas in predicting the properties of steel weld metals. Mater Des 31(5): 2649–2653
12. Yurioka N, Kasuya T (1995) A chart method to determine necessary preheat in steel welding. Weld World 35(5):327–334
13. Dearden J, O'Neil H (1940) A guide to the selection and welding of low alloy structural steels. Trans Int Weld 3(10):203–214
14. Suzuki H, Tamura H (1961) Weldability of high strength steels evaluated by synthetic HAZ ductility test. Rep NRIM 3(1):47–59
15. Hannerz NE (1980) The influence of silicon on the weldability of mild and high tensile structural steel, IIW Doc. IX-1169-80
16. Uwer D and Hohne H (1991) Determination of suitable minimum preheating temperatures for the cold-crack-free welding of steels, IIW Doc. IX-1631-9
17. Itoh Y, Bessho K (1968) Cracking parameter of high strength steels related to HAZ cracking. J Jpn Weld Soc 37(9):983–989
18. Duren C (1985) Equations for the prediction of cold cracking in field-welding large diameter pipes, IIW Doc. IX-1356-85
19. Graville BA Cold cracking in welds in HSLA steels, Proc. Conf. on Weldability of HSLA Structural Steel, Rome, ASM
20. Yurioka N, Ohshita S, Tamehiro H (1981) Study on carbon equivalents to assess cold cracking tendency in steel welding. AWRA Symposium on Pipeline Welding in the 80's, Melbourne
21. Lazor RB and Graville BA (1983) Effect of microalloying on weld cracking in low carbon steels. Can Welder and Fabricator, July, 21–23
22. Kasuya T, Yurioka N (1995) Determination of necessary preheat temperature to avoid cold cracking under varying ambient temperature. ISIJ Int 35(10):1183–1189
23. Kou S (2002) Welding metallurgy, 2nd edn. Wiley, New York
24. Alam N, Dunne D, and Barbaro F (1999) Weld metal crack testing for high strength cellulosic electrodes. In: First International Conference on Weld Metal Hydrogen Cracking in Pipeline Girth Welds, Wollongong, Australia, 9.1-9.23. WTIA
25. Signes EG, Howe P (1988) Hydrogen-assisted cracking in high-strength pipeline steels. Weld J 67(8):163s–170s
26. Kurji R, Griggs J, Linton V, Kotousov A, Gamboa E, Ghomashchi R, and Coniglio N (2013) An improved welding Institute of Canada test for evaluation of high strength pipeline steel weldability. In: Proc. 6th Pipeline Technology Conference, Ostend
27. Magudeeswaran G, Balasubramanian V, Madhusudhan Reddy G (2008) Hydrogen induced cold cracking studies on armour grade high strength, quenched, and tempered steel weldments. Int J Hydrog Energy 33:1897–1908
28. Sawhill JM Jr, Dix AW, Savage WF (1974) Modified implant test for studying delayed cracking. Weld J 53(13):554s–560s
29. Vasudevan R, Stout RD and Pense AW (1981) Hydrogen-assisted cracking in HSLA pipeline steels, Weld J, Sept, 155s-168s
30. Beachem CD (1972) A new model for hydrogen-assisted cracking (Hydrogen "Embrittlement"). Metall Trans 3:437–451
31. Law M, Nolan D, Holdstock R (2008) Method for the quantitative assessment of transverse weld metal hydrogen cracking. Mater Charact 59:991–997
32. Peterneder E and Königshofer H (1999) Capabilities and limitations of cellulosic electrodes—a producer's perspective. In: First International Conference on Weld Metal Hydrogen Cracking in Pipeline Girth Welds, Wollongong, Australia, 17.1-17.17. WTIA
33. Sarrafan S, Ghaini FM and Rahimi E (2010) Weld metal hydrogen cracking in transmission pipelines construction, In: Proceedings of the 8th International Pipeline Conference IPC2010, Calgary, Canada. IPC2010-31240
34. Alam N, Dunne D, Squires I, Barbaro F and Feng B (1996) Weldment cold cracking—the effect of hydrogen and other factors, In: Proceedings of Joint Seminar Hydrogen Management in Steel Weldments, Melbourne, Australia, 49–60. WTIA
35. Kinsey AJ. The welding of structural steels without preheat, Weld J, 79 (4), 79s-88s
36. Graville BA, McParlan M (1974) Weld-metal cold cracking. Met Constr Br Weld J 6(2):62–63
37. Sterjovski Z, Pitrun M, Nolan D, Dunne D, Norrish J (2007) Artificial neural networks for predicting diffusible hydrogen content and cracking susceptibility in rutile flux-cored arc welds. J Mater Process Technol 184:420–427
38. McParlan M, Graville BA (1976) Hydrogen cracking in weld metals. Weld J 55(4):95s–102s
39. Vasudevan R, Stout RD, Pense AW (1980) A field weldability test for pipeline steels—part I. Weld J 59(3):76s–84s
40. Suzuki H, Yurioka N, Okumura M (1983) A new cracking parameter for welded steels considering local accumulation of hydrogen. Weld World 21(5/6):110–132, Doc. IIS/IIW-755-83
41. Ushio M, Sugitani Y, Kanayama K, Aida I, Hara N and Nakano T (1999) Cracking in GMAW pipeline girth welds based on experiences in pipeline construction in Japan, in: First International Conference on Weld Metal Hydrogen Cracking in Pipeline Girth Welds, Wollongong, Australia, 10.1-10.19. WTIA
42. Katz Y, Tymiak N, Gerberich WW (2001) Nanomechanical probes as new approaches to hydrogen/deformation interaction studies. Eng Fract Mech 68(6):619–646
43. Costin WL, Lavigne O, Linton V, Brown IH, Kotousov AG, Barbaro FJ and Ghomashchi R (2013) Micromechanical examination of the relationship between weld metal microstructure and hydrogen assisted cold cracking, In: Proc. 6th Pipeline Technology Conference, Ostend
44. Bailey N (1994) Weldability of ferritic steels. Abington Publishing
45. Lippold JC (2005) Recent developments in weldability testing. In: Hot cracking phenomena in welds, Springer: 271–290
46. Cross CE, Boellinghaus T (2006) The effect of restraint on weld solidification cracking in aluminium. Weld World 50:51–54
47. Yurioka N (1999) Predictive methods for prevention and control of hydrogen assisted cold cracking, In: First International Conference on Weld Metal Hydrogen Cracking in Pipeline Girth Welds, Wollongong, Australia, 2.1-2.16. WTIA
48. Barbaro FJ (1999) Types of hydrogen cracking in pipeline girth welds, In: First International Conference on Weld Metal Hydrogen Cracking in Pipeline Girth Welds, Wollongong, Australia, 11.1-11.15. WTIA
49. Hirth JP (1980) Effect of hydrogen on the properties of iron and steel. Metall Trans 11A:861–890
50. Padhy GK, Komizo Y (2013) Diffusible hydrogen in steel weldments. Trans JWRI 42:39–62
51. Fletcher L, Yurioka N (2000) A holistic model of hydrogen cracking in pipeline girth welding. Weld World 44(2):29–36

52. Fletcher L and Yurioka N (1999) A holistic model of hydrogen cracking in pipeline girth welding, In: First International Conference on Weld Metal Hydrogen Cracking in Pipeline Girth Welds, Wollongong, Australia, 12.1-12.14. WTIA

53. A. Glover and B. Graville (1999) The risk of hydrogen cracking in multipass welds and its effect upon procedure design, In: First International Conference on Weld Metal Hydrogen Cracking in Pipeline Girth Welds, Wollongong, Australia, 9.1-9.23. WTIA